

# Oxidation Catalyst Studies on a Diesel Engine

Ye, Shifei

*Award date:*
2010

*Awarding institution:*
University of Bath

# Oxidation Catalyst Studies on a Diesel Engine

**Shifei Ye**

**A thesis submitted for the degree of Doctor of Philosophy**

**University of Bath**

**Department of Mechanical Engineering**

**December 2010**

# Acknowledgements

I am enormously grateful to the people who have been a part of my life during my PhD study, both professionally and personally.

First and foremost, I would like to express my sincerest thanks to my supervisors Prof. Stan Kolaczkowski and Dr. Kevin Robinson for giving me the opportunity to work on this project. There are not enough words to express my deep appreciation for their encouragement and tireless dedication to supporting me towards achieving my PhD.

I wish to express my thanks to all members of the PVRC for their support during my PhD study (Prof. Gary Hawley, Dr. Chris Brace, Dr. Sam Akeurst, Dr. Chris Bannister). Special thanks go to Mr. Allan Cox, Mr. Andy Lewis, Mr. Edward Chappell, Mr. Don Blake and Mr. Sam Hurly for their great help in engine tests.

My greatest thanks to my parents for looking after my daughter and financial support for my study in the UK.

我非常感激父母为我读书提供经济上的支持和照看我的女儿。

I would like to thank my wife Qianqian for her support and love.

我也想感谢妻子（倩倩）对我的支持和关爱。

Last but not least, I would like to express my love to my dearest daughter for keeping me motivated! This work would not have been achieved without the support and understanding of my family.

最后我想感谢我的女儿（叶梓），是她让我对生活和未来充满了动力。这篇论文的完成离不开家人的理解和支持。

The financial support provided by the EPSRC and Prof. Stan Kolaczkowski is very much appreciated.

# Abstract

In this thesis, the experimental test facilities consisted of a well instrumented live Ford 2.0 litre turbocharged diesel engine connected to a specially made exhaust can, which contained a diesel oxidation catalyst (DOC). Experiments were performed on DOCs, which were specially prepared by Johnson Matthey, and had thermocouples mounted in their walls to measure axial temperature profiles. These DOCs consisted of a Pt catalyst dispersed in an alumina washcoat on a cordierite monolith supports, and were representative of a commercial application. Experiments were performed on Full-scale DOCs (o.d. = 106 mm, length = 114 mm), and also on Thin-slice DOCs (length = 5 and 10 mm), which generate some interesting data, and enabled a technique that is normally only used in laboratory bench-top experiments to be applied to a live engine. A number of different methodologies were developed based on (a) the operation of the engine at pseudo-steady-state operating conditions, and (b) transient experiments (e.g. a pulse of CO was injected into the exhaust gas just before the DOC). For example, it was shown how experiments on a live engine can be used to explore: (a) the hysteresis between light-off and extinction curves, (b) how catalyst temperature rise during warm-up of a DOC, (c) the promotion effect that hydrogen has on the conversion of CO, (d) the extent of competition for active catalytic sites, e.g. between CO, THCs, propane or hydrogen. The main findings are: (a) the hysteresis between light-off and extinction curves are mainly caused by CO inhibition, (b) the promotion effect of hydrogen on CO oxidation is largely attributed to thermal effect, (c) LHHW form rate expression is not adequate for catalytic converter modelling under transient conditions, (d) the competition for active catalytic sites is not apparent at the test conditions performed in this thesis. Moreover, a number of case studies were also used to illustrate how the experimental results/techniques developed in this thesis, may be used to support modelling studies.

# Table of Contents


**Acknowledgements** **ii**

**Abstract** **iii**

**Table of Contents** **iv**

List of Figures vii

List of Tables xviii

**Nomenclature** **xxi**

Greek symbols xxiii

Subscripts xxiii

Abbreviations xxiv

**1. Introduction** **1**

1.1 Background 1

1.2 Emission standards 1

1.3 Exhaust emissions from engines 2

1.4 Catalytic converters 3

1.4.1 Structure of a catalytic converter 4

1.4.2 Substrate 4

1.4.3 Washcoat 6

1.5 Types of catalytic converters 7

1.6 Performance of DOCs 9

1.7 Development of catalytic converters 10

1.8 Scope of this thesis 11

References 14

**2. Literature review – to set the scene** **16**

2.1 Modelling studies on catalytic converter 16

2.1.1 Models using the NTU method 17

2.1.2 Correlations for heat and mass transfer coefficients 19

2.1.3 Reaction rate expressions 21

2.2 Effect of pulsating flow on the performance of catalytic converters 25

2.2.1 Effect of pulsating flow on the warm-up of a catalytic converter under non-reacting conditions 26
2.2.2 Effect of pulsating flow on the performance of catalytic converters 29
2.2.3 Conclusions 30
2.3 Experimental studies of catalytic converters 31
2.3.1 Three-way monolith converter: simulations *versus* experiments (Siemund *et al.,* 1996) 31
2.3.2 Experiments and numerical simulations of unsteady temperature fields in automotive catalytic converters (Wang *et al.,* 2001) 34
2.3.3 Catalyst temperature measurement 35
2.3.4 Experimental studies on catalyst light-off 36
2.3.5 CO self-inhibition 43
2.3.6 Effect of hydrogen on the oxidation of CO in a DOC 44
2.4 Physical properties 45
2.5 Concluding remarks 47
References 49
**3. Experimental studies 52**
3.1 Experimental facilities and equipment 53
3.1.1 Modified exhaust system 53
3.1.2 DOCs 55
3.1.3 Engine test cell 56
3.1.4 Temperature measurements 59
3.1.5 Full-scale DOC with embedded thermocouples 60
3.1.6 Differential reactor (Thin-slice DOC) 62
3.1.7 Gas injection device 63
3.1.8 Static in-line mixer 64
3.2 Preliminary tests on equipment 65
3.2.1 Checks on gas injection system and gas mixer 65
3.2.2 Baseline engine tests 67
3.2.3 Effect of pulsating flow 70
3.3 New European Driving Cycle (NEDC) 72
3.3.1 Cold NEDC 74
3.3.2 Hot NEDC 93

3.3.3 Concluding remarks 107
3.4 Light-off experiments 109
3.4.1 Pseudo-steady-state light-off experiments 110
3.4.2 Transient light-off experiments 120
3.4.3 Transient light-off (ignition) and extinction experiments 124
3.4.4 Investigating the main cause of hysteresis using a Thin-slice DOC 133
3.5 CO inhibition 137
3.5.1 Test on 10 mm Thin-slice DOC 138
3.5.2 Test on 5 mm Thin-slice DOC 140
3.5.3 THCs inhibition 143
3.6 Gas injection experiments 146
3.6.1 CO concentration pulse injection 146
3.6.2 Propane concentration pulse injection 153
3.6.3 Site competition 158
3.7 Hydrogen and CO oxidation 163
3.7.1 Promotion effect of hydrogen on CO oxidation using Full-scale DOC 164
3.7.2 Promotion effect of hydrogen on CO oxidation using Thin-slice DOC 167
3.7.3 Site competition 169
3.7.4 Effect of hydrogen addition during the cold NEDC using Full-scale DOC 171
3.7.5 Measurement of background level of hydrogen in diesel exhaust 172
3.8 Non-uniform distribution of washcoat and catalyst 173
3.9 Concluding remarks 177
Reference 180
**4. Case studies: applying modelling techniques 181**
4.1 Choice of models 182
4.2 Modelling tools 183
4.3 Case Study 1:Thermal models at non-reacting conditions 184
4.3.1 1-D heat transfer model in MATLAB 184
4.3.2 2-D heat transfer model in COMSOL Multiphysics 196
4.4 Case Study 2: Non-reacting heat transfer experiment 208

4.4.1 Warm-up experiment using a hot air rig 208
4.4.2 Warm-up experiment using the diesel engine 214
4.5 Case Study 3: Catalytic combustion of propane (steady-state) 220
4.5.1 Model construction 220
4.5.2 Simulation results 228
4.6 Case Study 4: Pseudo-steady state light-off experiments 232
4.7 Concluding remarks 238
Reference 239
**5. Conclusions and future work 240**
5.1 Conclusions 240
5.1.1 Based on experimental work in Chapter 3 240
5.1.2 Based on case studies illustrating modelling in Chapter 4 243
5.2 Future work 244
**Appendices 245**
Appendix 1: Useful conversions 245
Appendix 2: Nusselt number for different duct shapes 250
Appendix 3: Derivation of NTU method (based on Lubeski, 2000) 252
Appendix 4: Summary of Dimensionless Groups 257
Appendix 5: The cross-sectional area of washcoat 261
Appendix 6: Checks on gas analyser readings 265
Appendix 7: Experimental data 273
Appendix 8: Mathematical models in MATLAB 283

## List of Figures

**Figure 1.1** Progression of European emission standards for diesel passenger cars over the last 15 years. The Euro 2-6 correspond to the emission standards, e.g. Euro 2 standards for the European emission standards II for diesel passenger cars. Data was obtained from Euractiv (2008). 2

**Figure 1.2** Schematic drawing of the structure of a catalytic converter with a single substrate. 5

**Figure 1.3** A catalytic converter with metal substrate. Photograph supplied courtesy of Emitec GmbH, Lohmar, Germany. 6

**Figure 1.4** Illustration of the structure of a square channel monolith and magnified structure of washcoat and catalyst. 7

**Figure 1.5** An illustration of light-off curve for CO (adapted from Knafl *et al*., 2007). 10

**Figure 1.6** Summary of work performed in this thesis and link to a parallel PhD project. 13

**Figure 2.1** Schematic diagram of experimental apparatus and rotating disc system (adapted from Benjamin and Roberts, 2001). 26

**Figure 2.2** Schematic illustrates the position of thermocouples and obstacle in the inlet cone to distribute the flow (modified from Siemund *et al.*, 1996). 32

**Figure 2.3** Schematic of the experimental engine bench set-up (modified from Siemund *et al.*, 1996). 33

**Figure 2.4** Schematic of experiment rig (adapted from Wang *et al*., 2001). 34

**Figure 2.5** Sketch of the light-off curve for CO (500 ppm inlet concentration) generated in a bench-top experiment (adapted from Salomons *et al*., 2006). 37

**Figure 2.6** The percentages of different species in hydrocarbons emitted from a 1.7 litre 4 cylinder automotive diesel engine (operated at lean conventional condition) organised by carbon number. Fuel composition is also shown. (Adapted from Figure 3 in Bohac *et al*., 2006) 38

**Figure 2.7** Schematic of the bench-top reactor set-up adapted from diagram in Knafl *et al*. (2007). 41

**Figure 3.1** Overview of the experimental investigations in Chapter 3. 52

**Figure 3.2** Schematic of the modified exhaust systems. 54

**Figure 3.3** Configuration of the engine test cell. 56

**Figure 3.4** A photograph of Ford PUMA engine as installed on the test bed. 58

**Figure 3.5** Thermocouple arrangement inside the monolith channel. Ten thermocouples are inserted along the axial direction (r = 0), and another ten are inserted at r = ½ R and 7/8 R. 60

**Figure 3.6** Thermocouples were carefully placed into pre-marked positions (tips were in contact with monolith) and fixed in position with a little cement. 61

**Figure 3.7** Two halves were bonded with a very thin layer of cement (this shows the rear end of the monolith). 61

**Figure 3.8** The DOC housed in a metal can. 62

**Figure 3.9** An example of the 5mm Thin slices housed in the catalytic converter can: (a) is the thin slice embedded with three 0.5 mm K-type thermocouples (insulation mat is wrapped around the thin slice to prevent heat loss), and (b) is the thin slice housed in the stainless steel converter can. 62

**Figure 3.10** Schematic of gas injection system. 64

**Figure 3.11** Photographs of the paper model of the static in-line gas flow mixing plate. 64

**Figure 3.12** Measured pre and post-catalyst pressure, where the engine is operated at 2000 rpm speed and 45 Nm torque. The air mass flowrate was 60 kg $h^{-1}$. 70

**Figure 3.13** Calculated exhaust gas velocity as a function of time. 71

**Figure 3.14** Summary of experiments in Chapter 3. The highlighted experiments are discussed in Section 3.3. 72

**Figure 3.15** Vehicle speed during a NEDC. 73

**Figure 3.16** Time delay can be seen by plotting the valve signal and the response from the analyser on same graph. 75

**Figure 3.17** Engine speed during a NEDC. 77

**Figure 3.18** Engine torque during a NEDC. 78

**Figure 3.19** Inlet gas temperature profile in a cold NEDC. 79

**Figure 3.20** Axial wall (catalyst) temperature profiles in a cold NEDC. The overall length of the catalyst is 114 mm, the volume is 0.001 $m^3$ (1 litre). 80

**Figure 3.21** Radial wall (catalyst) temperature profiles at a 65 mm distance from the inlet of the DOC in a cold NEDC. 81

**Figure 3.22** Pre- and post-catalyst emissions of CO in a cold NEDC. 83

**Figure 3.23** Cumulative emissions of CO at pre- and post-catalyst positions in a cold NEDC. 84

**Figure 3.24** Pre- and post- catalyst emissions of THCs in a cold NEDC cycle. 85

**Figure 3.25** Cumulative emissions of THCs at pre- and post- catalyst positions in a cold NEDC cycle. 86

**Figure 3.26** Pre- and post- catalyst emissions of $NO_x$ in a cold NEDC cycle. 87

**Figure 3.27** Cumulative emissions of $NO_x$ at pre- and post-catalyst positions in a cold NEDC. 88

**Figure 3.28** Air mass flow in a cold NEDC. 90

**Figure 3.29** Gas hourly space velocity (GHSV) in a cold NEDC. 91

**Figure 3.30** Pressure drop across the DOC in a cold NEDC. 92

**Figure 3.31** Inlet gas temperature profile in a hot NEDC. 94

**Figure 3.32** Axial wall temperature profiles in a hot NEDC cycle. The total length of the DOC is 114 mm; the volume is 0.001$m^3$ (1litre). 95

**Figure 3.33** Pre- and post-catalyst CO emissions in a hot NEDC. 97

**Figure 3.34** Cumulative emissions of CO at pre- and post-catalyst positions in a hot NEDC. 98

**Figure 3.35** Pre- and post-catalyst concentrations of THCs in a hot NEDC. 99

**Figure 3.36** Cumulative emissions of THCs at pre- and post-catalyst position in a hot NEDC. 100

**Figure 3.37** Pre- and post-catalyst concentrations of $NO_x$ in a hot NEDC. 101

**Figure 3.38** Cumulative emissions of $NO_x$ at pre- and post-catalyst position in a hot NEDC 102

**Figure 3.39** Responses of different DOCs to the inlet gas temperature in a hot NEDC. 104

**Figure 3.40** Comparison of CO emissions when using Full-scale DOC (114 mm) and Thin-slice DOC (10mm) in a hot NEDC. 105

**Figure 3.41** Comparison of THCs emissions when using Full-scale DOC (114 mm) and Thin-slice DOC (10 mm) in a hot NEDC. 106

**Figure 3.42** Summary of experiments in Chapter 3. The experiments highlighted in red are discussed in Section 3.4. 109

**Figure 3.43** Schematic of the engine test cell, control and data acquisition system. 110

**Figure 3.44** Engine speed is fixed at 2000 rpm for the pseudo-state-steady light-off experiments. (a) Inlet gas temperature, (b) air mass flow, (c) inlet CO and (d) THCs concentrations 112

**Figure 3.45** Light-off curve for CO (no additional CO and propane, Full-scale DOC was used). 113

**Figure 3.46** Light-off curve for THCs (no additional CO and propane, Full-scale DOC was used). 113

**Figure 3.47** Light-off curve for CO (inlet CO concentration was maintained at 3000 ppm). 114

**Figure 3.48** Light-off curves for CO with different inlet CO concentrations: 2000, 3000 and 4000 ppm. For each CO inlet concentration, the THCs concentration was maintained at 1500 ppmC1 (equivalent to 500 ppm propane). 116

**Figure 3.49** Overall rate of CO oxidation (during light-off experiments with different fixed values of inlet CO concentrations). 117

**Figure 3.50** Light-off curve for CO and THCs (inlet CO concentration was 3000 ppm, and THCs were maintained at 1500 $ppmC_1$ (equivalent to 500 ppm propane)). 117

**Figure 3.51** Wall temperature profiles (at r = 0, i.e. centre of the monolith) along axial direction of the DOC at various inlet gas temperatures (inlet CO

concentration at 3000 ppm, inlet THCs concentration at 1500 ppm$C_1$, and using Full-scale DOC). 119

**Figure 3.52** Conditions for transient light-off experiments with engine speed fixed at 2000 rpm while the torque is ramped-up over 300 s: (a) inlet gas temperature profile, (b) air mass flow, (c) inlet CO and (d) THCs concentration. 121

**Figure 3.53** Light-off curve for CO for conditions in Figure 3.52. 122

**Figure 3.54** Light-off curve for THCs for conditions in Figure 3.52. 122

**Figure 3.55** Light-off curves for CO with different engine torque ramp-up times. 123

**Figure 3.56** The light-off and extinction curves for CO (3000 ppm) obtained from tests with a torque ramp-up time of 300 s. The inlet CO concentration was 3000 ppm and the inlet THCs concentration was 1500 ppm$C_1$. 125

**Figure 3.57** The light-off and extinction curves for THCs (1500 ppm$C_1$) obtained from the tests with a torque ramp-up time of 300 s. The Inlet CO concentration was 3000 ppm and the inlet THCs concentration was 1500 ppm$C_1$. 125

**Figure 3.58** Light-off and extinction experiment, which include: inlet gas temperature, outlet gas temperature and wall (or catalyst) temperatures at various axial positions along the centre of the DOC (r = 0). 127

**Figure 3.59** Conditions for transient light-off and extinction experiment with engine speed fixed at 2000 rpm while the torque is ramped-up over 90 s: (a) inlet gas temperature profile, (b) air mass flow, (c) inlet CO and (d) THCs concentration. 129

**Figure 3.60** The effect of inlet CO concentrations on CO light-off and extinction. These tests were performed at initial inlet CO concentrations of 3000, 4000 and 5000 ppm while the initial inlet THCs concentration was maintained at 1500 ppm$C_1$, and with an engine torque ramp-up time of 90 s. 130

**Figure 3.61** The effect of inlet CO concentration on the overall rate of CO oxidation during light-off and extinction. 130

**Figure 3.62** Comparison of the light-off and extinction curves for THCs at different background level of THCs: (a) 240 to 340 ppm$C_1$ (no propane addition); (b) maintained at 1500 ppm$C_1$ (*via* propane injection). The inlet CO concentration was maintained at 3000 ppm, and with torque ramp-up time of 90 s. 131

**Figure 3.63** The effect of inlet THCs concentration on the conversion of CO during light-off and extinction for conditions in Figure 3.62. 132

**Figure 3.64** The effect of inlet THCs concentration on the overall rate of CO oxidation during light-off and extinction phases for the conditions in Figure 3.62. 133

**Figure 3.65** The light-off and extinction curves for CO plotted as a function of the inlet gas temperature. These tests were performed at inlet CO concentrations

of 3000, 4000 and 5000 ppm while the THCs concentration was maintained at 1500 ppm$C_1$, and the engine torque ramp-up time was 90 s. 134

**Figure 3.66** The light-off and extinction curves for CO plotted as a function of the average wall (or catalyst) temperature for the conditions in Figure 3.65. 134

**Figure 3.67** The rate of CO oxidation is plotted as a function of the average wall (or catalyst) temperature. 135

**Figure 3.68** Summary of experiments in Chapter 3. The experiments highlighted in red are discussed in Section 3.5. 137

**Figure 3.69** The rate CO oxidation and CO conversion as functions of inlet CO concentrations. 139

**Figure 3.70** Average temperature of reactor as a function of inlet CO concentration. 139

**Figure 3.71** Effect of an increase in the inlet CO concentration on the rate of CO oxidation. 141

**Figure 3.72** Wall temperature as a function of the inlet CO concentration. 142

**Figure 3.73** Effect of an increase in the inlet THCs concentration on the rate of THCs oxidation. 144

**Figure 3.74** Effect of an increase in the inlet THCs concentration on the rate of CO oxidation. 144

**Figure 3.75** Wall temperature as a function of the inlet THCs concentration. 145

**Figure 3.76** Summary of experiments in Chapter 3. The experiments highlighted in red are discussed in Section 3.6. 146

**Figure 3.77** Injection of a concentration pulse of CO at an inlet gas temperature of 150$^o$C. The inlet THCs concentration was maintained at 1500 ppm$C_1$. 148

**Figure 3.78** Thermal response to a concentration pulse of CO for conditions in Figure 3.77. 148

**Figure 3.79** Injection of a CO concentration pulse of CO at an inlet gas temperature of 180$^o$C. The inlet THCs concentration was maintained at 1500 ppm$C_1$. 149

**Figure 3.80** Thermal response to a concentration pulse of CO for conditions in Figure 3.79. 149

**Figure 3.81** Injection of a concentration pulse of CO as inlet gas temperature of 190$^o$C. The inlet THCs concentration was maintained at 1500 ppm$C_1$. 150

**Figure 3.82** Thermal response to a concentration pulse of CO for conditions in Figure 3.81. 150

**Figure 3.83** Injection of a concentration pulse of CO as inlet gas temperature of 200$^o$C. The inlet THCs concentration was maintained at 1500 ppm$C_1$. 151

**Figure 3.84** Thermal response to a concentration pulse of CO for conditions in Figure 3.83. 152

**Figure 3.85** Injection of a concentration pulse of THCs at an inlet gas temperature of 146 $^{o}$C. The inlet CO concentration was maintained at 3000 ppm. 154

**Figure 3.86** Thermal responses to a concentration pulse of THCs for conditions in Figure 3.85. 154

**Figure 3.87** Injection of a concentration pulse of THCs at an inlet gas temperature of 189$^{o}$C. The inlet CO concentration was maintained at 3000 ppm. 155

**Figure 3.88** Thermal responses to a concentration pulse of THCs for conditions in Figure 3.87. 155

**Figure 3.89** Injection of a concentration pulse of THCs at an inlet gas temperature of 320$^{o}$C. The inlet CO concentration was maintained at 3000 ppm. 156

**Figure 3.90** Thermal responses to a concentration pulse of THCs for conditions in Figure 3.89. 156

**Figure 3.91** Effect of CO injection upon THCs conversion (Copied from Hammond, 2004). 158

**Figure 3.92** Pre- and post-catalyst concentrations of CO and THCs when a pulse of 1% CO is injected with an inlet gas temperature of 270$^{o}$C. The inlet THCs concentration was about 580 ppm$C_1$. 160

**Figure 3.93** Pre- and post-catalyst concentrations of CO and THCs throughout 1% CO injection when inlet gas temperature is 270$^{o}$C. The inlet THCs concentration was maintained at about 3500 ppm$C_1$. 160

**Figure 3.94** Concentrations of CO and THCs at the inlet and outlet of the Thin-slice DOC during CO injection. The inlet gas temperature was 153$^{o}$C. The wall (or catalyst) temperature is also plotted as a function of time. 162

**Figure 3.95** Concentrations of CO and THCs at the inlet and outlet of the Thin-slice DOC during CO injection. The inlet gas temperature was 277$^{o}$C. The wall (or catalyst) temperature is also plotted as a function of time. 162

**Figure 3.96** Summary of experiments in Chapter 3. The experiments highlighted in red are discussed in Section 3.7. 163

**Figure 3.97** Effect of hydrogen on the oxidation of CO in light-off and extinction phases. 165

**Figure 3.98** Effect of hydrogen on the overall rate of CO oxidation in light-off and extinction phases. 166

**Figure 3.99** Axial wall temperature profiles with different amounts of hydrogen, when the inlet gas temperature is 223$^{o}$C. 166

**Figure 3.100** Effect of hydrogen on the oxidation of CO in light-off and extinction phases. 168

**Figure 3.101** Wall temperature and its effect on the oxidation of CO in the presence of hydrogen. 168

**Figure 3.102** Wall temperature and its effect on the rate of CO oxidation in the presence of hydrogen. 169

**Figure 3.103** Influence of a pulse of 1125 ppm of hydrogen when the inlet gas temperature was 170$^{o}$C. 170

**Figure 3.104** Influence of a pulse of 1125 ppm of hydrogen when the inlet gas temperature was 232$^{o}$C. 170

**Figure 3.105** Summary of experiments in Chapter 3. The experiments highlighted in red are discussed in Section 3.8. 173

**Figure 3.106** Illustration of the positions of three 5 mm thin slices cut from the Full-scale DOC. 174

**Figure 3.107** Conversion of CO as a function of wall temperature. Inlet CO and THCs concentrations were maintained at 3000 ppm and 1500 ppm$C_1$, respectively. 175

**Figure 3.108** Overall rate of CO oxidation as a function of wall temperature. Inlet CO and THCs concentrations were maintained at 3000 ppm and 1500 ppm$C_1$, respectively. 175

**Figure 3.109** Conversion of THCs as a function of wall temperature. Inlet CO and THCs concentrations were maintained at 3000 ppm and 1500 ppm$C_1$, respectively. 176

**Figure 3.110** Overall rate of THCs oxidation as a function of wall temperature. Inlet CO and THCs concentrations were maintained at 3000 ppm and 1500 ppm$C_1$, respectively. 176

**Figure 4.1** Overview of the mathematical models developed in Chapter 4. 182

**Figure 4.2** Schematic of the single channel model. 184

**Figure 4.3** Example of discretization of the gas temperature represented in an *x, y*-coordinate system (mesh points), where *i* stand for mesh points along the axial direction along the monolith (also known as dimensionless length steps, $\Delta z$) and *j* stands for mesh points in time domain (also known as dimensionless time steps, $\Delta t$). 187

**Figure 4.4** Solid and gas temperature profiles in the first 5.7 s at the middle point (z = 57 mm) of the monolith channel, with $\Delta z$ =1.14 mm, and $\Delta t$ = 0.0057 s (simulated by implicit finite difference thermal model, the MATLAB code is in Appendix 8.1). 190

**Figure 4.5** Solid temperature profiles at entrance to the monolith channel (*z* = 1.14 mm). The MATLAB code for the NTU model is in Appendix 8.2. 192

**Figure 4.6** Temperature of the monolith substrate as a function of axial distance after 10 and 50 s, with $\Delta z$ =1.5 mm, and $\Delta t$ = 6.4e$^{-4}$ s (simulated by Code III, in Appendix 8.3). 195

**Figure 4.7** Air flow in a monolith channel (ID = 1.25 mm; length = 150 mm). (a) Check on velocity profile, (b) check on Nu number at constant wall temperature, and (c) check on Nu number at constant heat flux. 196

**Figure 4.8** Velocity profile in the radial direction when L = 75 mm. 197

**Figure 4.9** Example of radial temperature profiles at constant wall temperature. 198

**Figure 4.10** Calculated values of local *Nu* number as a function of channel length with a constant wall temperature. 199

**Figure 4.11** Example of radial temperature profiles at constant wall heat flux. 200

**Figure 4.12** Calculated values of local *Nu* number as a function of channel length with a constant wall heat flux condition. 200

**Figure 4.13** 2-D model in COMSOL, the square shape of the monolith is converted into a cylindrical shape. 201

**Figure 4.14** Schematics of the geometry of single channel model in COMSOL Multiphysics. 201

**Figure 4.15** Temperature of the solid wall as a function of axial distance: (a) after 10 s, and (b) after 50 s. 207

**Figure 4.16** Gas inlet temperature (z = 0 mm) as a function of time (experimental and polynomial equation). 211

**Figure 4.17** Outlet gas temperature as a function of time. Simulation results from MATLAB and COMSOL are compared with experimental results (MATLAB Code III using a time step $\Delta t = 1\times10^{-3}$ s, and a step length $\Delta z$ =1 mm). 212

**Figure 4.18** Monolith wall temperature as a function of axial distance when t = 10 s. Exp. r = 0 means the measured temperature profile at centre of the substrate. Exp. r = 46 mm means the measured wall temperature profile at r = 46 mm. 213

**Figure 4.19** Monolith wall temperature as a function of axial distance when t = 50 s. Exp. r = 0 means the measured temperature profile at centre of the substrate. Exp. r = 46 mm means the measured wall temperature profile at r = 46 mm. 213

**Figure 4.20** Monolith wall temperature as a function of axial distance when t = 90 s. Exp. r = 0 means the measured temperature profile at centre of the substrate. Exp. r = 46 mm means the measured wall temperature profile at r = 46 mm. 214

**Figure 4.21** Inlet gas velocity profile at t = 0 s (simulated by 2-D COMSOL model). 216

**Figure 4.22** Gas inlet temperature: comparison of measured and curve fitted polynomial (z = 0 mm) as a function of time. 216

**Figure 4.23** Gas outlet temperature: comparison of measured and simulated values (z = 114 mm). 217

**Figure 4.24** Monolith wall temperature: comparison of measured and simulated value when t = 100 s. The "Exp. r = 0.5R" means the axial temperature profile at 1/2 radius of the monolith. 217

**Figure 4.25** Monolith wall temperature: comparison of measured and simulated value when t = 500 s. The "Exp. r = 0.5R" means the axial temperature profile at 1/2 radius of the monolith. 218

**Figure 4.26** Pressure profiles along the monolith channel. In the COMSOL simulation the outlet pressure was assigned as atmospheric pressure (101325 Pa). 219

**Figure 4.27** Schematic of the catalytic combustion process inside a single monolith channel (wall coated with washcoat + catalyst). 221

**Figure 4.28** Converting the actual geometry into a cylindrical shape. 221

**Figure 4.29** Concentration profile of propane at steady-state with an inlet gas velocity of 0.5 m s-1 (STP). The red colour indicates higher propane concentration, and green colour indicates lower concentration. 229

**Figure 4.30** Results from the COMSOL 2-D simulation showing axial gas and wall temperature profiles. The dashed lines are the wall temperatures and the solid lines are the mean gas temperature. 230

**Figure 4.31** Axial gas and wall temperature profiles. The dashed lines are the wall temperatures and the solid lines are the gas temperature (simulated at $v_{av}$ = 0.5 m/s, at reference of 298 K). The results plotted in black colour are the output from Hayes and Kolaczkowski (1997; p. 325), and the results plotted in red colour are the output from the COMSOL 2-D model. 230

**Figure 4.32** Axial gas and wall mole fractions of propane. The dashed lines are the wall concentrations and the solid lines are the gas concentration (simulated at $v_{av}$ = 0.5 m/s, at reference of 298 K). The results plotted in black colour are the output from 1-D model in Hayes and Kolaczkowski (1997; p. 326), and the results plotted in red colour are the output from the COMSOL 2-D model. 231

**Figure 4.33** Comparison of measured and simulated light-off curves for CO (with inlet concentration of 3210 ppm). The inlet THCs concentration is maintained at 1500 ppm$C_1$ (equivalent to 500 ppm propane). LHHW rate expressions are used in the simulation. 234

**Figure 4.34** Comparison of measured and simulated light-off curves for THCs (with inlet concentration of 1500 ppm$C_1$, equivalent to 500 ppm propane). The inlet CO concentration is maintained at 3000 ppm. LHHW rate expressions are used in the simulation. 235

**Figure 4.35** Wall temperature 50 mm from the inlet. Simulations compared with experimental data. 235

**Figure 4.36** Wall temperature 105 mm from the inlet. Simulations compared with experimental data. 236

**Figure 4.37** Comparison of measured and simulated light-off curves for CO (with inlet concentration of 2100 and 4100 ppm). For two tests, the inlet THCs concentration was maintained at 1500 ppm$C_1$ (equivalent to 500 ppm propane). 237

**Figure A1** (a) Example of an SEM picture of a monolith channel (b) image after cutting, (c) image processed by Photoshop, (d) image processed into black and white for boundary trace in MATLAB. 261

**Figure A2** CO readings from MEXA1 and 2. 266

**Figure A3** The difference in CO readings between MEXA1 and 2, versus the CO readings on MEXA 1. 266

**Figure A4** THCs readings from MEXA1 and 2. 267

**Figure A5** The difference in THCs between MEXA1 and 2, versus the THCs readings on MEXA 1. 267

**Figure A6** Linearity check on CO readings. 268

**Figure A7** Linearity check on THCs readings. 269

**Figure A8** Calibration curves for CO readings from MEXA1 and 2. 269

**Figure A9** Calibration curves for CO readings from MEXA1 and 2. 270

**Figure A10** Difference between MEXA1 CO readings and actual concentration. 270

**Figure A11** Difference between MEXA2 CO readings and actual concentration. 271

**Figure A12** Pre- and post-catalyst concentrations of CO and THCs when a pulse of 3000 ppm CO is injected with an inlet gas temperature of 188$^oC$. The inlet THCs concentration was about 1500 ppm$C_1$. 275

**Figure A13** Pre- and post-catalyst concentrations of CO and THCs when a pulse of 3000 ppm CO is injected with an inlet gas temperature of 218$^oC$. The inlet THCs concentration was about 1500 ppm$C_1$. 275

**Figure A14** Pre- and post-catalyst concentrations of CO and THCs when a pulse of 3000 ppm CO is injected with an inlet gas temperature of 232$^oC$. The inlet THCs concentration was about 1500 ppm$C_1$. 276

**Figure A15** Pre- and post-catalyst concentrations of CO and THCs when a pulse of 3000 ppm CO is injected with an inlet gas temperature of 258$^oC$. The inlet THCs concentration was about 1500 ppm$C_1$. 276

**Figure A16** Pre- and post-catalyst concentrations of CO and THCs when a pulse of 3000 ppm CO is injected with an inlet gas temperature of 290$^oC$. The inlet THCs concentration was about 1500 ppm$C_1$. 277

**Figure A17** Cumulative emissions of CO at pre- and post-catalyst position in the cold NEDC. No addition of hydrogen. 278

**Figure A18** Cumulative emissions of THCs at pre- and post-catalyst position in the cold NEDC. No addition of hydrogen. 278

**Figure A19** Cumulative emissions of $NO_x$ at pre- and post-catalyst position in the cold NEDC. No addition of hydrogen. 279

**Figure A20** Cumulative emissions of CO at pre- and post-catalyst position in the cold NEDC, hydrogen was added at 0.575 litre/min. 279

**Figure A21** Cumulative emissions of THCs at pre- and post-catalyst position in the cold NEDC, hydrogen was added at 0.575 litre/min. 280

**Figure A22** Cumulative emissions of $NO_x$ at pre- and post-catalyst position in the cold NEDC, hydrogen was added at 0.575 litre/min. 280

**Figure A23** Cumulative emissions of CO at pre- and post-catalyst position in the cold NEDC, hydrogen was added at 0.9 litre/min. 281

**Figure A24** Cumulative emissions of THCs at pre- and post-catalyst position in the cold NEDC, hydrogen was added at 0.9 litre/min. 281

**Figure A25** Cumulative emissions of CO at pre- and post-catalyst position in the cold NEDC, hydrogen was added at 0.9 litre/min. 282

**Figure A26** Flowsheet of the 1-D heat transfer model solved using MATLAB. 291

**Figure A27** Flowsheet of the Reaction Engineering Lab in COMSOL Multiphysics. 292

**Figure A28** Flowsheet of the Chemical Engineering Module in COMSOL Multiphysics. 292

## List of Tables

**Table 2.1** Summary of key heat transfer equations developed in Lubeski *et al*. (2000). 18

**Table 2.2** Some examples of information on rate constants in the LHHW form of rate expression. 23

**Table 2.3** Rate constants after final optimisation in Sampara *et al.* (2007). 25

**Table 2.4** Composition of the synthetic gas used for light-off study of a diesel oxidation catalyst in Chandler *et al*. (2000). 39

**Table 2.5** Examples of relevant physical properties found in the literature. Note that: $T_w$ is the solid temperature in K, $T_g$ is air temperature in K, $P_2$ is air pressure in atm and $P_1$ is 1 atm. 46

**Table 3.1** Measurement performed on the catalyst samples provided by JM. 55

**Table 3.2** Properties of the DOCs. 56

**Table 3.3** Specifications of the Ford PUMA 2.0 litre diesel engine (turbocharged ). 57

**Table 3.4** Configuration of MEXA-7100 DEGR. 58

**Table 3.5** A matrix of engine test data obtained from Ford PUMA 2.0 litre diesel engine. 68

**Table 3.6** Some useful conversion factors. 116

**Table 3.7** Comparing experimental conditions with Hayes *et al*. (1995). 140

**Table 3.8** Conditions for CO inhibition experiments. 140

**Table 3.9** Conditions for THCs inhibition experiments. 143

**Table 3.10** Effect of hydrogen addition on the overall conversion of the major contaminants during the cold NEDC using Full-scale DOC. 171

**Table 3.11** Composition of exhaust gas for three different engine torques. 172

**Table 4.1** Test condition and physical parameters used in Code I. 190

**Table 4.2** Some experimental conditions and physical properties of the monolith and air that were used in Benjamin and Roberts (2001). 193

**Table 4.3** The typical physical parameters used by Benjamin and Roberts (2001) for CFD simulation. 204

**Table 4.4** Example of experimental conditions. 209

**Table 4.5** Operating conditions and physical parameters of monolith substrate. 210

**Table 4.6** Summary of operation conditions and physical parameters of JM substrate. 215

**Table 4.7** Physical dimensions of the monolith/washcoat modelled. 221

**Table 4.8** Diffusion volumes for use in the Fuller *et al.* correlations (copied from Hayes and Kolaczkowski, 1997; p. 229). 223

**Table 4.9** Boundary conditions for convection and diffusion. 227

**Table 4.10** Boundary conditions for convection and conduction. 227

**Table 4.11** Boundary conditions for momentum balance using Weakly Compressible Navier-Stokes. 228

**Table 4.12** Summary of the operating conditions for a pseudo-steady-state light-off experiment. 233

**Table 4.13** Initial rate constants (final rate constants from Kim and Kim, 2009) and tuned rate constants. 233

**Table A1** Fully developed Nusselt numbers for the more commonly encountered shapes (modified from Hayes and Kolaczkowski 1997; p.317). 251

**Table A2** Summary of the cross-sectional area of washcoat. 263

**Table A3** An example of the experiment conditions and conversion data obtained from the pseudo-steady-state light-off experiments, where the inlet CO concentration and the inlet THCs concentrations were maintained at 3000 ppm and 1500ppm$C_1$, respectively. (Matched to Figure 3.47 ) 273

**Table A4** An example of the temperature data obtained from the pseudo-steady-state light-off experiment, where the inlet CO concentration and the inlet THCs concentration were maintained at 3000 ppm and 1500 ppm$C_1$, respectively. (Matched to Figure 3.51). 274

# Nomenclature

| | |
|---|---|
| $A$ | Area of heat transfer, $m^2$ |
| $A$ | Pre-exponential rate constant, various units |
| $A_a$ | Pre-exponential adsorption rate constant, various units |
| $A_{geo}$ | Geometric surface area of the DOC tested, $m^2$ |
| $C_b$ | Mean bulk concentration, mol $m^{-3}$ |
| $C_p$ | Specific heat capacity (constant pressure), J $mol^{-1}$ $K^{-1}$ |
| $d$ | Inner diameter of monolith channel, m |
| $Da$ | Damköhler number |
| $D_{A,B}$ | Molecular diffusion coefficient of A in a mixture of A and B, $m^2$ $s^{-1}$ |
| $D_{eff}$ | Effective diffusivity, $m^2$ $s^{-1}$ |
| $D_H$ | Hydraulic diameter, m |
| $D_k$ | Knudsen diffusion coefficient, $m^2$ $s^{-1}$ |
| $D_v$ | Diffusion coefficient inside a pore, $m^2$ $s^{-1}$ |
| $E$ | Activation energy, J $mol^{-1}$ |
| $E_r$ | Activation energy, J $mol^{-1}$ |
| $E_a$ | Activation energy for adsorption, J $mol^{-1}$ |
| $f$ | Frictional factor |
| $G$ | Inhibition term in LHHW rate expression due to adsorption, units vary |
| $F$ | Molar flowrate, mol $s^{-1}$ |
| $F$ | Body force vector, N $m^{-3}$ |
| $h$ | Heat transfer coefficient, W $m^{-2}$ $K^{-1}$ |
| $H$ | Heat of reaction, J $mol^{-1}$ |
| $k$ | Thermal conductivity, W $m^{-1}$ $K^{-1}$ |
| $k$ | Apparent rate constants, various units |
| $k_{dv}$ | An added term in Stress tensor |
| $k_a$ | Adsorption rate constants, various units |
| $k^0_a$ | Pre-exponential adsorption rate constant, various units |
| $k_r$ | Apparent rate constants, various units |
| $k^0_r$ | Pre-exponential rate constant, various units |
| $K$ | Adsorption rate constants, various units |

| | |
|---|---|
| $L$ | Monolith length, characteristic length, m |
| $l$ | Element length, m |
| $L_c$ | Effect length of washcoat, m |
| $m$ | Mass, kg |
| $M$ | Molar mass, kg $mol^{-1}$ |
| $m_{air}$ | Air mass flow, kg $s^{-1}$ |
| $m_{Pt}$ | Platinum catalyst loading for the DOC tested, g |
| $M_{air}$ | Molar mass of air, kg $mol^{-1}$ |
| $n$ | Unit vector normal to boundary , pointing outward from computational domain, , dimensionless |
| $Nu$ | Nusselt number, dimensionless |
| $Nu_H$ | Nusselt number with constant surface flux boundary conditions, dimensionless |
| $Nu_T$ | Nusselt number with constant wall temperature boundary conditions, dimensionless |
| $Pr$ | Prandtl number, dimensionless |
| $q$ | Heat transfer rate, W $m^{-2}$ |
| $q$ | Heat flux vector, W $m^{-2}$ |
| $Q$ | Heat source, W $m^{-2}$ |
| $R$ | Rate of reaction, mol $m^{-3}$ $s^{-1}$ |
| $R$ | Radius of monolith channel or catalytic converter, m |
| $Re$ | Reynolds number, dimensionless |
| $r$ | Radius coordinate in cylindrical coordinate system, dimensionless |
| $r$ | Rate of reaction, Rate of reaction, mol $m^{-3}$ $s^{-1}$ |
| $r_e$ | Equivalent pore radius, m |
| $S$ | Strain rate tensor |
| $T$ | Temperature, K or $^oC$ |
| $T_{50}$ | Light-off temperature, K or $^oC$ |
| $t$ | Time, s |
| $u_{air}$ | Local air velocity, m $s^{-1}$ |
| $u_{air,0}$ | Initial air velocity, m $s^{-1}$ |
| $u_m$ | Mean average velocity of the gas, m $s^{-1}$ |
| $v_{av}$ | Average velocity of inlet gas, m $s^{-1}$ |
| $V$ | Volume of reactor, $m^{-3}$ |

| | |
|---|---|
| $V_{air}$ | Volumetric flowrate of air, $m^3\ s^{-1}$ |
| $x$ | Distance down the length of the catalyst, m |
| $X$ | Fractional conversion , dimensionless |
| $Y$ | Mole faction, dimensionless |
| $z$ | Axial coordinate in cylindrical coordinate system, m |
| $Z$ | Distance to inlet of converter, m |
| $\Delta p$ | pressure drop, Pa |
| $\Delta H_R$ | Heat of reaction, $J\ mol^{-1}$ |
| $R(\theta)$ | Inhibition term in LHHW rate expression due to adsorption, unit vary |

## Greek symbols

| | |
|---|---|
| $\alpha$ | Thermal diffusivity of gas, $m^2\ s^{-1}$ |
| $\beta$ | Parameter |
| $\delta$ | Wall thickness, m |
| $\varepsilon$ | Void volume of the catalyst |
| $\varepsilon_s$ | Solid heat transfer effectiveness, $W\ m^{-2}\ K^{-1}$ |
| $\eta$ | Effectiveness factor |
| $\theta$ | Time step, s |
| $\lambda$ | Thermal conductivity, $W\ m^{-1}\ K^{-1}$ |
| $\mu$ | Dynamic viscosity of the gas, $kg\ m^{-1}s^{-1}$ |
| $\sigma$ | Diffusion volume |
| $\rho$ | Density, $kg\ m^{-3}$ |
| $\tau$ | Tortuosity factor |
| $\tau$ | Viscous tress tensor, Pa |
| $\Phi$ | Washcoat porosity |

## Subscripts

| | |
|---|---|
| CO | Carbon monoxide |
| g | Gas phase |

| | |
|---|---|
| $H_2$ | Hydrogen |
| HCs | Hydrocarbons |
| $C_3H_6$ | Propene |
| $i$ | Substance ($i$) |
| $i$ | Length step |
| $j$ | Time step |
| NO | Nitrogen monoxide |
| s | Solid phase |
| w | Washcoat or wall |
| 0 | Initial conditions |

## Abbreviations

| | |
|---|---|
| 1-D | One dimensional |
| 2-D | Two dimensional |
| 3-D | Three dimensional |
| BDF | Backward difference formula |
| BiFo | Biot-Fourier number |
| BVP | Boundary value problem |
| BSP | British standard pipe |
| CID | Chemi-luminescence detection |
| CFD | Computational fluid dynamics |
| CO | Carbon monoxide |
| COV | Coefficient of variance |
| CPSI | Cells per square inch |
| DOC | Diesel oxidation catalyst |
| ECU | Engine control unit |
| EGR | Exhaust gas recirculation |
| EPA | Environmental protection agency (US) |
| EUDC | Extra urban driving cycle |
| FID | Flame ionization detection |
| FTP | Federal test procedure (US) |

| | |
|---|---|
| GC | Gas chromatography |
| HC | Hydrocarbon |
| HWA | Hot wire anemometry |
| IMEP | Indicated mean effective pressure |
| JM | Johnson Matthey |
| LHHW | Langmuir-Hinshelwood-Hougen-Watson |
| MPD | Magneto-pneumatic detection |
| MSDS | Material Safety Data Sheets |
| NDIR | Non-dispersive Infrared method |
| NEDC | New European driving cycle |
| UDC | Urban driving cycle |
| $NO_x$ | Nitric oxides |
| NTU | Number of transfer units |
| $NTU_h$ | Number of transfer units |
| ODE | Ordinary differential equation |
| PCI | Pre-mixed compression ignition |
| ppm | Parts per million (1 in $10^6$) |
| PRV | Pressure reduction valve |
| PVRC | Powertrain and Vehicle research centre |
| RPM | Revolutions per minute |
| SEM | Scanning electron microscope |
| SCR | Selective catalytic reduction |
| STP | Standard temperature and pressure |
| THCs | Total unburned hydrocarbons |

# 1. Introduction

## 1.1 Background

As the world develops, the number of vehicles manufactured is increasing rapidly year by year. In 2008, 34.27 million new cars were registered in Europe, China, Japan and USA (Motor Industry Facts 2009, UK, p. 18). As catalytic converters are required for exhaust treatment, their total global market is expanding rapidly.

Resources of the precious metals used in exhaust after treatment devices are limited yet emissions from vehicles must be controlled. Road transport accounts for around 85% of the transport sector's carbon emissions, which in turn accounts for 25% of the total UK emissions (National Statistics, UK, 2004; p. 310). Many decades will pass before the use of carbon based fuels in internal combustion engines starts to become replaced by alternatively-powered vehicles. As developing nations continue to grow, the number of cars will increase in the world, and demand for the limited resources of precious metals used in catalysts will increase. Thus the development of catalytic converters to reduce the usage of precious metals and to maintain, or even increase the efficiency of such systems, seems even more important. Moreover, as government legislation to reduce emissions from vehicles becomes stricter, the car manufacturers will be more interested in seeking improvements in the design of catalytic converters and how they are integrated with the engine management system in the vehicle.

## 1.2 Emission standards

Over the past fifteen years much progress has been achieved in improving air quality. Increasingly tight exhaust emission regulations have been imposed on automotive manufacturers, see Figure 1.1. These regulations restrict emissions from both petrol and diesel cars. Emissions of carbon monoxide (CO), total hydrocarbons (THCs), oxides of

nitrogen ($NO_x$) and particulate matters (PM), are all considered to be harmful to human health.

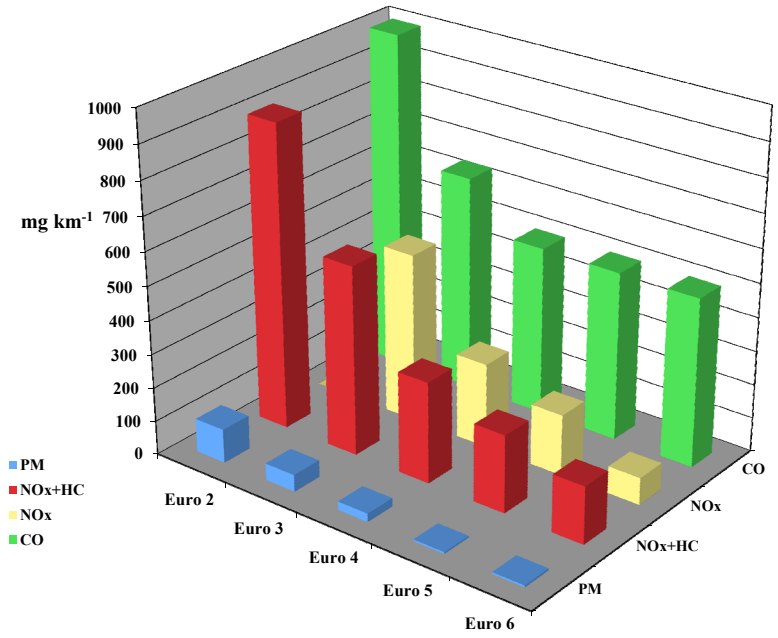


**Figure 1.1** Progression of European emission standards for diesel passenger cars over the last 15 years. The Euro 2-6 correspond to the emission standards, e.g. Euro 2 standards for the European emission standards II for diesel passenger cars. Data was obtained from Euractiv (2008).

The current emission standards in Europe are Euro 5. This was applied in September 2009 for new models of cars, and will apply in January 2011 for all new cars. The Euro 6 standard is only a draft directive now, and it may begin in April 2013. This will place demands on automotive manufacturers to seek improvements in the performance of post treatment systems, such as catalytic converters.

## 1.3 Exhaust emissions from engines

Exhaust emissions refer to the pollutants contained in the exhaust gas from an internal combustion engine. In an ideal situation (complete combustion), internal combustion engines that use hydrocarbon fuel should only produce CO and water. However, in practice complete combustion of the fuel is never achieved. A typical diesel engine produces the following major pollutants (Stone, 1999; p. 98).

(a) Oxides of nitrogen ($NO_x$): These are formed during the very high temperatures (>1500°C) of the combustion process resulting in thermal fixation of the nitrogen in the air which forms $NO_x$ (Heck and Farrauto, 2001). These oxides are irritant and harmful to human health. They also cause environmental problems, acting as a greenhouse gas, and causing photochemical smog (along with hydrocarbons), and they create nitric acid (Material Safety Data Sheets (MSDS) data sheet for $NO_2$).

(b) Total hydrocarbons (THCs): These are formed due to incomplete oxidation of carbon fuels. These are irritants, smelly and condense to form particulates. They may also take part in atmospheric reactions and some may be carcinogenic (MSDS data sheet for propane).

(c) Carbon monoxide (CO): This is a product from the incomplete combustion of fuel. It causes adverse effect on human health, by reducing the ability of oxygen to be carried in the blood. Environmental effects are not significant from CO although it may react with nitrogen dioxide to produce $O_3$ (ozone), which is the major source of tropospheric ozone formation (MSDS data sheet for CO).

(d) Particular matter (PM): These are very fine particles that are not visible but collectable by filtration. The effects of inhaling particular matter are considered to be directly related to causes of several diseases, e.g. asthma and lung cancer.

## 1.4 Catalytic converters

A catalytic converter is a catalytic device that is used to reduce harmful emissions from internal combustion engines. It was first introduced in the mid-1970s into the American market to comply with the tightening EPA (Environmental protection agency) regulation on tailpipe emissions. Since then, it is the most common and effective device for emissions control.

### 1.4.1 Structure of a catalytic converter

A catalytic converter has a substrate, which is wrapped with a metal mesh and an insulation mat, and is then housed in a metal case. The metal mesh isolates the substrate from any vibrations caused by the engine, or the movement of the vehicle. The mat provides good thermal insulation to prevent any unnecessary heat loss to the surroundings, in order to achieve an earlier light-off and higher conversion (Stone, 1999; p. 173). Usually a catalytic converter contains one monolith substrate (see Figure 1.2). However, two-substrate systems are also used. According to Stone (1999), two bricks reduce the likelihood of fracture through differential thermal expansion.

### 1.4.2 Substrate

The substrate is a core part of a converter since the catalytic reactions take place inside its monolith channels. Ceramic materials were chosen as a substrate and they still dominate the market (over 90%, Cybulski and Moulijn, 2006, p. 116) because of the relatively low manufacturing cost. Cordierite is often used as the ceramic material, and it has a formulation of 14% magnesia (MgO), 35% alumina ($Al_2O_3$) and 51% silica ($SiO_2$) (Hayes and Kolaczkowski, 1997; p. 665, reporting on values from Day and Thompson, 1991).

The most important mechanical properties of automotive catalytic converter substrates are the thermal shock resistance and the coefficient of thermal expansion (Williams, 2001). According to Alexander and Umehara (1995), the advantages of using cordierite as a substrate are:

(a) desirable low coefficient of thermal expansion,

(b) high temperature stability (softening point > 1300$^{o}$C),

(c) good porosity, and

(d) excellent oxidation resistance.

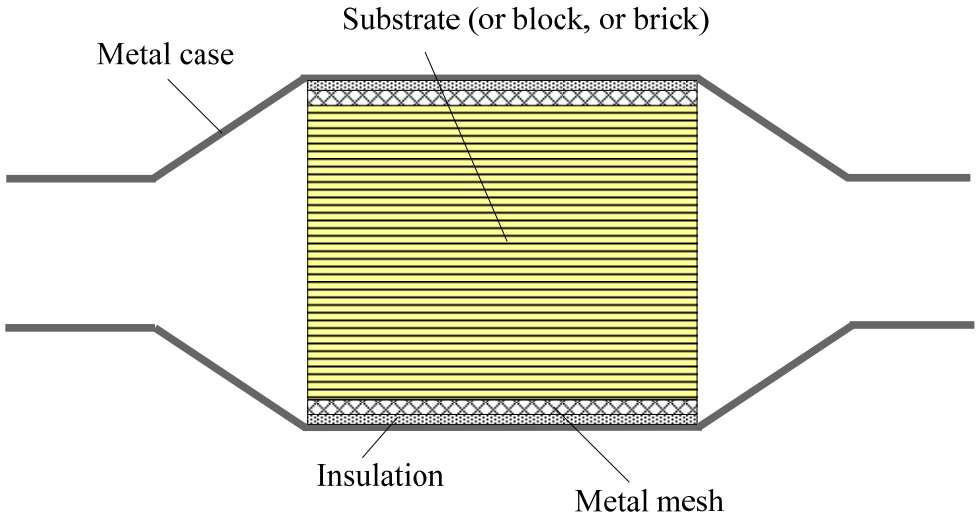


**Figure 1.2** Schematic drawing of the structure of a catalytic converter with a single substrate.

The dominant catalyst support for the automotive exhaust catalyst is a monolith or honeycomb structure (Heck and Farrauto, 2001). The monolith substrate has thousands of parallel small channels, e.g. with a cell density of 400 CPSI (cells per square inch). The channel shapes may vary, e.g. circular, triangle and square. Nevertheless, the square channel is the most popular shape in catalytic converters. The monolith structure offers a number of advantages in gas phase catalytic applications (Gulati, 1998; Heck and Farrauto, 2001):

a) high gas flow rate,

b) high surface/volume ratio, and

c) the particulate in the exhaust gas can pass easily through the channel since the diameter of the channel is much greater than that of the particles.

Alternatively, metal alloys can also be used as catalyst substrates. Figure 1.3 illustrates a typical configuration of a metallic substrate. The sinusoidal shaped cell is characterised by the width to height ratio, and this design aims to overcome problems with thermal shock and vibration effects (see Pelters *et al*., 1989).

Kaspar *et al.* (2003) states the advantages of using metal alloys: they can be made with thinner walls and have more open frontal areas (close to 90 %), allowing lower

pressure drop. On the other hand, larger cell density is achievable by using metallic substrate, which allows compact catalytic converter design for some special cases.

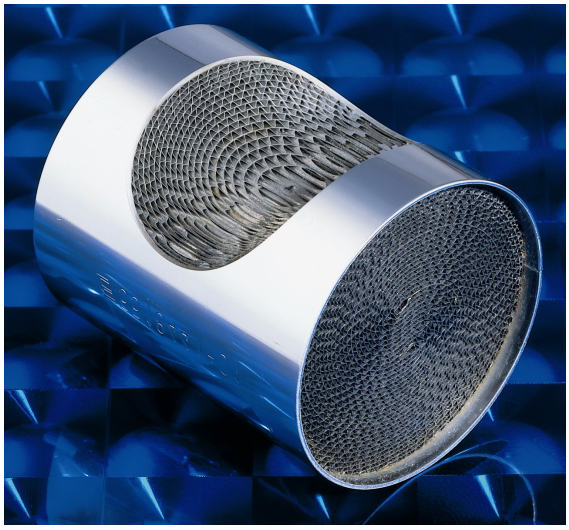

**Figure 1.3** A catalytic converter with metal substrate. Photograph supplied courtesy of Emitec GmbH, Lohmar, Germany.

In addition, Santos and Costa (2008) found another advantage of metallic substrate in manufacturing stage, "*A great advantage of the metal substrates is that the cell shape is produced in a pre-production step and can be easily modified*."

### 1.4.3 Washcoat

Unfortunately, ceramic substrates have a relatively low surface area (~0.2 $m^2$ $g^{-1}$, Yap, 2010), and that makes them unsuitable as a catalyst support in an automotive application. To achieve a high surface area for catalyst loading, a highly porous material is applied to the internal surface of the channels, known as a washcoat. The washcoat is commonly made from gamma-alumina ($\gamma$-$Al_2O_3$), which has a very high porosity. Its porous structure offers a high surface area (e.g.100 to 200 $m^2$ $g^{-1}$) for catalyst loading (Koltsakis and Stamatelos, 1997). According to Sideris (1998; p. 8), the thickness of the washcoat may vary from 20 to 60 μm.

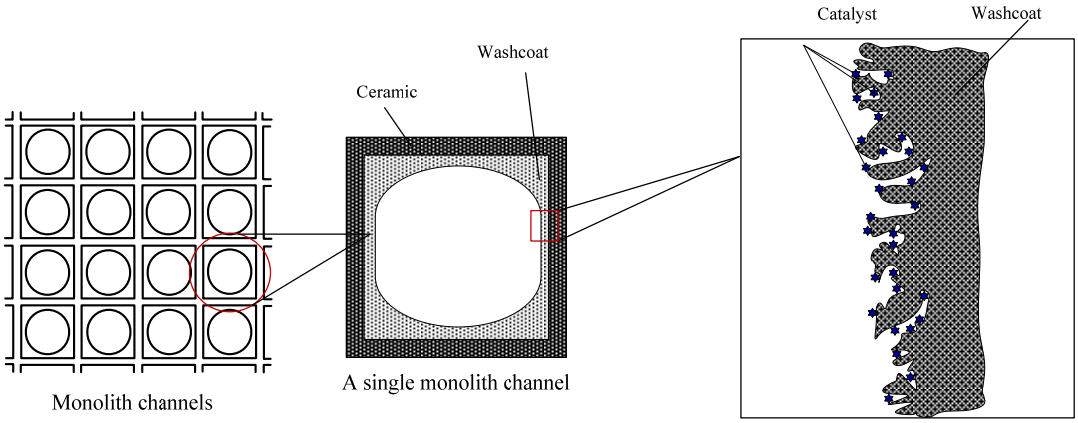


**Figure 1.4** Illustration of the structure of a square channel monolith and magnified structure of washcoat and catalyst.

The catalysts used in a converter are precious metals (e.g. Pt is generally used in diesel oxidation catalyst, DOC). They are present in a highly dispersed form over the porous structure of the washcoat, see Figure 1.4. Therefore the quantity of precious metals contained in a catalytic converter is about 2-3 g (Siders, 1998; p. 8).

## 1.5 Types of catalytic converters

Concerning the function of catalytic converters, two types of catalytic converter are available on the market. A diesel oxidation catalyst (DOC) is used for diesel engines and a three-way catalytic converter is used for gasoline engines.

**Diesel oxidation catalysts (DOCs):** these can lower the level of unburned THCs and CO emissions from a diesel engine. The following equations illustrate the process of oxidation. Oxidations of CO and THCs are summarised as follows (Hayes and Kolaczkowski, 1997; p. 68).

$$2CO + O_2 \longrightarrow 2CO_2 \qquad (1.1)$$

$$2C_xH_y + (2x + \frac{y}{2})O_2 \longrightarrow 2xCO_2 + yH_2O \qquad (1.2)$$

and, water-gas shift reaction:

$$CO + H_2O \longrightarrow CO_2 + H_2 \qquad (1.3)$$

The DOCs usually consist of platinum/palladium (Hayes and Kolaczkowski, 1997; p. 68). However, they have no, or very limited, ability to reduce the nitrogen oxides in the exhaust because of the "lean-burn" operating condition in diesel engines. The "lean-burn" condition refers to high air/fuel ratio, which leads to the presence of excess oxygen in the exhaust stream. This excess oxygen inhibits the reduction reactions of nitrogen oxides, but ensures the levels of CO and unburned THCs are minimised through both complete combustion in the engine and then maximum oxidation in the catalytic combustion process (Stone, 1999; p. 172). In general, the post treatment system in a diesel engine vehicle requires other devices or processes to control the nitrogen oxides emissions, e.g. exhaust gas recirculation (EGR), selective catalytic reduction (SCR) and $NO_x$ trap.

**Three-way catalytic converters**: they are employed for the control of gasoline engine emissions, which are capable of removing three pollutants in the exhaust gas simultaneously by oxidising CO, THCs and reducing $NO_x$. Since the air/fuel ratio in the gasoline engine is close to the stoichiometric condition (i.e. 14.7 g of air to 1 g of fuel), only a small amount of oxygen is present in the exhaust stream. Thus, the reduction of nitrogen oxides can be achievable while CO and THCs are oxidised. Reduction of nitrogen oxides is described as (Koltsakis and Stamatelos, 1997):

$$NO + CO \longrightarrow CO_2 + \frac{1}{2}N_2 \qquad (1.4)$$

$$C_xH_y + (2x + \frac{y}{2})NO \xrightarrow{\text{catalyst}} xCO_2 + \frac{y}{2}H_2O + (x + \frac{y}{4})N_2 \qquad (1.5)$$

$$NO + H_2 \longrightarrow H_2O + \frac{1}{2}N_2 \qquad (1.6)$$

The precious metal catalysts in a three-way catalytic converter contain platinum (as in an oxidation catalyst), and also small amounts of other precious metals, e.g. palladium and rhodium. In addition, the washcoat composition of the three-way catalyst is also different. Although only a small amount of ceria is needed, it plays an important role in the catalytic converter because of its several unique features. The important

features of ceria in catalytic combustion are listed as follows (Cybulski and Moulijn, 2006; p. 118).

(a) Ceria acts as an oxygen storage material, which absorbs oxygen from the exhaust gas under lean-burn conditions and then releases it under fuel-rich conditions. Thus, it controls the oxygen level within the desirable range where the optimum conversion can be achieved.

(b) Ceria is also a structural promoter, stabilising the precious metals and alumina during exposure to high temperature. Moreover, it inhibits the transformation of the alumina in the washcoat, from a gamma-alumina to a beta-alumina (which has a smaller surface area).

## 1.6 Performance of DOCs

Currently, provided the electronic engine management and operating temperatures are adequate, a DOC is able to reduce CO, and THCs emissions by about 99%. However, they do not work effectively until the light-off temperature is achieved, and a significant amount of pollutants can be emitted during this heat up period (Koltsakis and Stamatelos, 1997). About 60 to 80% of the THCs emissions are produced during this period in both the New European Driving Cycle (NEDC) and the Federal Test Procedure (FTP 75) for a diesel engine. This is known as the cold-start effect, and is discussed in detail in many publications, e.g. Ashley (1996) and Iliyas *et al.* (2007).

The light-off temperature commonly denotes the temperature of the catalytic converter for which the conversion reaches 50% of a specified reactant. For example, this temperature for CO usually ranges from 150 to 220$^{o}$C, see Figure 1.5.

From the brief discussion above, it is evident that the temperature of the catalyst has a close relationship to its performance. Therefore, it is important to understand the heat transfer characteristics of the catalytic converter in order to obtain a better understanding and improve the design of catalytic converters.

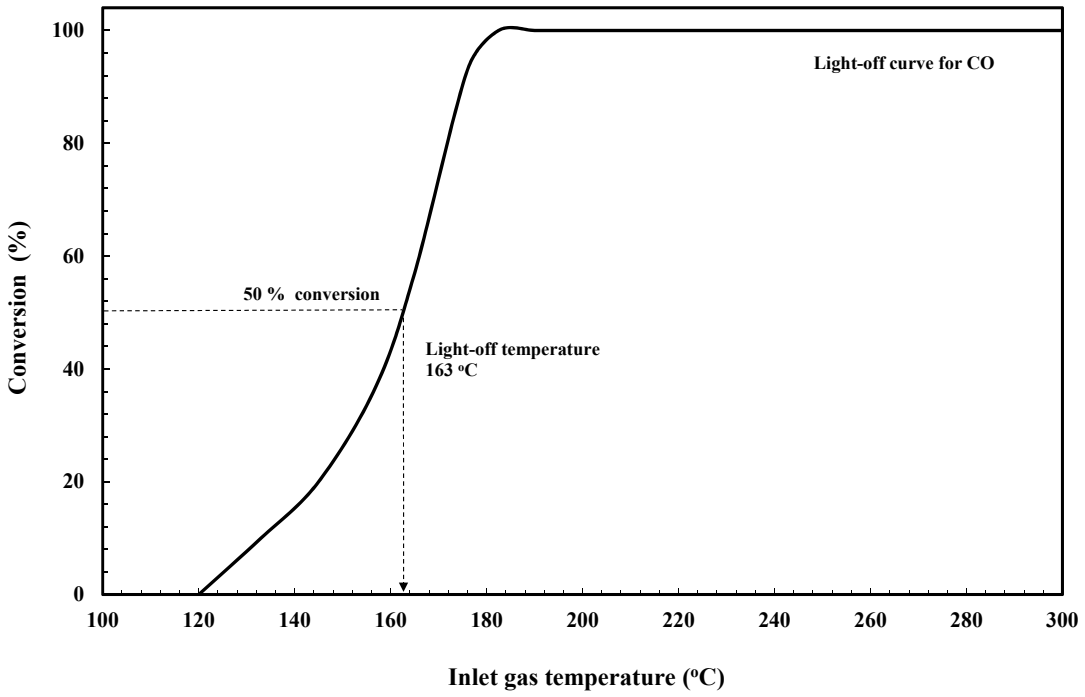


**Figure 1.5** An illustration of light-off curve for CO (adapted from Knafl *et al*., 2007).

## 1.7 Development of catalytic converters

Catalyst development for catalytic converters is somewhat piece-meal, occurring in a laboratory on small samples of powdered catalyst or small monolith structures. When trials are eventually done on real engines with full-scale converters, then the overall performance of the converter is evaluated, and an opportunity is lost to obtain a deeper understanding of the performance of the converter on-line.

Literature on the subject of catalytic converters is vast, although the number of rigorous scientific and fundamental studies is very limited. An extended review of the status of work in this field featured in Bennett *et al*. (1992). There are many papers that describe models of converters, but as many of the modellers work at a distance from the experimentalists, very few show any comparisons with experimental data. The need to assign values for the effective diffusivity of reactants in the catalyst layer is generally understood, but there is a lack of data to provide confidence in the method/values used. Models also vary in complexity, ranging from single channel to multi-channel monolith structures that are modelled as a continuum. Some of the models have many tuneable parameters, and the link between cause and effect is not transparent. Many researchers

develop their own in-house codes, or sometimes they adapt commercially available CFD codes such as Fluent to model the structures. In a number of instances, the work has been supported by transient experimental studies (e.g. Nibbelke, 1998; Harmasen *et al*., 2001), using small samples of catalyst in bench top studies. In this thesis it is timely to make a more significant contribution in this field, and this necessitates more fundamental work on real catalytic converters connected to an engine.

## 1.8 Scope of this thesis

This thesis aims to bridge a gap in knowledge between bench-top experiments performed in a laboratory (on small samples of catalyst), and trials that are performed on live engines with commercial catalysts.

The main focus of the work is on diesel oxidation catalysts (DOC), how techniques that have been used in bench-top experimental studies may be applied to experiments on a live engine, and how such data may be used to improve the design of DOC systems. The work described in this thesis was supported by a 3 year EPSRC grant for research on: 'On-line and on-engine catalyst characterization – a diagnostic technique to design a better catalyst'. Working on this project was one other PhD student (Y.Yap) who assisted with some of the experimental work, but whose research focussed more on the characterisation of the catalyst supports and the testing of mathematical mechanistic models of parallel/series reactions – this link is illustrated on the right hand side of Figure 1.6. To assist with the supervision of modelling work and application of available commercial modelling codes, some support was obtained from a PDRA in the Department of Chemical Engineering. To help with the day-to-day supervision of the engine test facilities some support was obtained from a Research Officer in the Department of Mechanical Engineering.

In the literature, there are many general reviews on the subject of catalytic converters and catalytic combustion, so to set the scene for the work that follows, this thesis starts with a brief review of more relevant literature (Chapter 2). This includes a discussion of: modelling techniques; forms of reaction rate expression; the effects of pulsating flow

on the performance of catalytic converters. This then influences the design of the experimental test facilities on the live Ford 2.0 litre turbocharged diesel engine, which are then described in Chapter 3. Here experiments are performed, mainly on DOCs that were specially prepared by Johnson Matthey for this project. These DOCs are prepared on cordierite monolith supports whose scale matches a commercial application. Experiments are performed on full 'monolith blocks, or bricks' (o.d. = 106 mm, length = 114 mm), and also on very short lengths of monolith (length = 5 and 10 mm). In many of these experiments, a known quantity of gas (e.g. carbon monoxide, propane, or hydrogen) is injected into the exhaust from the live engine, and the response of the catalyst system is monitored. This generates some very interesting data, and enables a technique that is normally only used in laboratory bench-top experiments to be applied to a live engine. In that chapter, the results of the experimental measurements are also presented. This then leads on to Chapter 4, where a number of case studies are considered in detail to illustrate:

(a) How the experimental results/techniques developed in this thesis may be used in modelling studies to facilitate catalyst system design.

(b) How mathematical modelling techniques can be applied to interpret the results obtained.

Finally in Chapter 5, conclusions and recommendations for further work are presented.

Nomenclature and abbreviations feature in a section at the start of the thesis, and a list of references is provided at the end of each chapter. In the appendices, useful terms, conversions, derivations are presented. Some additional experimental data is also provided, together with a description of the modelling codes.

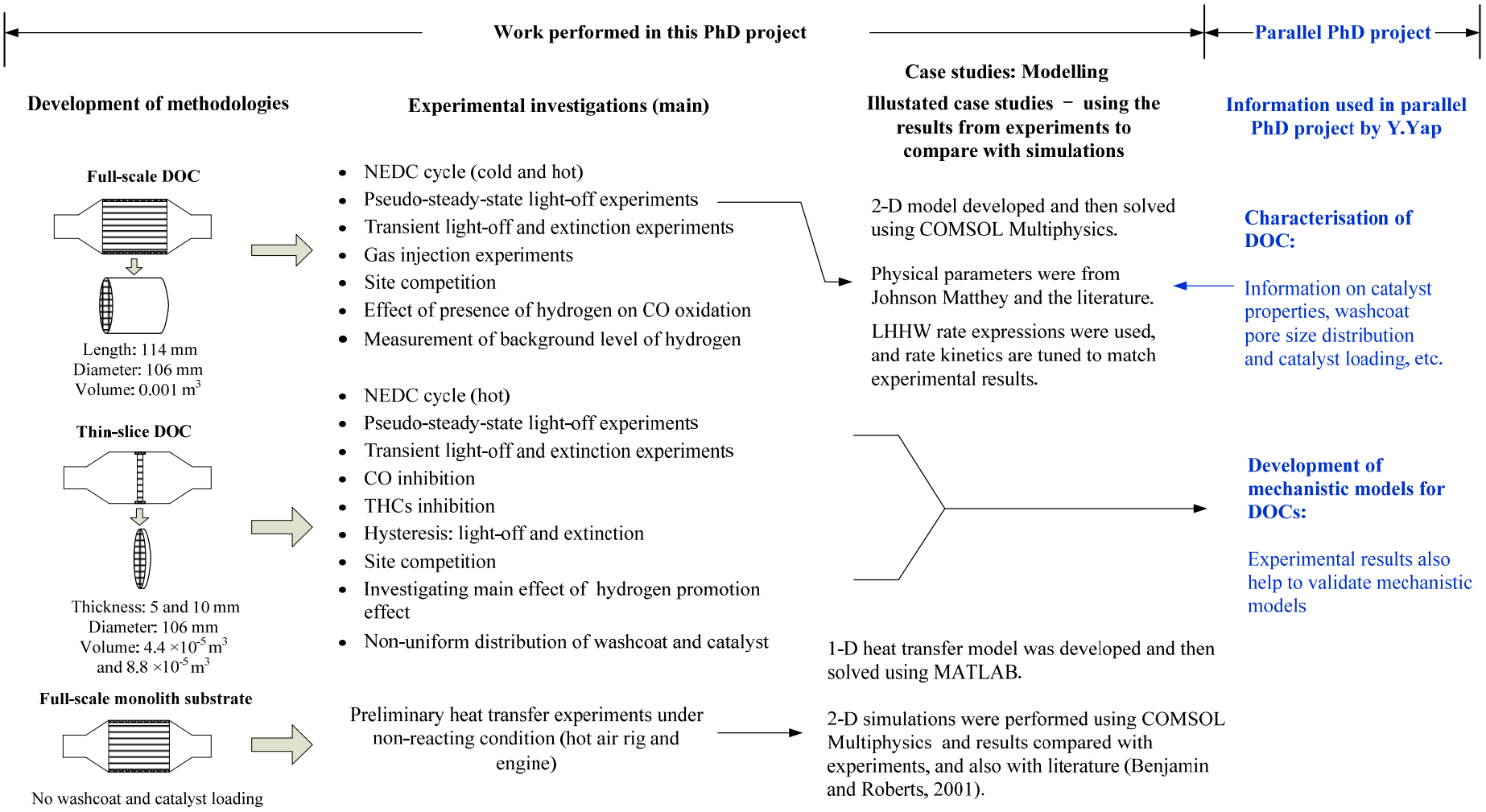


**Figure 1.6** Summary of work performed in this thesis and link to a parallel PhD project.

## References


Alexander, J.T. and Umehara, K. (1995) Ceramic Honeycomb for Air Pollution Control, NKG Insulator Ltd., Nagoya, Japan, Reference JH-952128, July.

Ashley, C. (1996) Future Strategies for Reducing Emission, *Automotive Engineering*, **21**(1),18-20.

Bennett, C. J., Hayes, R. E., Kolaczkowski, S. T. and Thomas, W. J. (1992) An Experimental and Theoretical Study of a Catalytic Monolith to Control Automobile Exhaust Emissions, Proc Royal Soc. Lond. A, **439**, 465 - 483.

Cybulski, A. and Moulijn J.A. (Ed.) (2006) *Structured Catalysts and Reactors*, 2nd Ed., CRC Press, New York.

Euractiv (2008) available from: http://www.euractiv.com/en/transport/euro-5-emissions-standards-cars/article-133325 [Accessed 7 February 2008].

Gulati,S.T. (1998) Physical Durability of Thin Wall Ceramic Substrates, SAE 982635.

Harmasen, J. M. A, Hoebink, J. H. B. J. and Schouten, J. C. (2001) Cetylene and Carbon Monoxide Oxidation Over a Pt/Rh/CeO2/γ-Alumina Automotive Exhaust Gas Catalyst: Kinetic Modelling of Transient Experiments, *Chemical Engineering Science*, **56**, 2019-2035

Heck, R. M. and Farrauto, R. J. (2001) Automobile Exhaust Catalysts, *Applied Catalysis A*: General **221**, 443-457.

Iliyas, A., Zahedi-Niaki, M.H., Eic, M. and Kaliaguine, S. (2007) Control of Hydrocarbon Cold-start Emissions: A Search for Potential Adsorbents, *Microporous and Mesoporous Materials*, **102**. 171-177,

Kaspar, J., Fornasiero, P., Hickey, N. (2003) Automotive Catalytic Converters: Current Status and Some Perspectives. *Catalysis Today*, **73**, 419–49.

Knafl, A., Bohac, S.V., Han, Assanis, D.N. and Szymkowicz, P. G. (2007) Comparision of Diesel Oxidation Catalyst Performance on an Engine and a Gas Flow Reactor, SAE 2007-01-0231.

Koltsakis, G.C., and Stamatelos, A.M. (1997) Catalytic Automotive Exhaust After Treatment, *Progress in Energy Combustion Science*, **43**, 1-39.

Motor Industry Facts (2009) Available from: http://www.smmt.co.uk/downloads/MotorIndustryFacts2009.pdf [Accessed 18 December 2009].

UK National Statistics Yearbook (2004) Available from: http://www.statistics.gov.uk/downloads/theme_compendia/UK2004/UK2004.pdf [Accessed 18 December 2009].

Nibbelke, R. (1998) *Steady State, Transient and Non-linear Kinetics in Automobile Exhaust Gas Catalysis*, PhD thesis, Technical University of Eindhoven.

Pelters, S., Kaiser, F.W., Mauss, W. (1989) The Development and Application of a Metal Supported Catalyst for Porsches 911 Carrera 4, SAE 890488.

Santos, H. and Costa, M. (2008) Evaluation of the Conversion Efficiency of Ceramic and Metallic Three Way Catalytic Converters, *Energy Conversion and Management*, **49**(2), 291-300.

Sideris, M. (1998) *Methods for Monitoring and Diagnosing the Efficiency of Catalytic Converters: A Patent-oriented Survey (Studies in Surface Science and Catalysis),* Elsevier Science, Amsterdam.

Stone, R. (1999) *Introduction to Internal Combustion Engines*, 3rd revised Ed, MacMillian Publishers, London.

Williams, J.L. (2001) Monolith Structures, Materials, Properties and Uses, *Catalysis Today*. **69**, 3-9.

Yap, Y. (2010) PhD thesis: *On-line and on-engine catalyst characterisation: effective diffusion and reaction mechanisms,* University of Bath.

# 2. Literature review – to set the scene

In the literature, there are many general reviews on the subject of catalytic converters and catalytic combustion (e.g. Koltsakis and Stamatelos, 1997; Farrauto and Heck, 1999; Heck and Farrauto, 2001; Cybulski and Moulijn, 2006), so this chapter considers more relevant literature to set the scene for the work that follows.

In this chapter, general modelling approaches and experimental techniques for both bench-top experiments and engine trials are considered. Based on information in the literature, useful conversions are presented in Appendix 1, then in Appendix 2, Nusselt numbers for different duct shapes are described.

## 2.1 Modelling studies on catalytic converter

The mathematical modelling of catalytic converters has been extensively studied over last decade. There are many examples in the literature where the energy balances are described in a rigorous manner in differential form, and a numerical method based on finite difference method, (e.g. Oh and Cavendish,1982), or finite element (e.g. Hayes *et al.*, 1992; Hayes and Mukadi, 2002) is used to solve the system of coupled equations.

In some of the models, equations are solved for gas flow in one of the monolith channels, and it is assumed that all of the other channels behave in an identical manner (e.g. Oh and Cavendish, 1982; Siemund *et al.*, 1996). In other models, the converter is represented as a continuum, consisting of a homogeneous structure containing both a gas and a solid phase (e.g. Zygourakis, 1989).The models may have been developed by the authors (e.g. Hayes and Mukadi, 2002), or the authors made use of a proprietary CFD code (e.g. Shamim *et al*., 2002, Wang *et al*., 2004; Chen *et al*., 2004; Mazumder, 2007; Arrighetti *et al*., 2007).

One major drawback of these rigorous techniques is that when these equations are coupled with the material balances (with nonlinear reaction terms), the resulting system of equations is complex and stability problems are often encountered. In the solution algorithm, this also leads to long simulation run times. Therefore, some modellers are seeking ways in which to reduce computational run times.

### 2.1.1 Models using the NTU method

The NTU (Number of Transfer Unit) method has been developed to reduce computational run time, and improve the stability of solutions. There are a number of examples in the literature where this technique has been used (e.g. Lubeski *et al*., 2000). The key heat transfer equations as presented in Lubeski *et al*. (2000) are summarised in Table 2.1.

The basis of the NTU method described in Lubeski *et al*. (2000) is a steady-state heat transfer model without reactions; thus, it is based on energy conservation in the gas phase and energy conservation in the solid phase. The equations were analytically rearranged to a format where the temperatures of the solid and the fluid at a current time step are functions of those at the last time step. On the other hand, the initial condition (temperature) is described in terms of air flow rate and change of air/fuel ratio (empirical equation from experimental data). The heat released from the reaction was determined from the reaction rate of CO oxidation.

Lubeski *et al*. (2000) constructed their model in a manner such as to predict only the average solid temperatures at the front and the rear of a catalytic converter. Moreover, the basis of the model is strongly dependent on their experimental data. Therefore, the capability and application of this earlier model is very limited. For example, it cannot predict the conversion of pollutants, or produce a solid temperature distribution along the monolith.

However, the basis of their heat transfer model using the NTU method was valuable to others. Blohm *et al*. (2003) modified the heat transfer equations from Lubeski *et al*. (2000) to account for heat conduction in the solid phase and heat loss to the surroundings. They concluded that the model showed comparable results with a full finite difference approach, yet had the potential for shorter computer run times. A derivation of the basis of the heat transfer model using the NTU method is presented in Appendix 3.

**Table 2.1** Summary of key heat transfer equations developed in Lubeski *et al*. (2000).

| | **Equations** |
|---|---|
| Heat transfer rate | $q = h\,A_s\,\Delta t\left(T_{g,0}\dfrac{\varepsilon_s}{\left(1+\dfrac{\varepsilon_s}{\varepsilon_t}-\varepsilon_s\right)}-T_{s,0}\dfrac{\varepsilon_t}{\left(1+\dfrac{\varepsilon_t}{\varepsilon_s}-\varepsilon_t\right)}\right)$ |
| Average gas temperature of a element length, $\ell$ | $T_{g,\ell}=T_{g,0}\text{-}NTU_h\left(T_{g,0}\dfrac{\varepsilon_s}{\left(1+\dfrac{\varepsilon_s}{\varepsilon_t}-\varepsilon_s\right)}-T_{s,0}\dfrac{\varepsilon_t}{\left(1+\dfrac{\varepsilon_t}{\varepsilon_s}-\varepsilon_t\right)}\right)$ |
| Average solid temperature of a time step, θ | $T_{s,\theta}=T_{s,0}+BiFo\left(T_{g,0}\dfrac{\varepsilon_s}{\left(1+\dfrac{\varepsilon_s}{\varepsilon_t}-\varepsilon_s\right)}-T_{s,0}\dfrac{\varepsilon_t}{\left(1+\dfrac{\varepsilon_t}{\varepsilon_s}-\varepsilon_t\right)}\right)$ |
| Gas heat transfer effectiveness | $\varepsilon_s=\dfrac{1-e^{-NTU_h}}{NTU_h}$ |
| Solid heat transfer effectiveness | $\varepsilon_t=\dfrac{1-e^{-BiFo}}{BiFo}$ |
| Biot-Fourier number | $BiFo=\dfrac{h\,A_s\theta}{(m\,C_P)_s}$ |
| The Number of Transfer Unit | $NTU_h=\dfrac{h\,A_s}{(m\,C_P)_g}$ |

### 2.1.2 Correlations for heat and mass transfer coefficients

An advantage of a 1-D model over a 2-D model is mainly in computation time. However, when using a 1-D model, heat and mass transfer coefficients need to be assigned. The heat transfer coefficient is obtained from a Nusselt number. The mass transfer coefficient is obtained from a Sherwood number. This aspect has been discussed in considerable detail in Hayes and Kolaczkowski (1997; pp. 313 – 318). They describe a number of correlations for the calculation of Nusselt Numbers (and Sherwood Numbers):

a) Heck *et al.* (1976) developed correlations for non-reacting fluids in circular channels using Graetz number for the case of a thermally developing flow with hydrodynamically fully developed flow). For the constant wall temperature the correlation is:

$$Nu_T = 3.657 + 6.874\left(\frac{1000}{Gz}\right)^{-0.488}\exp\left(-\frac{57.2}{Gz}\right) \qquad (2.1)$$

and for constant wall heat flux:

$$Nu_H = 4.364 + 8.68\left(\frac{1000}{Gz}\right)^{-0.5386}\exp\left(-\frac{48.2}{Gz}\right) \qquad (2.2)$$

b) Tronconi and Forzatti (1992) developed a correlation for the simultaneous (both hydrodynamiclly and thermally) boundary layer development for constant wall temperature:

$$Nu_T = 3.657 + 8.827\left(\frac{1000}{Gz}\right)^{-0.545}\exp\left(-\frac{48.2}{Gz}\right) \qquad (2.3)$$

the corresponding correlation for simultaneously developing flow with constant wall flux as determined by Hayes *et al.* (1996) is:

$$Nu_H = 4.364 + 13.18\left(\frac{1000}{Gz}\right)^{-0.524}\exp\left(-\frac{60.2}{Gz}\right) \qquad (2.4)$$

and,

$$Gz = \mathrm{Re}\,\mathrm{Pr}\frac{D_H}{z} \qquad (2.5)$$

c) The Sherwood number can be obtained by substituting the Schmidt number, *Sc*, for the Prandtl number in Equation (2.5):

$$Gz = \mathrm{Re}\, Sc \frac{\mathrm{D_H}}{\mathrm{z}} \qquad (2.6)$$

where *Re* is Reynolds number, *Pr* is Prandtl number and *z* is the distance from the entrance in the direction of gas flow in metres (the dimensionless numbers are summarised in Appendix 4).

d) The following expressions can be used for a square shaped channel (developed by Groppi *et al*., 1995), in the thermally developed region with hydro-dynamically developed flow:

For constant wall temperature:

$$Nu_T = 2.977 + 6.854 \left(\frac{1000}{Gz}\right)^{-0.5174} \exp\left(-\frac{42.49}{Gz}\right) \qquad (2.7)$$

and, for constant wall heat flux:

$$Nu_H = 3.095 + 8.933 \left(\frac{1000}{Gz}\right)^{-0.5386} \exp\left(-\frac{6.7275}{Gz}\right) \qquad (2.8)$$

e) Groppi *et al*. (1995) proposed that the value of *Nu* in a system with chemical reaction at the wall could be approximated by interpolating between $Nu_T$ and $Nu_H$ using the interpolation formula of Brauer and Fetting (1966):

$$\frac{Nu\text{-}Nu_H}{Nu_T\text{-}Nu_H} = \frac{Da \cdot Nu}{(Da + Nu) \cdot Nu_T} \qquad (2.9)$$

the Damköhler number, *Da*, is a ratio of the rate of reaction to the rate of diffusion to the wall and depends on the reaction kinetics (further explanation in Appendix 4).

f) For fully developed laminar flow, the Nusselt number can be a constant value (from which the heat transfer coefficient is calculated) and this depends on the shapes of the channel - this is described in Appendix 2. For developing laminar flow, the entrance effect should be considered. The local values of Nusselt number have to be determined using Equation (2.7) or (2.8), where the Graetz number describes entrance effects for the flow of gas in a monolith channel. The values of local Sherwood numbers can also be determined by substituting Equation (2.6).

### 2.1.3 Reaction rate expressions

There are many forms of kinetic expression available in the literature. In the classic work by Voltz *et al.* (1973), the kinetics of carbon monoxide and propylene oxidation were studied on a platinum-alumina catalyst (pellets) using a synthetic gas mixture under lean conditions. The kinetic expressions for the two reactants were proposed to be of a Langmuir-Hinshelwood-Hougen-Watson (LHHW) form, as follows:

Rate of CO oxidation:

$$r_{CO} = -\frac{k_{r1} C_{CO} C_{O_2}}{R(\theta)} \tag{2.10}$$

Rate of $C_3H_6$ oxidation:

$$r_{C_3H_6} = -\frac{k_{r2} C_{C_3H_6} C_{O_2}}{R(\theta)} \tag{2.11}$$

where the inhibition term, R(θ), was represented as:

$$\begin{aligned} R(\theta) = {} & (1 + k_{a1} C_{CO} + k_{a2} C_3 H_6)^2 \times \\ & (1 + k_{a3} C_{CO}{}^2 C_{C_3H_6}{}^2) \times (1 + k_{a4} C_{NO}{}^{0.7}) \end{aligned} \tag{2.12}$$

The temperature dependence of the kinetic parameters $k_{ri}$ and $k_{ai}$ are presented in an Arrhenius form:

$$k_{ri} = k^0{}_{ri} \exp\left( \frac{-E_{r\,i}}{R_g (T_s + 460)} \right) \tag{2.13}$$

$$k_{ai} = k^0{}_{ai} \exp\left( \frac{-E_{a\,i}}{R_g (T_s + 460)} \right) \tag{2.14}$$

The first term in Equation (2.12), $(1 + k_{a1} C_{CO} + k_{a2} C_3 H_6)^2$, is a function that accounts for the inhibition effects due to chemisorption of CO and $C_3H_6$. The second term, $(1 + k_{a3} C_{CO}{}^2 \; C_{C_3H_6}{}^2)$, is used to fit experimental data at higher concentrations of CO and $C_3H_6$. The last term, $(1 + K_{a4} C_{NO}{}^{0.7})$, represents the inhibition effects of NO on the oxidation of CO and $C_3H_6$.

These LHHW forms of rate expression have been widely used in the literature (e.g. Oh and Cavendish, 1982; Pontikakis *et al*., 2004; Triana *et al*., 2003; Kim and Kim, 2009). Oh and Cavendish (1982) used the slightly different specific reaction rate

expressions for the oxidation of CO, $C_3H_6$, and $CH_4$, which were obtained by calibrating the rate equations of Voltz *et al.* (1973) against the recycle reactor data obtained in their laboratory (Schlatter and Chou, 1978). In this calibration, only the pre-exponential factors of the rate constants were adjusted, without changing the activation energies and adsorption equilibrium constants given by Voltz *et al*.(1973). The rate expressions are shown as follows:

Rate of CO oxidation:

$$R_{CO} = \frac{k_1 C_{CO} C_{O_2}}{G} \quad \frac{\text{mol CO}}{\text{cm}^2\ (\text{Pt}) \cdot \text{s}} \tag{2.15}$$

Rate of $C_3H_6$ oxidation:

$$R_{C_3H_6} = \frac{k_2 C_{C_3H_6} C_{O_2}}{G} \quad \frac{\text{mol C}_3\text{H}_6}{\text{cm}^2\ (\text{Pt}) \cdot \text{s}} \tag{2.16}$$

Rate of $CH_4$ oxidation:

$$R_{CH_4} = \frac{k_3 C_{CH_4} C_{O_2}}{G} \quad \frac{\text{mol CH}_4}{\text{cm}^2\ (\text{Pt}) \cdot \text{s}} \tag{2.17}$$

where,

$$G = T \times (1 + K_1 C_{CO} + K_2 C_3 H_6)^2 \times (1 + K_3 C_{CO}{}^2 C_{C_3H_6}{}^2) \times (1 + K_4 C_{NO}{}^{0.7}) \tag{2.18}$$

$$k_1 = 6.699 \times 10^9 \ \exp\left(\frac{-12556}{T}\right) \tag{2.19}$$

$$k_2 = 1.392 \times 10^{11} \ \exp\left(\frac{-14556}{T}\right) \tag{2.20}$$

$$k_3 = 7.326 \times 10^6 \ \exp\left(\frac{-19000}{T}\right) \tag{2.21}$$

and

$$K_1 = 65.5 \ \exp\left(\frac{961}{T}\right) \tag{2.22}$$

$$K_2 = 2.08 \times 10^3 \ \exp\left(\frac{361}{T}\right) \tag{2.23}$$

$$K_3 = 3.98 \ \exp\left(\frac{11611}{T}\right) \tag{2.24}$$

$$K_4 = 4.97\times10^5 \ \exp\left(\frac{-3733}{T}\right) \tag{2.25}$$

Comparing the inhibition terms in Equation (2.12), and Equation (2.18), then in Equation (2.18), *T*, is added to represent a temperature dependence factor using the modified Arrhenius form in the reaction rate. These rate expressions have been widely used for converter modelling, e.g. Zygourakis (1989) and Siemund *et al.* (1996). Triana *et al*. (2003) adopted the activation energies of CO and THCs oxidations from Voltz *et al.* (1973) and Oh and Cavendish (1982), and the NO activation energy from Athanasios *et al.* (2000) to perform the model calibration, where the pre-exponential factors are fine tuned to match the experiment results from a diesel oxidation catalyst connected to a live engine. Kim and Kim (2009) carried out a similar study to Triana *et al*. (2003). To determine the kinetic parameters that best fit the experimental results (from engine trials using DOC), a two-step kinetic parameters estimation method was used. The final pre-exponential factors and activation energies were determined. These are listed and compared with the values from other data in the literature in Table 2.2. The K1 to K4 terms (in Equations (2.22) to (2.25)) where the same in all of the papers in Table 2.2.

**Table 2.2** Some examples of information on rate constants in the LHHW form of rate expression.

| | | **Pre-exponential factor (mol K $m^{-2}$ $s^{-1}$)** | **Activation energy (J $mol^{-1}$)** |
|---|---|---|---|
| **Siemond *et al.* (1996): 3-way Catalyst** | CO | $6.69\times10^{13}$ | 104390 |
| | HCs | $1.392\times10^{15}$ | 121018 |
| | $NO_x$ | $3.067\times10^{12}$ | 72922 |
| **Triana *et al.* (2003): DOC** | CO | $4.51\times10^{13}$ | 104390 |
| | HCs | $1.108\times10^{15}$ | 121018 |
| | $NO_x$ | $2.727\times10^{11}$ | 90622 |
| **Kim and Kim (2009): DOC** | CO | $4.49993\times10^{13}$ | 80140 |
| | HCs | $9.77310\times10^{6}$ | 33560 |
| | $NO_x$ | $3.6526\times10^{8}$ | 51930 |

Sampara *et al*. (2007) determined global oxidation kinetics for propylene ($C_3H_6$), CO, $H_2$, and NO over platinum (Pt) catalyst with simulated diesel exhaust between 200 and 415 °C and over a wide range of concenrations. Propylene ($C_3H_6$) was used to present the HCs from a diesel engine exhaust. An integral reactor with high space velocity capability (up to 2 million $h^{-1}$) was used to generate low and moderate

conversion data for the rate-generation process. Finally the proposed kinetics was employed in a mathematical model, and validated against the results of engine tests with a Full-scale DOC. The comparison showed the measured conversion efficiency increased more rapidly than the simulation.

Recently, some studies have proposed very detailed mechanistic reaction schemes for catalytic converter modelling. For example, Salomons *et al*. (2007) proposed detailed mechanisms for the oxidation of CO on converters with Pt catalyst. They believed that LHHW expressions are best suited for steady state operation, and are not well suited for transients. On the other hand, LHHW rate expressions do not capture the change in the adsorbed species on the surface with time, and are also less suited for extrapolation and engineering design, owing to the limited range of conditions over which they have been developed and hence are valid. In addition to Salomons'work, a few researchers proposed the full reaction schemes for three way catalytic converter (e.g. Koltsakis and Stamatelos, 1997; Nibbelke *et al.*,1998; Chatterjee *et al*., 2001; Kwon *et al.*, 2007).

In the literature review in Sampara *et al.* (2008), they concluded that using the rate expression forms suggested by Voltz *et al.* (1973), together with kinetic parameters calibrated against an experimentally measured light-off curve (e.g. Oh and Cavendish, 1982), then this would often (a) confine the kinetics to a narrow temperature window, and (b) not be adequate when applied to other reactor operating conditions. In addition, they believed that the reaction rates developed by them for DOC would be different from Voltz *et al*.(1973) since "*The reaction rates developed by Voltz et al. were under slightly lean conditions with high reductant concentrations* (CO, THCs, and $H_2$)*, which are typically seen in gasoline exhaust. Diesel exhaust on the other hand has substantially higher $O_2$ levels, and concentrations of CO, THCs, and $H_2$ are also lower*."

In Sampara *et al.* (2007), a commercial DOC was used, and THCs were split into two groups: (a) partially oxidized THCs (represented by $C_3H_6$), and (b) unburnt fuel, (represented by Swedish low sulfur diesel fuel (DF)). The rate expressions are listed as follows:

$$r_i = \frac{k_i c_{s,i} c_{s,O_2}}{G} \ \frac{\text{mol}}{\text{mol (site)} \cdot \text{s}} \quad i = \text{DF}, \text{C}_3\text{H}_6, \text{CO}, \text{H}_2 \tag{2.26}$$

$$r_{NO} = \frac{k_{NO} c_{s,O_2}}{G_{NO}} \left( c_{s,NO} \sqrt{c_{s,O_2}} - \frac{c_{s,NO_2} \sqrt{c_R}}{K_{eq}} \right) \frac{\text{mol}}{\text{mol (site)} \cdot \text{s}} \tag{2.27}$$

where:

$$k_i = A_i \exp\left(\frac{E_i}{RT}\right) \tag{2.28}$$

$$K_i = Aa_i \exp\left(\frac{Ea_i}{RT}\right) \tag{2.29}$$

$$G = \left(1 + K_{co} c_{s,CO}\right)^2 \left(1 + K_{NO} c_{s,NO}\right) \tag{2.30}$$

$$G_{NO} = \left(1 + K_{DF} c_{s,DF}\right)^2 \left(1 + K_{NO} c_{s,NO}\right) \tag{2.31}$$

The final rate constants are summarised in Table 2.3. Within the scope of this PhD study, only LHHW rate expressions would be used to model DOCs (in the case studies explored in Chapter 4). Mechanistic models would be explored in a parallel PhD project by Y.Yap.

**Table 2.3** Rate constants after final optimisation in Sampara *et al.* (2007).

| **Pre-exponential Rate constant** | **$m^6$ $mol^{-1}$ mol-site$^{-1}$ $s^{-1}$** | **Activation energy Rate constant** | **J $mol^{-1}$** |
|---|---|---|---|
| $A_{HC}$ | $1.123\times10^9$ | $E_{HC}$ | 51560 |
| $A_{CO}$ | $3.725\times10^6$ | $E_{CO}$ | 22130 |
| $A_{H2}$ | $1.335\times10^7$ | $E_{H2}$ | 30320 |
| $A_{NO}$ | 1086 | | |
| **Pre-exponential Adsorption constant** | **$mol^{-1}$ $m^{-3}$** | **Activation energy Adsorption constant** | **J $mol^{-1}$** |
| $Aa_{CO}$ | 10.57 | $Ea_{CO}$ | -9709 |
| $Aa_{NO}$ | 32.19 | $Ea_{NO}$ | -19010 |

## 2.2 Effect of pulsating flow on the performance of catalytic converters

In a real engine exhaust, pulsation is present due to the nature of engine operation. Zhao *et al.* (1997) characterized the exhaust flow structure inside a catalytic converter (under floor fitted) retro-fitted to a firing four-cylinder gasoline engine over different operating conditions using cycle-resolved laser doppler velocimetry (LDV) technique. Therefore, it is important to understand the effects of pulsation flow on the heat transfer of catalytic converter before developing the mathematical models. In the literature, most of the converter models ignored the pulsation flow without any explanations (e.g.

Zygourakis, 1989; Siemund *et al.*, 1996). Only a few researchers studied this effect experimentally (e.g. Benjamin and Roberts, 2001), or theoretically (using CFD modelling technique, e.g. Tsinoglou and Koltsakis, 2005). These aspects are reviewed in more detail, since they are not only helpful in understanding the pulsation flow effect, but also helpful in designing the experiments and the construction of mathematical models.

### 2.2.1 Effect of pulsating flow on the warm-up of a catalytic converter under non-reacting conditions

**Benjamin and Roberts (2001)**: they studied the flow pulsation effect on the warm-up of a catalytic converter at non-reacting condition. The motivation for this work was to improve the understanding of catalyst warm-up. According to Benjamin and Roberts (2001): "*It can take up to 60 s for the substrate to be warmed by the gases from the engine to a temperature at which the catalyst becomes active*." This period is important as unconverted exhaust gases escape to the environment (also known as 'cold-start' effect).

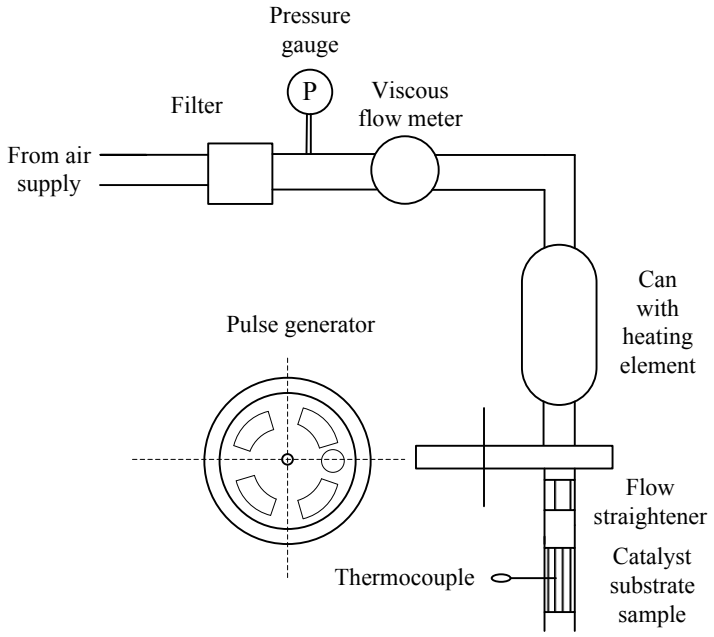


**Figure 2.1** Schematic diagram of experimental apparatus and rotating disc system (adapted from Benjamin and Roberts, 2001).

The authors took a special interest in the effect that pulsating flow from the movement of pistons in an engine may have on heat transfer. Their experiments were not performed on a live engine. Instead they used an air supply and an electric heater, and simulated the pulsations by interrupting the air flow with a rotating disc. They

performed experiments with mass flow pulsations in the range of 32 to 100 Hz. A schematic of the experimental apparatus is illustrated in Figure 2.1.

From the discussion in their literature review, and the discussion of their own work, the following important observations/statements have been captured that are relevant to this study:

(a) In a four cylinder four-stroke engine:

- There are two pulses per revolution (therefore at 1000 rpm pulsation correspond to 33 Hz).
- The exhaust mass flow fluctuates approximately sinusoidally without flow reversal.
- The pulsation amplitude is in the region of 80 to 90 percent of the mean.

(b) Views appear to differ about whether or not pulsating flow has a significant effect on heat transfer. However, in general, it appears to be accepted, that without flow reversal, the effect is small.

(c) Simulations of the warm-up of a converter were performed with the aid of a CFD code, and these were considered to be 'time consuming'. They found that a porous medium model (1-D) ran much more quickly, but required values of heat transfer coefficients as an input.

(d) Heat transfer coefficients were calculated from an assigned value of Nusselt Number = 3.608 (fully developed flow in square channel). Then to allow for entrance effects, they increased the value of the heat transfer coefficients by a factor of 1.9, 1.4, 1.2, 1.15 and 1.1, at 2.5 mm intervals in the entrance to the monolith.

(e) They presented in considerable detail the results of their transient experiments, and these could be used to test the heat transfer model developed in this thesis.

(f) A non-washcoated monolith substrate was used for this study, which was 50 mm o.d. and 150 mm long.

(g) Substrate temperatures were measured with 0.5 mm K-type thermocouples. These were inserted to a depth of 15 mm, through 0.7 mm holes and were taped so that their tips were forced into contact with a channel wall. [Note: this may create some uncertainty as to whether the gas, solid, or combined temperature was being measured].

(h) From their heat transfer study, they concluded that: *"When making Computational Fluid Dynamics* (*CFD*) *predictions for real systems, use of steady flow rather than pulsating flow would introduce negligible error and would have the advantage of providing significant reductions in computational effort"*. [Note: they did not study these effects under reaction conditions].

(i) They recognised that in real applications, there is a velocity distribution across the face of the catalyst (e.g. with conical diffusers), so the situation is more complex than they studied, and this was the subject of further work.

**Benjamin *et al.* (2002)**: In subsequent work, they studied the effect of pulsating flow on flow distribution. The following important observations/statements have been captured that are relevant to this thesis:

(a) They used two piezo-ceramic pressure sensors from Druck to measure the pulsating flow.

(b) They used a TSI IFA 300 constant temperature HWA (Hot wire anemometry) system to measure velocity.

(c) In their work, a two ceramic substrates system was used. Their o.d. was 118 mm, cell density was 62 cells $cm^{-2}$, and length was 152 mm and 102 mm.

(d) In non-pulsating flow experiments, at a Reynolds number of 20,000 (based on 48 mm i.d. inlet pipe) the static pressure drop was approximately 75 Pa (0.75 mbar). At $Re$ = 80,000 then pressure drop was approximately 270 Pa (2.7 mbar).

(e) From their experiment results, they concluded that: the pulsating flow would improve the flow uniformity, and it would also reduce the pressure drop.

This research group also had a number of publications in the topic of pulsating and flow distribution. For example, Liu *et al.* (2003) investigated the flow maldistribution across the monolith substrate and the results were compared with that obtained in an earlier study (Benjamin *et al.*, 2002). CFD was used to simulate different input pulse shapes, which were compared with experimentally measured pulse shapes. A number of observations/statements have been captured that are relevant to this thesis.

(a) They believed that flow maldistribution depends on three factors: mass flowrate (engine load), pulsation frequency (engine speed), and pulse shape (load, speed and engine configuration).

(b) They found that flow is more maldistributed with an increase in mass flow rate, and it is in general more uniformly distributed with an increase in pulsating frequency.

(c) They also found that the degree of flow maldistribution is largely influenced by the shape of inlet pulse shapes. The higher peak/mean ratio (means the peak gas velocity/the mean velocity of gas) leads to less flow maldistribution at all frequencies.

(d) They suggested that the net effect of these parameters on flow distribution needs to be evaluated on running engines.

### 2.2.2 Effect of pulsating flow on the performance of catalytic converters

Recently, Tsinoglou and Koltsakis (2005) extended the study of Benjamin and Roberts (2001) to assess the effect of pulsation on the performance of a close coupled three way catalytic converter. A fully transient 1-D channel problem was solved for some extremely transient operation modes. The simulation results were compared to that obtained by the models using quasi-steady-state approach. The main assumption of their model was that the pollutant conversion depends only on the mass transfer in the gas phase. In this case, they only considered THCs in their model, because they believed that the hydrocarbons are known to have the lowest diffusivity among the pollutants encountered in gasoline engine exhaust gas. A few observations/statements have been captured that are relevant to this thesis.

a) According to the simulation results, they found that the instantaneous pollutant emissions of a catalytic converter operating under pulsating flow were shown to depend on the gas residence time inside the channel, and the pulse duration. As a result, the quasi-steady-state approach used in many mathematical models may give different results (from a fully transient approach), especially in the case of extreme transients, which can be encountered in close-coupled applications.

b) A parametric analysis was performed to assess the effect of engine operating point, catalyst active length, and pulsation pattern on close-coupled catalyst performance under pulsating flow. Both for very low and for very high values of the residence time, the effect of pulsations is negligible. For residence time values found near the middle of the expected range, the pulsating flow

conversion presents a deviation from steady state conversion. The magnitude of this deviation depends significantly on pulsation pattern.

c) The pulsation pattern is a very critical parameter. The influence of pulsating flow starts to become important when the maximum pulse velocity is more than two times higher than the average velocity. For lower peak velocity values, the influence of pulsations on pollutant conversion is less than 4%, and the accuracy of the steady state approach is expected to be sufficient. At higher peak velocities, flow pulsations have a detrimental effect on pollutant conversion.

d) The exact shape and intensity of the pulsations depends on the engine and exhaust design and operational characteristics. They suggested that a more detailed investigation on this topic could involve using mass flow rate data from engine models as input to the simplified channel model.

### 2.2.3 Conclusions

From the literature review on the effect of pulsating flow on the performance of a catalytic converter, it has been decided not to simulate pulsating flow in mathematical models developed in this PhD thesis, for the following reasons:

a) The experimental data presented in Benjamin and Roberts (2001) confirms that the effect on heat transfer during warm-up caused by mass pulsations is small, and would not be significant in a practical situation of catalyst warm-up.

b) From the modelling study in Benjamin and Roberts (2001), they concluded that: *"When making Computational Fluid Dynamics (CFD) predictions for real systems, use of steady flow rather than pulsating flow would introduce negligible error and would have the advantage of providing significant reductions in computational effort."*

c) Although a theoretical study has showed that at certain conditions pulsation can become important to the performance of the catalytic converter; in this study, the DOC would be used as a under floor installation. Therefore, the effect of pulsating flow would be very much less than in a close coupled installation.

## 2.3 Experimental studies of catalytic converters

In the literature, there appear to be more papers focusing on the theory (e.g. modelling) than papers providing comparisons between simulations and experimental data. Although there are a number of experimental studies in the literature, the following are considered in more detail, as they provide information, which is very relevant to the design of the experiment in this thesis.

### 2.3.1 Three-way monolith converter: simulations *versus* experiments (Siemund *et al.*, 1996)

The objective in their work was to develop a simple adiabatic one-dimensional (1-D) model for a three-way catalytic converter. Although, Siemond *et al.* (1996) did not use a DOC for their study, there is some every useful information which will help. Following an extensive literature review on this topic, they divided the assumptions used in their model into three groups.

The 1st group is made of widely accepted and most probably reliable assumptions:

a) The monolith is a pseudo-homogeneous cylinder of circular cross section.
b) The gas phase is ideal at uniform and constant pressure.
c) The accumulation terms in the gas phase are neglected.
d) Transverse diffusion and laminar flow are accounted for by the film model.
e) Heat conduction in the gas phase is neglected.
f) The reactants are much diluted and the chemical expansion flux is neglected.

The validity of their 2nd group of assumptions is more questionable:

a) The catalyst does not deactivate.
b) Steady-state reaction kinetics can be used in the transient state.
c) Oxidation and reduction of the catalyst ($CeO_2$, Rh) is not accounted for.

The validity of their 3rd group of assumptions may also be debated:

a) Heat transfer by radiation, is neglected.
b) The residual HCs are accounted for by a single lumped species.
c) Only four reactions are accounted for ($CO/O_2$, $HC/O_2$, $H_2/O_2$ and $NO_x/CO$).
d) The development of a laminar flow zone is neglected.

The heat and mass transfer coefficients were obtained from Nusselt and Sherwood numbers. They chose the asymptotic number 2.89 for both Nusselt and Sherwood numbers at a constant wall flux situation (since they assumed the flow regime is fully developed and this number was proven to be successful in Chen and Cole (1989)). The rate expressions for the reactions were adopted from Oh and Cavendish (1982) in LHHW form (discussed earlier in Section 2.1.3).

A series of experiments was also performed on a gasoline engine and the results were compared with the simulations. From the description of their experiments, a number of important observations/statements have been captured, which are relevant to this study:

(a) A standard three-way catalyst (Corning, cordierite, square channels) in the form of a round ceramic monolith was used in their study. Prior to the experiment, the catalyst was conditioned for 2 hours at 550 to 600$^{o}$C under stoichiometric exhaust gas.

(b) To obtain time and space-resolved temperatures, 17 thermocouples were introduced in the monolith channels from the rear face, and they were evenly distributed. The front face of these channels was plugged with cement, see Figure 2.2.

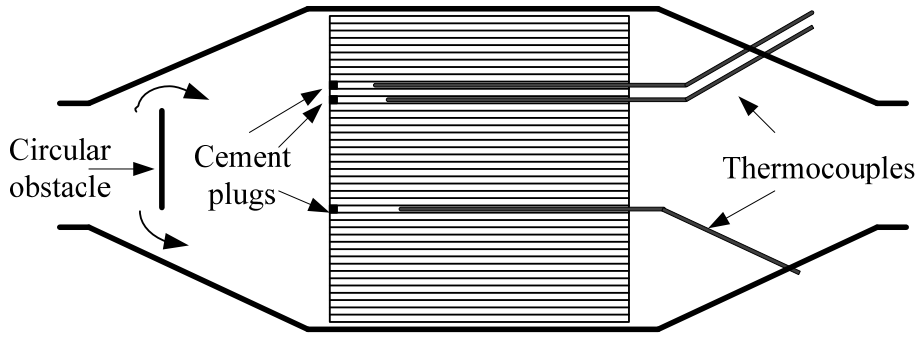


**Figure 2.2** Schematic illustrates the position of thermocouples and obstacle in the inlet cone to distribute the flow (modified from Siemund *et al.*, 1996).

(c) A four-cylinder Renault *J7T 754* gasoline engine was used, with a 2165 cm$^3$ displacement, and electronic fuel injection. All the tests at stoichiometry were made under closed loop air/fuel control using the original EFI computer on the engine. An external control unit (AMAP 3, Renault) was used for the other tests made in open loop.

(d) The exhaust gas temperature was maintained at a desired level by an electrical heater located between the engine and converter. This guaranteed a constant feed

temperature of exhaust gas or allowed the temperature to be manipulated without changing the exhaust gas composition and flowrate, see Figure 2.3.

(e) Gas analyzers: NDIR type for CO, FID type for hydrocarbons, and chemi-luminescence type for $NO_x$. However, $O_2$ was not measured directly; its concentration in the exhaust gas was computed from the lambda values and from other gas concentrations.

A series of validation experiments was performed on the engine system illustrated in Figure 2.3. Specifically, this included: changes in temperature (feed exhaust gas temperature increases-single step and multi-step); changes in air/fuel ratio changes; and changes in gas flowrate changes.

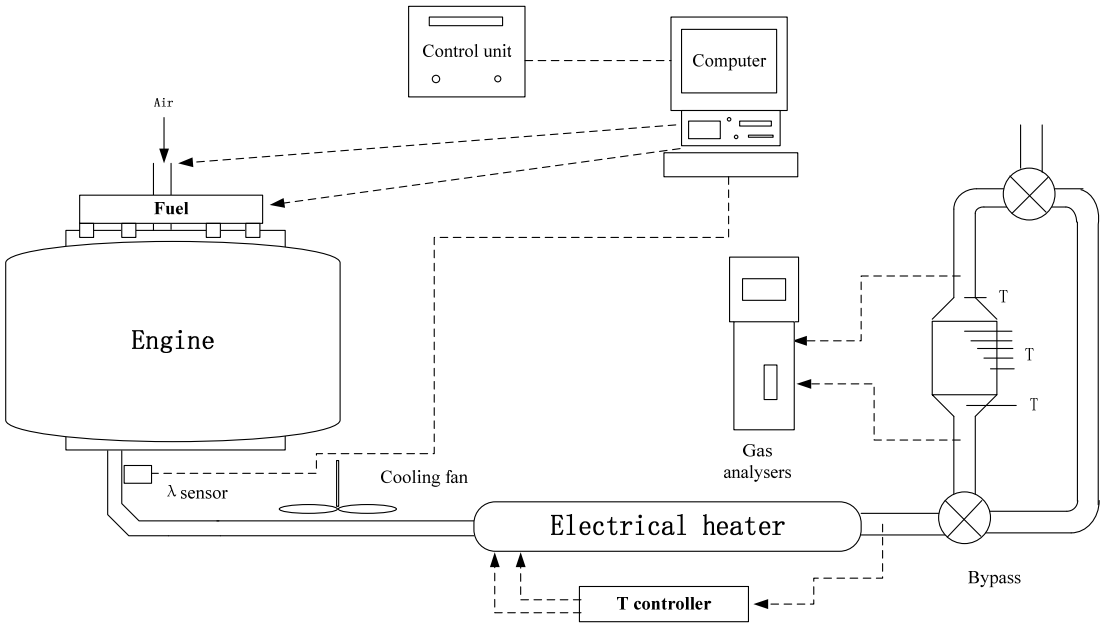


**Figure 2.3** Schematic of the experimental engine bench set-up (modified from Siemund *et al.*, 1996).

From their study the following information is drawn:

(a) "*Considering the simplifying assumptions made, and knowing that the calculations are performed with a unique set of parameters, the agreement between simulation and experimental results is satisfactory – especially under stoichiometric or slightly lean conditions*."

(b) However, the agreement became less satisfactory when the model was used to simulate experiments with fast and large temperature excursions. They suggested two possible reasons that caused the discrepancies:

- accuracy of the experimental data,

- and inaccurate parameters and inappropriate model assumptions.

(c) In their conclusion, they suggested that experimental and theoretical efforts must be put to account for internal diffusion in the catalyst layer.

### 2.3.2 Experiments and numerical simulations of unsteady temperature fields in automotive catalytic converters (Wang *et al*., 2001)

The purpose of this study was to investigate the unsteady warm-up characteristics of the monolith and the effect of inlet cone structure on temperature distribution. They measured unsteady temperature fields of uncoated-monolith and catalytic monolith under real engine operating conditions using thermocouples. A multi-dimensional flow mathematical model was also constructed with the aid of a CFD code, which includes turbulence, heat and mass transfer, and chemical reactions. The model was solved numerically in the entire flow field of the catalytic converter. An outline schematic of the experimental apparatus is illustrated in Figure 2.4.

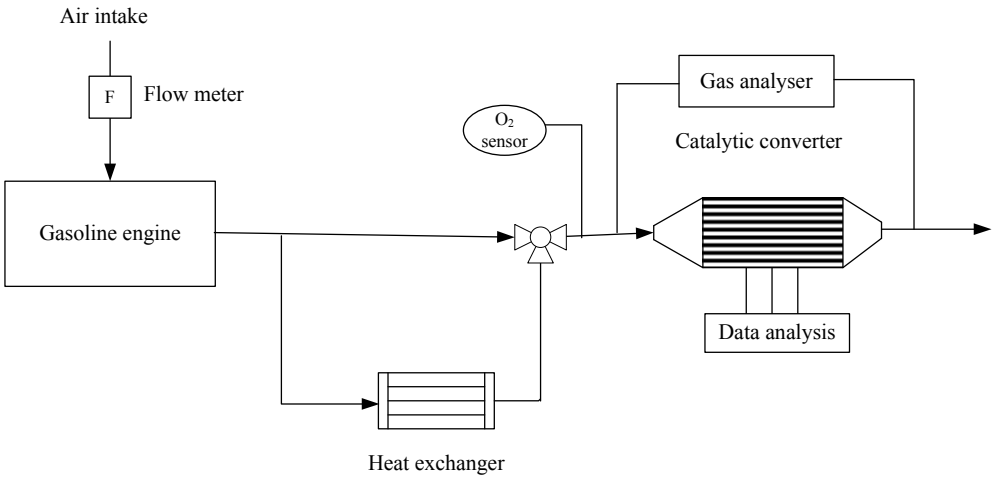


**Figure 2.4** Schematic of experiment rig (adapted from Wang *et al*., 2001).

From the discussion of their own experimental works, the following important observations/statements have been captured that are relevant to this thesis:

(a) They used BN492 S.I. engine (simple point injection system) for the test. The thermocouples (1mm NiCr-NiSi) were inserted into the monolith from the rear end of the monoliths, and the front ends of the channels with thermocouple in them were sealed with a temperature-resisting cement. The tips of some of the thermocouples protruded about 10 mm (out of the front end) for inlet gas temperature measurement. [ Note: this method of thermocouple installation was

similar to that used in some of the experimental studies already described, e.g. Siemund *et al.*, 1996; Benjamin and Roberts, 2001].

(b) A controlled step change in exhaust gas temperature was created by: operating the engine at 2000 rpm, with A/F ratio near the stoichiometric ratio, and mass flowrate at 33 g $s^{-1}$ and the exhaust gas was cooled to 150$^{o}$C by a heat exchanger. As soon as the engine ran steadily at this set of conditions, the valve was switched to allow the exhaust gas to flow directly into the monolith without passing through the heat exchanger, see Figure 2.4. Thus, a temperature step rise was obtained.

(c) Only oxidation reactions of CO and $C_3H_6$ were considered on the channel surface (as a preliminary investigation). Propane was assumed to be a representative of "fast oxidising hydrocarbons". [Note: The reaction rate expressions are identical to those presented in Oh and Cavendish (1982).]

(d) With the aid of CFD, they compared the temperature distributions at two different inlet cone angles, 40$^{o}$ and 120$^{o}$. During the warm-up phase, they found that the 40$^{o}$ cone catalytic converter had a more uniform temperature distribution across the radial direction, but no obvious difference in the axial direction during warm-up stage. However, the 120$^{o}$ cone had a better light-off performance.

### 2.3.3 Catalyst temperature measurement

The measurement of catalyst temperature is relatively difficult, and a number of techniques in the literature are reviewed and discussed. The use of 0.5 mm K-type thermocouples has been reported in a number studies in the literature, e.g. Siemund *et al.* (1996), Hall (2001) and Wang *et al.* (2001). The K-type thermocouple is capable of operating at a high temperature of 1200$^{o}$C. Moreover, the smaller the diameter of the thermocouple, the more sensitive it is to the temperature change (faster response).

Thermocouples may form a tight fit in the monolithic channel (e.g. Kolaczkowski, 1995 and Hayes *et al.*, 1996), ensuring good contact with the wall, such that no gas flow (hence no reactions) could occur in those channels. In Kolaczkowski (1999), the author reviewed Hayes *et al.* (1996) and pointed out that *"One of the interesting aspects described in this paper is the recognition and method of quantification of the lag that arose as a result of the thermal capacity of the thermocouple itself. The thermocouple blocks a channel so reactions do not proceed in that channel. Therefore the walls that*

*surround the thermocouple and the thermocouple itself will respond to a change more slowly than the rest of the monolith*."

In another widely adopted method (e.g. Siemund *et al*., 1996; Wang *et al*., 2001), thermocouples are introduced into the monolithic channels from the rear face. The front face of these channels is then plugged with cement. These methods have a number of drawbacks:

Firstly, if the thermocouple is too thick, then this may delay the thermal response (the diameter of the channel is 1.1mm).

Secondly, during assembly the position of the thermocouple may be accidently moved.

Finally, more than one thermocouple cannot be inserted into the same channel, so only one temperature measurement can be performed in that channel.

Some experimentalists have positioned thermocouples by drilling holes in the radial direction at different axial positions. In Hayes and Kolaczkowski (1997; p. 516), a potential disadvantage of this technique was identified: "*the flow in a greater number of channels may be influenced by the inserted thermocouples. This depends on the channel to thermocouple diameter ratio ($D_c/D_T$) and the proportion of channel affected."*

In Hall (2001) the monolith was cut in half along the length with a very fine-toothed band saw. Thermocouples were then inserted and the two parts were cemented together. The cement layer has to be as thin as practically viable since the thermocouples are carefully positioned within this cement layer and it has to be durable enough to hold the two monolith parts together. This method offers relatively better accuracy in the positioning of thermocouple and durability of the system, but the transient temperature readings from the thermocouple may be affected by the heat capacity of the cement. Nevertheless, this method was selected for this study. In Hall (2001), it was shown that axial temperature changes are more significant near the front the monolith, so it was decided to position the thermocouples closer together near the front face.

### 2.3.4 Experimental studies on catalyst light-off

The "light-off" curve of a catalyst is usually an effective tool not only to evaluate the performance of catalyst, but also to validate the mathematical models. In the literature, when catalyst 'light-off' temperatures are quoted, these arise from experiments that are performed in an experimental rig in the laboratory that consists of a catalyst mounted in

a tube (the reactor), using a constant mass flow of gas which contains the reactant gases at a fixed concentration. Then, as the gas inlet temperature is gradually increased, the inlet and outlet concentration of the reactant is measured, and from that the conversion is determined. These results are then plotted as a function of temperature that is known as the light-off curve, e.g. Salomons *et al.* (2006).

**Salomons *et al.* (2006):** they studied CO and hydrogen oxidations on a diesel oxidation catalyst. The monolith converter was loaded with 80 g/ft$^3$ Pt and had a cell density at 400 CPSI. The dimension of the converter was 2.54 cm in diameter and 7.62 cm in length. One of their experimental studies was to produce the CO light-off curve. Synthetic gas was used as feed gas, and its temperature was controlled using a heating element. The CO concentration was measure by IR spectrum after the catalyst. The inlet gas temperature was increased at approximately 0.133 K per second from 350 to 623 K (transient experiment), where it was held constant for 30 mins. Then this experiment was repeated for different inlet concentrations of CO at 500, 1000, 1500 and 2000 ppm, with a constant oxygen concentration of 6 vol%. The light-off curve of CO was produced, as shown in Figure 2.5.

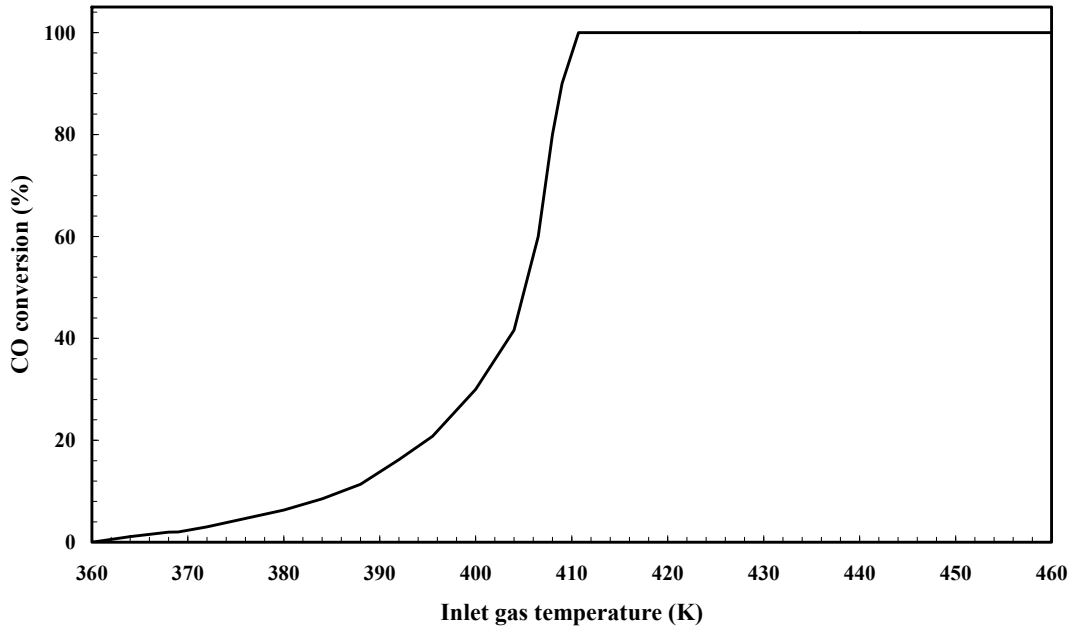


**Figure 2.5** Sketch of the light-off curve for CO (500 ppm inlet concentration) generated in a bench-top experiment (adapted from Salomons *et al*., 2006).

The 'light-off' temperature is normally assigned as the temperature at which 50 % conversion of the limiting reactant is achieved. In the case of a catalytic converter for a diesel engine (DOC), then such experiments should be performed for CO, and also for

HCs. However, THCs in a real diesel engine exhaust can consist of a wide range of different species (e.g. Bohac *et al.*, 2006; Knafl *et al.*, 2006).

**Bohac *et al.* (2006)**: they studied emissions from different engine operation modes. Their experiments were performed on a 1.7 litre 4-cylinder automotive diesel engine equipped with a DOC (400 CPSI, 0.5 litre and 150 g $ft^{-3}$ platinum loading). As one of the outcomes from their study, the hydrocarbon composition from the engine emission was measured using Gas Chromatography (GC) techniques and plotted according to its carbon number, see Figure 2.6.

A more detailed analysis on the individual hydrocarbon species from a diesel engine can be found in Han *et al.* (2008). However, for simplicity, THCs are normally represented by a single component such as propylene, or propane (in the bench-top experiments, e.g. Chandler *et al*., 2000), and also in most of the simulation studies (e.g. Triana *et al.*, 2003; Kim and Kim, 2009) for simplicity.

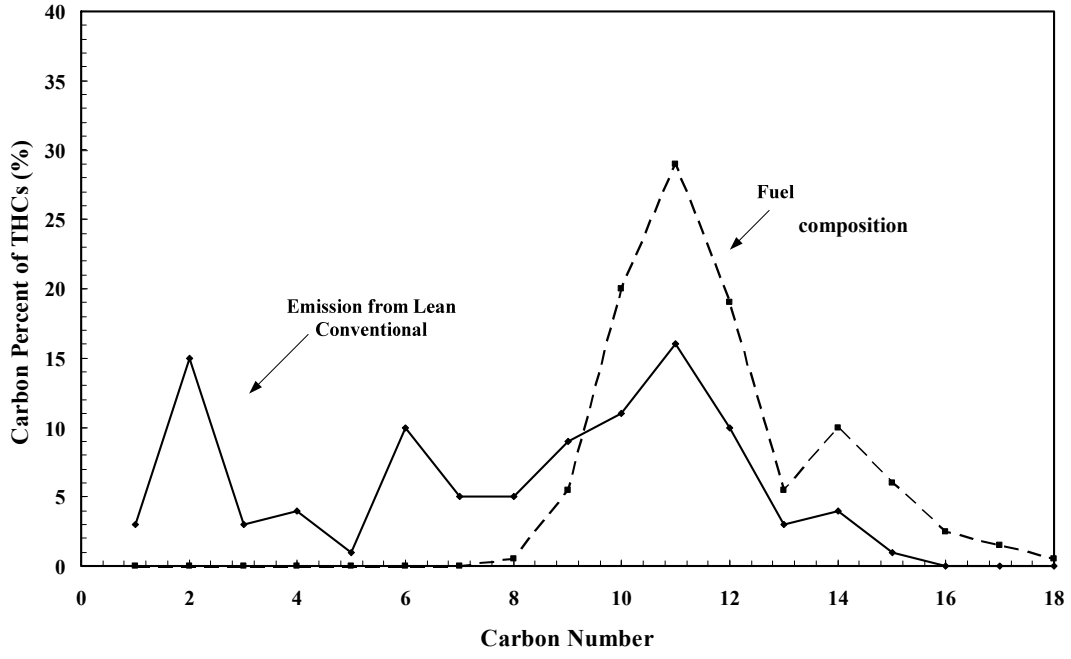


**Figure 2.6** The percentages of different species in hydrocarbons emitted from a 1.7 litre 4 cylinder automotive diesel engine (operated at lean conventional condition) organised by carbon number. Fuel composition is also shown. (Adapted from Figure 3 in Bohac *et al*., 2006)

When researchers perform experiments on laboratory bench-top rigs, then they simulate the exhaust gas from a diesel engine with a synthetic fuel mixture, and an example of such mixtures is illustrated in Table 2.4. Light-off experiments may also be performed on live engines, usually as pseudo-steady-state experiments (e.g. Knafl *et al.*, 2006).

**Table 2.4** Composition of the synthetic gas used for light-off study of a diesel oxidation catalyst in Chandler *et al*. (2000).

| Species | Concentration |
|---|---|
| $C_3H_6$ | 100 ppm |
| CO | 200 ppm |
| $CO_2$ | 8 % |
| $NO_x$ | 300 ppm |
| $O_2$ | 10.7 % |
| $N_2$ | balance |
| $SO_2$ | 20 ppm |
| $H_2O$ | 4.5 ppm |

**Knafl *et al*. (2006)**: they studied the degreening (aging) of oxidation catalyst by examining the light-off and light-down at different operating hours. The engine exhaust was also analyzed for HC species *via* gas chromatography (GC), and catalyst activity was determined for various HC species at different hours of degreening. The following important observations/statements have been captured that are relevant to this thesis:

a) The light-off experiments were performed using a 1.7 litre high-speed diesel engine equipped with a common rail fuel injection system and a light-loaded oxidation catalyst (7.7 g $ft^{-3}$ Pt loading). They believed that the lightly loaded catalyst formulation is chosen to better control and characterise the light-off behaviour. The monolith measured 114 mm in diameter and 76.2 mm in length.

b) The light-off curve was obtained by increasing the engine load at a fixed engine speeds (this is similar to our experiment). At each engine load the engine was stabilised for 5 minutes before exhaust concentrations were analysed pre- and post-catalyst, and the light-off curve was produced by plotting the conversion against inlet gas temperature. By repeating this procedure with decreasing engine load, the pseudo-steady-state light-down curve was also produced (hysteresis experiment). The above test run was repeated at 0, 1, 2, 3, 4, 6, 8, 10, 12, and 16 degreening hours.

c) As the catalyst is degreened, the catalyst light-down temperature increases. Light-down temperatures increase rapidly over the first 8 hours and then largely stabilise. The light-off increases by 14°C for CO and by 11°C for THCs through the degreening procedure. The shape of the light-down curves is not affected by the degreening process. Conversion efficiency of the fully lit-off catalyst is unaffected by degreening. The authors believed that the catalyst performance

changes due to coalescence of precious metal sites that have been exposed to high temperature.

d) As the hydrocarbons consist of a range of different species, the oxidation catalyst is not equally active for all hydrocarbon species. The oxidation catalyst is most active for acetylenes, then olefins and finally aromatics. Paraffins show the lowest activity as they pass through the oxidation catalyst. Little to no change in methane concentration was observed across the catalyst. Catalyst activity deteriorates with degreening across all HC groups but most severely for aromatics and normal paraffins.

e) In their work, they mentioned changes in gas velocity, inlet concentration of CO and HCs with changing engine loads; however, they did not explain how these would affect the catalyst light-off. However, they felt that such changes may cause the hysteresis between the light-off and light-down curves.

**Knafl *et al.* (2007)**: in subsequent work, they compared the performance of a DOC on an engine, and also on a gas flow reactor. Experiments were performed in two different modes of operation (namely premixed compression ignition (PCI) and conventional). The experimental set-up and procedure for operation of the engine are very useful for this thesis:

Pt/Pd (3:1) alumina catalyst with zeolite was used in both experiments with approximately 87.5 g/ft$^3$ loading, however the dimensions of the two reactors were different. The bench-top flow reactor was 10.9 mm long and 19 mm in diameter (3 ml in volume) and housed in a quartz tube, whereas the catalyst used in the engine experiment was a full-scale catalyst (152.4 mm long, 101.6 mm in diameter and 1.24 litre in volume) that was housed in a stainless steel can.

Figure 2.7 illustrates the bench-top reactor set-up.

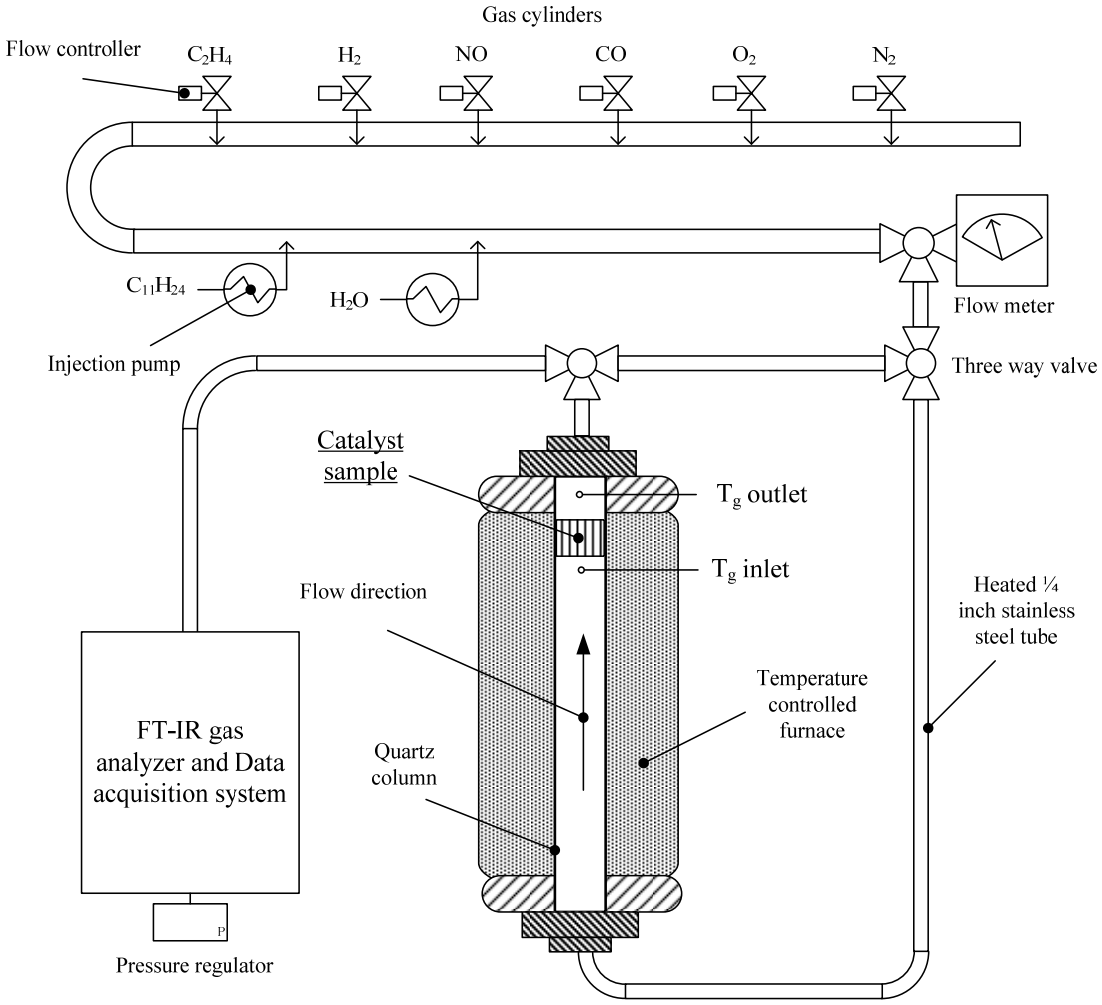


**Figure 2.7** Schematic of the bench-top reactor set-up adapted from diagram in Knafl *et al*. (2007).

In their paper, the following information is relevant:

a) The feed gas composition to the bench-top experiment was determined from measurements on a real exhaust with different engine operation modes. Repeatability of the feed gas composition was studied by 8 tests on different days and represented as coefficient of variance (COV). Space velocity was set to 50,000 $h^{-1}$ for both tests that simulated PCI and conventional combustion.

b) A 1.7 litre low compression (16:1) turbocharged diesel engine was used for the study. Thermocouples were placed 100 mm immediately before and after the catalytic converter to measure the gas temperature (no measurement of converter temperature was mentioned). An AVL CEB II single stream emissions bench was used to analyze pre- and post-catalyst emissions by switching a three-way valve. The measurement of emissions was taken intermittently with the assumption that engine-out emissions do not change significantly at steady-state engine operation.

c) Before the light-off tests, the catalyst was conditioned and purged at 350°C for 20 minutes in low CO and HC exhaust. No conditioning step was done before light-down tests. Five steady-state engine operating conditions were used to span the light-off and light-down temperature ramps. The temperature ramp started from 130 to 250$^{o}$C. The engine was run for 4 minutes at each operating point, and for 20 minutes at 250°C, which was the catalyst inlet temperature between light-off and light-down experiments.

d) In these two experiments, good repeatability was obtained in the light-off for CO and THC in the PCI exhaust gas. No repeatability tests were done for other light-off curves. The authors assumed that they behaved in a similar manner.

Based on their results and discussions, the following important observations/statements are very relevant to this thesis:

a) In many ways, both set-ups showed a similar shape of light-off and light-down curves, and the light-down temperature was lower than the light-off temperature.

b) The authors believed that the plotting of the light-off and light-down curves against the inlet gas temperature can be misleading, since the inlet gas temperature may fail to represent the actual temperature of the active catalytic sites.

c) The catalyst behaved differently in the two set-ups. The engine set-up showed higher initial apparent HC conversion efficiencies, higher CO and HC light-off temperatures, and lower fully-lit HC conversion. The authors explained the causes of these differences: "*Higher initial apparent HC conversion is caused by a higher fraction of trappable* (*i.e.high boiling point*) *HC*. *Engine light-off is delayed because in the tests performed*, *engine-out CO was 11-30% higher than on the reactor*, *causing significant self-inhibition*. *The engine DOC also experiences ambient cooling*, *which also delays light-off. Fully-lit HC conversion is lower on the engine because the reactor surrogate exhaust mixtures did not include methane* (*$CH_4$*), *which is unreactive at diesel light-off temperatures*. *Engine DOC heat loss and sample line HC desorption during post-DOC sampling also reduce fully-lit HC conversion on the engine*."

### 2.3.5 CO self-inhibition

The inhibition effect of CO, on oxidation reactions has been well studied. In Voltz (1973), the inhibition effect of CO on the oxidation of CO and $C_3H_6$ was investigated using a bench-top experimental rig with synthetic gas mixtures. The experiment was performed: (a) at high CO concentration (4%) and low CO concentration (0.7%), (b) with high $C_3H_6$ (800 ppm) and low $O_2$ (3%), and (c) low $C_3H_6$ (100 ppm) and high $O_2$ (4.5%). The Pt/alumina (pellets) was the catalyst and the reactor temperature was kept at 288$^{o}$C for all of the experiments. The velocity of gas in the stream was very low compared to a real engine exhaust. They found the increase in CO concentration from 0.7% to 4%, had the effect of decreasing sharply the conversion of both CO and $C_3H_6$. The CO concentration in their experiment is high compare to that in a diesel engine exhaust (e.g. 1500 to 6000 ppm). The $O_2$ concentration is lower than that in a diesel engine exhaust (e.g. 9%).

In Hayes *et al.* (1995), experiments were performed using a single channel tubular reactor (coated with Pt loaded washcoat ) by injecting CO at different concentrations while the inlet gas flowrate and temperature remained the same. These experiments showed a maximum rate of CO conversion at about 3.3% CO concentration followed by a decrease in rate of reaction. However, this experiment was done on a specially formed annular ring (not a Full-scale catalytic converter) and the hourly space velocity was therefore very high 1,500,000 $h^{-1}$, which is very much larger than the gas hourly space velocity of the exhaust from a 2.0 litre diesel engine in a Full-scale DOC (which usually lies between 20,000 to 280,000 $h^{-1}$).

In the literature, the CO inhibition effect has been considered as one of the major causes of the hysteresis phenomena between the light-off and the extinction process (Arnby *et al.*, 2004; Knafl *et al*., 2007). At low inlet gas temperatures, the CO oxidation is self-inhibited due to high CO surface coverage. The high conversion of CO leads to less vacant active sites available for oxygen and other species, e.g. THCs. As the temperature increases, CO desorbs from the sites, and more active sites become available for oxygen. Therefore, more oxidation reactions could take place, and even more active sites become available for oxygen and other species in the exhaust gas since more CO can be reacted. During the extinction process, the initial surface coverage of CO is low, and it increases as the inlet gas temperature decreases. This explains why the conversion of CO can remain high until the temperature drops to the point at which CO inhibition occurs again.

To sum up, it would be interesting to show the inhibition effect using real diesel engine exhaust, and to identify under what operating conditions of the engine this is most likely to occur.

### 2.3.6 Effect of hydrogen on the oxidation of CO in a DOC

Hydrogen is considered to be present in the engine exhaust as a product of the water-gas shift reaction. Oh and Cavendish (1982) included hydrogen as a separate species in their simulations. They also reported that the concentration of hydrogen was assumed to be determined by the equilibrium of the water-gas shift reaction; and that the molar ratio is approximately 1:3 between hydrogen and CO. Their simulations suggested that the presence of hydrogen would enhance the CO light-off.

Sun *et al.* (2003) studied the catalytic combustion of $H_2$ and CO mixture over a Pt alumina coated monolith catalyst. They observed that the catalytic rate of $H_2$ is inhibited by CO, and the presence of $H_2$ assists CO oxidation. The $H_2$ concentration range used in their study was from 0 to 2.5%. From their experimental results, the presence of $H_2$ assists CO light-off off. In their opinion this effect is attributed to the exotherm from hydrogen combustion, which increased the temperature of the catalyst, shifting the equilibrium between CO adsorption and desorption.

Salomons *et al.* (2006) studied CO and hydrogen oxidations on a Pt monolith DOC using a bench-top experiment rig. Some of the observations are consistent with other literature as follows:

a) CO inhibits hydrogen ignition,

b) hydrogen promotes CO oxidation, and

c) CO starts oxidising before hydrogen.

The new finding was that the light-off temperature of CO was lowered by 23 $^{o}$C with 500 ppm $H_2$ addition (1000 and 2000 ppm background concentration of CO), and it was only reduced further by 3 $^{o}$C when 2000 ppm of $H_2$ were added. They commented that "*small amount of hydrogen enhance significantly the ignition point, but the marginal benefit of additional hydrogen is small".* They believed that this also proves the promotion of CO oxidation by the presence of hydrogen (and not because of an increase in the catalyst temperature by hydrogen combustion). Instead, according to their literature review, researchers (Stetter and Blurton, 1980; Hoyle *et al*., 1999; Oh and cavendish, 1982) have attributed the promotion effect as the presence of hydrogen

influencing (and increasing) the desorption rate of CO. Other species would then have more opportunity to adsorb on the active sites. On the other hand, a model was used to simulate the experiment results, and found not to be able to predict the hydrogen enhancement effect on CO light-off.

More recently, Salomons *et al.* (2009) used an "oxygen compression" mechanism to model their experimental results. Their model captured the hydrogen enhancement effect on the light-off temperature by reducing the activation energy of desorption of CO as a function of the gas phase hydrogen concentration. Moreover, the authors commented that: "*From an automotive perspective, because hydrogen is always present in the exhaust gas as a result of the water gas shift reaction, addition of hydrogen to auto exhaust as a means of reducing light-off temperature is not likely to be very effective*".

Bhatia *et al*. (2009) proposed the formation and decomposition of an H-CO complex on platinum to explain the effect of hydrogen on light-off behaviour of CO oxidation. This also resulted in a decrease of activation energy of CO desorption with an increase in the coverage of hydrogen. The simulation results were compared with experimental data in Salomons *et al*. (2006), and good agreement was obtained.

## 2.4 Physical properties

When a mathematical model is developed, then it is important to assign appropriate valves for the physical properties of the catalyst system and the gases flowing through the DOC. Based on information in the literature, physical property data is summarised in Table 2.5. As formulations of the cordierite support and the washcoat may vary depending on the manufacturer, this may leads to slightly variations in properties. Some of these properties are dependent on the local temperature, e.g. heat capacity, and this will increase the complexity of mathematical models that include such temperature dependent terms.

**Table 2.5** Examples of relevant physical properties found in the literature. Note that: $T_w$ is the solid temperature in K, $T_g$ is air temperature in K, $P_2$ is air pressure in atm and $P_1$ is 1 atm.

| Material | Property | Value or correlation | Literature source |
|---|---|---|---|
| Cordierite | Thermal conductivity | $0.9558 - 2.09\times10^{-4}\mathrm{T_s}$ (W m$^{-1}$ K$^{-1}$) | Hayes and Kolaczkowski (1997; p. 655) reporting value from Oh and Bissett (1994) |
| | Heat capacity | $1071 + 0.156\mathrm{T_s} - 3.437\times10^{7}\mathrm{T_s^{-2}}$ (J kg$^{-1}$ K$^{-1}$) | Hayes and Kolaczkowski (1997; p. 655) reporting value from Oh and Bissett (1994) |
| | Density | 1770 (kg m$^{-3}$) | Santos and Costa (2008) |
| Washcoat | Thermal conductivity | 1 (W m$^{-1}$ K$^{-1}$) | Santos and Costa (2008) |
| | Heat capacity | 950 (J kg$^{-1}$ K$^{-1}$) | Santos and Costa (2008) |
| | Density | 2790 (kg m$^{-3}$) | Santos and Costa (2008) |
| Air | Thermal conductivity | $1.679\times10^{-2} + 5.073\times10^{5}\mathrm{T_g}$ (W m$^{-1}$ K$^{-1}$) | Hayes and Kolaczkowski (1997; p. 660) |
| | Heat capacity | $28.09 + 0.1965\times10^{-2}\mathrm{T_g} - 0.4799\times10^{-5}\mathrm{T_g^2} - 1.965\times10^{-9}\mathrm{T_g^3}$ (J mol$^{-1}$ K$^{-1}$) -Temperature ranges from 273 to 1800K | Hayes and Kolaczkowski (1997; p. 660) reporting value from Kyle (1984) |
| | Dynamic viscosity | $7.701\times10^{-6} + 4.166\times10^{-8}\mathrm{T_g} - 7.531\times10^{-12}\mathrm{T_g^2}$ (Pa.s) | Hayes and Kolaczkowski (1997; p. 660) |
| | Density (ideal gas) | $1.292\times\frac{273.15}{T_g}\times\frac{P_2}{P_1}$ (kg m$^{-3}$) | |

## 2.5 Concluding remarks

a) There are many papers that describe the construction of mathematical models for catalytic converter. However, very few of them show comparisons with experimental data. Models vary in complexity, and some have many tuneable chemical and physical parameters, e.g. heat capacity, rate constants. Hence, it is not clear how good they would really be when operated in predictive mode.

b) The NTU method provides an alternative modelling technique, which can be used to validate models that are constructed using the fnite-different method.

c) Correlations for heat and mass transfer coefficients that can be used in 1-D models are available in the literature, including correlations that consider a developing laminar flow profile.

d) The LHHW forms of rate expression are of use for CO oxidation , and are considered suitable to simulate the reaction under steady-state conditions. Althrough they have been used in transient simulations, they are not really suitable for that application. The rate expressions proposed by Voltz *et al*. (1973) are still popular, althrough mechanistic reaction steps have also been developed to model the transient behaviour of the catalyst. However, few of them have been compared with results obtained from engine trials. This illustrates the importance of generating data from engine trials, that could be used to validate mathematical models of DOC systems.

e) Based on the review of the literature, it was decided to follow the oxidation of CO in this thesis and to use propane to represent the hydrocarbons. Also for some of the experiments, the effect of hydrogen would also be studied.

f) From the review of work on pulsating flow, this is not considered to be for the range of experiments performed in this thesis.

g) To measure solid wall temperatures, thin thermocouples (0.5 mm) will be positioned between cut sections of monolith, that will then be cemented together.

h) Based on the review of the literature, the inlet cone of the catalytic converter (to be used in the experiments) will have an angle of $40^{o}$, in order to ensure a uniform temperature distribution across the radial direction.

i) CO inhibition has been widely studied, and observed in many experiments. However, many of these experiments were performed using bench-top rigs where the experimental conditions are quite different from conditions in a converter on an actual engine, e.g. gas flows rate are different, the composition of the synthetic gas mixtures is also different. It is therefore interesting to perform such experiments in engine trials, to show if this effect is real and to explore further its importance.

j) Similarly, because the experimental conditions are easier to control most of the light-off experiments on DOCs were also performed using bench-top rigs. Very few of them were performed using a real engine. In Knafl *et al*.(2006), engine trials were performed to produce a light-off curve. However, there were a number of uncertainties: as engine torques (loads) was increased, the gas velocity, inlet concentration of CO and THCs also varied. These changing factors may affect the light-off. Therefore it is important to improve this technique to produce more reliable light-off curves from live-engine experiments.

k) In bench-top experiments, the promotion effect of hydrogen on CO oxidation was observed. This promotion effect was considered to occur for two possible reasons. Firstly because of the exotherm resulting from the combustion of hydrogen, and secondly that hydrogen weakened the CO inhibition effect. It would be interesting to explore this aspect on a live-engine experiment.

l) Useful physical properties have been gathered, and these will be used in the modelling part of the thesis.

m) When light-off experiments are perfomed, then both catalyst light-off and extinction (light-down) will be studied. It is also important to assess any hysteresis.

## References


Arrighetti, C., Cordiner, S., Mulone, V. (2007) Heat and Mass Transfer Evaluation in the Channels of an Automotive Catalytic Converter by Detailed Fluid-Dynamic and Chemical Simulation. *Transactions of the ASME, Journal of Heat Transfer,* **129**, 536-547.

Benjamin, S. F. and Roberts C. A. (2001) Warming Automotive Catalysts with Pulsating Flows. *Proc Mech Engrs*, **215** (D), 891-910.

Benjamin, S.F., Roberts, C.A., Wollin, J. (2002) A Study of Pulsating Flow in Automotive Catalyst Systems. *Exp. in Fluids*, **33**, 629-639.

Bohac, S.V., Han, M., Jacobs, T.J., Lopez, A.J., Assanis, D.N. and Szymkowicz, P.G. (2006) Speciated hydrocarbon emissions from an automotive diesel engine and DOC utilizing conventional and PCI combustion, SAE 2006-01-0201.

Bhatia, D., Harold, M. P., Balakotaiah, V. (2009) Kinetic and Bifurcation Analysis of the Cooxidation of CO and $H_2$ in Catalytic Monolith Reactors, *Chemical Engineering Science*, **64**(7), 1544-1558.

Blohm, T., Zoz, S., Penning, R., Trappe, B. (2003) Thermal Modelling of Exhaust Catalysts, *VTMS 6: Vehicle Thermal Management Systems*, 475-484.

Chatterjee, D., Deutschmann, O. and Warnatz, J. (2001) Detailed Surface Reaction Mechanism in a Three-way Catalyst. *Faraday Discuss.*, **119**, 371-384.

Chen, D. K. S. and Cole, C. E. (1989) Numerical simulation and experimental verification of conversion and thermal responses for a Pt/Rh metal monolithic converter, SAE 890798.

Cybulski, A. and Moulijn J.A. (Ed.) (2006) *Structured Catalysts and Reactors*, 2nd Ed., CRC Press, New York.

Farrauto, R. J. and Heck, R. M. (1999) Catalytic Converters: State of the Art and Perspectives, *Catalysis Today*, **51**, 351-360.

Hayes, R.E., Kolaczkowski, S.T., Thomas, W. J. (1992) Finite element model for catalytic monolith reactor, *Computers them. Engng*, **16**(7), 645-657.

Hayes, R.E., Kolaczkowski S.T., Thomas, W.J. and Titiloye, J., 1995. Intraphase Diffusion and Interphase Mass Transfer Effects During the Catalytic Oxidation of CO in a Tube Wall Reactor, *Proc. R. Soc. Lond*. A, **448**, 321 – 334

Hayes, R.E. and Kolaczkowski S.T. (1997) *Introduction to catalytic combustion*, Amsterdam: Gordon and Breach Science Publishers.

Hayes, R. E. and Mukadi, L. S. (2002) Modelling the Three-way Converter with Mechanistic Kinetics using the Newton-Krylov Method on a Parallel Computer. *Computers and Chemical Engineering*, **26**, 439-455.

Hoyle, N.D., Kumarasamy, P., Self, V.A., Sermon, P.A., Vong, M.S.W. (1999) Catalysis of $H_2$, CO and Alkane Oxidation-combustion Over Pt/silica Catalysts: Evidence of Coupling and Promotion, *Catalysis Today*, **47**, 45-49.

Heck, R. M. and Farrauto, R. J. (2001) Automobile Exhaust Catalysts, *Applied Catalysis A*: General **221**, 443-457.

Knafl, A., Busch S.B., Han, M., Bohac, S.V., Assanis, D.N. (2006) Characterizing Light-off Behaviour and Species - Resolved Conversion Efficiencies During In-Situ Diesel Oxidation Catalyst Degreening, SAE 2006-01-0209.

Knafl, A., Bohac, S.V., Han, Assanis, D.N. and Szymkowicz, P. G. (2007) Comparision of Diesel Oxidation Catalyst Performance on an Engine and a Gas Flow Reactor, SAE 2007-01-0231.

Koltsakis, G.C., and Stamatelos, A.M. (1997) Catalytic Automotive Exhaust After Treatment, *Progress in Energy combustion Science*, **43**, 1-39.

Kim, Y. and Kim, W. (2009) Re-evaluation and Modelling of a Commercial Diesel Oxidation Catalyst. *Ind.Eng. Chem. Res*. **48**, 6579-6590.

Kwon, H.J., Baik, J.H., Kwon, Y.T., Nam, I. and Oh, S.H. (2007) Detailed Reaction Kinetics over Commercial Three-way Catalysts, *Chemical Engineering Science*, **62**(18-20), 5042-5047

Liu, Z., Benjiamin, S.F., Roberts, C.A. (2003) Pulsating flow maldistribution within an axisymmetric catalytic converter – flow rig experiment and transient CFD simulations, SAE, 2003-01-30.

Lubeski, A. (2000) Real-time Catalytic Converter Temperature Estimator in the Powertrain Controller, SAE 2000-01-065.

Mazumder, S. (2007) Modelling Full-scale Monolithic Catalytic Converters: Challenges and Possible Solutions. *ASME*, **129**, 526-535.

Nibbelke, R. (1998) *Steady State, Transient and Non-linear Kinetics in Automobile Exhaust Gas Catalysis*, PhD thesis, Technical University of Eindhoven.

Oh, S.H. and Cavendish, J. (1982) Transients of Monolithic Catalytic Converters: Response to Step Changes in Feed Stream Temperature as Related to Controlling Automobile Emissions. *Ind. Eng. Chem. Prod. Res. Dev*. **21**, 29-37.

Pontikakis, G.N., Konstantas, G.S. and Stamatelos, A.M. (2004) Three-Way Catalytic Converter Modeling as a Modern Engineering Design Tool, *ASME Transactions*, *Journal of Engineering for Gas Turbines and Power*, **126** (4), 906-923.

Salomons, S., Votsmeier, M., Hayes, R. E., Drochner, A., Vogel, H. and Gieshof, J. (2006) CO and $H_2$ Oxidation on a Platinum Monolith Diesel Oxidation Catalyst. *Catalysis Today*, **117**(4), 491- 497.

Salomons, S., Hayes R.E., Votsmeier M., Drochner A., Vogel H., Malmberg S. and Gieshof J. (2007) On the Use of Mechanistic CO Oxidation Models with a Platinum Monolith Catalyst. *Applied Catalysis*, *Part B*,**70**(1-4), 305-313.

Salomons, S., Hayes R.E. and Votsmeier M. (2009) The Promotion of Carbon Monoxide Oxidation by Hydrogen on Supported Platinum Catalyst, *Applied Catalysis A: General*, 352, 27-34

Shamim, T., Shen, H., Sengupta, S., Son S. and Adamczyk, A.A. (2002) A Comprehensive Model to Predict Three-way Catalytic Converter Performance, *Journal of Engineering for Gas and Turbines and Power-Transitions of the ASME*, **124**(2), 421-428.

Siemund, S., Leclerc, J. P., Schweich, D., Prigent, M. and Castagna, F. (1996) Three-way Monolithic Converter: Simulations versus Experiments, *Chemical Engineering Science*, **51**(15), 3709-3720.

Stetter, J. R. and Blurton, K.F. (1980). Catalytic Oxidation of CO and $H_2$ Mixtures in Air, *Industrial & Engineering Chemistry Product Research and Development*, **19** (2), 214-215.

Sun, M., Croiset, E.B., Hudgins, R.R. and Silveston P.L. (2003) Steady-State Multiplicity and Superadiabatic Extinction Waves in the Oxidation of $CO/H_2$ Mixtures over a $Pt/Al_2O_3$-Coated Monolith, *Ind. Eng. Chem. Res.*, **42** (1), 37–45.

Triana, A. P., Johnson, J. H., Yang S. L., and Baumgard K. J. (2003) An Experimental and Numerical Study of the Performance Characteristic of the Diesel Oxidation Catalyst in a Continuously Regenerating Particulate Filter, SAE 2003-01-3176.

Tsinoglou, D. H. and Koltsakis, G.C. (2005) Influence of Pulsating Flow on Close-coupled Catalyst Performance, *ASME*, **127**, 676-682

Voltz,S.E., Morgan,C.R., Liederman, D. And Jacob, S.M. (1973) Kinetic Study of Carbon Monoxide and Propylene Oxidation on Platinum Catalysts. *Idn. Engng Chem. Prod. Res. Dev*. **12**, 294-301.

Wang, J.X., Shuai, S.J. and Zhuang R.J. (2001) Experiment and Numerical Simulation of Unsteady Temperature Fields in Automotive Catalytic Converters, SAE 2001-01-3563.

Zygourakis, K. (1989) Transient Operation of Monolith Catalytic Converter: a Two-dimensional Reactor Model and the Effects of Radially Nonuniform Flow Distributions, *Chemical Engineering Science*, **44**, 2075–2086.

# 3. Experimental studies

In this chapter, the experimental test facilities are described, and how the exhaust system on a Ford 2.0 litre turbocharged diesel engine was modified to accommodate the specially prepared catalyst units.

Experiments were performed, mainly on DOCs that were specially prepared by Johnson Matthey for this project. These DOCs were prepared on cordierite monolith supports whose scale matches a commercial application. Experiments were performed on Full-scale DOC (length 114 mm), and also on very short lengths of monolith (length = 5 and 10 mm) which are described as 'Thin-slice DOC'. The range of experiments is summarized in Figure 3.1. At the start of the sections that describe experimental results, this figure features as a reminder of the sequence of experiments, and where the section fits in the overall scheme.

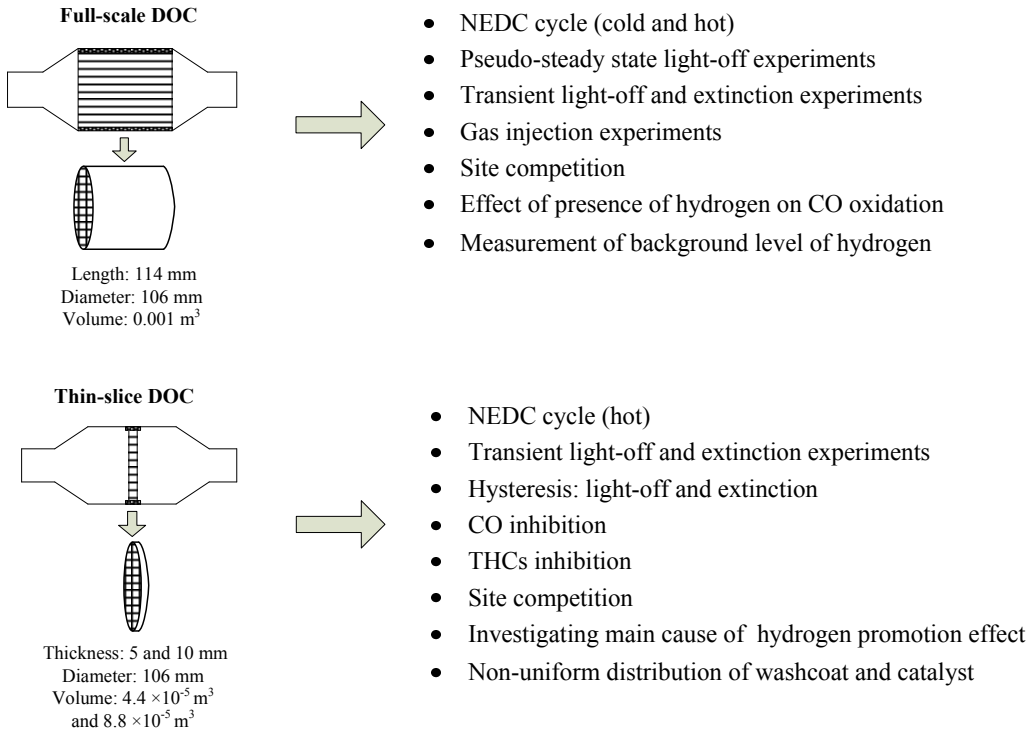


**Figure 3.1** Overview of the experimental investigations in Chapter 3.

In many of these experiments, a known quantity of gas (e.g. carbon monoxide, propane, or hydrogen) was injected into the exhaust from the live engine, and the response of the catalyst system was monitored. This generates some very interesting data, and enables a technique that is normally only used in laboratory bench-top experiments to be applied to a live engine. This then leads to the development of methodologies that are suitable for a live engine.

## 3.1 Experimental facilities and equipment

The experimental system consisted of a number of key parts:

- an exhaust system, that was specially modified,
- DOCs into which thermocouples were positioned and then the DOC was mounted in a special housing (can), and
- an engine test cell with: a diesel engine, emission measurement equipment, engine control and data acquisition systems.

These aspects are described in this section.

### 3.1.1 Modified exhaust system

This modified exhaust system was specially built for this research project. A schematic of an exhaust section is shown in Figure 3.2. It has a total length of 2 metres, and is made from 50.8 mm O.D. stainless steel (300 series) with a 1.6 mm wall thickness. The catalyst cans were constructed of stainless steel (400 series). The catalyst inside the can was wrapped with thermal mats supplied by Johnson Matthey (JM), and these reduce heat loss and damage to the catalyst from vibrations. The catalyst can was also wrapped with thermal insulation fabrics to minimise heat loss during the tests.

A “4-point measurement” technique was used for pressure measurement; four 2 mm holes were drilled through the pipe wall and then covered with a metal outer shell. Then the pressure measurement was taken from the outer shell, see Item 4 in Figure 3.2. Measurements were made pre- and post- catalyst.

The exhaust gas was sampled through a 6 mm stainless steel tube (with a few small holes drilled across its surface), which was inserted into the middle of the exhaust pipe. There were two sampling ports, one at the inlet and the other at the outlet of the catalyst.

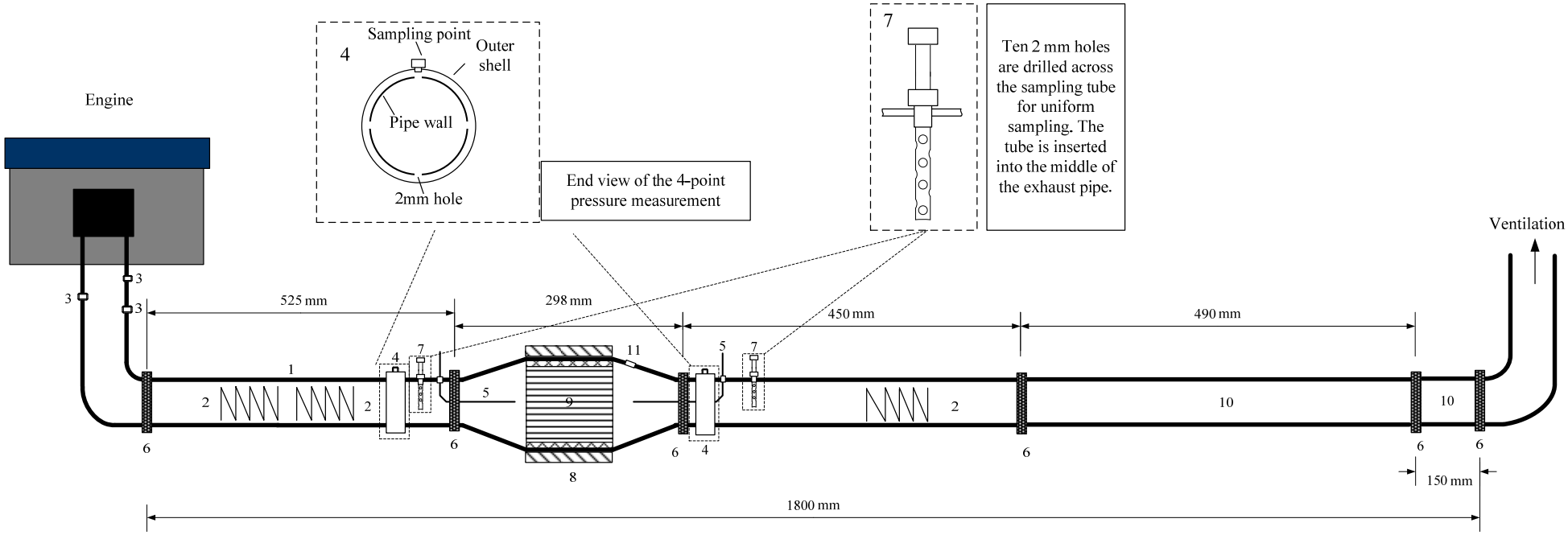


**1 - Exhaust pipe (Nominal pipe size 63 mm o.d. schedule 5 stainless steel pipe (welded) )**
**2 - Gas flow mixer**
**3 - Gas injection ports (¼" BSP compression fittings)**
**4 - 4-point pressure measurement (¼" BSP compression fitting)**
**5 - Gas temperature measurement (1mm K-type thermocouple, 1/16" )**
**6 - Marmon flanges (64 mm o.d.)**
**7 - Gas sampling points (¼" BSP compression fittings)**
**8 - Insulation on catalyst can**
**9 - Diesel oxidation catalyst**
**10 - Spool piece**
**11 - Exit of embedded thermocouples (0.5mm K-type) for catalyst temperature measurement**

**Figure 3.2** Schematic of the modified exhaust systems.

The whole exhaust system was assembled from several sections for ease of fabrication and transportation. Marmon flanges (Item 6) were used to facilitate assembly of these pipe sections. There were a number of tappings (6 mm compression fittings), which could be used to insert thermocouples, attach pressure transducers or used for gas sampling. There is a spool-piece, which could be adapted to match future needs. The unused tappings were sealed using stainless steel balls (ball-bearings) or high temperature exhaust putty.

### 3.1.2 DOCs

The Full-scale (i.e. commercial scale) DOC samples were supplied by Johnson Matthey (JM). They were in three forms: (a) as clean cordierite monolith substrate, (b) as monolith substrate with washcoat only, and (c) as DOCs. The cordierite substrate is a clean monolith brick without alumina washcoat. The monolith substrate with washcoat is a cordierite monolith with a $\gamma$ -$Al_2O_3$ washcoat, but no catalyst. These DOCs were specially prepared for the purpose of this research project. All of the samples had been aged in a furnace at 650$^{o}$C for 16 hours. The average weight of the samples is summarised in Table 3.1, and the specifications of the DOCs are shown in Table 3.2.

A technique was developed using Photoshop and MATLAB (described in Appendix 5), which helped to determine the area of an irregular object. This was used to calculate the cross sectional area of washcoat. More characterisation studies of the DOCs, such as pore volume and catalyst distribution, were carried out in the parallel PhD project.

**Table 3.1** Measurement performed on the catalyst samples provided by JM.

| Types of sample | Average weight (g) | Error (g) |
|---|---|---|
| Cordierite | 434 | ±1 |
| Cordierite + washcoat | 625 | ±1 |
| Cordierite + washcoat + Pt | 629 | ±1.5 |
| | **Loadings (g/DOC)** | |
| Average washcoat loading | 191 | ±1 |
| Average catalyst loading | 3.5 | ±0.5 |
| Theoretical loading | 4.3 | N/A |

**Table 3.2** Properties of the DOCs.

| Supplier | Johnson Matthey | |
|---|---|---|
| Manufacture of substrate | NGK | |
| Cell structure | Square | Supplied |
| Cell density | 400 cpsi | Supplied |
| Cell width (without washcoat) | 1.1 mm | Supplied |
| Average washcoat cross-sectional area per channel | 0.2643mm$^2$ | Calculated |
| Catalyst loading (Pt) | 120 g ft$^{-3}$ | Provided by JM |
| Density of DOC | 1430 kg m$^{-3}$ | Calculated |
| Substrate length | 114.3 mm | Measured |
| Substrate diameter | 105.7 mm | Measured |
| Volume of substrate | 1000 cm$^3$ | calculated |

### 3.1.3 Engine test cell

The engine trials were performed using an engine test-bed within the Powertrain and Vehicle Research Centre (PVRC) in the Department of Mechanical Engineering at the University of Bath. This test cell is capable of performing full driving cycle and transient tests with emission measurements. The configuration of the engine test cell is illustrated in Figure 3.3. The engine was mounted on a test bed and coupled to a McClure 215 kW transient dynamometer.

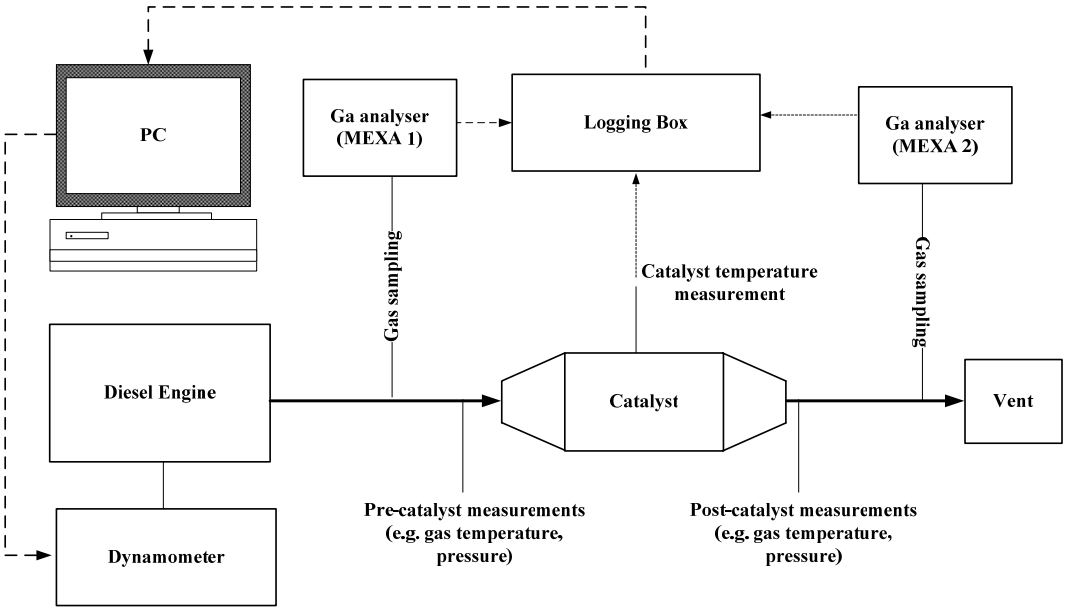


**Figure 3.3** Configuration of the engine test cell.

It was controlled and manipulated through CP CADET V14 control and data acquisition system (supplied by CP Engineering Ltd.). Downstream of the exhaust manifold, the following parameters were measured and recorded:

- gas temperature at exhaust manifold,
- gas temperatures at inlet and outlet of the catalyst,
- catalyst temperature,
- pressure at inlet and outlet of the catalyst, and
- exhaust emissions at inlet and outlet of the catalyst.

The exhaust gas was emitted through a ventilation pipe. The whole test cell was also well ventilated. This reduced the risk of inhaling any leaking exhaust gas, or any leaking gas from the gas cylinders.

**Diesel engine**

The engine used in this study was a Ford PUMA 2.0 litre turbocharged diesel engine (featuring high-pressure common rail fuel injection). It is representative of modern diesel engine design practice, and features in the Ford "Mondeo" and "Transit". The specification of the engine is summarised in Table 3.3. A photograph of this engine on the test bed is also shown in Figure 3.4.

**Table 3.3** Specifications of the Ford PUMA 2.0 litre diesel engine (turbocharged ).

| Engine details | Ford Puma 2.0 L VGT |
|---|---|
| Engine type | Compression ignition |
| Stroke | 4 |
| Cylinder | 4 |
| Fuel type | diesel |
| Fuel injection system | High pressure Common Rail Direct Injection |
| Injection pressure (bar) | 1400 |
| Compression ratio | 16 |
| Engine displacement (cc) | 1998 |
| EGR | Mass flow controlled |
| Turbocharger | Garrett variable geometry |
| Max torque (Nm) | 310 at 1800 – 2500 rev/min |
| Max power (kW) | 96 at 3800 rpm |

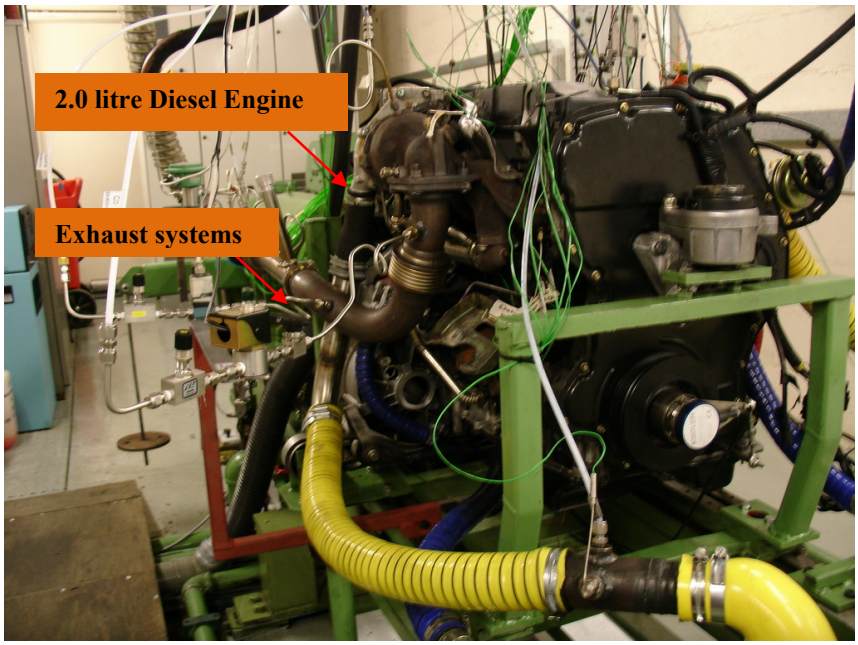


**Figure 3.4** A photograph of Ford PUMA engine as installed on the test bed.

## Emission analysers

Two Horiba MEXA 7100 DEGR gas analysers were available to measure simultaneously the emissions at the inlet and outlet of the DOC. The Horiba MEXA 7000 series gas analyser is a reliable analytical system designed to measure exhaust emissions from diesel or gasoline engines, and is capable of measuring CO, CO2, NOx, THCs and $O_2$, see Table 3.4. It is capable of second by second emission measurements which are ideal for driving cycle and steady-state testing.

**Table 3.4** Configuration of MEXA-7100 DEGR.

| **MEXA-7100 FX System Configuration** | |
|---|---|
| Components and Measured Range | CO: min. range 0 ppm to 100 ppm, max. range 0-12 vol%<br>$CO_2$: min. range 0-5000 ppm, max. range 0-20 vol%<br>$NO/NO_x$: min. range 0-10 ppm, max. range 0-10000 ppm<br>THC: min. range 0-10 ppm$C_1$, max. range 0-50000 ppm<br>$O_2$ : min. range 0-5 vol%, max. range 0-25 vol% |
| Principle | CO: non-dispersive Infrared method (NDIR)<br>$CO_2$: non-dispersive Infrared method (NDIR)<br>$NO/NO_x$: chemi-luminescence detection (CLD), heated, vacuum-type<br>THCs: flame ionization detection (FID), heated<br>$O_2$: magneto-pneumatic detection (MPD) |
| Sample Gas Flow Rate | Approx. 15 litres minute$^{-1}$ |

The gas analysers had been calibrated for the tests. Prior to each test, the gas analysers were purged to clear the residuals from previous runs. The emission analysers were checked daily, and the filters were changed daily (or even more frequently depending on the test frequency). Moreover, these emission analysers were serviced and maintained by professional engineers (from Horiba).

**Engine control and data acquisition system**

The test cell was equipped with data logging facilities made by CP Engineering. The data logging box consisted of three pressure and thirty temperature channels. The computer in the control room used CADET V14 software, which recorded all the temperatures, pressures, gas concentrations and engine operating conditions from the test. The CADET V14 operates in a windows XP environment. It allows system customisation using Visual Basic 6.0 and also contains Real Time multi-tasking direct digital control functions. Its interface supports input from the dynamometer, engine control unit (ECU), fuel weighers, sensors and controllers. This comprehensive system eliminated the need for laborious data synchronisation (between temperature and gas composition measurements) post testing.

The CP128 system capture cards are capable of sampling data at rates of up to 100 kHz at 16 bit resolution and at up to 1 MHz at eight resolutions (Tan, 2007). The hardware interface connecting options are serial, IEEE, and Ethernet.

### 3.1.4 Temperature measurements

A key objective in this study was to measure the thermal responses of a DOC at different operating conditions. For the measurement of gas temperatures, two 1 mm diameter K-type thermocouples were used, and placed 30 mm apart from the inlet and outlet of the converter.

The catalyst (solid or wall) temperature was measured with 0.5 mm K-type thermocouples (manufactured by Labfacility, UK). As illustrated in Figure 3.5, the thermocouples were inserted at various positions, ten of which were aligned along the axial direction at a spacing of 5 mm (for the first five thermocouples), and then 10 mm spacing for the rest of them. At two radial positions the thermocouples are spaced at 20 mm intervals (in the axial direction). In total, twenty thermocouples were used to measure the radial and axial temperature variations in a Full-scale DOC.

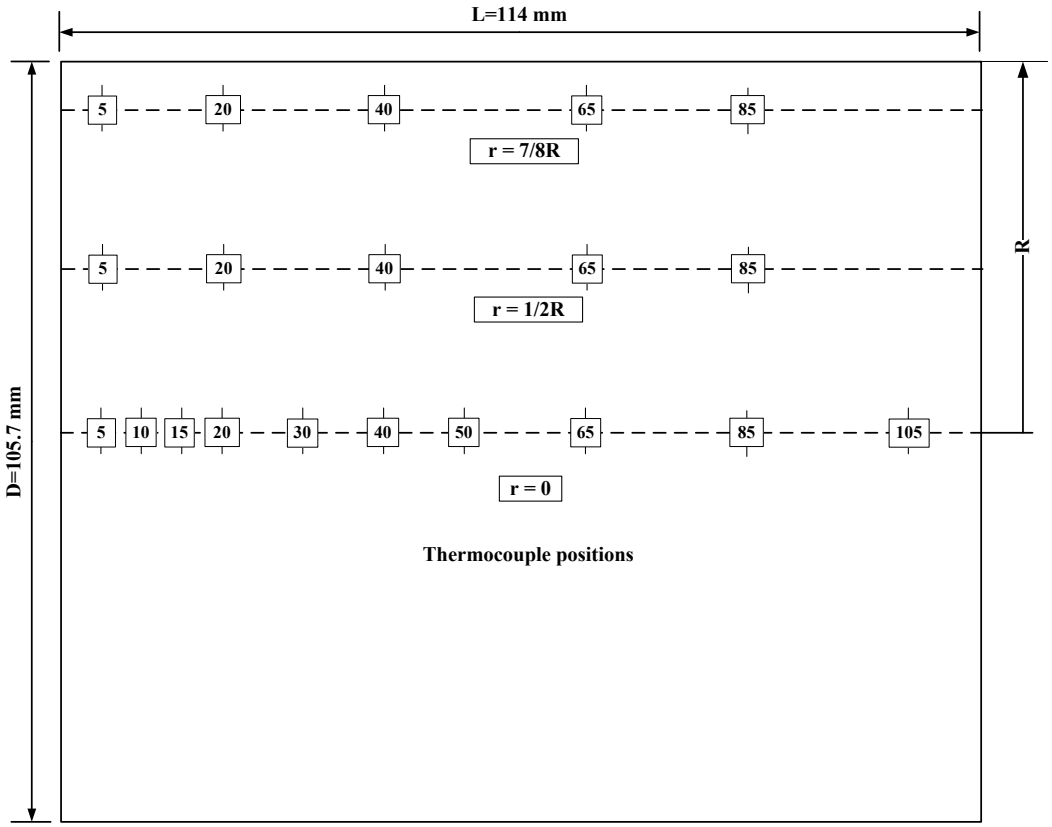


**Figure 3.5** Thermocouple arrangement inside the monolith channel. Ten thermocouples are inserted along the axial direction (r = 0), and another ten are inserted at r = ½ R and 7/8 R.

### 3.1.5 Full-scale DOC with embedded thermocouples

To perform this thermocouple installation, a DOC was cut in half (along the axial direction) using a fine-tooth hack saw, and then the cut surface was polished. The positions for the thermocouples were marked, and then thermocouples were placed into pre-marked positions (tips were in contact with the monolith) and fixed in position using a small amount of "Holts Gun Gum paste", then dried with a hot air gun, see Figure 3.6. Each thermocouple was labelled accordingly. After placing all of the thermocouples in position, the two monolith halves were bonded with a very thin layer of "Holts Gun Gum paste", see Figure 3.7. Finally, the thermocouple leads were fed through a ¼" (6 mm) BSP compression fitting boss.

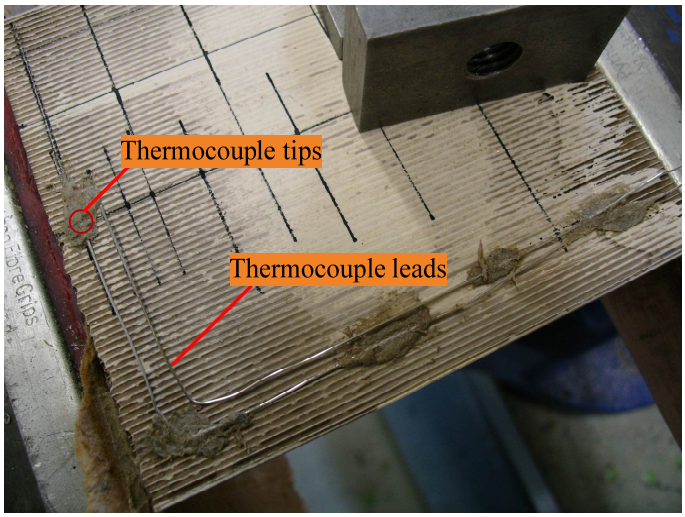


**Figure 3.6** Thermocouples were carefully placed into pre-marked positions (tips were in contact with monolith) and fixed in position with a little cement.

The DOC with thermocouples was housed into a stainless steel can with 40$^{o}$ inlet and outlet cone, see Figure 3.8. The BSP compression boss was carefully welded onto the can. The thermocouple leads must not contact the boss during welding, or they would either be earthed or burnt out. Due to the fragile nature of the 0.5mm K-type thermocouples, they had to be adequately supported. The thermocouple leads were therefore strapped together using heat shrunk sleeving, and then kept in a fixed position using P-clips mounted from the exhaust clamps. The thermocouple leads were then connected to the data logger. The catalytic converter can was wrapped with insulation material to minimise heat loss to surroundings.


**Front view** **Rear view**

**Figure 3.7** Two halves were bonded with a very thin layer of cement (this shows the rear end of the monolith).

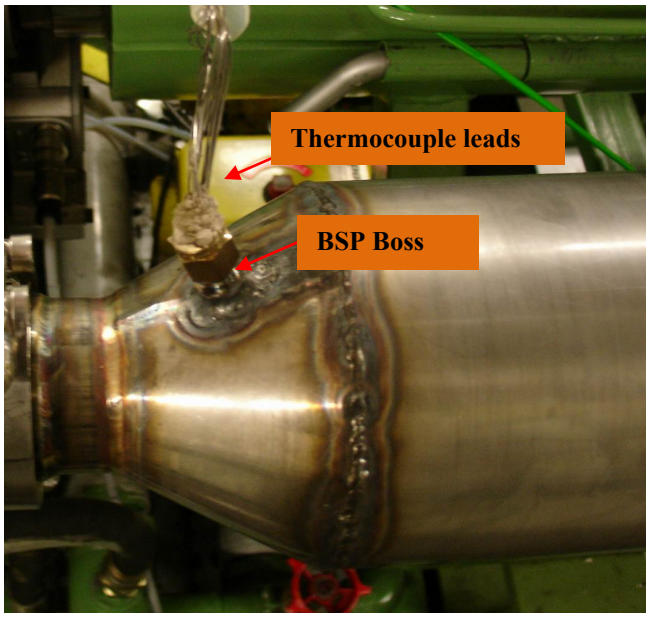


**Figure 3.8** The DOC housed in a metal can.

### 3.1.6 Differential reactor (Thin-slice DOC)

The differential reactor was made from a thin slice cut from the Full-scale DOC (e.g. 5 mm and 10 mm thick, see Figure 3.9a). One advantage of using a differential reactor is to calculate the rate of reaction. A derivation of the relevant equations is described in Hayes and Kolaczkowski (1997; pp. 512 - 513), on which the following is based:

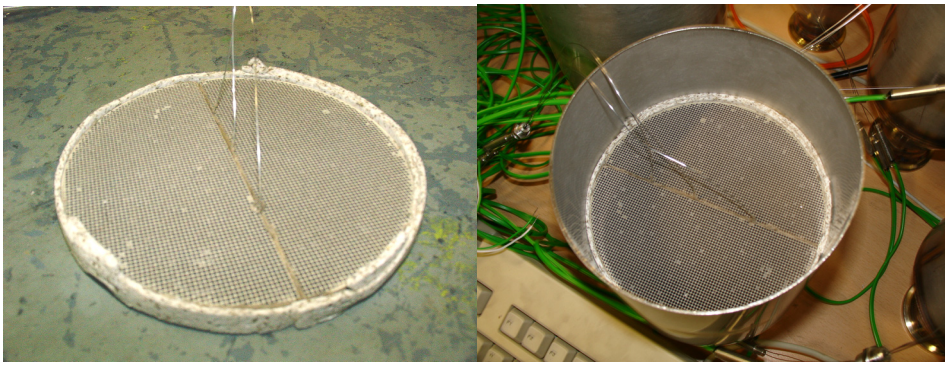

**(a)** **(b)**

**Figure 3.9** An example of the 5mm Thin slices housed in the catalytic converter can: (a) is the thin slice embedded with three 0.5 mm K-type thermocouples (insulation mat is wrapped around the thin slice to prevent heat loss), and (b) is the thin slice housed in the stainless steel converter can.

The mole balance on the catalyst is shown as:

$$-\frac{dF_i}{dV_s} = (-R_i) \tag{3.1}$$

For a differential reactor it is assumed that the concentration change is small enough so that the plug flow equation can be approximated by:

$$-\frac{F_{i,L} - F_{i,0}}{V_s} = \frac{F_{i,0} \cdot X_i}{V_s} = (-R_i) \tag{3.2}$$

where $X_i$ is the fractional conversion of species, $i$, and $F_{i,0}$ and $F_{i,L}$ represent the molar flowrates of species $i$ at inlet (z = 0) and outlet (z = $L$), and ($-R_i$) is the reaction rate (expressed in mol $m^{-3}$ (reactor) $s^{-1}$) and $F_{i,L} = F_{i,0}(1 - X_i)$. $V_s$ is the volume of a Thin-slice DOC ($m^{-3}$).

Another advantage of using a Thin-slice DOC in this project is that it would magnify changes (e.g. in catalyst temperature and conversion) during the transient operation of the engine (e.g. NEDC). It is small and thin, and this enables it to have a more rapid response to inlet gas temperature (rather than a Full-scale DOC). Also, it has simpler temperature profile than a Full-scale DOC.

The Thin-slice DOC was also installed with 0.5 mm K-type thermocouples using the same technique described in Section 3.1.5. Three thermocouples were used in the 5 mm thin slice, and six thermocouples were used in the 10 mm thin slice. These were positioned at radial locations (r = 0, r = 1/2 R and r = 7/8 R). The thin slice was wrapped with thermal insulation matting, and then housed in the middle of a Full-scale catalytic converter can, see Figure 3.9b. Six small metal brackets secured the position of this thin-slice in the metal can.

### 3.1.7 Gas injection device

Upstream of the catalyst, a few gas injection ports were attached to the exhaust pipe allowing the injection of gases (e.g. CO, $C_3H_8$ and $H_2$). For some of the investigations synthetic gas was injected into the exhaust pipe to maintain a constant background level, or to create a step change/pulse of concentration.

Figure 3.10 shows the schematic of the gas injection system. The gas is fed from a gas bottle (supplied by BOC). For each gas bottle, the appropriate gas regulator

(supplied by BOC) was fitted. An on/off switch valve (Swagelok) was used as a safety valve in case the gas needed to be switched off in an emergency. A flexible 6 mm plastic pipe connected the safety valve to a high resolution needle valve (16 turns, Cole Palmer). The solenoid valve was placed very close to the exhaust pipe (to reduce injection delay). Stainless steel tube (6 mm) was used between the needle valve and the exhaust pipe which provided a steady support for both the solenoid valve and the needle valve. Gas injection was activated by triggering the solenoid valve through a computer, and the needle valve was used to regulate the quantity of gas injected. For safety reasons two CO detectors were placed close to the CO gas bottle to detect any leakage of CO.

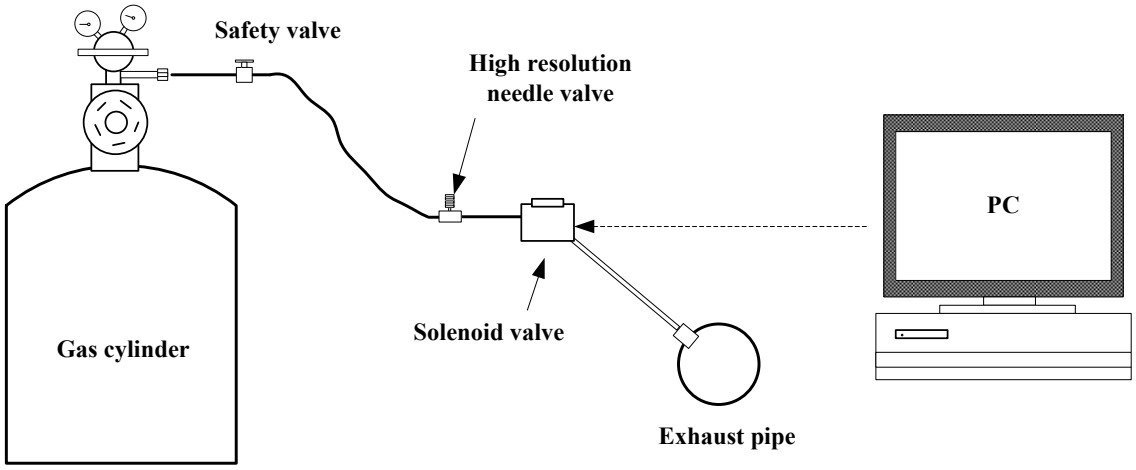


**Figure 3.10** Schematic of gas injection system.

### 3.1.8 Static in-line mixer

The static in-line mixer was positioned inside the exhaust pipe, downstream of the gas injection ports to provide good mixing of injected gas and exhaust gas. Figure 3.11 shows photographs of the paper model of the gas flow mixer plate. In the experiment, it was made from stainless steel sheet.

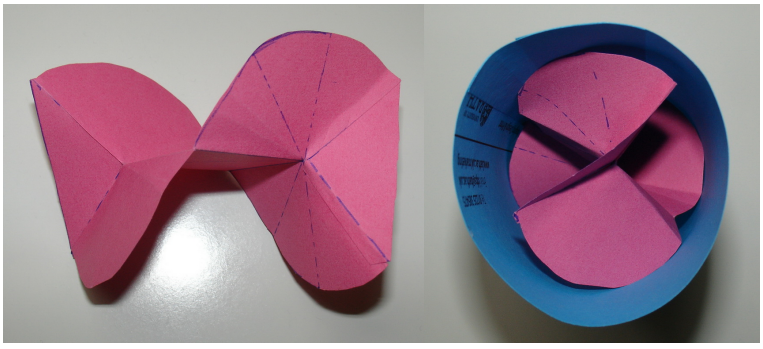

**Figure 3.11** Photographs of the paper model of the static in-line gas flow mixing plate.

## 3.2 Preliminary tests on equipment

Before carrying out the major investigations, a few preliminary tests need to be performed to ensure the experimental apparatus was working properly.

### 3.2.1 Checks on gas injection system and gas mixer

For this first set of experiments, only one gas analyser was used to avoid any uncertainty from reading differences between the two gas analysers. A three-way solenoid valve was installed to enable measurements to be taken either from the inlet or the outlet of the DOC. A cordierite monolith substrate was used instead of a reacting catalyst (to make sure the gas concentrations were the same at the inlet and the outlet). The engine was operated at 2000 revolutions per minute (rpm) and 25 Nm torque, which produced an inlet (to substrate) gas temperature of 235$^{o}$C, and inlet CO of 1200 ppm, and THCs of 200 ppm$C_1$. The exhaust gas flow rate was approximately 57 kg $h^{-1}$. Then the tests had been carried out in the following orders.

**Valve positions**

The first test was to identify the best position for the needle valve. Initially, the needle value was placed close to the gas cylinder, rather than close to the injection point. This was for safety reasons, since the needle valve had to be adjusted in some of the engine trials. However, following a set of experiments, it was decided to place the needle valve close to the exhaust pipe. This ensured that a sharp concentration pulse was obtained.

**Gas mixing**

The second test was to check the uniformity of gas mixing. During a series of tests, the exhaust gas was sampled at pre- and post-catalyst positions, and the analyser readings for CO and THCs were compared between these two positions. The results show that the two readings were the same, and thus the substrate was inert. Therefore, CO injection was switched on, and then the CO concentration readings at the inlet and the outlet of the substrate were compared. The readings remained consistent, which means the injected CO was well mixed. The same test was performed for propane, and it was found that the outlet concentration of THCs is higher than inlet. This might be a sign of non-uniform mixing. In order to identify the cause of this problem, propane was

injected from the CO injection port and the difference in readings was not observed this time; CO was injected from the propane port, and outlet CO concentration reading was higher than the inlet. From these observations, the following conclusions were formed: The gas injected from the CO injection port was well mixed since this injection port is 65 cm away from the gas mixers. The propane injection port is too close to the gas mixers (10 cm away from the gas mixers), so the injected propane did not have time to mix.

Therefore, a few modifications had made to the exhaust sections. The propane injection port was moved 5 cm upstream of the CO injection port. Another gas mixer was made and installed in front of the existing two gas mixers. Then the test was repeated, and it was found that the injected gas from both ports mixed well with exhaust.

**Checks on two gas analysers' readings**

When performing the transient emission measurement, two Horiba MEXA-7000 series gas analysers (Horiba MEXA-7100 DEGR and Horiba MEXA-7170 DEGR) would be used to measure inlet and outlet emissions simultaneously. Therefore, prior to any transient tests, checks must be performed on the readings of these two gas analysers to identify if there are any discrepancies between the readings. This check was concluded with following procedures:

- A cordierite monolith substrate was used as dummy section between the two sampling points (in order to prevent any possible reactions that may disturb the readings). Also, it acted as a flow straighter.
- The engine was operated at a constant condition (2000 rpm and 25 Nm torque). At this condition, the inlet gas temperature to the monolith substrate was around 220$^{o}$C (this is above 190$^{o}$C where the THCs storage problem may occur). The air mass flowrate was around 57 kg h$^{-1}$.
- As steady-state was achieved (the "steady-state" means the mass flowrate and engine-out emissions do not change significantly), twenty readings were taken at 10 s intervals in 5 minutes.
- Then by injecting CO, the CO concentration was increased from 1000 to 6000 ppm (incrementally). By injecting propane, the THCs concentration was increased from 100 to 3450 ppm$C_1$.

- The two gas analyser readings were compared, and it was found that the two gas analysers were reading differently. Then, the sampling positions of the two gas analysers were swopped, and the readings remained the same. Hence, the difference between two analysers could be confirmed.

Therefore, the two gas analysers were tested by a technician, and then calibrated by an engineer from Horiba. To check THCs readings, a bottle of 2000 ppm alpha grade propane in nitrogen was used. The engineer spanned the concentration from 0 to 6000 ppm$C_1$ using a special piece of kit and compared these concentrations with the readings on the two analysers. It was found that the THCs readings from the two analysers were close to the actual concentration. To calibrate the CO readings a similar process was repeated using 4000 ppm of CO in nitrogen, and then a calibration equation was created for each analyser to estimate the actual concentration from its reading. Some of the results are also presented in Appendix 6.

### 3.2.2 Baseline engine tests

These consisted of measurements on the diesel engine, which included: emissions, air mass flowrate and exhaust temperature. The engine was run from 1000 to 3500 rpm (at increments of 500 rpm). At each engine speed, the engine torque was increased from 5 to 200 Nm (at increments of 5 Nm). The EGR valve was maintained fully open during the tests. Data was taken at each combined speed and torque reading. Thus, a matrix of test data was formed, see Table 3.5.

**Table 3.5** A matrix of engine test data obtained from Ford PUMA 2.0 litre diesel engine.

| Engine Speed RPM | Engine torque Nm | Gas Temp. $^{o}C$ | CO ppm | $O_2$ % | THCs $ppmC_1$ | NOx ppm | Air Mass Flow kg/h |
|---|---|---|---|---|---|---|---|
| 1000 | 20.8 | 219.7 | 461 | 13.68 | 107 | 118 | 36.1 |
| 1000 | 40.2 | 250.9 | 328 | 12.95 | 67 | 236 | 45.03 |
| 1000 | 59.6 | 312 | 374 | 10.95 | 56 | 273 | 50.51 |
| 1000 | 79.6 | 372.2 | 420 | 8.73 | 51 | 277 | 54.24 |
| 1000 | 99.2 | 414.4 | 327 | 7.49 | 51 | 433 | 57.05 |
| 1000 | 119.4 | 452.5 | 205 | 6.91 | 45 | 917 | 66.14 |
| 1000 | 160.8 | 571.7 | 3720 | 2.27 | 42 | 1233 | 69.37 |
| 1500 | 20.6 | 270.4 | 2958 | 10.42 | 1033 | 23 | 36.37 |
| 1500 | 40 | 282.4 | 883 | 12.33 | 174 | 119 | 64.37 |
| 1499 | 59.2 | 331.4 | 704 | 11.04 | 107 | 174 | 73.57 |
| 1500 | 79.5 | 371.2 | 505 | 9.67 | 69 | 237 | 80.25 |
| 1500 | 99.4 | 406.8 | 305 | 9 | 48 | 343 | 90.56 |
| 1499 | 119.5 | 445.9 | 231 | 8.22 | 45 | 411 | 103.81 |
| 1499 | 139.7 | 477.2 | 164 | 7.81 | 41 | 611 | 116.47 |
| 1499 | 159.8 | 495.4 | 99 | 8.49 | 36 | 1241 | 138.53 |
| 1501 | 179.7 | 530.7 | 94 | 7.35 | 33 | 1296 | 142.02 |
| 1501 | 199.7 | 574.5 | 107 | 6.11 | 32 | 1378 | 146.01 |
| 1499 | 219.8 | 613 | 171 | 5.02 | 31 | 1405 | 151.35 |
| 1499 | 239.7 | 641.6 | 285 | 4.07 | 30 | 1444 | 157.68 |
| 1501 | 249.4 | 669 | 2636 | 1.69 | 30 | 1163 | 149.46 |
| 2000 | 20.1 | 242 | 894 | 17.06 | 126 | 214 | 151.32 |
| 2000 | 39.7 | 282.4 | 929 | 15.9 | 96 | 294 | 161.86 |
| 2000 | 59.2 | 325.5 | 769 | 14.83 | 71 | 409 | 169.26 |
| 2000 | 79.6 | 369.9 | 570 | 13.81 | 48 | 568 | 175.79 |
| 2000 | 99.7 | 405.1 | 404 | 12.8 | 43 | 672 | 184.66 |
| 2000 | 119.7 | 432.5 | 300 | 11.89 | 35 | 760 | 193.82 |
| 2000 | 139.7 | 466.3 | 200 | 10.89 | 32 | 915 | 197.39 |
| 2000 | 139.8 | 465.6 | 205 | 10.63 | 34 | 887 | 191.46 |
| 2000 | 159.7 | 505.8 | 155 | 9.67 | 32 | 927 | 197.95 |
| 2000 | 179.7 | 526.3 | 130 | 8.95 | 29 | 1031 | 206.84 |
| 2000 | 199.7 | 548.1 | 113 | 8.11 | 28 | 1165 | 212.84 |
| 2000 | 220 | 582.4 | 140 | 6.51 | 27 | 1276 | 209.61 |
| 2000 | 240.2 | 620.8 | 248 | 4.89 | 27 | 1321 | 208.68 |
| 2000 | 260.6 | 606.8 | 106 | 6.02 | 27 | 1329 | 240.24 |
| 2000 | 268.3 | 635.3 | 155 | 5.21 | 24 | 1383 | 237.52 |
| 2000 | 281.1 | 562.2 | 74 | 7.16 | 23 | 1164 | 266.56 |
| 2000 | 301.1 | 580.5 | 78 | 6.51 | 21 | 1211 | 275.38 |
| 2000 | 326.6 | 608.2 | 110 | 5.66 | 20 | 1223 | 286.89 |

| Engine Speed RPM | Engine torque Nm | Gas Temp. $^{o}C$ | CO (low) ppm | $O_2$ % | THCs $ppmC_1$ | NOx ppm | Air Mass Flow kg/h |
|---|---|---|---|---|---|---|---|
| 2500 | 21.3 | 279.5 | 2718 | 14.58 | 2243 | 45 | 116.45 |
| 2500 | 40.4 | 320 | 2165 | 12.78 | 961 | 75 | 122.91 |
| 2500 | 60.2 | 349.3 | 1748 | 11.59 | 340 | 111 | 136.24 |
| 2500 | 80.1 | 383.6 | 1346 | 10.55 | 164 | 138 | 151.09 |
| 2500 | 100.3 | 406.8 | 1078 | 9.95 | 105 | 167 | 169.69 |
| 2500 | 120.1 | 423.8 | 800 | 9.95 | 72 | 243 | 195.2 |
| 2500 | 140 | 444 | 561 | 10.3 | 55 | 284 | 228.36 |
| 2500 | 160 | 449.8 | 282 | 10.85 | 41 | 450 | 265.92 |
| 2500 | 179.8 | 455.9 | 100 | 11.33 | 31 | 643 | 310.48 |
| 2500 | 199.7 | 477.6 | 92 | 10.83 | 31 | 735 | 324.26 |
| 2500 | 219.7 | 494.8 | 85 | 10.27 | 30 | 820 | 336.13 |
| 2500 | 239.7 | 515.4 | 79 | 9.58 | 28 | 887 | 344.1 |
| 2500 | 259.4 | 536.8 | 73 | 8.84 | 28 | 986 | 350.03 |
| 2500 | 279.3 | 562.3 | 71 | 7.95 | 30 | 1078 | 352.33 |
| 2500 | 313.3 | 622.3 | 178 | 5.81 | 37 | 1093 | 350.54 |
| 2999 | 21.4 | 264.7 | 1254 | 15.69 | 669 | 95 | 167.51 |
| 2999 | 40.3 | 305.1 | 732 | 14.71 | 276 | 132 | 195.97 |
| 2999 | 60.1 | 332.3 | 546 | 14.19 | 140 | 156 | 233.88 |
| 2999 | 80.2 | 354.5 | 510 | 13.69 | 89 | 190 | 267 |
| 2999 | 100.1 | 384.8 | 514 | 13.39 | 70 | 242 | 302.38 |
| 2999 | 119.9 | 410.3 | 418 | 13.05 | 53 | 333 | 329.54 |
| 2999 | 140 | 435 | 386 | 12.56 | 46 | 350 | 357.22 |
| 3002 | 160.1 | 458.7 | 504 | 12.09 | 37 | 387 | 380.55 |
| 3002 | 179.6 | 489.9 | 412 | 11.59 | 33 | 502 | 401.23 |
| 3002 | 198.8 | 514 | 342 | 10.86 | 31 | 560 | 411.99 |
| 3002 | 219.5 | 535.4 | 195 | 9.94 | 29 | 644 | 413.1 |
| 3002 | 238.9 | 562.1 | 120 | 8.98 | 27 | 757 | 413.56 |
| 3002 | 259.1 | 591.8 | 113 | 8.02 | 28 | 899 | 413.23 |
| 3002 | 283.6 | 632.8 | 158 | 6.76 | 29 | 961 | 420.01 |
| 3500 | 19.8 | 266.4 | 853 | 16.59 | 365 | 160 | 264.21 |
| 3500 | 39.6 | 305.2 | 745 | 15.71 | 218 | 187 | 294.23 |
| 3500 | 59.4 | 344.6 | 655 | 14.79 | 136 | 230 | 312.03 |
| 3500 | 79.6 | 363.6 | 160 | 14.33 | 53 | 251 | 364.78 |
| 3500 | 99.8 | 400.3 | 141 | 13.73 | 44 | 297 | 394.69 |
| 3500 | 119.9 | 431.4 | 139 | 12.86 | 39 | 378 | 400.69 |
| 3499 | 139.9 | 471 | 150 | 12.05 | 36 | 419 | 415.34 |
| 3500 | 159.8 | 502.1 | 134 | 11.41 | 34 | 524 | 432.41 |
| 3500 | 179.6 | 528.3 | 115 | 10.73 | 33 | 664 | 445.93 |
| 3500 | 199.6 | 558.3 | 103 | 9.97 | 31 | 816 | 456.37 |

### 3.2.3 Effect of pulsating flow

Following the literature review and discussion on the effect of pulsating flow on the performance of catalytic converters in Section 2.2, a simple test was carried out to determine the pattern and intensity of exhaust flow pulsation from the current engine set-up, and to explore its effect on the warm-up process and the performance of the DOC.

The engine was operated at a fixed speed of 2000 rpm, and at a fix torque of 45 Nm, such that it would produce an exhaust gas at temperature of 260$^{o}$C, and a mass flowrate of 60 kg h$^{-1}$. These operating conditions are considered to be representative of the trials performed in this project. The pressure at the inlet and the outlet of the DOC was monitored by two pressure transducers at a rate of 80 *Hz*. An example of such pressure data (presented as gauge pressure) is plotted as a function of time in Figure 3.12.

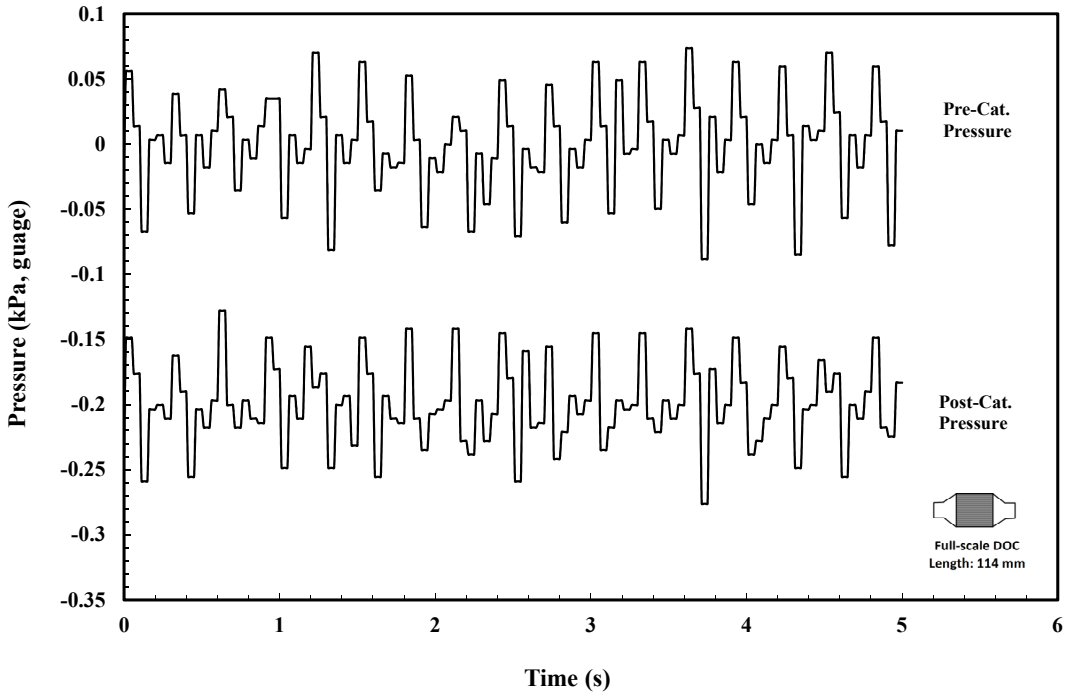


**Figure 3.12** Measured pre and post-catalyst pressure, where the engine is operated at 2000 rpm speed and 45 Nm torque. The air mass flowrate was 60 kg h$^{-1}$.

In the literature, the intensity of pulsation is usually represented as a ratio of peak velocity to mean velocity. However, in the current engine set-up, the exhaust gas velocity is not measured. Nevertheless, the exhaust gas velocity can be estimated from the pressure drop data. A sample calculation is shown in Appendix 1.5. The calculated

mean velocity has a value of 4.56 m $s^{-1}$, and this is close to the velocity calculated from the air mass flow from engine control unit (ECU), which is 4.78 m $s^{-1}$.

Figure 3.13 shows the calculated velocity from pressure drop as a function of time. As can be seen, the maximum peak velocity is only ± 8% more than the mean velocity. If this is compared with results of work by Tsinoglou and Koltsakis (2005) (discussed earlier in Section 2.2.2), then this variation of ±8% in velocity is not considered to have a big impact on the performance of the DOC.

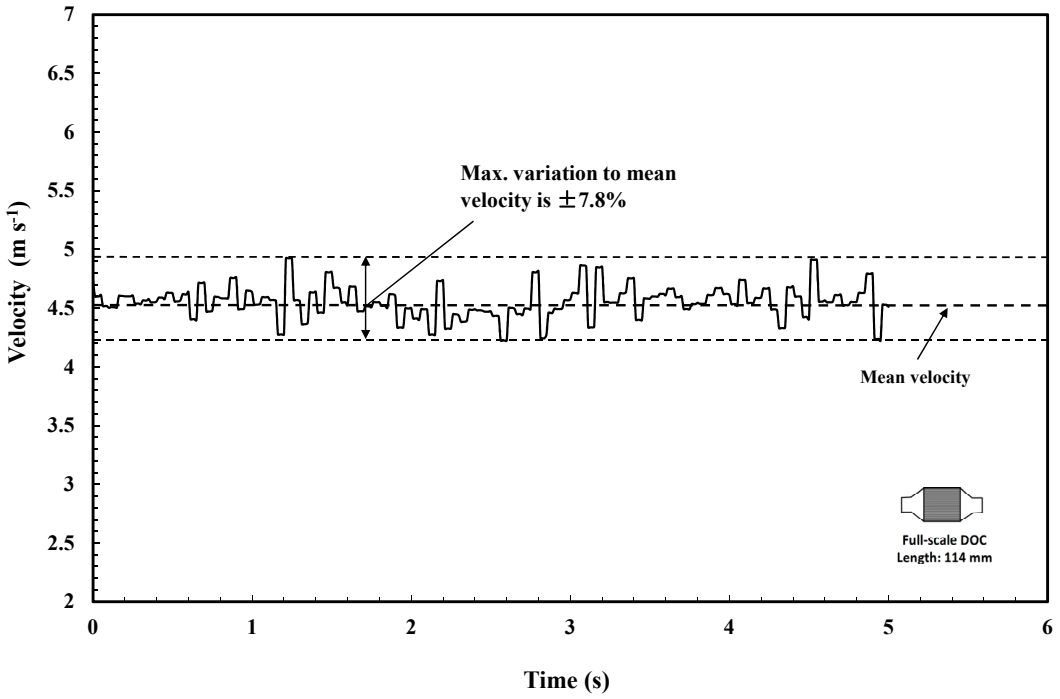


**Figure 3.13** Calculated exhaust gas velocity as a function of time.

## 3.3 New European Driving Cycle (NEDC)

In this section, measurements are made that assess the performance of the DOC as the engine is operated to simulate the NEDC. This will help to identify conditions that are of interest, and at which catalyst 'light-off' experiments would be desirable. The experiments highlighted in red in Figure 3.14 will be described in this section.

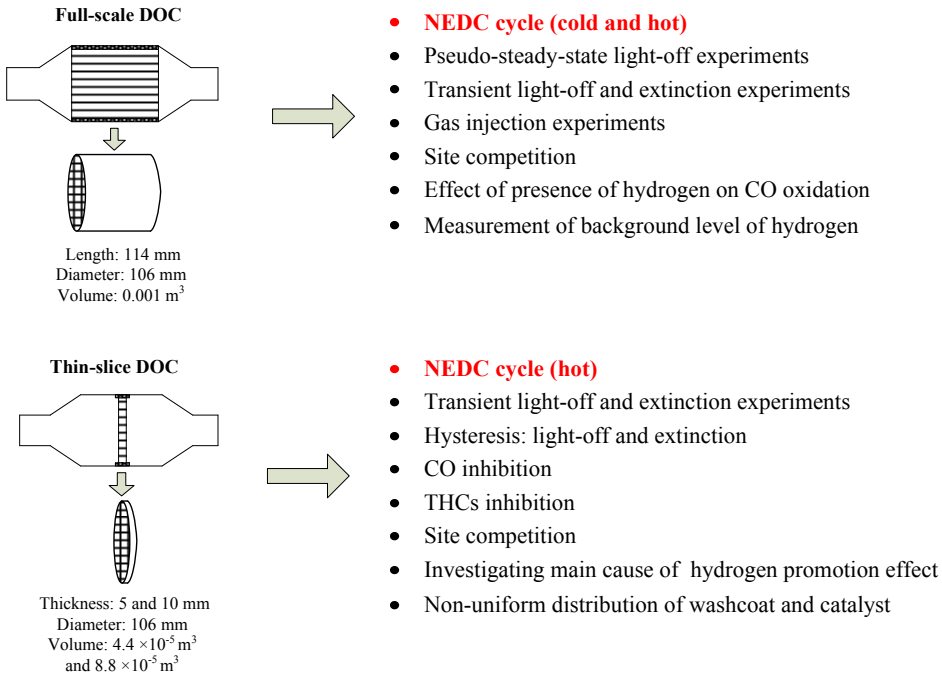


**Figure 3.14** Summary of experiments in Chapter 3. The highlighted experiments are discussed in Section 3.3.

The NEDC is used to evaluate emission levels from car engines. It consists of a repeated urban driving cycle (UDC) and an extra urban driving cycle (EUDC). Figure 3.15 shows the NEDC in terms of vehicle speed. The UDC represents the driving mode in an urban area, and the EUDC is devised to simulate high speed and aggressive driving modes on highways.

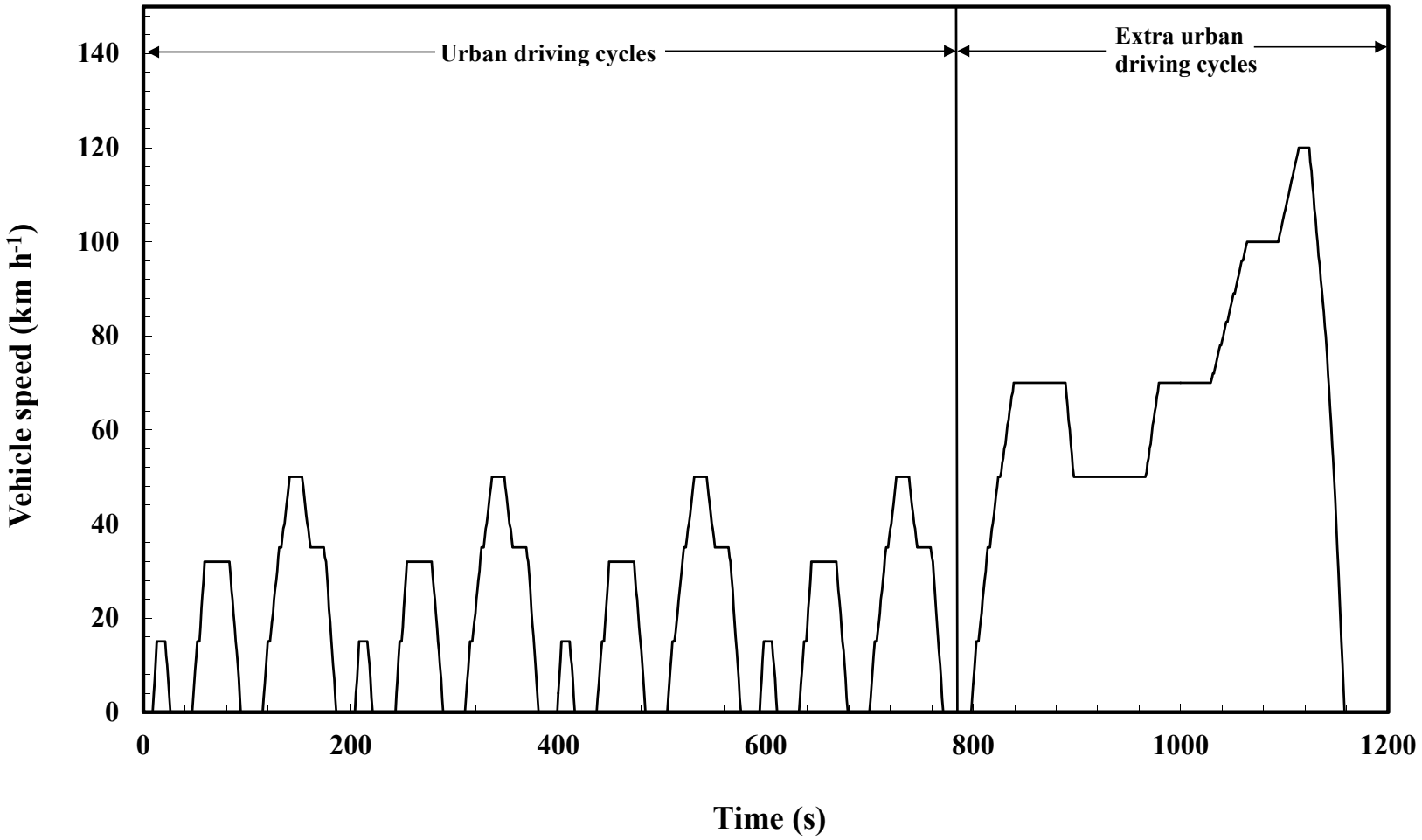


**Figure 3.15** Vehicle speed during a NEDC.

### 3.3.1 Cold NEDC

The cold NEDC test means the NEDC is performed starting with a low engine temperature (the engine is rested overnight). This represents a “cold-start” situation. This test enables an operating map of the engine to be developed. This helps to select the test conditions in this thesis, which helps to ensure that they are realistic. The cold NEDC was performed on a Full-scale DOC. Exhaust gas emissions were measured both at the inlet and the outlet of the DOC. The engine was programmed to run the test automatically. All the experimental data was stored automatically in a trace file, which was then converted into a spread-sheet.

When taking measurements, there is a time difference (delay) between temperature measurements and emission measurements due to the time delay of the emission analysers. The time delay of the emission analysers mainly consists of two parts. The first is a transport time delay through the pipe work, and the second is the response time of the gas analysers (includes transport time in the heated line). Generally speaking, the transport time through the pipe work is much less significant than the response time of the gas analysers. The exhaust gas velocity is fast, and this leads to short residence time in the pipe section. This normally has a magnitude of 0.1 s. In contrast, the gas sample has to travel through a much longer (approximately 12 metres) heated sampling pipe connected to the analyser that results in a significant time delay. According to the gas analyser manual, the response time measured by the manufacturer can be as long as 6 s. Nevertheless, this response time varies with different gas species analysed.

This time delay could be determined from experiments in which a pulse of CO was injected into the exhaust pipe. Two gas analysers were used to measure the CO concentration at the inlet and the outlet of the DOC. Therefore, the transient response was captured. An example of such an experiment is shown in Figure 3.16. The time at which the valve was opened is indicated as a red line, and the time delay before the CO concentration ramp appears is about 7 s. This is close to the value provided by the analyser manufacturer. From this test data, the time delay between the two gas analysers is negligible.

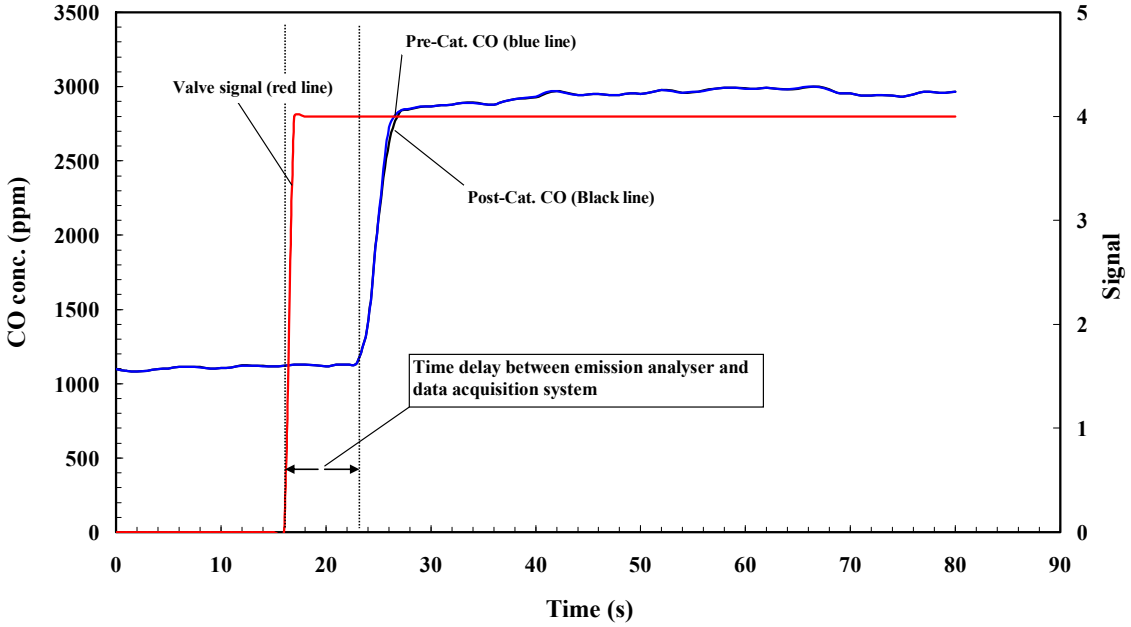


**Figure 3.16** Time delay can be seen by plotting the valve signal and the response from the analyser on same graph.

## Results and discussions

The cold NEDC was repeated three times to test the repeatability. By comparing the emission data between different tests, a repeatable trend was observed. The absolute emission value changed from test to test, but the variations were small and acceptable (CO emission variation is within ± 5%; THCs emission variation is within ± 20%; and $NO_x$ emission variation is within ± 2%). In general, considering the complexity of operating an engine the repeatability of the NEDC was good. The results obtained from the cold NEDC performed on 19/03/2010 are presented in this section. The operating conditions (engine speed and torque) for the engine are shown in Figures 3.17 and 3.18.

The inlet gas temperature to the DOC is plotted as a function of time in Figure 3.19. It can be seen that the inlet gas temperature varies with time (i.e. engine operating conditions). The test is started from cold, so that the inlet gas temperature is relatively low (40$^{o}$C) at the beginning, and then warms up gradually as time passes. Finally, it reaches a peak at approximately 400$^{o}$C. In the repeating UDC (0 - 800s), the inlet gas (i.e. exhaust) temperature was relatively low (around 130$^{o}$C). In the EUDC, the inlet gas temperature increased much faster (than UDC) since the engine was run under more

harsh conditions. The trend in the inlet gas temperature reflects the trend in the engine temperature.

Figure 3.20 shows the wall (or catalyst) temperature profiles along the axial length of the DOC in the cold NEDC. The wall temperatures follow the same trend of inlet gas temperature in Figure 3.19. The wall temperature is also cold at the beginning of the cycle (27$^{o}$C) and then gradually increases to 420$^{o}$C in the EUDC. Comparing this with Figure 3.19, the initial wall temperature is lower than the inlet gas temperature, and the peak wall temperature is higher than the gas temperature (due to the heat released from reactions at the catalyst surface).

Figure 3.20 also demonstrates how the DOC works under transient conditions. When the vehicle accelerates (creating a high inlet gas temperature and high emission), the entire length of the DOC is reacting to remove the pollutants. This is evident over the 800 to 840 s in the UDC. When the vehicle decelerates (lower inlet gas temperature and emission), the front part of the DOC is cooled rapidly by the inlet gas temperature, and the temperature at the rear of the DOC decreases more slowly. This indicates that the reactions are retained in the rear part of the DOC. This also explains why the Full-scale DOC is very effective at removing pollutants.

Figure 3.21 shows the wall (or catalyst) temperature profiles (at 65 mm to the inlet of the DOC) in the radial direction of the catalyst, during the cold NEDC. The wall temperatures at three different radial locations (i.e. r = 0, r =1/2 R and r = 7/8 R) have a similar trend, however, temperature gradients can be observed in the radial direction. The wall temperature measured at the centre of the DOC (r = 0) has the highest value; and the wall temperatures measured at the outer (r = 1/2 R and 7/8 R) have lower values. This may be caused by heat loss to the surroundings (in the radial direction), or the presence of more complex flow patterns across the face of the DOC

Next, emissions are examined.

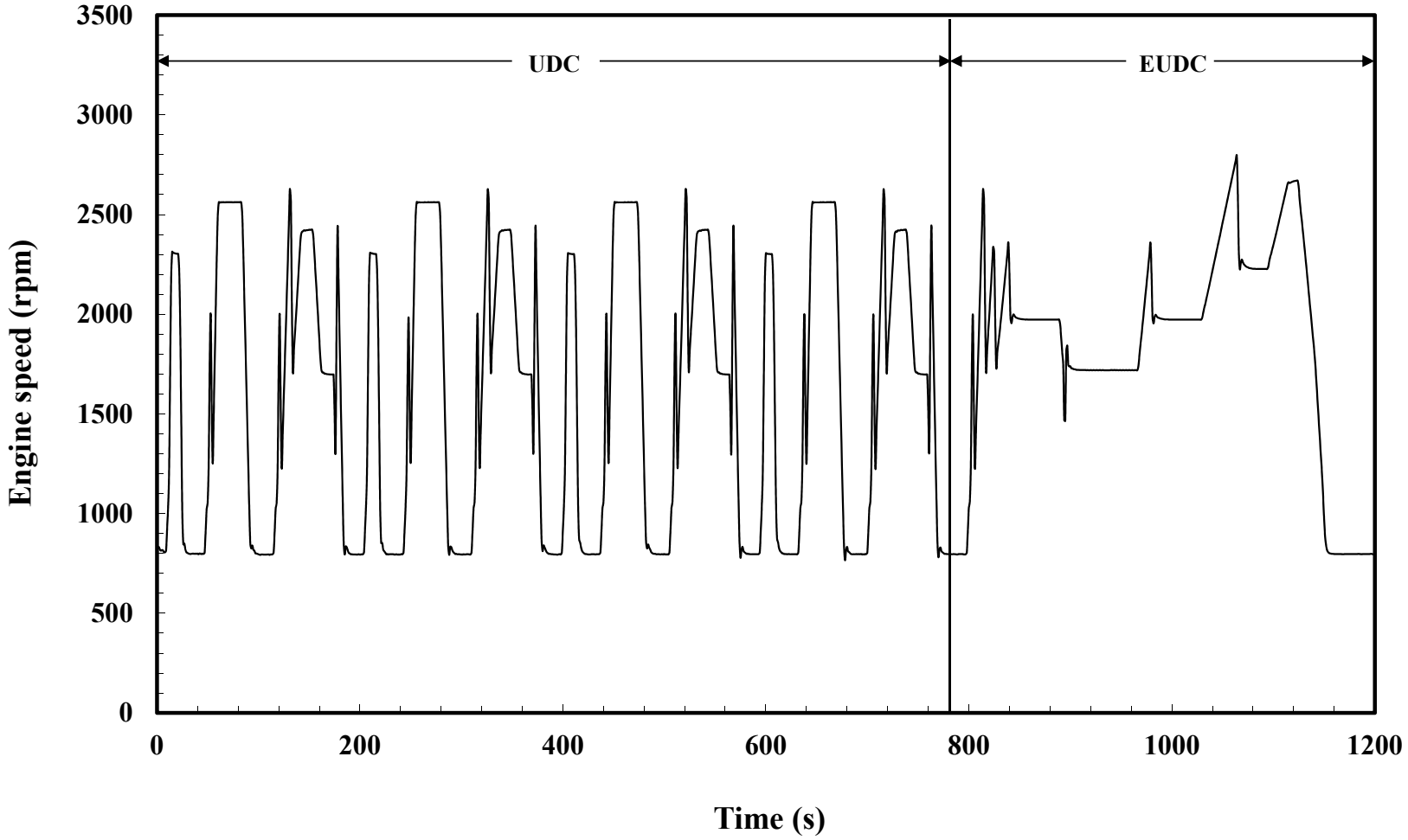


**Figure 3.17** Engine speed during a NEDC.

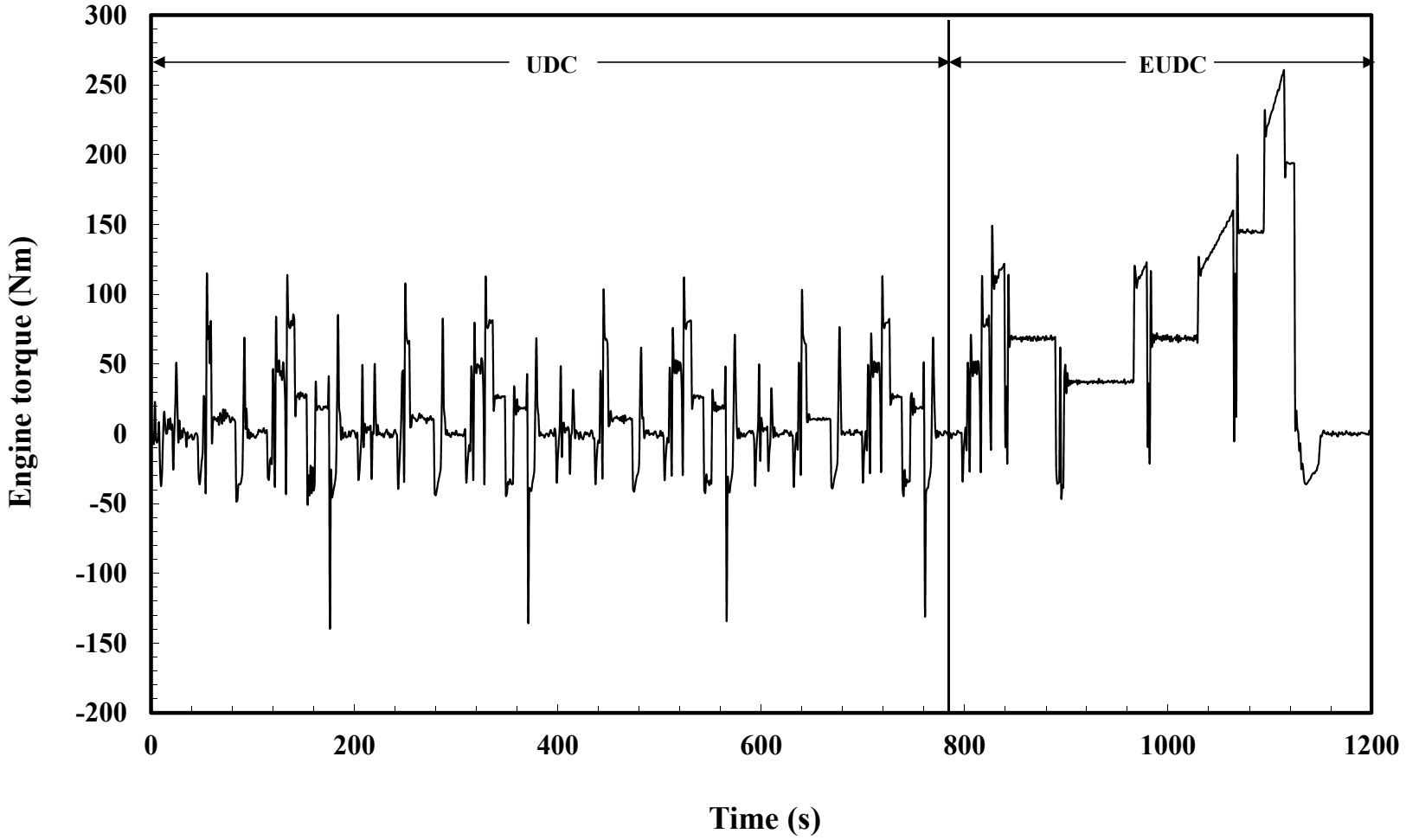


**Figure 3.18** Engine torque during a NEDC.

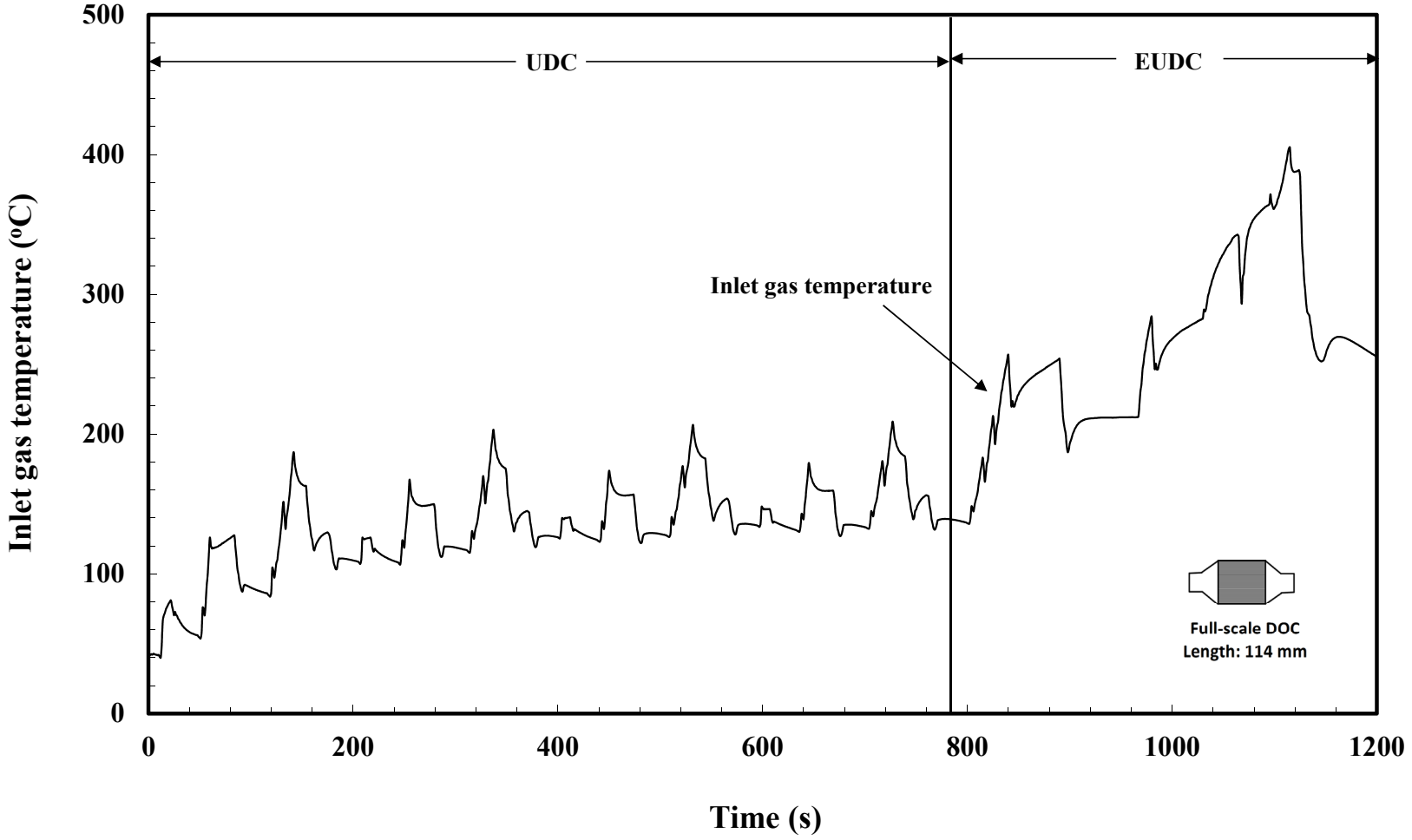


**Figure 3.19** Inlet gas temperature profile in a cold NEDC.

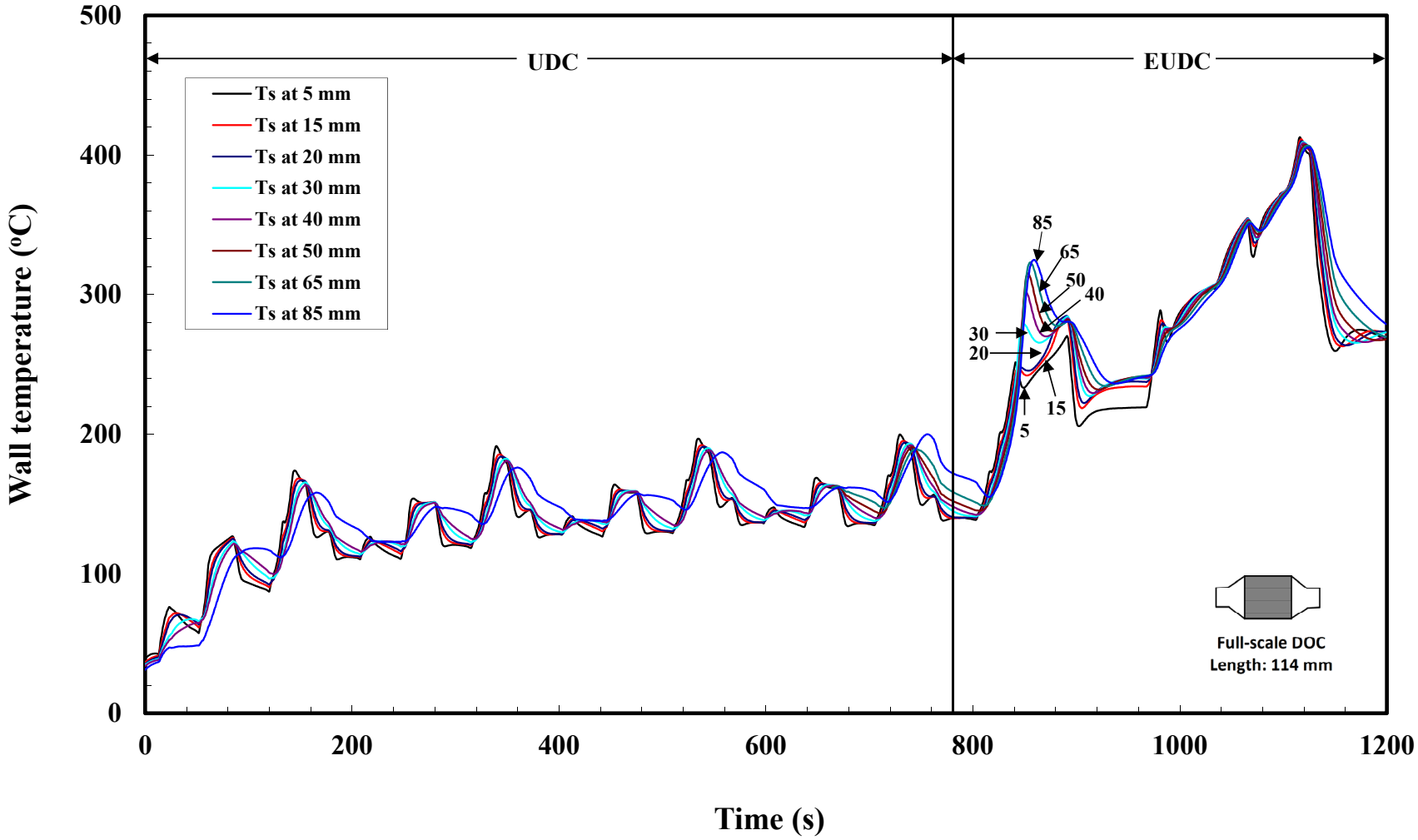


**Figure 3.20** Axial wall (catalyst) temperature profiles in a cold NEDC. The overall length of the catalyst is 114 mm, the volume is 0.001 $m^3$ (1 litre).

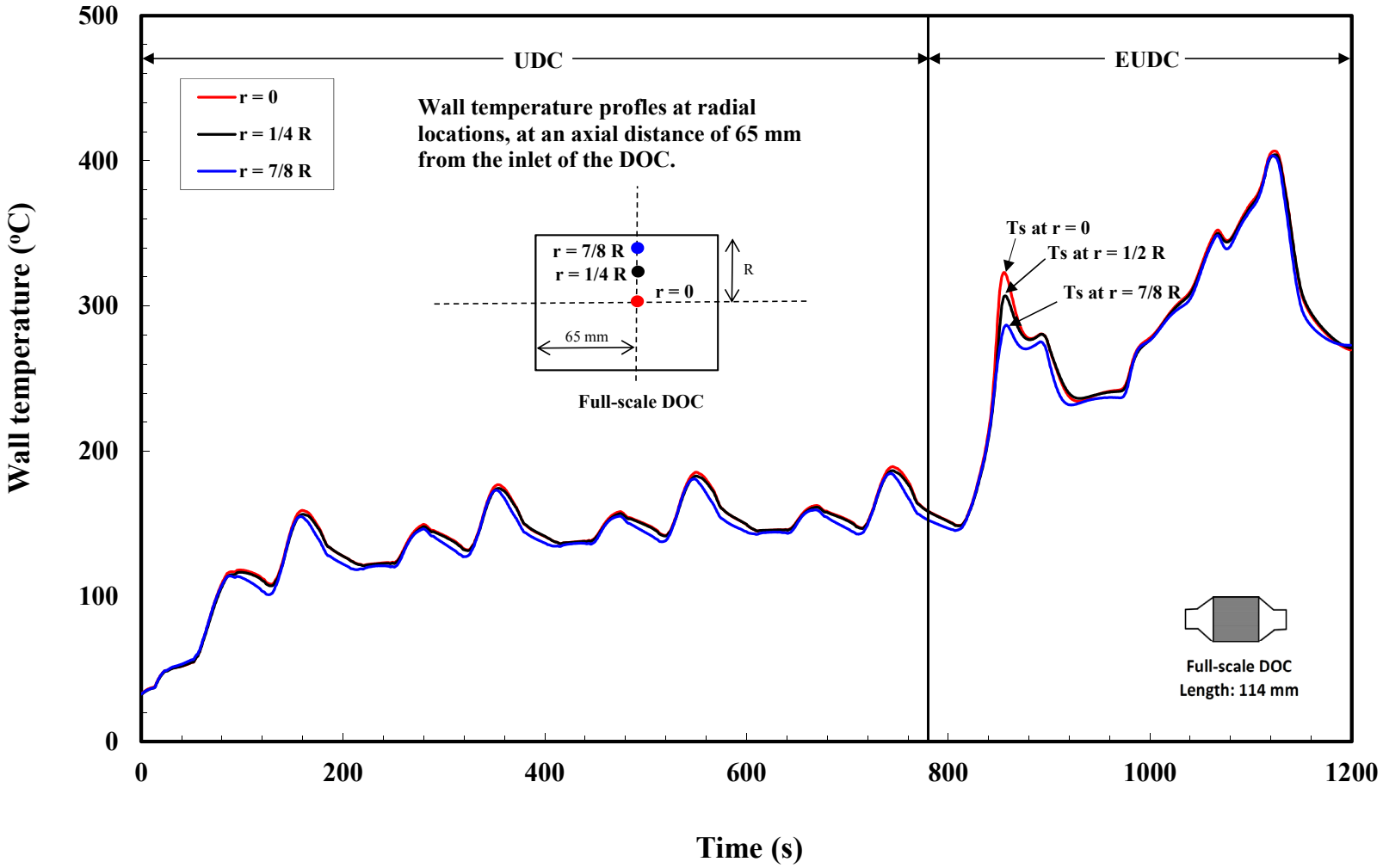


**Figure 3.21** Radial wall (catalyst) temperature profiles at a 65 mm distance from the inlet of the DOC in a cold NEDC.

Figure 3.22 shows the pre-and post-catalyst CO emissions in the cold NEDC. In the UDC, the pre-and post-catalyst emission are high. The high pre-catalyst CO emission is due to low engine temperature, which resulted from incomplete fuel combustion. The low conversion of CO (i.e. high post-catalyst CO emission) is also because the catalyst temperature is below the light-off temperature. Therefore, as the engine gets warmer in the EUDC, the pre-catalyst CO emission becomes lower. The conversion of CO is improved significantly. The emission data is also processed and presented as cumulative emission data, see Figure 3.23. This was obtained from the following equation:

$$Cumulative\ CO_{emission} = \sum_{i=1:1200} \left( \frac{C_{CO,i} \times F_{exhaust,i} \times M_{CO}}{10^6} \right) \text{g} \qquad (3.3)$$

where $C_{co,i}$ is concentration of CO at time $i$ (ppm), and $F_{exhaust}$ is the molar flowrate of exhaust at time $i$ (mol $s^{-1}$), and $M_{co}$ is the molar mass of CO (g $mol^{-1}$). It can be seen that the overall conversion of CO in the cold NEDC is 24.4%. Of this amount 85% is converted in the EUDC part of the cycle.

Figure 3.24 shows the pre- and post-catalyst THCs emission data in the cold NEDC. The pre-catalyst THCs emissions have peaks that correspond to CO peaks throughout the test cycle. However, THCs emissions decrease much faster as the engine warms up. In addition, conversion of THCs can be seen to occur at the beginning of the cycle. This may occur because the heavy components of THCs (> $C_6$) could be stored (or trapped) on the catalyst structure (at low temperature (< 190$^o$C)); and these trapped THCs could then be released as the temperature increased above 190$^o$C. The conversion of THCs also increases with temperature.

Figure 3.25 shows the cumulative emissions of THCs. In this cycle the overall conversion of THCs was 27.2%, and this was uniform throughout the test cycle.

Figure 3.26 shows the pre- and post-catalyst $NO_x$ emissions in the cold NEDC. This is also plotted as cumulative emissions in Figure 3.27. From these figures, the pre-catalyst $NO_x$ emission is relatively low in the UDC, and increases significantly in the latter phase of EUDC. This is because the engine temperature has an adverse effect on $NO_x$ emissions. As engine temperature increases more $NO_x$ is produced (Stone, 1999; p. 101). As expected, the DOC has very little effect on the reduction of $NO_x$ emission (4.7% conversion from Figure 3.27).

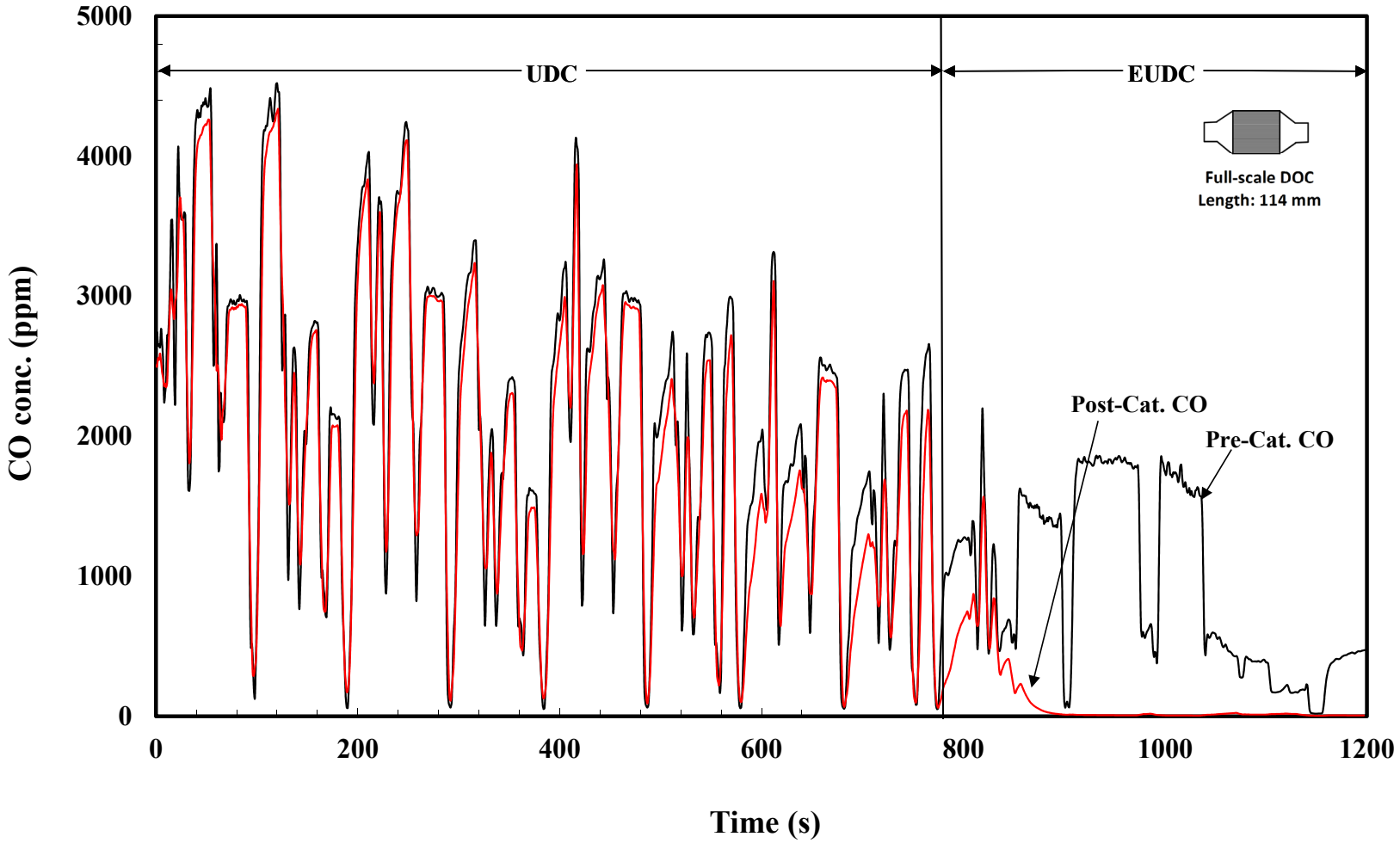


**Figure 3.22** Pre- and post-catalyst emissions of CO in a cold NEDC.

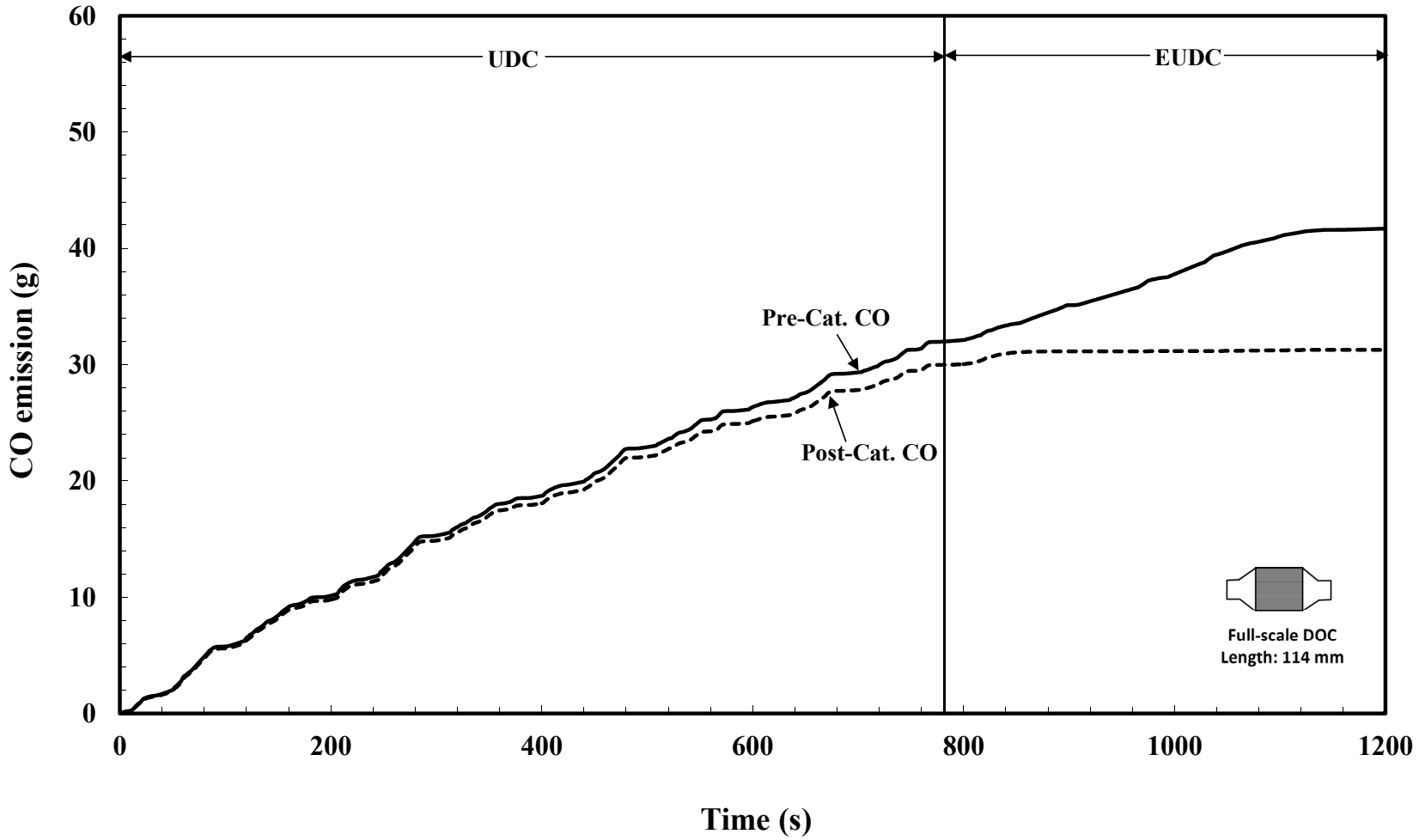


**Figure 3.23** Cumulative emissions of CO at pre- and post-catalyst positions in a cold NEDC.

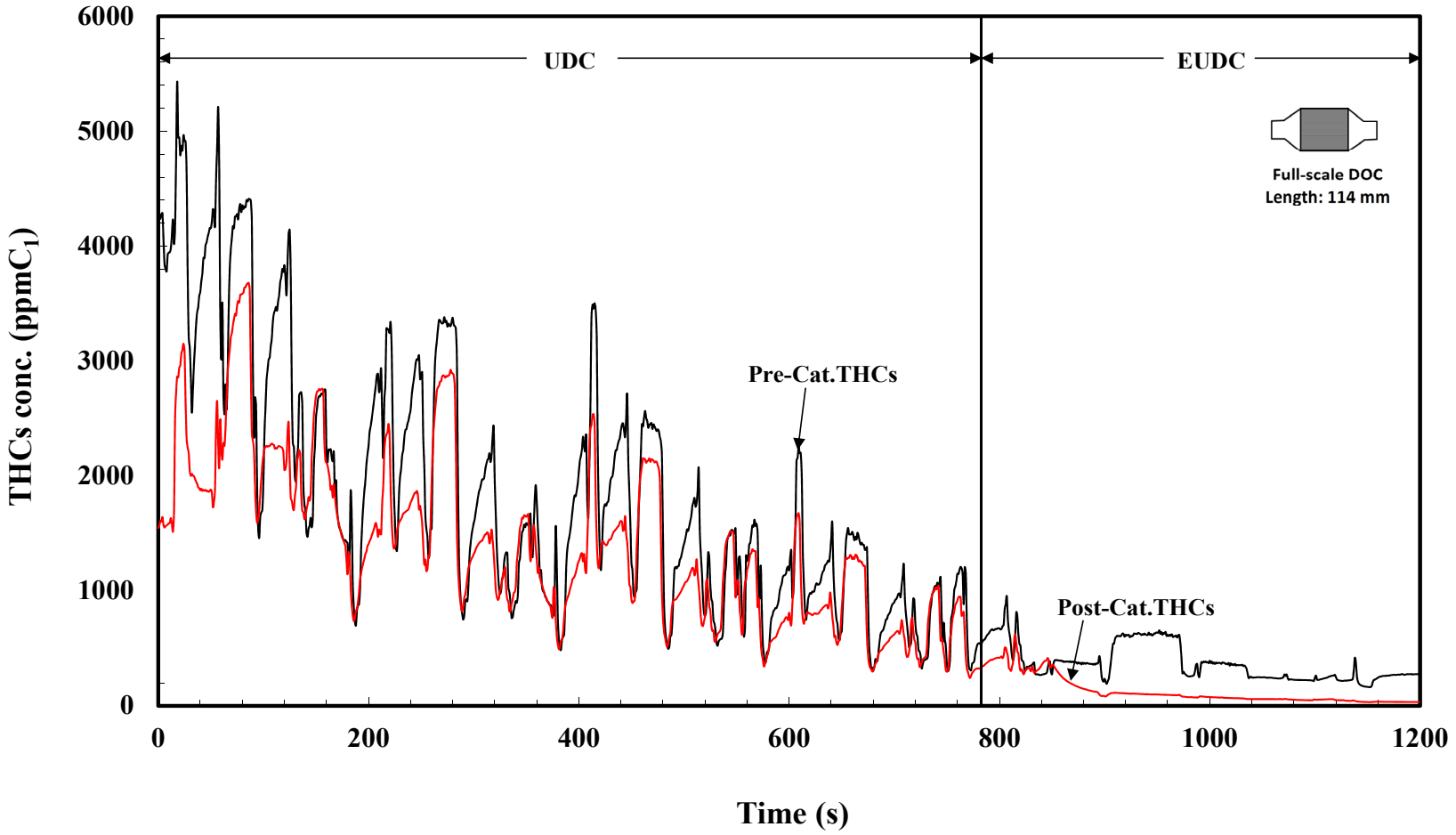


**Figure 3.24** Pre- and post- catalyst emissions of THCs in a cold NEDC cycle.

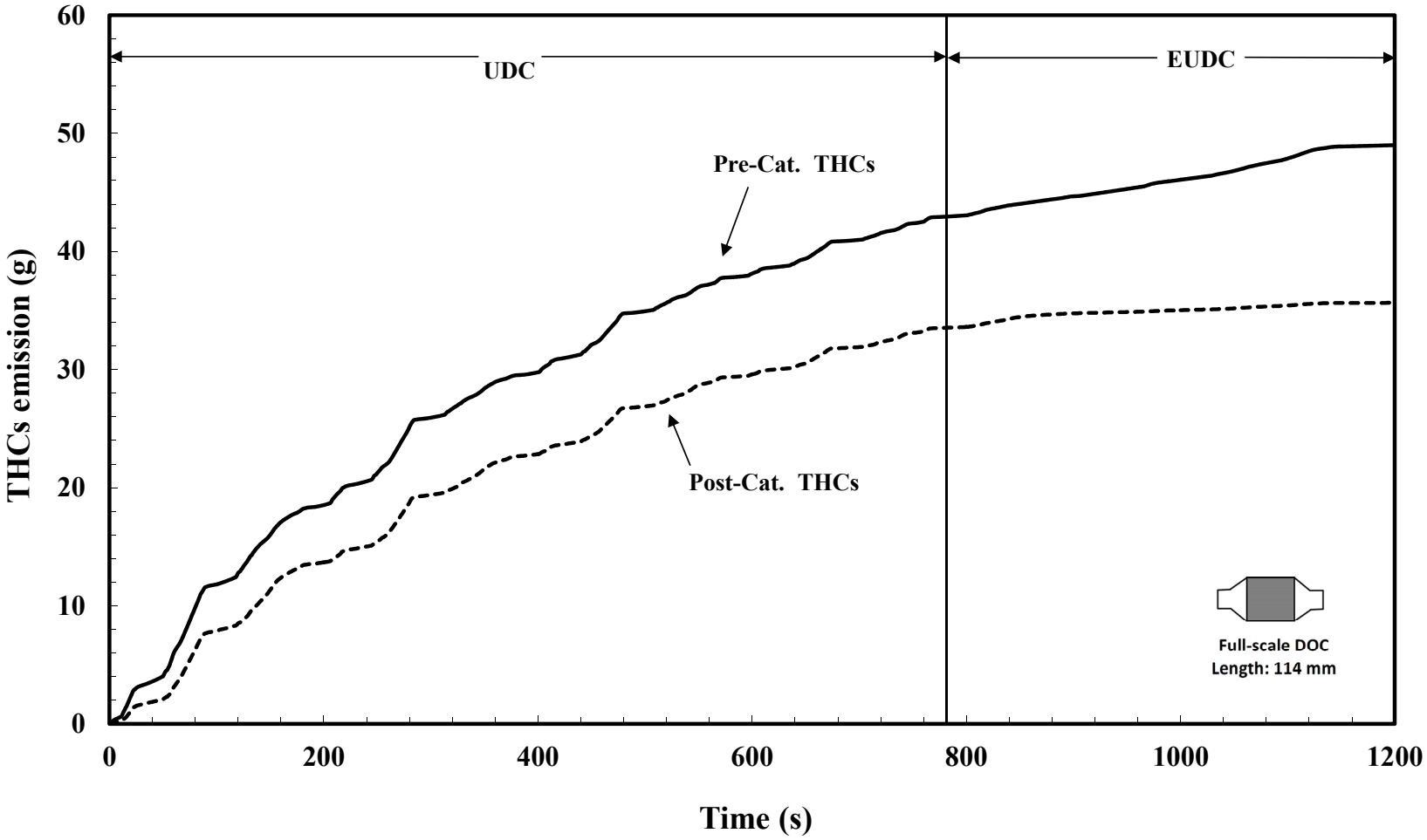


**Figure 3.25** Cumulative emissions of THCs at pre- and post- catalyst positions in a cold NEDC cycle.

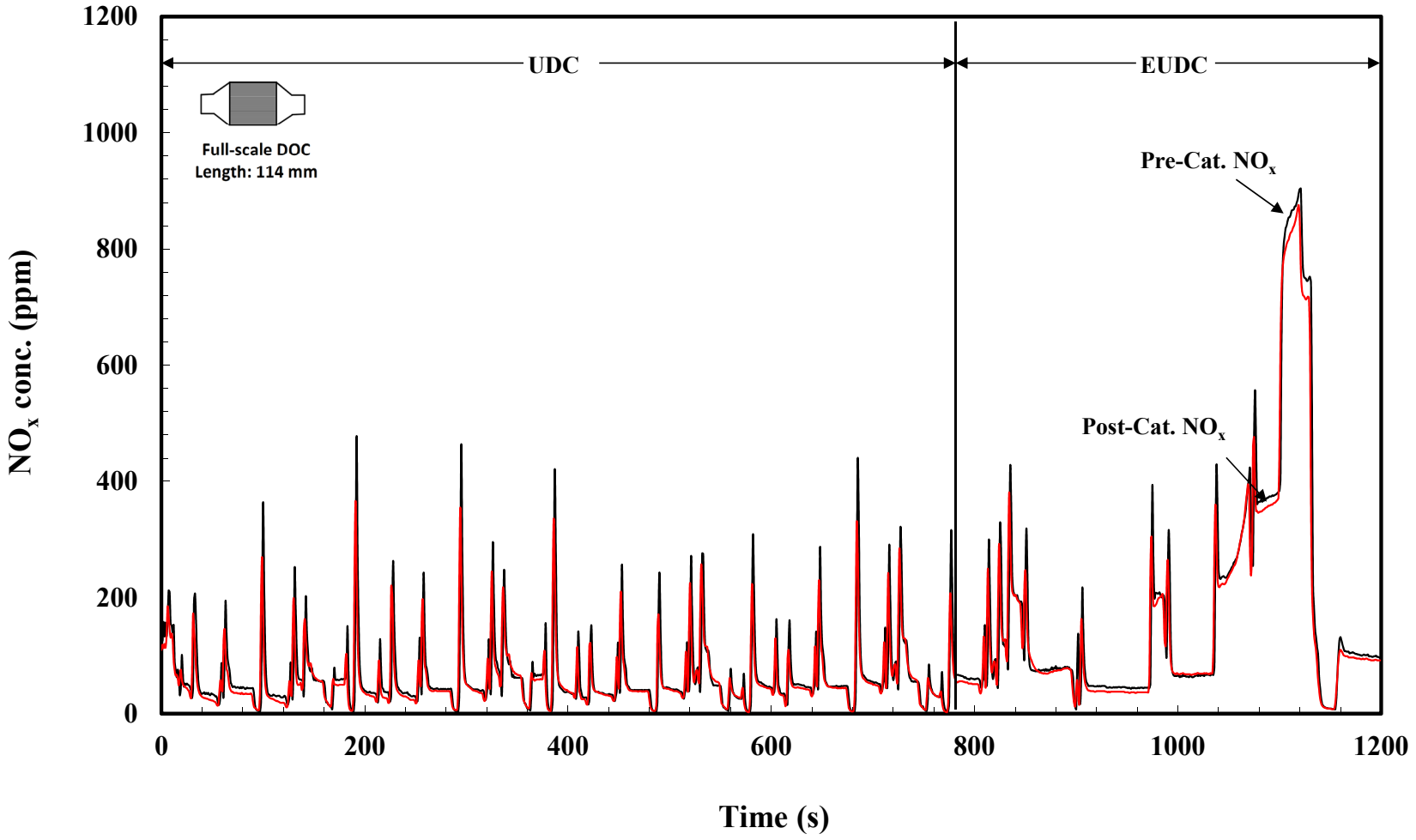


**Figure 3.26** Pre- and post- catalyst emissions of $NO_x$ in a cold NEDC cycle.

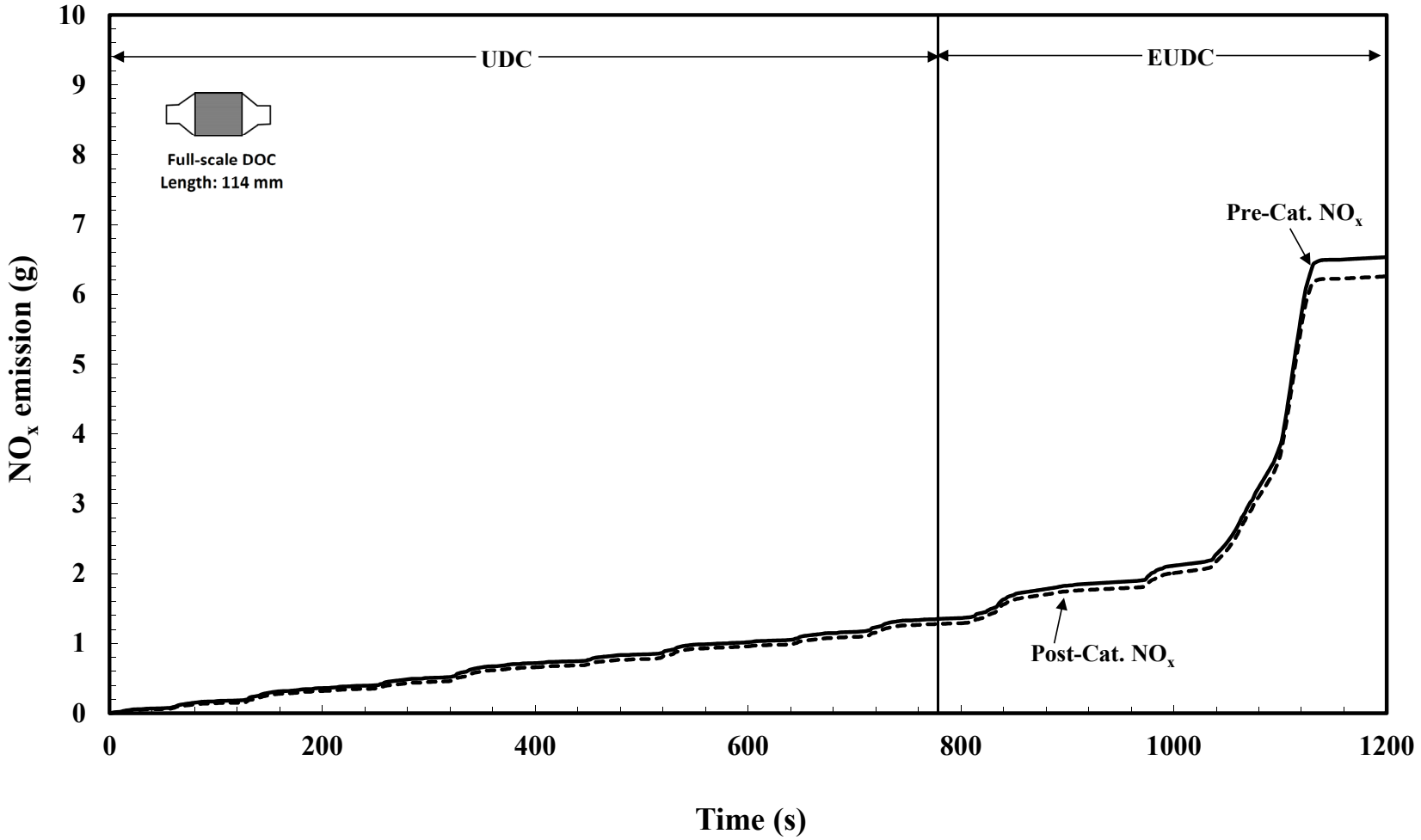


**Figure 3.27** Cumulative emissions of $NO_x$ at pre- and post-catalyst positions in a cold NEDC.

Figure 3.28 shows the air mass flow in the test cycle, and the gas hourly space velocity (GHSV) is plotted in Figure 3.29. The pressure drop across the Full-scale DOC in the test cycle is shown in Figure 3.30. As can be seen from these figures, the pressure drop has the same trend as the air mass flow.

From this set of experiments, useful information has been obtained about the DOC during the cold NEDC. It is also interesting to note, that the 'cold-start period' of the DOC lasts more than ten minutes. Next experiments will be performed for the hot NEDC.

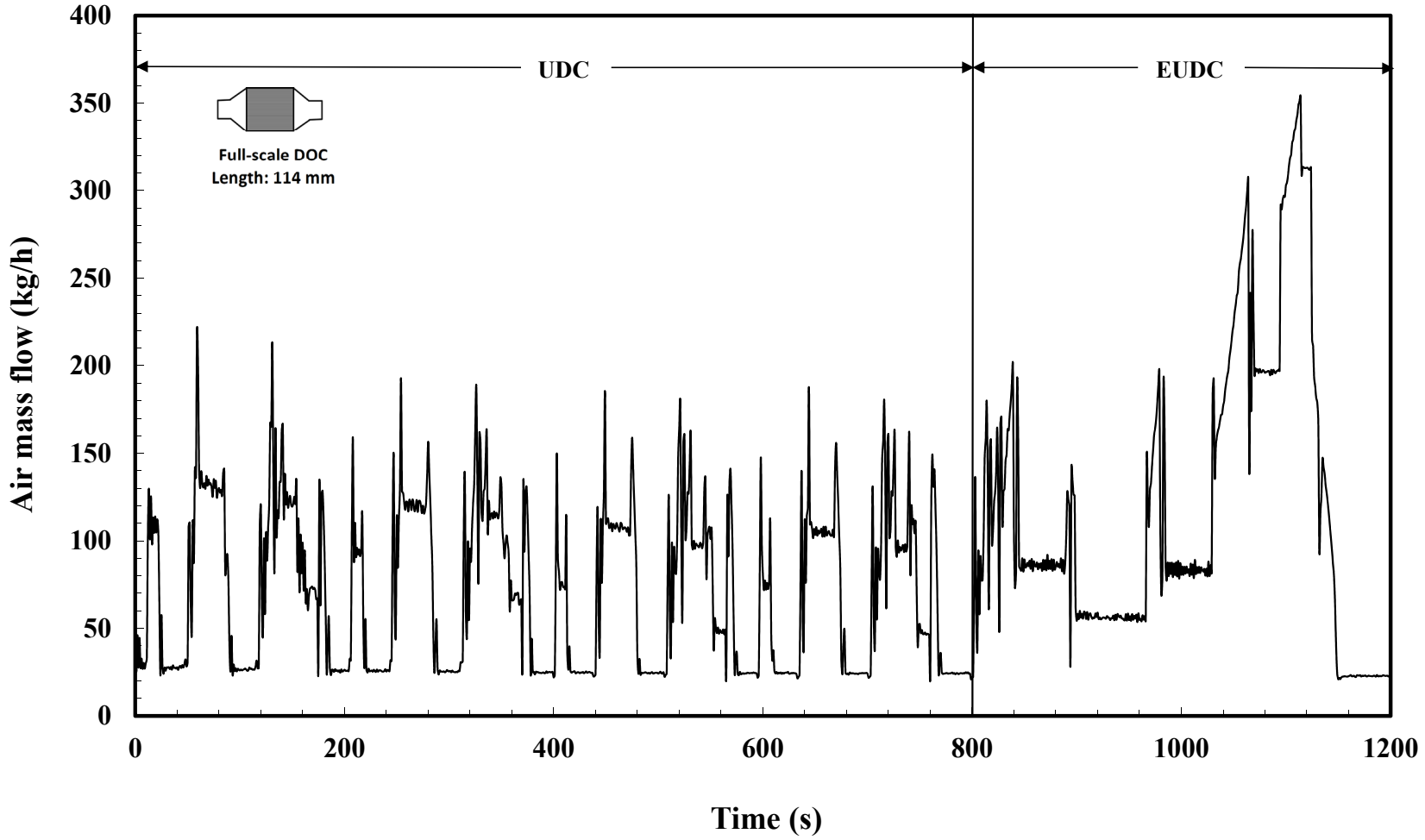


**Figure 3.28** Air mass flow in a cold NEDC.

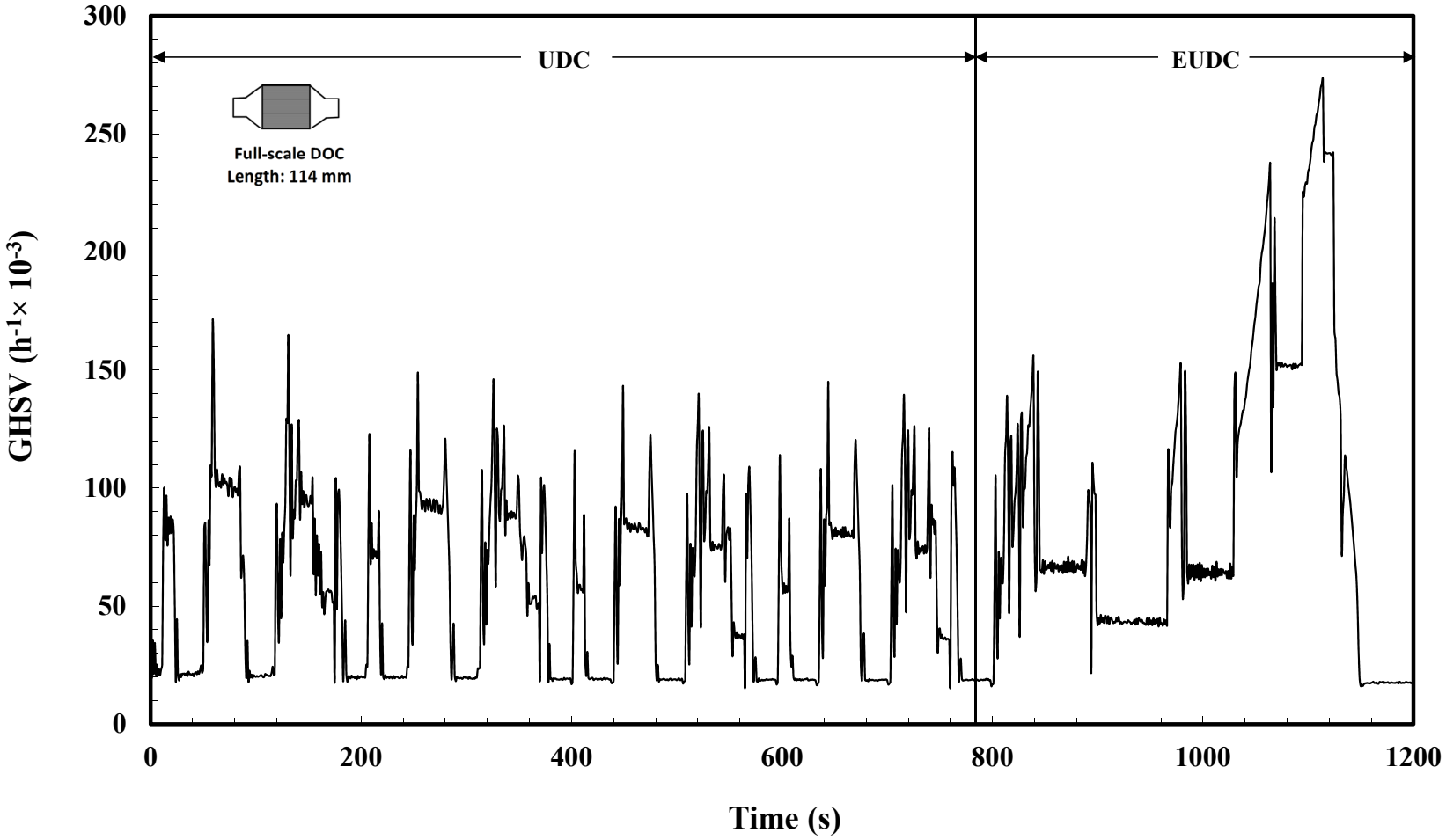


**Figure 3.29** Gas hourly space velocity (GHSV) in a cold NEDC.

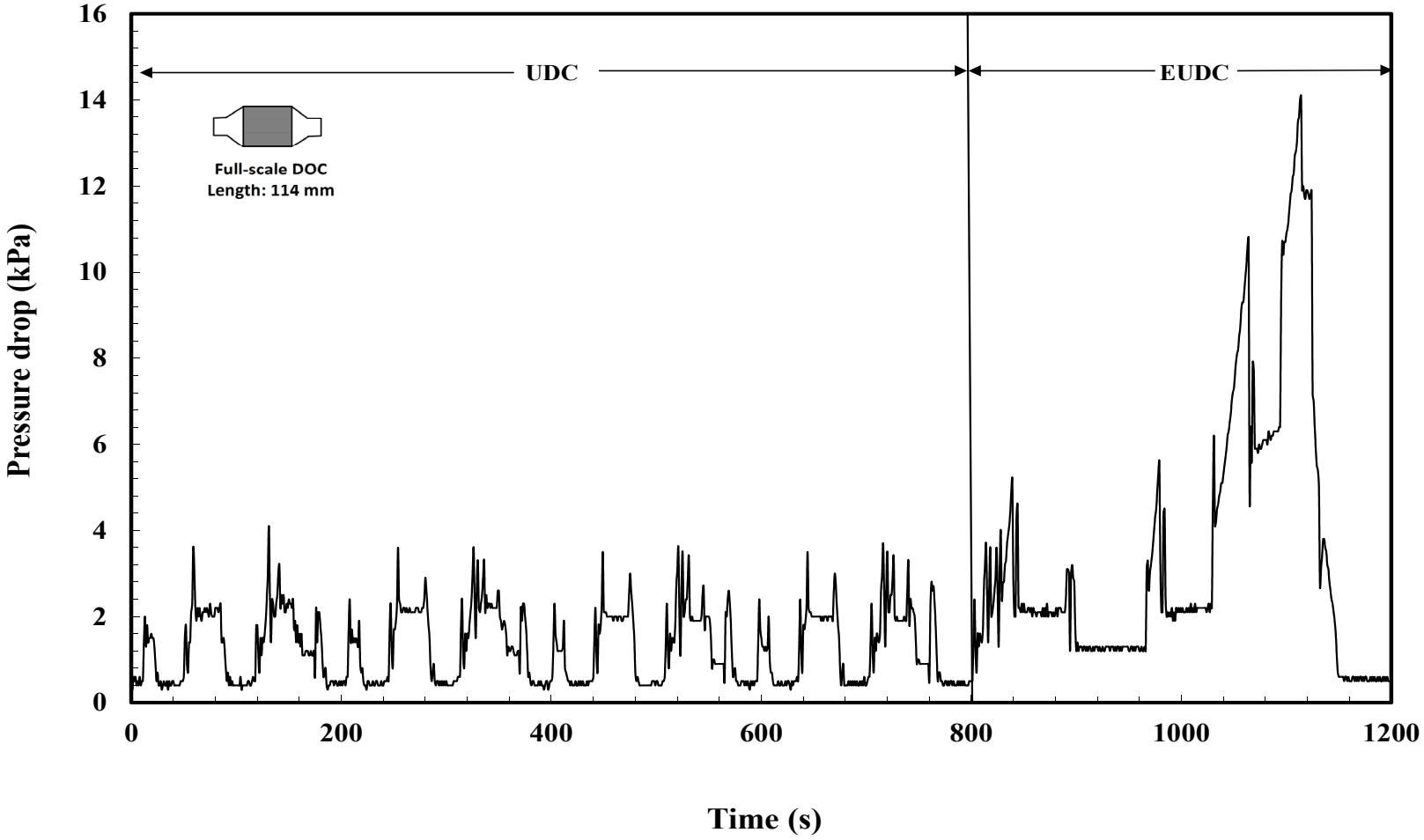


**Figure 3.30** Pressure drop across the DOC in a cold NEDC.

### 3.3.2 Hot NEDC

The hot NEDC simulates driving conditions when the engine is fully warmed-up. Under these conditions, the DOC is also warmed-up before the start of the test cycle. Hence, the cold-start problem should not be observed in this test.

#### 3.3.2.1 Test on Full-scale DOC

The hot NEDC was performed on a Full-scale DOC. The cold NEDC was repeated three times to test the repeatability. The absolute emission value changed from test to test, but the variations were small and acceptable (CO emission variation is within ± 3%; THCs emission variation is within ± 5%; and $NO_x$ emission variation is within ± 2%). In general, considering the complexity of operating an engine the repeatability of the NEDC was good. The results obtained from the hot NEDC performed on 15/06/2010 are presented in this section. The engine speed and torque are the same as for cold NEDC.

The inlet gas temperature to the DOC is plotted as a function of time in Figure 3.31. It can be seen that the inlet gas temperature varies with time (i.e. engine operating conditions). The test is started from warm, so that the inlet gas temperature is relatively high (210$^{o}$C) at the beginning. Finally, it reaches a peak at approximately 400$^{o}$C. In the repeating UDC (0 – 800 s), the inlet gas temperature was relatively low (around 200$^{o}$C). In the EUDC, the exhaust gas temperature increased much faster (than UDC) since the engine was run under more harsh conditions. The trend in the inlet gas temperature reflects the trend in the engine temperature.

Figure 3.32 shows the wall temperature profiles along the axial length of the DOC in the hot NEDC, which follows a similar trend as the inlet gas temperature. The DOC is warm at the beginning of the cycle (225$^{o}$C), and then it decreases slightly (approximately 5$^{o}$C) throughout the repeating UDC (as the inlet gas temperature decreases). Then the wall temperature gradually reaches a peak at 420$^{o}$C in the EUDC. Comparing this with Figure 3.31, the initial wall temperature is similar to the inlet gas temperature, and the peak wall temperature is higher than the gas temperature (due to the heat released from reactions at the catalyst surface). Comparing the wall temperature profiles in the cold and hot NEDCs (Figures 3.20 and 3.32), when the DOC was warmed-up (EUDC), then similar trends were followed.

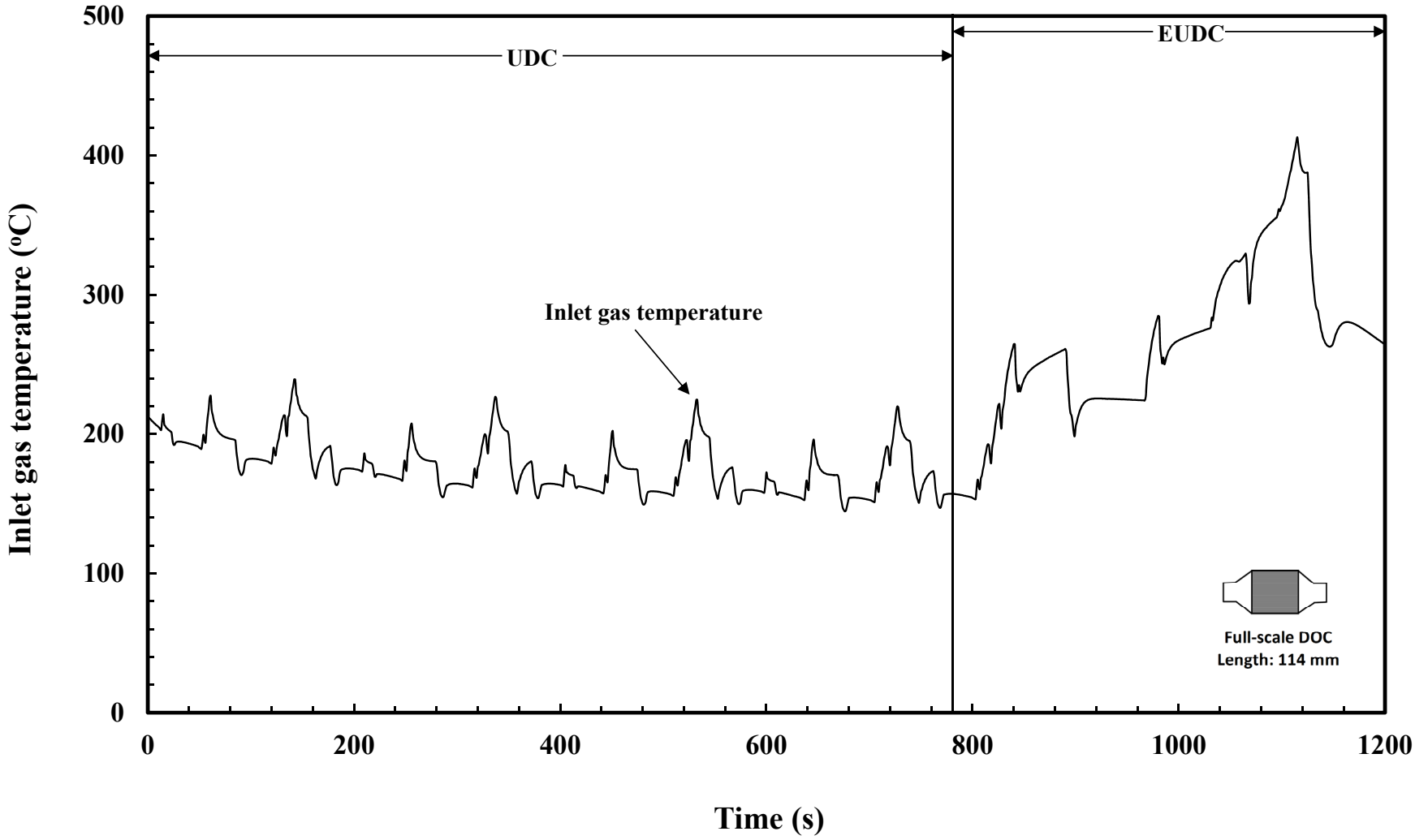


**Figure 3.31** Inlet gas temperature profile in a hot NEDC.

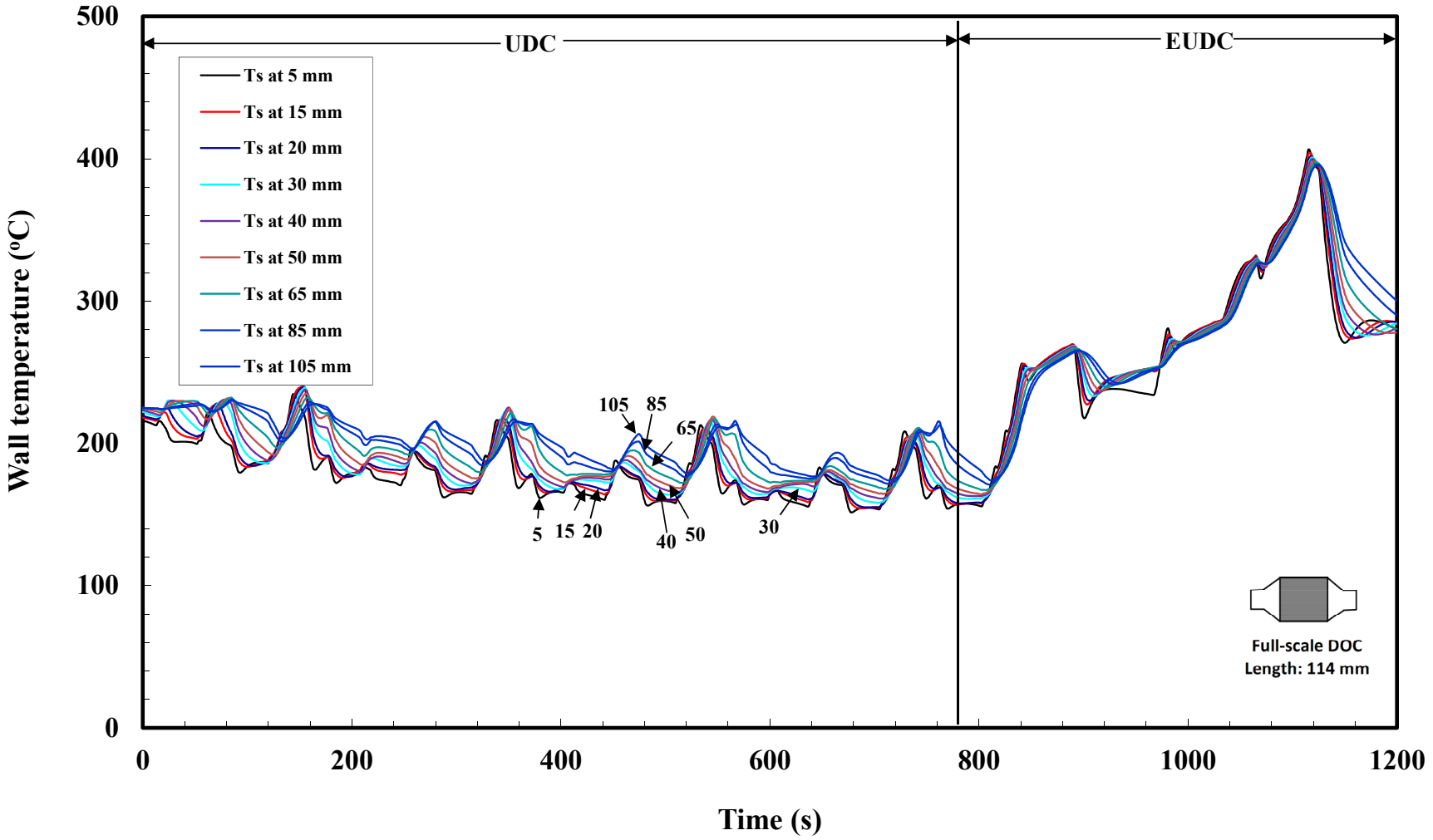


**Figure 3.32** Axial wall temperature profiles in a hot NEDC. The total length of the DOC is 114 mm; the volume is 0.001m$^3$ (1litre).

Figure 3.33 shows the pre- and post-catalyst CO emissions in the hot NEDC cycle. As expected, pre-catalyst emissions are lower than in the cold NEDC (Figure 3.22), and the post-catalyst emissions are also lower because the engine is warmer. In the repeating UDC cycle, the pre-catalyst CO emissions have a repeatable trend. The post-catalyst emissions are low at the beginning of the cycle, and then these increase in the middle of the cycle (as the inlet gas temperature decreases). As the engine gets warmer in the EUDC, the pre-catalyst CO emissions become lower, and the conversion of CO is improved significantly. The emission data is also processed and presented as cumulative emission data, see Figure 3.34. It can be seen that the overall conversion of CO in the hot NEDC was 90%. Comparing this with the CO cumulative emissions in the cold NEDC (see Figure 3.23), the overall conversion for CO increased from 24.4 to 90%. However, it should be observed that the cumulative pre-catalyst CO levels were 25% lower in the hot NEDC cycle.

Figure 3.35 shows the pre- and post-catalyst THCs emission data in the hot NEDC. The pre-catalyst THCs emissions have peaks that correspond to CO peaks throughout the test cycle, and these are low compared to the THCs emissions in cold NEDC. The post-catalyst THCs emissions are low at the beginning and the end of the test cycle, and these are slightly higher in the middle (where the inlet gas temperature is relatively low).

Figure 3.36 shows the cumulative emissions of THCs. Comparing these with the emissions in the cold NEDC (see Figure 3.25), the overall conversion increased from 27.2 to 80%. However, it should be observed that the cumulative pre-catalyst THCs were 73% lower in the hot NEDC.

Figure 3.37 shows the pre- and post-catalyst $NO_x$ emissions in the hot NEDC. These are also plotted as cumulative emissions in Figure 3.38. From these figures, the observations are similar to those in the cold NEDC. However, the pre-catalyst $NO_x$ levels were 22% higher than in the cold NEDC.

Measurements of pressure drop during the hot NEDC were similar to the measurements in the cold NEDC.

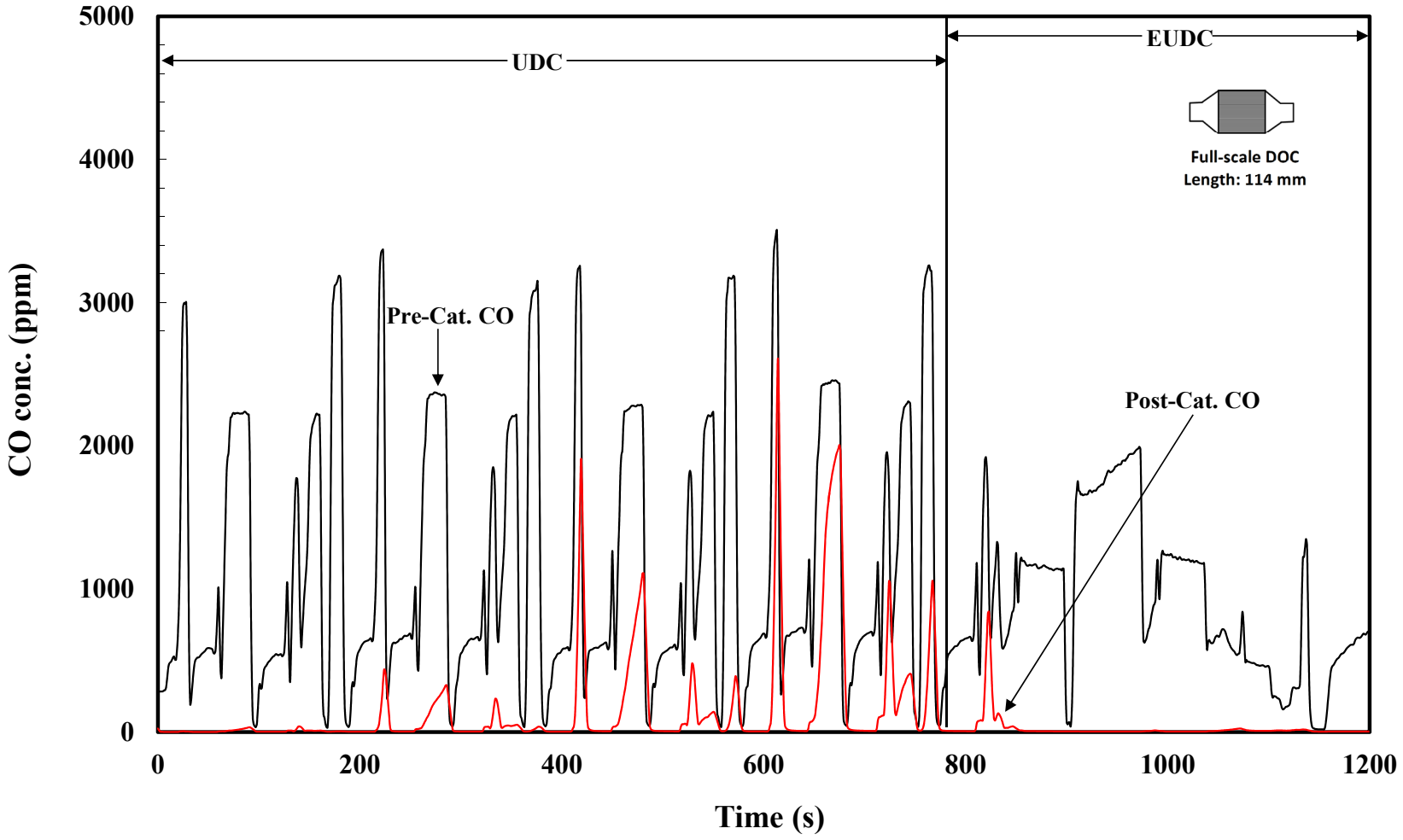


**Figure 3.33** Pre- and post-catalyst CO emissions in a hot NEDC.

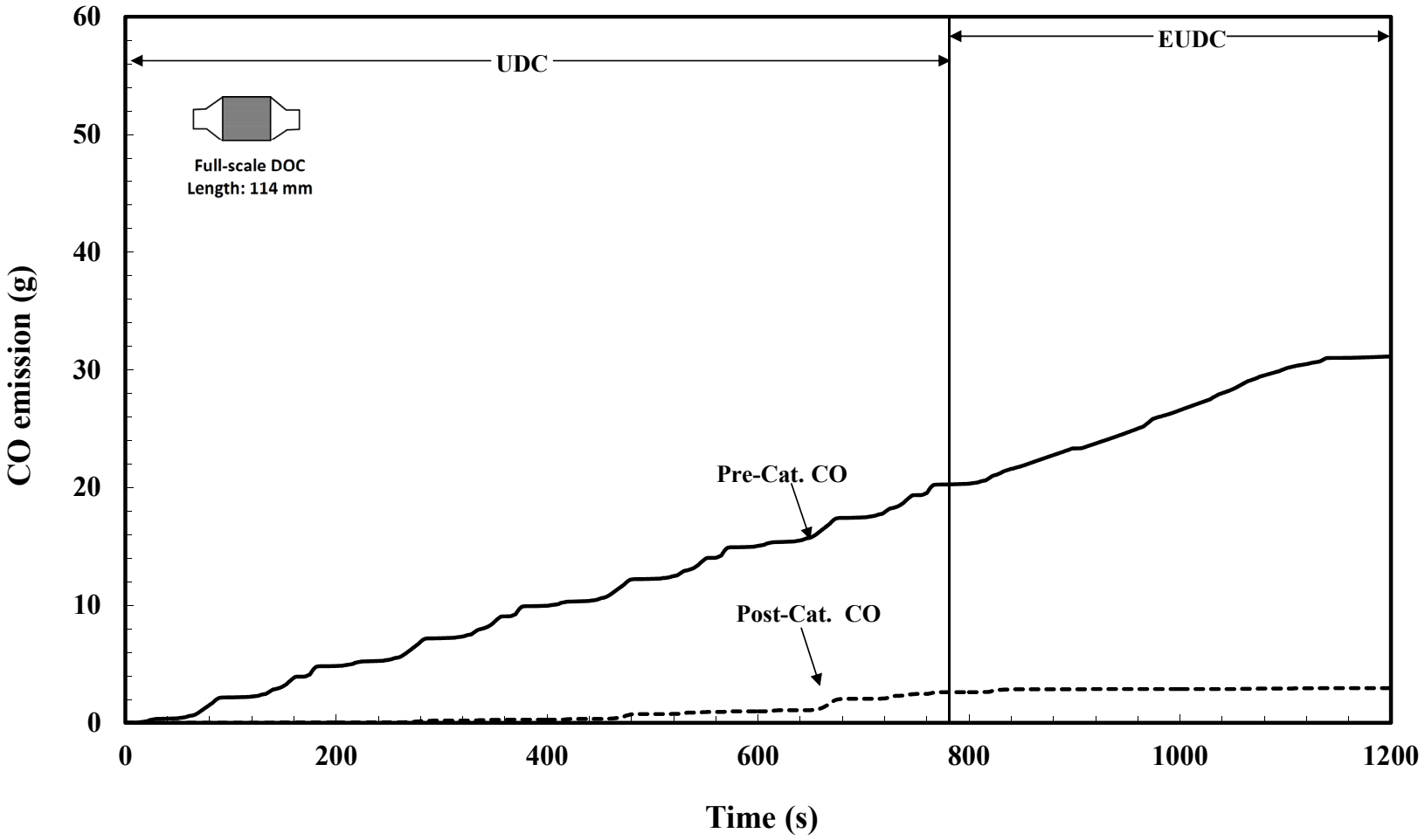


**Figure 3.34** Cumulative emissions of CO at pre- and post-catalyst positions in a hot NEDC.

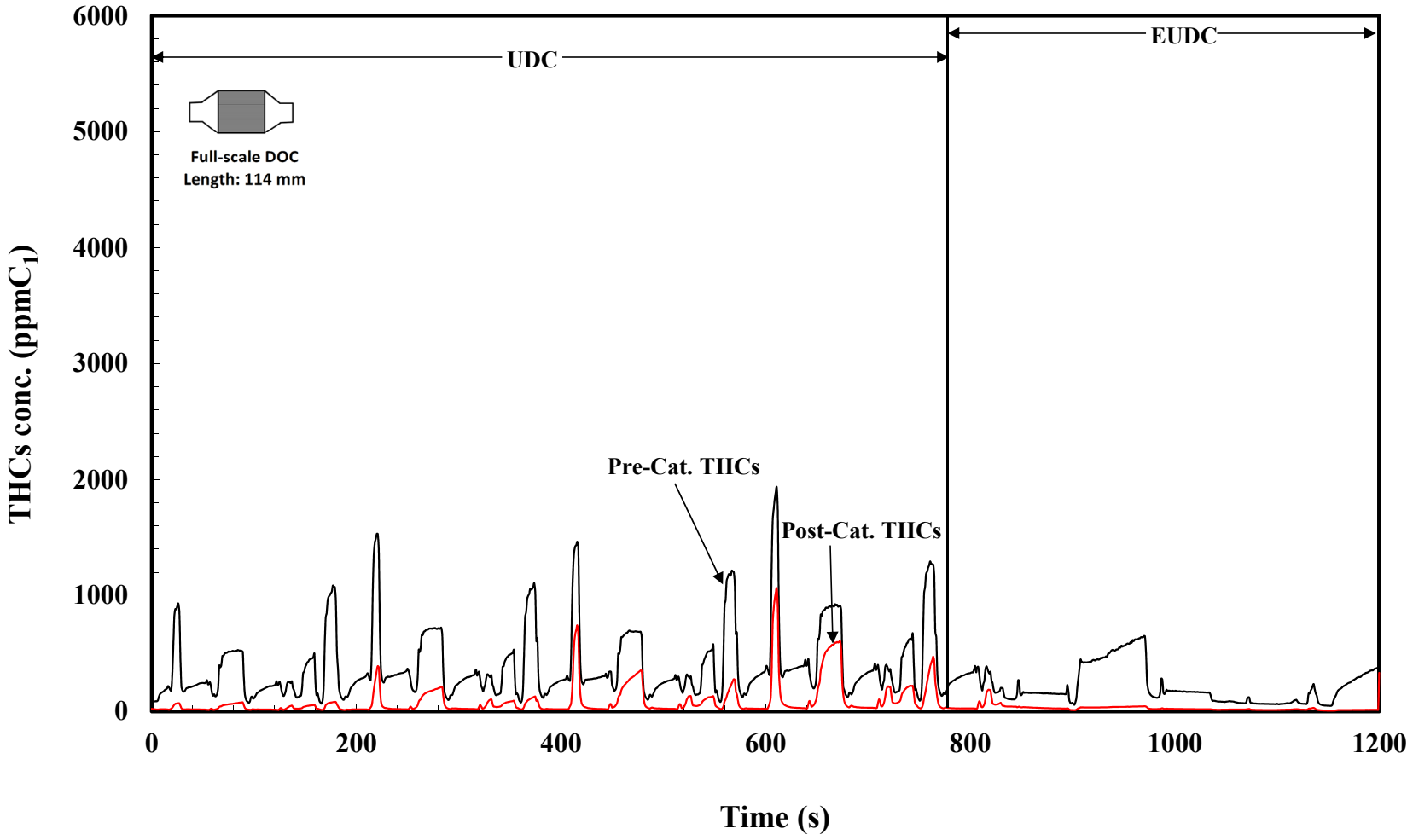


**Figure 3.35** Pre- and post-catalyst concentrations of THCs in a hot NEDC.

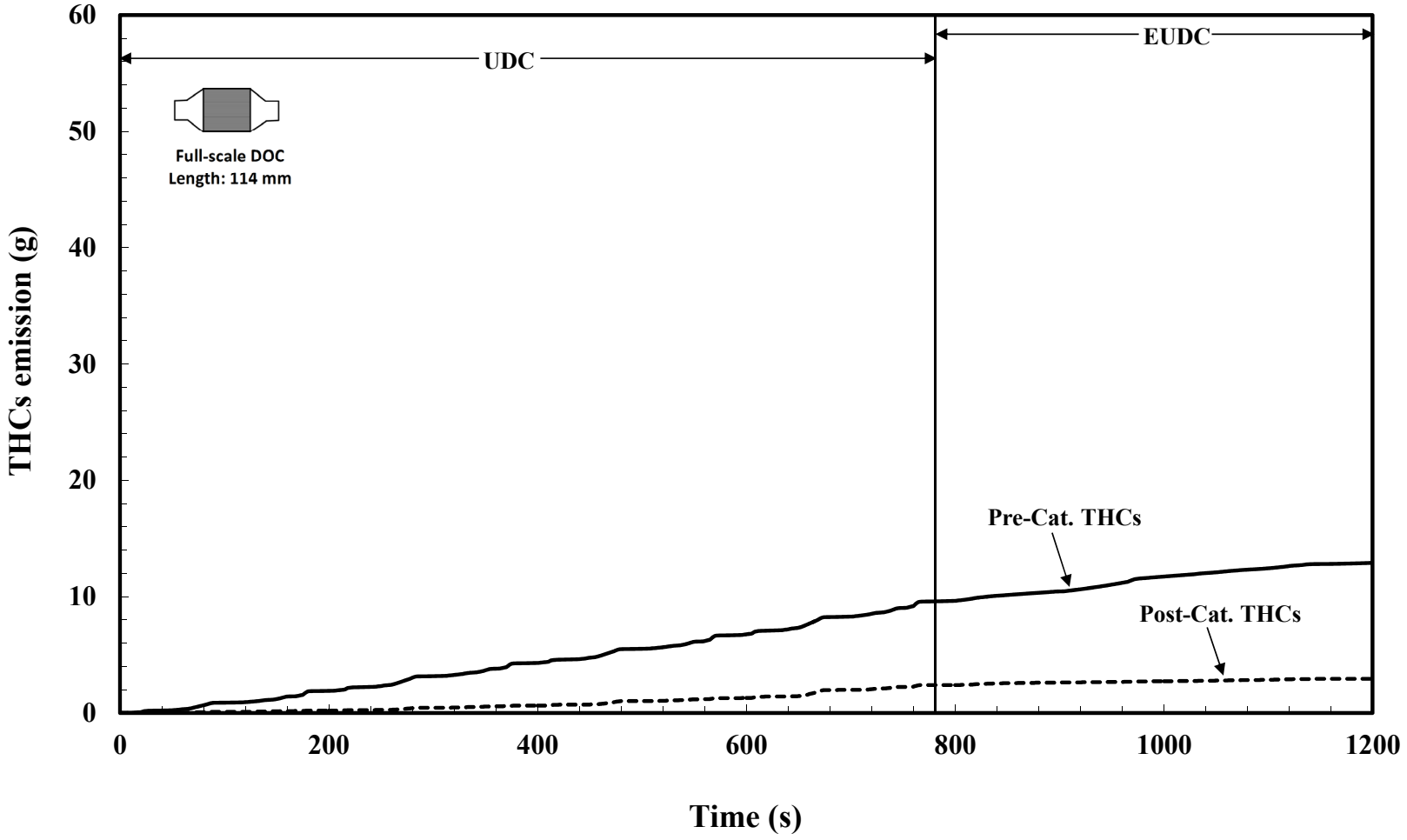


**Figure 3.36** Cumulative emissions of THCs at pre- and post-catalyst position in a hot NEDC.

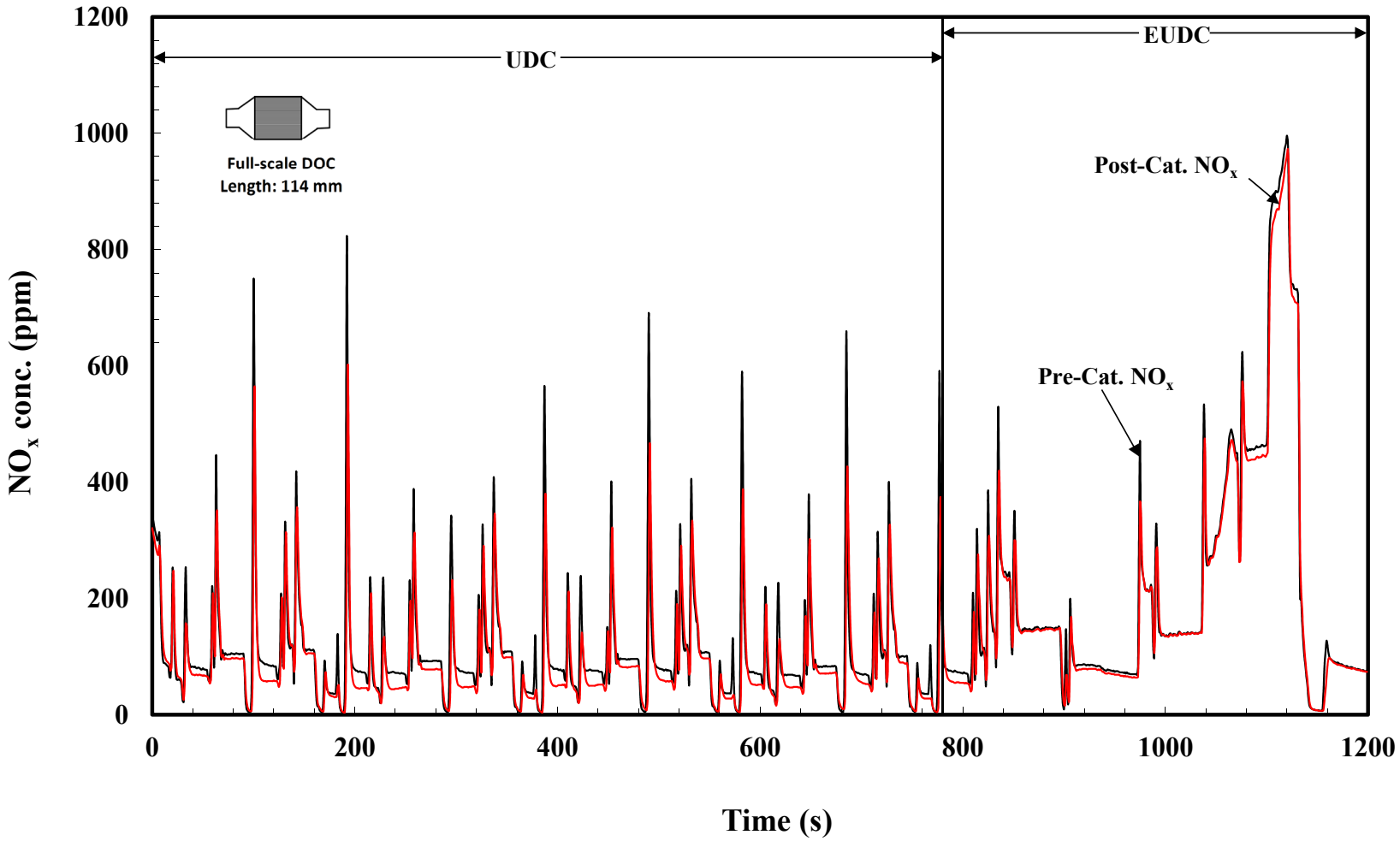


**Figure 3.37** Pre- and post-catalyst concentrations of $NO_x$ in a hot NEDC.

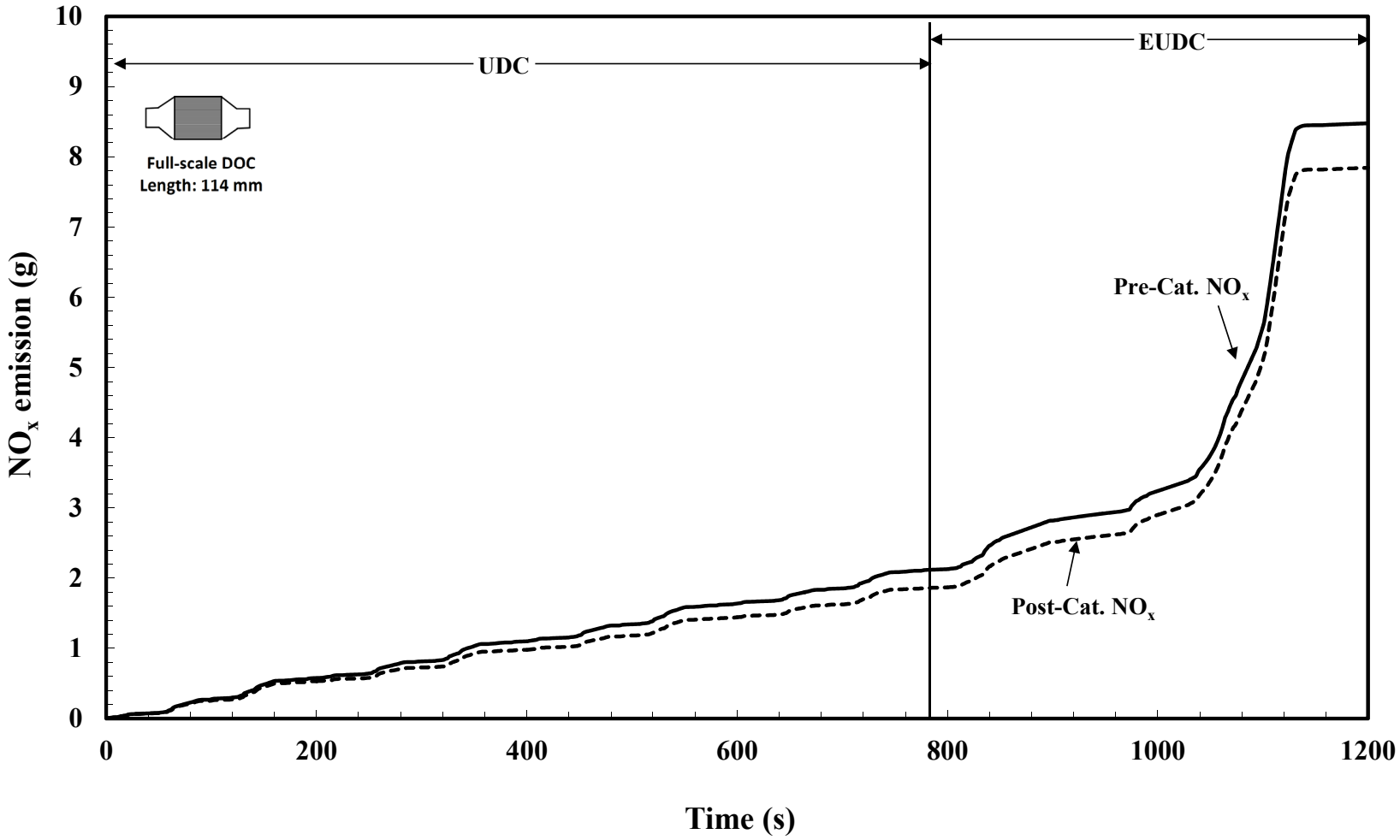


**Figure 3.38** Cumulative emissions of $NO_x$ at pre- and post-catalyst position in a hot NEDC

#### 3.3.2.2 Test on 10 mm Thin-slice DOC

The hot NEDC cycle was also performed using a 10 mm Thin-slice DOC. The aim of this test was to:

(a) see how feasible it was to perform measurement across such a thin slice,

(b) see what extra information may be provided, and

(c) compare the performance of the Thin-slice DOC with the Full-scale DOC.

Figure 3.39 shows the comparison of the average wall temperature between the Full-scale DOC and Thin-slice DOC in the hot NEDC, and the inlet gas temperature. It is interesting to observe:

(a) That the average temperature of Thin-slice DOC closely follows the trend of the inlet gas temperature.

(b) The average temperature of the Thin-slice DOC is very close to the gas inlet gas temperature.

(c) The average wall temperature of the Full-scale DOC also follows the trend of the inlet gas temperature, but it is approximately 10 to 20$^{o}$C higher than the inlet gas temperature.

(d) The post-catalyst emissions from a hot NEDC using the Thin-slice DOC and Full-scale DOC are compared in Figures 3.40 and 3.41. Across the Thin-slice DOC the conversion of CO and THCs is low. This is an important feature, as it will be easier to observe across a Thin-slice DOC, the effect of any changes in inlet conditions. Hence it will be very much easier to make a link between small changes and the performance of the DOC.

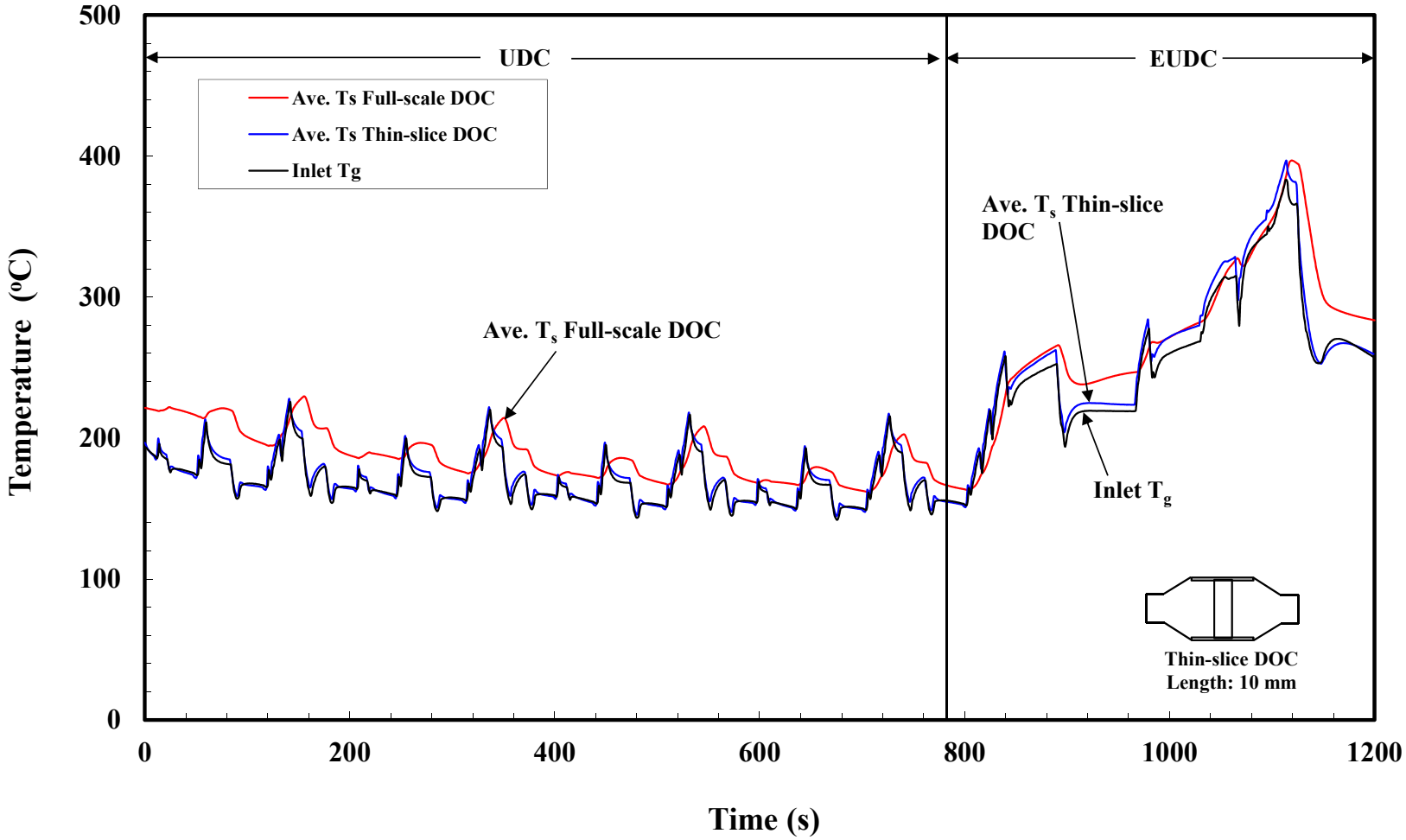


**Figure 3.39** Responses of different DOCs to the inlet gas temperature in a hot NEDC.

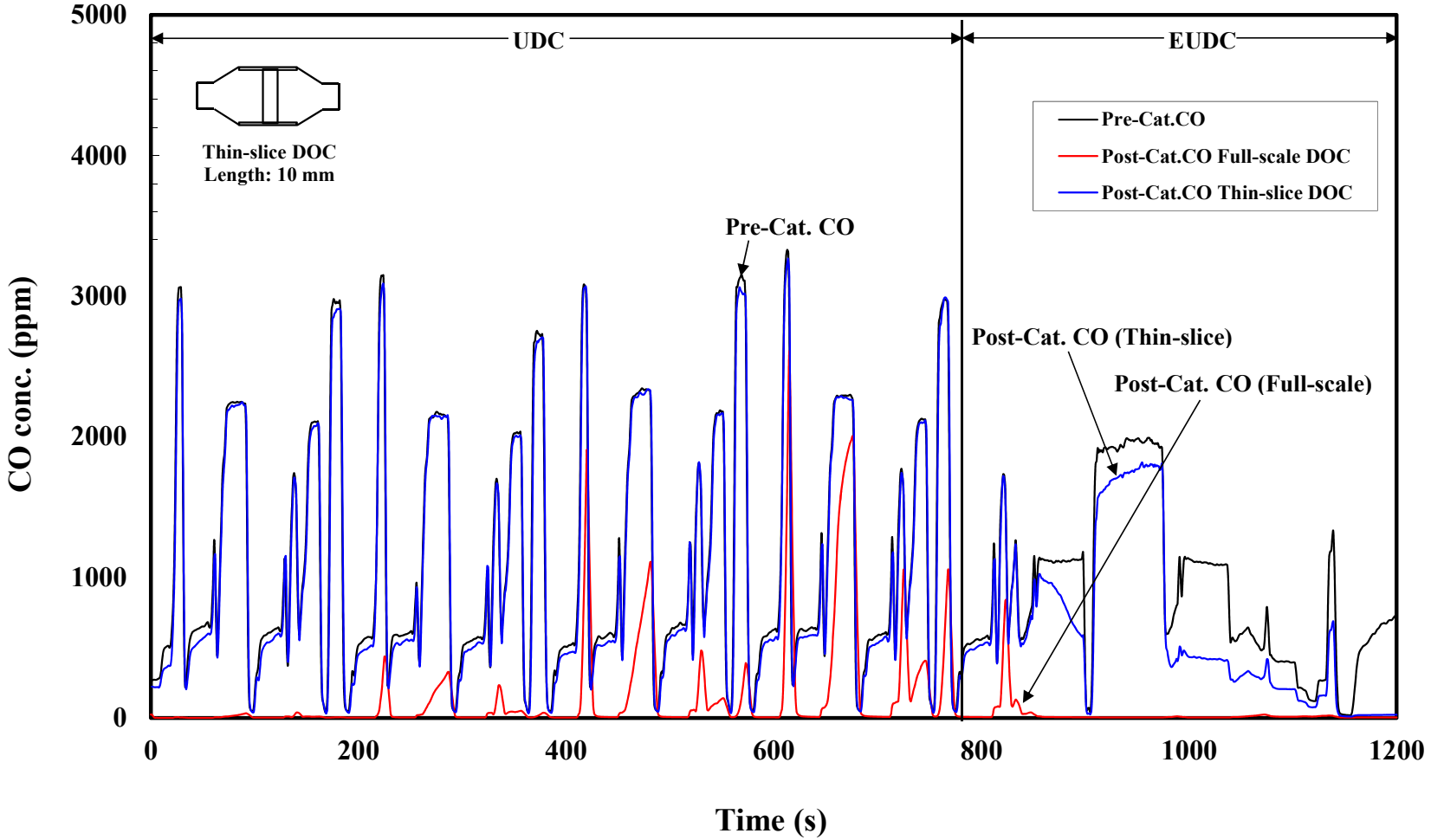


**Figure 3.40** Comparison of CO emissions when using Full-scale DOC (114 mm) and Thin-slice DOC (10mm) in a hot NEDC.

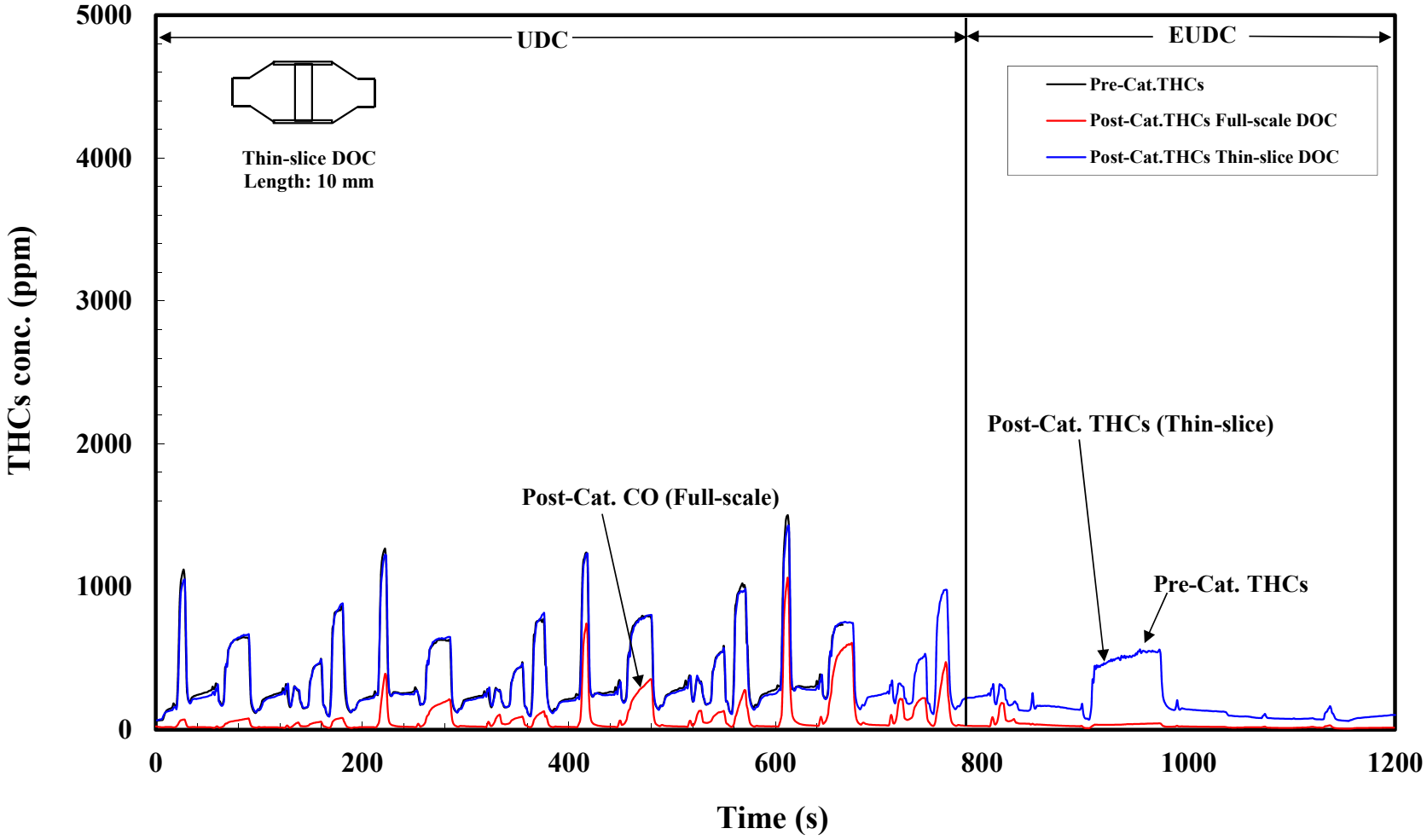


**Figure 3.41** Comparison of THCs emissions when using Full-scale DOC (114 mm) and Thin-slice DOC (10 mm) in a hot NEDC.

### 3.3.3 Concluding remarks

**Time alignment:** this was shown to be important, and a method was developed to test and allow for this aspect. After time-alignment was taken into account, the difference between the two analysers was considered to be negligible.

**Full-scale DOC:** From experiments in which the performance of the Full-scale DOC was monitored over both cold and hot NEDCs:

(a) It is very clear in which regions the catalyst (or wall) temperature is insufficient to sustain high conversions of CO or THCs.

(b) Emissions of THCs are reduced throughout the cycles, whereas CO emissions are very temperature sensitive. It is interesting to note, that hardly any conversion of CO occurs in UDC phase of the cold NEDC, and the UDC part of the cycle contributes 85 % of the cumulative CO emissions. This identifies most clearly a region for improvement in the design/operation of the catalyst system.

(c) In the hot NEDC, and even in the UDC phase, the temperature of the catalyst is high enough to sustain CO oxidation reactions, and in general their conversion across the DOC is high.

(d) As expected, $NO_x$ emissions remain in general unchanged across the catalyst, with only a slight reduction of about 5 % in the cold and hot NEDCs.

(e) The pressure drop across the catalyst block during the cold NEDC, was found to vary between 0.2 to 14 kPa.

**Thin-slice DOC:** From experiments in which the hot NEDC was followed, there were a number of very interesting observations:

(a) It was shown, that is was feasible to mount a Thin-slice of DOC into an exhaust can, and to monitor its performance, and the results were consistent. However, great care had to be taken in the way in which this Thin-slice was mounted in the exhaust can.

(b) When comparing the performance of the Thin-slice with the Full-scale DOC, then as a result of using this technique, it was very clear that extra information was obtained. As the conversion across this Thin-slice is relatively low in many points in the NEDC, it is a lot easier to see the difference between small changes

in inlet conditions, and their impact on the performance of the DOC. This feature will be exploited in the sections that follow, to make a clearer link between cause and effect. However, in some parts of the EUDC, it is very interesting to observe that the conversion of CO across the Thin-slice is high (e.g. 61% at 1000 s in Figure 3.40). This is an interesting experimental observation, and coincides with a region of high wall temperature in the cycle, which ensures that the catalyst remains very active. The results also show clearly, how at low gas inlet temperatures in the cycle, the wall/gas temperatures can gradually increase along the length of the Full-scale DOC reaching a point at which reactions are significant and high conversion are achieved across the DOC.

(c) From data gathered on the Full-scale DOC, it is clear, that: (i) in parts of the cycle, the wall temperatures vary significantly in the axial direction, whereas (ii) in the Thin-slice DOC, the wall temperatures do not vary to that extent. In the Thin-slice they remain (for a greater part of the cycle) a lot closer to gas inlet temperatures, and in subsequent parts of this thesis, these two features will be shown to be beneficial - especially when trying to determine/validate chemical kinetics.

**Identification of conditions for subsequent experiments:** Based on the results of these experiments, it was decided to operate the engine, such that:

- an exhaust gas flow of about 60 kg/h was obtained (this matched the UDC region in the NEDC),
- an exhaust gas inlet temperature range of 100 to 280$^{o}$C (this matched the gas inlet temperature range in the NEDC).

This could be achieved by operating the engine at the speed of 2000 rpm, and varying the engine torque from 5 to 45 Nm.

In addition, it was decided to perform experiments in which:

- a step-up, and step-down in CO concentration of 3000 ppm could be achieved (this matched the peak pre-catalyst CO concentration in the hot NEDC), and
- a step-up, and step-down in THC concentration of 3000 ppm$C_1$ could be achieved (this matched the range of pre-catalyst THCs emission in the cold NEDC).

## 3.4 Light-off experiments

In the literature, when catalyst 'light-off' temperatures are quoted, these arise from experiments that are performed in an experimental rig in the laboratory that consists of a catalyst mounted in a tube (the reactor), using a constant mass flow of gas which contains the reactant gases at a fixed concentration. Then, as the gas inlet temperature is gradually increased, the inlet and outlet concentration of the reactant is measured, and from that the conversion is determined. The 'light-off' temperature is normally assigned as the temperature at which 50% conversion of the limiting reactant is achieved. In the case of a catalytic converter for a diesel engine, then such experiments would be performed for CO, and also for THCs.

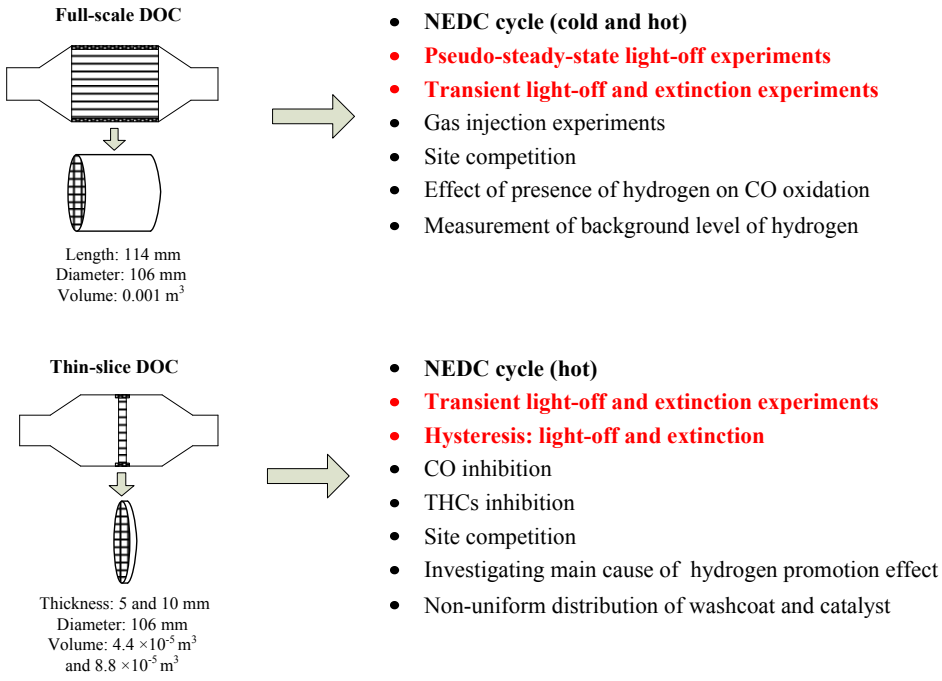


**Figure 3.42** Summary of experiments in Chapter 3. The experiments highlighted in red are discussed in Section 3.4.

From a scientific/engineering perspective it is recognised, that information on the light-off characteristics is most helpful in understanding the behaviour of the catalyst system, although the importance of this 'S' shaped curve is not always fully appreciated. Catalyst light-off characteristics are also used by researchers who develop mathematical simulation models of converters, and they use them to tune unknown parameters in their models. When a catalyst supplier finally provides a manufactured catalyst that is tested on

a real diesel engine test-bed, then how can the 'light-off' characteristics for this particular catalyst be quantified? How can these be compared with any data that may have been supplied by the catalyst manufacturer?

In this section, these questions are addressed and a few methodologies are described which could be used by engine developers and car manufacturers who are interested in the performance of converters. Valuable experimental data is also provided, which will be helpful to workers who develop mathematical simulation models of converters.

### 3.4.1 Pseudo-steady-state light-off experiments

The first methodology was developed to obtain the "light-off" curve under pseudo-steady-state engine operation condition. The set-up of the engine test cell was shown in Figure 3.43. This set-up is similar to that for the NEDC, apart from the gas injection system.

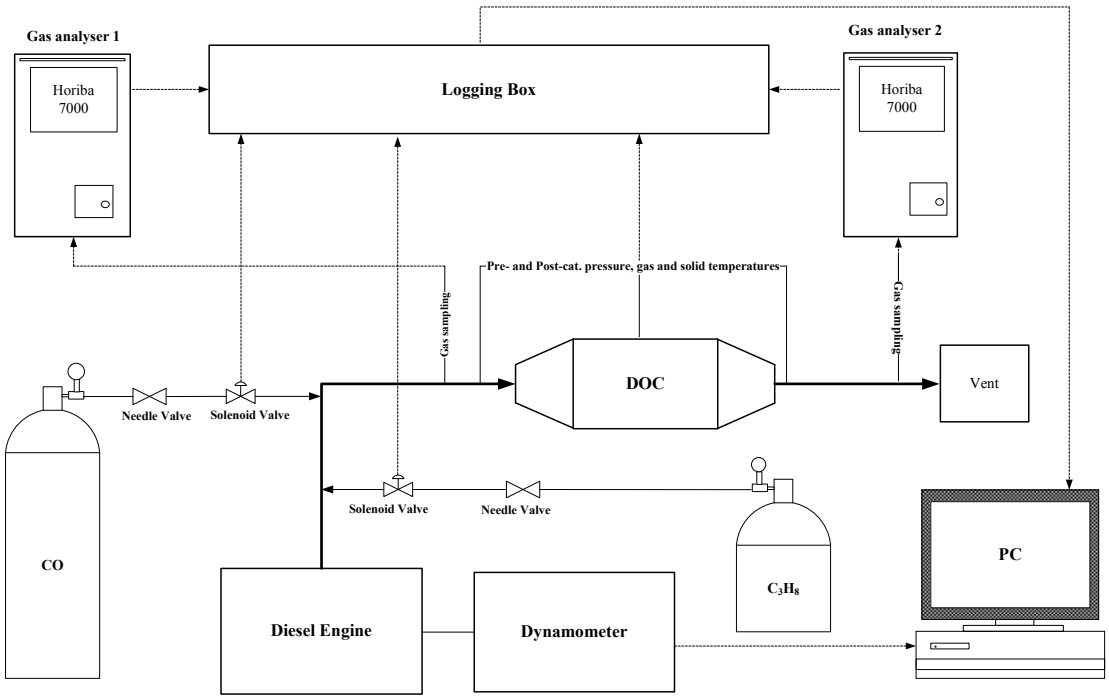


**Figure 3.43** Schematic of the engine test cell, control and data acquisition system.

To illustrate the methodology, the engine was operated at a constant speed at 2000 rpm, which is a typical engine speed when driving a vehicle. Then different settings of engine torque were applied, then the gas inlet temperature to the DOC would also have a range of values, and it should increase with engine torque. However, there would also be small changes in the air mass flow, CO and THCs concentrations. As the engine torque

was varied from 5 to 47 N.m, then at each torque setting, the engine was allowed to reach an approximate steady-state condition, and then three data measurement points were taken to obtain an average value. A few plots show the variations in air mass flow and emissions in Figure 3.44.

From Figure 3.44, it can be seen that:

- the inlet gas temperature increases from 146 to 285$^{o}$C,
- the CO concentration varies from 954 to 1201 ppm,
- the THCs concentration varies from 191 to 264 ppm$C_1$, and
- the air mass flow varies from 52 to 60 kg/h (GHSV: 40,165 to 46,344$h^{-1}$).

It is encouraging to see, that across a 146 to 285$^{o}$C temperature range, the mass flow only varied by ± 15%.

Now the conversion of CO, and THCs can be plotted as a function of temperature as illustrated in Figures 3.45 and 3.46, respectively. This now starts to take the shape of a 'light-off' curve. However, in this plot the concentrations of both the CO and THCs are relatively low. As engine torque is varied, they still remain low, but increase by 20 and 30% respectively. To improve on this technique, additional CO was added up-stream of the converter, and this was adjusted such that the inlet CO concentration was 3100 ppm (± 100 ppm). This has the effect of magnifying the response from the converter, approximating a situation as if CO alone was the main pollutant. This now enables a clearer picture of a 'light-off' curve to be generated, as by increasing the CO level in the feed the response of the system will be magnified. The results of such an experiment are illustrated in Figure 3.47.

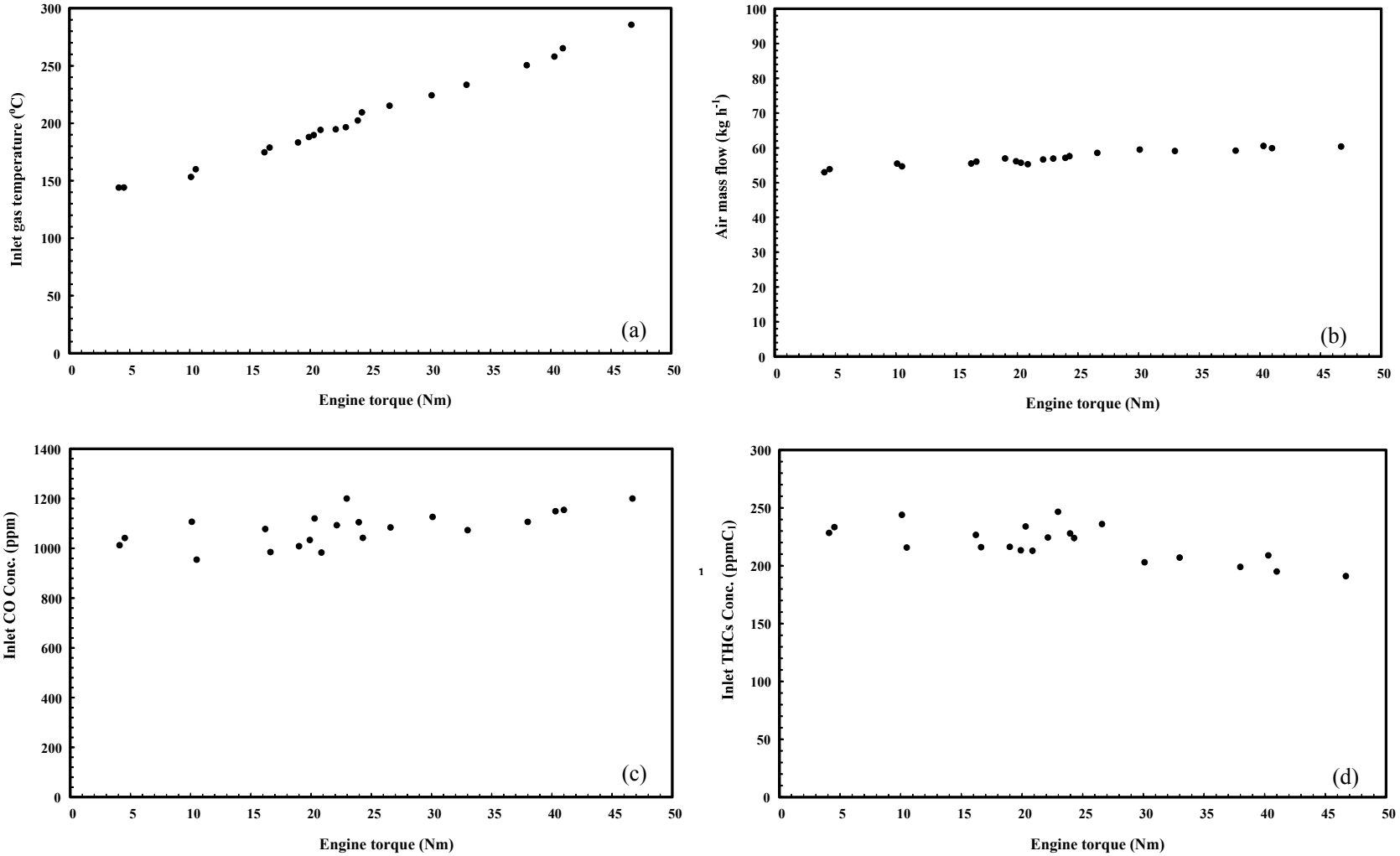


**Figure 3.44** Engine speed is fixed at 2000 rpm for the pseudo-state-steady light-off experiments. (a) Inlet gas temperature, (b) air mass flow, (c) inlet CO and (d) THCs concentrations

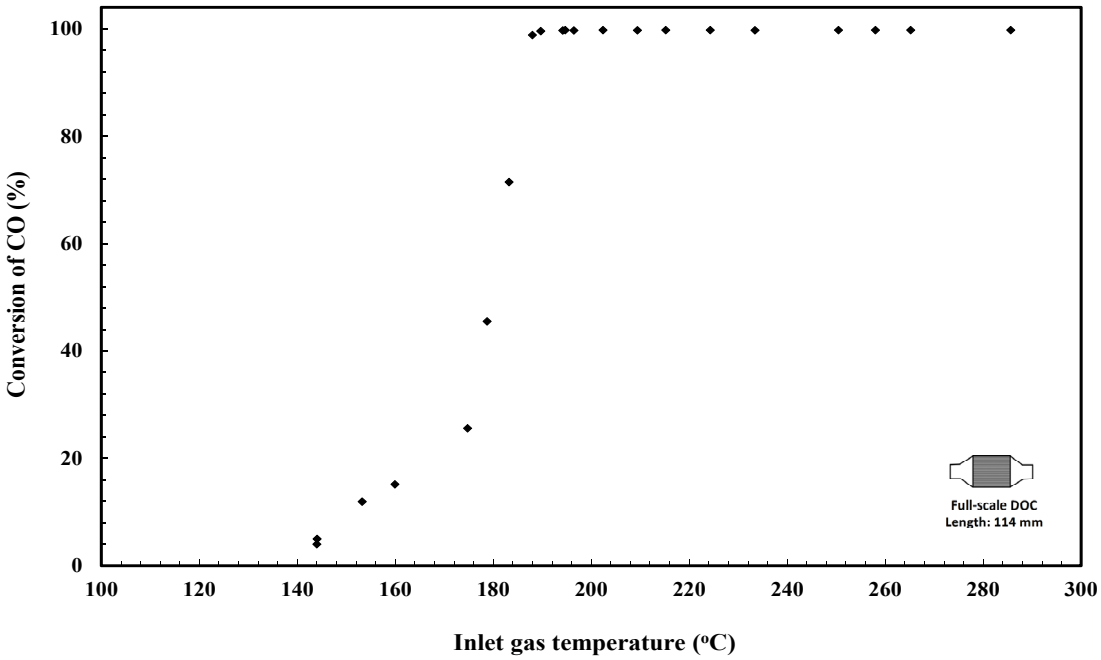


**Figure 3.45** Light-off curve for CO (no additional CO and propane, Full-scale DOC was used).

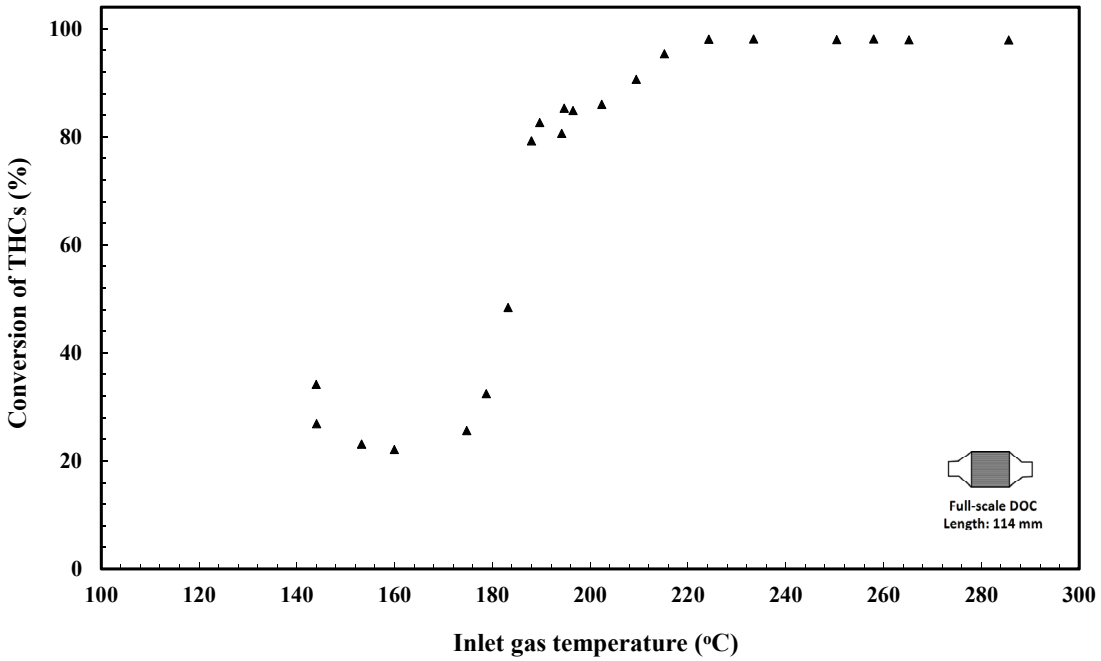


**Figure 3.46** Light-off curve for THCs (no additional CO and propane, Full-scale DOC was used).

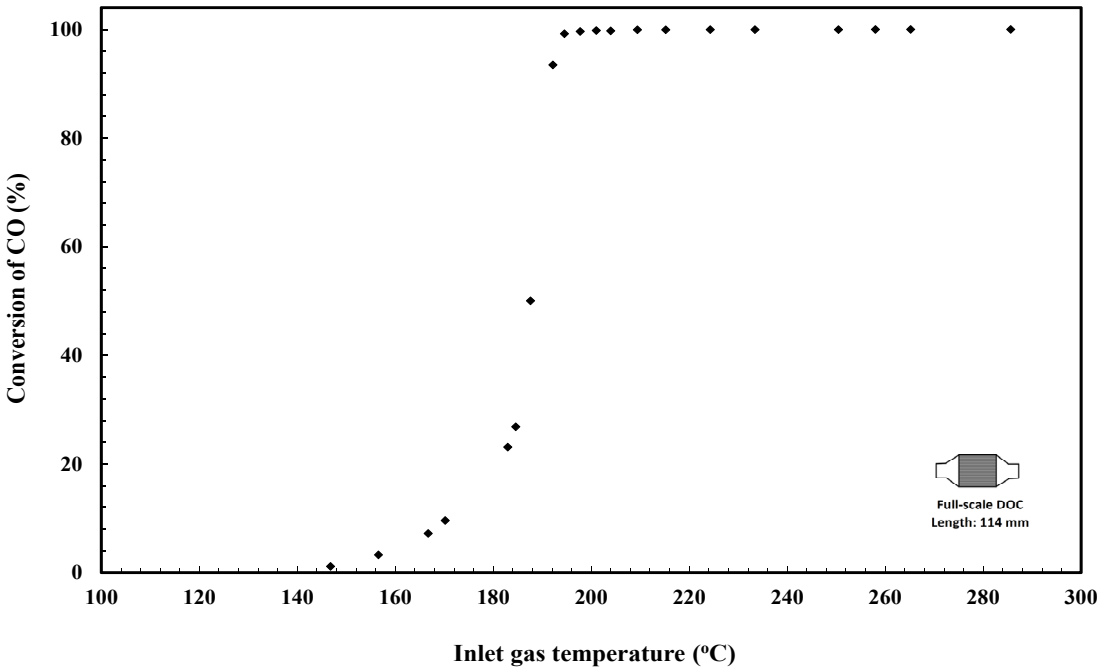


**Figure 3.47** Light-off curve for CO (inlet CO concentration was maintained at 3000 ppm).

This technique now creates a wide range of opportunities, for example:

- Experiments could be performed with different fixed values of CO concentration e.g. 2000, 3000 and 4000 ppm, and the influence of CO concentration on catalyst light-off could be studied.
- Using a similar technique (while the CO remained at the background level of 900 to 1000 ppm) a known quantity of propene or propane (to represent THCs) could be added, to create a fixed inlet concentration of hydrocarbons (e.g. 1500 ppm$C_1$). Light-off for THCs could then be ascertained.
- In addition, experiments could be performed with the simultaneous addition of both CO (e.g. 3000 ppm) and propene/propane (500 ppm).

The data from such studies can then be used to help identify the functional characteristics of the catalyst system that has been supplied, the performance characteristics of different catalysts can be compared more easily and a weakness, or strength, of a particular formulation identified more easily. This type of data can also be used to determine unknown coefficients in a mechanistic model. This involves making adjustments to the unknown/uncertain parameters in a converter simulation model, until a good match is obtained with the light-off characteristic.

The validity of a converter model, that had been tuned on the basis of bench-top experiments and was used to help design the catalyst system that was provided as a

commercial product, can then also be tested in this manner. In the example illustrated in Figure 3.45, the converter model may be run and results compared with the experimental curves - no tuning of parameters would be allowed. In this example, as the CO response of the system has been magnified, it will soon become apparent how good the converter model is in describing CO aspects in the simulation. Similar studies could then be performed for the hydrocarbons. In this manner, it would be a lot easier to make a clear link between the cause and effect than in the current practice, where simulations with the model are compared with engine performance data which follows an engine test cycle that simulates driving conditions. In such cases, the modellers claim that because of the complexity of the system modelled, they need to tune many of the parameters in their model before they can match the data. One is then left feeling uncertain about the validity of the model, as it has not been tested in an independent manner. The areas where the model had short-comings are also not very clear, as many variables and parameters are changing in such a study.

An example of experiments with different CO concentrations is illustrated in Figure 3.48. Higher inlet CO concentrations clearly increase the light-off temperature. If bench-top experiments had been performed, then this outcome would have been expected (e.g. Salomons *et al.*, 2006; Zervas, 2008), and it is encouraging to see that by using the methodology described in this section, then this trend is also observed in a real engine test-bed situation. As an aside, some researchers may view this as a loss in performance of the catalyst as the light-off temperature has increased. However, if the overall rate of reaction across the converter is plotted as a function of temperature (see Figure 3.49), then in the low temperature range the overall rates look very similar. Although at the higher temperatures, the rates are clearly higher as there is a greater quantity of CO to react. For information, the light-off curve for the background level of THCs is plotted in Figure 3.50.

**Note**

In this chapter, it was decided to plot the reaction rate in terms of the change across the reactor, e.g. see Figure 3.49. This is obtained from:

$$\text{Reaction rate} = \frac{\text{Moles of CO inlet}}{\text{s}} - \frac{\text{Moles of CO outlet}}{\text{s}} = \frac{\text{Moles of CO}}{\text{s}} \text{ reacted}$$

To convert to other units:

(a) if a rate is required based on the mass of Pt catalyst, then:

$$\text{Reaction rate} = \frac{\text{Moles of CO}}{\text{s}} \text{ reacted} \times \frac{1}{m_{Pt}}$$

where $m_{Pt} = \text{mass of catalyst loading in the actual DOC tested}$

(b) To convert to a rate based on geometric external surface area, then:

$$\text{Reaction rate} = \frac{\text{Moles of CO}}{\text{s}} \text{ reacted} \times \frac{1}{A_{geo}}$$

where $A_{geo} = \text{geometric surface area of actual DOC tested}$

Further information is available in Appendix 1.4, and some useful conversion factors are presented in Table 3.6.

**Table 3.6** Some useful conversion factors.

| | Full-scale DOC | Thin-slice DOC | |
|---|---|---|---|
| | 114 mm long | 10 mm | 5 mm |
| Mass of Pt catalyst (g) | 4.3 | 0.38 | 0.19 |
| Geometric surface area ($m^2$) | 2.115 | 0.186 | 0.093 |

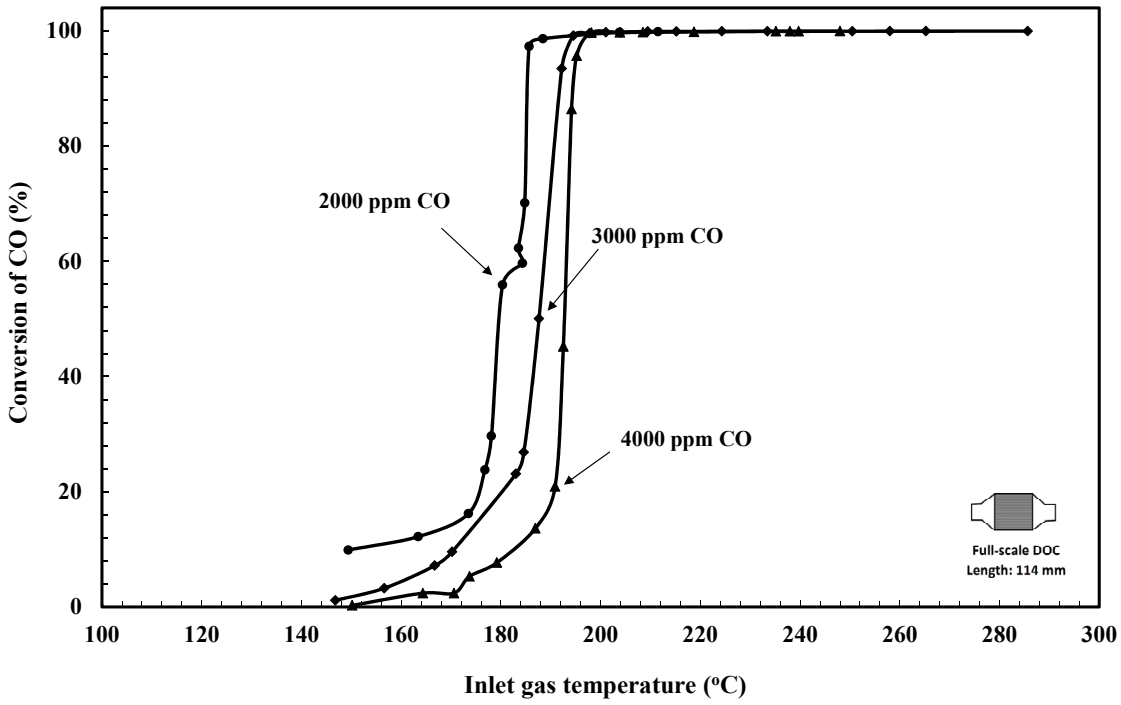


**Figure 3.48** Light-off curves for CO with different inlet CO concentrations: 2000, 3000 and 4000 ppm. For each CO inlet concentration, the THCs concentration was maintained at 1500 ppm$C_1$ (equivalent to 500 ppm propane).

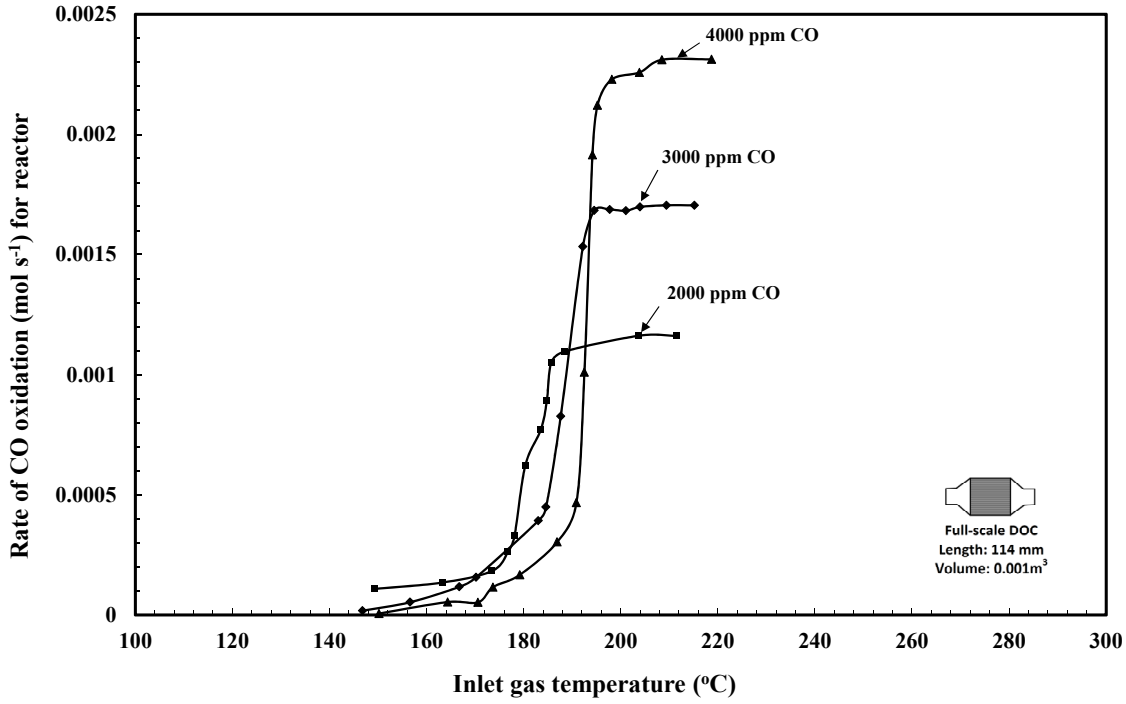


**Figure 3.49** Overall rate of CO oxidation (during light-off experiments with different fixed values of inlet CO concentrations).

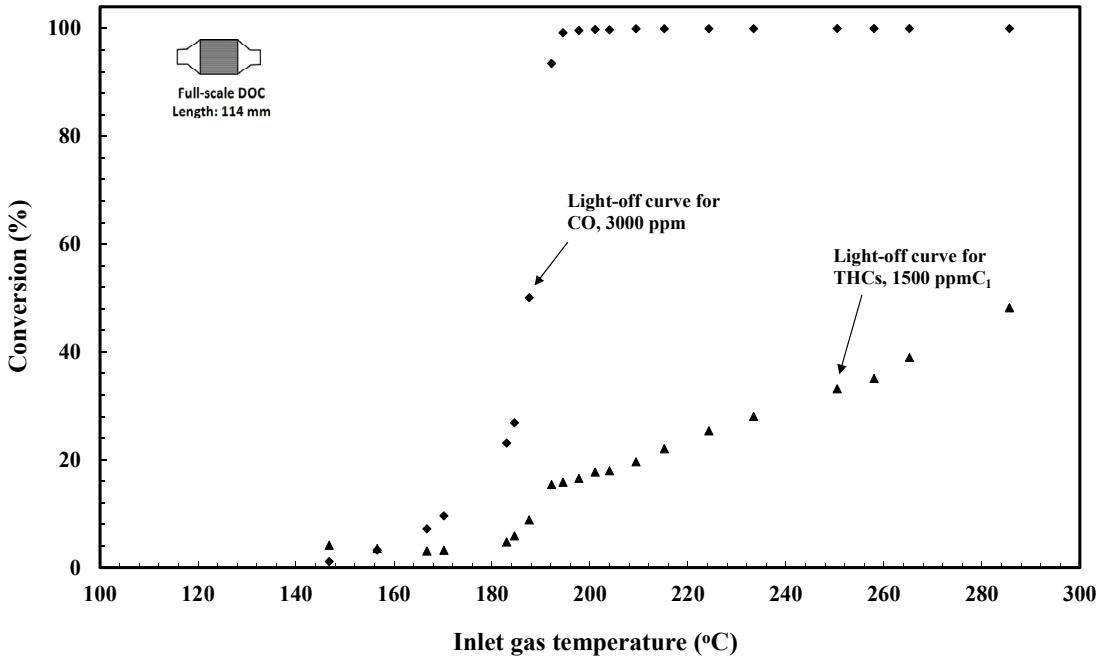


**Figure 3.50** Light-off curve for CO and THCs (inlet CO concentration was 3000 ppm, and THCs were maintained at 1500 ppm$C_1$ (equivalent to 500 ppm propane)).

The embedded thermocouples also provide important information about how the DOC is warmed-up as the inlet gas temperature increases. An example is provided for illustration, see Figure 3.51. The warm-up trend observed in the plot is consistent with simulation results in Oh and Cavendish (1982), when a step-increase in the inlet exhaust temperature was simulated: “at early times, the hot exhaust heats up the upstream portion of the monolith primarily by convective heat transfer. As time elapses, however, the downstream section of the monolith becomes hotter than the upstream section because the reaction exotherm generated in the upstream section is constantly carried downstream by the exhaust flow. This leads to the development of a temperature peak in the downstream section as a result of a vigorous reaction in that region, and then this temperature peak moves rather slowly toward the inlet of the monolith.” During the light-off process, wall temperatures at the rear of the DOC increase a lot faster than in the front section. The oxidation reactions start light-off in the rear part of the converter. As the gas inlet temperature increases, then this zone of high temperature moves towards the inlet. Finally, a uniform wall temperature profile is achieved, and the DOC will be above the light-off temperature.

As this appears to be the first study of its type (where light-off experiments on a real DOC are performed with the additional CO and THCs) the data to match the figures is presented in Appendix 7.1. Unfortunately, in the literature there is a scarcity of numerical data of this type, and this makes it very difficult for researchers that focus on modelling to advance their work.

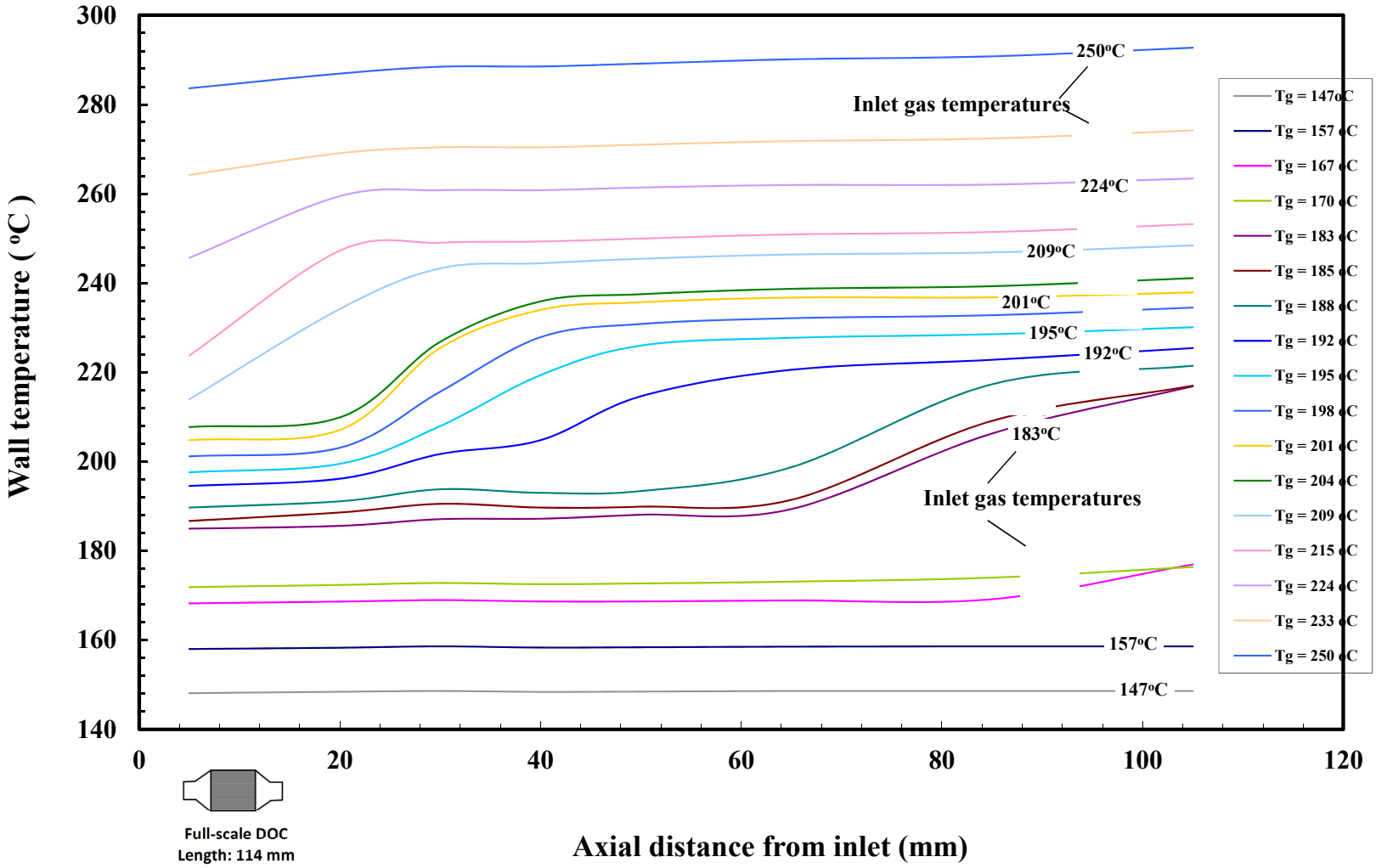


**Figure 3.51** Wall temperature profiles (at r = 0, i.e. centre of the monolith) along axial direction of the DOC at various inlet gas temperatures (inlet CO concentration at 3000 ppm, inlet THCs concentration at 1500 ppm$C_1$, and using Full-scale DOC).

### 3.4.2 Transient light-off experiments

In bench top light-off experiments described in the literature, the inlet gas temperature is ramped up while all other parameters are maintained constant (such as inlet concentration and air mass flowrate). This type of experimental data can be used to validate transient models of catalytic converters, especially mechanistic models. In this section, a methodology is described, which helps to investigate the transient response of a DOC connected to a live diesel engine.

As a demonstration of the technique, experimental trials were performed with the same engine test set-up as described for the pseudo-steady-state light-off experiments. Prior to the transient tests, a conditioning step was carried out in which the engine was operated at high speed and load, to heat the DOC temperature up to 450$^{o}$C for 30 minutes (to purge the DOC) to burn any carbon deposits that may have formed on the pipe wall or on the DOC.

After completing the conditioning step, the engine was operated at idle conditions to allow the exhaust pipe and DOC to cool down to 120$^{o}$C. The EGR valve was kept open for all of these tests. Then the engine was operated at a constant speed of 2000 rpm speed and 6 Nm torque to produce an inlet gas temperature around 146$^{o}$C.Then CO and propane were injected at pre-catalyst positions to maintain the background level at 3000 ppm CO and 1500 ppm$C_1$. As steady-state was achieved, the engine torque was programmed to ramp up to 47 Nm in a pre-determined time period (e.g. 300 s). When the engine torque changed from 5 to 47 Nm, the inlet gas temperature would take longer time (e.g. 880 s) to increase from 146 to 275$^{o}$C, and the inlet CO and THCs concentrations, and air mass flow would also change; these are plotted in Figure 3.52.

From Figure 3.52, it can be seen that:

(a) the exhaust flow rate changes approximately from 55 to 62 kg $h^{-1}$,
(b) the inlet CO concentration increases from 3000 to 3500 ppm during the engine torque ramp up period (0 to 300 s), and then drops back to 3000 ppm when the engine torque ramp is finished, and
(c) the inlet THCs concentrations increase from 1500 to 1550 ppm$C_1$ (during the torque ramp up period (0 to 300 s)) and then drop gradually to 1300 ppm$C_1$ (as the engine temperature gets warmer).

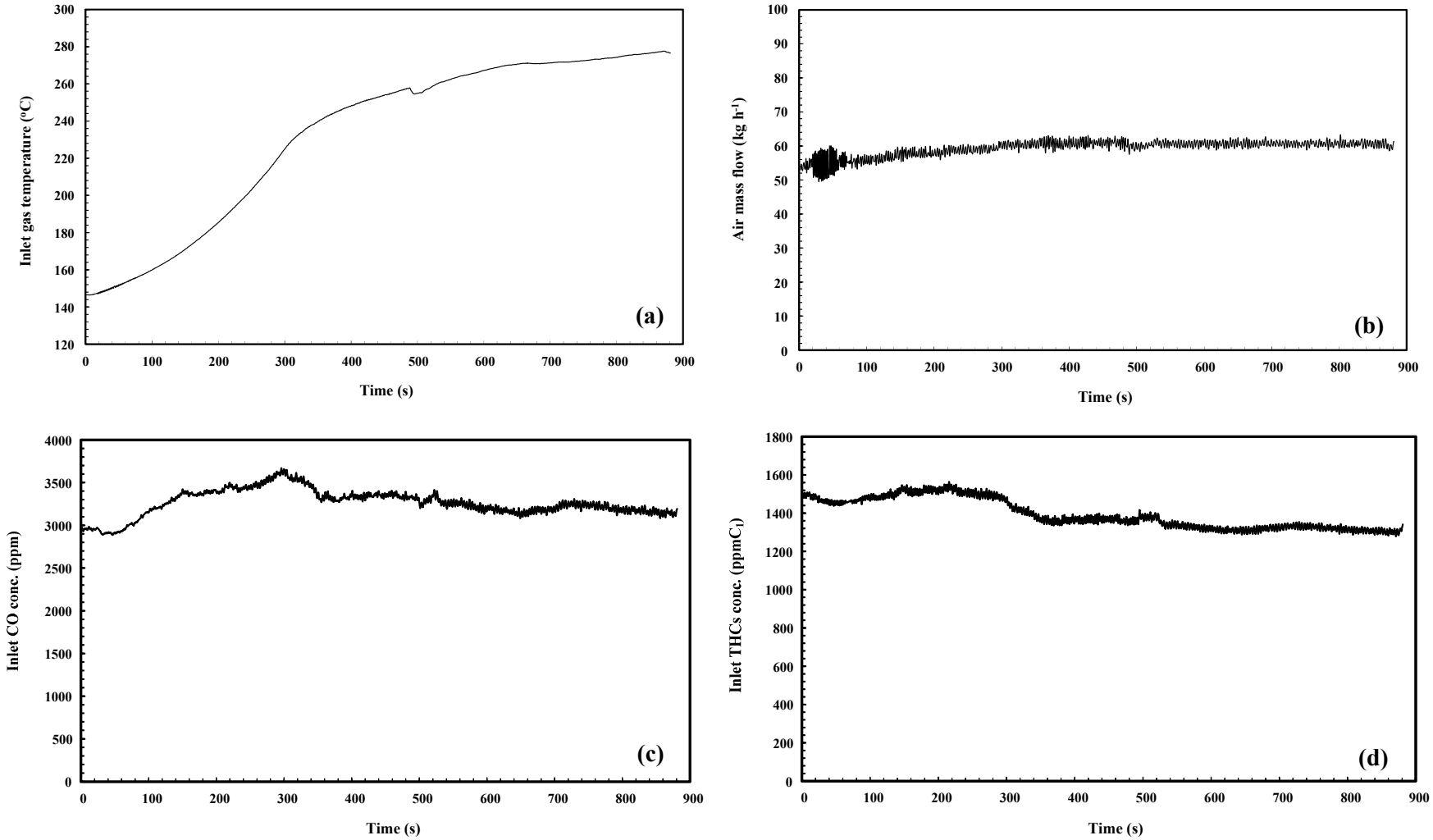


**Figure 3.52** Conditions for transient light-off experiments with engine speed fixed at 2000 rpm while the torque is ramped-up over 300 s: (a) inlet gas temperature profile, (b) air mass flow, (c) inlet CO and (d) THCs concentration.

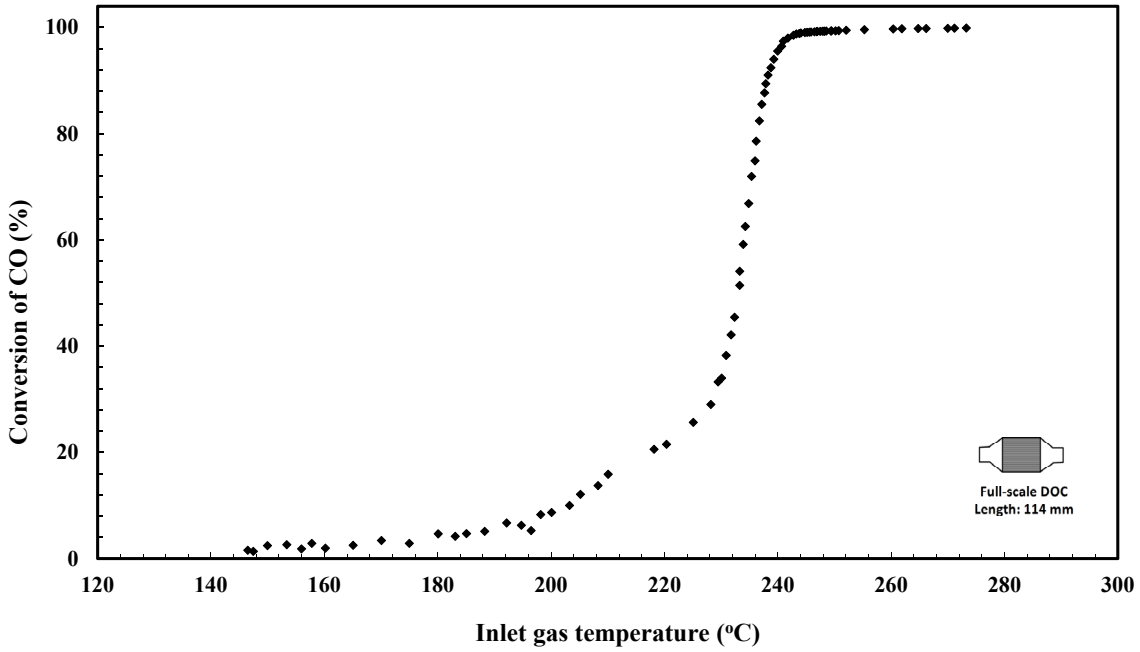


**Figure 3.53** Light-off curve for CO for conditions in Figure 3.52.

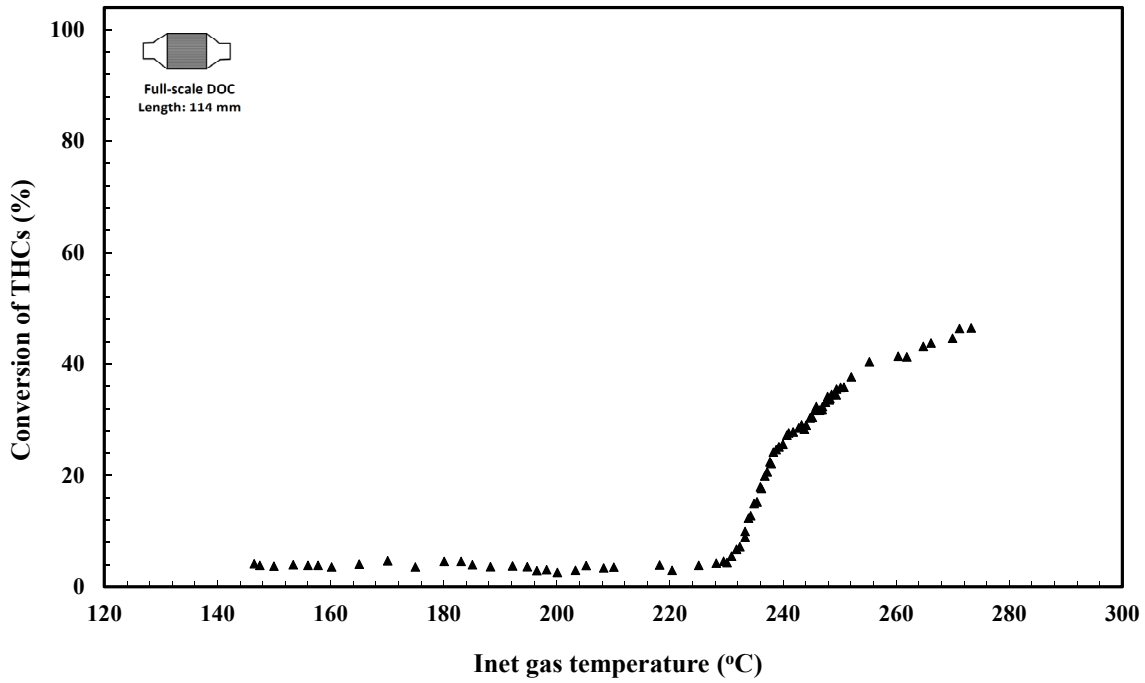


**Figure 3.54** Light-off curve for THCs for conditions in Figure 3.52.

It is encouraging to see, the variations (in CO, THCs and mass flow) are small, and will not affect the shape of the light-off curve. Furthermore, as they are recorded, they can be used as an input condition (function of time) in a mathematical model (if required). The conversions of CO and THCs can be plotted as functions of inlet gas temperature to produce light-off curves, as shown in Figures 3.53 and 3.54.

The transient light-off experiment was repeated with different values of engine torque ramp-up time, e.g. 90 and 600 s. In Figure 3.55, the conversion of CO is plotted as a function of the inlet gas temperature for each engine torque ramp-up time, and this is also compared with the light-off obtained from the earlier pseudo-steady-state experiments. From this figure, it is clear that the light-off temperature for CO decreases as the engine torque ramp-up time is increased. This shows most clearly the importance of maintaining a consistent test procedure when assessing the light-off temperature for a DOC. Also, that this light-off temperature cannot be considered an absolute number, as it depends on many factors.

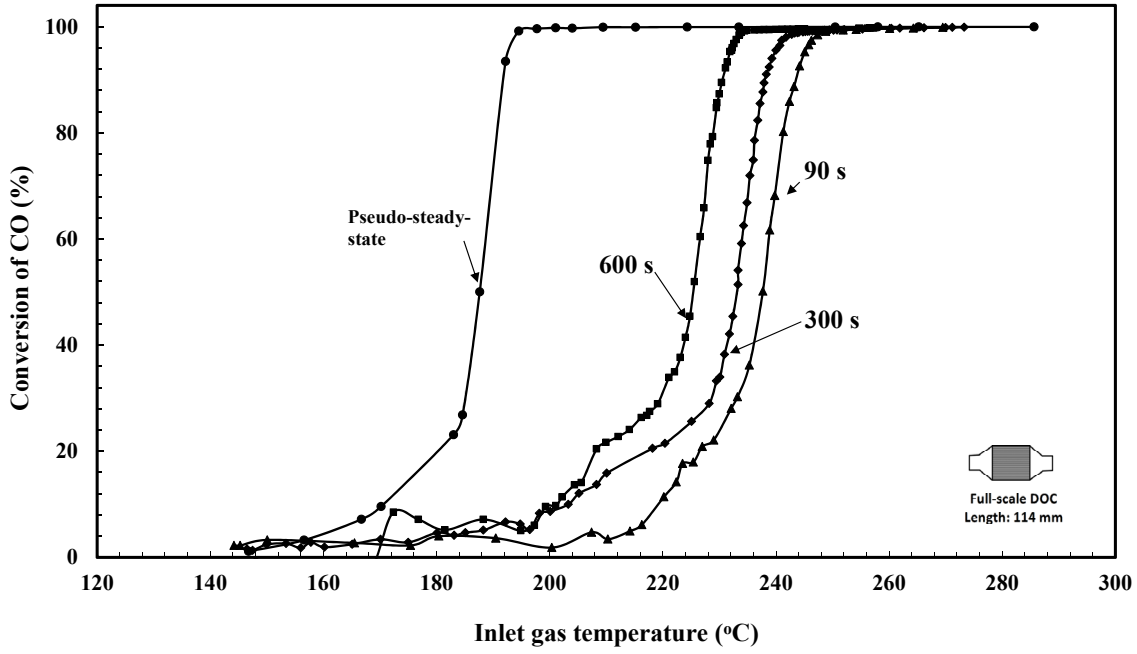


**Figure 3.55** Light-off curves for CO with different engine torque ramp-up times.

### 3.4.3 Transient light-off (ignition) and extinction experiments

In the literature, when a transient light-off experiment is performed using a bench-top experimental rig, then an extinction process is also performed after the light-off experiment, where the inlet gas temperature is then decreased in a similar manner. From such an experiment, if the conversion is plotted against inlet gas temperature, a hysteresis effect is often observed between the 'light-off curve' and 'extinction curve'.

This type of experiment was also performed on the DOC connected to the engine. For the extinction phase, the torque was decreased from 47 to 5 N.m. The results of such an experiment are illustrated in Figures 3.56 and 3.57.

Figure 3.56 shows the conversion of CO follows a typical light-off and extinction process for CO oxidation over platinum as the inlet gas temperature ramps up and then down. The conversion of CO reaches 50% at an inlet gas temperature ($T_{50}$) of 237$^{o}$C in the light-off phase, and is maintained above 50% until the inlet gas temperature drops to 162$^{o}$C (in the extinction phase). This hysteresis (approximately 70$^{o}$C) between light-off and extinction curves is very distinct from the plot. There are two main reasons for this ignition-extinction hysteresis: (i) CO self-inhibition (Arnby *et al*., 2004), and (ii) a thermal effect (Carlsson *et al*., 2004; Salomon, 2008). At low inlet gas temperatures, the CO oxidation is self-inhibited due to high CO surface coverage. The high converge of CO leads to less vacant active sites available for oxygen and other species, e.g. THCs. As the temperature increases, CO desorbs from the sites, and more active sites become available for oxygen. Therefore, more oxidation reactions can take place, and even more active sites become available for oxygen and other species. During the extinction phase, at high temperatures the initial surface converge of CO is low, but it increases as the inlet gas temperature decreases, and CO inhibition occurs again. On the other hand, once the catalyst has been lit-off, the heat released from the chemical reactions promotes the reaction and high CO desorption rates counteract the CO self-inhibition effects (Carlsson *et al*., 2004). In the extinction phase, the wall (or catalyst) temperature decreases with the inlet gas temperature but at a much slower rate. The significance of these two reasons will be investigated in more detail in a subsequent section.

From Figure 3.57, the conversion of THCs increases a lot slower as the gas inlet temperature rises. The maximum conversion of THCs is only 45%, and the inlet gas temperature is clearly not high enough to achieve full conversion during this test. As the inlet gas temperature ramps down, then it is interesting to observe that hysteresis also

occurs between the light-off and extinction phases. This may be attributed to CO inhibition and/or thermal effects.

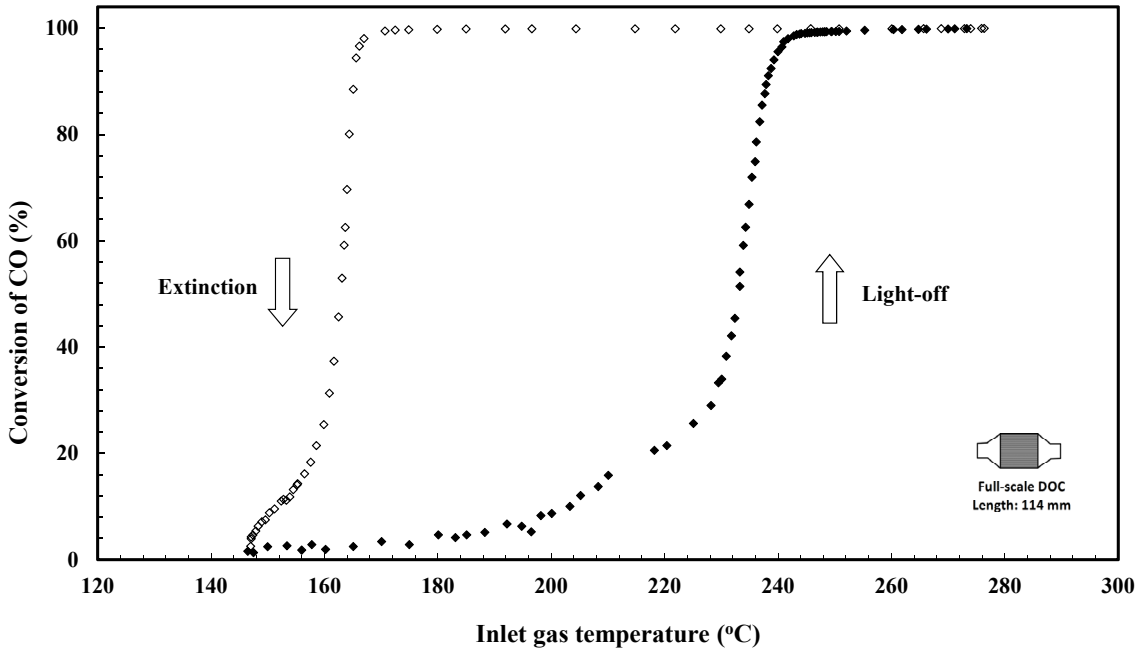


**Figure 3.56** The light-off and extinction curves for CO (3000 ppm) obtained from tests with a torque ramp-up time of 300 s. The inlet CO concentration was 3000 ppm and the inlet THCs concentration was 1500 ppm$C_1$.

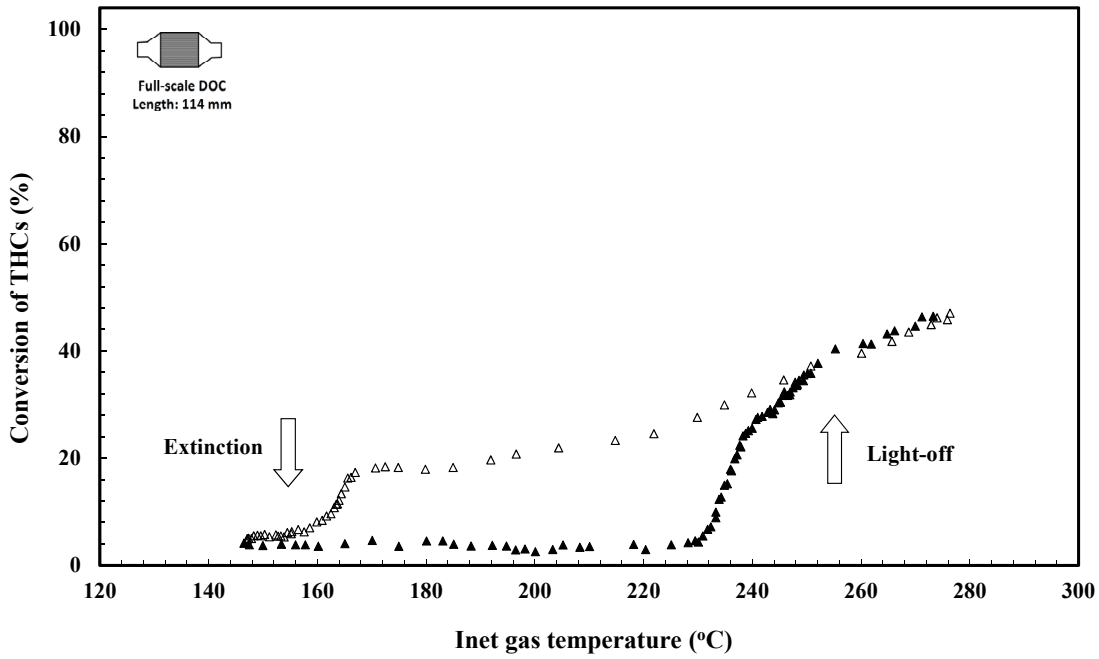


**Figure 3.57** The light-off and extinction curves for THCs (1500 ppm$C_1$) obtained from the tests with a torque ramp-up time of 300 s. The Inlet CO concentration was 3000 ppm and the inlet THCs concentration was 1500 ppm$C_1$.

In addition, transient wall temperature profiles also provide some very important information on the light-off and extinction phases. In Figure 3.58, the inlet gas temperature, outlet gas temperature and wall temperatures are plotted as functions of time. The wall temperatures are measured along the centre line (r = 0), at an axial distance 5, 20, 30, 40, 50, 65, 85 and 105 mm from the front face (inlet) of the DOC. from Figure 3.58, the following observations were made:

(a) Before reactions take place ( t = 0 to 315 s), the order of the temperatures from high to low is inlet gas temperature, 5 to 105 mm wall temperatures, and outlet gas temperature.

(b) As reactions start to take place (t = 315 s), the exotherm from the reactions starts in the rear part of the DOC, therefore, the wall temperature at 85 and 105 mm become the highest. The temperature difference between the front and the rear of the DOC is approximately 45$^{o}$C.The outlet gas temperature also increases and overtakes the inlet gas temperature.

(c) When the DOC is fully lit-off (t = 400 to 1417 s), the temperature difference between the front and the rear of the DOC becomes smaller (approx. 8$^{o}$C), although the rear part of the DOC still remains the hottest.

(d) During the extinction process (t = 900 to 2050 s), the rear part of the DOC remains the hottest. But as reactions stop, the outlet gas temperature drops slightly below the inlet gas temperature.

(e) These results also start to answer the question relating to thermal inertia and connection with hysteresis. If thermal inertia played a major role, then the wall temperature profiles at 50% CO conversions in the light-off and extinction phases should be close to one another. However, a difference of about 70$^{o}$C in exists.

As a reminder, these types of experiments can now be used to help to tune mathematical models. They can also be used to compare simulations with experimental measurements.

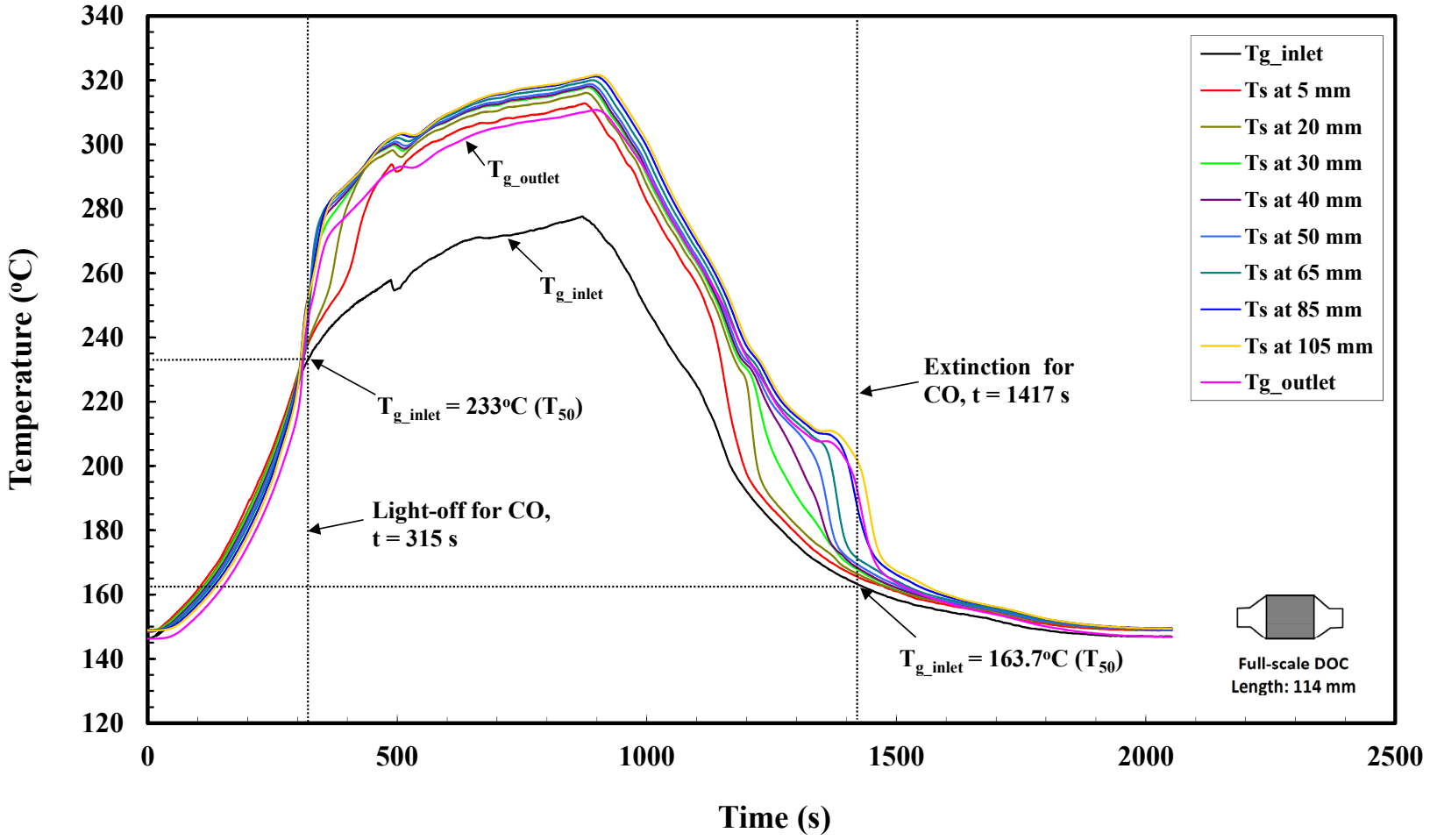


**Figure 3.58** Light-off and extinction experiment, which include: inlet gas temperature, outlet gas temperature and wall (or catalyst) temperatures at various axial positions along the centre of the DOC (r = 0).

#### 3.4.3.1 Effect of inlet CO concentration on light-off and extinction

These transient experiments were repeated with different fixed values of inlet CO concentration (3000, 4000 and 5000 ppm). In the tests, the inlet THCs concentration was maintained at 1500 ppm$C_1$ (*via* propane injection). The engine torque ramp-up time was 90 s. The engine output conditions (with inlet CO concentration at 3000 ppm) are summarised in Figure 3.59. The experimental results are shown in Figure 3.60.

A repeatable trend is observed among the light-off and extinction curves for CO. As expected, the light-off temperatures ($T_{50}$) increases with inlet CO concentration, and the extinction temperatures ($T_{50}$) decreases with inlet CO concentrations, and hysteresis between the light-off and extinction phase is similar. These observations are consistent with other bench-top experimental results in the literature.

The overall rate of CO oxidation is also plotted as a function of inlet gas temperature for different inlet CO concentration, as shown in Figure 3.61. A similar trend to Figure 3.60 is observed. During the early phase of the light-off process, it is interesting to observe that the overall rate of CO oxidation shows a similar trend to the pseudo-steady-state light-off experiment (see Figure 3.49). However, the reaction rate with a 3000 ppm CO inlet seems identical to that with a 4000 or 5000 ppm level. However, at higher temperatures and CO concentrations the rate increases as more CO is available for reaction. During the extinction process, a similar reverse pattern is followed.

Unfortunately, some uncertainty may still remain with the interpretation of results from these plots; because the inlet gas temperature does not always reflect the wall (or catalyst) temperature, where the reactions actually take place. Therefore, such plots may mislead. In the literature, light-off curves are usually plotted as a function of inlet gas temperature. This may be attributed to two reasons, (a) the inlet gas temperature is easier to measure than the wall temperature, and (b) even when the wall temperature is measured, it is difficult to find a representative value since a Full-scale DOC may have complex temperature profiles.

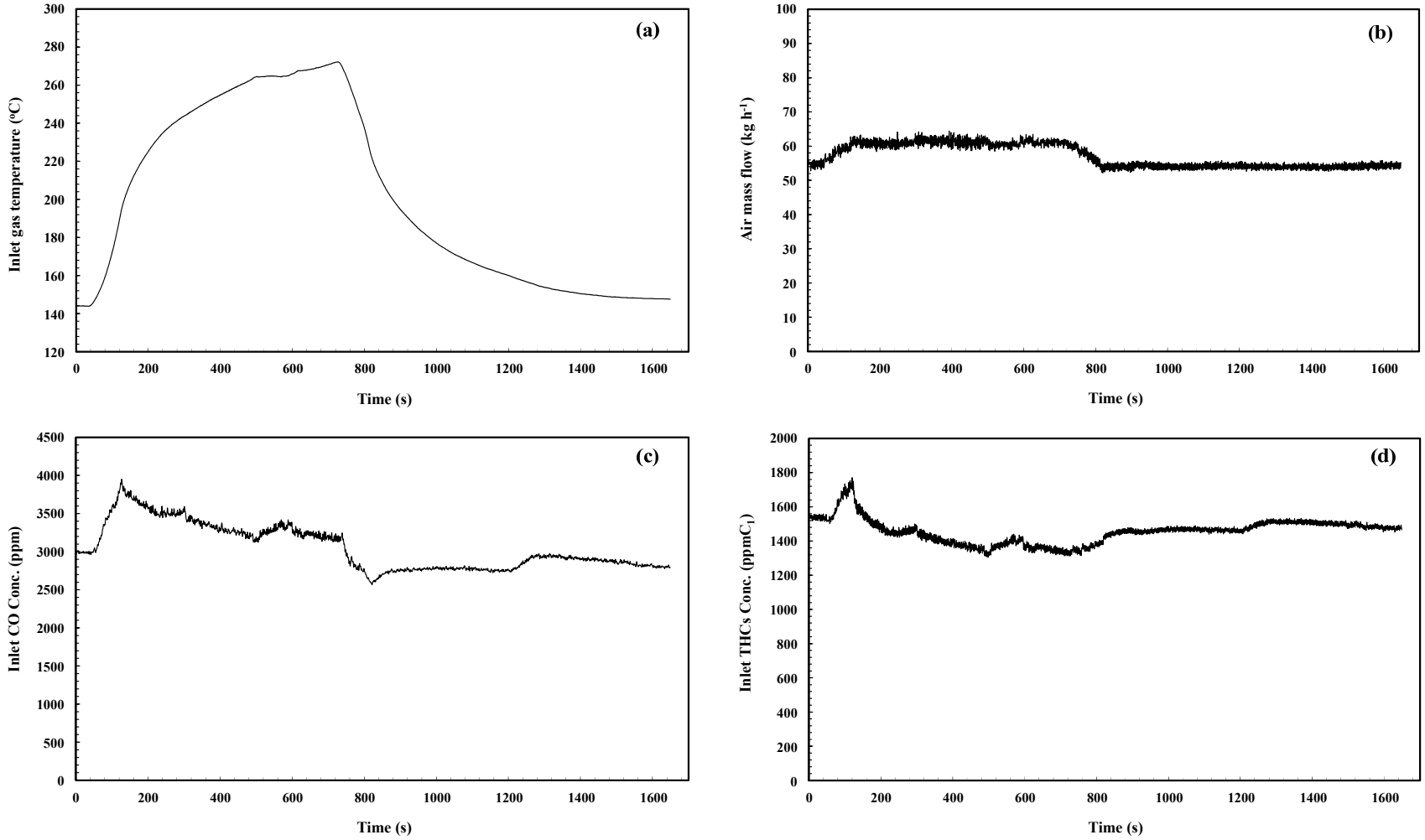


**Figure 3.59** Conditions for transient light-off and extinction experiment with engine speed fixed at 2000 rpm while the torque is ramped-up over 90 s: (a) inlet gas temperature profile, (b) air mass flow, (c) inlet CO and (d) THCs concentration.

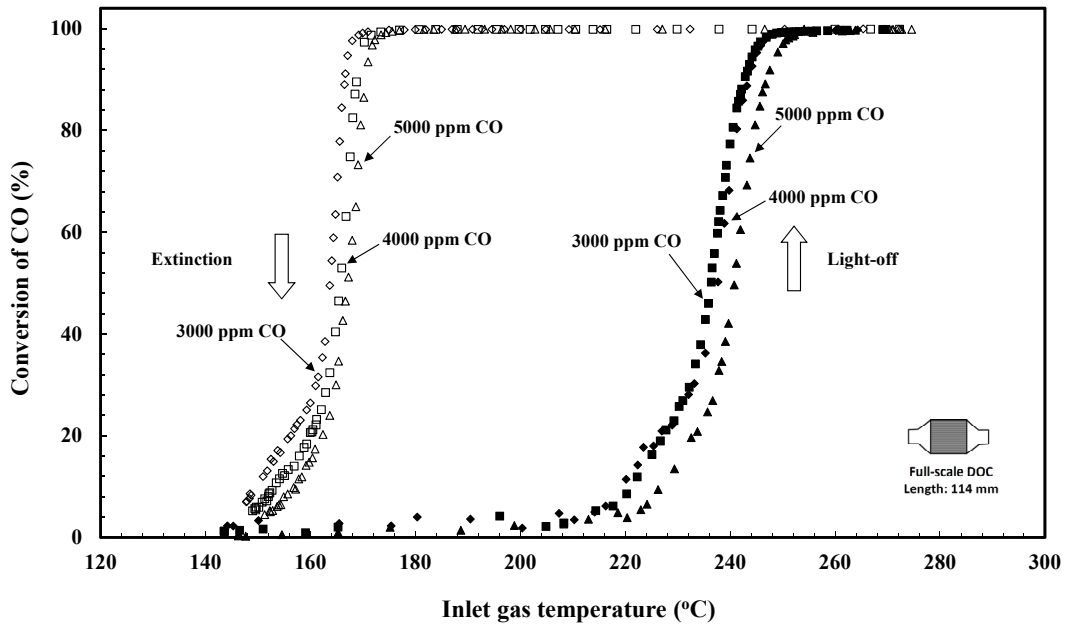


**Figure 3.60** The effect of inlet CO concentrations on CO light-off and extinction. These tests were performed at initial inlet CO concentrations of 3000, 4000 and 5000 ppm while the initial inlet THCs concentration was maintained at 1500 ppm$C_1$, and with an engine torque ramp-up time of 90 s.

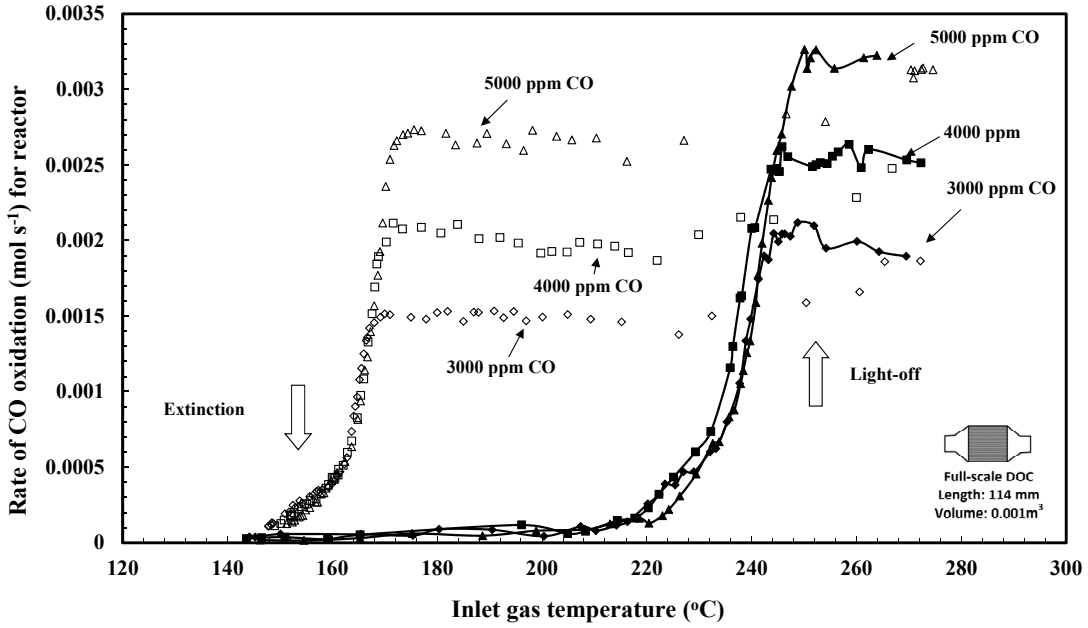


**Figure 3.61** The effect of inlet CO concentration on the overall rate of CO oxidation during light-off and extinction.

### 3.4.3.2 Effect of inlet concentration of THCs on light-off and extinction

In the first set of experiments the initial inlet CO concentration was maintained at 3000 ppm and no extra hydrocarbon were added. In the test, the engine torque ramp-up time was 90 s, and the background level of THCs concentration varied from 240 to 340 ppm$C_1$ (due to increasing engine torque). Experiments were then performed with the addition of propane to provide a background level of 1500 ppm$C_1$ THCs, and the results are plotted in Figure 3.62.

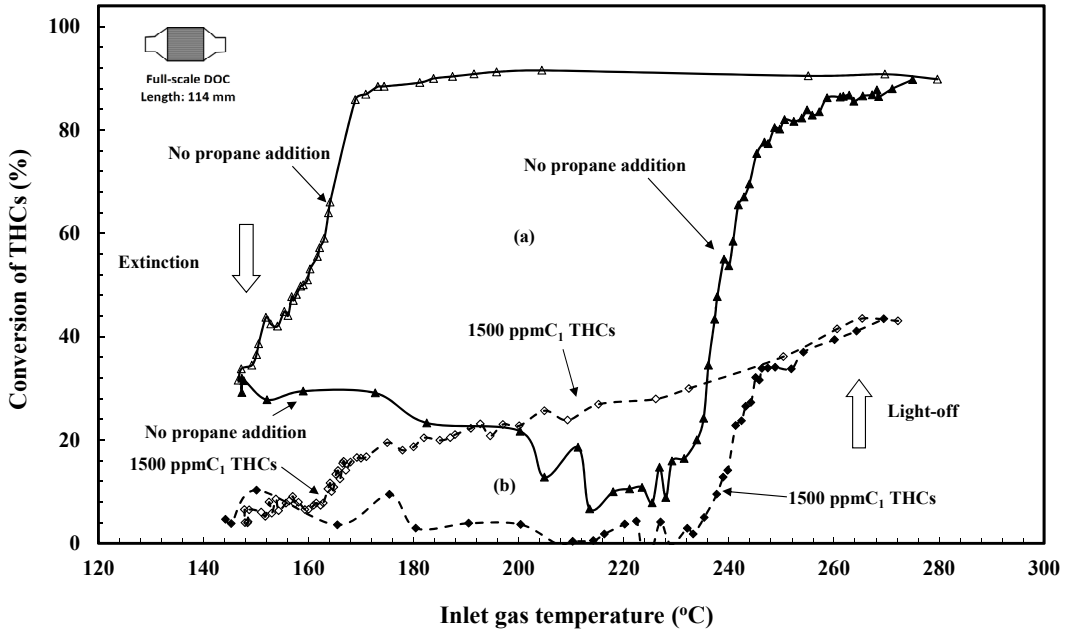


**Figure 3.62** Comparison of the light-off and extinction curves for THCs at different background level of THCs: (a) 240 to 340 ppm$C_1$ (no propane addition); (b) maintained at 1500 ppm$C_1$ (*via* propane injection). The inlet CO concentration was maintained at 3000 ppm, and with torque ramp-up time of 90 s.

From Figure 3.62, there is an indication that during the early phase of the light-off process, THCs may be adsorbed/stored on the surface of the DOC. The conversion appears to be high at low temperatures, and then it drops as the temperature is increased. However, when 1500 ppm$C_1$ propane is added, then a similar effect is also observed, but the shape is different. According to Knafl *et al.* (2007), this decrease in THCs conversion is because of hydrocarbons with a carbon number $C_5$ and higher being trapped at low temperatures on the DOC. In their engine experiments, THCs conversion dropped from 70% down to 0% before it started to increase at higher temperatures. Also in their study, they found that about 72% of pre-catalyst emission was $\geq C_6$.

In the next set of figures the change in CO is plotted as a function of inlet gas temperature for different inlet THCs concentration. From Figure 3.63, it can be seen that without propane injection, the light-off curve for CO is almost identical to that with 1500 ppm$C_1$ THCs. However, during the extinction phase, the test with propane injection (1500 ppm$C_1$ THCs) shows an earlier drop in conversion. This could occur because of the extra amount of THCs reducing the surface coverage available for oxygen to reacting with CO sites, resulting in an increase in the surface coverage of CO.

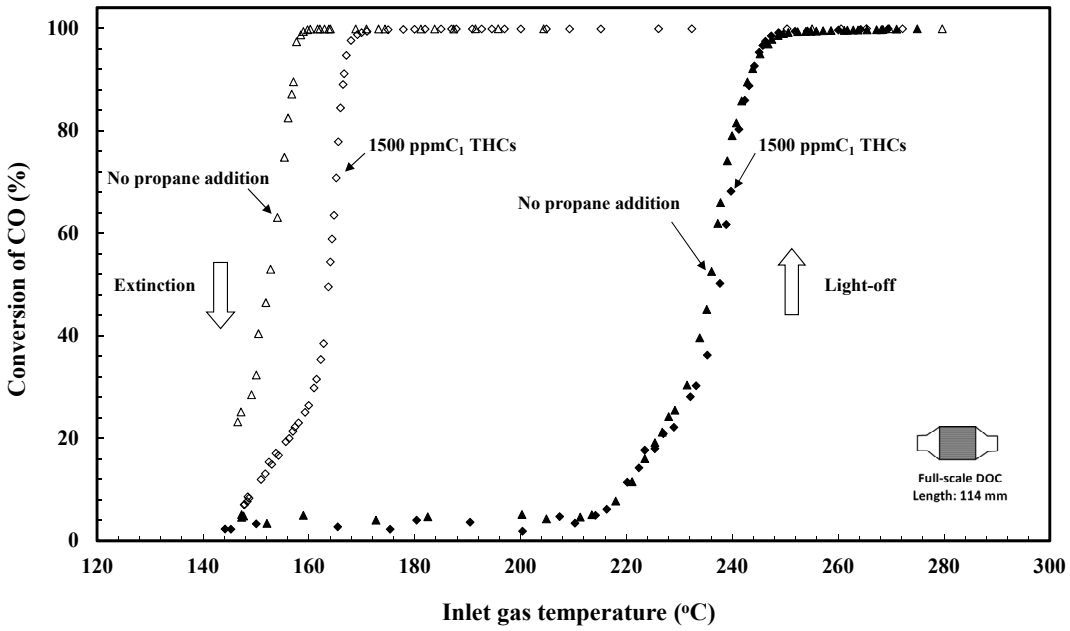


**Figure 3.63** The effect of inlet THCs concentration on the conversion of CO during light-off and extinction for conditions in Figure 3.62.

However, if the overall rate of CO oxidation is plotted as a function of inlet gas temperature, the overall rate of CO oxidation does not appear to be affected by propane injection during the light-off and extinction phases, see Figure 3.64. However, it is important to remember that, especially during the extinction phase, the inlet gas temperature does not represent the actual wall temperature.

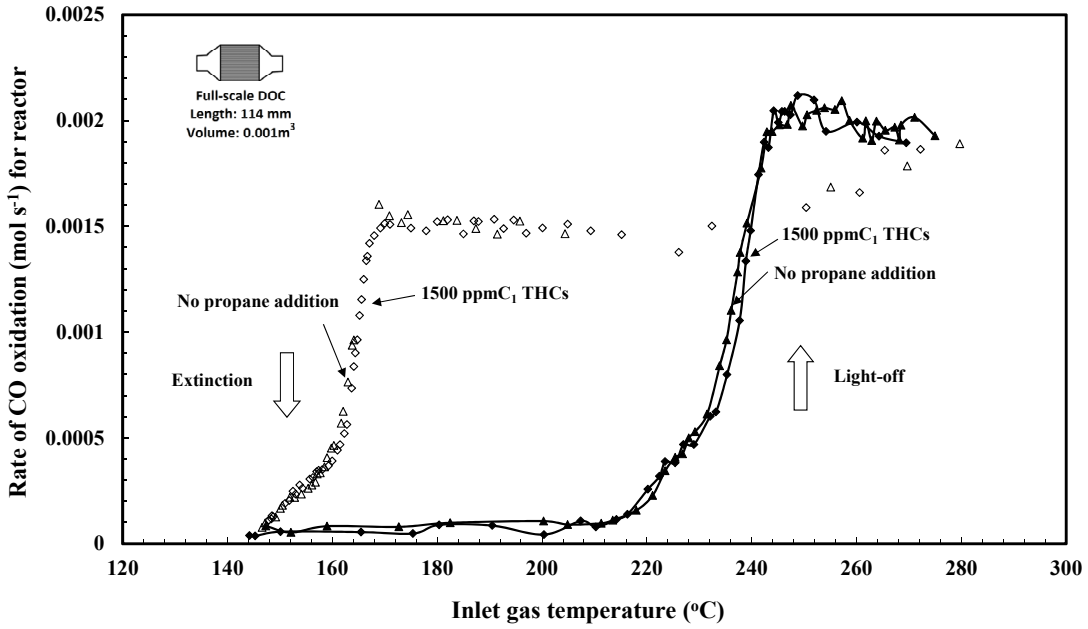


**Figure 3.64** The effect of inlet THCs concentration on the overall rate of CO oxidation during light-off and extinction phases for the conditions in Figure 3.62.

### 3.4.4 Investigating the main cause of hysteresis using a Thin-slice DOC

The main advantage of using, a Thin-slice DOC for this test is that it has a simple wall temperature profile (compared to a Full-scale DOC). Thus the average wall temperature can be used to represent the temperature of the DOC, and this can be used to plot the results. The transient light-off and extinction experiments were repeated using a 5 mm Thin-slice DOC. This was 50% thinner than the 10 mm Thin-slice used in the earlier experiments. The reason for this, was to reduce the conversion across this Thin-slice DOC even further (especially at high temperatures). Inlet CO concentrations were 3000, 4000 and 5000 ppm, and the inlet THCs concentration was maintained at 1500 ppm$C_1$. The engine torque was ramped up from 5 to 47 Nm in 90 s.

In Figure 3.65, the trend in the light-off and extinction curves is similar to Figure 3.60, and as expected the maximum conversions of CO are lower than in the Full-scale DOC. Hysteresis between light-off and extinction phases can be clearly observed. Another observation from the comparison between the Thin-slice DOC (Figure 3.65) and the Full-scale DOC (Figure 3.60), is the relatively sharp rise in the light-off curve for the Thin-slice DOC.

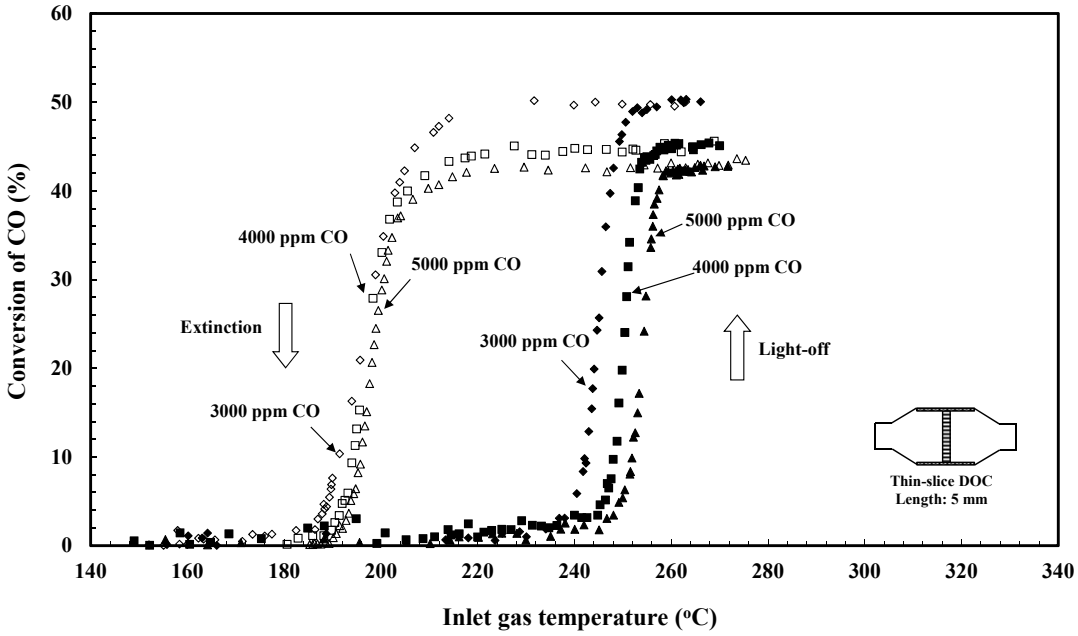


**Figure 3.65** The light-off and extinction curves for CO plotted as a function of the inlet gas temperature. These tests were performed at inlet CO concentrations of 3000, 4000 and 5000 ppm while the THCs concentration was maintained at 1500 ppm$C_1$, and the engine torque ramp-up time was 90 s.

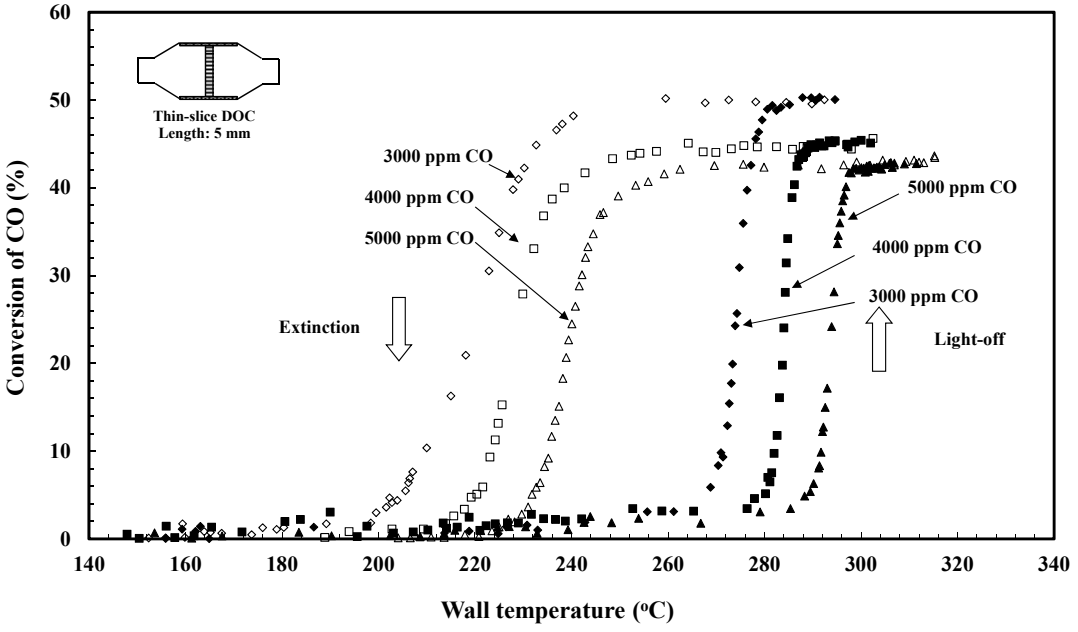


**Figure 3.66** The light-off and extinction curves for CO plotted as a function of the average wall (or catalyst) temperature for the conditions in Figure 3.65.

In Figure 3.66, when conversion is plotted against the average wall temperatures, the differences in the extinction curves are more distinct showing that the conversion of a 5000 ppm feed of CO drops at a higher temperature than feeds of 4000 and 3000 ppm of CO. This is because at a higher inlet CO concentration, it is easier to cover the active sites. The discrepancy in extinction curves between Figures 3.62 and 3.65 emphasises the importance of monitoring the wall temperature during these experiments.

As discussed earlier, the two main reasons that can give rise to hysteresis between light-off and extinction phases are mechanistic (CO inhibition) and/or thermal effects (inertia). From Figure 3.66, it is clear that this is not a thermal effect as conversion is plotted as a function of wall temperature. Taking the results from a 3000 ppm inlet CO concentration (for illustration), the hysteresis for 3000 ppm CO in Figure 3.65 is approximately 60$^{o}$C, and in Figure 3.66, this is approximately 55$^{o}$C. This indicates that hysteresis is largely attributed to CO inhibition, and thermal inertia plays a minor role. This conclusion is consistent with the simulation results in Salomon's PhD thesis (Salomon, 2008).

Figure 3.67 shows the effect of inlet CO concentrations on the rate of CO oxidation. Again, the hysteresis between light-off and extinction phases can be clearly observed.

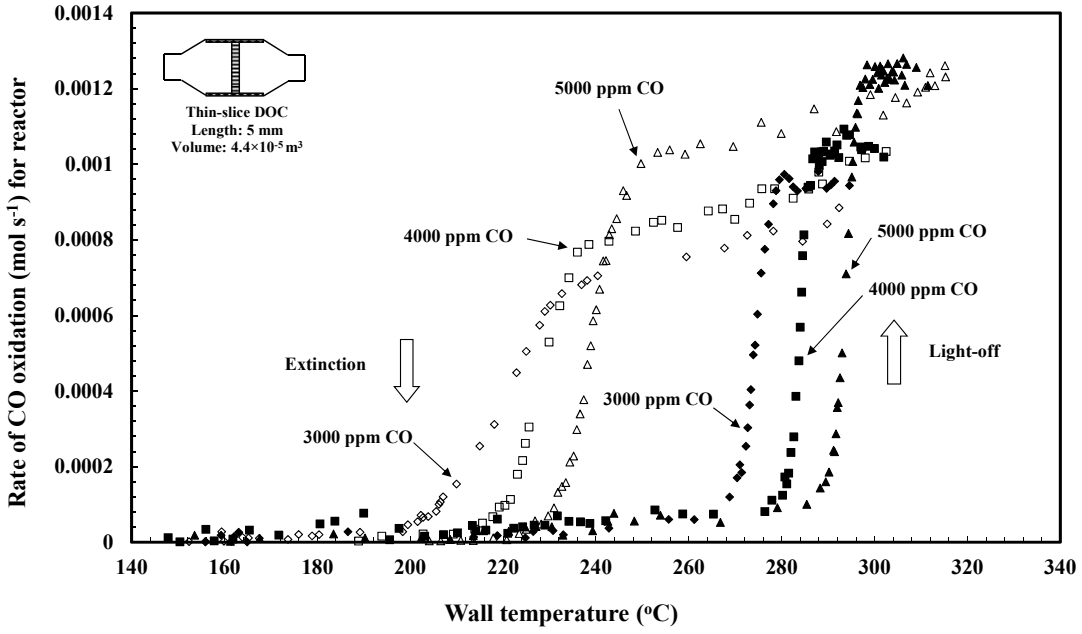


**Figure 3.67** The rate of CO oxidation is plotted as a function of the average wall (or catalyst) temperature.

In general, such experimental results will be very useful for the development of mechanistic mathematical models of DOCs. These results also confirm that the LHHW forms of rate expressions will not be adequate to simulate these kinds of transient experiments, as they do not consider the transient nature in the availability of active sites on the catalyst surface.

## 3.5 CO inhibition

CO inhibition and its effect on the oxidations of CO and THCs had been well studied in the literature (e.g. Voltz, 1973; Herskowitz and Kenny, 1983), however, these studies were all performed on bench-top experimental rigs using synthetic gas mixtures. In this section, a technique is described, which helps to see the CO inhibition effect on a real engine exhaust system.

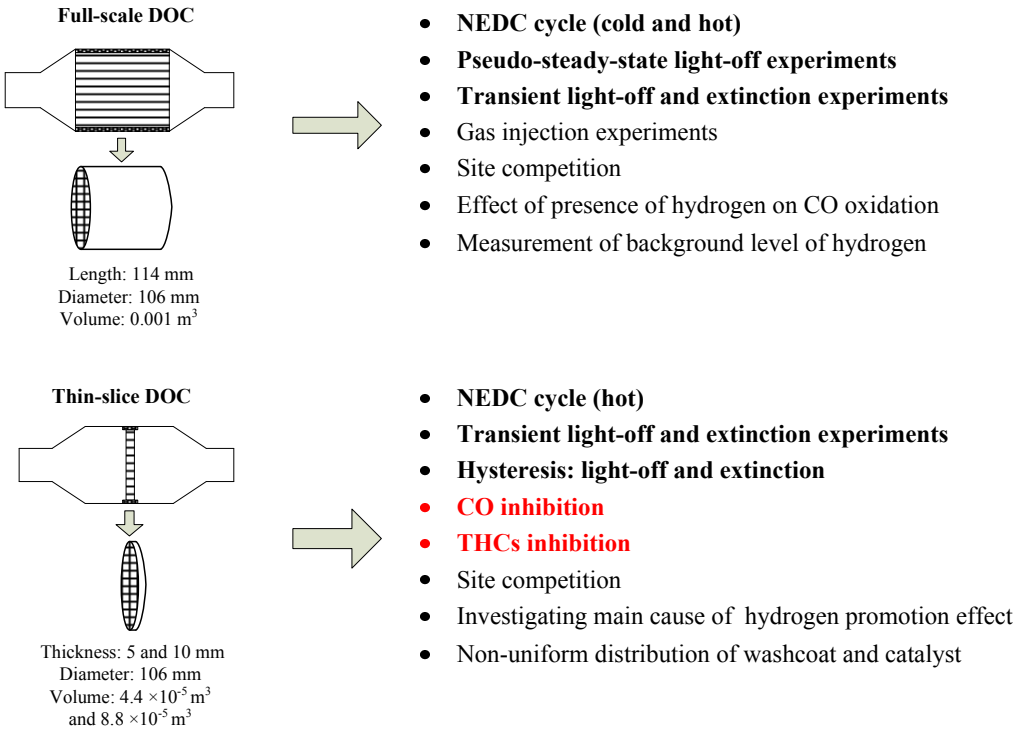


**Figure 3.68** Summary of experiments in Chapter 3. The experiments highlighted in red are discussed in Section 3.5.

The inhibition effect is difficult to observe if a Full-scale DOC is used, because it has many active sites, often high conversion, and a varying wall temperature profile along the axis.

Using a Thin-slice DOC is a good option for this type of experiment, as:

(a) Local rates of reaction may be calculated (provided that the inlet and outlet concentrations and flowrates are known).

(b) There are less available active sites, and this leads to:

- Sites are more easily fully covered by CO, i.e. resulting in inhibition.

- Conversion is low; hence the system has less temperature variation along the axis.

(c) There is less thermal mass, and the wall temperature profile is simpler.

(d) Because of entrance effects in such short DOC, the heat and mass transfer coefficients are high.

The overall effect is to highlight more clearly the behaviour of the DOC.

### 3.5.1 Test on 10 mm Thin-slice DOC

Initial experiments were performed in a 10 mm Thin-slice DOC. To illustrate the technique, the engine was operated at a constant speed of 2000 rpm and a constant engine torque of 45 Nm to produce a fixed average inlet gas temperature of 265$^{o}$C (actually varied from 261 to 267$^{o}$C). At this temperature, external mass transfer limitations were considered not to be significant (Volts *et al.,* 1973; Hayes *et al*., 1995). Then CO was added to raise its concentration from 0.012 to 8 vol% in an incremental manner (Note: the concentration range to cover background CO concentrations from a typical diesel engine in the NEDC, varied from 0.01 to 0.05 vol%). The exhaust gas was sampled simultaneously at pre- and post-catalyst positions using two emission analysers. The experimental data was automatically saved as a trace file, and could be easily converted into editable format.

In this experiment, a very high concentration of CO was investigated, to see how the results compared with literature data at high concentrations. Figure 3.69 shows the rate of CO oxidation and CO conversion as functions of inlet CO concentration. It is interesting to note, that the reaction rate increases almost linearly with the inlet CO concentration, hence, the expected CO self-inhibition is not observed. To explore why the inhibition is not seen, the test conditions are compared in Table 3.7 with work by Hayes *et al*. (1995) where CO inhibition was observed.

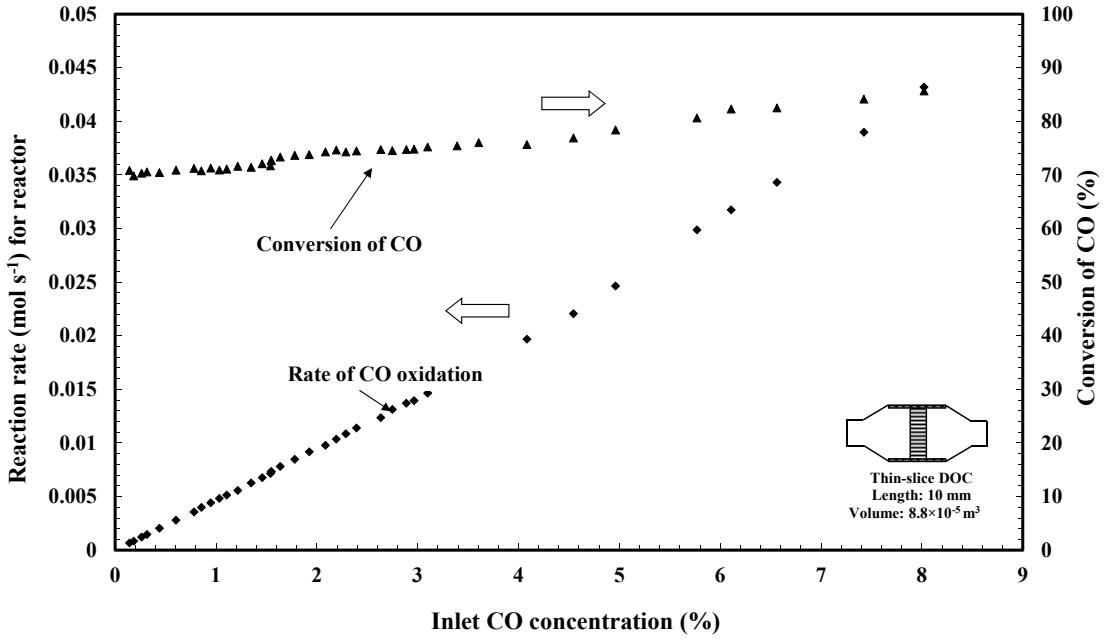


**Figure 3.69** The rate CO oxidation and CO conversion as functions of inlet CO concentrations.

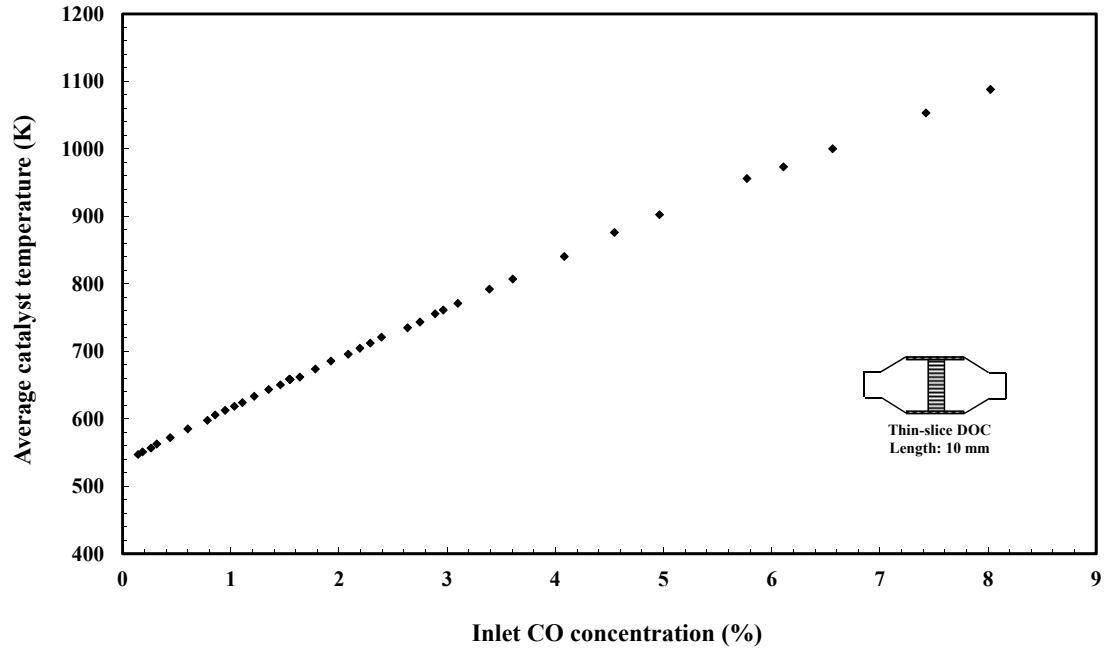


**Figure 3.70** Average temperature of reactor as a function of inlet CO concentration.

**Table 3.7** Comparing experimental conditions with Hayes *et al*. (1995).

| | **This experiment** | **Hayes *et al*. (1995)** |
|---|---|---|
| **Type of experiment** | Engine test | Bench-top |
| **Reactor** | 10 mm long, 106 mm diameter | 5 mm long, 15 mm diameter |
| **Inlet gas temperature ($^oC$)** | 261 to 267 | 260 |
| **Conversion of CO** | 70 to 85% | 4.4 to 11.1% |
| **Reactor temperature ($^oC$)** | 260 to 850 | 280 |
| **Inhibition observed** | No | Yes (at 3 % CO) |
| **Gas inlet velocity** | 3.13 to 3.35 m $s^{-1}$ at STP | 2 m $s^{-1}$ at STP |
| **Monolith channel size** | 1.1 mm | N/A |
| **Catalyst loading** | 120 g/$ft^3$ | N/A |

The main difference arises from the use of an annular ring (in Hayes *et al.*, 1995) which is coated with catalyst, and for this low surface area the conversion of CO is maintained very low. As illustrated in Figure 3.70, as the conversion increases then so does the average wall temperature, and this may be masking the inhibition effect. So it was decided to reduce the length of the Thin-slice DOC, so as to reduce the conversion of CO across it.

### 3.5.2 Test on 5 mm Thin-slice DOC

A few experimental trails were performed, in which the engine was operated at a constant engine speed of 2000 rpm and different engine torques were used in order to produce inlet gas temperatures. These conditions are summarised in Table 3.8.

Table 3.8 Conditions for CO inhibition experiments.

| **Engine torque (Nm)** | **27** | **30** | **34** |
|---|---|---|---|
| **Inlet gas temperature ($^oC$)** | 208 | 219 | 229 |
| **Air mass flow (kg/h)** | 59.48 | 59.49 | 60.45 |
| **GHSV ($h^{-1}$)** | $10.4\times10^5$ | $10.4\times10^5$ | $11.5\times10^5$ |
| **Inlet THCs (ppm$C_1$)** | 348 | 282 | 265 |
| **$O_2$ (vol%)** | 11 | 11.5 | 10.11 |
| **NOx (ppm)** | 57 | 55 | 61 |
| **$CO_2$ (vol%)** | 6.55 | 7.09 | 7.32 |

Prior to each test the conditioning step was run to purge the DOC. For each test, as steady-state was reached, the inlet concentration of CO was gradually increased from 1000 to 7000 ppm by adding CO from a gas cylinder. All tests were run at GHSV of approximately 1,100,000 $h^{-1}$, and the results are shown in Figure 3.71.

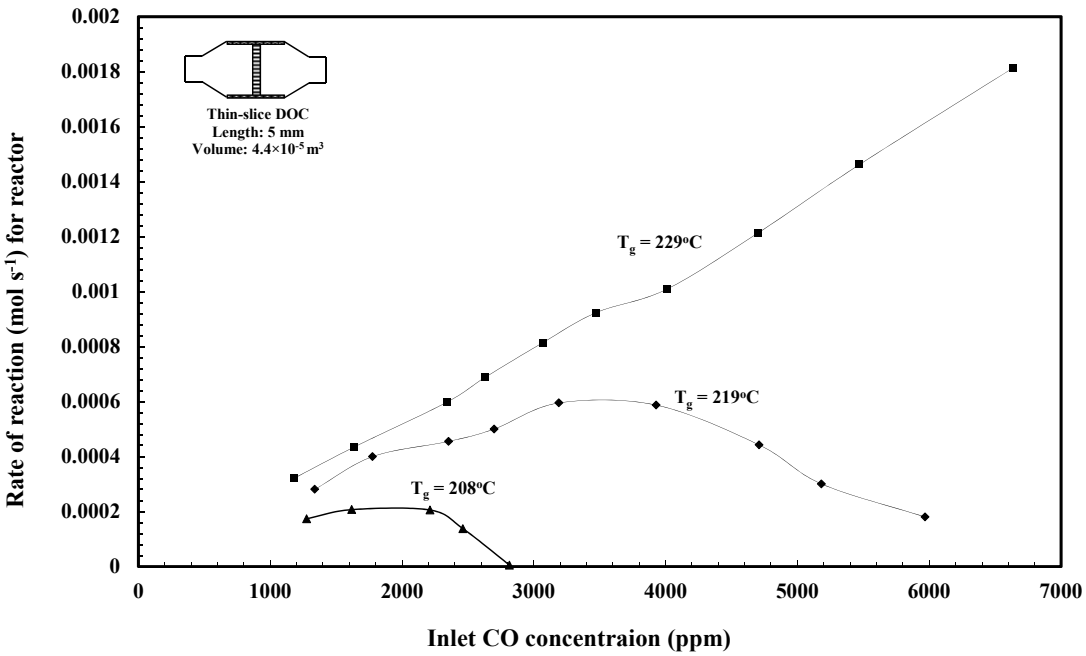


**Figure 3.71** Effect of an increase in the inlet CO concentration on the rate of CO oxidation.

For this experiment the wall temperature profiles are plotted as a function of inlet concentration of CO in Figure 3.72, and the following observations can be made:

- When the test was performed with an inlet gas temperature of 208°C, the rate of CO oxidation slightly increases with inlet CO concentrations, and then at 2200 ppm, the rate starts to decrease and become inhibited.
- When the test was performed at an inlet gas temperature of 219°C, inhibition starts at an inlet CO concentration of 3500 ppm;
- When the test was performed at an inlet gas temperature of 229°C, the rate of CO oxidation continues to increase linearly, and there are no signs of CO self-inhibition.
- Although CO self-inhibition was observed in these tests, the wall temperature was also observed to increase during the tests.

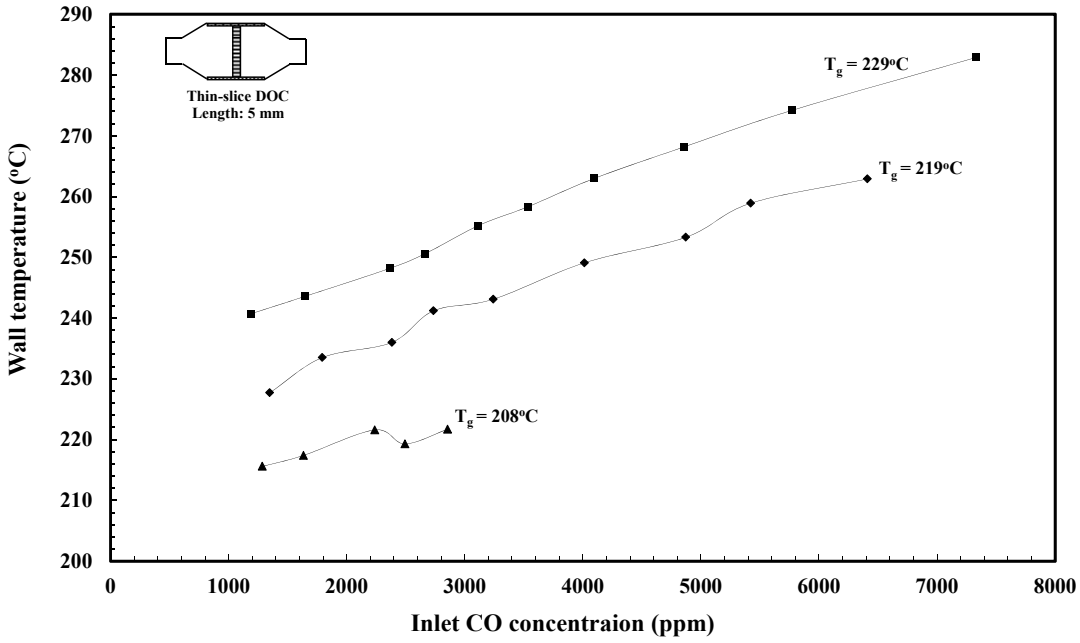


**Figure 3.72** Wall temperature as a function of the inlet CO concentration.

### 3.5.3 THCs inhibition

The same technique was then used to see if THCs were likely to show any inhibition effects. The engine was operated at a constant speed of 2000 rpm and different engine torques was used in order to produce different inlet gas temperatures, see Table 3.9.

**Table 3.9** Conditions for THCs inhibition experiments.

| **Engine torque (Nm)** | **8.4** | **30.1** | **50.8** | **74.6** |
|---|---|---|---|---|
| **Inlet gas temperature ($^oC$)** | 160 | 218 | 300 | 360 |
| **Air mass flow (kg/h)** | 55 | 59 | 63 | 92 |
| **GHSV ($h^{-1}$)** | $9.5\times10^5$ | $10.4\times10^5$ | $11.1\times10^5$ | $16.3\times10^5$ |
| **Inlet CO (ppm)** | 886 | 1022 | 1111 | 746 |
| **$O_2$ (vol%)** | 15 | 11.5 | 7.88 | 8.66 |
| **NOx (ppm)** | 73 | 65 | 55 | 100 |
| **$CO_2$ (vol%)** | 4.25 | 6.77 | 9.42 | 8.83 |

Prior to each trial the conditioning step was run to purge the DOC. For each trial, the inlet concentration of THCs was increased gradually from 1000 to 8000 ppm$C_1$ (by adding propane from a gas cylinder). During these tests, CO was not injected, and its concentration changed with engine torque. When the engine torque was 8.4, 30.1 and 50.8 Nm, the background CO concentration was around 1000 ppm, and when the engine torque was 74.6 Nm, the background CO concentration was about 750 ppm. The GHSV varied from approximately 950,000 to 1,600,000 $h^{-1}$. The experimental results are present in Figures 3.73 to 3.75. From these the following observations are made:

(a) From Figure 3.73, there is no evidence of any inhibition in the oxidation of THCs, however, in Figure 3.74, there is an indication of a slight inhibition effect on CO when $T_g = 218^oC$. However at higher temperatures (e.g. $300^oC$) inhibition effect on CO is not occurring.

(b) From Figure 3.75, when $T_g = 160$ and $230^oC$, then the wall (or catalyst) temperature is relatively constant. However, as $T_g$ increases to $300^oC$, then wall temperature starts to increase (as THCs increase). From Figure 3.73 this contribution must be coming from the oxidation of THCs.

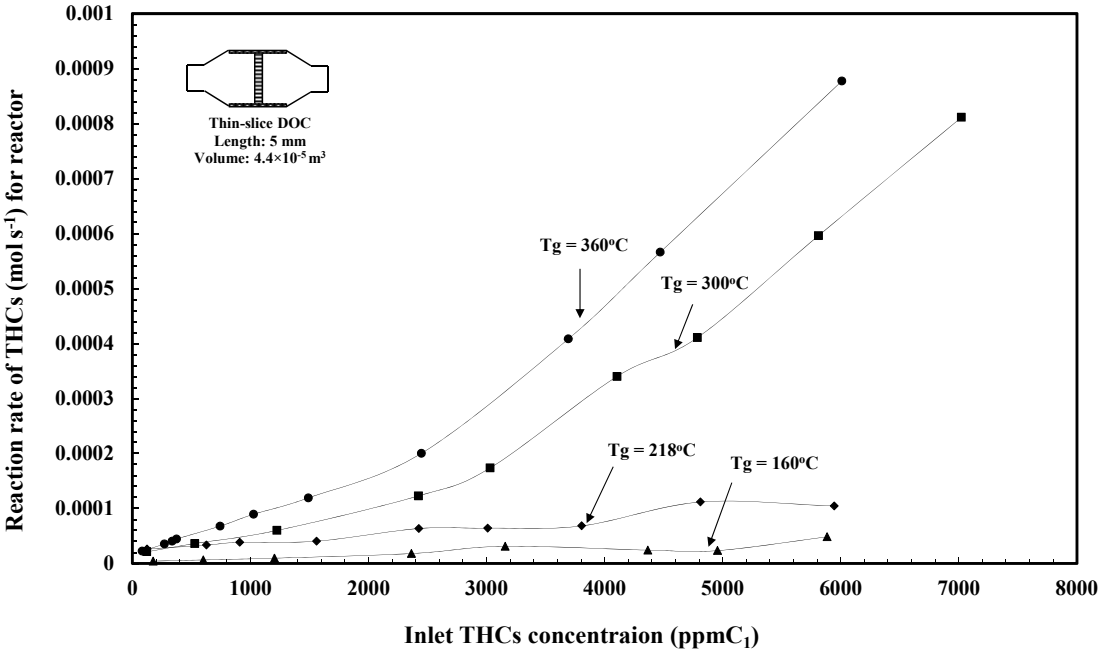


**Figure 3.73** Effect of an increase in the inlet THCs concentration on the rate of THCs oxidation.

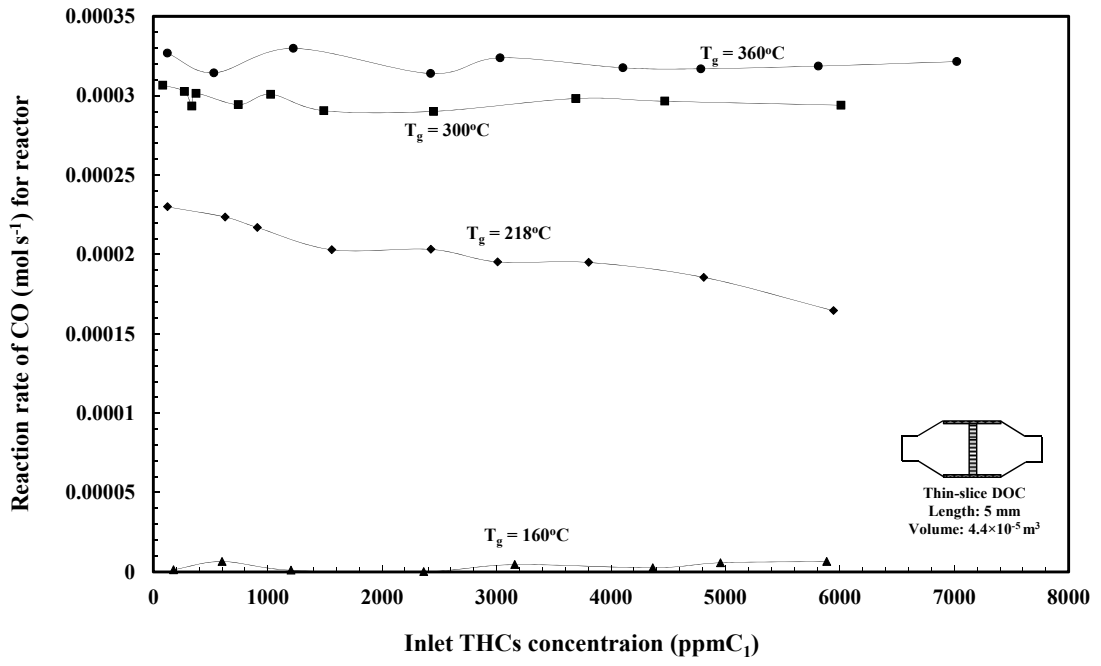


**Figure 3.74** Effect of an increase in the inlet THCs concentration on the rate of CO oxidation.

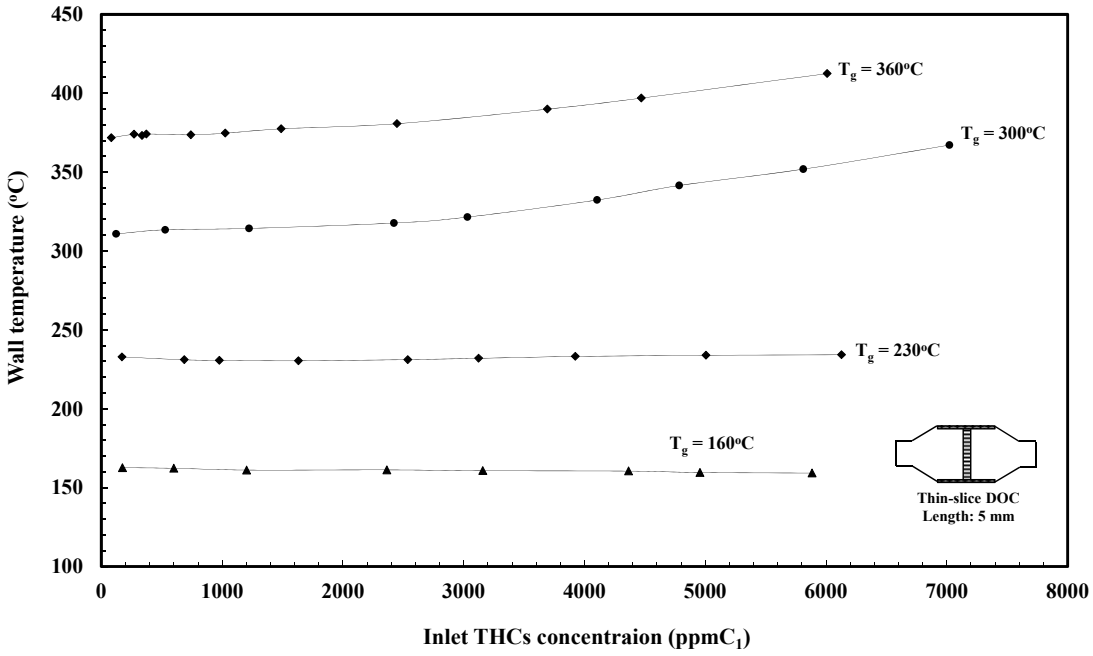


**Figure 3.75** Wall temperature as a function of the inlet THCs concentration.

## 3.6 Gas injection experiments

In this section, a methodology is described, which may help to see the transient response of a DOC to changing inlet conditions. To illustrate the technique, engine trials were performed to investigate the responses of a Full-scale DOC to concentration pulses of CO and THCs. For all of the engine trials, the engine was operated at a constant speed (e.g. 2000 rpm), and engine torque was changed to produce different exhaust gas temperatures. During the test, the EGR valve was kept open to maintain a realistic mode of operation.

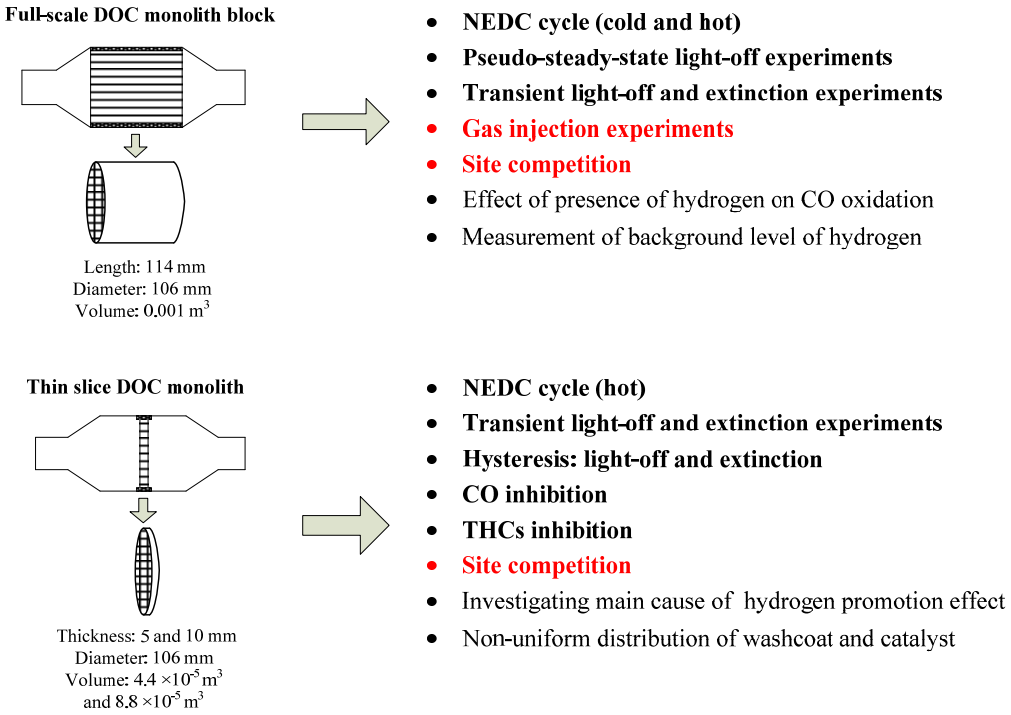


**Figure 3.76** Summary of experiments in Chapter 3. The experiments highlighted in red are discussed in Section 3.6.

### 3.6.1 CO concentration pulse injection

During the CO pulse injection experiments, propane was also added to maintain a background level of THCs at 1500 ppm$C_1$, and to magnify the response of THCs. Prior to the tests the needle valve was adjusted to inject a fixed amount of CO into the exhaust, which gives a final concentration of 3000 ppm after injection. The CO injection lasted 30 s and this created a concentration pulse. The solid wall temperature

was measured with thermocouples. The pre- and post- catalyst emissions were monitored simultaneously by two gas analysers. The experiment was repeated at different inlet gas temperatures. Some of the experiment results are shown in the sections that follow.

As illustrated in Figure 3.77, at an inlet gas temperature of 146$^{o}$C, the DOC has not lit-off. The step change in the inlet and the outlet concentration of CO is captured, and the injection of CO has no effect on the conversion of THCs.

Figure 3.78 displays the thermal response to the injection of CO, and the inlet gas temperature is slightly higher (~3$^{o}$C) than the outlet gas temperature. The catalyst wall temperatures are higher (~1$^{o}$C) than the inlet gas temperature.

At an inlet gas temperature of 180$^{o}$C, about 28.5% of CO conversion was achieved (equivalent to a 400 ppm reduction in CO, see Figure 3.79). Then after CO injection, the conversion does not change. Similarly, the conversion of THCs is not affected by the injection of CO, see Figure 3.79.

Figure 3.80 shows the thermal response to the injection of CO. As can be seen, the wall temperatures have increased, especially the temperature at rear end of the DOC (85 mm from the inlet), which has risen by 3$^{o}$C. However, these changes are still very small.

Figure 3.81 shows the concentration responses of CO and THCs at the inlet and outlet of the DOC, at an inlet gas temperature of 190$^{o}$C, then the conversion of CO is about 90% (equivalent to a 1350 ppm reduction in CO). Then when CO is injected, the conversion of CO reduces to about 75%, but the total amount of CO converted amounts to a reduction of 2300 ppm.

Figure 3.82 shows the gas and wall temperatures. As the CO is injected, the front part of the DOC remains close to the inlet gas temperature, but in the middle and rear parts (40 to 85 mm from the inlet) the wall temperatures have increased by 25 to 30$^{o}$C (due to the release of extra heat from CO oxidation). However, the increase in wall temperature still does not promote the conversion of THCs as the wall temperatures are still too low to initiate significant oxidation of THCs.

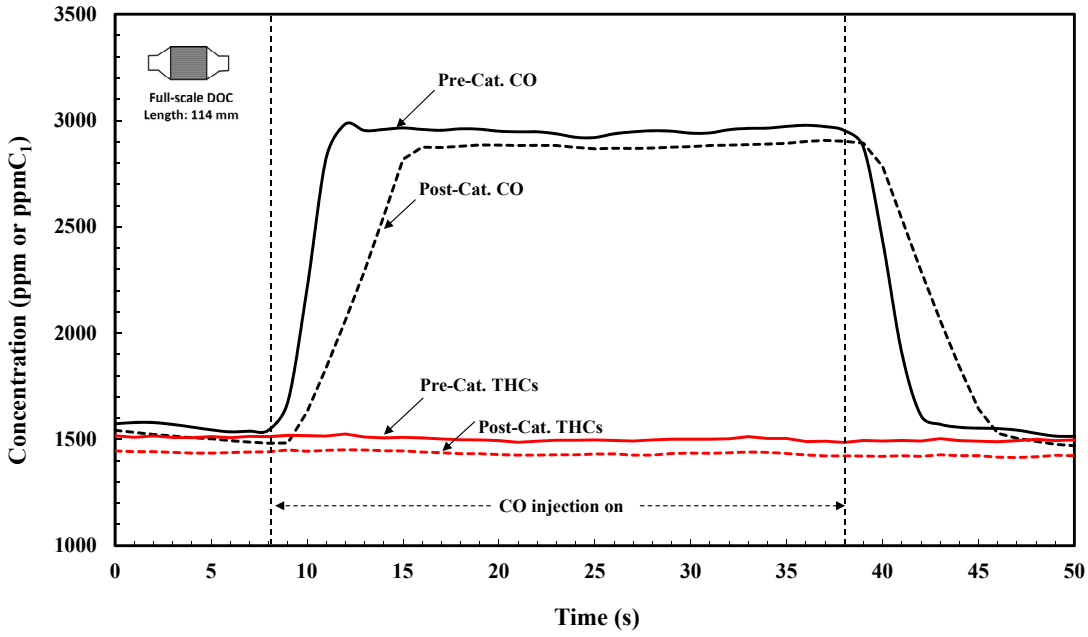


**Figure 3.77** Injection of a concentration pulse of CO at an inlet gas temperature of 150°C. The inlet THCs concentration was maintained at 1500 ppm$C_1$.

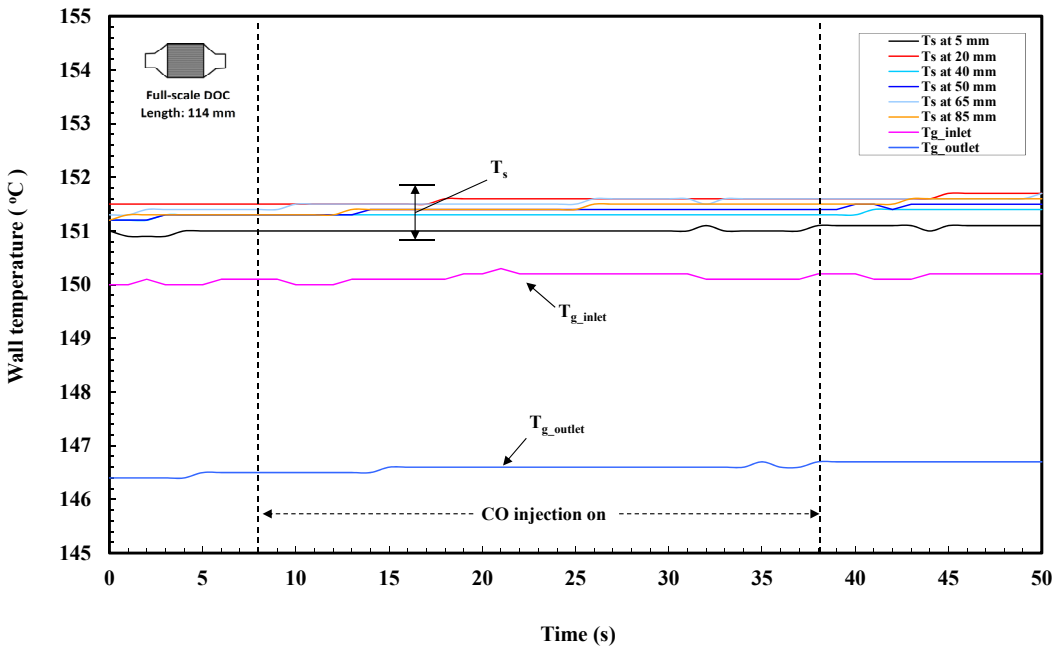


**Figure 3.78** Thermal response to a concentration pulse of CO for conditions in Figure 3.77.

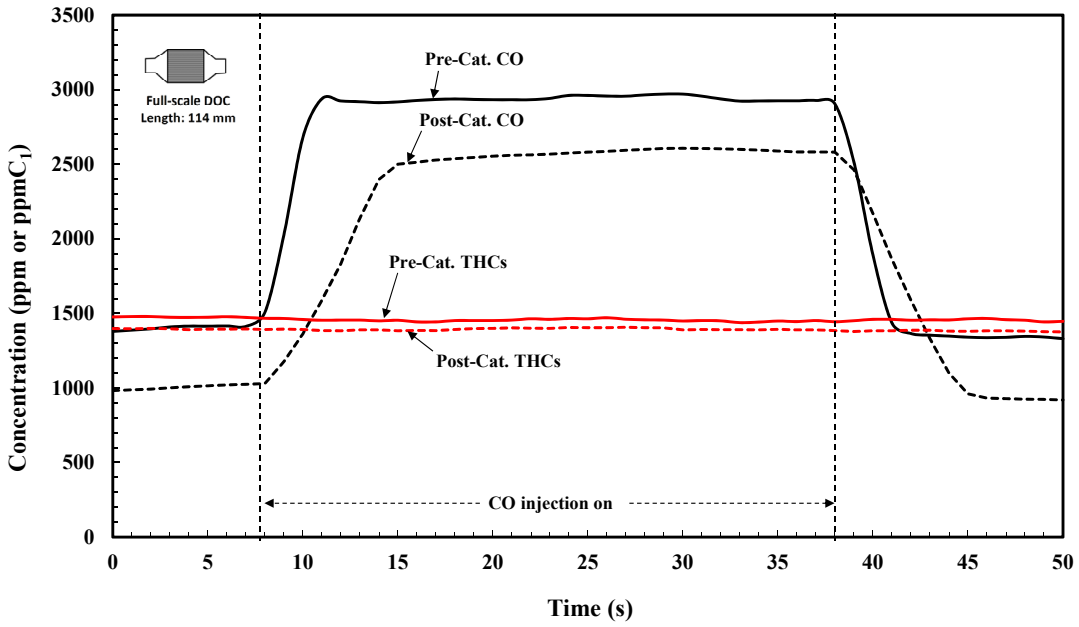


**Figure 3.79** Injection of a CO concentration pulse of CO at an inlet gas temperature of 180°C. The inlet THCs concentration was maintained at 1500 ppm$C_1$.

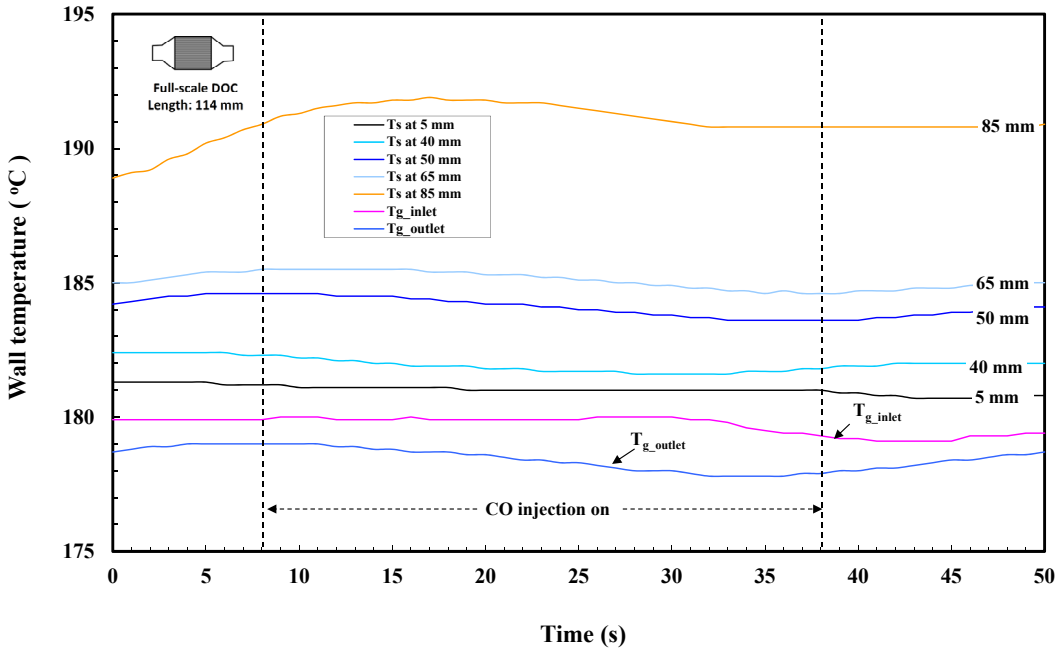


**Figure 3.80** Thermal response to a concentration pulse of CO for conditions in Figure 3.79.

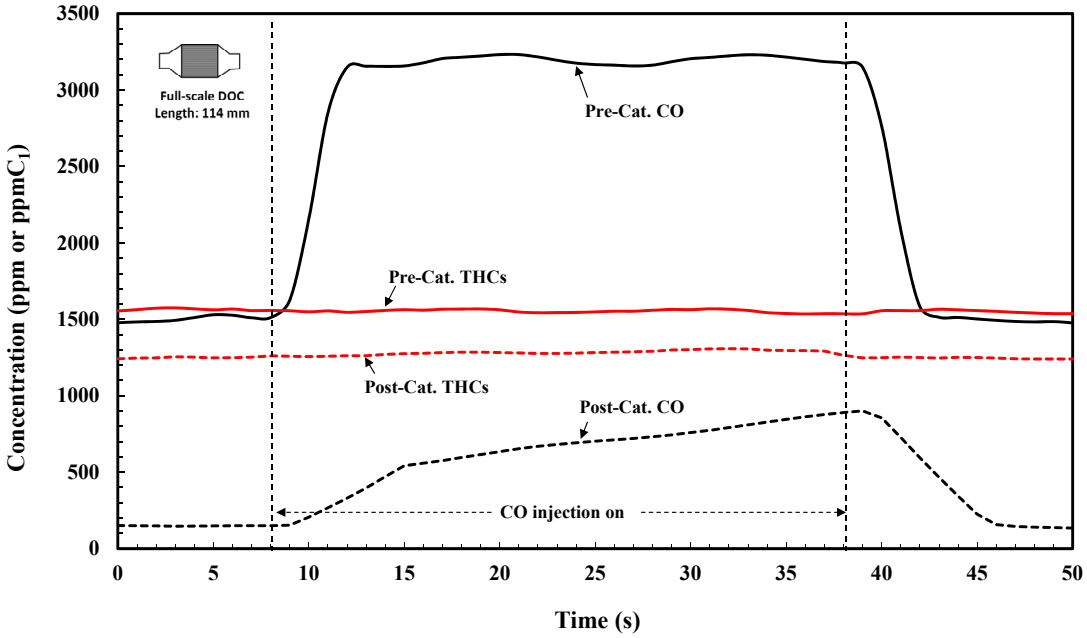


**Figure 3.81** Injection of a concentration pulse of CO as inlet gas temperature of 190°C. The inlet THCs concentration was maintained at 1500 ppm$C_1$.

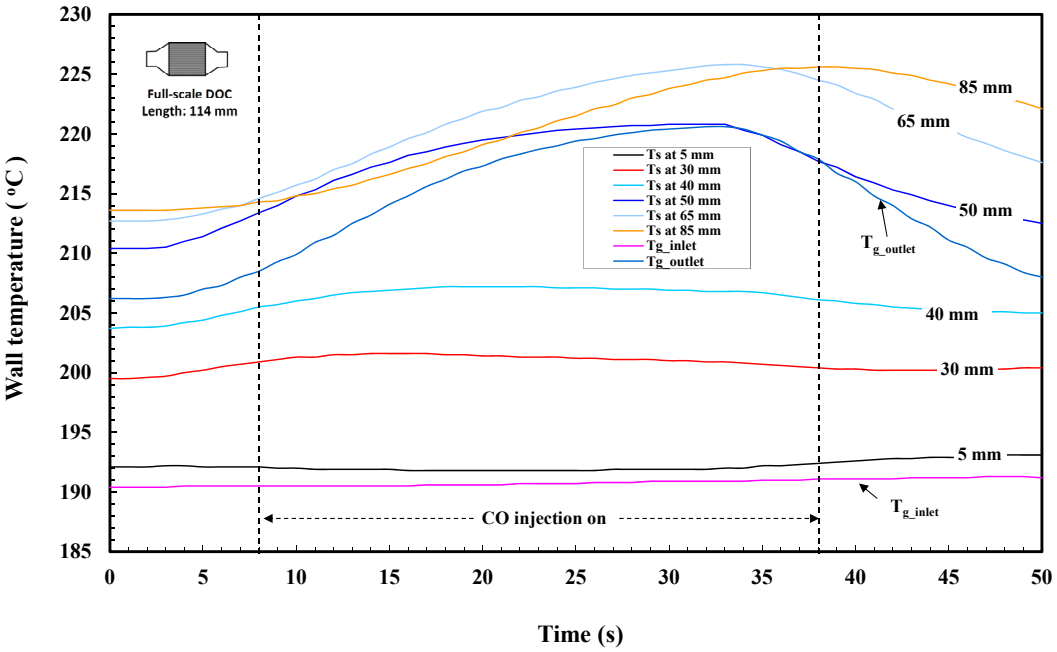


**Figure 3.82** Thermal response to a concentration pulse of CO for conditions in Figure 3.81.

Figure 3.83 shows the concentration responses of CO and THCs. At an inlet gas temperature of 200°C, the conversion of CO is about 100%. Then when CO is injected, 100% conversion of CO is still achieved (a reduction of 3000 ppm).

Figure 3.84 shows the gas and wall temperatures. As the CO is injected, in the very front of the DOC (5 mm and 20 mm from the inlet of the DOC), the wall temperatures remain unaffected (4 and 7°C above the inlet gas temperature). It is interesting to note that the wall temperatures at front of the DOC (30 and 40 mm from the inlet) responds first, and then temperatures rise from the front to the rear of the DOC. This indicates that the reaction starts at the front of the DOC, and then the reaction zone moves towards the back of the DOC. Again, the increase in wall temperature still does not promote the conversion of THCs.

At an inlet gas temperature of 200°C, the wall temperatures across the DOC are above the light-off temperature for CO. Therefore, the additional CO is ignited in the front part of the DOC. It does not contradict observations in the light-off experiments (described earlier Section 3.4.1). In the light-off experiments, the wall temperatures were increased gradually, and during that process, the rear part of the DOC was always the hottest. Therefore, the reactions were always ignited from the rear part of the DOC.

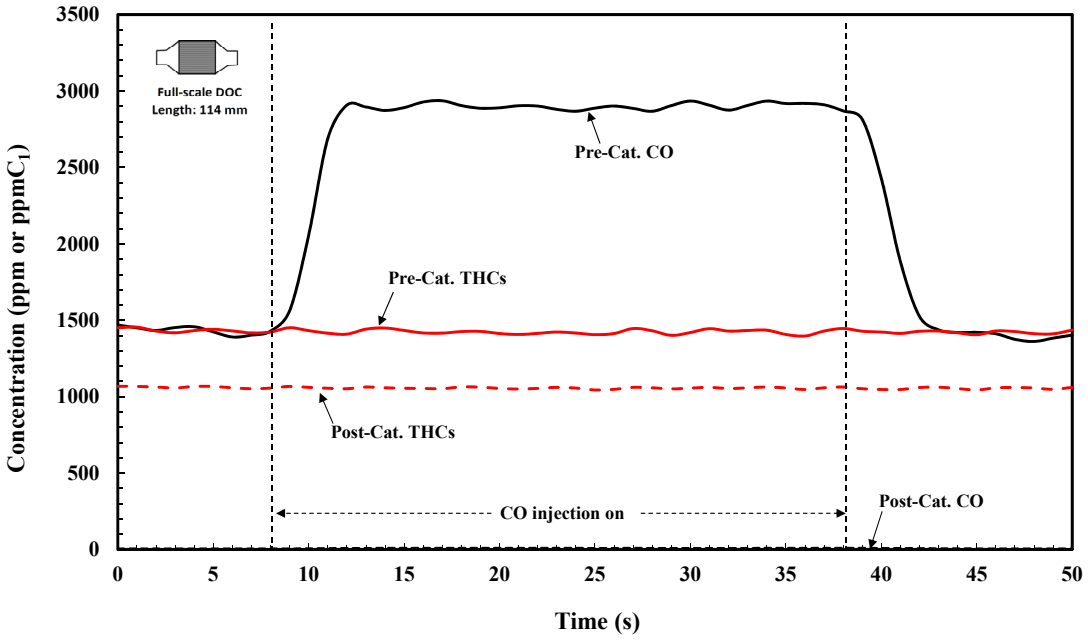


**Figure 3.83** Injection of a concentration pulse of CO as inlet gas temperature of 200°C. The inlet THCs concentration was maintained at 1500 ppm$C_1$.

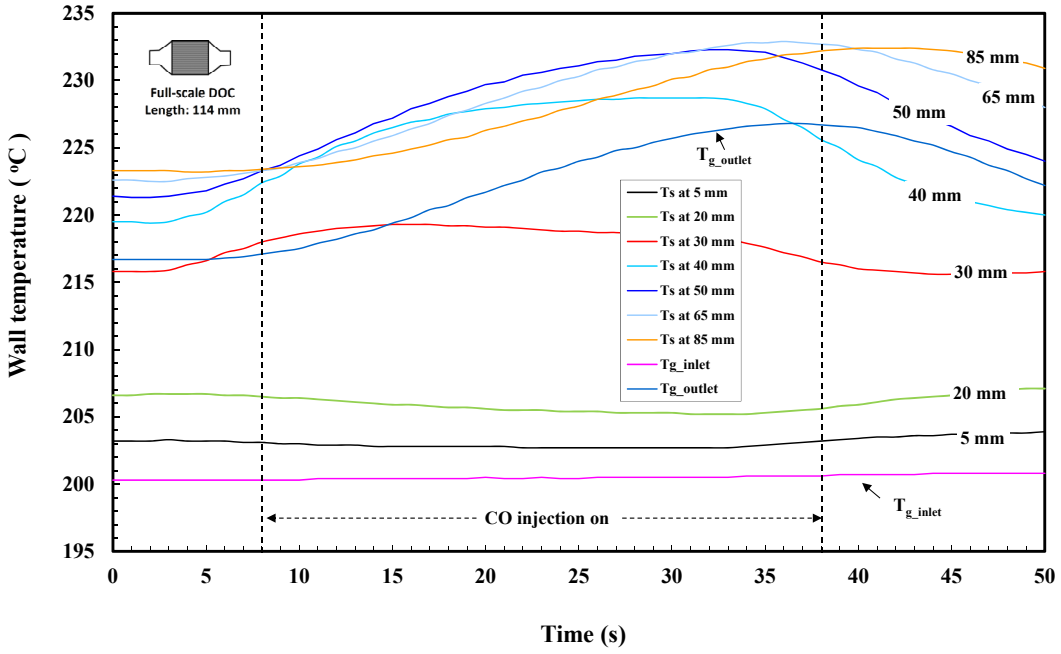


**Figure 3.84** Thermal response to a concentration pulse of CO for conditions in Figure 3.83.

### 3.6.2 Propane concentration pulse injection

In this set of experiments, the engine was operated at a constant speed of 2000 rpm, and engine torque was varied to produce the desired inlet gas temperature to the DOC. Here, propane was used to represent the THCs, and a Full-scale DOC was used. The background CO concentration was kept at 3000 ppm (by the addition of CO), and propane was injected as a pulse with a peak concentration of THCs = 3000 ppm$C_1$. Some of the experimental results are shown in the sections that follow.

As illustrated in Figure 3.85, when the inlet gas temperature is 146$^o$C, a clear concentration pulse of THCs can be observed at the inlet and outlet of the DOC. The conversions of THCs and CO are low since the temperature is below the light-off.

Figure 3.86 shows the thermal response to the injection of propane, and the temperatures remain stable. The gas temperature is slightly higher at the inlet compared with the gas outlet of the DOC.

As illustrated in Figure 3.87, when the inlet gas temperature is 189$^o$C, the conversion of CO is high approximately 64 %. At this temperature the conversion of THCs is low (9.5%), and when propane is injected, the amount of converted THCs remains about the same.

Figure 3.88 shows the thermal response to the injection of propane. It is interesting to observe, that despite the addition of propane, the reduction in the ppm of THCs has not changed much, and the wall temperatures have only increased very slightly. This provides a clear indication that for propane, temperatures are below the light-off for propane. However, other hydrocarbon species (background levels from engine) are clearly reacting.

When the inlet gas temperature was increased to 320$^o$C, then from Figure 3.89 it can be seen, that CO is fully converted and THCs conversion is more significant. The amount of THCs converted increases from 300 (before propane injection) to 2300 ppm$C_1$ (during propane injection). Therefore it is not surprising to see in Figure 3.90 that after the addition of propane heat is released and the wall temperatures increase, and the gas outlet temperature increases. It is also interesting to note that the wall temperature at the front of the DOC responds first, and then temperatures rise from front to the rear of the DOC. This indicates that the reaction starts at the front of the DOC, and then the reaction zone moves towards the back of the DOC. This is

consistent with an earlier observation in the CO injection experiment with an inlet gas temperature of 200°C.

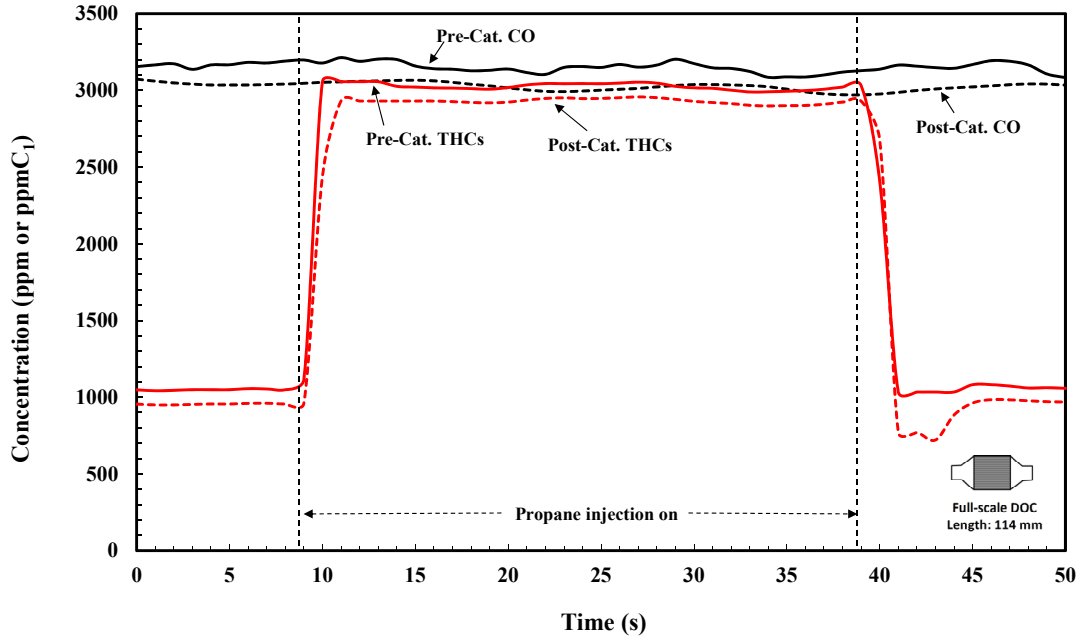


**Figure 3.85** Injection of a concentration pulse of THCs at an inlet gas temperature of 146 °C. The inlet CO concentration was maintained at 3000 ppm.

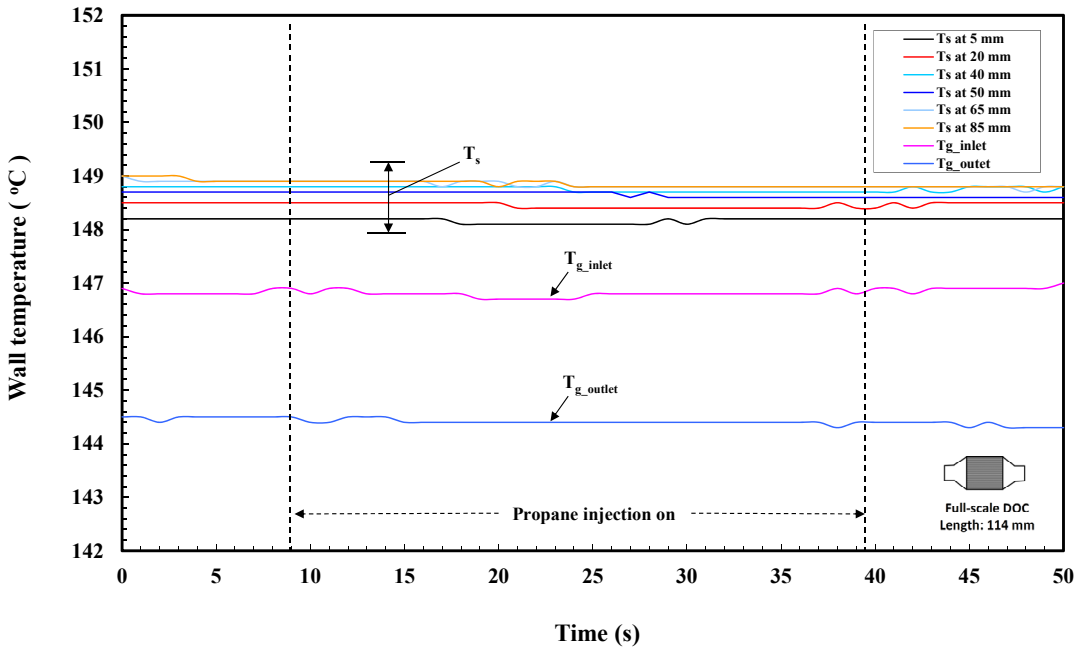


**Figure 3.86** Thermal responses to a concentration pulse of THCs for conditions in Figure 3.85.

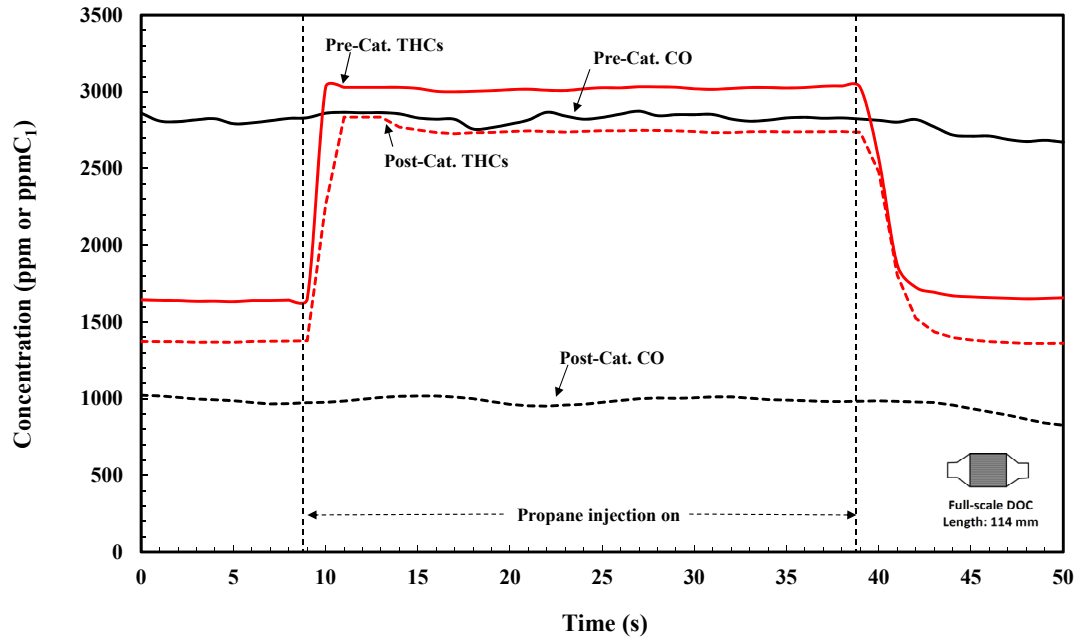


**Figure 3.87** Injection of a concentration pulse of THCs at an inlet gas temperature of 189°C. The inlet CO concentration was maintained at 3000 ppm.

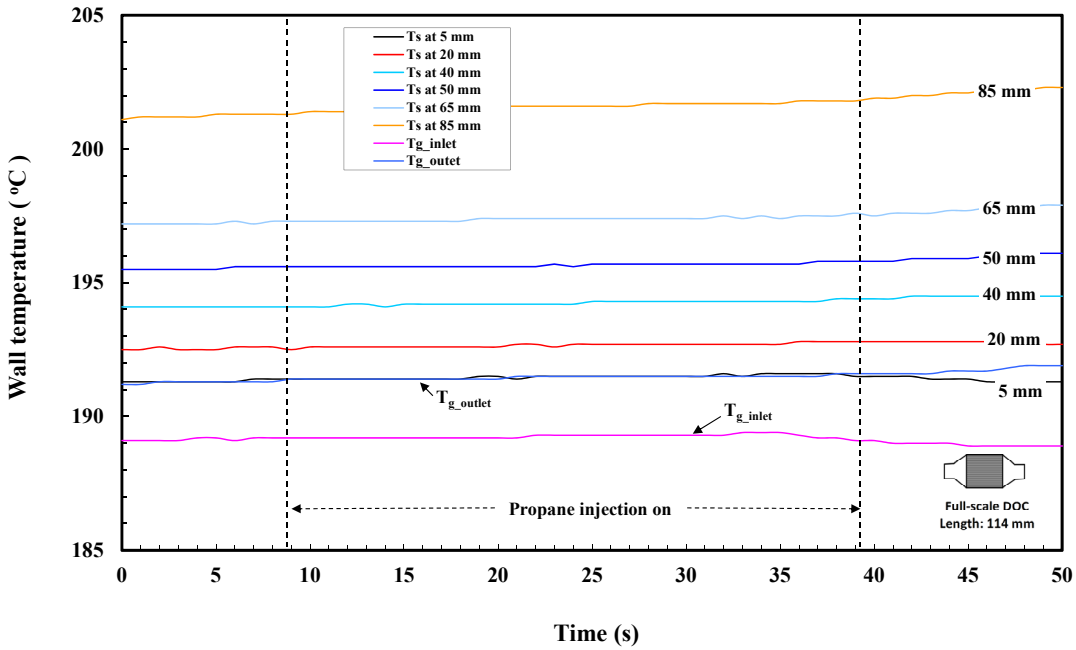


**Figure 3.88** Thermal responses to a concentration pulse of THCs for conditions in Figure 3.87.

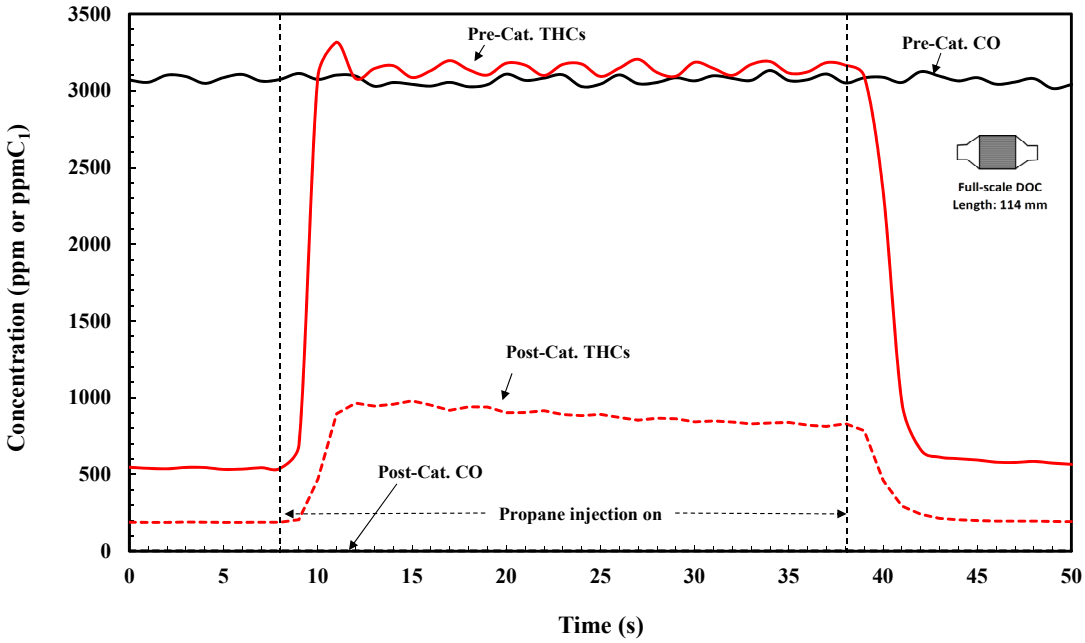


**Figure 3.89** Injection of a concentration pulse of THCs at an inlet gas temperature of 320°C. The inlet CO concentration was maintained at 3000 ppm.

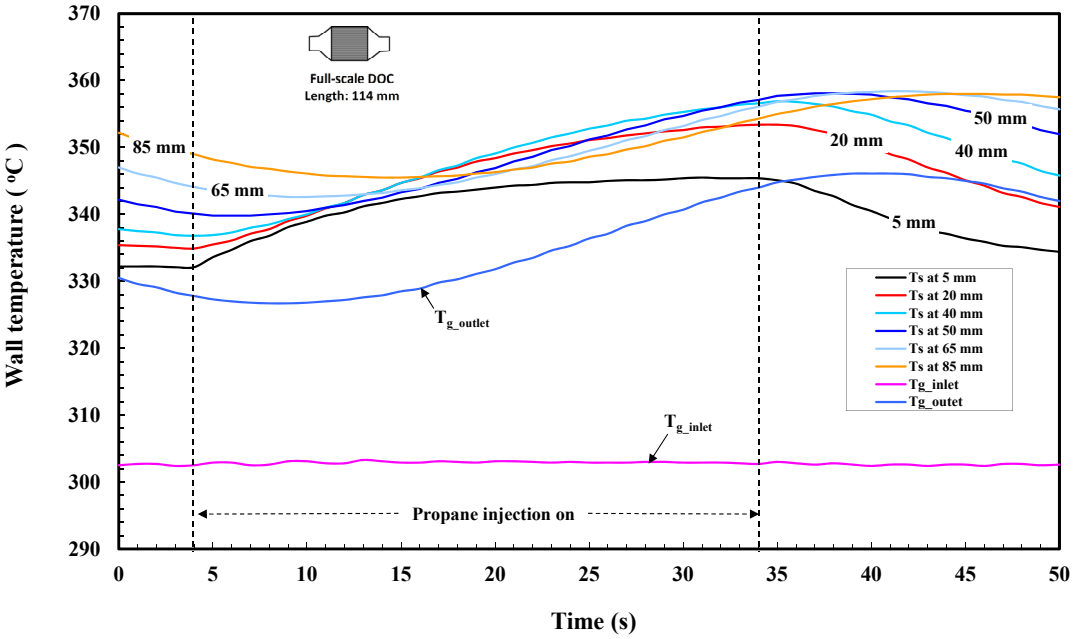


**Figure 3.90** Thermal responses to a concentration pulse of THCs for conditions in Figure 3.89.

In general, the gas injection experiments provide a good opportunity to observe the transient response (temperature and concentration) of the DOC to a change in inlet concentration of different pollutants. The results will also be of great use to validate DOC models and to see how well they can capture the observed transient response. This gas injection technique can also be used to investigate the interactions between different species, e.g. competition for available active sites.

### 3.6.3 Site competition

In very early and preliminary work by Hammond (2004) at the University of Bath, the CO injection experiment was performed to determine the light-off point (i.e. temperature) of a Full-scale Degussa DOC connected to a live engine. To perform the trials, the engine was operated at 1500 rpm with EGR closed, and the torque was varied from 20 to 100 Nm at 5 Nm increments to produce different inlet gas temperatures. CO at 1 vol% (10,000 ppm) was injected in the inlet of the DOC and the response from the outlet was monitored.

From the experimental results, when the inlet gas temperature was approximately 270$^{o}$C, competition between CO and THCs appeared to be observed, as the outlet THCs level increased as the pulse of CO was injected, see Figure 3.91. Hammond explained that: "*A brief look at total hydrocarbon levels in the exhaust gas stream pre and post-catalyst showed a marked increase in total hydrocarbon concentration (post-catalyst) during periods of CO injection. (CO injection was a square pulse of CO increasing concentration from 200 ppm to 10000 ppm pre-catalyst). It would appear that the facilitation of Carbon Monoxide combustion in the catalyst is detrimental to the limited amount of Hydrocarbon reduction already taking place*".

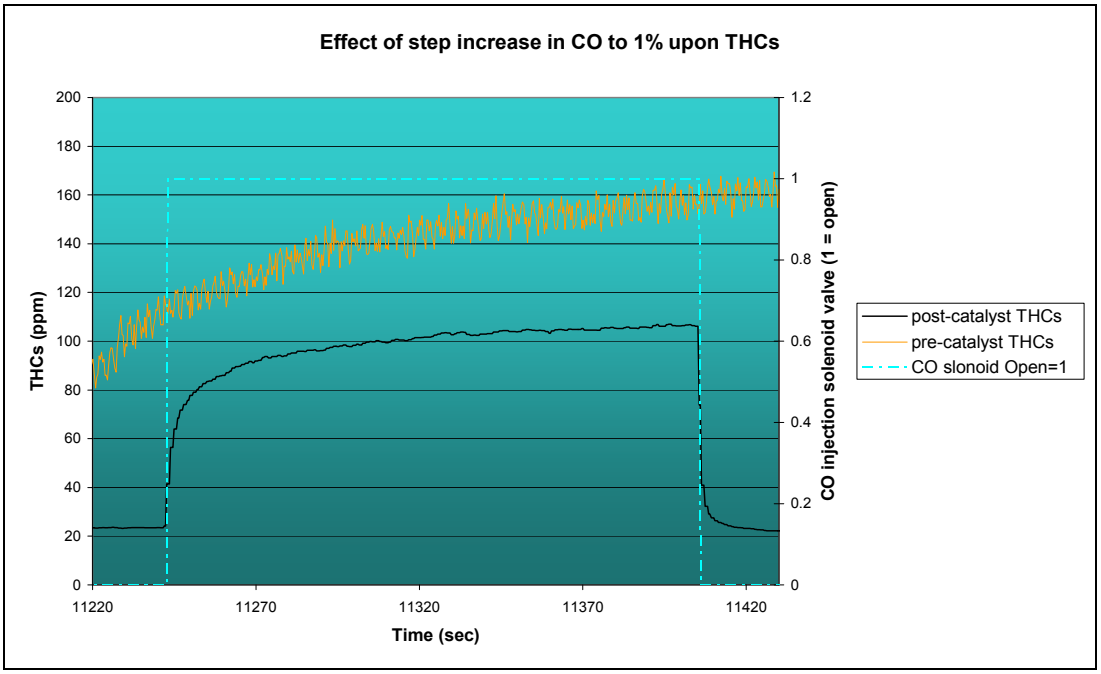


**Figure 3.91** Effect of CO injection upon THCs conversion (Copied from Hammond, 2004).

In a proposed (Salomons *et al*., 2006) mechanistic reaction scheme for CO oxidation over Pt sites, the CO must first attach itself to an active site and then it can react with an attached oxygen to form $CO_2$. Similarly, a hydrocarbon has to do the same. If the number of active sites is limited, then there would be competition for the active sites between CO and THCs. Before the injection of 1% CO, relative rates of the oxidation reactions of CO and THCs must be at an equilibrium. As a Full-scale DOC was used, there are many catalytic sites for CO and THCs, especially as the background level of CO and THCs was low (CO concentration is 200 ppm, THCs concentration is 100 ppm$C_1$). When 1vol% of CO was injected, the number of free active sites may become insufficient to sustain these two reactions. Since CO has a lower activation energy for its attachment to an active site, this means that CO adsorbs on an active site easier than THCs. Therefore, there would be less active site left for the THCs to attach, so the outlet concentration of THCs would increase. However, in the experiments in this thesis, no sign of site competition has been observed. Therefore, a series of tests were carried out, at conditions where the "site competition" phenomena – was considered possible.

In the first test (Test 1) Hammond's experiment was repeated at similar operating conditions. The inlet concentration of THCs was higher (580 ppm$C_1$ rather than 100 ppm$C_1$ in Hammond, 2004), but this should not stop the possibility of seeing competition. To repeat the experiment, the engine was run at 2000 rpm and 45 Nm torque. At this engine operating condition, the exhaust gas temperature was approximately 270$^o$C, at which the CO is fully converted and the conversion of THCs is around 50%. When the system reached steady-state, a pulse of 1 vol% CO was injected. The transient responses are plotted in Figure 3.92. No sign of competition is observed, and the concentration of THCs at the outlet remains unchanged. On the other hand, this test also proves that, the Full-scale DOC is able (at $T_g$ = 270$^o$C) to convert completely 1 vol% CO and is above light-off temperature.

In order to increase the possibility of seeing any competition between CO and THCs, the background level of THCs was increased to 3500 ppmC1 (Test 2). Other conditions remained the same as Test 1. The results are plotted in Figure 3.93. Again, this is no sign of site competition. On the contrary, the conversion of THCs appears to be promoted by the injection of CO. Oxidation of CO will produce extra heat which raises the wall temperatures and hence oxidation rates of THCs.

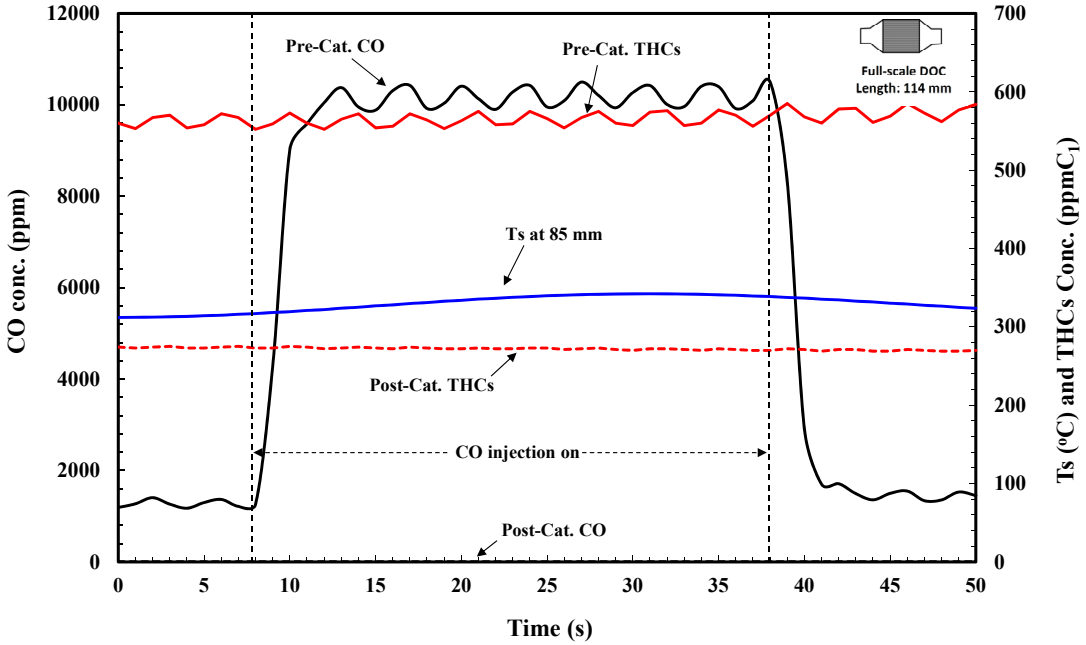


**Figure 3.92** Pre- and post-catalyst concentrations of CO and THCs when a pulse of 1% CO is injected with an inlet gas temperature of 270°C. The inlet THCs concentration was about 580 ppm$C_1$.

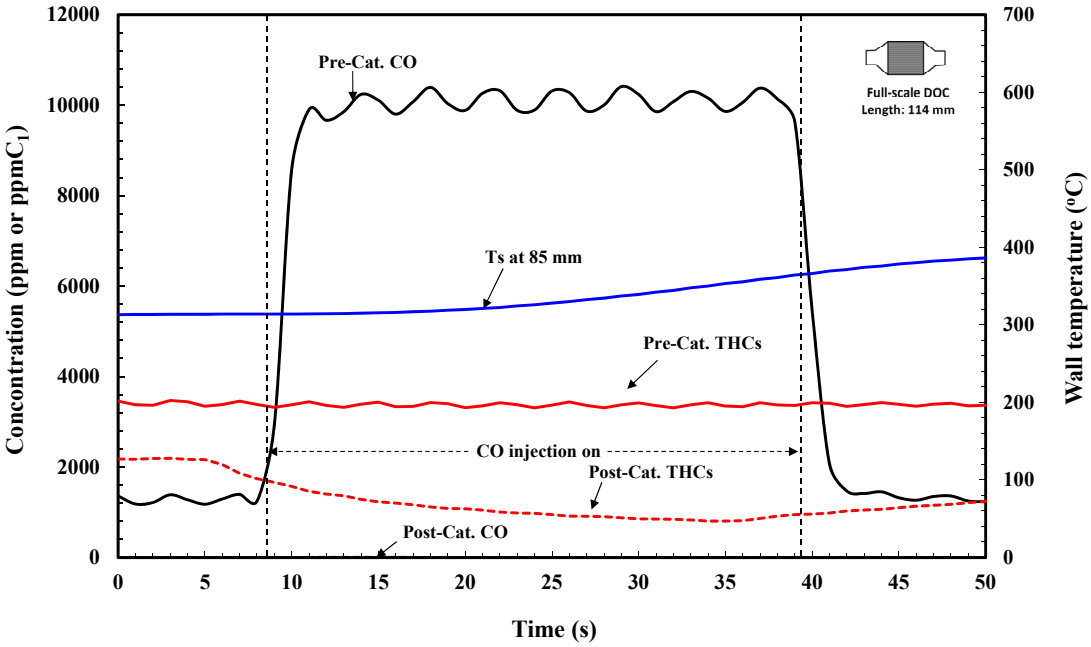


**Figure 3.93** Pre- and post-catalyst concentrations of CO and THCs throughout 1% CO injection when inlet gas temperature is 270°C. The inlet THCs concentration was maintained at about 3500 ppm$C_1$.

From the results of Tests 1 and 2, there does not appear to be any site competition between CO and THCs. This may be due to two possible reasons. Firstly, the Full-scale DOC has plenty of active sites for CO and THCs. Secondly, as CO was fully converted (in the two tests) this may leave plenty of active sites for THCs (i.e. the turnover rate of CO is high). Therefore, a 5 mm Thin-slice DOC was used to reduce the amount of active sites, which may force the CO to compete with THCs for active sites.

This Test 3 was performed following the same procedure as Tests 1 and 2 but at different inlet gas temperatures (i.e.153 to 290$^{o}$C). A pulse of CO was injected to achieve a peak concentration of 0.3 vol% (3000 ppm) instead of 1vol%. The background level of THCs was increased to a level of 1500 ppm$C_1$, by the addition of propane. Some of the experimental results are shown in the figures, and the rest of the results are presented in Appendix 7.2.

Figure 3.94 shows the results obtained with a low inlet gas temperature test of 153$^{o}$C. Figure 3.95 shows the results obtained from higher inlet gas temperature (at 277$^{o}$C), and the following observations can be made.

When the inlet gas temperature is 153$^{o}$C, the conversion of THCs is very low, and CO conversion is about 50%. Following the injection of the CO pulse, more CO (200 ppm) is converted which leads to an increase of about 1$^{o}$C in the wall (or catalyst) temperature. No increase in the outlet concentration of THCs is observed.

When the inlet gas temperature is increased to 277$^{o}$C, the CO conversion is about 40% (equivalent to 450 ppm of CO is converted); and THCs are reduced by about 100 ppm$C_1$. Following the injection of the CO pulse, conversion of CO increases to 50% (equivalent to 1500 ppm of CO is converted) and this leads to a significant increase of about 10$^{o}$C in the wall temperature. However, there is no increase in the outlet concentration of THCs.

The experiment was also repeated, but this time a 5000 ppm pulse of CO was used. The background concentration of THCs was maintained at 1500 ppm$C_1$. Once again, there was no evidence of site competition between CO and THCs for the active sites.

In summary, from this series of tests there was no evidence of site competition between CO and THCs (over the range of condition tested). So the reason for why it was observed by Hammond remains a mystery. The answer may lie in the way in which Hammond performed the preliminary experiments. For example, steady-state

conditions may have not been achieved at the start and/or the DOC may have not been purged clean prior to that trial.

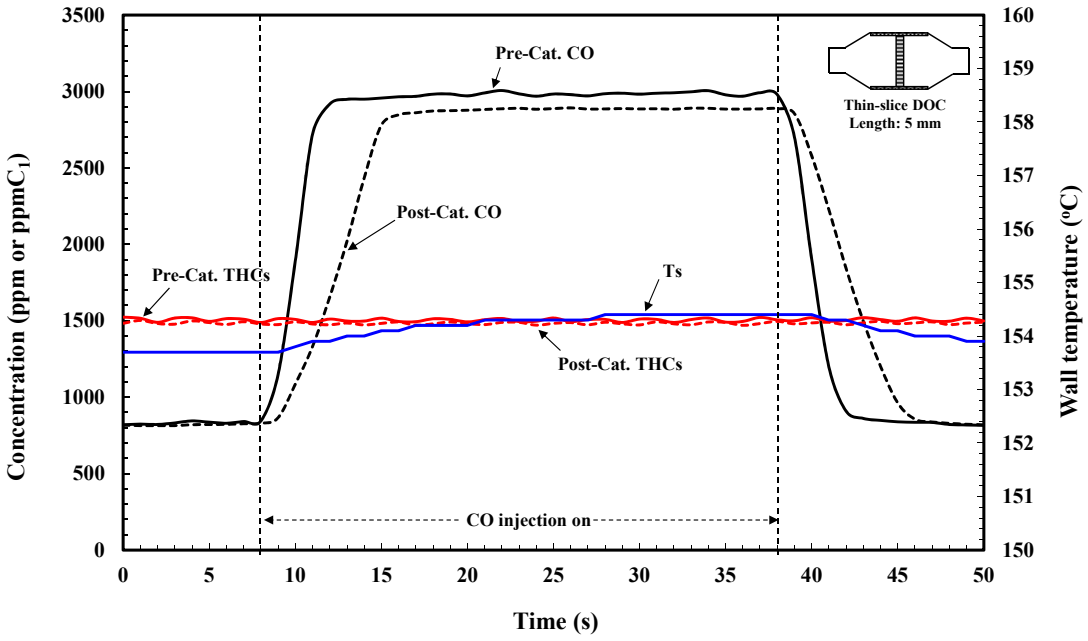


**Figure 3.94** Concentrations of CO and THCs at the inlet and outlet of the Thin-slice DOC during CO injection. The inlet gas temperature was 153°C. The wall (or catalyst) temperature is also plotted as a function of time.

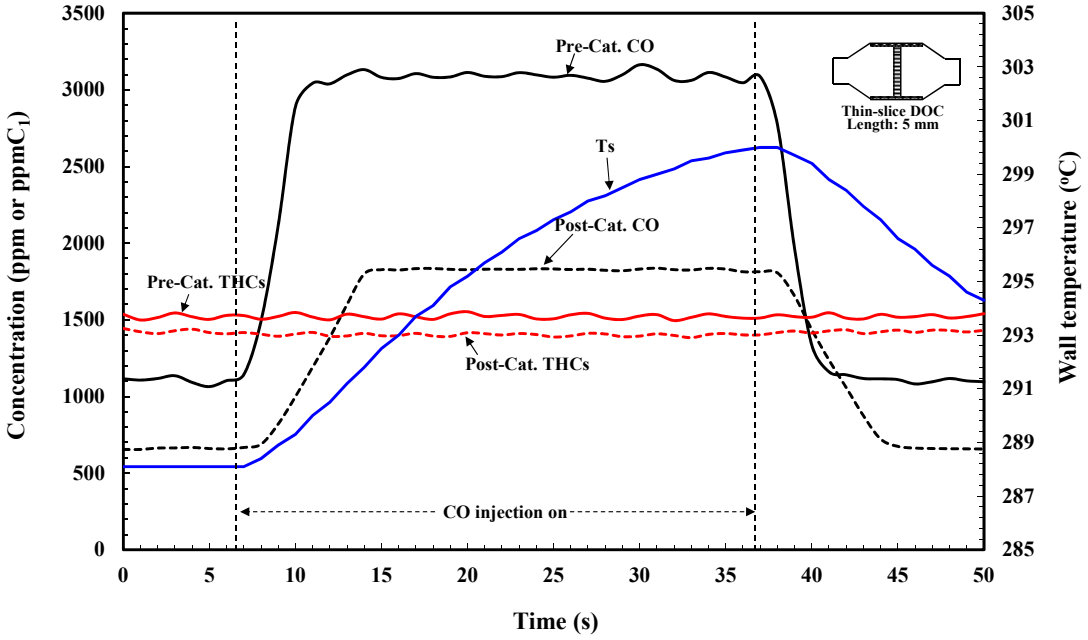


**Figure 3.95** Concentrations of CO and THCs at the inlet and outlet of the Thin-slice DOC during CO injection. The inlet gas temperature was 277°C. The wall (or catalyst) temperature is also plotted as a function of time.

## 3.7 Hydrogen and CO oxidation

The effect of hydrogen on the oxidation of CO over $Pt/Al_2O_3$ catalysts has been studied extensively in the literature, and its presence has been found to promote the oxidation of CO. However, these types of experiments do not appear to have been performed on a Full-scale DOC under real engine operating conditions. In this section, a methodology is described to perform such trials using a Full-scale DOC (and a Thin-slice DOC) connected to a real diesel engine. The possibility of site competition between hydrogen and other species is also examined.

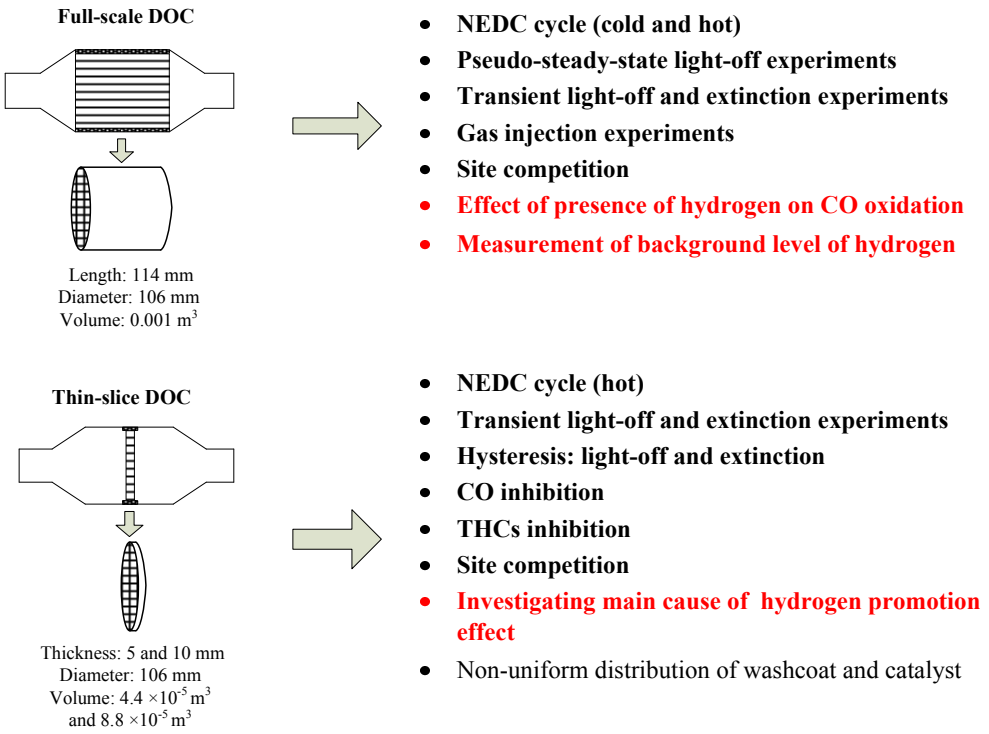


**Figure 3.96** Summary of experiments in Chapter 3. The experiments highlighted in red are discussed in Section 3.7.

### 3.7.1 Promotion effect of hydrogen on CO oxidation using Full-scale DOC

These experiments follow the same procedures as the transient light-off and extinction experiments in Section 3.5. The engine was operated at a constant speed of 2000 rpm and a torque of 5 Nm until steady-state was reached. Then CO was added to maintain a background concentration around 3000 ppm, and propane was also added to maintain a THCs concentration around 1500 ppm$C_1$. Hydrogen was then injected at a flow of 0.3 litre minute$^{-1}$ (equivalent to 375 ppm at an exhaust gas flow of 60 kg h$^{-1}$). Due to a lack of instrumentation for the measurement of hydrogen concentration, a rotameter was calibrated using a bubble flow meter in order to monitor the addition of hydrogen. Knowing the flow rate of the exhaust gas, the readings from the rotameter can then be converted into a concentration (in ppm). A sample calculation is provided in Appendix 1.6. In the calculation, the inlet gas temperature was assumed to be 10$^{o}$C.

When the system reached steady-state again (after the addition of gases), the engine torque was programmed to ramp up from 5 to 47 Nm in 90 s. As the engine torque increased, the exhaust gas temperature would increase from 145 to 280$^{o}$C, but at a slower rate than the torque ramp-up. When the inlet gas temperature reached 280$^{o}$C, the whole system was kept for 5 minutes to reach steady-state; and then the engine torque was ramped-down to 5 Nm in 90 s, in turn the inlet gas temperature dropped back to 145$^{o}$C. All of this experimental data was recorded automatically by CADET 14.

Then, the same experiment was repeated with a higher flow of hydrogen at 0.9 litre minute$^{-1}$ (equivalent to 1125 ppm at an exhaust gas flow of at 60 kg h$^{-1}$). The results of these experiments are plotted in Figures 3.95 to 3.97, from which the following observations are made:

(a) The addition of hydrogen does not change the trends in the shape of the light-off and extinction curves, and hysteresis can be observed.

(b) As expected, the addition of hydrogen promotes the conversion of CO (earlier light-off).

These observations are consistent with the observations from the results obtained from the bench-top CO light-off experiment with addition of hydrogen in Salomons *et al*. (2006). The presence of hydrogen is also observed to delay the extinction phase.

These results are also presented in Figure 3.98 in terms of the overall rate of CO oxidation.

In the literature (e.g. Sun *et al*., 2003; Salomons *et al.*, 2006), two possible causes of this promotion effect have been mentioned: a) hydrogen coverage promotes the desorption of CO and, b) the additional exotherm provided by hydrogen oxidation promotes the oxidation of CO. Some researchers (e.g.Salomons *et al.*, 2006) believe that the promotion effect is mostly attributed to the first reason, and a number of mechanistic reaction schemes have been proposed.

By looking at the axial wall temperature profiles in Figure 3.99, it is clear that hydrogen oxidation increases significantly the wall (or catalyst) temperatures. However, the wall temperature profile inside the Full-scale DOC is complex, so it was decided to repeat these experiments in a Thin-slice DOC.

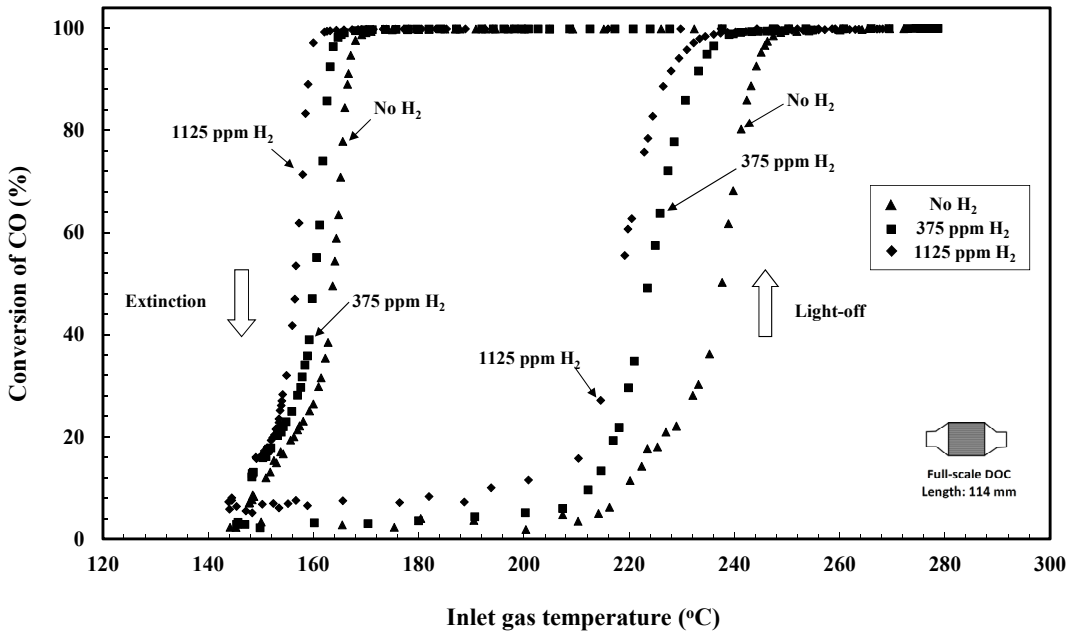


**Figure 3.97** Effect of hydrogen on the oxidation of CO in light-off and extinction phases.

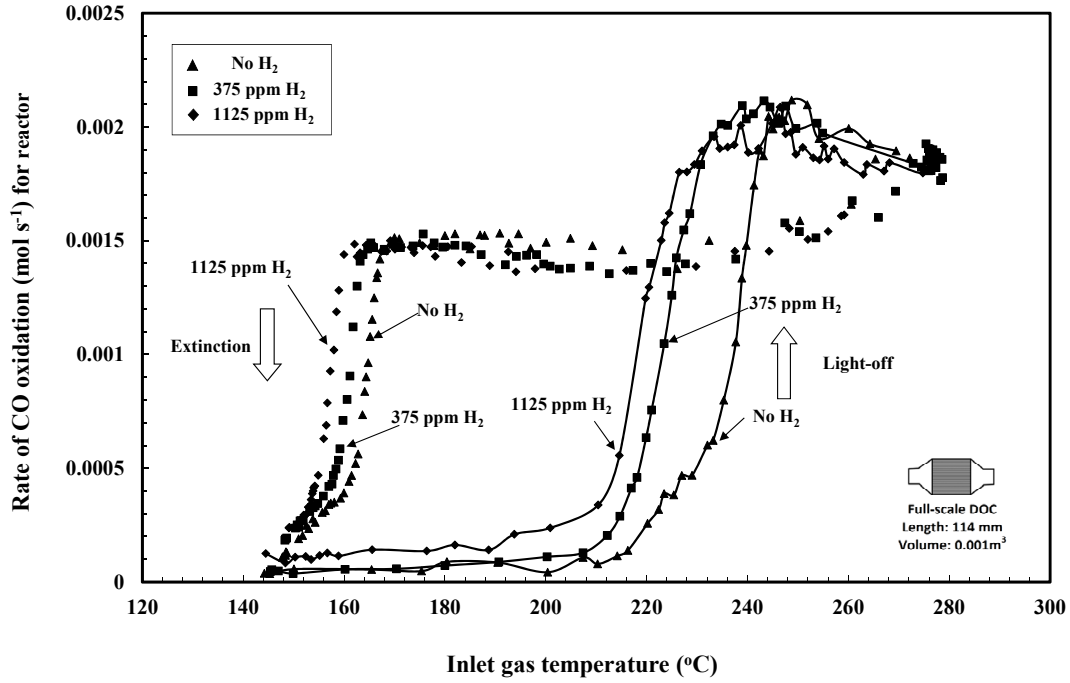


**Figure 3.98** Effect of hydrogen on the overall rate of CO oxidation in light-off and extinction phases.

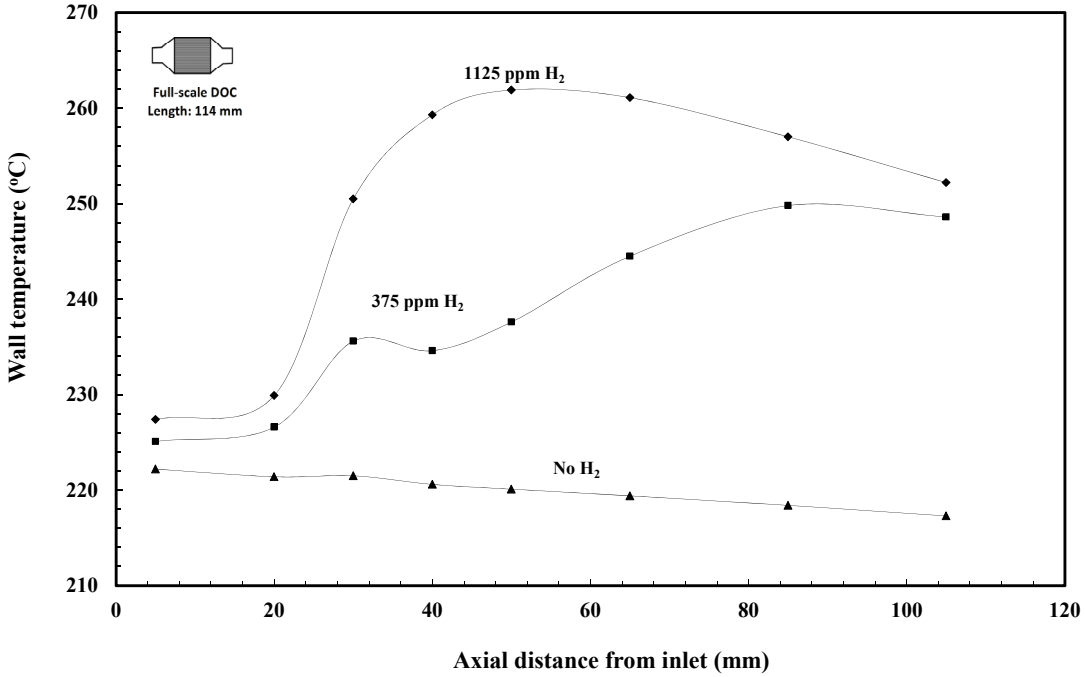


**Figure 3.99** Axial wall temperature profiles with different amounts of hydrogen, when the inlet gas temperature is 223$^o$C.

### 3.7.2 Promotion effect of hydrogen on CO oxidation using Thin-slice DOC

A 5mm Thin-slice DOC was used, and an extra test was done with 763 ppm of hydrogen. This series of tests was performed twice on different days, and good repeatability from the test results was observed. The experiment results on 01/06/2010 are shown in Figure 3.100.

As a thin-slice DOC is used, the conversion of CO is lower than in the Full-scale DOC (since the size of thin-slice DOC is only about 4.5% the length of the Full-scale DOC). The promotion effect of hydrogen on the oxidation of CO is clearly evident. The first 375 ppm of hydrogen lowers the light-off temperature by 3$^{o}$C; the 763 ppm of hydrogen lowers the light-off temperature by 8$^{o}$C, and the 1125 ppm of hydrogen lowers the light-off temperature by 10.5$^{o}$C. The presence of hydrogen also delays the extinction process.

The thin-slice DOC has a thickness of 5 mm, so that the axial wall temperature gradient can be neglected. The radial wall temperature profile was monitored with three thermocouples, and the results suggest the temperature gradient from the centre of the slice to the outer wall is less than 3$^{o}$C. Therefore, the radial temperature profile is averaged, and it is a good representation of the wall temperature.

If the promotion effect of CO was mainly due to a mechanistic influence from the presence of hydrogen, then the promotion effect would still be clearly seen in a plot of conversion against wall temperature. This plot is shown in Figure 3.101, and it is clear that, the promotion effect of hydrogen is not evident. The light-off temperature (in terms of wall temperature) is not affected by the presence of hydrogen. Therefore, it can be concluded that the promotion effect of hydrogen on the oxidation of CO is largely attributed to the extra exotherm from the oxidation of hydrogen.

However, from the early phase in the light-off curves in Figure 3.100, the oxidation of CO starts slightly earlier than in the test without extra hydrogen. This may be a sign of a small mechanistic influence from hydrogen (i.e. the surface converge of hydrogen lowers the activation energy of CO desorption). The rate of CO oxidation is also calculated and plotted against the wall temperature in Figure 3.102.

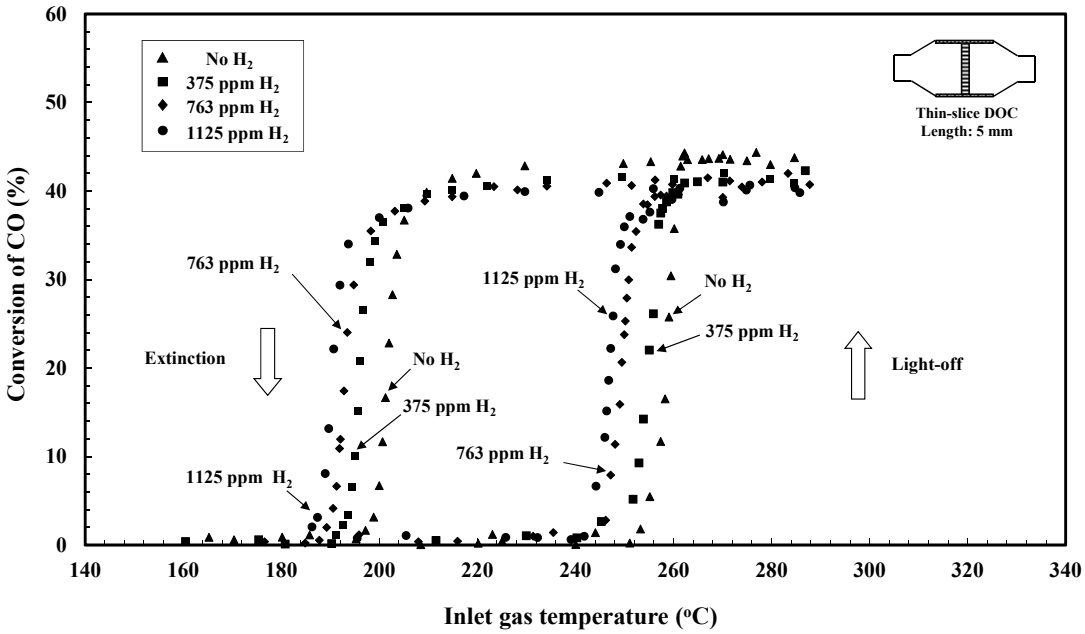


**Figure 3.100** Effect of hydrogen on the oxidation of CO in light-off and extinction phases.

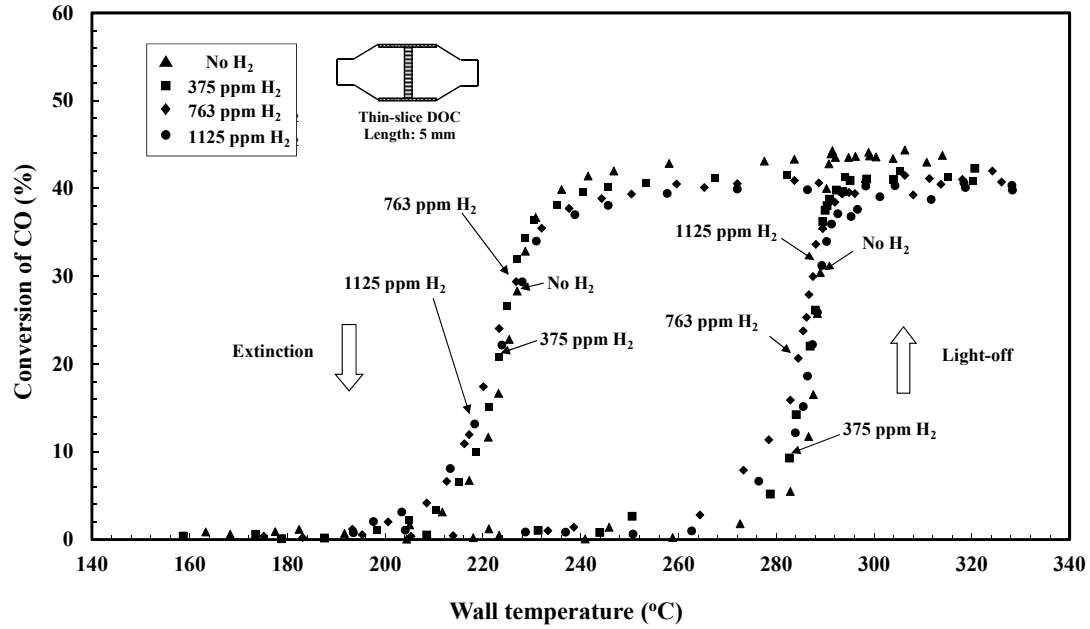


**Figure 3.101** Wall temperature and its effect on the oxidation of CO in the presence of hydrogen.

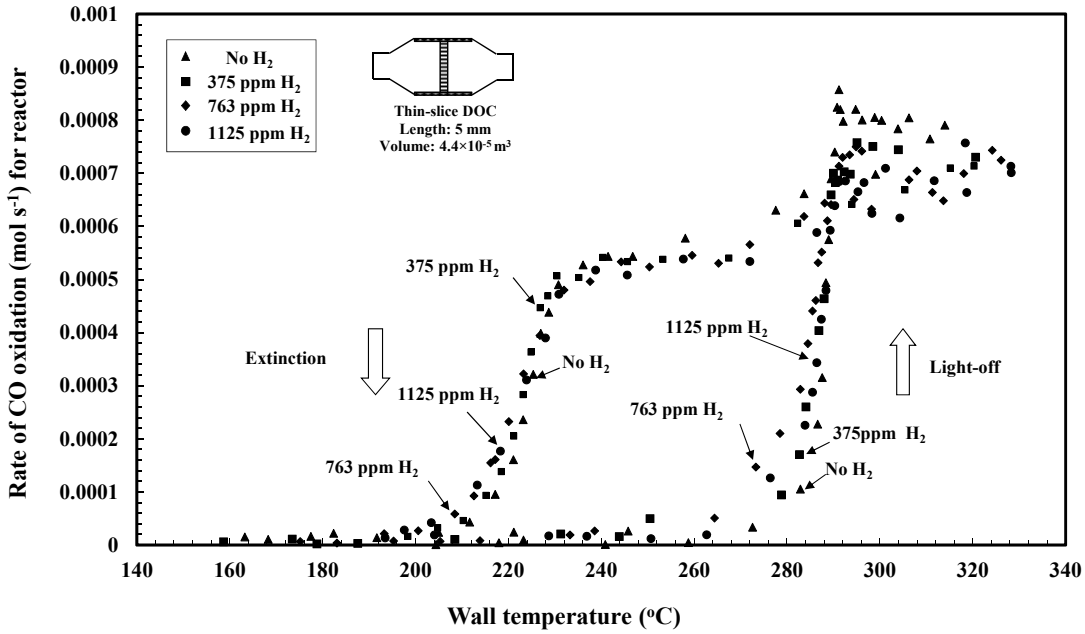


**Figure 3.102** Wall temperature and its effect on the rate of CO oxidation in the presence of hydrogen.

### 3.7.3 Site competition

To investigate for the presence of any site competition, the technique described in Section 3.6 was applied. A quantity of hydrogen was injected at two different gas inlet temperatures (170 and 232$^{o}$C). A concentration pulse of 1125 ppm of hydrogen was injected, while, the background concentration of CO and THCs was maintained at 3000 ppm and 1500 ppm$C_1$, respectively. These results are shown in Figures 3.101 and 3.102, from which the following observations can be made.

At an inlet gas temperature of 170$^{o}$C, the DOC is not active, and the conversion of CO and THCs are both low. The wall temperature remains relatively steady during the injection of hydrogen, which also indicates the conversion of hydrogen is also very low at this temperature. This provides a good base-case study.

Next, at an inlet gas temperature of 232oC, the DOC is clearly active for CO and hydrogen (see Figure 3.104). However, the conversion of THCs still remains low (approx. 6%). A clear rise in the wall temperature (approx. 6$^{o}$C) is observed and this must have arisen from the oxidation of the injected hydrogen. However, this slightly higher wall temperature does not promote the conversions of CO and THCs. Again, the outlet concentrations of CO and THCs remain unchanged during the hydrogen injection phase.

At a mechanistic level interactions between hydrogen and CO or THCs are not observed. The thermal effect from hydrogen injection is clear.

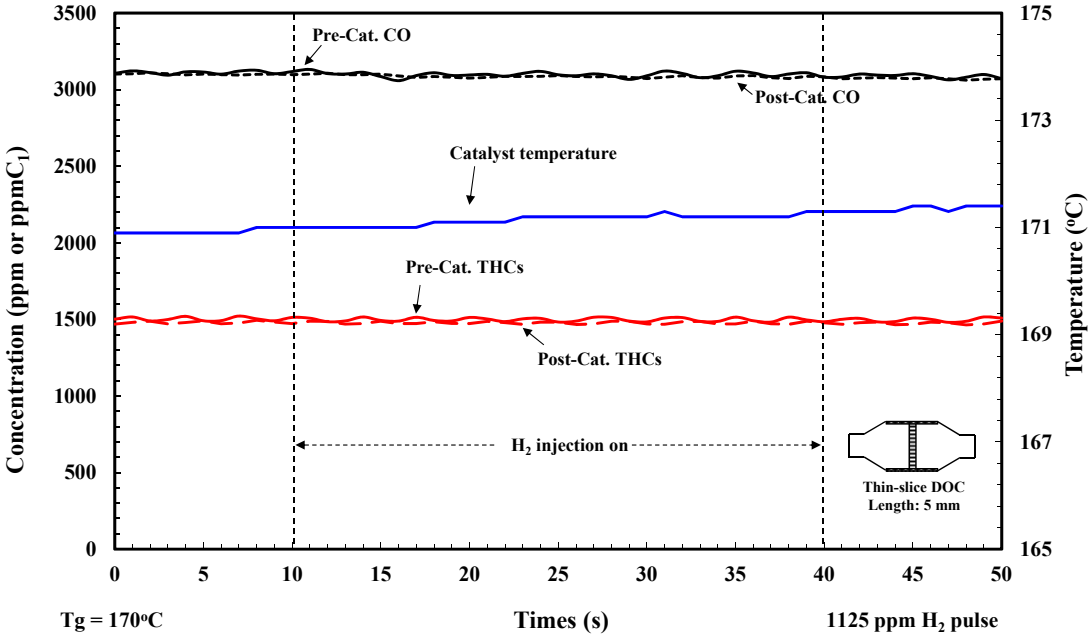


**Figure 3.103** Influence of a pulse of 1125 ppm of hydrogen when the inlet gas temperature was 170°C.

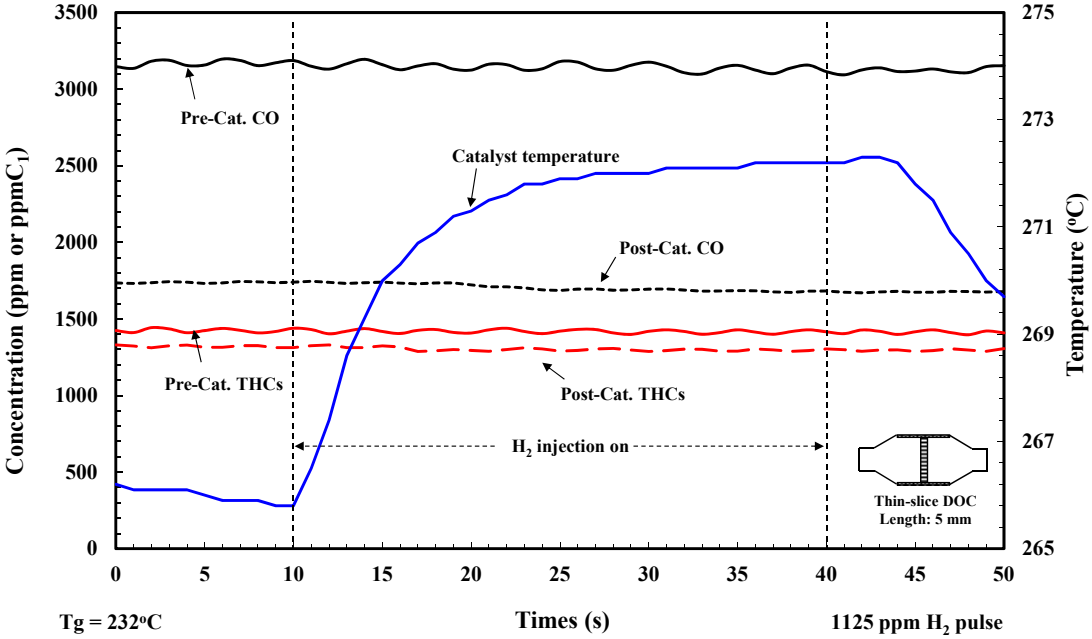


**Figure 3.104** Influence of a pulse of 1125 ppm of hydrogen when the inlet gas temperature was 232°C.

### 3.7.4 Effect of hydrogen addition during the cold NEDC using Full-scale DOC

Three cold NEDC were performed with different levels of hydrogen addition:

(a) Test cycle 1: with no hydrogen injection;
(b) Test cycle 2: hydrogen was injected at 0.456 litre minute$^{-1}$ (equivalent to 570 ppm when the exhaust gas flowrate is 60 kg h$^{-1}$);
(c) Test cycle 3: hydrogen was injected at 0.9 litre minute$^{-1}$ (equivalent to 1125 ppm when the exhaust gas flowrate is 60 kg h$^{-1}$).

The performance of the DOC is summarised in Table 3.10. Other relevant information is summarised in Appendix 7.3.

**Table 3.10** Effect of hydrogen addition on the overall conversion of the major contaminants during the cold NEDC using Full-scale DOC.

| Hydrogen injection (litre minute$^{-1}$) | Overall conversion (%) | | |
|---|---|---|---|
| | CO | THCs | $NO_x$ |
| 0 | 34.9 | 36.4 | 7.8 |
| 0.456 | 38.7 | 37.2 | 7.48 |
| 0.9 | 44.78 | 44.3 | 8.6 |

From Table 3.10, it is clear that the injection of hydrogen creates a significant improvement in the overall conversion of CO and THCs. However, the level of improvement is limited, as an increase in the temperature of the wall (or catalyst) has to reach a minimum level at which the oxidation reactions for CO and THCs will become significant.

In this experimental rig, the DOC is mounted about 0.5 m away from the exhaust manifold, which may delay catalyst light-off because of heat loss from this short section of pipe work. The exhaust gas temperature at the exhaust manifold can be more than 30$^{o}$C higher than the inlet gas temperature to the DOC. In a vehicle the DOC is directly mounted onto the exhaust manifold. In such a configuration, the wall temperature will increase quicker and the hydrogen will start to react earlier in the NEDC, so the effect of hydrogen on the overall conversion efficiency would be improved.

### 3.7.5 Measurement of background level of hydrogen in diesel exhaust

Hydrogen in the engine exhaust gas is considered to arise as a product of water-gas shift reaction (Oh and Cavendish, 1982). Oh and Cavendish (1982) included hydrogen as a separate species in their simulations. They also reported that the concentration of hydrogen was assumed to be determined by the equilibrium of the water-gas shift reaction, and they assigned a mole ratio of 1:3 between hydrogen and CO. Unfortunately, there are very few experimental studies in which the hydrogen concentration is measured. For example, Abu-Jrai and Tsolakis (2007) measured the composition of hydrogen and CO, and they found the ratio between hydrogen and CO depended on operating conditions and was:

- 1 : 2.5 ($H_2$ : CO) at 25% load, speed:1500 rpm and IMEP: 3.0 bar
- 1 : 1.25 ($H_2$ : CO) at 50% load, speed:1500 rpm and IMEP: 4.3 bar
- 1 : 1.3 ($H_2$ : CO) at 75% load, speed:1500 rpm and IMEP: 5.9 bar

In this project, the hydrogen background concentration was also measured by a fast mass spectrometer (manufactured by Hiden Analytical Ltd. UK). In the tests, the engine was running at constant speed of 2000 rpm and samples were taken at three different torques (loads): 10, 40 and 100 Nm. For each engine torque, the exhaust gas sample was taken from the pre-catalyst position. A gas sampling pump was used to fill a gas sampling bag. Since the mass spectrometer has restriction on the water content in the sample gas, a spiral stainless tube was connected between the sampling port and the pump, and this was submerged in a bucket of cold water to reduce the water vapour content in the gas. Meanwhile, the MEXA 7000 gas analyser was also used. The results are summarised in Table 3.11. From these it can be seen that the background level of hydrogen is only about 15% of the CO concentration, and the molar $H_2$ : CO ratio is approximately 1: 9. This is very different to the values reported in the literature. Unfortunately, there was a lack of time to explore this aspect further.

**Table 3.11** Composition of exhaust gas for three different engine torques.

| | Speed: 2000 rpm<br>Torque: 15 Nm | Speed: 2000 rpm<br>Torque: 36 Nm | Speed: 2000 rpm<br>Torque: 47 Nm |
|---|---|---|---|
| CO (ppm) | 1450 | 1120 | 1450 |
| THCs (ppm$C_1$) | 144 | 200 | 214 |
| $NO_x$ (ppm) | 225 | 287 | 472 |
| $H_2$ (ppm) | 156 | 121 | 152 |

## 3.8 Non-uniform distribution of washcoat and catalyst

The non-uniform distribution of washcoat and catalyst was discovered when preparing the Thin-slice DOCs. As the Full-scale DOC was cut into thin slices, from a visual observation it was clear that the distribution of washcoat was non-uniform. In order to investigate the effect of this variance on the performance of a DOC, three aspects were studied:

(a) Visual inspection of a number of thin-slices.
(b) Measurement of the number of active catalytic sites on different thin-slices.
(c) Testing the relative activity of thin-slices in the Thin-slice DOC reactor connected to a live engine.

Parts (a) and (b) were performed in the parallel PhD project by Yap. From his visual inspection, it was clear that the distribution of the washcoat exhibited an egg or spinning top structure, aligned along the centre-line axis of the DOC.

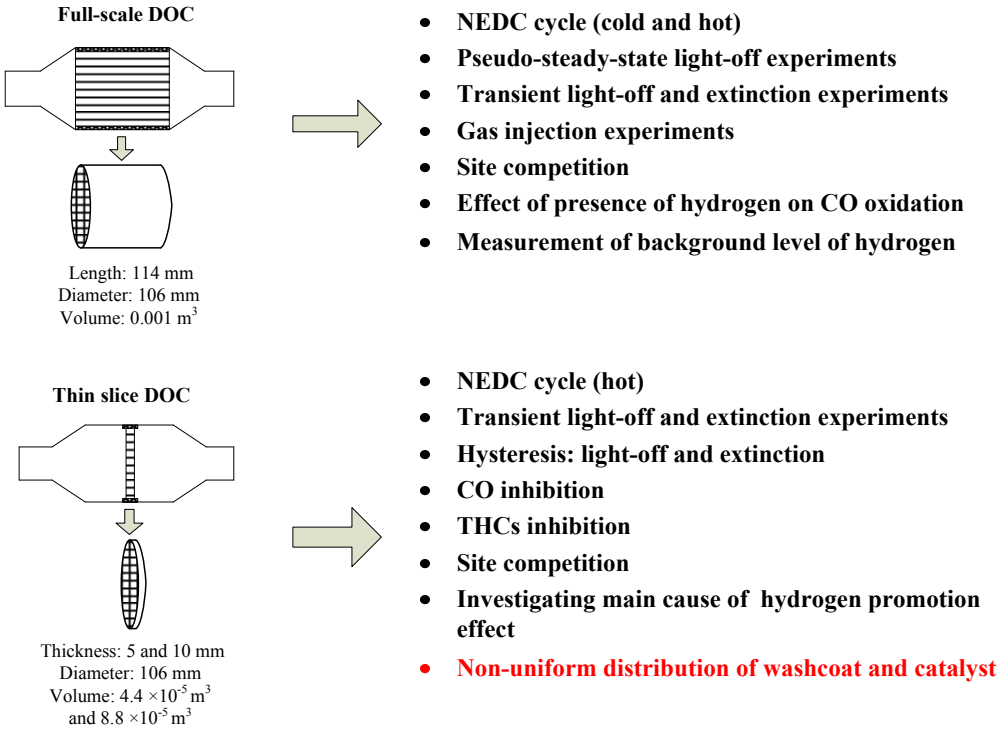


**Figure 3.105** Summary of experiments in Chapter 3. The experiments highlighted in red are discussed in Section 3.8.

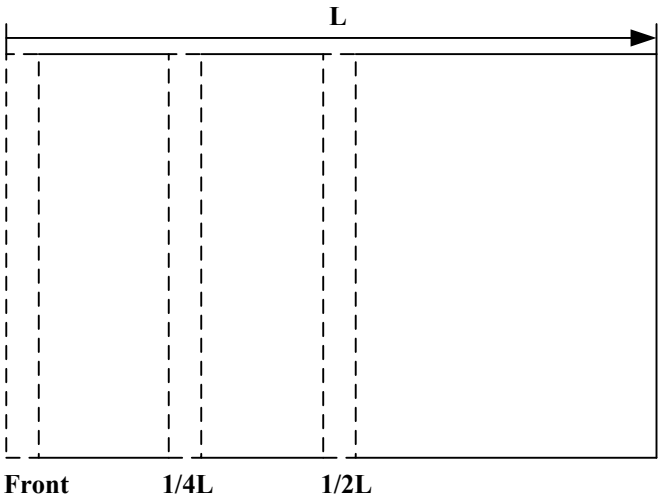


**Figure 3.106** Illustration of the positions of three 5 mm thin slices cut from the Full-scale DOC.

Therefore, three (5 mm) thin-slices were cut from three axial positions of a Full-scale DOC, starting at the front, then ¼ L, then ½ L, see Figure 3.106. To explore the effect of non-uniform washcoat and catalyst distribution, the catalytic oxidations of CO and THCs were studied using the pseudo-steady-state experimental technique described in Section 3.5.1.

For all of the tests, the inlet concentrations of CO and THCs were maintained at 3000 ppm and 1500 ppm$C_1$, respectively. The results are shown in Figures 3.105 to 3.108. Although variations can be seen, the main difference occurred at high temperatures for the ½ L slice. This was linked to a fracture in this thin-slice, and so the results at high temperature should be neglected from the ½ L slice. However, this was useful as it was very clear that something was at fault with this sample.

The relative activity of the slices for the oxidation of CO and THCs followed the same sequence i.e. order of activity was ¼ L, ½ L and then Front. Otherwise, the difference was not as great as expected (from the visual observation of variations in washcoat thickness between the slices). The front slice had the thinnest layer and hence it is not surprising to see CO light-off delayed by about 25$^{o}$C.

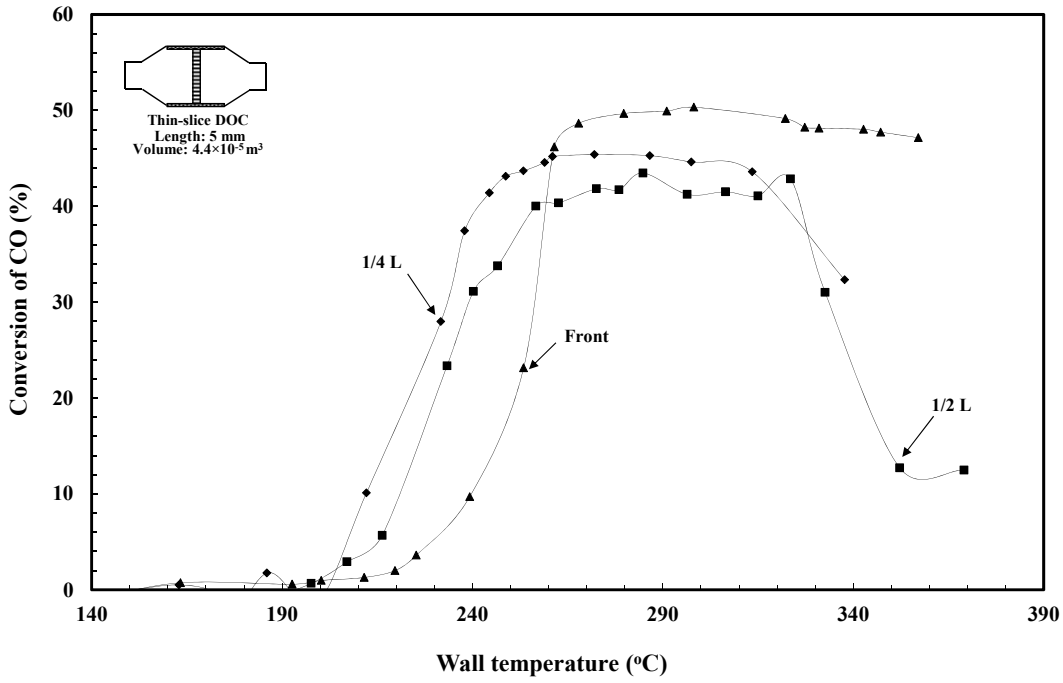


**Figure 3.107** Conversion of CO as a function of wall temperature. Inlet CO and THCs concentrations were maintained at 3000 ppm and 1500 ppm$C_1$, respectively.

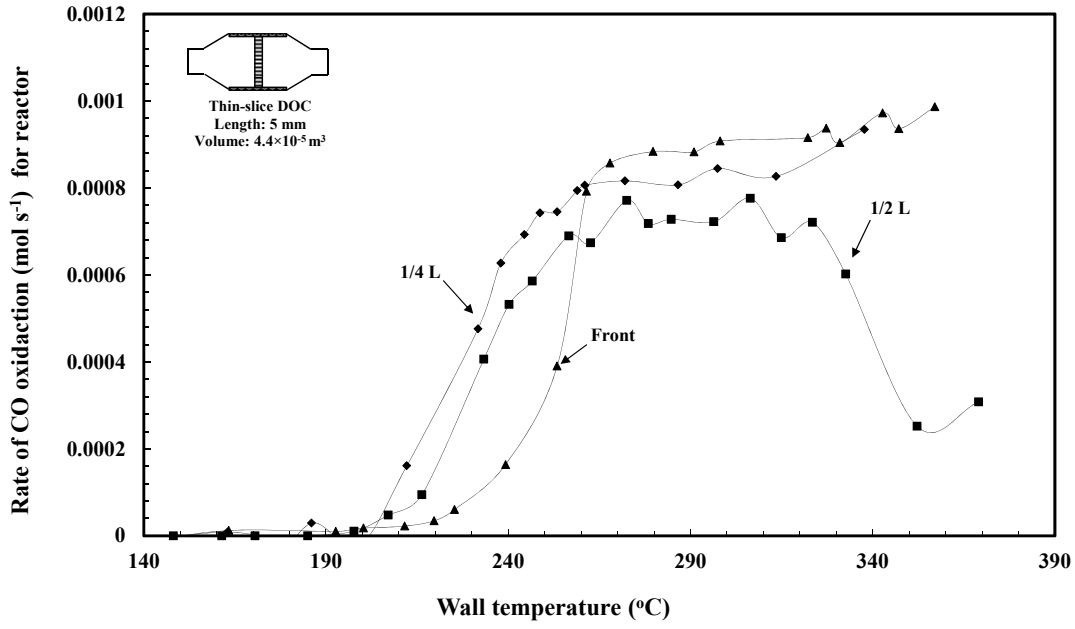


**Figure 3.108** Overall rate of CO oxidation as a function of wall temperature. Inlet CO and THCs concentrations were maintained at 3000 ppm and 1500 ppm$C_1$, respectively.

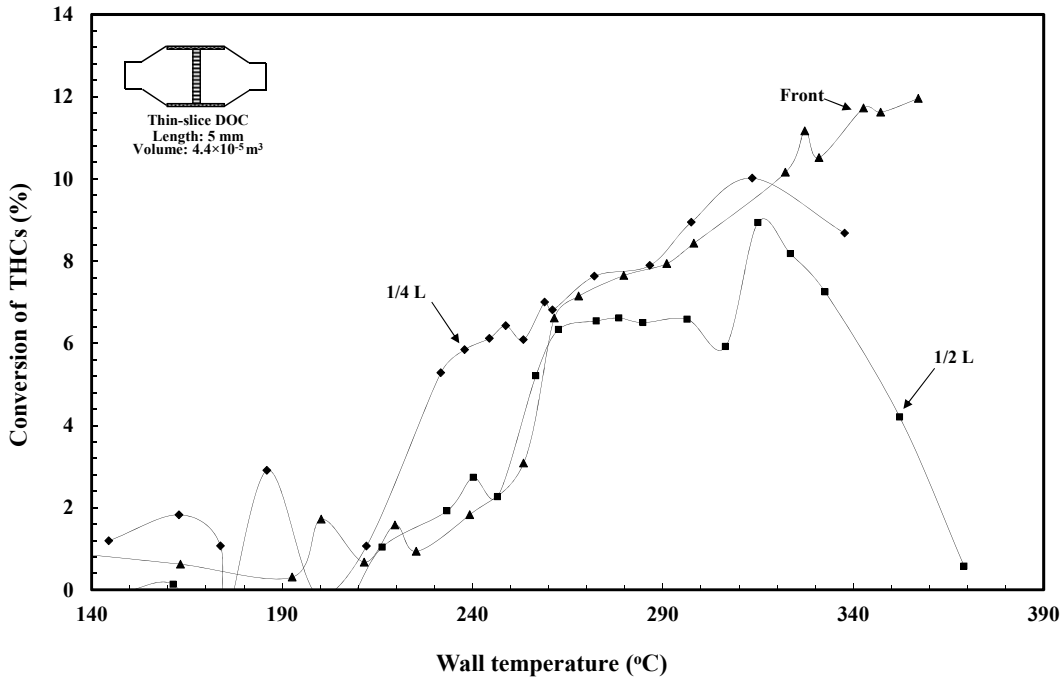


**Figure 3.109** Conversion of THCs as a function of wall temperature. Inlet CO and THCs concentrations were maintained at 3000 ppm and 1500 ppm$C_1$, respectively.

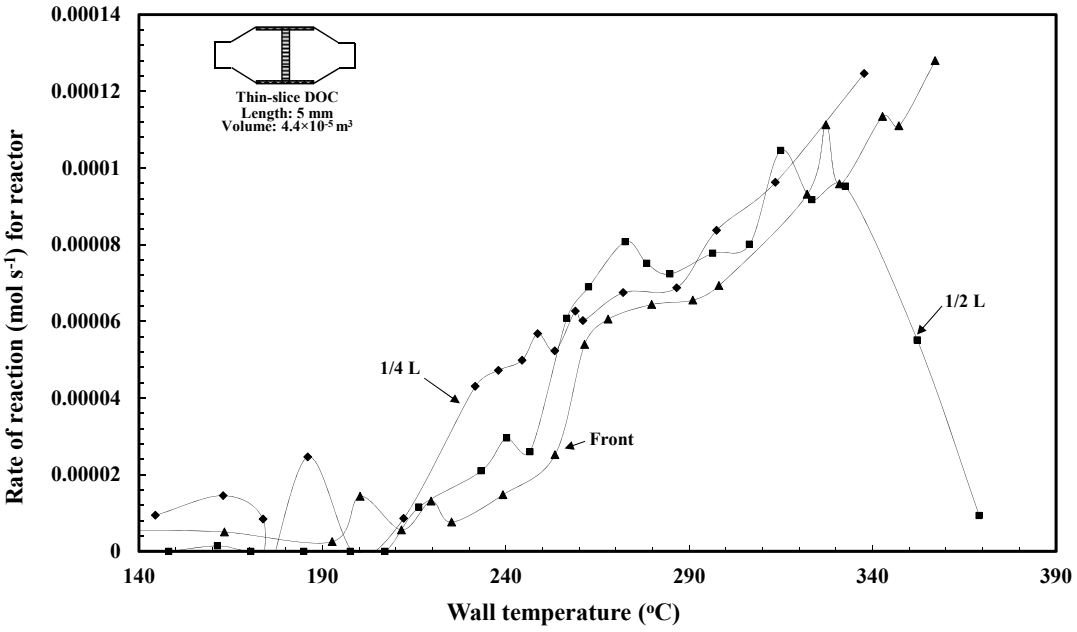


**Figure 3.110** Overall rate of THCs oxidation as a function of wall temperature. Inlet CO and THCs concentrations were maintained at 3000 ppm and 1500 ppm$C_1$, respectively.

## 3.9 Concluding remarks

In this chapter a number of techniques have been developed and demonstrated, which will help to acquire a deeper understanding of how the DOC is performing. Techniques that have in general only been used in bench-top laboratory experiments on small catalyst samples/powders with simulated exhaust gases, have now been used (probably for the first time) successfully on DOCs connected to a live diesel engine.

Throughout this chapter, a number of experimental techniques are explored, and it is shown how to make use of a Full-scale DOC and a Thin-slice DOC, to gather fundamental data on the performance of the DOC, and how to combine information on wall temperature profiles in the DOC with information on conversion and reaction rates, in order to draw conclusions on what is taking place. The following techniques were demonstrated:

(a) **Baseline data:** How to start such a study, by gathering relevant baseline performance data for the engine, so as to establish a matrix of operating conditions.

(b) **NEDC:** How to gather data on cold and hot NEDCs, and how to present this information so that it is in a useful form to interpret what is happening inside the DOC.

(c) **Light-off:** A methodology has been developed and demonstrated, which enables catalyst light-off curves to be generated, by running the engine at a range of pseudo-steady-state conditions. This also involves the addition of known background levels of CO and THCs.

(d) **Light-off and extinction:** A methodology has been developed and demonstrated, which illustrates how background levels of CO and THCs influence light-off and extinction. Clear evidence is provided to show the presence of hysteresis.

(e) **Hysteresis:** A methodology has been developed and demonstrated, which helps to unravel the difference between thermal and mechanistic effects. It is shown that for CO oxidation, there is a clear mechanistic effect.

(f) **Pulse injection:** A methodology has been developed, in which a pulse concentration of a reactant is added, whilst a known gas inlet (to DOC)

background concentration of other contaminants is maintained constant. The transient response of the DOC is then monitored. This is a transient experiment, as in response to the pulse input, the DOC responds. From this type of experiment a very wide range of mechanistic aspects can be explored. For example, is there any evidence of competition for the active site between CO and THCs, which would affect the performance of the DOC?

In the course of developing this methodology, many important observations where made, which helped to clarify how the catalyst was performing. This will help to design better catalyst systems, and in any simulations (mathematical models) of the DOC, these features can be used to check the validity of the code. These features included:

(i) **Light-off during NEDC:** How during the simulated cold & hot NEDCs, catalyst light-off starts from the back of the DOC.

(ii) **Light-off (CO/propane):** How, in the pulse experiments with CO, the catalyst light-off starts from the back of the DOC, yet in the experiments with a pulse of propane, light-off starts from the front of the DOC.

(iii) **Hysteresis:** How different background CO and THCs levels affect the shape of the light-off and extinction curves, and magnitude of hysteresis.

(iv) **Catalyst wall temperatures:** How information from a Thin-slice DOC may be interpreted and the usefulness of having a relatively constant catalyst axial wall temperature profile, which helps to identify more clearly any enhancements from a thermal rather than a chemical mechanistic effect.

It was also shown:

- **Propane:** That propane is not a good representative for the THCs from a diesel engine. *This aspect was not explored further, but is recommended in future work.*
- **Site competition:** For the range of conditions tested, there appeared to be no significant competition for active catalytic sites, between CO, THCs, or propane. *This has important implication on the form of rate expressions that could be used in converter models.*
- **Hydrogen enhancement:** From a short study on the effect of hydrogen addition on enhancement in conversion, its contribution is considered to be

mainly from a thermal rather than a chemical reaction mechanistic aspect. *This observation will help to clarify some of the confusion in the literature.*

- **Relative catalyst activity (axial direction):** From a short study on the relative performance of thin-slices cut from different parts of the DOC (front, ¼ L, and ½ L), although the activity can be seen to vary, this effect in a Full-scale DOC is considered to be most probably small. *However, this could be important when using a Thin-slice DOC to acquire fundamental data (which is then assumed to apply over the entire DOC).*
- **Background ratio of CO to hydrogen:** From a very short study it was found that the molar ratio of hydrogen to CO in the exhaust gas from the diesel engine was close to 1 : 9. This background level is very different from some values reported in the literature data, which suggests ratios of 1:3. However, it is recognised that the measurement of hydrogen is difficult, and there is very little data in the literature on its value. *This aspect was not explored further, but is recommended in future work.*

As the experimental techniques were developed and described, experimental errors were discussed and this sometimes led to a need to re-calibrate the equipment. In these concluding remarks, a brief summary is provided:

(a) To reduce experimental errors, it was important to ensure that the gas analysis equipment was routinely calibrated. In general, measurements were within the following limits: CO ± 1% ; THCs ± 1% ; $NO_x$ ± 1.5%.

(b) The gas flows from the engine, were estimated to be within ± 2%.

(c) Temperatures were measured with thermocouples, and these were estimated to read within ± 1ºC (for the 0.5 mm thermocouples mounted in the monolith/DOC), and ± 1ºC for the thicker 1 mm thermocouples that measured gas temperatures.

(d) The axial and radial locations, at which the wall thermocouples were positioned, were within ± 1 mm of the reported location.

(e) Pressure drop was measured using pressure transducer, was within ± 0.2kPa.

(f) Especially in the transient experiments, time alignment of the various sources of data was critical to ensure that the changes could be represented as ‘real time’ plots. It is estimated that this was achieved within ± 1 s.

# Reference


Abu-Jrai, A. and Tsolakis, A. (2007) The Effect of $H_2$ and CO on the Selective Catalytic Reduction of NOx under Real Diesel Engine Exhaust Conditions over $Pt/Al_2O_3$. *Int. J. Hydrogen Energy*, **32**, 2073 -2080.

Arnby, K., Törncrona, A., Andersson, B.and Skoglundh, M. (2004) Investigation of $Pt/\gamma$ - $Al_2O_3$ Catalysts with Locally High Pt Concentrations for Oxidation of CO at Low Temperatures. *Journal of Catalysis,* **221**, 252-261.

Carlsson, P., Skoglundha, M., Thorma, P.and Anderssona, B. (2004) Low-temperature CO Oxidation over a $Pt/Al_2O_3$ Monolith Catalyst Investigated by Step-response Experiments and Simulations, *Topics in Catalysis*, **30/31**, 375-381.

Hammond, E. (2004) *Student Research Project: Exhaust Catalyst Investigations*, University of Bath.

Hayes, R.E., Kolaczkowski S.T., Thomas, W.J. and Titiloye, J. (1995) Intraphase Diffusion and Interphase Mass Transfer Effects During the Catalytic Oxidation of CO in a Tube Wall Reactor, *Proc. R. Soc. Lond*. A, **448**, 321 – 334

Knafl, A., Bohac, S.V., Han, Assanis, D.N. and Szymkowicz, P. G. (2007) Comparision of Diesel Oxidation Catalyst Performance on an Engine and a Gas Flow Reactor, SAE 2007-01-0231.

Oh, S.H. and Cavendish, J. (1982) Transients of Monolithic Catalytic Converters: Response to Step Changes in Feed Stream Temperature as Related to Controlling Automobile Emissions. *Ind. Eng. Chem. Prod. Res. Dev*. **21**, 29-37.

Salomons, S., Votsmeier, M., Hayes, R. E., Drochner, A., Vogel, H. and Gieshof, J. (2006) CO and $H_2$ Oxidation on a Platinum Monolith Diesel Oxidation Catalyst. *Catalysis Today*, **117**(4), 491- 497.

Salomons, S. (2008) PhD thesis: *Kinetic models for a diesel oxidation catalyst*, University of Alberta.

Sun, M., Croiset, E.B., Hudgins, R.R. and Silveston P.L. (2003) Steady-State Multiplicity and Superadiabatic Extinction Waves in the Oxidation of $CO/H_2$ Mixtures over a $Pt/Al_2O_3$-Coated Monolith, *Ind. Eng. Chem. Res.*, **42** (1), 37–45.

Tan, Y. P. (2007) PhD thesis: *Automotive diesel turbocharger investigation*, University of Bath.

Voltz,S.E., Morgan,C.R., Liederman, D. And Jacob, S.M. (1973) Kinetic Study of Carbon Monoxide and Propylene Oxidation on Platinum Catalysts. *Idn. Engng Chem. Prod. Res. Dev*. **12**, 294-301.

Zervas, E. (2008) Parametric Study of the Main Parameters Influencing the Catalytic Efficiency of a Diesel Oxidation Catalyst, *International Journal of Automotive Technology*, **9**(6), 641-647.

# 4. Case studies: applying modelling techniques

In this chapter, a number of case studies are considered in detail to illustrate:

(a) How some of the experimental results/techniques developed in this thesis, may be used in modelling studies to facilitate catalyst system design.

(b) How mathematical modelling techniques can be applied to interpret the results obtained.

This starts with a consideration of heat transfer aspects in a DOC, under conditions when there are no reactions take place. The results of such simulations are compared with work by Benjamin and Roberts (2001), and such simulations are also performed and compared with experimental data obtained in this thesis. As illustrated in Figure 4.1, models have been developed using two approaches:

- In Case Study 1, the formulated set of one-dimensional (1-D) equations have been solved using MATLAB.
- In Case Study 2, a two-dimensional (2-D) option in COMSOL has been selected to simulate the problem set.

Then reaction conditions are included in the model, and in Case Study 3, the model is tested by simulating conditions reported in the literature by Hayes and Kolaczkowski (1997, pp. 310 - 324) on the catalytic combustion of propane. This provides confidence in the way the model has been constructed.

Then finally in Case Study 4, it is shown how the model could be used to back-calculate the coefficients in a rate expression, and this is illustrated for the LHHW form of rate expression.

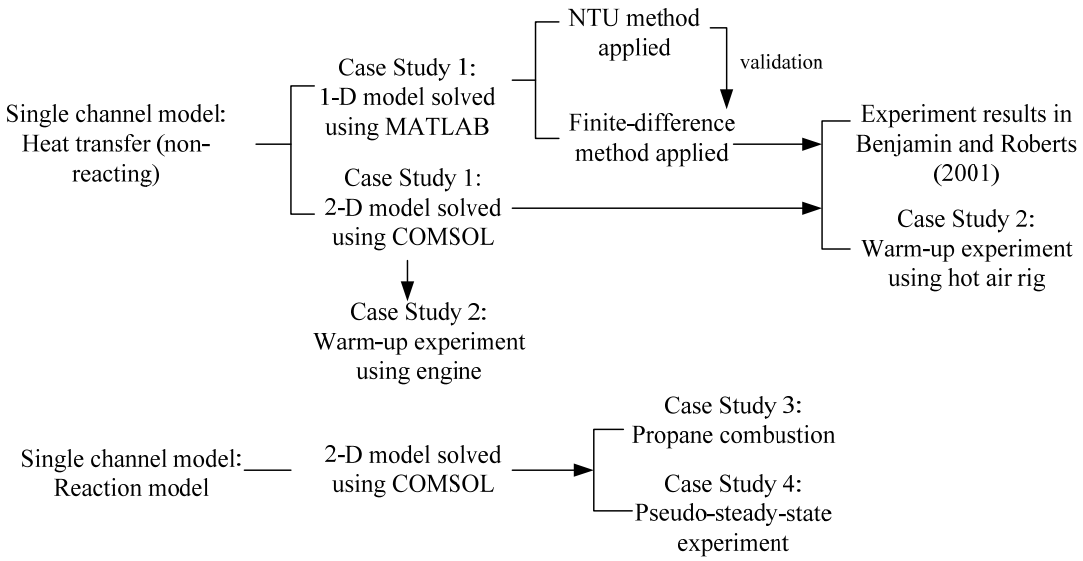


**Figure 4.1** Overview of the mathematical models developed in Chapter 4.

## 4.1 Choice of models

To develop an appropriate catalytic converter model, a number of decisions must be made concerning the number of dimensions in a model. Based on discussions in Hayes and Kolaczkowski (1997; p. 292), a one-dimensional (1-D) model assumes the gas properties are uniform over the cross-section of the channel and thus the gradients in temperature, concentration and velocity in the radial and angular directions are ignored. Therefore, the accuracy of a 1-D model depends on the magnitudes of the gradients in the radial and angular directions. However, they offer a number of advantages. They are simpler to construct, have shorter computer run time and it is easier to identify causes when problems occur. 2-D models account for the radial gradients in temperature, velocity and concentration but ignore those gradients in an angular direction. They are more complex than a 1-D model, and can take up to ten times the computer execution time of 1-D models (Hayes and Kolaczkowski, 1997; p. 293). Ideally, 3-D models are the most realistic models. Nevertheless, they may be computationally prohibitive and they are probably not justified in terms of accuracy (Hayes *et al*., 1992). Thus, as a compromise, 2-D models are often encountered as the more rigorous form of model in the literature (e.g. Zygourakis, 1989; Hayes *et al*., 1992; Koltsakis *et al*., 1997).

In the literature review section in Chapter 2, the importance of building-up models in a gradual manner has already been emphasised, thus a 1-D simple transient heat transfer model is a good starting point. Although a number of simplifying assumptions

are made at this stage, which could be debated e.g. Siemund *et al.* (1996), by following this simplified approach a better understanding can be obtained of the physical and chemical aspects in the system modelled.

## 4.2 Modelling tools

Two pieces of software, namely MATLAB (R2009b) and COMSOL Multiphysics (Version 3.5a), were used to solve the models. In the MATLAB environment, users need to construct the equations and this provides an opportunity to gain a deeper understanding of modelling.

The literature review in Chapter 2 shows that commercial CFD codes have been used to model the performance of catalytic converters. There are a number of CFD codes available, and many of them use a finite element technique for discretizing a flow field domain and then they solve the generalised transport equations (e.g. Kolaczkowski *et al*., 2007).

In COMSOL Multiphysics, the physics (i.e. governing equations and boundary condition) are pre-defined, and users only have to choose the suitable options and define the inlet conditions, and other physical parameters. Thus the package solves the problem automatically using a chosen solver.

## 4.3 Case Study 1:Thermal models at non-reacting conditions

In this case study, equations are developed to model heat transfer in one monolith channel that represents a channel in a DOC. In this analysis, it is assumed that all of the channels behave in the same manner.

### 4.3.1 1-D heat transfer model in MATLAB

A single channel 1-D heat transfer model was developed and then this was solved with the aid of MATLAB.

**Energy balance in a single channel**

This is developed assuming that plug-flow conditions are valid. The basis of this single channel (non-reacting) heat transfer model is illustrated in Figure 4.2.

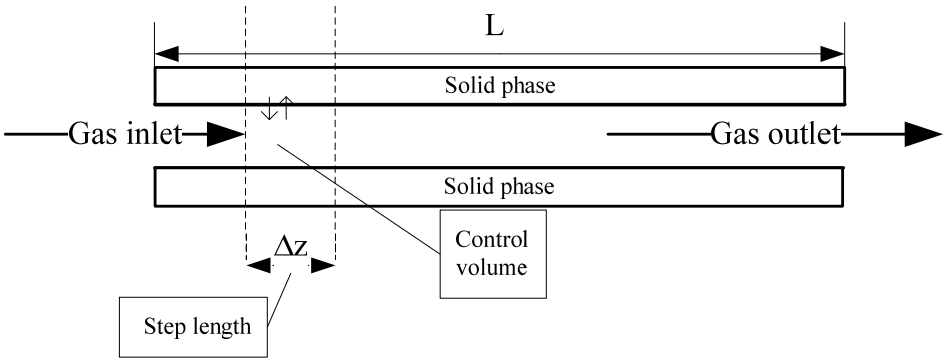


**Figure 4.2** Schematic of the single channel model.

Based on equations described in Hayes and Kolaczkowski (1997; pp. 339-340), the transient energy balances in the gas phase and the solid phase in a control volume can be summarised as:

The gas phase energy balance is:

$$-u\,\rho_g C_{Pg}\frac{dT_g}{dz}+\frac{4}{D_H}h\,(T_s-T_g)\;-\sum_{i=1}^{n}(-R_i)_g(\Delta H_R)_i=\rho_g C_{Pg}\frac{\partial T_g}{\partial t} \tag{4.1}$$

The solid phase energy balance is

$$\frac{d}{dz}\left(k_w\delta_w\frac{dT_s}{dz}\right)-q_{rad}-h\ (T_S-T_g)-\sum_{i=1}^{n}\eta_i(\text{-}R_i)_s(\Delta H_R)_i=\rho_s\delta_w\,C_{Ps}\frac{\partial T_s}{\partial t} \tag{4.2}$$

where:

| | | |
|---|---|---|
| $u$ | mean gas velocity | m $s^{-1}$ |
| $T$ | temperature | K |
| $T$ | time | s |
| $\rho$ | density | kg $m^{-3}$ |
| $C_p$ | heat capacity | kJ $kg^{-1}$ $K^{-1}$ |
| $D_H$ | hydraulic diameter | m |
| $h$ | heat transfer coefficient | W $m^{-2}$ $K^{-1}$ |
| $k_w$ | thermal conductivity of washcoat | W $m^{-1}$ $K^{-1}$ |
| $\delta_w$ | thickness of washcoat | m |
| $q_{rad}$ | radiant heat flux | W $m^{-2}$ |
| $\eta$ | effectiveness factor | |
| $R_i$ | reaction rate of substance *i* | |
| $(\Delta H_R)_i$ | enthalpy of the reaction of substance *i* | J $kg^{-1}$ |

*Subscripts*

| | |
|---|---|
| g | Gas phase |
| s | Solid phase |

The following assumptions are applied:

- plug flow,
- fully developed flow regime,
- heat transfer by radiation is neglected,
- heat loss to surroundings is neglected,
- both ends of the channel are insulated,
- axial heat conduction in the monolith wall is neglected, and
- no chemical reactions take place.

For a typical monolith reactor it has been shown that the axial heat conduction in the gas phase is not significant (Oh and Cavendish, 1982; Hayes, *et al*., 1992). The

speed of the response of the gas is several orders of magnitude higher than the response of the solid. At a typical inlet velocity of the order of 1 to 10 m $s^{-1}$ or higher, the residence time, in a 120 mm long channel would be of the order of 0.12 to 0.012 s. This implies that the transient term in the gas phase could be neglected. However, the term needs to be included in order to solve the transient nature of the problem. The transient term has to be retained in the solid phase energy balance. Thus, the transient energy balance in the gas phase can be simplified:

$$-u\,\rho_g C_{Pg}\frac{\partial T_g}{\partial z}+\frac{4}{D_H}h\,(T_s-T_g)=\rho_g C_{Pg}\frac{\partial T_g}{\partial t} \qquad (4.3)$$

and, the corresponding boundary conditions for Equation 4.3 are:

$$\frac{dT_g}{dz}=0 \qquad \text{at} \qquad z=0 \text{ and at } z=L \qquad (4.4)$$

The solid phase energy balance can also be simplified:

$$h\,(T_g-T_s)=\rho_s\delta\,C_{Ps}\frac{\partial T_s}{\partial t} \qquad (4.5)$$

and, the corresponding boundary conditions for Equation (4.4) are:

$$\frac{dT_s}{dz}=0 \qquad \text{at} \qquad z=0 \text{ and at } z=L \qquad (4.6)$$

**Formulating the finite-difference expressions**

A mathematical description of the catalytic converter produces a system of ordinary differential equation (ODEs) and partial differential equations (PDEs) with boundary conditions. This becomes a boundary value problem (BVP). The essence in solving most BVPs is to divide the solution domain into a finite number of *nodes* or *mesh points*. This is known as *discretization* (Hayes and Kolaczkowski, 1997; p. 284). The derivatives in the BVP are substituted with algebraic equations at each of these mesh points, such as finite-difference approximation (detailed description of this method can be found in Smith, 1985). Thus, the algebraic equations at different mesh points form a system of algebraic equations that contain the unknown dependent variables, which can be solved using an appropriate numerical method, such as an implicit method or an explicit method.

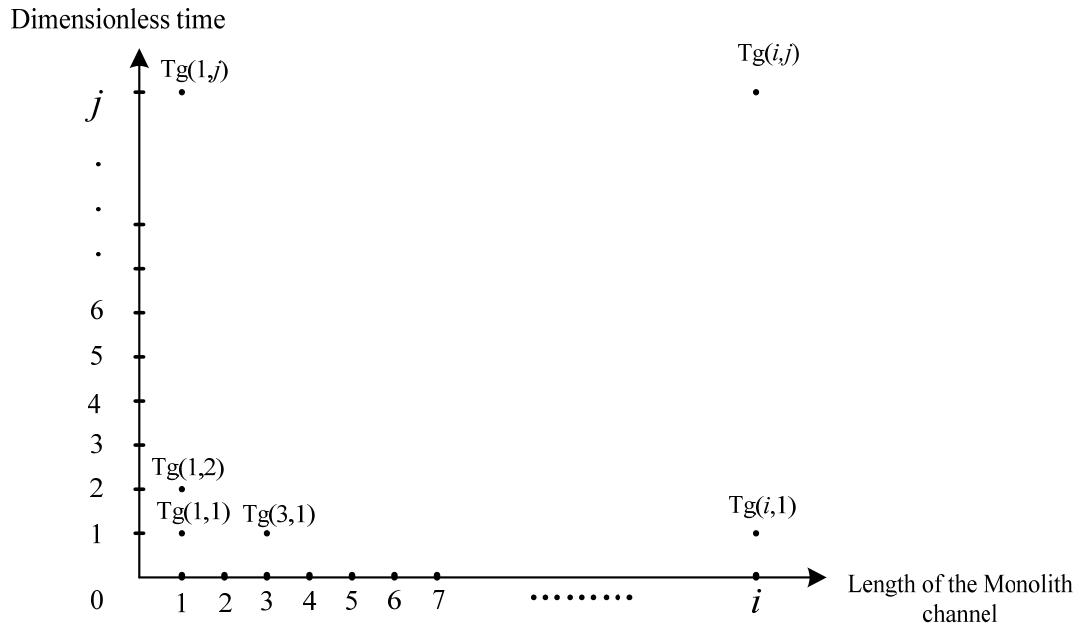


**Figure 4.3** Example of discretization of the gas temperature represented in an *x, y*-coordinate system (mesh points), where *i* stand for mesh points along the axial direction along the monolith (also known as dimensionless length steps, $\Delta z$) and *j* stands for mesh points in time domain (also known as dimensionless time steps, $\Delta t$).

Firstly, in order to solve this simple transient model, the dependent variables (gas and solid temperature) have to be discretized, see Figure 4.3. The solutions of gas temperatures are represented as mesh points in *x* and *y*-coordinates, where on the *x*-axis, (*i*) stands for the mesh points along the length axial direction of the monolith and on the *y*-axis, (*j*) stands for discrete mesh points in the time domain. This system also applies to solid temperatures. Therefore, the temperature can be written in T (*i*, *j*) format. As an illustration, $T_g(1, 2)$ stands for the gas temperature at position $\Delta$z away from the monolith entrance after two time steps.

Secondly, the derivatives in the energy balance equations are substituted by backward finite-difference approximations. The application of the finite-difference method is illustrated with the following initial conditions:

$$T_s(i,1) = T_g(i,1) = T_1 \tag{4.7}$$

The energy balance in the solid phase at mesh point (1, 2) can be represented as:

$$h\left[T_g(1,2) - T_s(1,2)\right] = \rho_s \, \delta \, C_{Ps} \frac{\partial T_s}{\partial t} \tag{4.8}$$

The derivative term of solid temperature can be approximated using the backward-difference approximation.

$$\frac{\partial T_s}{\partial t} \approx \frac{T_s(1,2) - T_s(1,1)}{\Delta t} \tag{4.9}$$

Substituting Equation (4.9) into Equation (4.8), and rearranging gives:

$$T_s(1,2) - T_s(1,1) = -\frac{h\,\Delta t}{\delta_w\,\rho_s\,C_{ps}}\left[T_s(1,2) - T_g(1,2)\right] \tag{4.10}$$

Let,

$$\beta = -\frac{h\,\Delta t}{\delta_w\,\rho_s\,C_{ps}} \tag{4.11}$$

Substituting Equation (4.11) into Equation (4.10), and rearranging gives:

$$(1+\beta)\;\; T_s(1,2) - \beta\, T_g(1,2) = T_s(1,1) \tag{4.12}$$

Therefore, the general form of solid phase energy balance for all the mesh points can be written as:

$$(1+\beta)\, T_s(i,j) - \beta\, T_g(i,j) = T_s(i,j-1) \tag{4.13}$$

A similar derivation can be applied to the gas phase energy balance. The energy balance for the gas phase at mesh point (1, 2) is:

$$-u\,\rho_g C_{Pg}\frac{\partial T_g}{\partial z} + \frac{4}{D_H}h\left[T_s(1,2) - T_g(1,2)\right] = \rho_g C_{Pg}\frac{\partial T_g}{\partial t} \tag{4.14}$$

In addition, the backward-difference approximations of the derivative terms are:

$$\frac{\partial T_g}{\partial t} \approx \frac{T_g(1,2) - T_g(1,1)}{\Delta t} \tag{4.15}$$

$$\frac{\partial T_g}{\partial z} \approx \frac{T_g(2,1) - T_g(1,1)}{\Delta z} \tag{4.16}$$

Thus, substituting Equations (4.15) and (4.16) into Equation (4.14), and rearranging gives:

$$\left(1 + \frac{u\,\Delta t}{\Delta z} + \frac{4\,h\,\Delta z}{D_H \rho_g C_{pg}}\right) T_g(1,2) - \frac{4\,h\,\Delta t}{D_H \rho_g C_{pg}} T_s(1,\,2)$$

$$= \frac{u\;\Delta t}{\Delta z} T_g(1,1) + T_g(1,1) \tag{4.17}$$

Let,

$$\alpha = \frac{4h\,\Delta t}{D_H \rho_g C_{pg}} \tag{4.18}$$

$$\gamma = 1 + \frac{u\,\Delta t}{\Delta z} + \frac{4h\,\Delta z}{D_H \rho_g C_{pg}} \tag{4.19}$$

$$\lambda = \frac{u\,\Delta t}{\Delta z} \tag{4.20}$$

Substituting Equations (4.18), (4.19) and (4.20) into Equation (4.17) gives:

$$\gamma\, T_g(1,2) - \alpha\, T_s(1,2) = \lambda\, T_g(1,1) + T_g(1,1) \tag{4.21}$$

Thus, based on Equation (4.21), the general energy balance for the gas phase at all mesh points can be created:

$$\gamma\, T_g(i,j) - \alpha\, T_s(i,j) = \lambda\, T_g(i-1,j) + T_g(i,j-1) \tag{4.22}$$

The algebraic equations that are discrete forms of the differential equations for each mesh point form a system of algebraic equations. The unknown dependent variables (namely $T_g(i,j)$ and $T_s(i,j)$) at each mesh point can be calculated simultaneously with the initial and boundary conditions, and this is known as the implicit method. Therefore, these equations can be solved simultaneously in MATLAB. In order to have confidence in the output from this model, and to ensure that the finite-difference method has been implemented correctly in the MATLAB code, simulations have been performed and compared with data from the literature.

**Testing the MATLAB code without heat transfer**

Firstly, the heat transfer model (Code I) was tested by setting the heat transfer coefficient to zero to ensure no heat transfer between the gas and solid phases. Thus, if a step change in inlet gas temperature is introduced, then the code should predict a step change in the inlet gas temperature at the monolith entrance, while the temperature of the solid should remain constant throughout the process. Information on these test conditions and physical parameters is summarised in Table 4.1. The code is presented in Appendix 8.1.

**Table 4.1** Test condition and physical parameters used in Code I.

| Conditions and parameters | Values |
|---|---|
| Gas velocity (m $s^{-1}$) | 2 |
| Initial gas temperature (K) | 500 |
| Gas temperature after step change (K) | 400 |
| Initial solid temperature (K) | 500 |
| Final time (s) | 5.7 |
| Number of step length in axial direction | 100 |
| Time step (s) | 0.0057 |
| Heat transfer coefficient (W $m^{-2}K^{-1}$, set to zero) | 0 |
| Density of air (kg $m^{-3}$) | 0.5 |
| Heat capacity of air (J $kg^{-1}K^{-1}$) | 1012 |
| Hydraulic diameter (m) | 0.00109 |
| Effective wall thickness (m) | 0.000139 |
| Density of monolith (kg $m^{-3}$) | 2500 |
| Heat capacity of wall (J $kg^{-1}K^{-1}$) | 1100 |
| Length of monolith (m) | 0.15 |

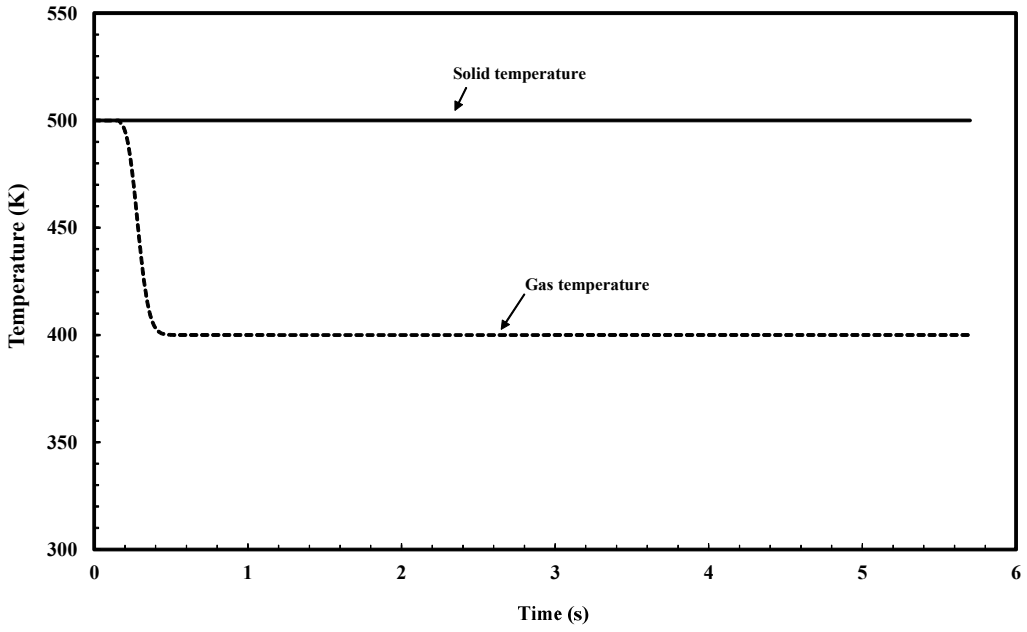


**Figure 4.4** Solid and gas temperature profiles in the first 5.7 s at the middle point (z = 57 mm) of the monolith channel, with $\Delta z$ =1.14 mm, and $\Delta t$ = 0.0057 s (simulated by implicit finite difference thermal model, the MATLAB code is in Appendix 8.1).

The gas and solid temperature at the middle of the channel are as a function of time plotted in Figure 4.4. As can be seen from the plot, Code I captures the step-down in inlet gas temperature, while the solid temperature remains at the initial temperature throughout the process since no heat transfer happens. However, the shape of the

predicted inlet gas temperature is not exactly the shape that was imposed as a boundary condition. This may be caused by the heat accumulation term in the gas phase, which delayed slightly the temperature drop process because of residual heat from the last time step that raised the gas temperature. However, in general this provides confidence in the internal consistency of the code and the way it has been implemented.

**Validation with NTU method**

The NTU method was discussed earlier in Section 2.1.2, and a heat transfer model was developed using the NTU method (Code II) as described in Appendix 3. The NTU model was solved with the aid of MATLAB, and the code is shown in Appendix 8.2. The purpose of this exercise was to check that sensible results were being produced by the finite-difference model, and to compare these two approaches.

The conditions and parameters used in the simulation are the same as those summarised in Table 4.1, except the heat transfer coefficient is set at a constant value of 78.15 $Wm^{-2}$ $K^{-1}$. This value was calculated from the *Nu* number provided in Benjamin and Roberts (2001). The transient response of the solid temperature at the entrance to the monolith channel ($z$ = 1.14 mm), to a step change in inlet gas temperature was simulated. These two results are plotted in Figure 4.5, and the following observations can be made.

- The results from the finite-different model are not identical to that from the NTU model, but similar trends are obtained.
- A decreasing solid temperature profile is sensible since the inlet gas is at a lower temperature and cools down the solid gradually, until they reach the same temperature.
- The NTU model predicts lower solid temperature than that predicted by the finite-difference model during first 15 s, and then a longer time for the solid and gas temperatures to approach one another.
- These simulations provide additional confidence in the way in which the MATLAB code has been constructed.

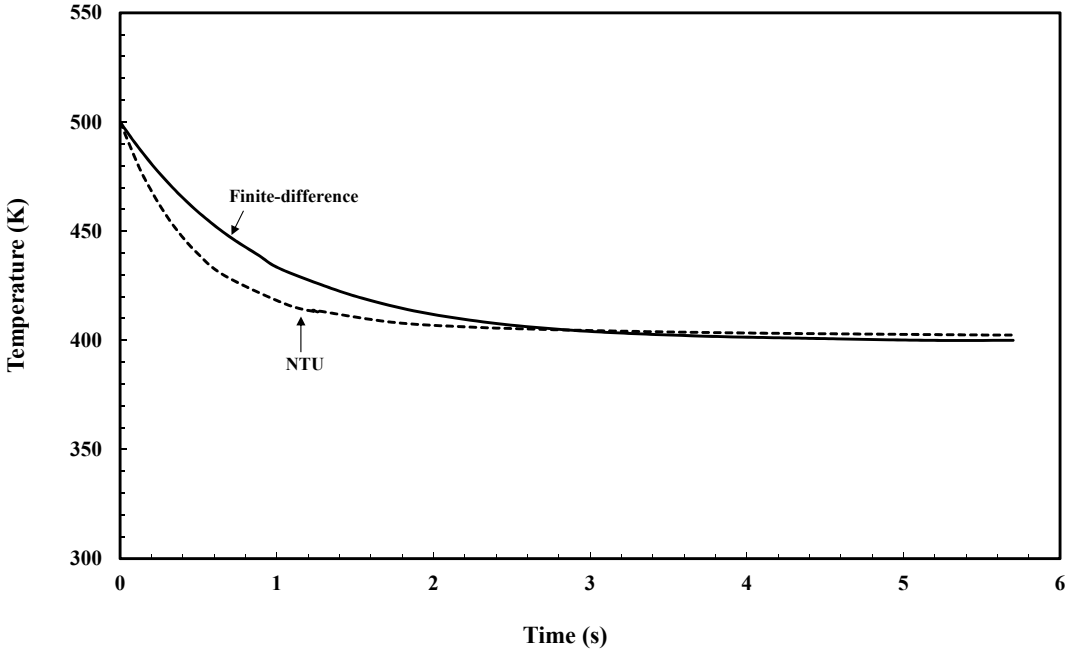


**Figure 4.5** Solid temperature profiles at entrance to the monolith channel ($z$ = 1.14 mm). The MATLAB code for the NTU model is in Appendix 8.2.

## Validation with experimental data in the literature

Benjamin and Roberts (2001) published some useful results that can be used to test the simple heat transfer models that have been developed in this study. Their experiment No.3 was run under a condition of steady air flow, and then the inlet air was heated up gradually by an air heater. Meanwhile, the transient response of the solid temperature along the axial direction of the monolith was measured (with five embedded 0.5 mm K-type thermocouples). The experimental conditions and physical parameters used in their experiment are summarised in Table 4.2. As shown, the physical parameters (e.g. heat capacities of air and solid) in Table 4.2, also have constant values, and these were also used in the modelling work by Benjamin and Roberts (2001). The modelling work was started using the simple model (Code I) with constant parameters, and then the complexity of the model was gradually increased. The output from each step was compared with earlier models and the experimental data from literature. Finally, the complete model is called Code III, and this is shown in Appendix 8.3. A simple flowsheet is used to illustrate the structure of Code III in Figure A26, presented in Appendix 8.4.

Code III includes axial heat conduction in the solid phase, and the energy balance for the solid phase becomes:

$$\frac{d}{dz}\left(k_w \delta_w \frac{dT_s}{dz}\right) - h\,(T_S - T_g) = \rho_s \delta_w\, C_{Ps} \frac{\partial T_s}{\partial t} \qquad (4.23)$$

Temperature dependent correlations for heat capacities for the gas and solid are also included (as previously presented in Table 2.5, Chapter 2).

For air: (within $T$ = 273 to 1800 K)

$$C_{Pg} = 28.9 + 0.1965 \cdot T_g - 0.4799 \times 10^{-5} \cdot T_g^2 - 1.965 \times 10^{-9} T_g^{\,2} \ \text{(J mol}^{-1}\ \text{K}^{-1}\text{)} \qquad (4.24)$$

For the monolith wall (cordierite substrate):

$$C_{Ps} = 1071 + 0.156\, T_s - 3.437 \times 10^{7} T_s^{\,2} \ \text{(J kg}^{-1}\ \text{K}^{-1}\text{)} \qquad (4.25)$$

Equation (4.25) has been widely used in modelling studies, e.g. Oh and Cavendish, 1982.

In addition, a correlation for the heat transfer coefficient as a function of the length of monolith ($z$) that for a square channel (developed by Groppi *et al*., 1995) was used to account for 'entrance effects'. In this case, constant wall heat flux was assumed (see Equation (2.8)), although real conditions most probably varied between constant wall heat flux and constant wall temperature.

**Table 4.2** Some experimental conditions and physical properties of the monolith and air that were used in Benjamin and Roberts (2001).

| **Parameters or conditions** | **Value** |
|---|---|
| Gas velocity in the duct (m $s^{-1}$) | 2.34 |
| Initial gas temperature (K) | 299 |
| Initial solid temperature (K) | 293 |
| Operation time (s) | 50 |
| Nusselt number for square channel | 3.608 |
| Heat transfer coefficient (W $m^{-2}$ $K^{-1}$) | 78.15 |
| Thermal conductivity of air (W $m^{-1}$ $K^{-1}$) | 0.024 |
| Hydraulic diameter (m) | 0.001108 |
| Density of air (kg $m^{-3}$) | 1.2 |
| Heat capacity of air (J $kg^{-1}$ $K^{-1}$) | 1012 |
| Effective wall thickness (m) | $0.081\times10^{-3}$ |
| Density of wall (kg $m^{-3}$) | 1750 |
| Heat capacity of wall (J $kg^{-1}$ $K^{-1}$) | 1100 |
| Length of monolith (m) | 0. 15 |

Prior to obtaining the local heat transfer coefficients, a number of dimensionless numbers had to be calculated (e.g. *Re*, *Gz* and *Pr*), which are also temperature dependent, The *Gz* number describes the entrance effects for the flow of gas in the monolith channel (a description of these dimensionless numbers can be found in Appendix 4).

The local air density was calculated from the ideal gas law:

$$\rho_{air} = \frac{PM_{air}}{RT_g} \tag{4.26}$$

The local air velocity was calculated from:

$$u_{air} = u_{air,0}\frac{T_g}{T_{g,0}} \tag{4.27}$$

where $P$ is the atmospheric pressure (101325 pa), $M_{air}$ is the molecular weight of air (28.97 g $mol^{-1}$), $R_g$ is the universal gas constant (8.314 J $K^{-1}$ $mol^{-1}$), $u_{g,0}$ is the initial air velocity (m $s^{-1}$), and $T_{g,0}$ is the initial air inlet temperature.

Code III was solved using finite-difference method (Backward Euler), and the code is shown in Appendix 8.3. Code III was used to simulate the experiment in Benjamin and Roberts (2001). The operating conditions have already been summarised in Table 4.2. The inlet gas temperature ramp (experimental data) was approximated by a 6$^{th}$ order polynomial equation.

$$T_g = 1.0266\times10^{-20}t^6 - 3.2302\times10^{-16}t^5 + 3.7596\times10^{-12}t^4 - 1.8773\times10^{-8}t^3 + 2.6306\times10^{-5}t^2 + 0.0828t + 298.43 \tag{4.28}$$

The simulations of solid temperature profiles along the axial direction of the monolith substrate at 10 and 50 s of the experiment are compared with the experimental results and CFD simulations in Benjamin and Roberts (2001), see Figure 4.6.

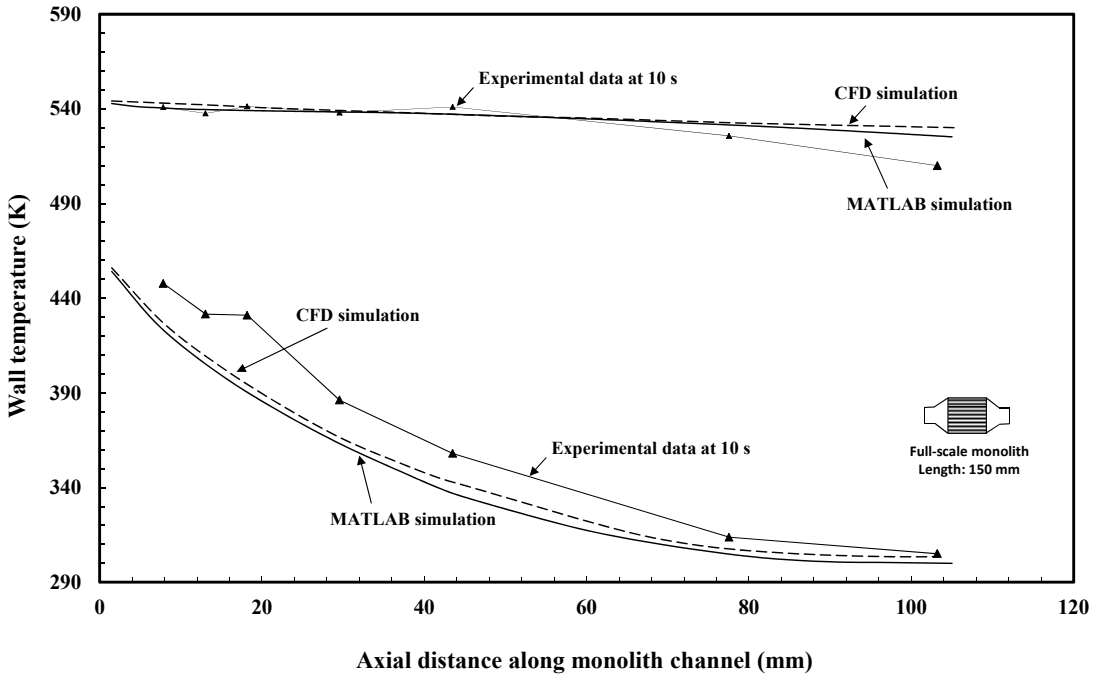


**Figure 4.6** Temperature of the monolith substrate as a function of axial distance after 10 and 50 s, with $\Delta z$ =1.5 mm, and $\Delta t = 6.4\times10^{-4}$ s (simulated by Code III, in Appendix 8.3).

From Figure 4.6, a number of observations/conclusions can be made as follows.

- Simulation of Code II captures the trend in solid temperature profiles. The simulation is very close to the CFD simulation results in the literature.
- Code II predicts lower temperature profile at $t$ = 10 s, and gives a close result to experiment data when t = 50 s. The simulated temperature profile at the rear of the monolith is higher than the experimental data. This may be attributed to the convective heat loss from the back of the monolith.

Code II was also used to simulate the experiment without the axial heat conduction term in the solid phase, and this produced almost identical results to those obtained with the term. The difference between these two simulation results was less than 0.05 K. This is consistent with the explanation in Hayes and Kolaczkowski (1997). In a thin walled monolith, heat transfer by axial heat conduction plays less of an important role than the convective heat transfer term. However, it may become a significant when a large temperature difference (driving force for heat conduction) is present in the axial direction of the solid phase. For example, when reaction terms are added into the model, and especially during catalyst light-off. Then the rate of reaction could release a large amount of heat (exothermic reactions) and this could create a large temperature gradient along the substrate (at point of light-off).

### 4.3.2 2-D heat transfer model in COMSOL Multiphysics

A 2-D heat transfer model was developed using COMSOL Multiphysics.

#### 4.3.2.1 Preliminary checks on the modelling in COMSOL Multiphysics

Before constructing more sophiscated models with chemical reactions, a number of preliminary simulations were performed, to check some of the basic working aspects in COMSOL Multiphysics. These could be visualized as blank tests in the experiment studies. These also help to gain confidence with the basic building blocks (or governing equations) in COMSOL Multiphysics. In these non-reacting simulations, diffusion is not considered as there are no concentration gradients. In all of these preliminary simulations, a circular monolith channel was modelled. The feed to the channel is air, and the operating conditions are summarised in Figure 4.7.

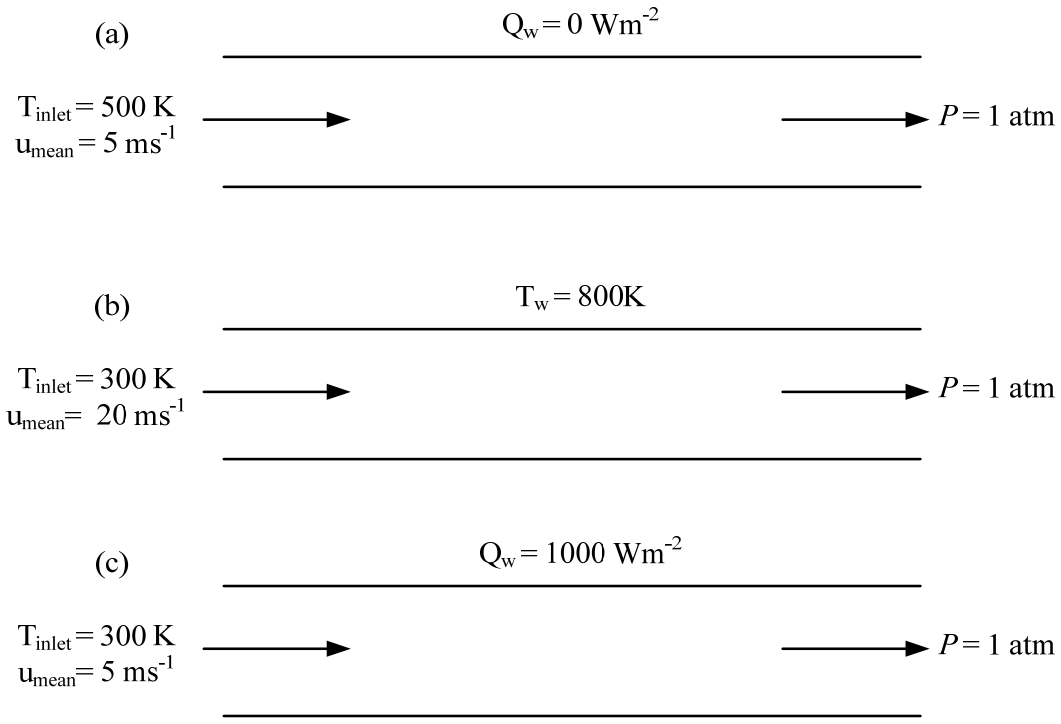


**Figure 4.7** Air flow in a monolith channel (ID = 1.25 mm; length = 150 mm). (a) Check on velocity profile, (b) check on Nu number at constant wall temperature, and (c) check on Nu number at constant heat flux.

**(a) Check on velocity profile**

In the simulation, a parabolic velocity profile is imposed as an inlet condition to the monolith channel. The boundary conditions on the solid wall are 'non-slip' and 'thermal insulation', so that the velocity at the wall is zero and there is no energy transfer across the wall. One of the results of velocity profile such a simulation is shown in Figure 4.8. As expected, the velocity profile maintains a parabolic shape.

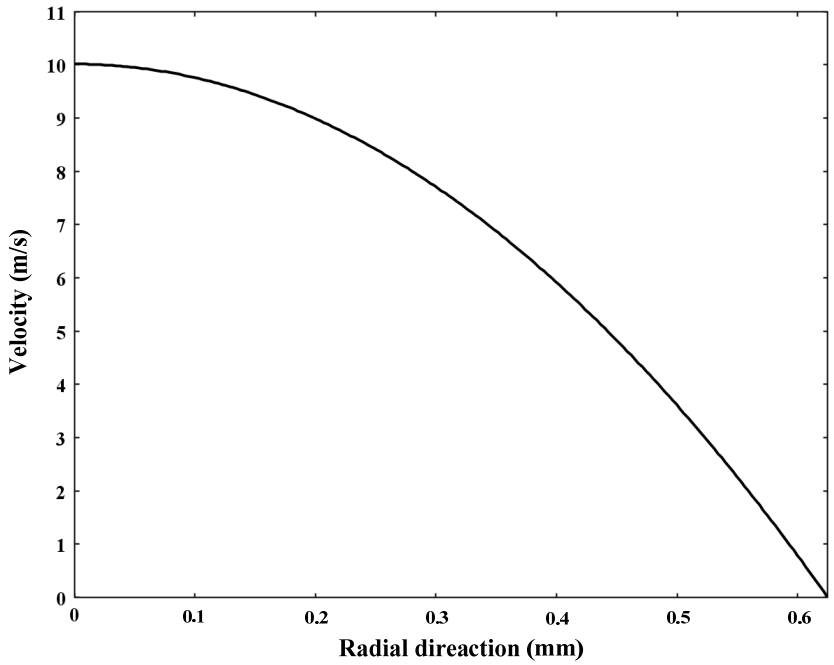


**Figure 4.8** Velocity profile in the radial direction when L = 75 mm.

**(b) Check on Nusselt number at constant wall temperature**

Flat velocity and gas temperature profiles are imposed as an inlet condition to the channel, and a wall temperature of 800 K is set as boundary condition along the channel wall, see Figure 4.7(b). The pre-defined air properties were selected, with air behaving as an ideal gas. For the simulation, the regular mesh size was further refined to give 22,016 elements along the structure modelled. As expected, the temperature of the gas increases along the length of the channel, and the temperature also varies in the radial direction. This is illustrated in Figure 4.9 at different values of L from the inlet to the channel. Making use of the simulation data, local values of the *Nu* number were calculated at various axial distances along the channel. This was achieved by

obtaining from COMSOL information on the average gas temperature at step intervals of 10 mm in the axial direction. Calculating:

$$Q = m \cdot C_P \cdot (T_1 - T_2) \tag{4.29}$$

where $T_1$ is the mass weighted average temperature at Position 1, and $T_2$ is the mass weighted average temperature at Position 2 (a distance of 10 mm from Position 1). Then temperature,

$$T_b = \frac{(T_1 + T_2)}{2} \tag{4.30}$$

then, calculating:

$$h = \frac{Q}{A \cdot (T_s - T_b)} \tag{4.31}$$

where $T_s$ is the average surface temperature of the wall.

Then the Nu number was determined from:

$$Nu = \frac{D \cdot h}{k_f} \tag{4.32}$$

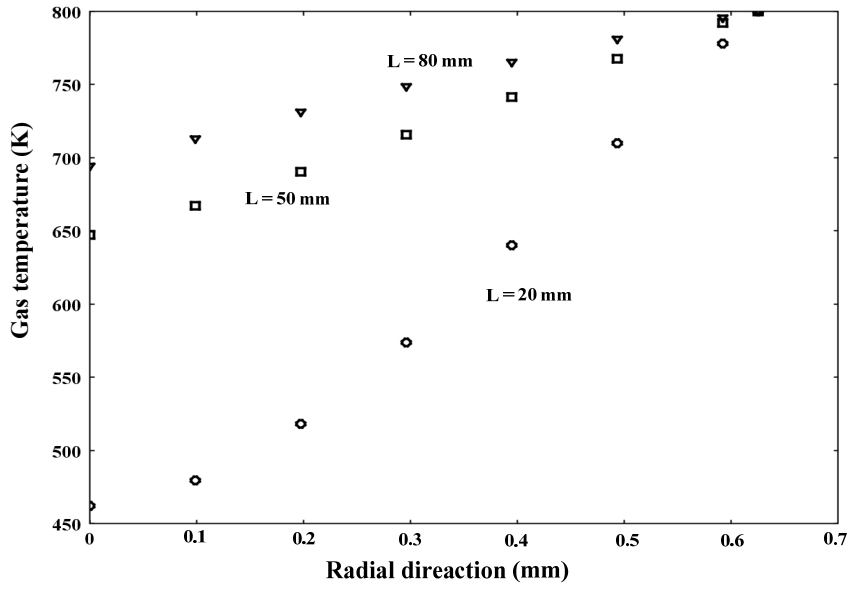


**Figure 4.9** Example of radial temperature profiles at constant wall temperature.

These values are plotted in Figure 4.10. From these values, it can be seen that the Nu number is around a value of 3.4, which is close to the value of 3.657, the reported

analytical solution in Shah and London (1978), for fully developed laminar flow when the wall temperature is constant.

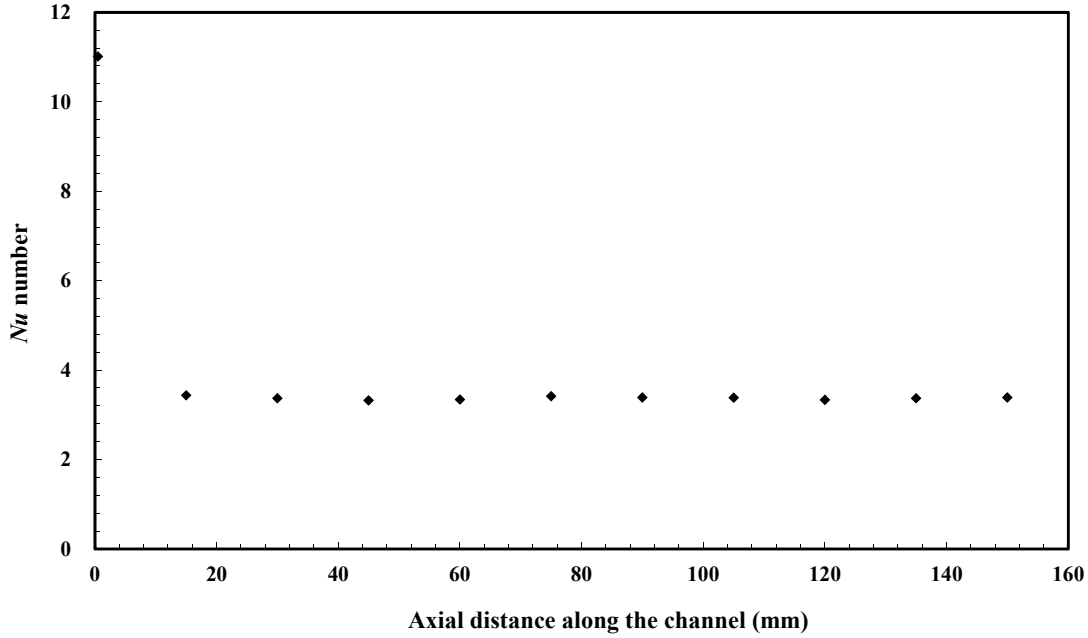


**Figure 4.10** Calculated values of local *Nu* number as a function of channel length with a constant wall temperature.

**(c) Check on the Nusselt numbers at constant heat flux**

Finally, flat velocity and temperature profiles are imposed as an inlet condition to the monolith channel, and now a heat flux of 1000 W $m^{-2}$ is set as a boundary condition along the channel wall, see Figure 4.7(c). For the simulation the regular mesh size was refined to give 22,016 elements. As the wall temperature is higher than the gas temperature, energy will flow from the wall to the gas phase. Some of the results of such a simulation are shown in Figure 4.11. As expected, the gas temperature increases along the length of the channel, and the temperatures vary in the radial direction. Making use of the data from such a simulation, local values of Nu number were calculated at various axial distances along the channel. These values are plotted in Figure 4.12. From these values, it can be seen that the *Nu* number is around a value of 4.3, which is close to the value of 4.364, the reported analytical solution in Shah and London (1978), for conditions of uniform heat flux along the wall.

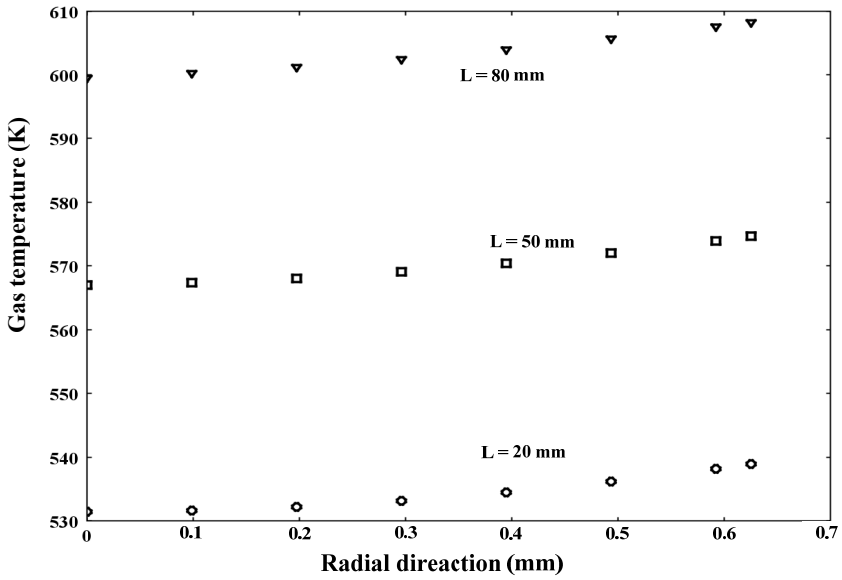


**Figure 4.11** Example of radial temperature profiles at constant wall heat flux.

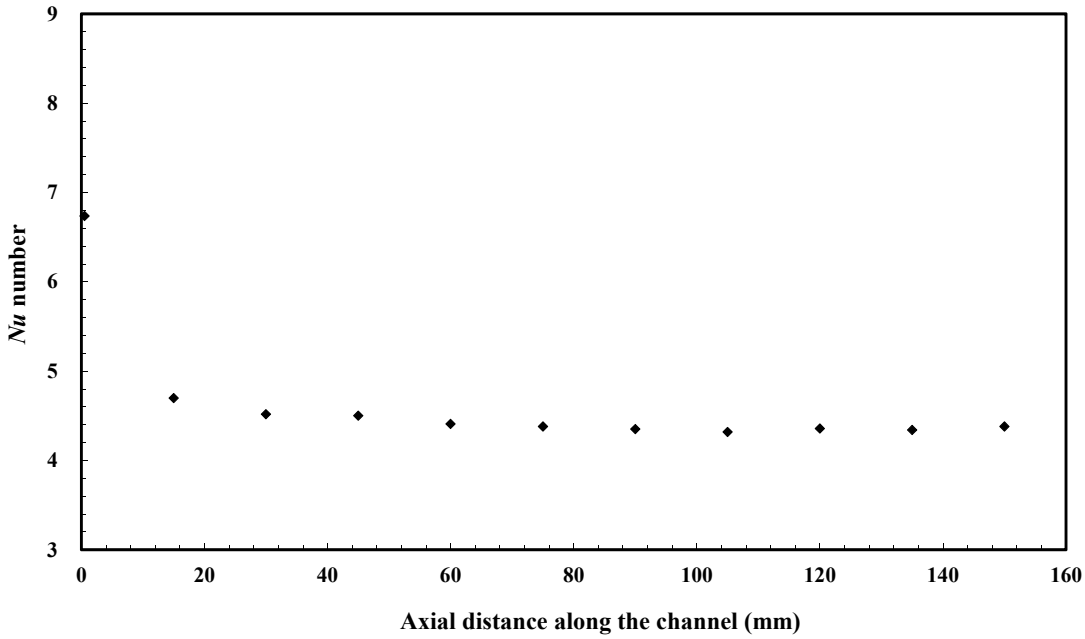


**Figure 4.12** Calculated values of local *Nu* number as a function of channel length with a constant wall heat flux condition.

These three preliminary simulations provide a degree and confidence, that the way in which the COMSOL model is being used is producing sensible results. In the 'velocity profile check', the simulation produces exactly the same parabolic velocity profile along the channel as in the input. Although two simulated *Nu* numbers did not match the literature value exactly, they are very close to each other.

#### 4.3.2.2 Construction of heat transfer model in COMSOL

COMSOL was now used to construct a more complicated model, to simulate some of the heat transfer experiments in Benjamin and Roberts (2001). The space dimension of the model was set as 2-D Axial symmetric. Having set this, the dimension of the square monolith channel had to be converted into a cylindrical channel, and the total mass of solid and flow area in the channel must should the same. This conversion is shown in Figure 4.13.

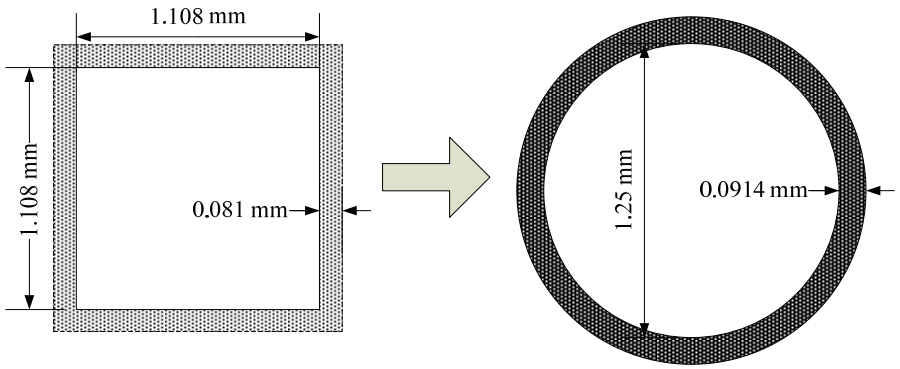


**Figure 4.13** 2-D model in COMSOL, the square shape of the monolith is converted into a cylindrical shape.

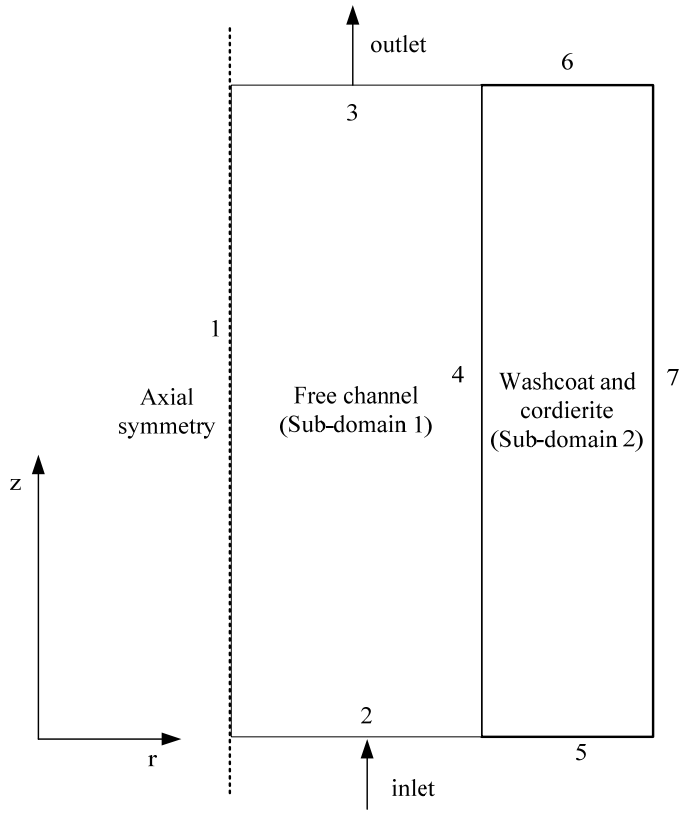


**Figure 4.14** Schematics of the geometry of single channel model in COMSOL Multiphysics.

The geometry of such a channel can be represented in COMSOL, is shown in Figure 4.14. This represents half of the actual geometry of the monolith channel, as the space dimension was set as 'axial symmetric'. Hence only half of the geometry needs to be simulated, and this saves on computation power and simulation time.

Then, the governing equations, inlet and boundary conditions are discussed. The following explanation is provided based on information in the COMSOL Multiphysics Chemical Engineering Module User's Guide (2009; pp. 116 - 236).

**Free channel (Sub-domain 1) setting:**

For the momentum balance, the **Weakly Compressible Navier-Stokes** application mode was chosen. It allows the calulation of local gas density as a function of temperature and pressure, i.e. Non-isothermal flow. It contains the fully compressible formulation of the continuity and the momentum equations:

$$\frac{\partial \rho_g}{\partial t} + \nabla \cdot \left(\rho_g \cdot u\right) = 0 \qquad \rho_g = \rho_g(P,T) \tag{4.33}$$

$$\rho_g \frac{\partial u}{\partial t} + \rho_g \cdot u \cdot \nabla u = -\nabla P + \nabla \cdot \left( \eta \cdot \left(\nabla u + (\nabla u)^T\right) - \left(\frac{2}{3}\eta - k_{dv}\right) \cdot (\nabla \cdot u) \cdot I \right) + F \tag{4.34}$$

where

$$\nabla = \left( \frac{d}{dz} + \frac{d}{dr} \right) \tag{4.35}$$

where $T$ is the absolute temperature in K, $u$ represents the velocity vector in both $r$ and $z$ directions (m $s^{-1}$), $\eta$ was entered as a correlation of viscosity of air, and $P$ is the pressure (Pa). The stress tensor used in Equation (4.35) describes a Newtonian fluid, with an added term $k_{dv}$. This term expresses the deviation from Stokes' assumption, which states that the fluid particles are in thermodynamic equilibrium with their neighours. It is very rare that a fluid shows a significant deviation from Stokes' assumption, and $k_{dv}$ is therefore by default set to zero. $F$ is a body force vector (N $m^{-3}$), and it was set to zero for both $x$ and $y$ directions. The flow was set as "non-isothermal flow"; this couples the density to temperature change. In order to achieve full functionality, the "Galerkin least-squares streamline diffusion" and "Crosswind diffusion" are activated for both the Weakly Compressible Navier-Stokes application

mode and for the Convection and Conduction application mode. The initial velocity in this domain is set to zero, and the initial pressure was set to 101325 Pa.

For the energy balance, both heat conduction and convection were included. In the **Conduction and Convection** application mode, the most general energy balance is one of the compressible Navier-Stokes equations:

$$\rho_g \cdot C_{pg}\left(\frac{\partial T_g}{\partial t} + (u \cdot \nabla) \cdot T_g\right) = -(\nabla \cdot q) + \tau : S - \frac{T_g}{\rho_g} \cdot \frac{\partial \rho_g}{\partial T_g}\Big|_P \left(\frac{\partial P}{\partial t} + (u \cdot \nabla) \cdot P\right) + Q \tag{4.36}$$

Where:

| | | |
|---|---|---|
| $\tau$ | viscous stress tensor | Pa |
| $C_{pg}$ | specific heat capacity at constant pressure | J $kg^{-1}K^{-1}$ |
| $q$ | heat flux vector | $Wm^{-2}$ |
| $Q$ | heat sources | $Wm^{-3}$ |
| $S$ | strain rate tensor: $S = \frac{1}{2} \cdot \left(\nabla u + (\nabla u)^T\right)$ | (4.37) |

The operation ":" is a contraction and can in this case be written in the following form:

$$a : b = \sum_n \sum_m a_{nm} b_{nm} \tag{4.38}$$

The **Convection and Conduction** application mode uses Fourier's law of conduction which states that the heat flux, $q$, is proportional to the temperature gradient:

$$q_i = -k \cdot \frac{\partial T_g}{\partial x_j} \tag{4.39}$$

where $k$ is the thermal conductivity. Inserting Equation (4.39) into Equation (4.36) gives the energy balance used in the **Convection and Conduction** application mode:

$$\rho_g \cdot C_{pg}\left(\frac{\partial T_g}{\partial t} + u \cdot \nabla T\right) = \nabla \cdot \left(k_g \cdot \nabla T_g\right) + Q \tag{4.40}$$

The second and third terms on the right-hand side of Equation (4.36) are usually small and are not included by default. The other heat source $Q$ was set to zero.

The thermal conductivity of air was entered as a correlation with temperature, is:

$$k_g = 1.679\times10^{-2} + 5.073\times10^{5} T_g \ (\text{W m}^{-1}\ \text{K}^{-1}) \qquad (4.41)$$

The heat capacity of air $C_{pg}$ was also a correlation with temperature, as shown in Euqation (4.24). The initial temperature of gas was set to room temperature 297 K.

**Sub-domain 2(Solid phase) setting:**

Since there is no gas flow inside the solid phase, the **Weakly Compressible Navier-Stokes** application mode is not activated for the solid phase.

In the **Conduction and Convection** application mode, the solid domain uses the same energy balance equation as gas phase, see Equation (4.40). The physical parameters of solid wall are presented in Table 4.3.

$$\rho_s \cdot C_{ps}\left(\frac{\partial T_s}{\partial t} + u\cdot\nabla T_s\right) = \nabla\cdot\left(k_s\cdot\nabla T_s\right) + Q \qquad (4.42)$$

**Table 4.3** The typical physical parameters used by Benjamin and Roberts (2001) for CFD simulation.

| Parameters | Values |
|---|---|
| Heat capacity of wall (J $kg^{-1}K^{-1}$) | 1100 |
| Wall density (kg $m^{-3}$) | 1750 |
| Wall conductivity (W $m^{-1}K^{-1}$) | 1.4 |
| Channel area ($mm^2$) | $1.108^2$ |
| Cell density (cells $cm^{-2}$) | 62 |
| Porosity (%) | 76.0 |

**Boundary conditions**

Boundary 1 is the axial symmetric boundary for both momentum and energy balances.

Boundary 2 is the inlet boundary, where the inlet gas temperature and velocity are defined. The inlet gas temperature was entered as a 9th order polynomial equation that matched the temperature ramp:

$$T_{g\_inlet}(t) = 1.0282\times10^{-13}\cdot t^9 - 2.2632\times10^{-11}\cdot t^8 + 2.8276\times10^{-9}\cdot t^7 + 4.9294\times10^{-7}\cdot t^6 - 9.7859\times10^{-5}\cdot t^5 + 0.0059\cdot t^4 - 0.1492\cdot t^3 + 1.0497\cdot t^2 + 16.5493\cdot t + 298.5 \tag{4.43}$$

The initial velocity in the *r* direction was set to zero; and a parabolic velocity profile was imposed in the *z* direction which is a function of *r*:

$$u_0 = 2\cdot u_{\text{mean}}\cdot\left(1-\left(\frac{r}{R}\right)^2\right) \tag{4.44}$$

Boundary 3 is the outlet boundary. For the energy balance, it was set as "convective flux" so the conduction was ignored. For the momentum balance, it was set as "no viscous stress", so that:

$$n\left(\eta\cdot\left(\nabla u+(\nabla u)^T\right)-\left(\frac{2}{3}\eta-k_{dv}\right)\cdot(\nabla\cdot u)\cdot I\right)=0 \tag{4.45}$$

In all expressions, *n* denotes the unit vector normal to the boundary, pointing outward from the computational domain, and the pressure was set to 101325 Pa.

Boundary 4 is the wall boundary. The no slip wall assumption was assumed so that the gas velocity at the wall was zero. For the energy balance, this boundary setting cannot be edited.

For Boundaries 5, 6 and 7, adiabatic condition was assumed so that they are thermally insulated from surroundings. These boundaries are not active in the momentum balance because there is no gas flowing inside the solid wall.

**Solver**

**UMFPACK** direct solver was used. It is a highly efficient solver for non-symmetric system. **Backward differentiation formula (BDF)** time stepping method was used. It is a multistep formula based on numerical differentiation for solutions to *ordinary differential equations*. A BDF method of order *n* computes the solution using an *n*th-grade polynomial in terms of backward differences. The degree of the interpolating polynomial used was set between 1 to 5 (default setting).

**Results**

An experiment was simulated, where the inlet air temperature was increased from 299 to 545K in 50 s, and the monolith substrate was warmed-up by the gas. Using a mesh of 50,486 elements, the model was solved. The number of degrees of freedom (solved for) was 295,474, and the simulation time was 917 s. The simulation results from the COMSOL model are compared with those from the MATLAB Code III, and the experimental results and CFD simulations in Benjamin and Roberts (2001). Solid temperature profiles along the monolith after 10 and 50 s are plotted in Figure 4.15.

As can be seen from Figure 4.15(a), the COMSOL model closely matches the results from MATLAB Code III and also the CFD results in Benjamin and Roberts (2001). Small variations may result from differences in modelling strategies and physical parameters used. This simulation exercise provided confidence in the way the 2-D heat transfer model had been constructed in COMSOL.

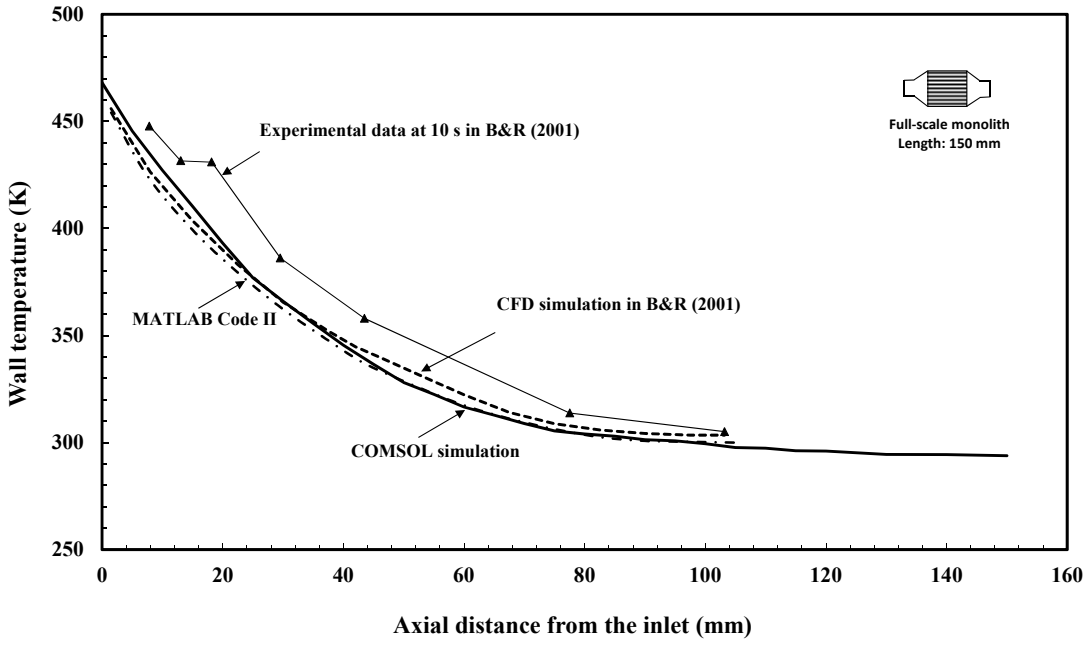


(**a**,10 s)

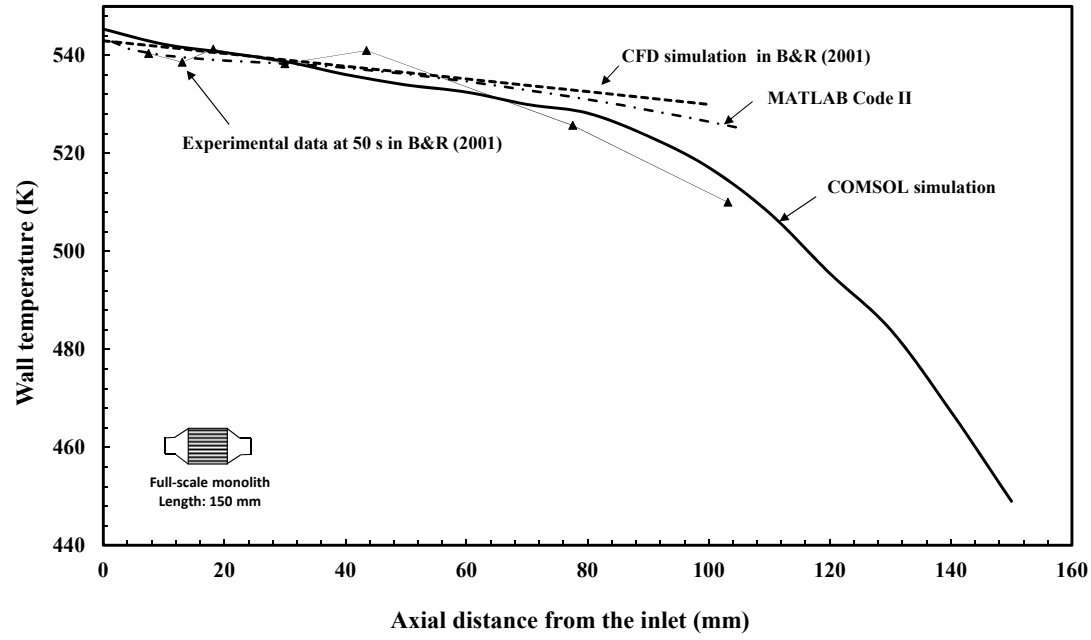


**(b,** 50 s**)**

**Figure 4.15** Temperature of the solid wall as a function of axial distance: (a) after 10 s, and (b) after 50 s.

## 4.4 Case Study 2: Non-reacting heat transfer experiment

When a mathematical model is constructed of a DOC, it is essential to ensure that the method used to model the basic heat transfer aspects is appropriate. Otherwise, as the reactions are exponentially dependent on temperature, small errors in temperature can have a significant effect on the method of calculating reaction rates, especially under transient conditions. Therefore, a heat transfer experiment was designed to validate the heat transfer models by monitoring the thermal response of a non-reacting monolith substrate to a 'ramp' in the temperature of the inlet gas.

### 4.4.1 Warm-up experiment using a hot air rig

**Experimental set-up**

This experiment was a non-engine experiment. Air was supplied by a hot air supply unit and used to simulate the exhaust gas. The air supply system is called a "Charging Air Handing Unit", and it was originally designed to investigate the performance of a turbo charger on a diesel engine. More detailed information on this air supply system is shown in Akehurst and Piddock (2008). This apparatus is controlled by a specially developed in-house program, through which the conditions for the supply of air are set, e.g. air mass flowrate, temperature and pressure. Air is fed from the compressed air supply in the test cell. A manual valve controls the amount of air intake, and the air pressure can be reduced through a pressure-reduction valve (PRV) (as the compressed air is supplied at 6 bar). By either controlling the main air inlet valve, or the dump valve connected with the air mass flowmeters (AFM), the desired air mass flowrate can be achieved. Similarly, the desired outlet air temperature can be achieved by either controlling the heating element (12 KW) or the balance value, which regulates air temperature through mixing. All of these controlling mechanisms are automatically regulated by the computer program. However, it did not work as originally planned. It struggled to heat the air temperature higher than 110 $^{o}$C. Nevertheless, a few experiments were performed with smaller temperature step changes and this was adequate.

In order to prevent any possible reactions, the monolith cordierite substrate was used. The physical properties of the monolith are close to the DOC. The monolith housed in a metal can was wrapped with insulation to maintain adiabatic conditions.

The pre- and post- monolith temperature was measured by two 1 mm K-type thermocouples. The wall temperature was monitored by twenty 0.5 mm K-type thermocouple at both axial and radial positions in the monolith wall.

**Experimental procedures**

The hot air rig was first set to run at a constant air mass flowrate (100 kg $h^{-1}$) and constant temperature (310 K) until steady-state was reached, i.e. the monolith has the same temperature as the inlet air temperature. Then a step change in the inlet gas temperate was made from 310 to 410 K in a specified time period of 20 s. The system was left running until steady-state was achieved. This experiment was also repeated at air mass flowrates of 200 and 300 kg $h^{-1}$. The experiment conditions are summarised in Table 4.4.

Table 4.4 Example of experimental conditions.

| | **Air mass flow (kg $h^{-1}$)** | **Temperature ramp (K)** | **Experiment duration (s)** |
|---|---|---|---|
| 1 | 100 | 310 to 410 in 20 s | 200 |
| 2 | 200 | 310 to 410 in 20 s | 200 |
| 3 | 300 | 310 to 410 in 20 s | 200 |

**Data processing: time alignment of temperature data**

Good time alignment is vital when the experimental data is analysed. The inlet gas temperature ramp is an important input in mathematical models that simulate the warm-up process. As described in Section 3.1.3, the inlet gas temperature thermocouple was placed 60 mm from the actual inlet of the monolith, so this would create a small time delay. This time delay consists of two parts, namely the response of the thermocouple, and the time to reach actual inlet to the monolith. Usually the response of the thin thermocouple is almost instant, and can be neglected. Therefore, the time delay becomes dependent on the transport time. A sample calculation is performed to determine the significance of the time delay.

Air flows into the monolith at a mass flowrate of 100 kg $h^{-1}$ and it was generally heated up from 50 to 150 $^{o}$C within 20 s.

Density of air at 50$^{o}$C:

$$\rho_{air} = \frac{p\,M_{air}}{R_g T} = \frac{101325 \times 0.029}{8.314 \times (273+50)} = 1.094\,\frac{kg}{m^3} \tag{4.46}$$

Volumetric flow of air at 50°C:

$$V_{air} = \frac{m_{air}}{\rho_{air}} = \frac{100}{3600 \times 1.094} = 0.0254\,\frac{m^3}{s} \tag{4.47}$$

$$u_{air} = \frac{V_{air}}{A} = \frac{0.0254}{0.75 \times \pi \times 0.053^2} = 3.787\,\frac{m}{s} \tag{4.48}$$

$$t_{transport} = \frac{L}{u_{air}} = \frac{0.06}{3.787} = 0.016\,s \tag{4.49}$$

According to this sample calculation, the time delay of the thermocouple would be insignificant compared to the frequency of data recording which is 1 *Hz*.

**Experimental results and simulations**

An experiment was performed with an air mass flowrate of 100 kg $h^{-1}$, and it was simulated using both MATLAB Code III and 2-D heat transfer COMSOL model. Some of the characteristics of monolith substrate, and operating conditions are summarised in Table 4.5.

**Table 4.5** Operating conditions and physical parameters of monolith substrate.

| Parameters | Values |
|---|---|
| Cordierite density (kg $m^{-3}$) | 1700 |
| Cordierite conductivity (W $m^{-1}K^{-1}$) | 1.4 |
| Substrate length (mm) | 114 |
| Substrate width (mm) | 105.7 |
| Channel area ($mm^2$) | 1.108×1.108 |
| Cell density (cells $cm^{-2}$) | 62 |
| Initial gas temperature (K) | 310 |
| Air mass flowrate (kg $h^{-1}$) | 100 |
| Initial wall temperature (K) | 303 |
| Time (s) | 90 |

The inlet gas temperature was represented by a polynomial equation ($9^{th}$ order, generated by MATLAB Curve fit tool) providing a best-fit curve to the experimental data (see Figure 4.16).

$$T_{g\_inlet}(t) = -3.8786\times10^{-14}\cdot t^{9} + 1.6201\times10^{-11}\cdot t^{8} - 2.8035\times10^{-9}\cdot t^{7} + 2.573\times10^{-7}\cdot t^{6} - 1.314\times10^{-5}\cdot t^{5} + 0.0034\cdot t^{4} - 0.0017\cdot t^{3} + 0.1222\cdot t^{2} + 3.2078\cdot t + 309.65 \quad (4.50)$$

Using Equation (4.50) as an inlet condition, and with an air mass flow of 100 kg $h^{-1}$, a number of simulation results are compared with experiment results in Figures 4.17 to 4.20. In the simulations with MATLAB Code III, the *Nu* number was determined from:

$$Nu_H = 3.095 + 8.933\left(\frac{1000}{Gz}\right)^{-0.5386}\exp\left(-\frac{6.7275}{Gz}\right) \quad (4.51)$$

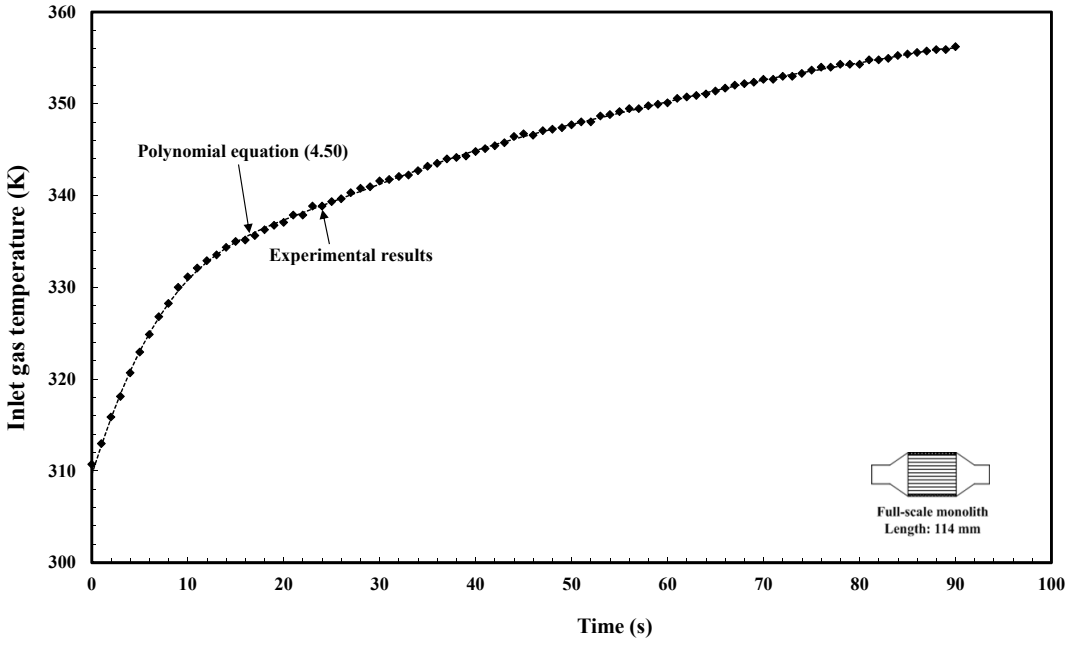


**Figure 4.16** Gas inlet temperature (z = 0 mm) as a function of time (experimental and polynomial equation).

Figure 4.17 shows the outlet gas temperature as a function of time. It can be seen that, both the COMSOL and MATLAB Code III models captured the general trend in the transient behaviour of the monolith as the inlet gas temperature was increased. However, the simulated temperature profiles are lower in the first 30 s, and then become higher. The MATLAB Code III model predicts slightly higher outlet gas temperature than the COMSOL model. The discrepancy between the simulations and

experimental results may be attributed to a heat loss, as the outlet gas temperature was measured about 10 cm downstream of the monolith outlet.

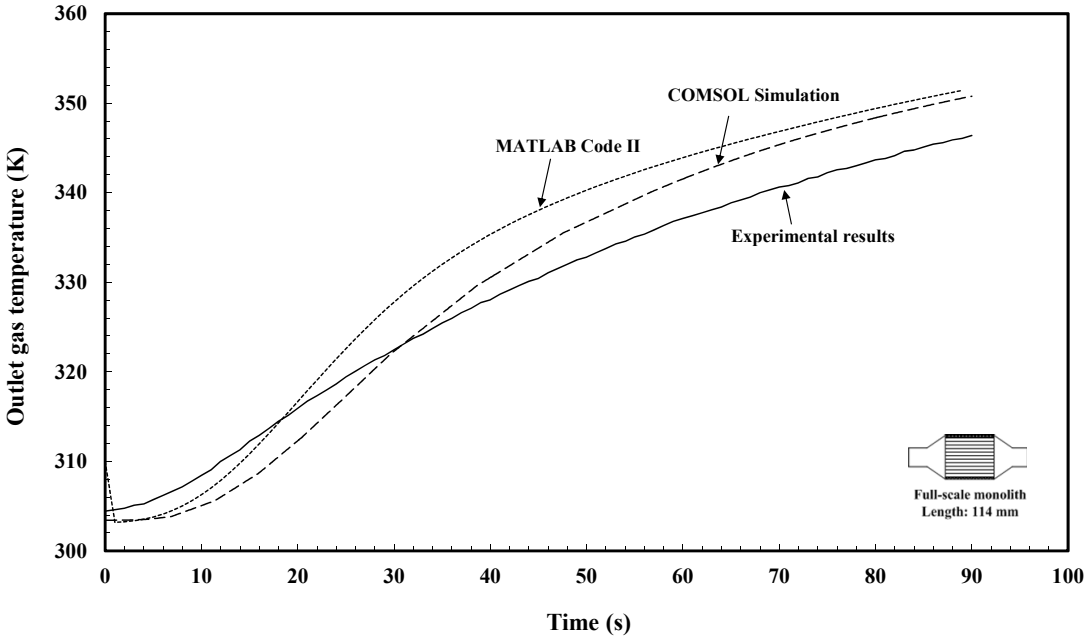


**Figure 4.17** Outlet gas temperature as a function of time. Simulation results from MATLAB and COMSOL are compared with experimental results (MATLAB Code III using a time step $\Delta t = 1\times10^{-3}$ s, and a step length $\Delta z$ =1 mm).

Figures 4.18 to 4.20 show the monolith wall temperature as a function of axial distance at $t$ = 10, 50 and 90 s, from which a number of observations/conclusions can be formed:

- In all three figures, the wall temperature profiles measured at the two different radial positions (r = 0 and r = 46 mm) are close to one another confirming that the assumption of no radial heat loss is reasonable, and that the use of a single channel model is therefore also acceptable.
- In all three figures, the simulations capture the trend in the monolith wall temperature profiles. However, the models predicted higher wall temperature profiles than measured.
- Comparing the simulation results, using COMSOL mode lower wall temperature profiles were predicted which is consistent with observations made earlier in Section 4.3.2.

Although the simulation results do not exactly match the experiments, they do capture the trends in outlet gas temperature and the wall temperature profiles. On

further investigation, the discrepancies were attributed to the experimental technique, as it was shown that the air flow controller needed to be re-calibrated. However, these experiments were useful, as experience was gained which could then be used in the next experiment.

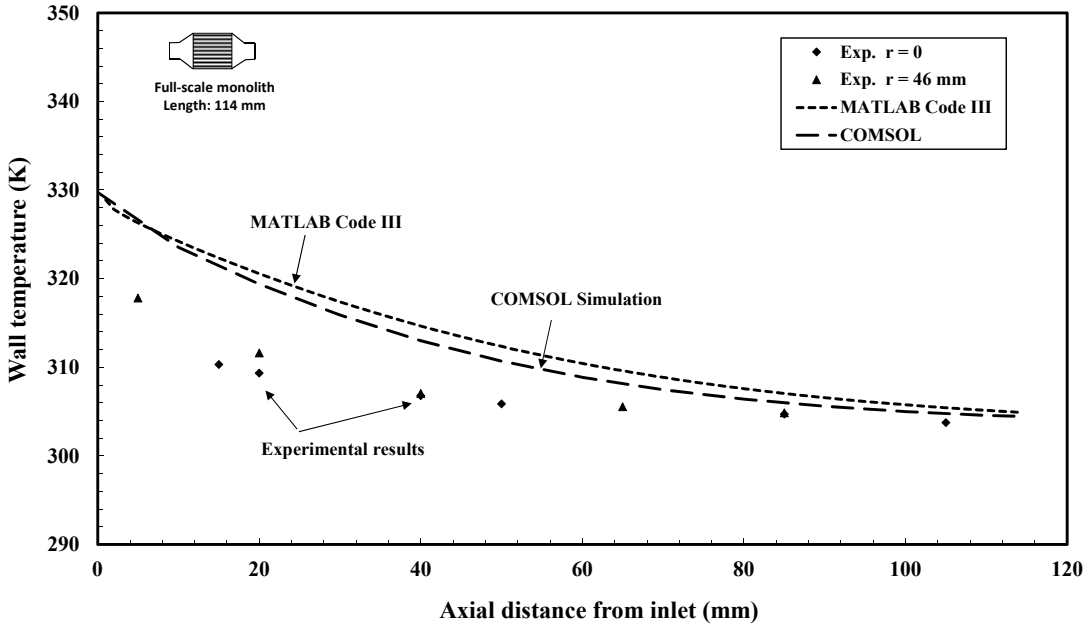


**Figure 4.18** Monolith wall temperature as a function of axial distance when t = 10 s. Exp. r = 0 means the measured temperature profile at centre of the substrate. Exp. r = 46 mm means the measured wall temperature profile at r = 46 mm.

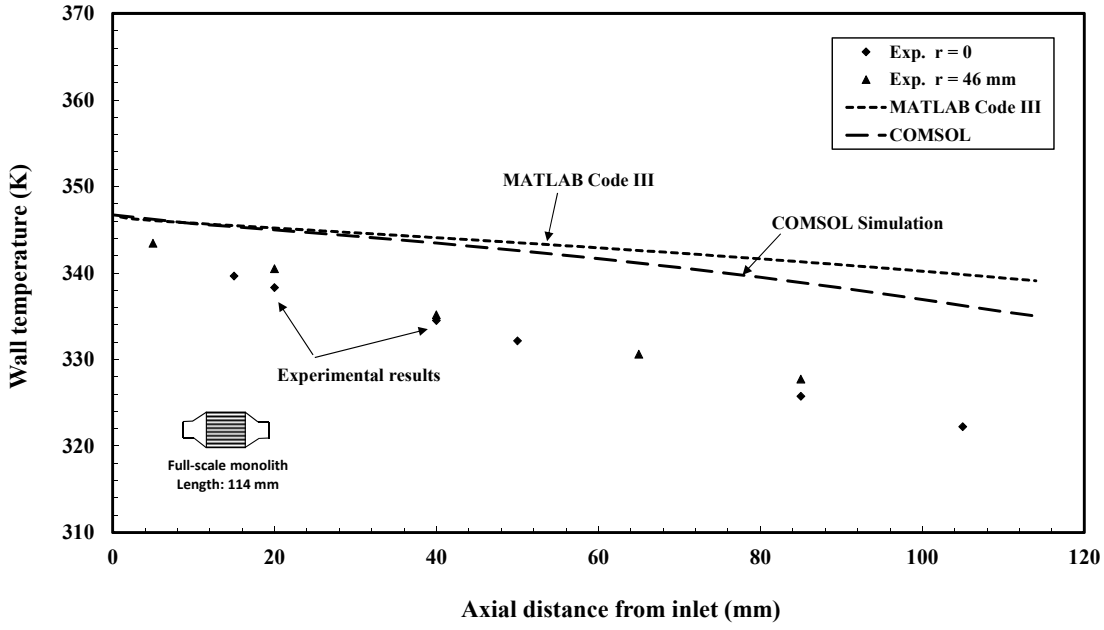


**Figure 4.19** Monolith wall temperature as a function of axial distance when t = 50 s. Exp. r = 0 means the measured temperature profile at centre of the substrate. Exp. r = 46 mm means the measured wall temperature profile at r = 46 mm.

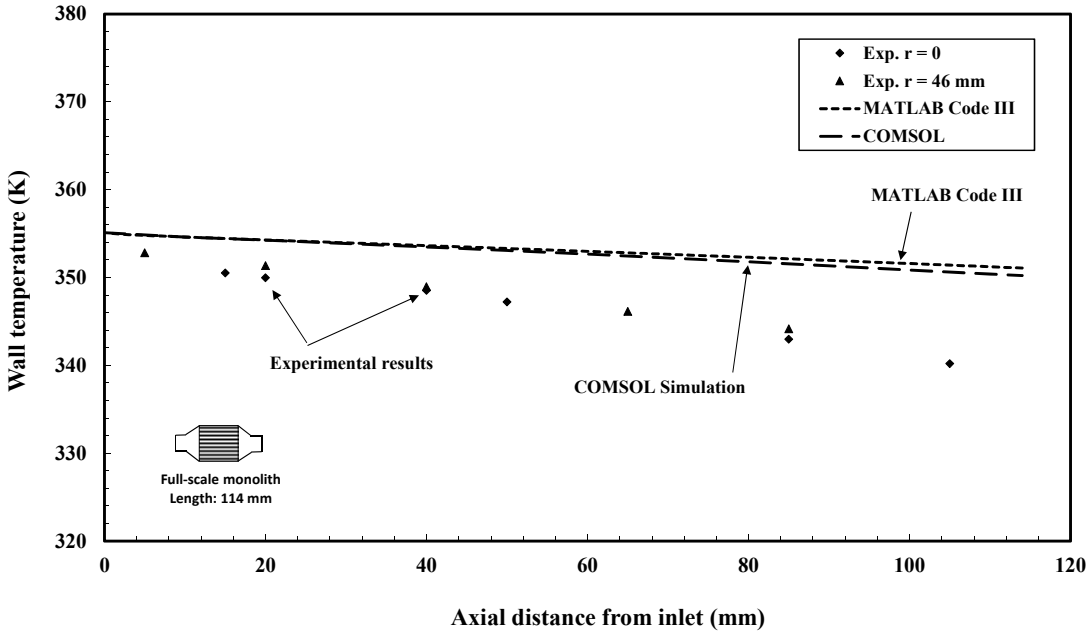


**Figure 4.20** Monolith wall temperature as a function of axial distance when t = 90 s. Exp. r = 0 means the measured temperature profile at centre of the substrate. Exp. r = 46 mm means the measured wall temperature profile at r = 46 mm.

### 4.4.2 Warm-up experiment using the diesel engine

**Experimental set-up**

A monolith warm-up experiment was performed using a Full-scale monolith substrate connected to the diesel engine. There was no catalyst on the monolith substrate to avoid the initiation of chemical reactions.

To perform the experiment, the engine was operated at constant speed of 2000 rpm, and an initial engine torque of 5 Nm. When the system reached steady-state, the engine toque was ramped up to 45 Nm in 300 s. As the torque ramps up, the inlet gas temperature increased from 420 to 540 K. During the experiment, the wall temperatures and the outlet gas temperature were recorded.

**Model set-up**

The 2-D COMSOL model developed in Section 4.3.2, was modified to simulate this experiment. The physical parameters and operating conditions are summarised in Table 4.6.

**Table 4.6** Summary of operation conditions and physical parameters of JM substrate.

| Parameters | Values |
|---|---|
| Cordierite density (kg $m^{-3}$) | 1700 |
| Cordierite conductivity (W $m^{-1}K^{-1}$) | 1.4 |
| Cordierite heat capacity (J $kg^{-1}K^{-1}$) | 800 |
| Substrate length (mm) | 114 |
| Substrate width (mm) | 105.7 |
| Channel area ($mm^2$) | $1.108^2$ |
| Cell density (cells $cm^{-2}$) | 62 |
| Initial wall temperature (K) | 420 |
| Mean velocity (m $s^{-1}$) | 3.2 |
| Time (s) | 800 |

The inlet gas temperature was entered as a 9th order polynomial equation, which provides a best-fit curve to the measured inlet gas temperature, see Equation (4.51).

$$T_{g\_inlet}(t) = 1.97\times10^{-22}\cdot t^9 - 8.384\times10^{-19}\cdot t^8 + 1.51\times10^{-15}\cdot t^7 - 1.508\times10^{-12}\cdot t^6 + 9.06\times10^{-10}\cdot t^5 - 3.3\times10^{-7}\cdot t^4 + 6.93\times10^{-5}\cdot t^3 - 7.09\times10^{-7}\cdot t^2 + 0.485\cdot t + 431.62 \quad (4.52)$$

Similarly, since the actual engine exhaust flow slightly changed with time, a 6th order polynomial equation was curve fitted:

$$F(t) = 7.21\times10^{-17}\cdot t^6 - 2.64\times10^{-13}\cdot t^5 + 3.43\times10^{-10}\cdot t^4 - 1.934\times10^{-7}\cdot t^3 + 3.7\times10^{-5}t^2 + 4.532\times10^{-3}\cdot t + 15.79 \quad (4.53)$$

The physical properties of the exhaust gas were assumed to be represented by air.

**Experimental results and simulations**

In Figures 4.21 to 4.25, some of the simulation results are compared with experimental data.

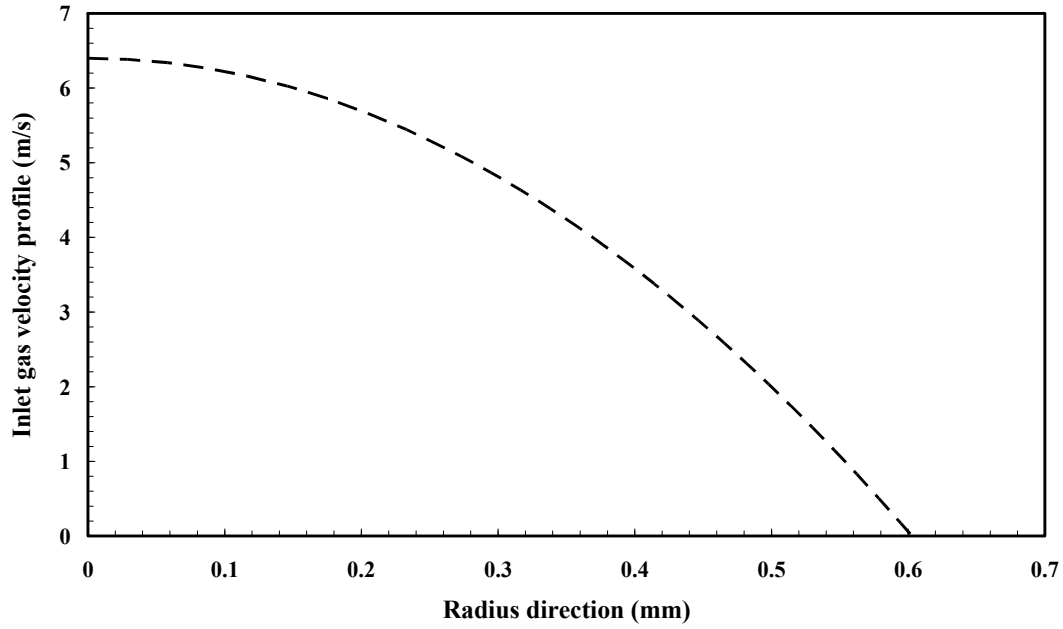


**Figure 4.21** Inlet gas velocity profile at t = 0 s (simulated by 2-D COMSOL model).

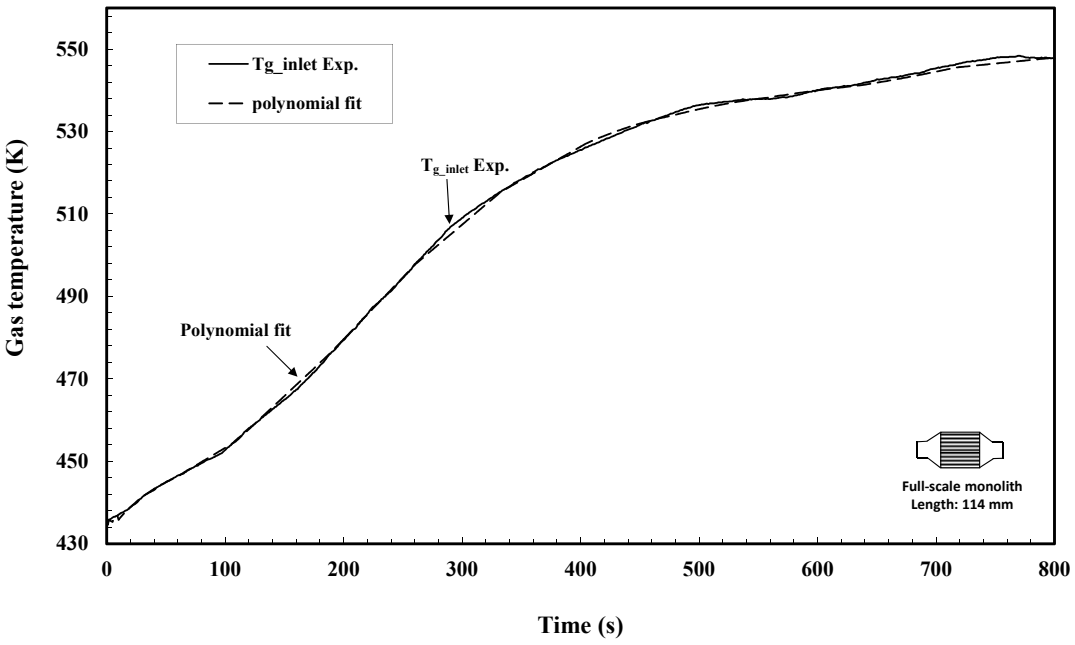


**Figure 4.22** Gas inlet temperature: comparison of measured and curve fitted polynomial (z = 0 mm) as a function of time.

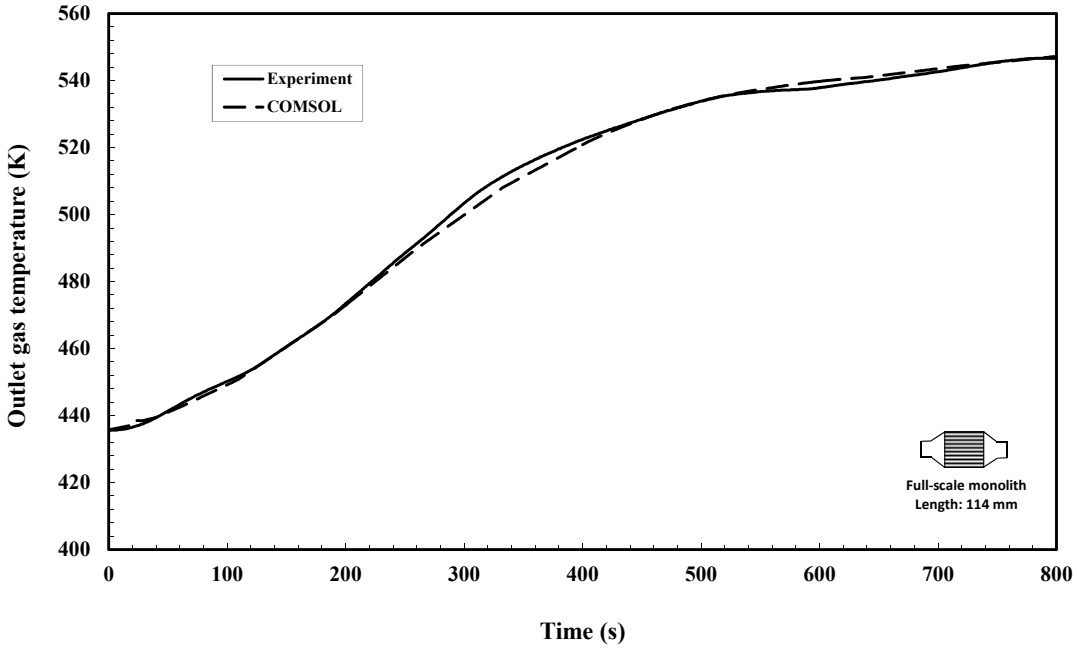


**Figure 4.23** Gas outlet temperature: comparison of measured and simulated values (z = 114 mm).

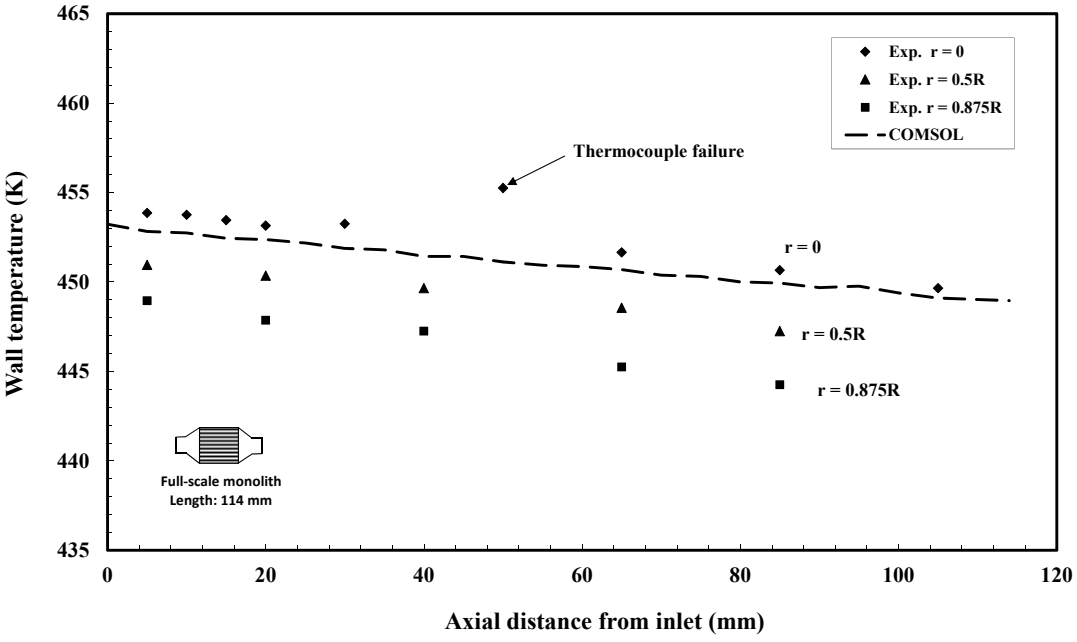


**Figure 4.24** Monolith wall temperature: comparison of measured and simulated value when t = 100 s. The "Exp. r = 0.5R" means the axial temperature profile at 1/2 radius of the monolith.

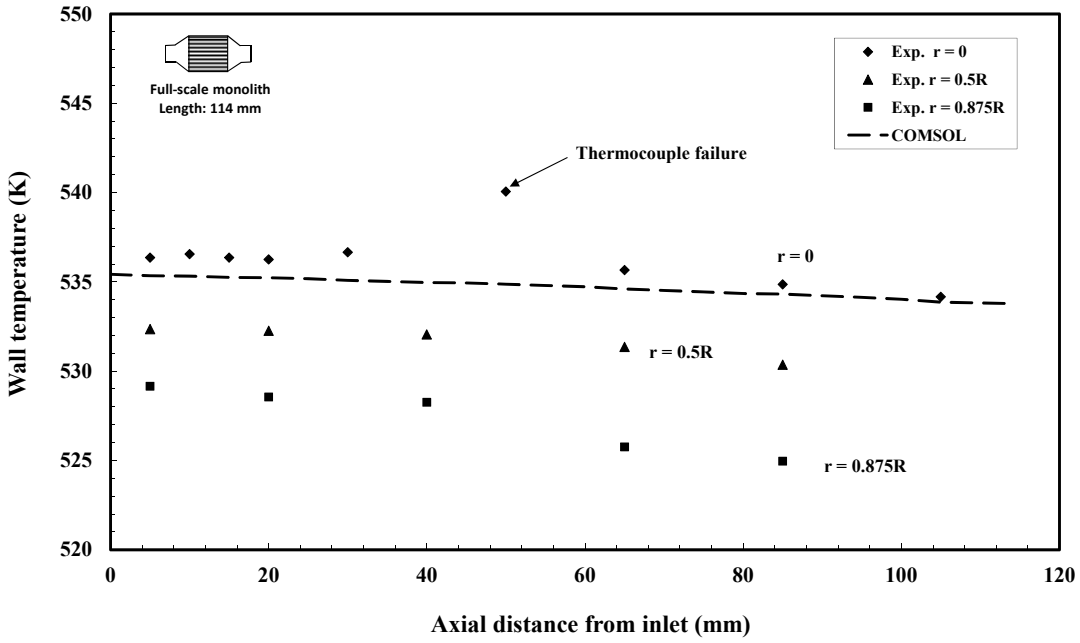


**Figure 4.25** Monolith wall temperature: comparison of measured and simulated value when t = 500 s. The "Exp. r = 0.5R" means the axial temperature profile at 1/2 radius of the monolith.

From Figure 4.23 the simulated outlet gas temperature provides a good match with the experimental results.

Figures 4.24 and 4.25 show the temperature profile of the substrate along axial direction of the substrate at 100 and 500 s, respectively. As expected, the axial wall temperature profiles are higher at the front and lower at the rear of the monolith. In addition, the axial wall temperature profile in Figure 4.25 is relatively flatter than that in Figure 4.24 – this is expected as it has been warmed-up longer (t = 500 s).

The presence of radial wall temperature profiles is interesting and may be attributed to:

(a) radial heat loss, and/or

(b) flow maldistribution because of the way in which the gas enters the monolith, from the exhaust inlet cone.

Although in these figures these radial variation may appear large (because of scale), actually they are relatively small (± 5 K) when compared with temperature variations during catalyst light-off in a Full-scale DOC.

Figure 4.26 shows the simulated pressure profiles along the axial direction of substrate at t = 0 and 800 s. The pressure drop at t = 800 s is greater than the pressure

drop as t = 0 s, because the gas velocity at t = 800 s is higher than at t = 0 s due to higher exhaust gas mass flowrate and temperature. The simulated pressure drop (approximately 0.2 kPa) from the COMSOL simulation is much smaller than the measured pressure drop in the experiment (approximately 0.4 to 0.9 kPa). This difference is not surprising, as in the real installation the flow pattern will be more complex as the gas enters and leaves the exhaust can. The presence of small pulsations from the engine (discussed earlier in Section 2.2), will also have an effect.

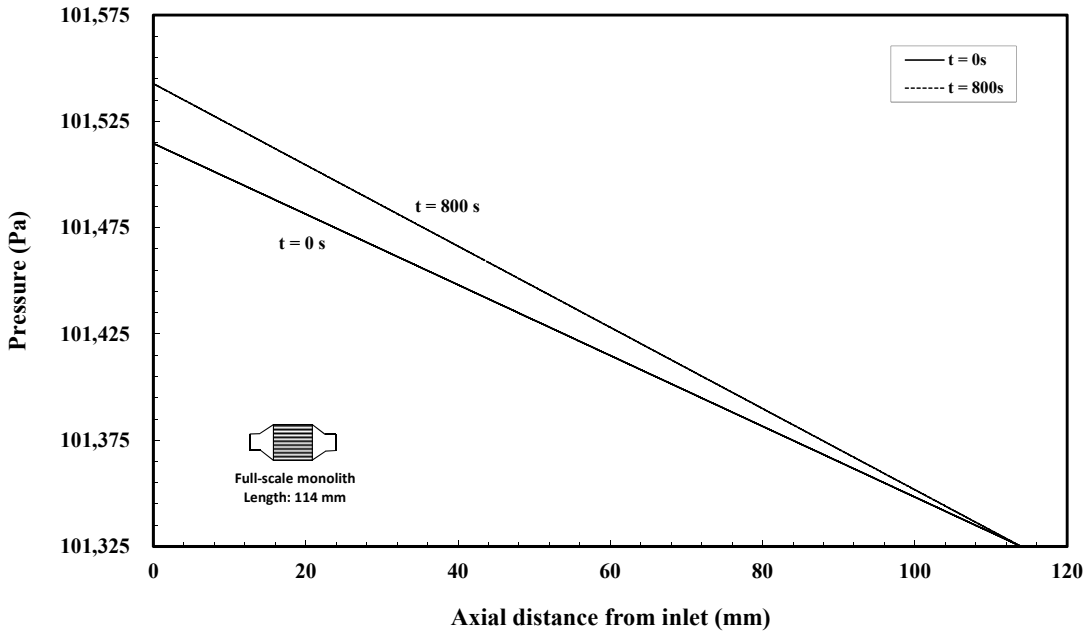


**Figure 4.26** Pressure profiles along the monolith channel. In the COMSOL simulation the outlet pressure was assigned as atmospheric pressure (101325 Pa).

In conclusion, it has been shown how the results of experiments on a live diesel engine, can be used to help validate some of the heat transfer aspects in a mathematical model of a DOC.

## 4.5 Case Study 3: Catalytic combustion of propane (steady-state)

Having gained experience with the use of COMSOL to model transient heat transfer in a monolith, the package was then used to include chemical reactions. Two simple flowsheets are then used to illustrate the structure of this model in Figures A28 and A29, in Appendix 8.4. In order to compare such simulations with published data, the catalytic combustion of propane was simulated. To ensure that the method of constructing this model has been implemented correctly in the COMSOL, this was compared with simulations in Hayes and Kolaczkowski (1997; pp. 324-325).

### 4.5.1 Model construction

The physical dimensions of the monolith channel and the physical properties of the gas and solid phases were taken from Hayes and Kolaczkowski (1997; pp. 310-324).

**Model setting**

The catalytic combustion of propane in a single monolith channel is illustrated in Figure 4.27. A mixture of air and propane is fed into the channel, and the gases reacted in the catalytic washcoat layer. A 2-D model was selected and following the same procedure as described in Hayes and Kolaczkowski (1997; pp. 310-313) the actual geometry of the monolith channel was converted into a cylindrical shape (see Figure 4.28). In the 2-D axisymmetric geometries in COMSOL Multiphysics, the *x*-axis represents the radial direction, and the *y*-axis represents the distance along the channel. The physical dimensions of the channel and the inlet conditions are summarised in Table 4.7.

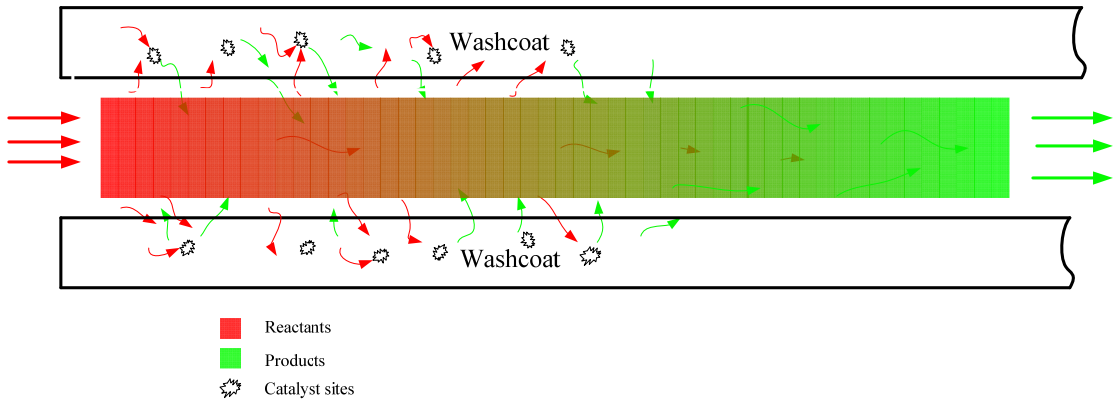


**Figure 4.27** Schematic of the catalytic combustion process inside a single monolith channel (wall coated with washcoat + catalyst).

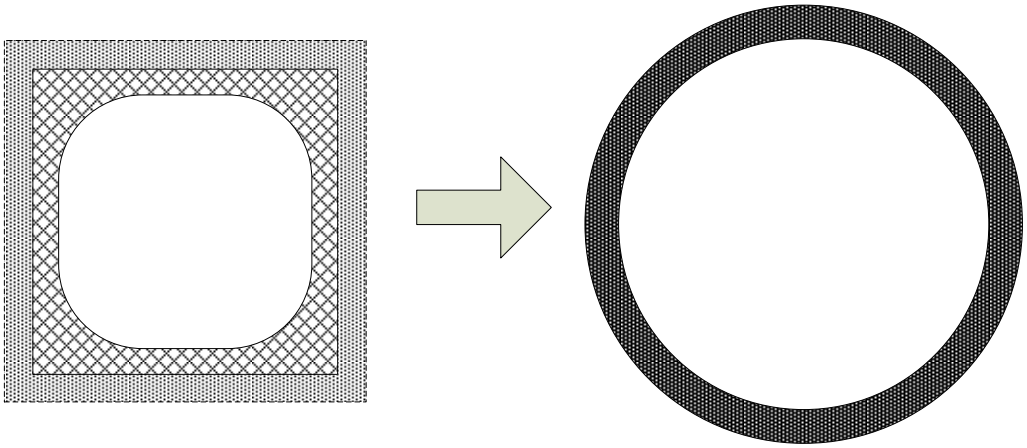

**Figure 4.28** Converting the actual geometry into a cylindrical shape.

**Table 4.7** Physical dimensions of the monolith/washcoat modelled.

| | |
|---|---|
| Actual physical dimensions of monolith channel | |
| Reactor length | 50 mm |
| Inside channel width (uncoated) | 1.1 mm |
| Wall thickness between channels | 0.15 mm |
| Washcoat cross-sectional area | 0.175 $mm^2$ |
| Free channel area | 1.035 $mm^2$ |
| Wetted parameters of channel (with washcoat) | 3.8 mm |
| Physical dimensions of the monolith channel after conversion | |
| Diameter of the channel | 1.21 mm |
| Effective thickness of the washcoat | 0.46 mm |
| Effective thickness of the substrate | 0.93 mm |
| Inlet conditions | |
| Inlet mole fraction propane | 0.002 |
| Inlet air velocity | 0.5, 1.0 and 2.0 m/s (STP) |
| Initial wall and gas temperature | 650 K |
| Pressure | 101.3 kPa |

**Reaction conditions**

The combustion of propane can be described as:

$$C_3H_8 + 5O_2 \rightarrow 3CO_2 + 4H_2O \tag{4.54}$$

Using the rate expression in the example in Hayes and Kolaczkowski (1997; p. 320):

$$(-R_{C_3H_8}) = 2.4\times10^5 \exp(-\frac{1.08\times10^4}{T})\, C_{C_3H_8}\ \frac{\text{mol}}{\text{m}^2\cdot s} \tag{4.55}$$

where $(-R_{C_3H_8})$ is reaction rate of propane, $T$ is the local temperature of the solid phase, and $C_{C3H8}$ is the local concentration of propane. However, in COMSOL, the reaction rate expression is presented based on reactor volume rather than on the basis of surface area. Making use of information presented in Table 4.7, the ratio of surface area to the volume of the solid phase was determined. In this case, the washcoat and the substrate were considered as a single phase, having an effective thickness of 0.139 mm, and the ratio was calculated:

$$\frac{A_s}{V_s} = \frac{W_p\, L}{(A_T - A_c)\, L} = \frac{W_p}{\frac{\pi\,(D+2\delta_w)^2}{4} - \frac{\pi D^2}{4}} = \frac{3.8}{\frac{\pi\,(1.21+2\times0.139)^2}{4} - \frac{\pi\,1.21^2}{4}}$$
$$= 6.454\,\frac{mm^2}{mm^3} = 6454\,\frac{m^2}{m^3} \tag{4.56}$$

then Equation (4.54) was adjusted to form:

$$(-R_{C_3H_8})_v = 2.4\times10^5 \exp(-\frac{1.08\times10^4}{T}) C_{C_3H_8}\ \frac{\text{mol}}{\text{m}^2\cdot s}\times 6454\,\frac{\text{m}^2}{\text{m}^3}$$
$$= 1.55\times10^9 \exp(-\frac{1.08\times10^4}{T}) C_{C_3H_8}\ \frac{\text{mol}}{\text{m}^3\cdot s} \tag{4.57}$$

**Heat of reaction**

This was expressed as a function of temperature using the equation derived in Hayes and Kolaczkowski (1997; p. 321).

$$H_{C_3H_8} = -2.059\times10^6 + 72.3\times10^{-2}T - 9.69\times10^{-2}T^2 + 4.34\times10^{-5}T^3 - 7.56\times10^{-9}T^4$$
$$(\text{J mol}^{-1}) \tag{4.58}$$

**Diffusion**

According to Hayes and Kolaczkowski (1997; p. 228), a method developed by Fuller *et al.* (1966) gives the following formula for a binary system diffusion coefficient, $D_{AB}$, which is:

$$D_{AB} = \frac{1.013\times10^{-2}\ T^{1.75}\left(\frac{1}{M_A}+\frac{1}{M_B}\right)^{0.5}}{P\left(\left(\sum v_i\right)_A^{1/3}+\left(\sum v_i\right)_B^{1/3}\right)^2} \qquad (4.59)$$

where $P$ is the pressure in $Pa$ and $v_i$ are diffusion volumes. Values of the latter for simple atoms and molecules are given in Table 4.8.

**Table 4.8** Diffusion volumes for use in the Fuller *et al*. correlations (copied from Hayes and Kolaczkowski, 1997; p. 229).

| Atomic and Structural Diffusion Volume Increments | | | |
|---|---|---|---|
| C | 16.5 | Cl | 19.5 |
| H | 1.98 | S | 17.0 |
| O | 5.48 | Aromatic rings | -20.2 |
| N | 5.69 | | |
| **Diffusion Volumes of Common Simple Molecules** | | | |
| $H_2$ | 7.07 | $CO_2$ | 26.9 |
| $N_2$ | 17.9 | $N_2O$ | 35.9 |
| $O_2$ | 16.6 | $H_2O$ | 12.7 |
| Air | 20.1 | $NH_3$ | 14.9 |
| CO | 18.9 | | |

Air is considered as a single component, and the molar mass is 28.96 g mol$^{-1}$. From Table 4.8 the diffusion volume of air is given as 20.1. The value of propane is not given; therefore, this has to be calculated using the diffusion volume increments. Propane contains three carbon atoms and eight hydrogen atoms, so the diffusion volume is: $16.5\times3+1.98\times8=65.34$. The molar mass of propane is 44. Substituting these values into Equation (4.58) with a temperature of 650 K and a pressure of 101325 Pa gives:

$$D_{AB} == \frac{1.013\times10^{-2}\ (650)^{1.75}\left(\frac{1}{44}+\frac{1}{28.96}\right)^{0.5}}{101325\ \left((65.34)^{1/3}+(20.1)^{1/3}\right)^2} = 5.0\times10^{-5}\ \frac{m^2}{s} \qquad (4.60)$$

In COMSOL Multiphysics, the way to calculate the diffusion of gas molecules inside the porous material is to multiply the bulk diffusivity with an effective coefficient. In this model, the Knudsen diffusion coefficient was calculated from the formula (as presented in Hayes and Kolaczkowski, 1997; p. 245):

$$D_K = 97\, r_e \left(\frac{T}{M}\right)^{0.5} \tag{4.61}$$

where $r_e$ is the equivalent pore radius in m, $T$ is in K.

Frequently the equivalent pore radius is taken as the average radius of the pores in the pellet. Using information from the case study in Hayes and Kolaczkowski (1997; p. 321), the effective length of the washcoat, $L_c$, is the ratio of the cross-section of the washcoat divided by the wetted parameter. This value is 46 μm. The average pore diameter is 12.6 nm, the porosity of the washcoat is 0.4 and the tortuosity factor is 4.0.

The molar mass of propane is 44 g mol$^{-1}$, therefore with an average pore radius of 6.3 nm the Knudsen diffusion coefficient at 650 K can be calculated as:

$$D_K = 97 \times 6.3 \times 10^{-9} \left(\frac{650}{44}\right)^{0.5} = 2.348 \times 10^{-6}\ \frac{m^2}{s} \tag{4.62}$$

Then following the procedure described in Kolaczkowski (1997; pp. 321 - 323):

The bulk diffusion coefficient, $D_{AB}$, can be combined with Knudsen diffusion coefficient in the pores, $D_V$:

$$\frac{1}{D_v} = \frac{1}{D_{AB}} + \frac{1}{D_K} \tag{4.63}$$

The effective diffusivity in the washcoat may then be calculated by multiplying the diffusion coefficient in the pores by the washcoat porosity, $\phi$, and dividing by the tortuosity factor, $\tau$.

$$D_{eff} = \frac{\phi\, D_v}{\tau} \tag{4.64}$$

For the propane in air, if the temperature is 650 K and pressure is 101325 Pa, then:

$$D_v = \left(\frac{1}{D_{AB}} + \frac{1}{D_K}\right)^{-1} = \left(\frac{1}{5 \times 10^{-5}} + \frac{1}{2.348 \times 10^{-6}}\right)^{-1} = 2.242 \times 10^{-6}\ \frac{m^2}{s} \tag{4.65}$$

and, then:

$$D_{eff} = \frac{\phi D_v}{\tau} = \frac{0.4 \times 2.242 \times 10^{-6}}{4} = 2.242 \times 10^{-7} \frac{m^2}{s} \qquad (4.66)$$

**Physical properties of the gas phase**

It is assumed that the physical properties of air may be represented by $N_2$.

**Description of model**

As a schematic this has already been illustrated in Figure 4.14. The descriptions of the equations that follow, are based on description in the COMSOL user guide (COMSOL Multiphysics Chemical Engineering Module User Guide, 2009; pp. 239-243)

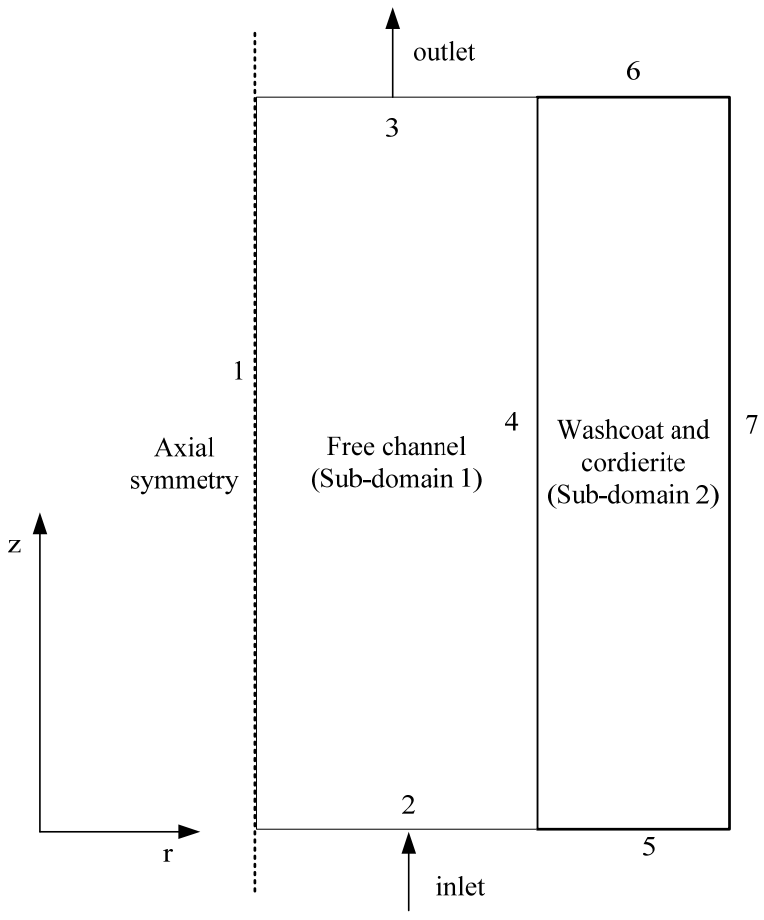


**Figure 4.14** Schematics of the geometry of single channel model in COMSOL Multiphysics.

**Mass balance**

The stationary mass balance equation implemented in the **Convection and Diffusion** application mode is given by:

$$\nabla \cdot \left(-D_i \nabla C_i\right) = R_i - u \nabla C_i \tag{4.67}$$

where

| | | |
|---|---|---|
| $C_i$ | concentration of species $i$ | mol $m^{-3}$ |
| $D_i$ | diffusion coefficient | mol $m^{-3}$ $s^{-1}$ |
| $R_i$ | the reaction rate for species $i$ | W $m^{-3}$ |
| $u$ | the velocity vector | m $s^{-1}$ |

The first term describes the diffusional transport, accounting for interaction between the dilute species (propane) and the solvent (air). On the right-hand side, the first term represents a source or sink, typically due to chemical reaction; arbitrary kinetic expressions of the reacting species can be introduced in the application mode interface. Finally, the second term on the right-hand side accounts for the convective transport due to a velocity field $u$. This field can be expressed analytically or be obtained by coupling a momentum balance to the equation system (COMSOL Multiphysics Chemical Engineering Module User Guide, 2009; p. 239).

In the sub-domain 1 (see Figure 4.14), the reaction rate was zero since no homogenous reaction happened in the gas phase. Thus, the mass balance equation in the gas phase becomes:

$$\nabla \cdot \left(-D_i \nabla C_i\right) = u \nabla C_i \tag{4.68}$$

In sub-domain 2, there is no velocity field inside the washcoat, therefore, the mass balance equation is:

$$\nabla \cdot \left(-D_i \nabla C_i\right) = R_i \tag{4.69}$$

The boundary conditions are summarised in Table 4.9.

**Table 4.9** Boundary conditions for convection and diffusion.

| Boundary | Conditions |
|---|---|
| 1 | Axial symmetry ($r = 0$) |
| 2 | Inlet concentrations of gas mixture |
| 3 | Convective flux $n \cdot \left(- D_i \nabla C_i\right) = 0$ |
| 4 | N/A |
| 5 | Insulation $n \cdot N = 0$ |
| 6 | Insulation $n \cdot N = 0$ |
| 7 | Insulation $n \cdot N = 0$ |

**Energy balance**

The stationary energy balance equation used in the **Convection and Conduction** application mode was:

$$\rho C_p u \nabla T = \nabla \cdot \left(k \nabla T\right) + Q \tag{4.70}$$

In the sub-domain 1, the heat source term was zero, since there were no chemical reactions taking place in the gas phase. Hence Equation (4.69) becomes:

$$\rho C_p u \nabla T = \nabla \cdot \left(k \nabla T\right) \tag{4.71}$$

In the sub-domain 2, the first term on the left-hand side in Equation (4.69) was eliminated because no velocity field in the solid phase. Thus, the energy balance was:

$$0 = \nabla \cdot \left(k \nabla T\right) + Q \tag{4.72}$$

The boundary conditions are summarised in Table 4.10.

**Table 4.10** Boundary conditions for convection and conduction.

| Boundary | Conditions |
|---|---|
| 1 | Axial symmetry ($r = 0$) |
| 2 | Inlet gas temperature |
| 3 | Convective flux $n \cdot \left(- k \nabla T\right) = 0$ |
| 4 | N/A |
| 5 | Thermal insulation $- n \cdot \left(- k \nabla T\right) = 0$ |
| 6 | Thermal insulation $- n \cdot \left(- k \nabla T\right) = 0$ |
| 7 | Thermal insulation $- n \cdot \left(- k \nabla T\right) = 0$ |

**Momentum**

The **Weakly Compressible Navier-Stokes** application mode was chosen. It contains the fully compressible formulation of the continuity equation and the momentum equation:

$$\nabla \cdot \left(\rho_g \cdot u\right) = 0 \qquad \rho_g = \rho_g(P,T) \tag{4.73}$$

$$\rho_g \cdot u \cdot \nabla u = -\nabla P + \nabla \cdot \left( \eta \cdot \left(\nabla u + (\nabla u)^T\right) - \left(\frac{2}{3}\eta - k_{dv}\right) \cdot (\nabla \cdot u) \cdot I \right) + F \tag{4.74}$$

The boundary conditions are summarised in Table 4.11.

**Table 4.11** Boundary conditions for momentum balance using Weakly Compressible Navier-Stokes.

| Boundary | Conditions |
|---|---|
| 1 | Axial symmetry ($r = 0$) |
| 2 | Inlet velocity profile (parabolic) |
| 3 | Pressure, no viscous stress $\eta\left(\nabla u + (\nabla u)^T\right) = 0$, $P = P\_ref$ |
| 4 | No slip ($u = 0$) |

### 4.5.2 Simulation results

The 2-D COMSOL model was used to simulate the catalytic combustion of propane at different inlet gas velocities, and the simulation results are compared with the simulation results obtained from the 1-D model in Hayes and Kolaczkowski (1997; pp. 325- 326). The operating conditions are summarised in Table 4.7. A number of selected results are illustrated in Figures 4.29 to 4.32, and following observations can be made:

Figure 4.29 shows the concentration distribution of propane when the inlet gas velocity is 0.5 m $s^{-1}$. As can be seen, the concentration of propane reduces along the length of the monolith channel. As expected, the concentration of propane at the wall is lower than that in the gas phase as the reactions take place in the catalyst layer at the wall.

Figure 4.30 shows the axial gas and wall temperature profiles determined with the COMSOL 2-D model. Note that the temperature profiles decrease with an increasing

gas velocity. As expected the solid temperature profiles are higher than the gas temperature profiles. For an inlet gas velocity of 0.5 m $s^{-1}$, in Figure 4.31 the wall and gas temperature profiles are compared with simulation results in Hayes and Kolaczkowski (1997; p. 325), and good agreement is observed.

Similarly, in Figure 4.32, the axial gas and wall mole fractions of propane are also compared and good agreement is observed. Having tested the way in which catalytic reactions in a washcoat layer may be modelled in COMSOL, confidence has been gained in using COMSOL to model DOC light-off.

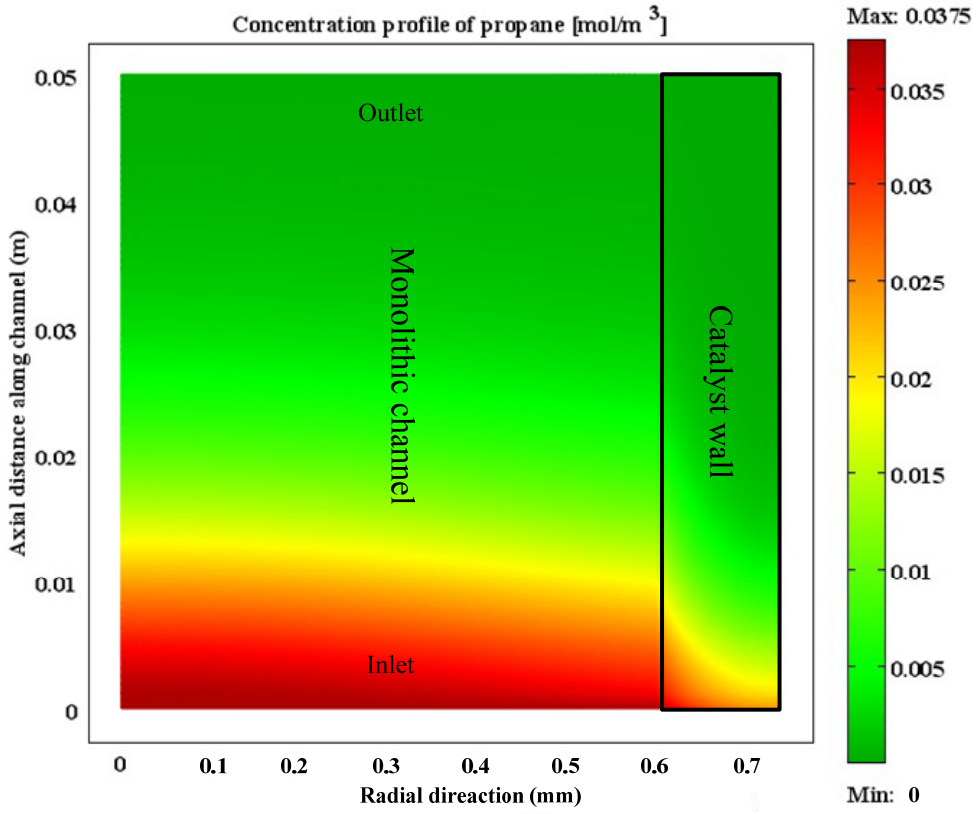


**Figure 4.29** Concentration profile of propane at steady-state with an inlet gas velocity of 0.5 m $s^{-1}$ (STP). The red colour indicates higher propane concentration, and green colour indicates lower concentration.

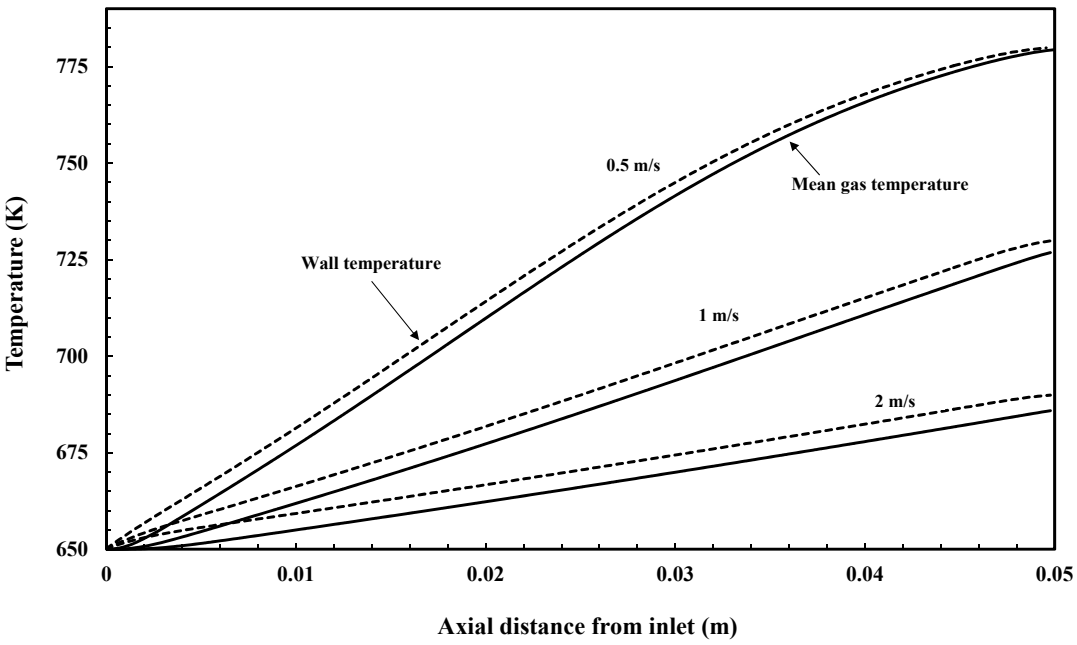


**Figure 4.30** Results from the COMSOL 2-D simulation showing axial gas and wall temperature profiles. The dashed lines are the wall temperatures and the solid lines are the mean gas temperature.

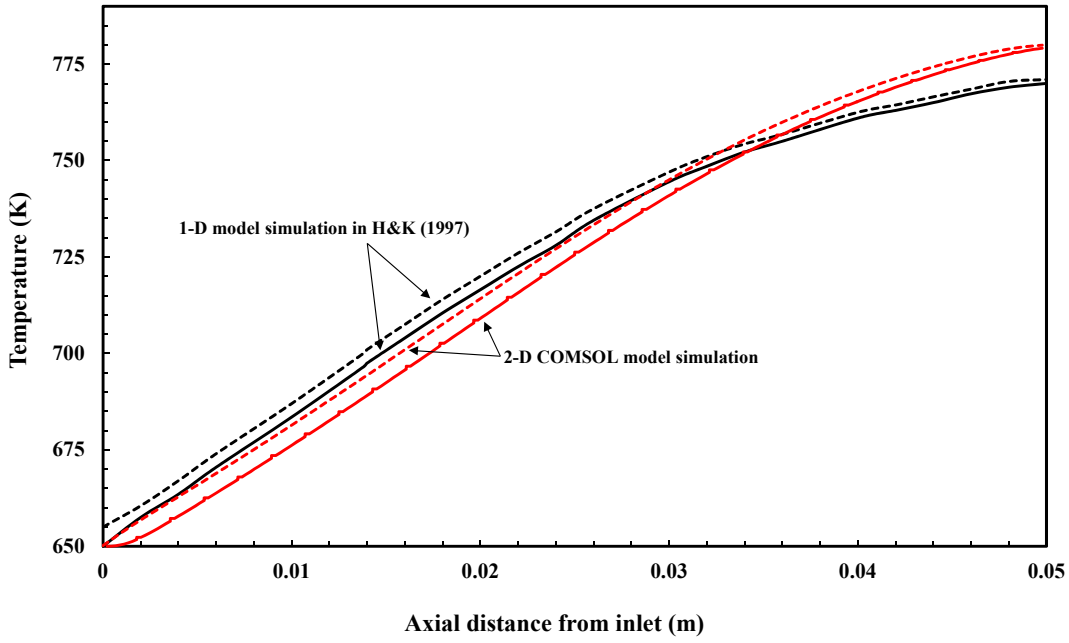


**Figure 4.31** Axial gas and wall temperature profiles. The dashed lines are the wall temperatures and the solid lines are the gas temperature (simulated at $v_{av}$ = 0.5 m/s, at reference of 298 K). The results plotted in black colour are the output from Hayes and Kolaczkowski (1997; p. 325), and the results plotted in red colour are the output from the COMSOL 2-D model.

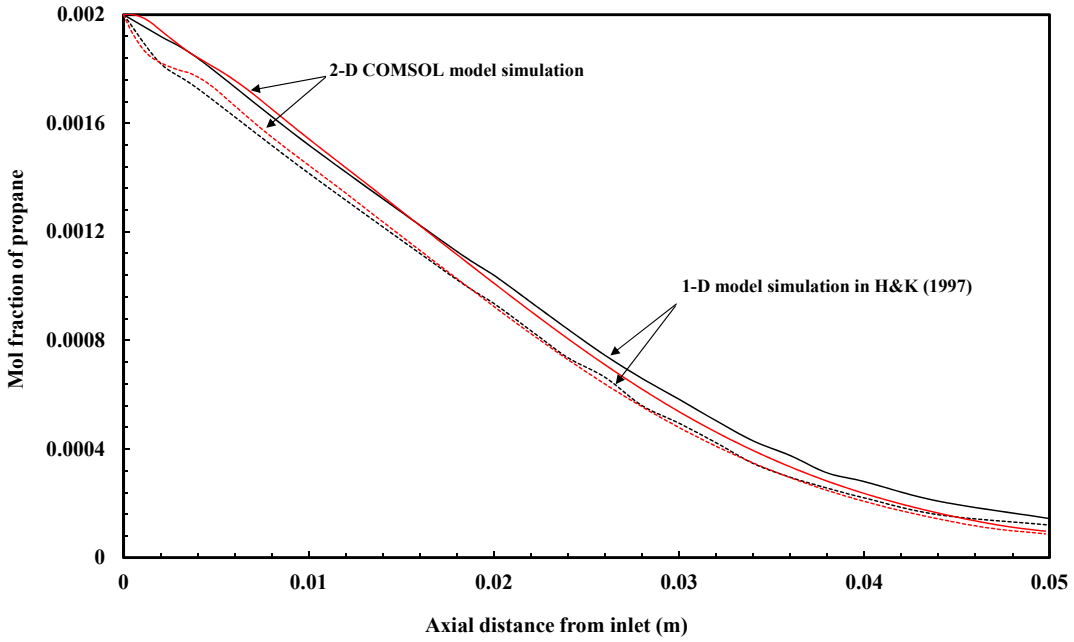


**Figure 4.32** Axial gas and wall mole fractions of propane. The dashed lines are the wall concentrations and the solid lines are the gas concentration (simulated at $v_{av}$ = 0.5 m/s, at reference of 298 K). The results plotted in black colour are the output from 1-D model in Hayes and Kolaczkowski (1997; p. 326), and the results plotted in red colour are the output from the COMSOL 2-D model.

## 4.6 Case Study 4: Pseudo-steady state light-off experiments

The COMSOL model developed in Case Study 3 was modified to simulate a set of pseudo-steady-state light-off experiment. In this simulation, only two oxidation reactions were considered (CO and THCs). Since the conversion of $NO_x$ is very small across the DOC, this is neglected. The reaction of hydrogen was also neglected, as the concentration of hydrogen is not directly measured in this study, although this reaction is believed to release significant amount of heat, which could affect wall temperatures (Oh and Cavendish, 1982; Siemond *et al.*, 1996).

As discussed earlier (Section 2.3.4), although THCs in diesel exhaust consist of a wide range of hydrocarbons, propane ($C_3H_8$) is chosen to represent the hydrocarbons. Also in the experiments, propane was injected in some of the experiments. There are many kinetic expressions available in the literature, and in this case study, the rate expressions are of the LHHW form and are based on the classic work by Voltz *et al*. (1973) and Oh and Cavendish (1982). These are:

CO oxidation:

$$R_{CO} = \frac{k_1 Y_{CO} Y_{O_2}}{G} \frac{\text{mol CO}}{\text{cm}^2\ \text{(Pt)}\ \text{s}} \tag{4.75}$$

$C_3H_8$ oxidation:

$$R_{C_3H_8} = \frac{k_2 Y_{C_3H_8} Y_{O_2}}{G} \frac{\text{mol C}_3\text{H}_8}{\text{cm}^2\ \text{(Pt)}\ \text{s}} \tag{4.76}$$

where

$$G = T_s \left(1 + K_1 Y_{CO} + K_2 Y_{C_3H_8}\right)^2 \left(1 + K_2 Y_{CO}{}^2 Y_{C_3H_8}{}^2\right)\left(1 + K_4 Y_{NO}{}^{0.7}\right) \tag{4.77}$$

The first term, $T_s$, represents a temperature dependence factor using the modified Arrhenius form in the rate expression. The second term, $\left(1 + K_2 Y_{CO}{}^2 Y_{C_3H_8}{}^2\right)$, is a function that accounts for the inhibition effects due to the chemisorption of CO and $C_3H_8$. The third term, $\left(1 + K_2 Y_{CO}{}^2 Y_{C_3H_8}{}^2\right)$, is used to fit experimental data at higher concentrations of CO and $C_3H_8$. The last term, $(1 + \mathrm{K_4 Y_{NO}}^{0.7})$, represents the inhibition effects of NO on the CO and $C_3H_8$ oxidation rates (Voltz *et al*., 1973, Oh and Cavendish, 1982). Since the model does not account for $NO_x$ oxidation, the last NO inhibition term was neglected. These forms of expressions have already been

discussed in Section 2.1.3.

The operating conditions and physical parameters used in the model are summarised in Table 4.12. The values of the initial kinetic constants are selected from the final rate constants presented in Kim and Kim (2009), see Table 4.13.

**Table 4.12** Summary of the operating conditions for a pseudo-steady-state light-off experiment.

| **Parameters or conditions** | **Value** |
|---|---|
| Hydraulic diameter (m) | $1.108\times10^{-3}$ |
| Effective wall thickness (m) | $0.175\times10^{-3}$ |
| Density of wall (kg $m^{-3}$) | 1750 |
| Heat capacity of wall (J $kg^{-1}$ $K^{-1}$) | 1100 |
| Thermal conductivity of wall (W $m^{-1}$ $K^{-1}$) | 1.1 |
| Length of monolith (m) | 0. 114 |
| **Initial conditions** | |
| Air mass flow (average) (kg $h^{-1}$) | 58 |
| Initial gas temperature ($^{o}$C) | 147 to 267 |
| Initial solid temperature ($^{o}$C) | 140 |
| CO (ppm) | 3210 |
| THCs (Propane, ppm$C_3$) | 500 |
| $CO_2$ (%) | 5 |
| $O_2$ (%) | 12 |
| $NO_x$ (ppm) | 60 |

**Table 4.13** Initial rate constants (final rate constants from Kim and Kim, 2009) and tuned rate constants.

| | **Reactions** | **Activation energy** [J $mol^{-1}$] | **Pre-exponential factor** [mol K $m^{-2}$ $s^{-1}$] |
|---|---|---|---|
| Initial | CO | $8.014\times10^{4}$ | $4.49993\times10^{13}$ |
| | THCs | $3.356\times10^{4}$ | $9.77310\times10^{6}$ |
| | | **[J $mol^{-1}$]** | **[mol K $m^{-3}$ $s^{-1}$]** |
| Tuned* | CO | $7.2\times10^{4}$ | $2.4\times10^{18}$ |
| | THCs | $1.0\times10^{5}$ | $4.5\times10^{17}$ |

* these tuned rate constants were used to simulate results in Figures 4.34 to 4.38.

This COMSOL model was solved using the UMFPACK solver with 16,384 meshes. The conversion of CO is plotted against the inlet gas temperature to produce a light-off curve for CO, and this is compared with experimental results, see Figure 4.33. A similar trend is observed in the simulated and experimental light-off curves. However, the simulated light-off curve for CO has a higher light-off temperature. Therefore, the

kinetic constants in the rate expression where tuned to match the experimental data. The final kinetic constants, expressed in terms of the washcoat volume, are shown in Table 4.13.

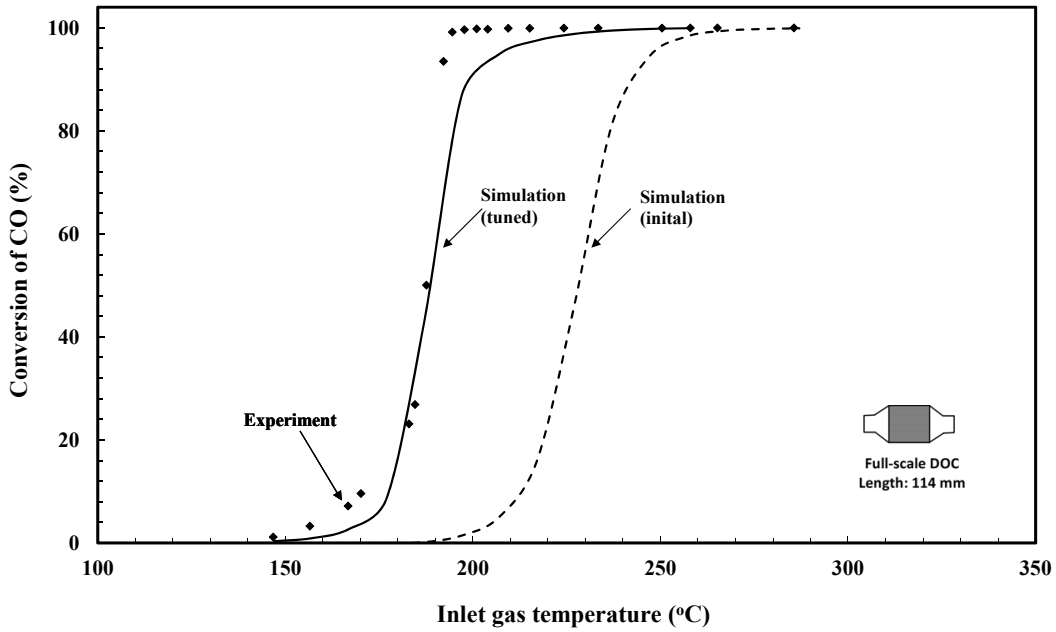


**Figure 4.33** Comparison of measured and simulated light-off curves for CO (with inlet concentration of 3210 ppm). The inlet THCs concentration is maintained at 1500 ppm$C_1$ (equivalent to 500 ppm propane). LHHW rate expressions are used in the simulation.

In the tuning process, the pre-exponential factor for CO oxidation is increased by a factor of 1200 (from initial guess), and the activation energy is reduced by 10%. After tuning the parameters, the simulated light-off curve for CO has a very good agreement with the experiment results. This shows that the rate constants in the LHHW form of rate expression are very dependent on the properties of the individual catalyst system tested.

Despite attempts to tune the coefficient in the rate constant for propane oxidation, the simulated light-off curve for THCs did not quite match the experimental results, see Figure 4.34. The shape of the light-off curve for THCs is not a conventional 'S' shape, so that the simulated light-off curve from an LHHW form of rate expression may not match this shape. This is interesting, as the shape of the THCs light-off is very gradual, and does not exhibit what is expected from an exponential form of rate expression.

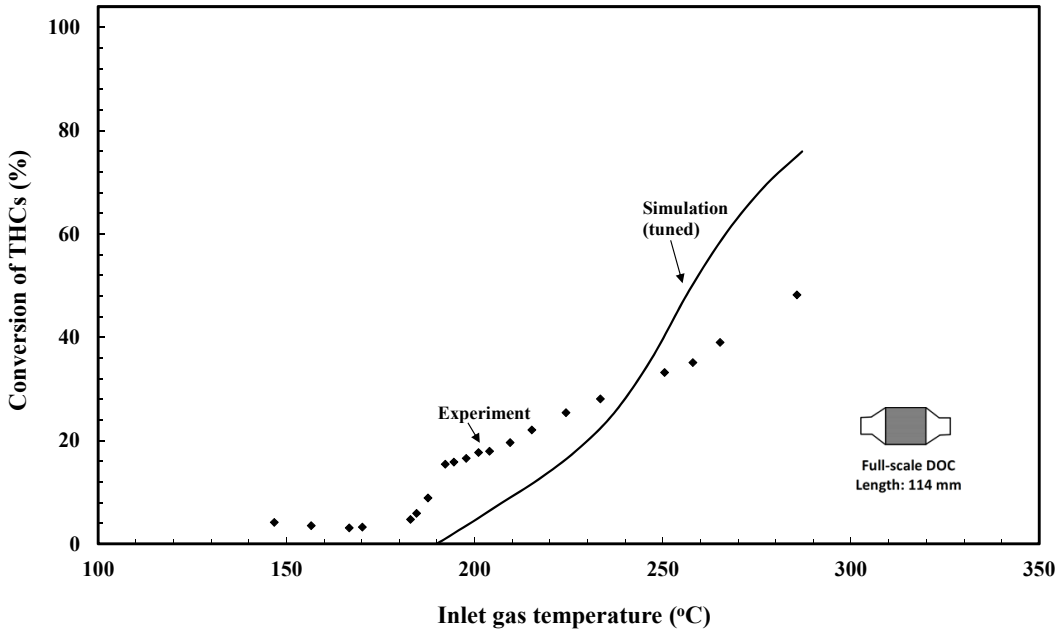


**Figure 4.34** Comparison of measured and simulated light-off curves for THCs (with inlet concentration of 1500 ppm$C_1$, equivalent to 500 ppm propane). The inlet CO concentration is maintained at 3000 ppm. LHHW rate expressions are used in the simulation.

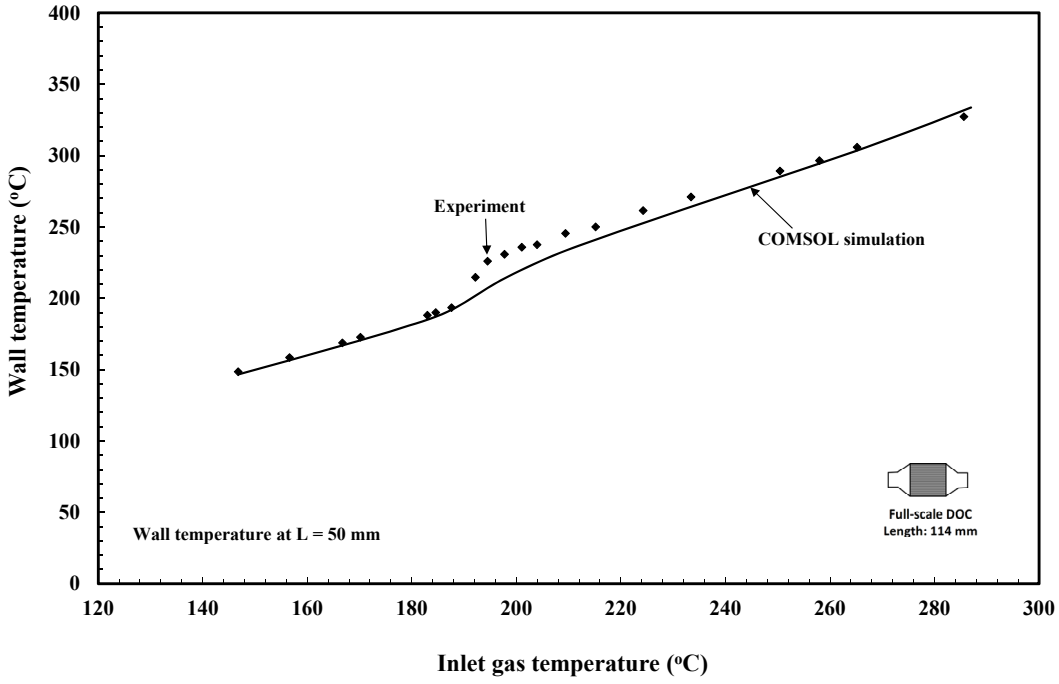


**Figure 4.35** Wall temperature 50 mm from the inlet. Simulations compared with experimental data.

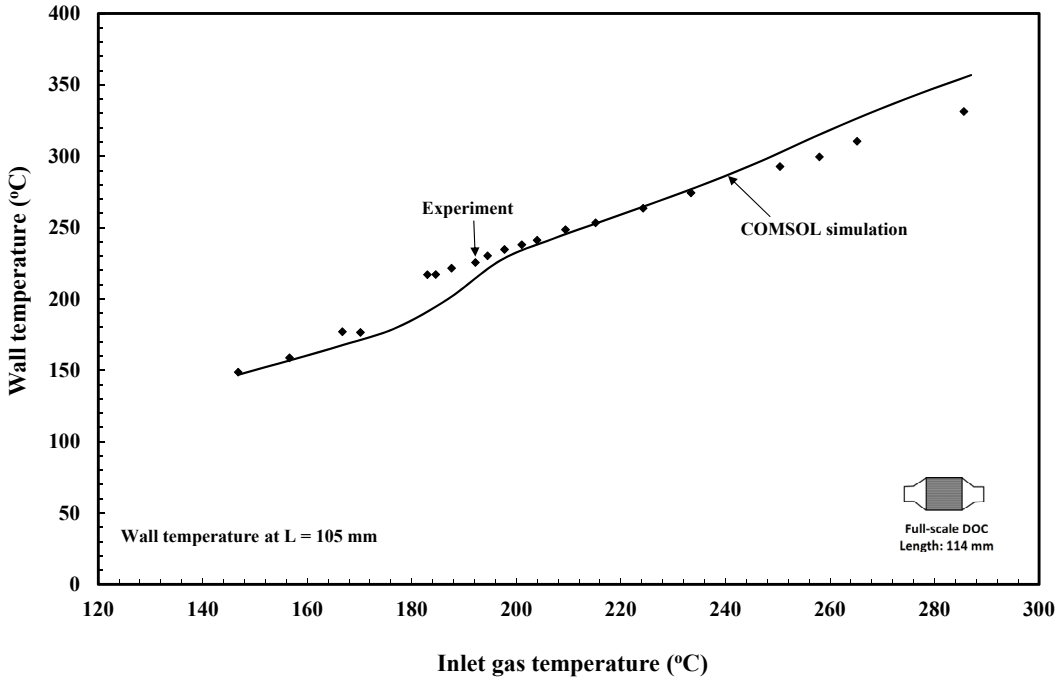


**Figure 4.36** Wall temperature 105 mm from the inlet. Simulations compared with experimental data.

Looking at wall temperatures, the simulated values at 50 and 105 mm from the inlet of the DOC are also compared with the experiment results in Figures 4.36 and 4.37. As can be seen from the plots, the simulations in general match the experimental results.

The COMSOL 2-D model was also used to simulate the light-off curve for CO, at two different inlet concentrations of CO (2100 and 4100 ppm). For these two simulations, the tuned kinetic constants in Table 4.13 were used. Figure 4.37 shows the comparisons and simulated light-off curve for CO with 4100 ppm inlet matches the experimental light-off curve. For the light-off curve with 2100 ppm of CO, the simulation provides a good match with the experiment results until the gas inlet temperature reaches 186$^{o}$C. After this point, the simulated light-off curve starts to approach the asymptote more slowly than the measured values in the experiment.

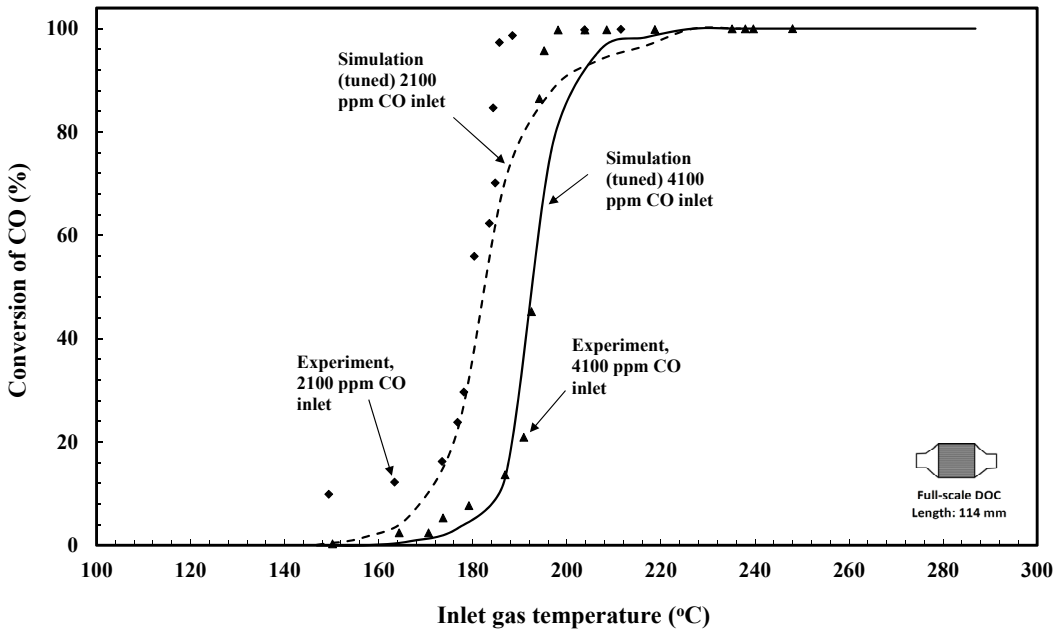


**Figure 4.37** Comparison of measured and simulated light-off curves for CO (with inlet concentration of 2100 and 4100 ppm). For two tests, the inlet THCs concentration was maintained at 1500 ppm$C_1$ (equivalent to 500 ppm propane).

## 4.7 Concluding remarks

As planned at the start of this chapter, mathematical models were developed in a gradual manner, starting with just a consideration of heat transfer aspects, and finally building up to a model that also included chemical reactions terms, which were used to simulate pseudo-steady-state light-off in a Full-scale DOC. These studies were done to illustrate how the experimental methodologies developed in this thesis, could be used to test the validity of models, or to back-calculate coefficients in such models. In the course of this work, the following interesting additional observations were made:

(a) The inclusion of the axial heat conduction term along the wall (axial direction) of the DOC may not be necessary, and this helps to reduce the complexity of the model.

(b) Following preliminary experiments on the hot air rig, it was shown that although the experimental techniques worked, there were problems with the air-flow controller, which then had to be re-calibrated. Also, the distance between the back end of the monolith and the location of the thermocouple measuring the gas outlet temperature can result in some heat loss (and hence lower recorded values of gas temperatures).

(c) In general, the technique to perform warm-up experiments with an engine was considered a success, and comparisons with simulations were encouraging. Small variations occurred in measured radial temperatures (± 5ºC), which probably arose from the presence of complex flow patterns at the inlet and outlet of the monolith in the exhaust can.

(d) Pressure drops determined from the use of a single channel model in COMSOL 2-D, were a factor of 2 to 4 times lower than in the actual experiments. This is not surprising, because of the presence of more complex flow patterns and pulsating flow.

(e) It is possible, to adjust a rate expression (based on geometric surface area) into a volume basis and to then to use them successfully in COMSOL to model reactions occurring in the catalytic washcoat layer in a DOC.

(f) In experiments, it was found that the shape of the light-off curve for THCs is very shallow (almost linear), and this is not what would be expected from an exponential form of rate expression. This aspect would be worthy of further exploration, in work that follows this thesis.

## Reference


Akehurst, S. and Piddock, M. (2008) A Multiple Factor Simulation and Emulation Approach to Investigate Advanced Air Handling Systems for Future Diesel Engines, SAE 2008-01-0297.

Benjamin, S. F. and Roberts C. A. (2001) Warming Automotive Catalysts with Pulsating Flows, *Proc Mech Engrs*, **215** (D), 891-910.

COMSOL Multiphysics Chemical Engineering User Guide, 2009.

Groppi, G., Belloli, A., Tranconi, E.,Forzatti,P. (1995) Comparison of Lumped and Distributed Models of Monolith Catalytic Combustors, *Chemical Engineering Science*, **50** (17), pp. 2705-2515.

Hayes, R.E. and Kolaczkowski S.T. (1997) *Introduction to catalytic combustion*, Amsterdam: Gordon and Breach Science Publishers.

Hayes, R.E., Kolaczkowski, S.T., Thomas, W. J. (1992) Finite Element Model for Catalytic Monolith Reactor, *Computers them. Engng*, **16**(7), 645-657.

Kolaczkowski, S.T., Chao R., Awdry, S. and Smith, A. (2007) Application of a CFD Code (FLUENT) to Formulate Models of Catalytic Gas Phase Reactions in Porous Catalyst Pellets, *Chemical Engineering Research & Design*, **85**(A11), 1539-1552.

Koltsakis, G.C. and Stamatelos, A.M. (1997) Catalytic Automotive Exhaust After-treatment, *Progress in Energy combustion Science*, **43**, 1-39.

Oh, S.H. and Cavendish, J. (1982) Transients of Monolithic Catalytic Converters: Response to Step Changes in Feed Stream Temperature as Related to Controlling Automobile Emissions. *Ind. Eng. Chem. Prod. Res. Dev*. **21**, 29-37.

Shah, R. K. and London, A. L., 1978. *Laminar Flow Forced Convection in Ducts: A Source Book for Compact Heat Exchanger Analytical Data*. New York: Academic Press.

Siemund, S., Leclerc, J. P., Schweich, D., Prigent, M. and Castagna, F. (1996) Three-way Monolithic Converter: Simulations versus Experiments, *Chemical Engineering Science*, **51**(15), 3709-3720.

Smith, G.D. (1985) *Numerical solution of partial differential equations: Finite difference methods*. 3rd Ed. Oxford: Clarendon.

Zygourakis, K. (1989) Transient Operation of Monolith Catalytic Converter: a Two-dimensional Reactor Model and the Effects of Radially Nonuniform Flow Distributions, *Chemical Engineering Science*, **44**, 2075–2086.

# 5. Conclusions and future work

Catalyst development for DOCs usually occurs in a laboratory on small samples of powdered catalyst, or small monolith structures. When trials are eventually done on a real engine with a Full-scale DOC an opportunity is lost to obtain a deeper understanding of the performance of the catalytic converter. The gap between the experiments in the laboratory and Full-scale engine trials is large. In this thesis, a number of techniques have been developed and demonstrated, which will help to acquire a deeper understanding of how the DOC is performing. Techniques that have in general only been used in bench-top laboratory experiments on small catalyst samples/powders (with simulated exhaust gases), have now been used (probably for the first time) successfully on DOCs connected to a live diesel engine.

## 5.1 Conclusions

### 5.1.1 Based on experimental work in Chapter 3

A number of experimental techniques are explored, and it is shown how to make use of a Full-scale DOC and a Thin-slice DOC, to gather fundamental data on the performance of the DOC, and how to combine information on wall temperature profiles in the DOC with information on conversion and reaction rates, in order to draw conclusions on what is taking place. The following techniques were demonstrated:

(a) **Baseline data:** How to start such a study, by gathering relevant baseline performance data for the engine, so as to establish a matrix of operating conditions.

(b) **NEDC:** How to gather data on cold and hot NEDCs, and how to present this information so that it is in a useful form to interpret what is happening inside the DOC.

(c) **Light-off:** A methodology has been developed and demonstrated, which enables catalyst light-off curves to be generated, by running the engine at a

range of pseudo steady-state conditions. This also involves the addition of known background levels of CO and THCs.

(d) **Light-off and extinction:** A methodology has been developed and demonstrated, which illustrates how background levels of CO and THCs influence light-off and extinction. Clear evidence is provided to show the presence of hysteresis.

(e) **Hysteresis:** A methodology has been developed and demonstrated, which helps to unravel the difference between thermal and mechanistic effects. It is shown that for CO oxidation, there is a clear mechanistic effect.

(f) **Pulse injection:** A methodology has been developed, in which a pulse concentration of a reactant is added, whilst a known gas inlet (to DOC) background concentration of other contaminants is maintained constant. The transient response of the DOC is them monitored. This is a transient experiment, as in response to the pulse input, the DOC responds. From this type of experiment a very wide range of mechanistic aspects can be explored. For example, is there any evidence of competition for the active site between CO and THCs, which would affect the performance of the DOC?

In the course of developing this methodology, many important observations where made, which help to clarify how the catalyst is performing. This will help to design better catalyst systems, and in any simulations (mathematical models) of the DOC, these features can be used to check the validity of the code. These features included:

(i) **Light-off during NEDC:** How during the simulated cold & hot NEDCs, catalyst light-off starts from the back of the DOC.

(ii) **Light-off (CO/propane):** How, in the pulse experiments with CO, the catalyst light-off starts from the back of the DOC, yet in the experiments with a pulse of propane, light-off starts from the front of the DOC.

(iii) **Hysteresis:** How different background CO and THCs levels affect the shape of the light-off and extinction curves, and magnitude of hysteresis.

(iv) **Catalyst wall temperatures:** How information from a Thin-slice DOC may be interpreted and the usefulness of having a relatively constant catalyst axial wall temperature profile, which helps to identify more clearly any enhancements from a thermal rather than a chemical mechanistic effect.

It was also shown:

- **Propane:** That propane is not a good representative for the THCs from a diesel engine. *This aspect was not explored further, but is recommended in future work.*
- **Site competition:** For the range of conditions tested, there appeared to be no significant competition for active catalytic sites, between CO, THCs, or propane. *This has important implication on the form of rate expressions that could be used in converter models.*
- **Hydrogen enhancement:** From a short study on the effect of hydrogen addition on enhancement in conversion, its contribution is considered to be mainly from a thermal rather than a chemical reaction mechanistic aspect. *This observation will help to clarify some of the confusion in the literature.*
- **Relative catalyst activity (axial direction):** From a short study on the relative performance of thin-slices cut from different parts of the DOC (front, ¼ L, and ½ L), although the activity can be seen to vary, this effect in a Full-scale DOC is considered to be most probably small. *However, this could be important when using a Thin-slice DOC to acquire fundamental data (which is then assumed to apply over the entire DOC).*
- **Background ratio of CO to hydrogen:** From a very short study it was found that the molar ratio of hydrogen to CO in the exhaust gas from the diesel engine was close to 1 : 9. This background level is very different to some values reported in the literature data, which suggests ratios of 1:3. However, it is recognised that the measurement of hydrogen is difficult, and there is very little data in the literature on its value. *This aspect was not explored further, but is recommended in future work.*

As the experimental techniques were developed and described, experimental errors were discussed and this sometimes led to a need to re-calibrate the equipment. In these concluding remarks, a brief summary is provided:

(a) To reduce experimental errors, it was important to ensure that the gas analysis equipment was routinely calibrated. In general, measurements were within the following limits: CO ± 1%; THCs ± 1%; $NO_x$ ± 1.5%.

(b) The gas flows from the engine, were estimated to be within ± 2%.

(c) Temperatures were measured with thermocouples, and these were estimated to read within ± 1ºC (for the 0.5 mm thermocouples mounted in the monolith/DOC), and ± 1ºC for the thicker 1 mm thermocouples that measured gas temperatures.

(d) The axial and radial locations, at which the wall thermocouples were positioned, were within ± 1 mm of the reported location.

(e) Pressure drop was measured using pressure transducer, was within ± 0.2kPa.

(f) Especially in the transient experiments, time alignment of the various sources of data was critical to ensure that the changes could be represented as 'real time' plots. It is estimated that this was achieved within ± 1 s.

### 5.1.2 Based on case studies illustrating modelling in Chapter 4

A number of case studies in mathematical modelling are also considered in detail to illustrate:

(a) How mathematical modelling techniques can be applied to interpret the results obtained.

(b) How some of the experimental results/techniques developed in this thesis, may be used in modelling studies to facilitate catalyst system design.

These mathematical models were developed in a gradual manner, starting with just a consideration of heat transfer aspects, and finally building up to a model that also included chemical reactions terms, which were used to simulate pseudo-steady-state light-off in a Full-scale, DOC. These studies were done to illustrate how the experimental methodologies developed in this thesis, could be used to test the validity of models, or to back-calculate coefficients in such models. In the course of this work, the following interesting additional observations were made:

(a) The inclusion of the axial heat conduction term along the wall (axial direction) of the DOC may not be necessary, and this helps to reduce the complexity of the model.

(b) Following preliminary experiments on the hot air rig, it was shown that although the experimental techniques worked, there were problems with the air-flow controller, which then had to be re-calibrated. Also, the distance between the back end of the monolith and the location of the thermocouple

measuring the gas outlet temperature can result in some heat loss (and hence lower recorded values of gas temperatures).

(c) In general, the technique to perform warm-up experiments with an engine was considered a success, and comparisons with simulations were encouraging. Small variations occurred in measured radial temperatures (± 5ºC), which probably arose from the presence of complex flow patterns at the inlet and outlet of the monolith in the exhaust can.

(d) Pressure drops determined from the use of a single channel model in COMSOL 2-D, were a factor of 2 to 4 times lower than in the actual experiments. This is not surprising, because of the presence of more complex flow patterns and pulsating flow.

(e) It is possible, to adjust rate expression (based on geometric surface area) into a volume basis and to then to use them successfully in COMSOL to model reactions occurring in the catalytic washcoat layer in a DOC.

In experiments, it was found that the shape of the light-off curve for THCs is very shallow (almost linear), and this is not what would be expected from an exponential form of rate expression.

## 5.2 Future work

The following is recommended:

(a) To perform on-line measurement of hydrogen concentration pre- and post-catalyst, which could then be used to validate rate expressions.

(b) The shape of the light-off curve for THCs needs further exploration.

(c) The experimental methodologies presented in this study may also be used to develop other types of models such as for the three-way catalytic converter, and the Selective Catalytic Reduction (SCR).

# Appendices

## Appendix 1: Useful conversions

### A1.1 Hydraulic diameter, $D_H$

Adapted from explanations presented in Hayes and Kolaczkowski (1997; p. 651).

$$D_H = \frac{4 \times \text{inside cross - sectional area of channel}}{\text{inside perimeter of channel}} \qquad \text{(A1.1)}$$

Examples:

a. For a square-shaped cell, if the inside dimensions of the cell are 1.1mm × 1.1mm:

$$D_H = \frac{4 \times 1.1^2}{4 \times 1.1} = 1.1\,\text{mm}$$

b. For a circular shaped cell, if the inside diameter is 1.1 mm, then

$$D_H = \frac{4 \times \pi \times \left(\frac{1.1^2}{2}\right)}{\pi \times 1.1} = 1.1\,\text{mm}$$

### A1.2 Open frontal area (porosity)

Adapted from explanations presented in Hayes and Kolaczkowski (1997; p. 651).

This is often presented as a percentage, and represents the % free cross-sectional area available for the gas flow, e.g. calculate the % open frontal area for 62 cell/cm$^2$ monolith substrate with a square shaped cells, i.e.1.1 mm×1.1 mm.

Each cell has an opening 1.1×1.1=1.21 mm$^2$

In one square centimetre, there are 64 cells, thus the area of cell openings in one square inch = 64×1.21=77.44 $mm^2$

$$\text{The \% open frontal area} = \frac{77.44}{100} \times 100\% = 77.44\%$$

Note: this is the open frontal area without washcoat. Application of washcoat reduces the open frontal area.

### A1.3 ppm (parts per million on a volumetric basis)

Adapted from explanations presented in Hayes and Kolaczkowski (1997; p. 651).

This presents parts per million on a volumetric basis, where a million is $10^6$.To convert from X ppm to Y $mg/m^3$, which is on a mass basis

$$\text{X ppm} = \frac{X \times (\text{molar mass}) \times 1000}{0.02241 \times 10^6} = \text{Y mg m}^{-3} \qquad \text{(A1.2)}$$

e.g. convert 1000 ppm of CO to mg $m^{-3}$. The molar mass of CO is 28 g $mol^{-1}$, therefore:

$$100 \text{ ppm} = \frac{100 \times 28 \times 1000}{0.02241 \times 10^6} \frac{\text{g mol}^{-1} \times \text{mg g}^{-1}}{\text{m}^3 \text{ mol}^{-1}} = 124.94 \text{ mg m}^{-3}$$

### A1.4 Rate of reaction

In parts of this thesis, the rate of reaction is sometimes presented in a unit of: mol/s for the reactor. This can be visualised as:

$$\frac{\text{mol}}{\text{s}} \cdot \frac{1}{\text{reactor}} \qquad \text{(A1.3)}$$

A number of conversions are performed to show how to convert this into other forms of units used in the literature. Starting with Equation (A1.3), then if volume of the reactor is known, and the surface area of active sites (Pt) per unit volume is known, then:

$$\frac{\text{mol}}{\text{s}} \cdot \frac{1}{\text{reactor}} \times \frac{\text{reactor}}{\text{volume}} \times \frac{\text{volume}}{\text{surface area (Pt)}} = \frac{\text{mol}}{\text{s} \cdot \text{m}^2} \qquad \text{(A1.4)}$$

If the concentration of active site (Pt) per unit volume is also known, then:

$$\frac{\text{mol}}{\text{s}} \cdot \frac{1}{\text{reactor}} \times \frac{\text{reactor}}{\text{volume}} \times \frac{\text{volume}}{\text{mol (Pt)}} = \frac{\text{mol (CO)}}{\text{s} \cdot \text{mol (Pt)}} \qquad \text{(A1.5)}$$

e.g. rate of CO oxidation is 0.45 mol $s^{-1}$ for a Full-scale DOC, and the volume of a Full-scale DOC is 0.001 $m^{-3}$, and the catalyst surface area to reactor volume ratio is 268950 $m^{-1}$, and the molar surface area of active sites is 2.72 $\times 10^{-5}$, then:

Converting to moles of CO reacted per square metre (platinum surface area) per second:

$$\frac{0.045 \text{ mol}}{\text{s}} \cdot \frac{1}{\text{reactor}} \times \frac{\text{reactor}}{0.001 \text{ m}^3} \times \frac{1}{268950} \cdot \frac{\text{m}^3\text{(reactor)}}{\text{m}^2\text{(Pt )}}$$
$$= 1.67 \times 10^{-4} \frac{\text{mol}}{\text{m}^2\text{(Pt )} \cdot \text{s}}$$

Converting to moles of CO reacted per mole of active sites (Pt) per second:

$$\frac{0.045 \text{ mol}}{\text{s}} \cdot \frac{1}{\text{reactor}} \times \frac{\text{reactor}}{0.001 \text{ m}^3} \times \frac{1}{268950} \cdot \frac{\text{m}^3\text{(reactor)}}{\text{m}^2\text{(Pt )}}$$
$$\times \frac{1}{2.72 \times 10^{-5}} \frac{\text{m}^2\text{(Pt）}}{\text{m}^3\text{(reactor)}} = 6.15 \frac{\text{mol}}{\text{m}^2\text{(Pt )} \cdot \text{s}}$$

### A1.5 Pressure drop across the DOC to velocity

The pressure drop is measured experimentally, and then the velocity can be estimated using the following equations:

$$u = \sqrt{\frac{\Delta p \, 2\text{d}}{f \, \text{L} \, \rho}} \qquad \text{(A1.6)}$$

$$f = \frac{64}{\text{Re}} \text{ ( for Laminar flow)} \qquad \text{(A1.7)}$$

Where

| | | |
|---|---|---|
| $\Delta p$ | pressure drop | Pa |
| $u$ | velocity | m $s^{-1}$ |
| $f$ | friction factor | |
| $L$ | length monolith | m |
| $\rho$ | density of air | kg $m^{-3}$ |
| $d$ | inner diameter of monolith channel | m |

e.g. If the pressure difference across the DOC is 0.398 kPa, the diameter of the monolith is 1.09 mm, length of the monolith is 114 mm and width is 106 mm, the inlet gas temperature is 533 K, the air mass flow is 60 kg $h^{-1}$, and the absolute pressure is 101,325 Pa, then:

The density of gas:

$$\rho = \frac{pM_{air}}{RT} = \frac{101325 \times 0.029}{8.314 \times 533} = 0.664 \text{ m}^3\text{s}^{-1}$$

The velocity of gas calculated based on air mass flow:

$$u_1 = \frac{m_{air}}{\rho A_c} = \frac{60}{3600 \times 0.664 \times \left(0.76 \times \pi \times \frac{0.106^2}{4}\right) \frac{\text{s}}{\text{h}} \cdot \frac{\text{m}^3}{\text{s}} \cdot \text{m}^2} \frac{\frac{\text{kg}}{\text{h}}}{} = 4.79 \text{ m s}^{-1}$$

Then, for laminar flow:

$$f = \frac{64}{\text{Re}} = \frac{64\mu}{\rho u_1 d} = \frac{64 \times 2.77 \times 10^{-5}}{0.664 \times 4.79 \times 0.00109} = 0.512$$

and hence:

$$u = \sqrt{\frac{\Delta p \, 2\text{d}}{f \, \text{L} \, \rho}} = \sqrt{\frac{398 \times 2 \times 0.00109}{0.512 \times 0.114 \times 0.664}} = 4.732 \text{ m s}^{-1}$$

## A1.6 Rotameter readings used to calculate hydrogen concentration in the exhaust

When performing the experiments with hydrogen addition, the amount of hydrogen added must be calculated, and a sample calculation is shown.

For example, using a rotameter, the flowrate of hydrogen was 0.1 litre/min at 10$^{o}$C and 1.013 bar (as measured with bubble flow meter). The engine exhaust flowrate varies from 55 to 60 kg h$^{-1}$ during the test. The molar mass of the exhaust gas was assumed to be 29 g mol$^{-1}$.

Molar volume of hydrogen at 10$^{o}$C and 1.5 bar pressure:

$$\text{Molar volume} = \frac{V}{n} = \frac{RT}{P} = \frac{8.314 \times (273.15 + 10)}{1.013 \times 10^{5}} \frac{\frac{\text{J}}{\text{K} \cdot \text{mol}} \times \text{K}}{\frac{\text{kg}}{\text{m} \cdot \text{s}^{2}}} = 0.0232 \frac{\text{m}^{3}}{\text{mol}} \tag{A1.8}$$

Molar flowrate of hydrogen:

$$F_{H_2} = V_f \times \frac{n}{V} = \frac{0.1 \times 10^{-3}}{60} \times \frac{1}{0.0232} \frac{\text{m}^{3}}{\text{s}} \cdot \frac{\text{mol}}{\text{m}^{3}} = 7.2 \times 10^{-5} \frac{\text{mol}}{\text{s}} \tag{A1.9}$$

Molar flowrate of exhaust gas:

$$F_{exhaust} = \frac{m_f}{M_{exhaust}} = \frac{60}{3600 \times 0.029} \frac{\frac{\text{kg}}{\text{h}}}{\frac{\text{s}}{\text{h}} \cdot \frac{\text{kg}}{\text{mol}}} = 0.575 \frac{\text{mol}}{\text{s}} \tag{A1.10}$$

Mole fraction of hydrogen in exhaust gas:

$$Y_{H_2} = \frac{F_{H_2}}{F_{exhaust}} = \frac{7.2 \times 10^{-5}}{0.575} \times 10^{6} = 125 \text{ ppm} \tag{A1.11}$$

## Reference

Hayes, R.E. and Kolaczkowski S.T. (1997) *Introduction to catalytic combustion*, Amsterdam: Gordon and Breach Science Publishers.

## Appendix 2: Nusselt number for different duct shapes

The Nusselt number is a key dimensionless quantity in heat transfer applications, which quantifies the convective heat transfer from a surface. As explained in Hayes and Kolaczkowski (1997; p. 664), it is defined as the ratio of the convective resistance to heat transfer in the gas phase to the convective resistance to the heat transfer in the gas phase.

$$Nu = \frac{D_H h}{k_f} = \frac{\frac{D_H}{k_f}}{\frac{1}{h}} = \frac{\text{conductive resistance to heat transfer in the gas phase}}{\text{convective resistance to the heat transfer in the gas phase}} \qquad \text{(A2.1)}$$

Where:

| | | |
|---|---|---|
| $D_H$ | characteristic length | m |
| $h$ | connective heat transfer coefficient | W $m^{-2}$ $K^{-1}$ |
| $k_f$ | thermal conductivity of gas | J $m^{-1}K^{-1}$ |

The analytically derived Nusselt numbers are a function of dimensionless groups characterizing duct geometry, and boundary conditions, these vary the parameters affecting heat transfer (Shah and London, 1978; p. 57).

According to the literature review in Hayes and Kolaczkowski (1997): channel shapes other than square and circular may be used in monolith reactors, for example, equilateral triangles and hexagonal shapes have also been reported, complete information on these shapes is lacking in the literature. Tronconi and Forzatti (1992) investigated monolith channels with equilateral triangular cross-sections. Groppi *et al* (1995) developed a correlation of Nusselt number for a square duct. Other values for different duct shapes may be found in Table 136 in Shah and London (1978) page 386.

Some examples of Nusselt number used for different duct shapes are summarised in Table A1.

**Table A1** Fully developed Nusselt numbers for the more commonly encountered shapes (modified from Hayes and Kolaczkowski 1997; p. 317).

| **Duct shape** | $\mathbf{Nu_T}$ | $\mathbf{Nu_{H2}}$ |
|---|---|---|
| Circular | 3.655 | 4.364 |
| Square | 2.977 | 3.095 |
| Equilateral triangle | 2.47 | 1.89 |
| Hexagonal | 3.34 | 3.862 |

Triangular and square channels often undergo a change in cross-section after application of the washcoat. Fillets of washcoat accumulate in the corners, thus rounding them.

## Reference


Groppi, G., Belloli, A., Tranconi, E.,Forzatti,P. (1995) Comparison of Lumped and Distributed Models of Monolith Catalytic Combustors, *Chemical Engineering Science*, **50** (17), 2705-2515.

Hayes, R.E. and Kolaczkowski S.T. (1997) *Introduction to catalytic combustion*, Amsterdam: Gordon and Breach Science Publishers.

Shah, R. K. and London, A. L. (1978) *Laminar flow forced convection in ducts: A source book for compact heat exchanger analytical data*. New York: Academic Press.

Tronconi, E. and Forzatti, P. (1992) Adequacy of Lumped Parameter Models for SCR Reactor with Monolith Structure, AIChE Journal, **38**, 201-210.

## Appendix 3: Derivation of NTU method (based on Lubeski, 2000)

The following derivation is based on an explanation in Lubeski (2000), which starts with the following assumptions:

- No heat loss to surrounding.
- No axial conduction along the substrate.
- Steady-state, and no accumulation terms.

In order to develop the equation for the average gas temperature across an element, both the heat transfer rate equation and the conservation of energy for the gas stream are required.

The heat transfer rate of the gas phase can be expressed as:

$$\delta q = h\,\delta A_s\,(T_g - \overline{T}_s) \tag{A3.1}$$

The rate of internal energy change for the gas phase:

$$\delta q = -(m C_P)_g\,\delta A_s \frac{dT_g}{dA_s} \tag{A3.2}$$

According to the gas phase energy balance, the rate of heat transferred to the solid equals the rate of internal energy change of the gas. Thus, combining Equations (A3.1) and (A3.2):

$$-(m C_P)_g\,\delta A_s \frac{dT_g}{dA_s} = h\,\delta A_s\,(T_g - \bar{T}_s) \tag{A3.3}$$

Eliminating $\delta A_s$ from both sides of Equation (A3.3), and after rearranging, it becomes:

$$\frac{dT_g}{(T_g - \overline{T}_s)} = -\frac{h\,dA_s}{(m C_P)_g} \tag{A3.4}$$

This is then integrated from $T_{g,0}$ to $T_{g,x}$, as well as from 0 to As', as shown:

$$\int_{T_{g,0}}^{T_{g,x}} \frac{dT_g}{(T_g - \overline{T}_s)} = -\int_0^{A_s} \frac{h\, dA_s}{(m\, C_P)_g} \tag{A3.5}$$

$$\ln\left(\frac{T_{g,x} - \overline{T}_s}{T_{g,0} - \overline{T}_s}\right) = -\frac{h\, A_s}{(m\, C_P)_g} \tag{A3.6}$$

Let:

$$-\frac{h\, A_s}{(m\, C_P)_g} = -\beta\, X \tag{A3.7}$$

Substituting Equation (A3.7) into (A3.6):

$$\ln\left(\frac{T_{g,x} - \overline{T}_s}{T_{g,0} - \overline{T}_s}\right) = -\beta\, X \tag{A3.8}$$

Taking the exponential:

$$\frac{T_{g,x} - \overline{T}_s}{T_{g,0} - \overline{T}_s} = e^{-\beta X} \tag{A3.9}$$

Rearranging Equation (A3.9):

$$T_{g,x} = (T_{g,0} - \overline{T}_s)e^{-\beta X} + \overline{T}_s \tag{A3.10}$$

Defining the arithmetic mean for an element of length $\ell$, and integrating respectively:

$$\overline{T}_g \equiv \frac{1}{\ell}\int_0^{\ell} T_{g,x}\, dx = \frac{1}{\ell}\int_0^{\ell} \left[(T_{g,0} - \overline{T}_s)e^{-\beta X} + \overline{T}_s\right] dx \tag{A3.11}$$

$$\overline{T}_g = (T_{g,0} - \overline{T}_s)\frac{1 - e^{-\beta \ell}}{\beta \ell} + \overline{T}_s \tag{A3.12}$$

By assuming that:

$$Ntu_h = \beta\, \ell \tag{A3.13}$$

for a single element.

Defining the gas heat transfer effectiveness in space as:

$$\varepsilon_s = \frac{1 - e^{-Ntu_h}}{Ntu_h} \tag{A3.14}$$

Substituting Equation (A3.14) into (A3.12), the average gas temperature across an element becomes:

$$\overline{T}_g = (T_{g,0} - \overline{T}_s)\varepsilon_s + \overline{T}_s \tag{A3.15}$$

The average solid temperature in time can be found in the same fashion; however, the heat transfer coefficient is produced from the difference between the average gas and the solid temperature.

$$\delta q = -(m C_P)_s \frac{dT_g}{dt} \tag{A3.16}$$

$$\delta q = h\, \delta A_s\, (\overline{T}_g - T_s) \tag{A3.17}$$

Next, then equations are combined resulting in:

$$\frac{dT_s}{(\overline{T}_g - T_s)} = -\frac{h\, \delta A_s}{(m C_P)_s} dt \tag{A3.18}$$

Once integrated from $T_{s,0}$ to $T_{s,t}$ and from 0 to t, the equation evolves into:

$$\int_{T_{s,0}}^{T_{s,t}} \frac{dT_g}{(\overline{T}_g - T_s)} = -\int_0^t \frac{h\, \delta A_s}{(m C_P)_s} dt \tag{A3.19}$$

$$\ln\left(\frac{\overline{T}_g - T_{s,t}}{\overline{T}_g - T_{s,0}}\right) = -\frac{h\, \delta A_s}{(m C_P)_s} t \tag{A3.20}$$

Let

$$\frac{h\, \delta A_s}{(m C_P)_s} t = \gamma\, t \tag{A3.21}$$

Substituting Equation (A3.21) into (A3.20):

$$\ln\left(\frac{\overline{T}_g - T_{s,t}}{\overline{T}_g - T_{s,0}}\right) = -\gamma\ t \tag{A3.22}$$

Taking the exponential from Equation (A3.22) and rearranging:

$$T_{s,t} = (T_{s,0} - \overline{T}_g)e^{-\gamma t} + \overline{T}_g \tag{A3.23}$$

Then defining the arithmetic for a time step θ yields the average temperature for the substrate:

$$\overline{T}_s \equiv \frac{1}{\theta}\int_0^{\theta} T_{s,t}dx = \frac{1}{\theta}\int_0^{\ell}\left[(T_{s,0} - \overline{T}_g)e^{-\gamma t} + \overline{T}_g\right]dt \tag{A3.24}$$

$$\overline{T}_s = (T_{s,0} - \overline{T}_g)\frac{1 - e^{-\gamma\theta}}{\gamma\theta} + \overline{T}_g \tag{A3.25}$$

A second integration takes place. Then using the Biot-Fourier dimensionless number:

$$\mathrm{BiFo} = \gamma\theta = \frac{h\,\delta A_s}{(m\,C_P)_s}\theta \tag{A3.26}$$

The solid heat transfer effectiveness in time is defined as:

$$\varepsilon_t = \frac{1 - e^{-\mathrm{BiFo}}}{\mathrm{BiFo}} \tag{A3.27}$$

Consequently, the average solid temperature during a time step becomes:

$$T_{s,t} = (T_{s,0} - \overline{T}_g)\varepsilon_t + \overline{T}_g \tag{A3.28}$$

The combination of both the average gas temperature across an element with the equation derived for the average solid temperature during a time step yields:

$$\overline{T}_g = \frac{T_{g,0} + T_{s,0}\left(\frac{\varepsilon_t}{\varepsilon_s} - \varepsilon_t\right)}{\left(1 + \frac{\varepsilon_t}{\varepsilon_s} - \varepsilon_t\right)} \tag{A3.29}$$

This above equation is substituted into the heat transfer rate Equation (A3.17). Afterwards, it is multiplied by the time step $\Delta t$ producing:

$$q = h\, A_s\, \Delta t \left( T_{g,0} \frac{\varepsilon_s}{\left(1 + \frac{\varepsilon_s}{\varepsilon_t} - \varepsilon_s\right)} - T_{s,0} \frac{\varepsilon_t}{\left(1 + \frac{\varepsilon_t}{\varepsilon_s} - \varepsilon_t\right)} \right) \tag{A3.30}$$

These derivations lead to these resulting equations for the conservation of energy in the fluid and the conservation of energy in the solid respectively:

$$T_{g,\ell} = T_{g,0} - Ntu_h \left( T_{g,0} \frac{\varepsilon_s}{\left(1 + \frac{\varepsilon_s}{\varepsilon_t} - \varepsilon_s\right)} - T_{s,0} \frac{\varepsilon_t}{\left(1 + \frac{\varepsilon_t}{\varepsilon_s} - \varepsilon_t\right)} \right) \tag{A3.31}$$

$$T_{s,\theta} = T_{s,0} + BiFo \left( T_{g,0} \frac{\varepsilon_s}{\left(1 + \frac{\varepsilon_s}{\varepsilon_t} - \varepsilon_s\right)} - T_{s,0} \frac{\varepsilon_t}{\left(1 + \frac{\varepsilon_t}{\varepsilon_s} - \varepsilon_t\right)} \right) \tag{A3.32}$$

## Reference

Lubeski, A. (2000) Real-time Catalytic Converter Temperature Estimator in the Powertrain Controller, SAE 2000-01-065.

# Appendix 4: Summary of Dimensionless Groups

The following explanations are in part copied and adapted from explanations in Hayes and Kolaczkowski (1997; pp. 661-669). Dimensionless groups are often used in engineering applications, including the catalytic converter studies. In the following, the dimensionless parameters that have been used are summarised in this thesis, and the physical meanings of these dimensionless group is also given.

**Graetz number, *Gz***

It is used for prediction of the convective heat transfer coefficient, *h*, since it is important for the calculation of the value of *Nu* number correlation.

Formula:

$$Gz = \mathrm{Re}\,\mathrm{Pr}\frac{D_H}{z} = \frac{\rho v D_H}{\mu}\frac{C_P \mu}{k_f}\frac{\mathrm{D_H}}{\mathrm{z}} = \frac{\left(\frac{D_H}{k_f}\right)}{\left(\frac{1}{\rho C_P v_m}\right)}\left(\frac{D_H}{\mathrm{z}}\right)^{*} = \frac{v_m D_H^2}{\alpha z} \qquad \text{(A4.1)}$$

Symbols:

| | | |
|---|---|---|
| $h$ | Convective heat transfer coefficient | W $m^{-2}$ $K^{-1}$ |
| $k_f$ | Thermal conductivity of gas | W $m^{-1}$ $K^{-1}$ |
| $\mu$ | Dynamic viscosity of the gas | kg $m^{-1}s^{-1}$ |
| $\rho$ | Mass density of the gas | kg $m^{-3}$ |
| $C_p$ | Mass heat capacity of gas | J $mol^{-1}$ $K^{-1}$ |
| $D_H$ | Hydraulic diameter | m |
| $Pr$ | Prandtl number | |
| $Re$ | Reynolds number | |
| $v_m$ | Mean average velocity of the gas | m $s^{-1}$ |
| $z$ | Distance from the entrance in the direction of gas flow | m |
| α | Thermal diffusivity of the gas (= $k_f$ / $\rho$ $C_p$) | |

* Meaning: $\frac{\text{conductive resistance to heat transfer in the gas phase}}{\text{convective resistance to the heat transfer in the gas phase}}$

Comments: The Graetz number is used in heat transfer to flowing fluids, especially where entrance effects are important. Note that product of the Reynolds and Prandtl number is the Peclet number for heat transfer, which is defined subsequently. A Graetz number for mass transfer can also be defined by replace the Prandtl number by the Schmidt number.

**Nusselt number, *Nu***

(e.g. for a gas flowing in a monolith channel)

Formula:

$$Nu = \frac{\left(\frac{D_H}{k_f}\right)^*}{\left(\frac{1}{h}\right)} = \frac{h\,D_H}{k_f} \qquad \text{(A4.2)}$$

Symbols:

| | | |
|---|---|---|
| $h$ | Convective heat transfer coefficient | W $m^{-2}$ $K^{-1}$ |
| $k_f$ | Thermal conductivity of gas | W $m^{-1}$ $K^{-1}$ |
| $D_H$ | Hydraulic diameter | m |

* Meaning: $\frac{\text{conductive resistance to heat transfer in the gas phase}}{\text{convective resistance to the heat transfer in the gas phase}}$

Comments: The Nusselt number is used to describe heat transfer to or from a flowing fluid.

**Reynolds number, *Re***

Formula:

$$\mathrm{Re} = \frac{\rho\, v_m D_H}{\mu} \qquad \text{(A4.3)}$$

Symbols:

| | | |
|---|---|---|
| $\mu$ | Dynamic viscosity of the gas | kg $m^{-1}s^{-1}$ |
| $\rho$ | Mass density of the gas | kg $m^{-3}$ |
| $D_H$ | Hydraulic diameter | m |
| $v_m$ | Mean average velocity of the gas | m $s^{-1}$ |

* Meaning: $\dfrac{\text{non - viscous forces}}{\text{viscous forces}}$

Comments: The Reynolds number is a dimensionless parameter that is often used to characterise a flow pattern. Many variations exist.

**Prandtl number, *Pr***

(e.g. describing flow of gas in a monolith channel)

Formula:

$$\mathrm{Pr} = \frac{\left(\dfrac{\mu}{\rho}\right)^*}{\left(\dfrac{k_f}{\rho\, C_p}\right)} = \frac{\mu C_p}{k_f} \qquad \text{(A4.4)}$$

Symbols:

| | | |
|---|---|---|
| $h$ | Convective heat transfer coefficient | W $m^{-2}$ $K^{-1}$ |
| $k_f$ | Thermal conductivity of gas | W $m^{-1}$ $K^{-1}$ |
| $\mu$ | Dynamic viscosity of the gas | kg $m^{-1}s^{-1}$ |
| $\rho$ | Mass density of the gas | kg $m^{-3}$ |
| $C_p$ | Mass heat capacity of gas | J $mol^{-1}$ $K^{-1}$ |

* Meaning: $\dfrac{\text{molecular diffusivity of momentum}}{\text{molecular diffusivity of heat}}$

Comments: The Prandtl number is used to describe heat transfer to or from a flowing fluid.

**Damköhler number, *Da***

(e.g. to describe a reaction in the catalyst layer and diffusion in the gas phase)

Formula:

$$Da = \frac{\left[\eta \cdot \left(-R_A\right)_s\right]^*}{\left(4 \cdot C_{A,s} \cdot \dfrac{D_{A,B}}{D_H}\right)} = \frac{\eta \cdot \left(-R_A\right)_s \cdot D_H}{4 \cdot C_{A,s} \cdot D_{A,B}} \qquad \text{(A4.5)}$$

Symbols:

| | |
|---|---|
| $\eta$ | Effectiveness factor |
| $C_{A,s}$ | Concentration of species A at the surface |
| $D_H$ | Hydraulic diameter of a channel |
| $D_{A,B}$ | Molecular diffusion coefficient for species A |
| $(-R_A)_s$ | Rate of disappearance of A evaluated at conditions on the external surface of the catalyst |

* Meaning: $\dfrac{\text{rate of reaction in the catalyst layer}}{\text{rate of external diffusion from the gas phase to the catalyst surface}}$

Comments: The Damköhler number is used to describe mass transfer with chemical reaction. There are many forms of the *Da* number described in the literature and the one shown here is only one possible form.

**Reference**

Hayes, R.E. and Kolaczkowski S.T. (1997) *Introduction to catalytic combustion*, Amsterdam: Gordon and Breach Science Publishers.

## Appendix 5: The cross-sectional area of washcoat

The cross sectional area of the washcoat is an important parameter. However, because of the irregular shape of the washcoat, the direct measurement of its cross sectional area becomes difficult. Therefore, a method was developed to calculate this area from images of the monolith channel using specialised software. The method uses a combined of image processing software (e.g. Adobe Photoshop) and the image process toolbox in MATLAB. An example of a magnified front view of a monolith channel taken using SEM is illustrated in Figure A1(a).

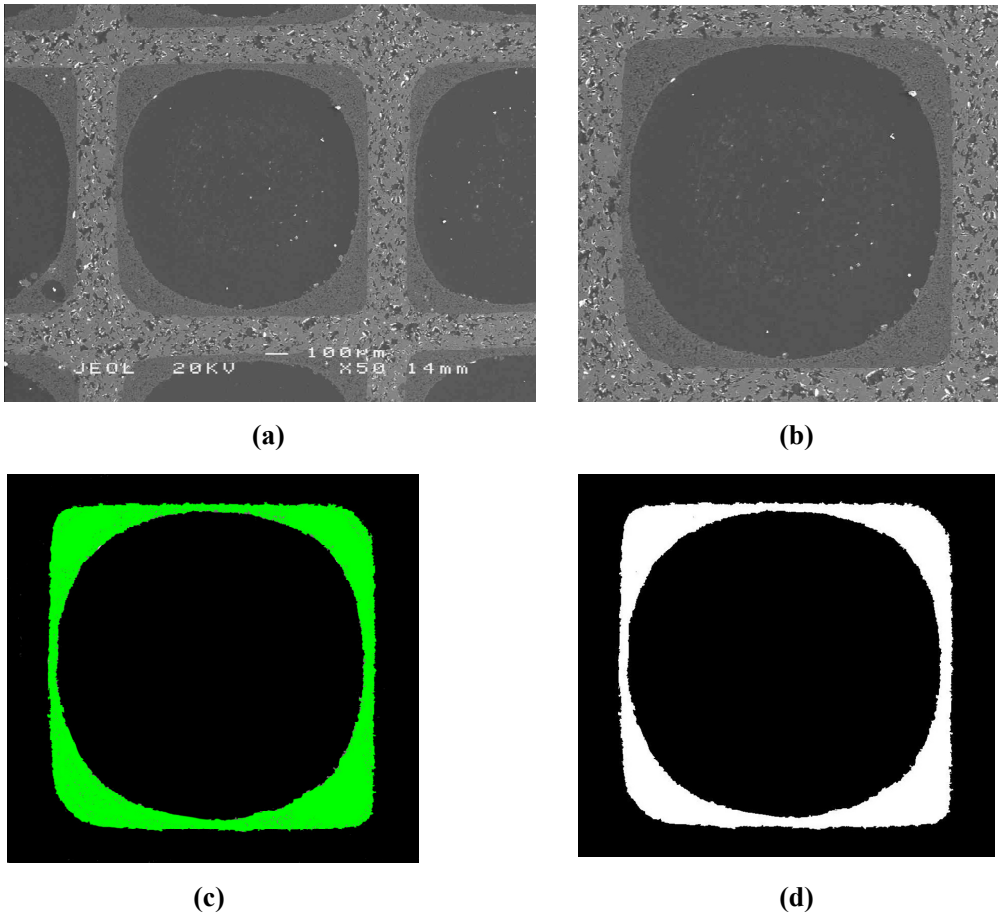


**Figure A1** (a) Example of an SEM picture of a monolith channel (b) image after cutting, (c) image processed by Photoshop, (d) image processed into black and white for boundary trace in MATLAB.

**Image processing in Photoshop**

The image process in Photoshop involves cutting and painting. Cutting captures the interested object for further processing (i.e. an image of a single channel in this case), see Figure A1(b).

The painting step is to enhance the contrast between the washcoat and other parts of the image, and this helps with the next step in MATLAB. The colour differences between the substrate, washcoat and open channel area are easily seen by the eye. A function called 'magic stick' in Photoshop can help to select certain parts of the image based on colour differences between them. Therefore each part can be selected and painted in two colours. The free channel and substrate were painted in dark colour and the washcoat was painted in a bright colour, this increased the contrast (e.g. green), see Figure A1(c).

**Further processing and calculating area of the washcoat in MATLAB**

A MATLAB code was written to process the image and calculate the area of the washcoat. First of all the image in Figure A1(b) was read in MATLAB and the pixels are converted into a the unit length scale (mm). In this case, 1 mm = 600 pixels.

Then Figure A1(c) was processed into black and white for boundary trace, see Figure A1(d). Therefore, the area of the white part of the image was calculated using MATLAB (in term of the number of pixels that is the area of washcoat). This area was originally presented in pixels and converted into $mm^2$ using the scale determined in the first place. This same process was applied to other SEM pictures of the monolith channel and similar results were found. The results are shown in Table A2.

**Table A2** Summary of the cross-sectional area of washcoat.

| Images | Washcoat area ($mm^2$) |
|---|---|
| 1 | 0.2824 |
| 2 | 0.2509 |
| 3 | 0.2511 |
| 4 | 0.2729 |
| **Average** | **0.2643** |

## Checks on this technique

In order to validate method, the code was used to calculate the area of a square in a picture, which had an area of 5813.86 $mm^2$. The area calculated using this method was found to be 5776.5 $mm^2$. The error was 0.64% which is considered to be acceptable, especially when considering the process of picture taking and then the processing of the image, which may create small changes to the actual area.

## MALAB code

```
% This code is developed to calculate the cross-sectional area of the washcoat .
clear all;
close all;
% Ask you to select the interested image from a file
[fname pname] = uigetfile('*.*', 'Select the first image');
cd (pname);
% Read the image
rgb=imread(fname);
% Threshold the image:convert the image to black and white in order to prepare for boundary tracing
using 'bwboundaries'
I = rgb2gray(rgb);
threshold = graythresh(I);
bw = im2bw(I,threshold);
imshow(bw); % show the black and white image
% Remove the niose:using morphology functions, remove pixels which do not belong to the objectives
of interest.
bw = bwareaopen(bw,30);   % Remove all object containing fewer than 30 pixels.
imshow(bw);
```

```
% Find the Boundaries: Concentrating only on the exterior boundaries. Option' noholes' will accelerate the processing by preventing 'bwboundaries'from searching for inner contours.
[B,L] = bwboundaries(bw,'noholes');
% Deterime free channel area and perimeter.
stats = regionprops(L,'Area','Centroid');
% Loop over the boundaries
for k = 1:length(B);
% Obtain (X,Y) boundary coordinates corresponding to label'k'
boundary = B{k};
% Compute a simple estimate of channel perimeter
delta_sq = diff(boundary).^2;
% Compute the area of the washcoat in pixels.
perimeter = sum(sqrt(sum(delta_sq,2)));
a(k) = stats(k).Area;
a=a';
% Show the areas in unit of mm^2
m=600; % 600 pixels for 1 mm
disp('washcoat area in mm^2:')
area =a/m^2
disp(area)
% compute the roundness metric
metric = 4*pi*a(k)/perimeter^2;
end
```

# Appendix 6: Checks on gas analyser readings

Figure A2 shows the CO concentration readings from two gas analysers (MEXA 1 and 2). The MEXA 1 reads consistently higher than MEXA 2 (when the inlet CO concentration was below 3000 ppm), and the MEXA 2 reads consistently higher (150 ppm) than MEXA 1 (when the inlet CO concentration above 3000 ppm).

Figure A3 shows the CO concentration reading differences between MEXA 1 and 2 against the readings from MEXA 1. It can be seen that the differences in CO readings were relatively stable when the inlet CO concentration was below 3000 ppm. However these increased linearly (with the inlet CO concentration) when the inlet CO concentration was above 3000 ppm.

Figure A4 shows the THCs concentration readings from two gas analysers. It can be seen that, within the low concentration range of THCs (below 300 ppm$C_1$) the two gas analysers' readings on THCs are very close. If the inlet THCs concentration was above 300 ppm$C_1$, then MEXA 2 reads higher.

Figure A5 shows the differences in THCs readings between MEXA 1 and 2, against the readings from MEXA 1.

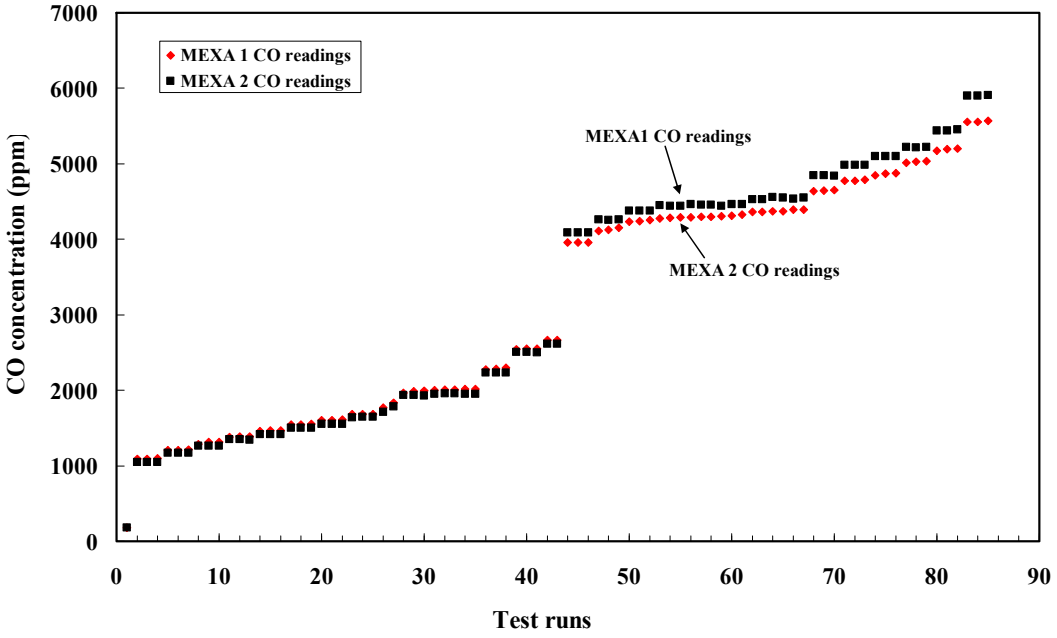


**Figure A2** CO readings from MEXA1 and 2.

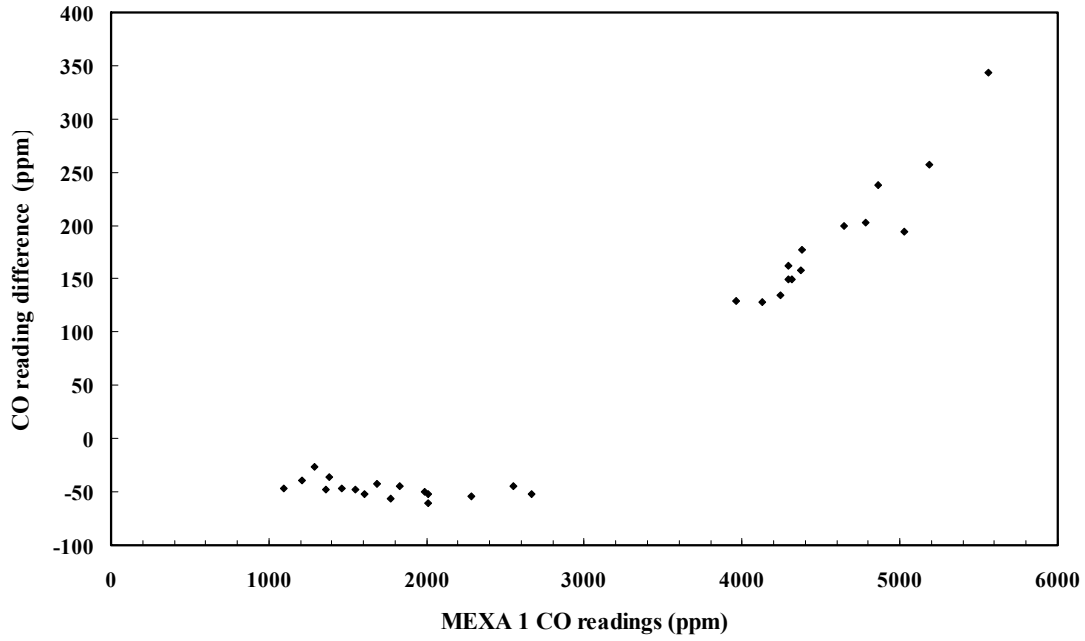


**Figure A3** The difference in CO readings between MEXA1 and 2, versus the CO readings on MEXA 1.

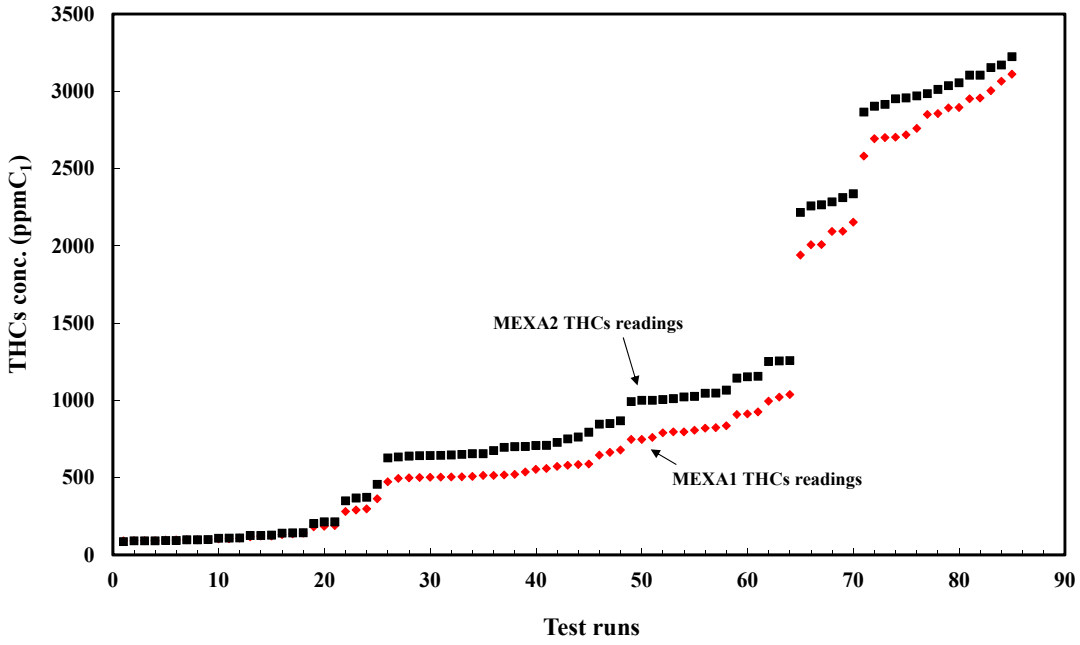


**Figure A4** THCs readings from MEXA1 and 2.

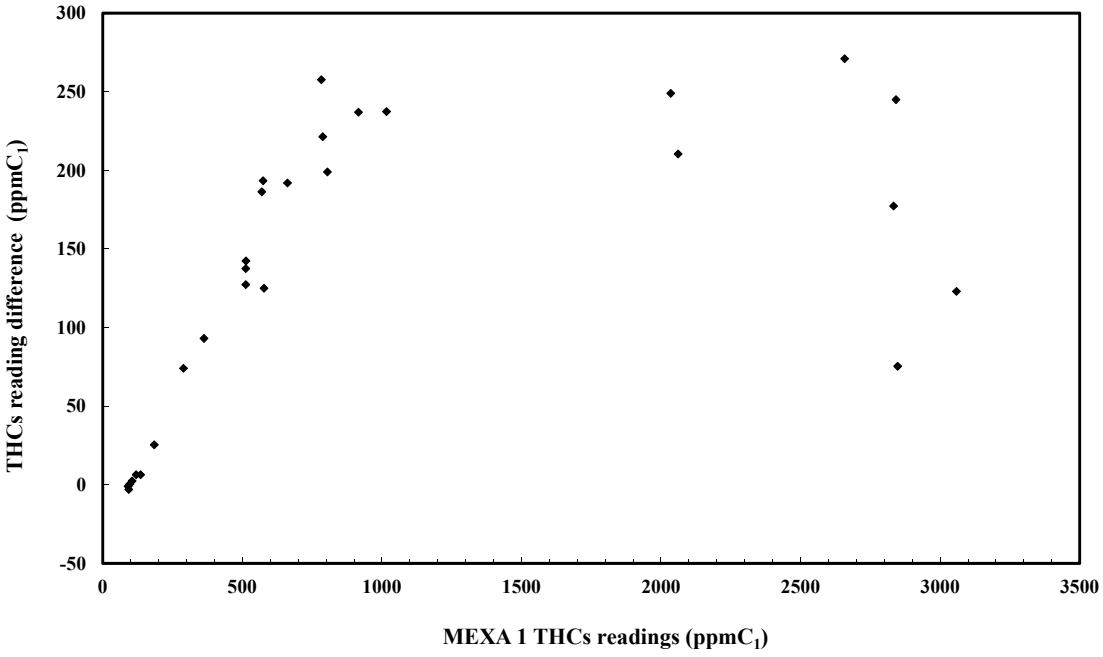


**Figure A5** The difference in THCs between MEXA1 and 2, versus the THCs readings on MEXA 1.

A Horiba engineer was invited to check the gas analysers. To check THCs readings, a bottle of 2000 ppm alpha grade propane in nitrogen was used. The engineer spanned the concentration from 0 to 6000 ppm$C_1$ using a special piece of kit and compared these concentrations with the readings on the two analysers. It was found that the THCs readings from the two analysers were close to the actual concentration. To calibrate the CO readings a similar process was repeated using 4000 ppm of CO in nitrogen, and then a calibration equation was created for each analyser to estimate the actual concentration from its reading.

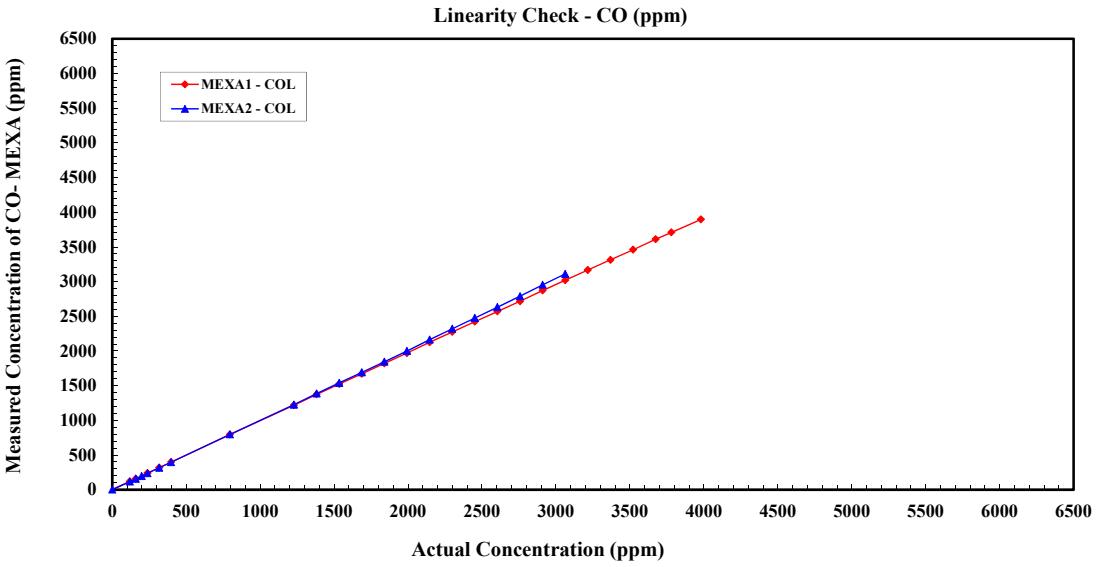


**Figure A6** Linearity check on CO readings.

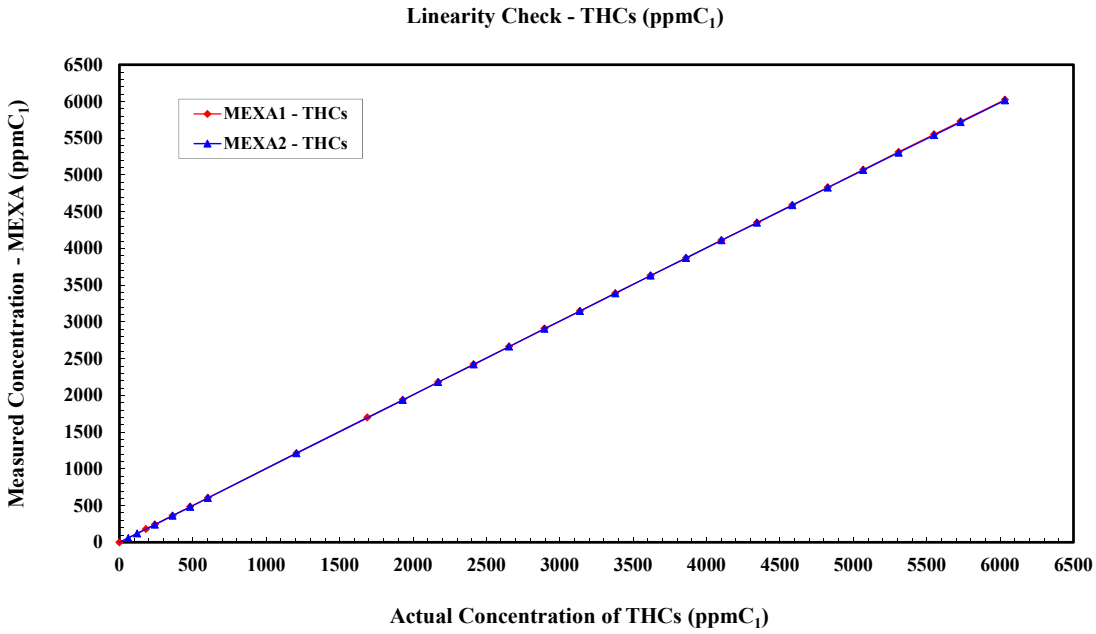


**Figure A7** Linearity check on THCs readings.

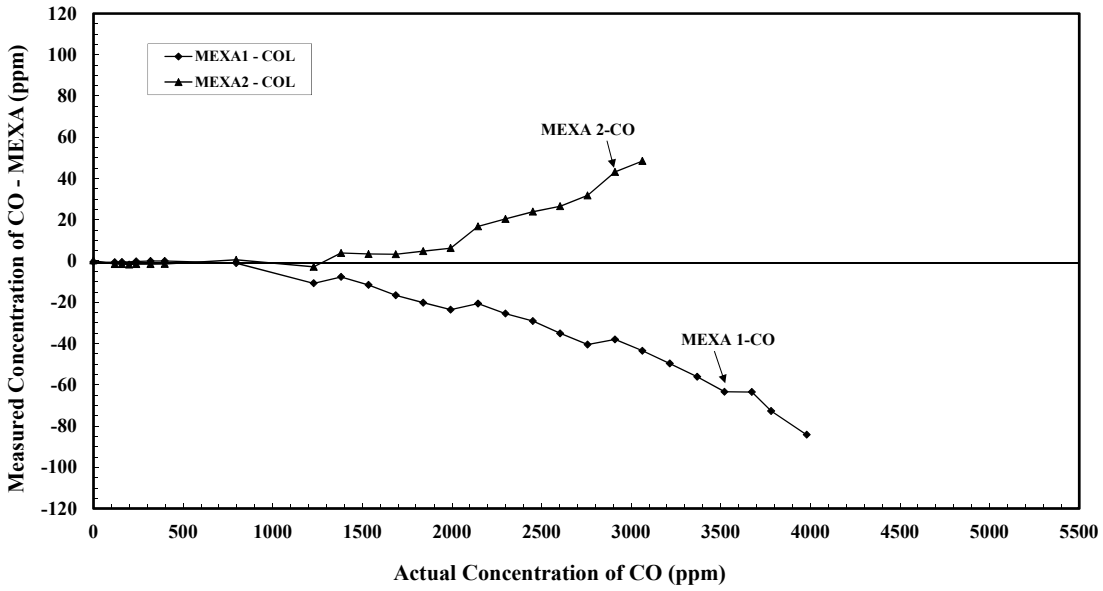


**Figure A8** Calibration curves for CO readings from MEXA1 and 2.

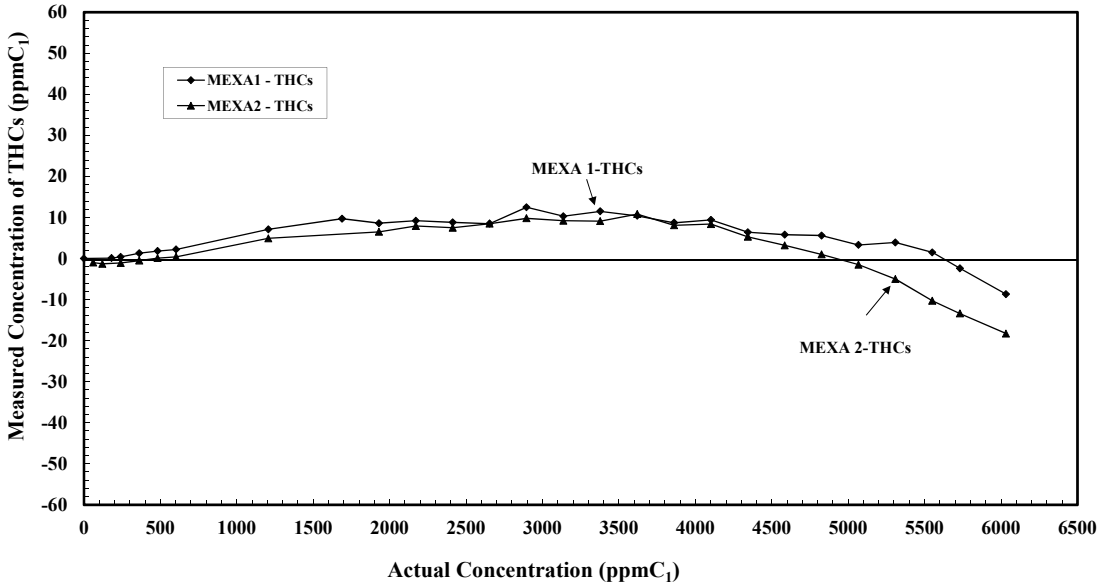


**Figure A9** Calibration curves for CO readings from MEXA1 and 2.

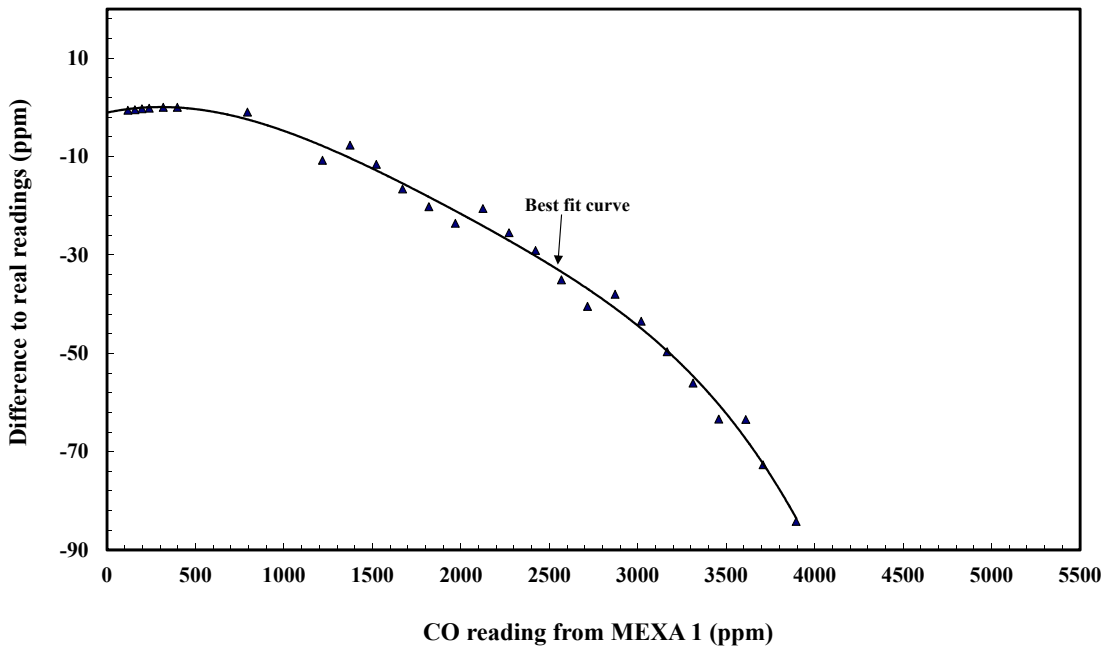


**Figure A10** Difference between MEXA1 CO readings and actual concentration.

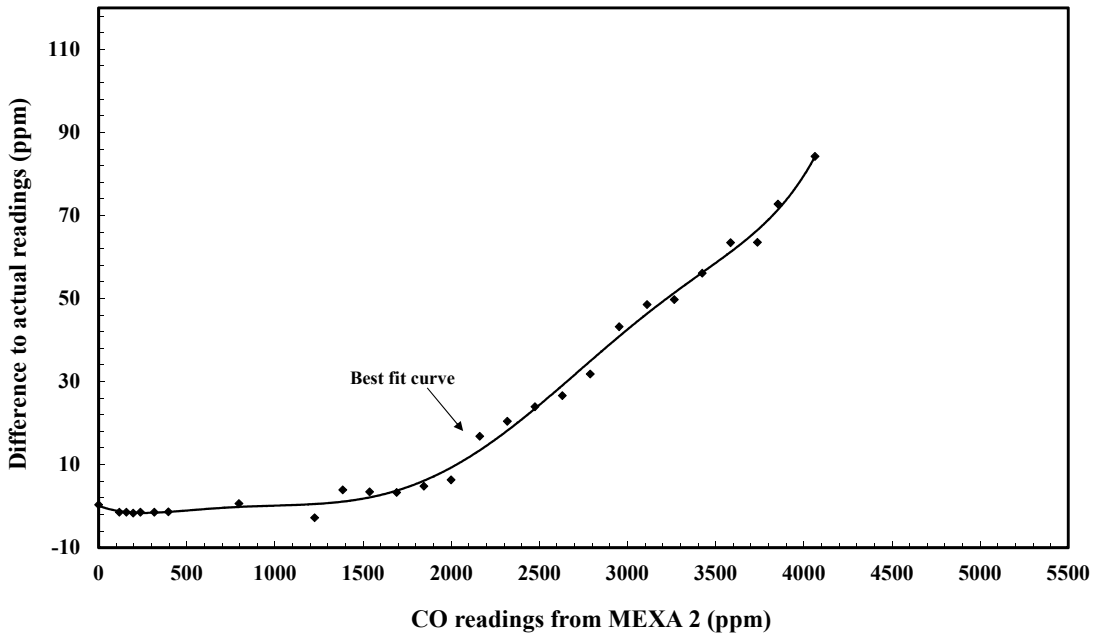


**Figure A11** Difference between MEXA2 CO readings and actual concentration.

**The correlations are:**

MEXA 1 CO reading correlation (ranges from 0 to 4000 ppm):

Actual CO concentration = $0.000000000000000000027465012837 \times CO^6 - 0.000000000000000441887133782804 \times CO^5 + 0.000000000015940576148543 \times CO^4 + 0.00000000022639064437315 \times CO^3 - 0.0000126373960171458 \times CO^2 + 0.0075119347212162 \times CO - 1.06348902621675$

MEXA 2 CO reading correlation (ranges from 0 to 4000 ppm):

Actual CO concentration = $0.000000000000000000712244651646 \times CO^6 - 0.000000000000008188886676186481 \times CO^5 + 0.000000000034124712041889 \times CO^4 - 0.00000006163831363080 54 \times CO^3 + 0.0000513647801703698 \times CO^2 - 0.0163410595396805 \times CO + 0.0924559408178391$

MEXA 1 CO reading correlation (used from 4000 to 5500 ppm):

Actual CO concentration = $-0.000000000000000000258943256581 \times CO^6 + 0.000000000000003976502961553790 \times CO^5 - 0.000000000022999934439786 \times CO^4 + 0.00000006167758657947 19 \times CO^3 - 0.000080778558665 1653 \times CO^2 + 0.0350630968244188 \times CO - 3.45146256623797$

MEXA 2 CO reading correlation (used from 4000 to 5500 ppm):

Actual CO concentration = $0.000000000000000000131051110802 \times CO^6 - 0.000000000000001740121389299 75 \times CO^5 + 0.000000000008150900752946 41 \times CO^4 - 0.000000015846283001263 4 \times CO^3 + 0.000018372863127864 8 \times CO^2 - 0.0098712699035086 6 \times CO - 0.0132951789779309$

**Note:**

CO is the CO readings from gas analysers.

# Appendix 7: Experimental data

## A7.1 Pseudo-steady-state light-off experiment data

**Table A3** An example of the experiment conditions and conversion data obtained from the pseudo-steady-state light-off experiments, where the inlet CO concentration and the inlet THCs concentrations were maintained at 3000 ppm and 1500ppm$C_1$, respectively. (Matched to Figure 3.47 )

| Avg Dyno Speed | Avg Torque | Mass Air Flow | Pre-Cat. CO | Post-Cat. CO | CO Conversion | Pre-Cat. HCs | Post Cat. HCs | THCs Conversion |
|---|---|---|---|---|---|---|---|---|
| rpm | Nm | kg/h | ppm | ppm | % | ppmC1 | ppmC1 | % |
| 1988 | 4 | 52.3 | 3065 | 3031 | 1.14 | 1488 | 1426 | 4.14 |
| 2000 | 8.1 | 55.0 | 3049 | 2949 | 3.25 | 1478 | 1426 | 3.52 |
| 2000 | 11.2 | 55.0 | 3024 | 2807 | 7.18 | 1509 | 1463 | 3.07 |
| 2000 | 12.2 | 55.2 | 3103 | 2805 | 9.58 | 1509 | 1460 | 3.23 |
| 2000 | 17 | 57.2 | 3100 | 2384 | 23.11 | 1490 | 1420 | 4.72 |
| 2000 | 17.1 | 56.4 | 3091 | 2261 | 26.85 | 1461 | 1375 | 5.89 |
| 2000 | 18.2 | 55.7 | 3101 | 1549 | 50.03 | 1464 | 1334 | 8.86 |
| 2000 | 19.3 | 55.3 | 3054 | 200 | 93.47 | 1462 | 1237 | 15.39 |
| 2000 | 19.4 | 57.3 | 3055 | 25 | 99.17 | 1532 | 1289 | 15.82 |
| 2000 | 20.1 | 57.1 | 3126 | 12 | 99.61 | 1569 | 1310 | 16.53 |
| 2000 | 21.8 | 56.9 | 3203 | 7 | 99.78 | 1562 | 1286 | 17.69 |
| 2000 | 23.4 | 57.5 | 3133 | 9 | 99.71 | 1529 | 1255 | 17.94 |
| 2000 | 24.3 | 57.6 | 3170 | 3 | 99.91 | 1541 | 1239 | 19.60 |
| 2000 | 26.6 | 58.5 | 3045 | 3 | 99.90 | 1484 | 1157 | 22.04 |
| 2000 | 30.1 | 59.5 | 3096 | 2 | 99.94 | 1477 | 1102 | 25.37 |
| 2000 | 33 | 59.1 | 3110 | 2 | 99.94 | 1460 | 1051 | 28.03 |
| 2000 | 38 | 59.2 | 3152 | 2 | 99.95 | 1531 | 1023 | 33.14 |
| 2000 | 40.3 | 60.5 | 3146 | 1 | 99.96 | 1516 | 984 | 35.08 |
| 2000 | 41 | 59.9 | 3179 | 1 | 99.96 | 1516 | 925 | 38.96 |
| 2000 | 46.7 | 60.4 | 3120 | 1 | 99.97 | 1445 | 749 | 48.18 |

**Table A4** An example of the temperature data obtained from the pseudo-steady-state light-off experiment, where the inlet CO concentration and the inlet THCs concentration were maintained at 3000 ppm and 1500 ppm$C_1$, respectively. (Matched to Figure 3.51).

| Inlet Gas Temperature | Outlet Gas Temperature | Solid temperatures ($^oC$) at different locations to inlet (mm) | | | | | | | |
|---|---|---|---|---|---|---|---|---|---|
| $^oC$ | $^oC$ | 5 | 20 | 30 | 40 | 50 | 65 | 85 | 105 |
| 146.8 | 145.8 | 148.1 | 148.4 | 148.6 | 148.4 | 148.5 | 148.6 | 148.6 | 148.6 |
| 156.6 | 155.5 | 158.0 | 158.3 | 158.6 | 158.3 | 158.4 | 158.5 | 158.6 | 158.6 |
| 166.7 | 165.8 | 168.2 | 168.6 | 169.0 | 168.7 | 168.7 | 168.9 | 169.2 | 177.0 |
| 170.2 | 170.4 | 171.9 | 172.4 | 172.8 | 172.5 | 172.7 | 173.1 | 174.0 | 176.4 |
| 183.0 | 208.4 | 185.0 | 185.6 | 187.1 | 187.2 | 188.1 | 189.4 | 206.3 | 216.9 |
| 184.6 | 210.2 | 186.7 | 188.6 | 190.5 | 189.7 | 189.9 | 191.4 | 209.1 | 217.0 |
| 187.6 | 215.7 | 189.7 | 191.1 | 193.8 | 193.0 | 193.4 | 198.7 | 217.3 | 221.5 |
| 192.2 | 219.9 | 194.5 | 196.2 | 201.7 | 204.8 | 214.6 | 220.6 | 222.8 | 225.4 |
| 194.5 | 223.6 | 197.6 | 199.5 | 208.0 | 219.4 | 226.0 | 227.7 | 228.5 | 230.1 |
| 197.8 | 227.3 | 201.2 | 203.1 | 215.7 | 227.9 | 230.8 | 232.1 | 232.8 | 234.5 |
| 201.1 | 230.8 | 204.8 | 207.1 | 225.5 | 234.0 | 235.7 | 236.7 | 236.8 | 237.9 |
| 204.0 | 233.6 | 207.7 | 209.9 | 226.8 | 235.9 | 237.5 | 238.7 | 239.3 | 241.1 |
| 209.4 | 240.3 | 214.0 | 234.2 | 243.3 | 244.4 | 245.4 | 246.4 | 246.9 | 248.4 |
| 215.2 | 245.4 | 223.8 | 247.3 | 249.0 | 249.3 | 250.0 | 250.9 | 251.4 | 253.2 |
| 224.3 | 254.8 | 245.7 | 259.5 | 260.8 | 260.8 | 261.4 | 262.0 | 262.1 | 263.4 |
| 233.4 | 264.7 | 264.2 | 269.1 | 270.4 | 270.4 | 271.0 | 271.8 | 272.4 | 274.2 |
| 250.5 | 282.2 | 283.6 | 286.9 | 288.5 | 288.5 | 289.2 | 290.1 | 290.8 | 292.7 |
| 258.0 | 288.8 | 291.1 | 294.3 | 295.8 | 295.8 | 296.4 | 297.2 | 297.7 | 299.5 |
| 265.2 | 298.7 | 299.2 | 302.8 | 304.7 | 304.9 | 305.8 | 307.1 | 308.1 | 310.3 |
| 285.6 | 318.5 | 320.6 | 324.1 | 326.1 | 326.4 | 327.2 | 328.4 | 329.3 | 331.2 |

## A7.2 Site competition (CO injection experiments)

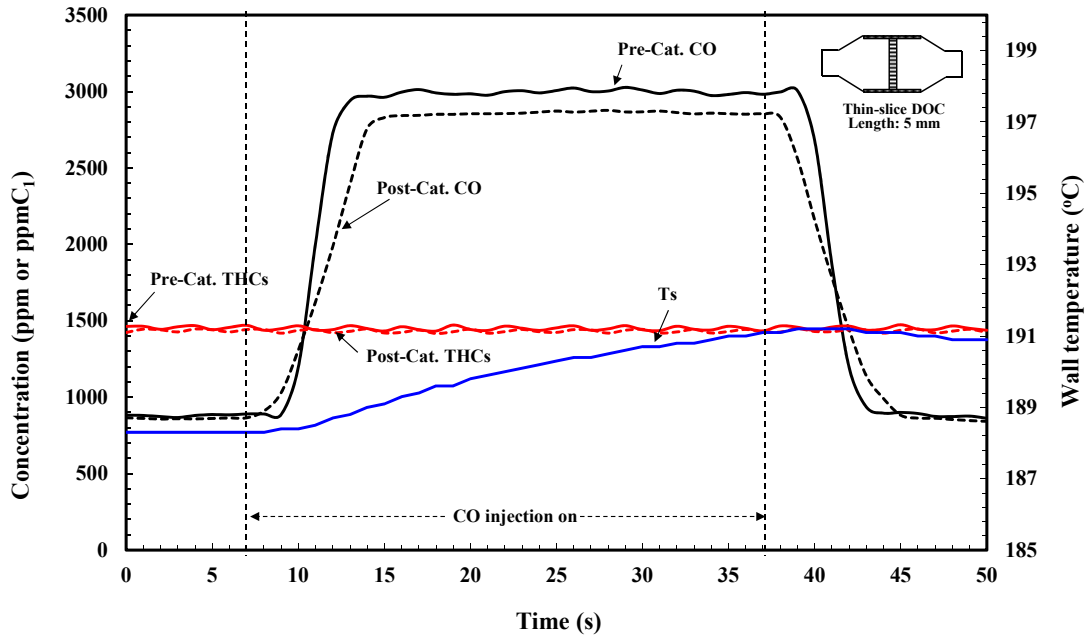


**Figure A12** Pre- and post-catalyst concentrations of CO and THCs when a pulse of 3000 ppm CO is injected with an inlet gas temperature of 188°C. The inlet THCs concentration was about 1500 ppm$C_1$.

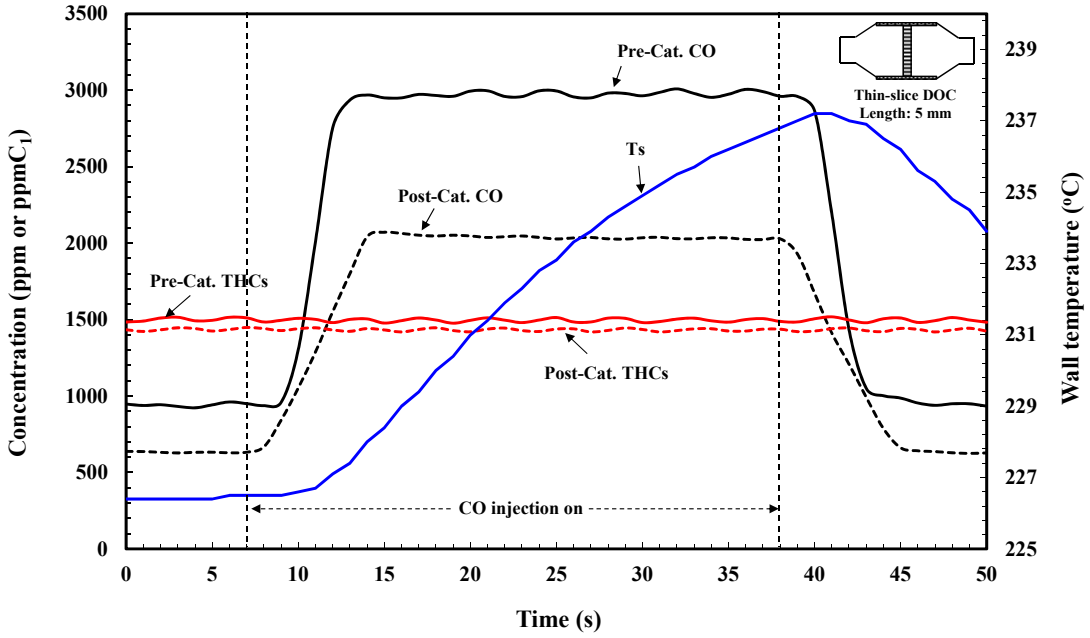


**Figure A13** Pre- and post-catalyst concentrations of CO and THCs when a pulse of 3000 ppm CO is injected with an inlet gas temperature of 218°C. The inlet THCs concentration was about 1500 ppm$C_1$.

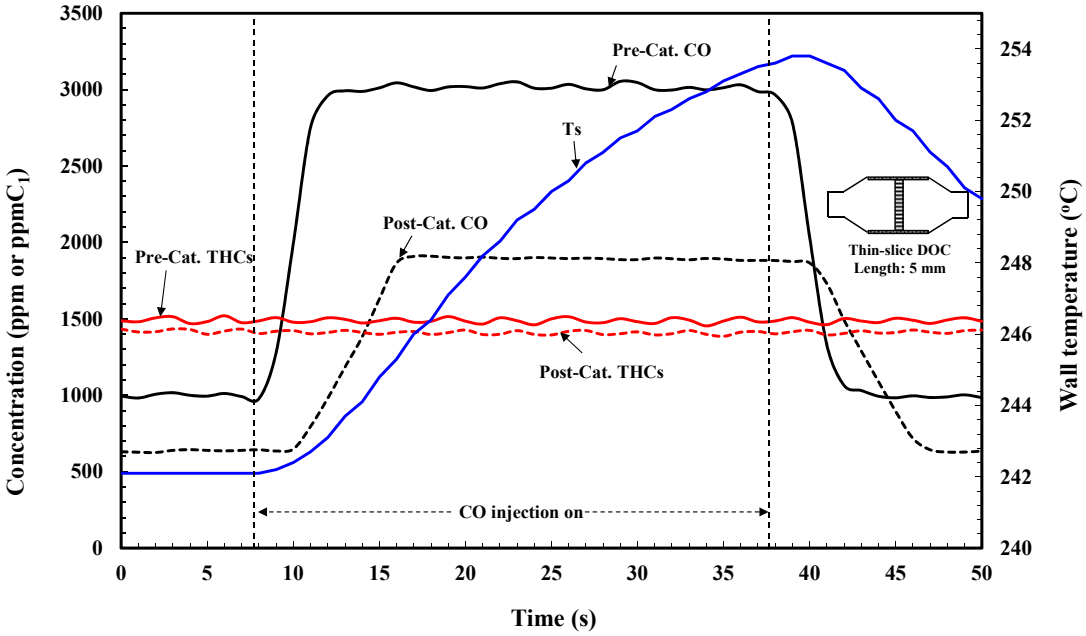


**Figure A14** Pre- and post-catalyst concentrations of CO and THCs when a pulse of 3000 ppm CO is injected with an inlet gas temperature of 232°C. The inlet THCs concentration was about 1500 ppm$C_1$.

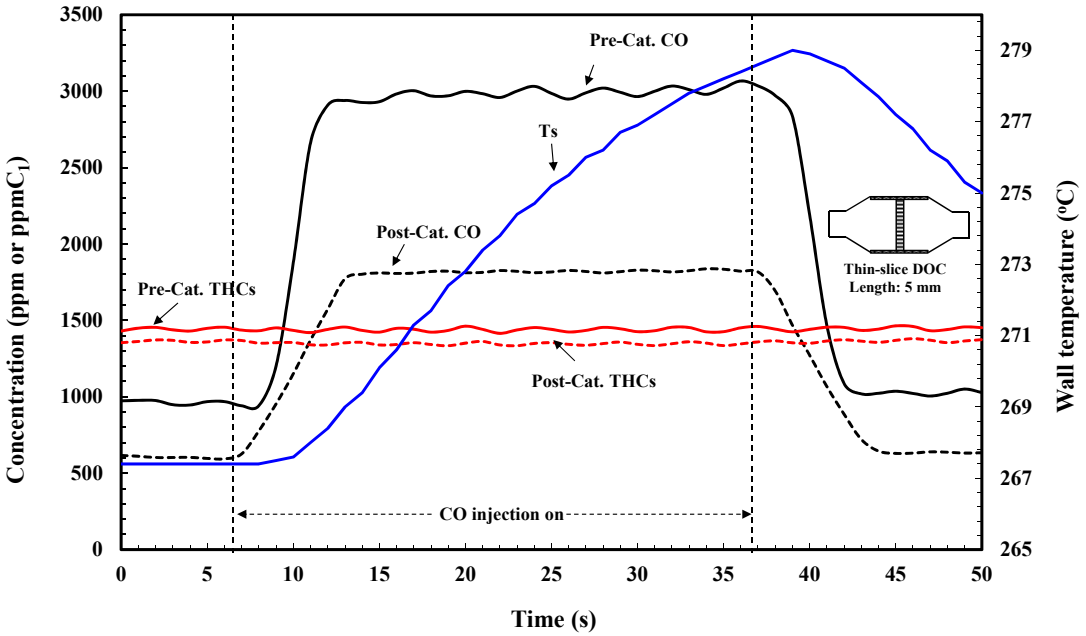


**Figure A15** Pre- and post-catalyst concentrations of CO and THCs when a pulse of 3000 ppm CO is injected with an inlet gas temperature of 258°C. The inlet THCs concentration was about 1500 ppm$C_1$.

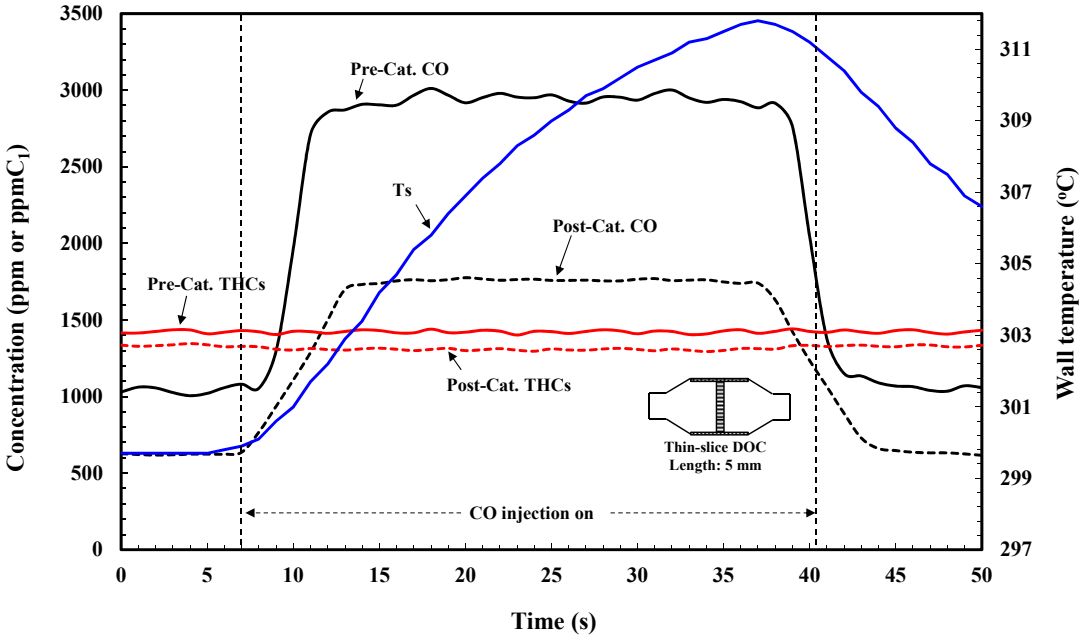


**Figure A16** Pre- and post-catalyst concentrations of CO and THCs when a pulse of 3000 ppm CO is injected with an inlet gas temperature of 290°C. The inlet THCs concentration was about 1500 ppm$C_1$.

## A7.3 Effect of the presence of hydrogen on the cold NEDC

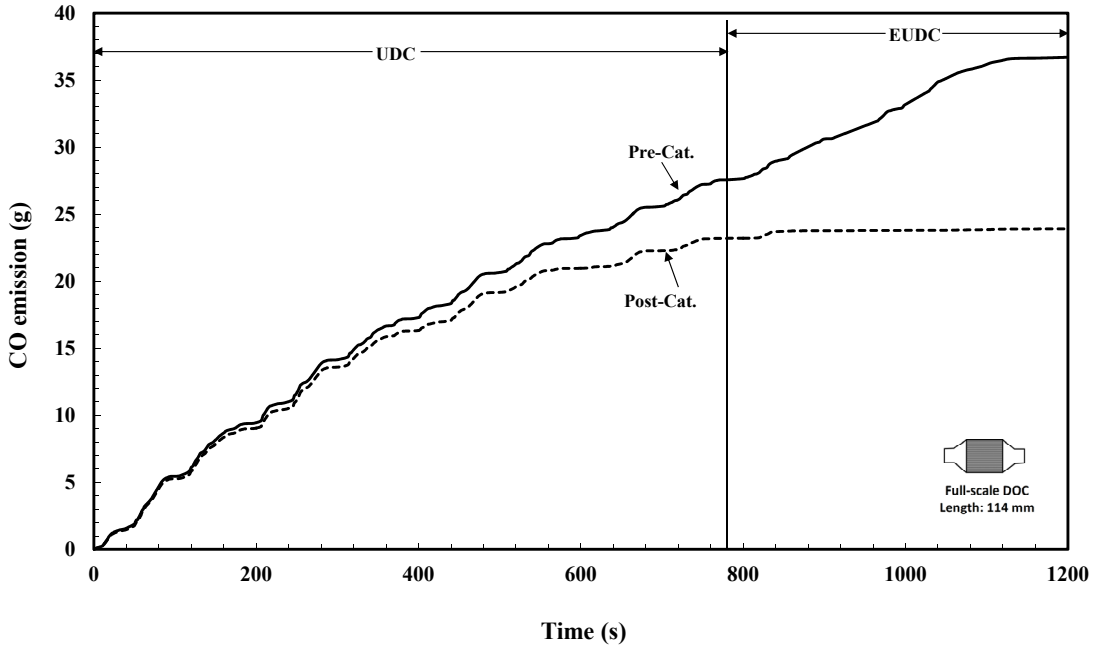


**Figure A17** Cumulative emissions of CO at pre- and post-catalyst position in the cold NEDC. No addition of hydrogen.

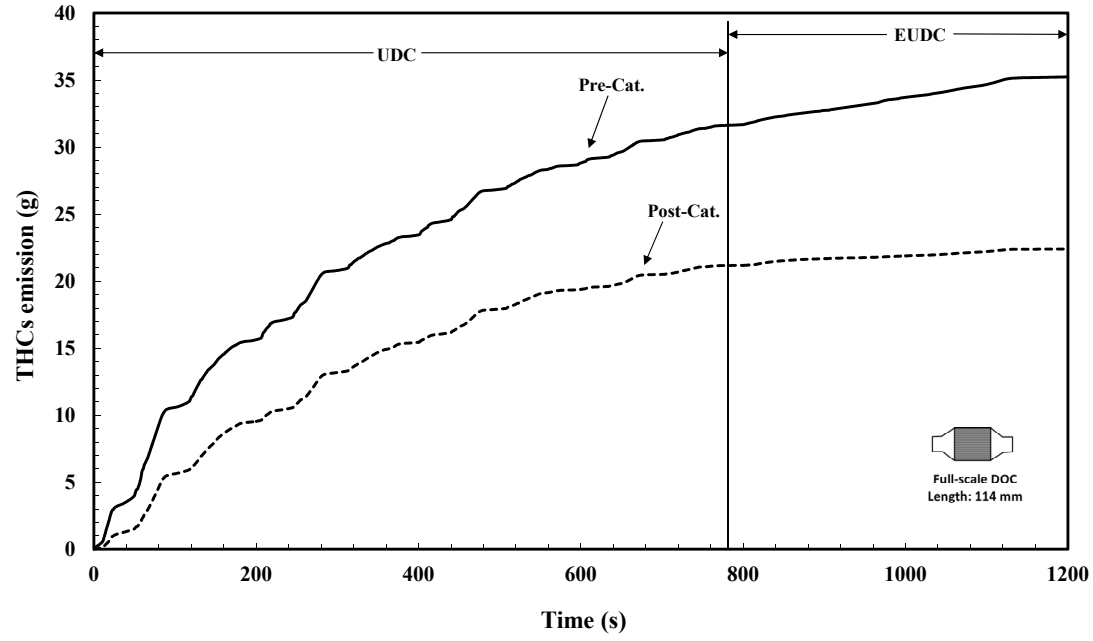


**Figure A18** Cumulative emissions of THCs at pre- and post-catalyst position in the cold NEDC. No addition of hydrogen.

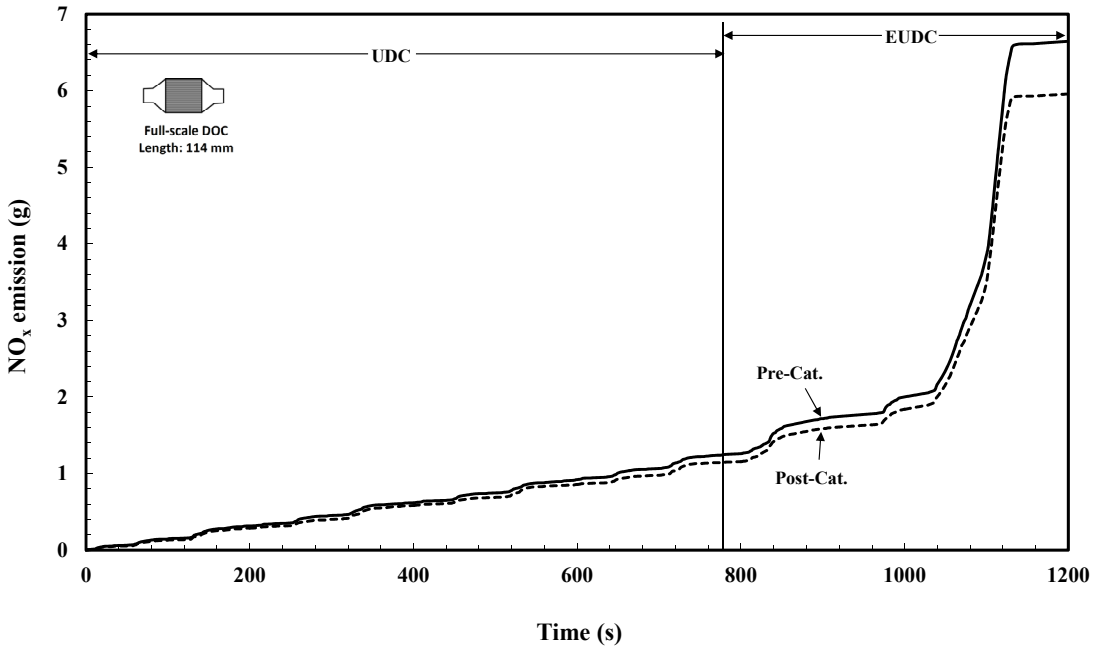


**Figure A19** Cumulative emissions of $NO_x$ at pre- and post-catalyst position in the cold NEDC. No addition of hydrogen.

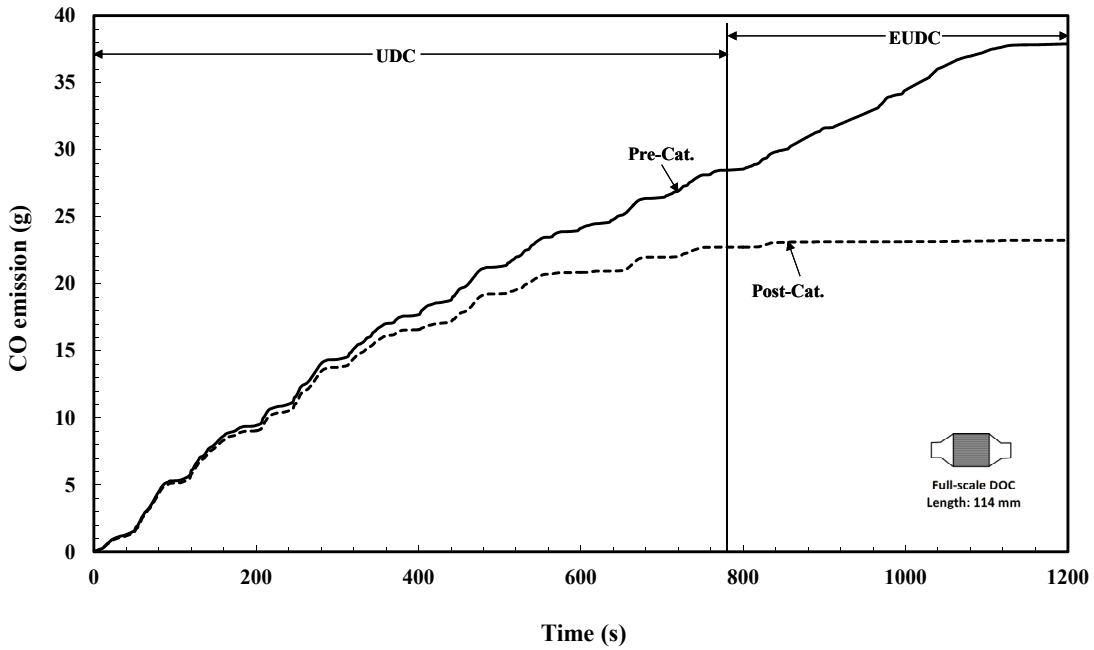


**Figure A20** Cumulative emissions of CO at pre- and post-catalyst position in the cold NEDC, hydrogen was added at 0.575 litre/min.

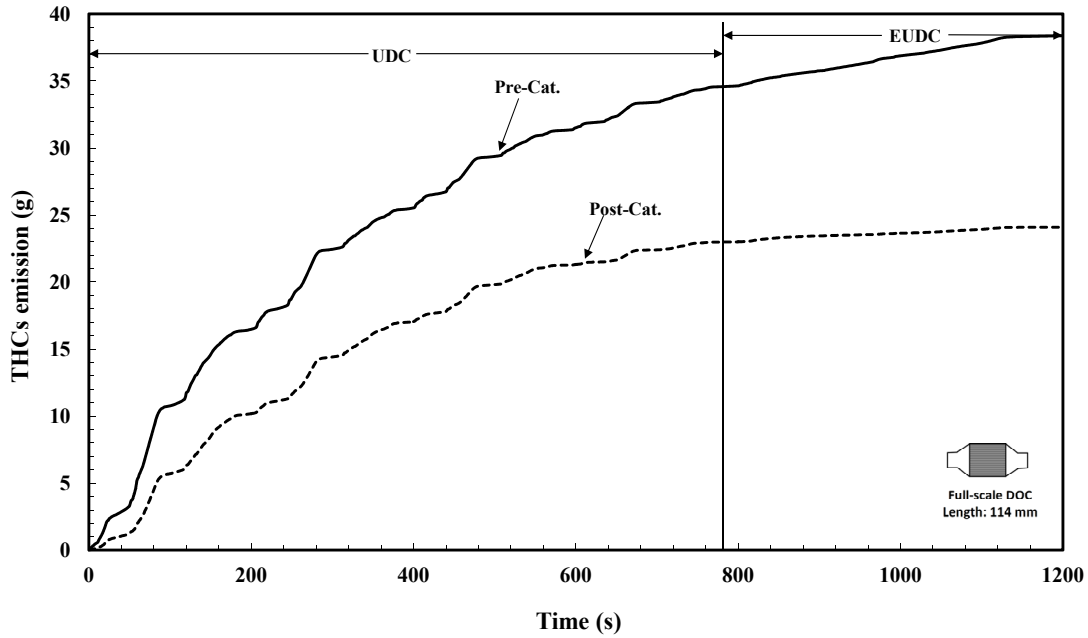


**Figure A21** Cumulative emissions of THCs at pre- and post-catalyst position in the cold NEDC, hydrogen was added at 0.575 litre/min.

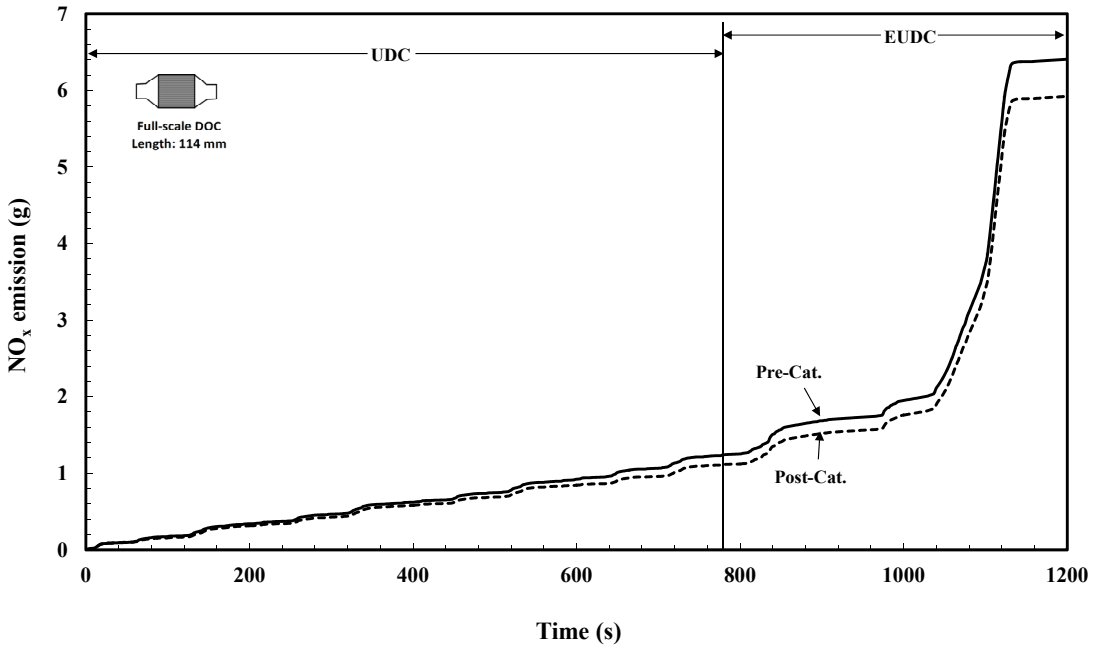


**Figure A22** Cumulative emissions of $NO_x$ at pre- and post-catalyst position in the cold NEDC, hydrogen was added at 0.575 litre/min.

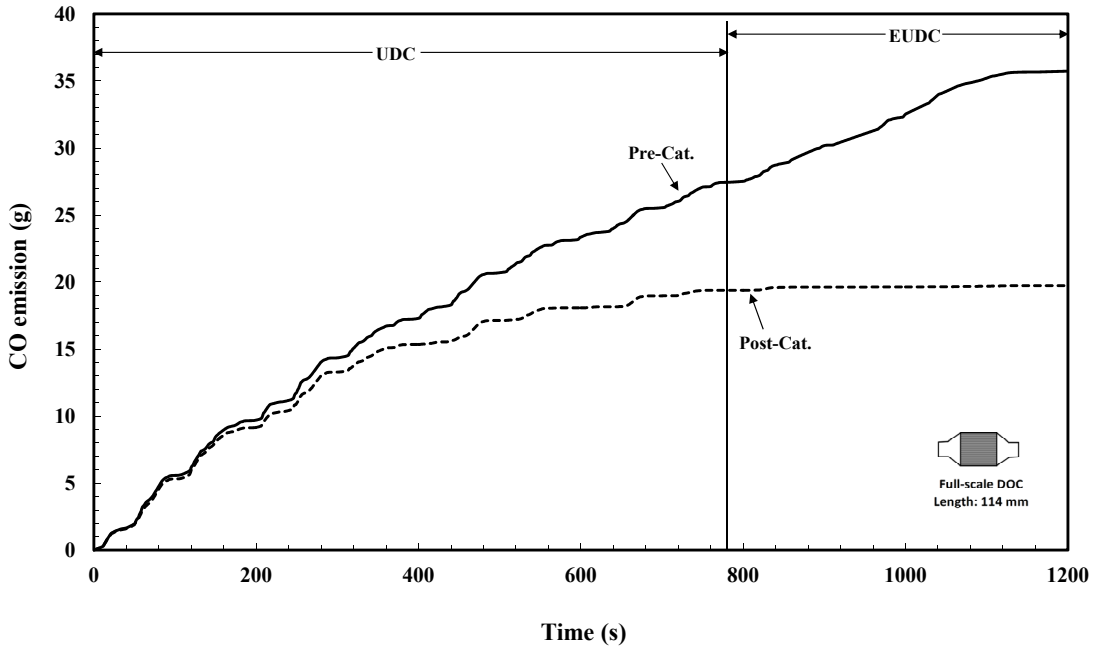


**Figure A23** Cumulative emissions of CO at pre- and post-catalyst position in the cold NEDC, hydrogen was added at 0.9 litre/min.

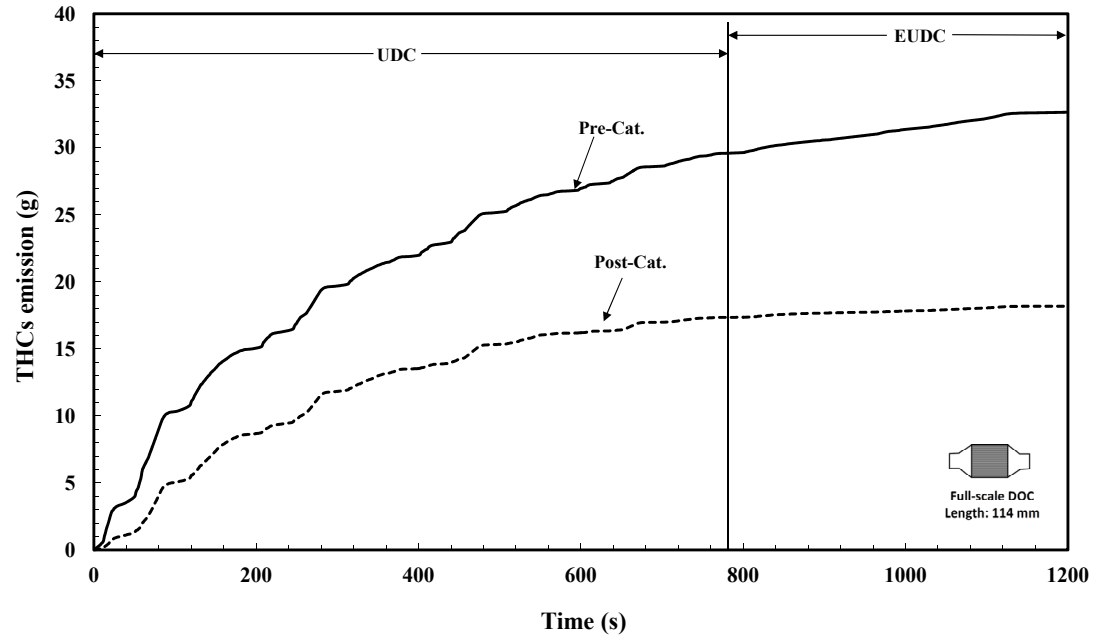


**Figure A24** Cumulative emissions of THCs at pre- and post-catalyst position in the cold NEDC, hydrogen was added at 0.9 litre/min.

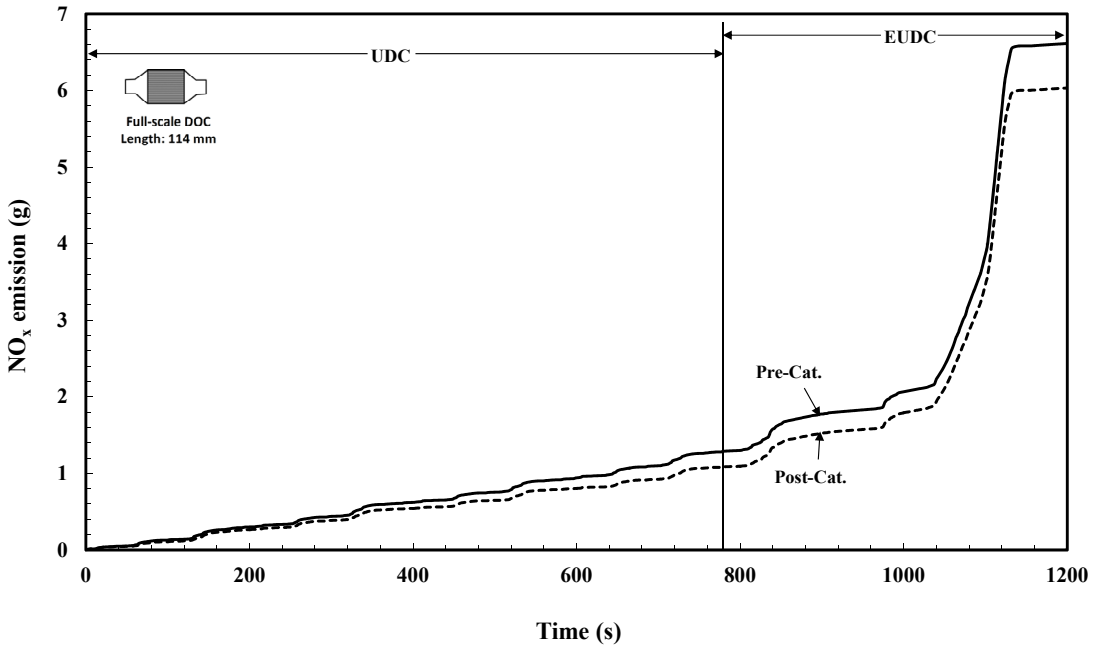


**Figure A25** Cumulative emissions of CO at pre- and post-catalyst position in the cold NEDC, hydrogen was added at 0.9 litre/min.

# Appendix 8: Mathematical models in MATLAB

## A8.1 Code I: Implicit finite difference thermal model (used to simulate Figure 4.4)

```
% First MATLAB code of implicit method
% Two equations (solid phase and gas phase) PDE
% Solved with Backward Euler method
% Governing equations:
% Solid phase     h (Ts- Tb) = gwrhoCpw(dTs/dt)
% Gas phase       rhoCpv(dT/dz) + 4/DH h (Ts-Tb) =rhoCpdT/dt

clear                   % This removes any previously created variables
% Physical parameters
vel =2;                 % Air velocity m/s
t=0 ;                   % Initial time s
z=0;                    % Initial length
tend =5.7;              % Finishing time s
N = 100;                % Number of steps in z-direction
Len = 0.114;            % Length of channel m
dz = Len/N;             % Step size in z-direction m
Tgo = 400;              % Initial Gas Temperature K
Tso = 500;              % Initial Solid Temperature K
dt = dz/vel;            % Step size in time s
M =tend/dt;             % Number of points in time domain
h= 0;                   % Heat transfer coefficient   W/m2/K
den = 0.5;              % Density of air kg/m3
Cp= 1012;               % Heat capacity of air at 20oC J/kg/K
DH = 1.09e-3;           % Hydraulic diameter m
g_w = 0.139e-3;         % Effective wall thickness m
rho_w = 2500;           % Density of monolith kg/m3
Cp_w = 1005;            % Solid wall heat capacity J/kg/K

% Set up matrix for temperatures
Tg=zeros(N,M);
Ts=zeros(N,M);
history_Tg = Tg;
history_Ts = Ts;

alpha = (4*h)/(DH *den*Cp)  ;
beta = h/(g_w*rho_w*Cp_w);
gamma = 1+ ((vel*dt)/(dz))+ alpha*dt;
% Enter the boundary conditions
for J=1:M
Tg(1,J)=400;
end
% Enter the coefficients
a1= gamma;
b1= alpha*dt;
c1= vel*dt/(dz);
```

```
a2 =(beta*dt);
b2= (1+beta*dt);
c2= 1;
RHS=ones(2,1);
A=zeros(2,2);
% Set up matrix for RHS
% Enter initial conditions
for j=1
Tg(1,1)=400;
Tg(2:N, j)=500;
Ts(1:N, j)=500;
end

for i=2:N                % z step loop
for j=2:M                % Time step loop
% Calculating solid temperature at i = 2:N, j = 2
Ts(1,j)=((Ts(1,j-1)+beta*dt*Tg(1,j))/(1+beta*dt));

A(1,1) = a1 ;
A(1,2)= -b1;
A(2,1)= -a2 ;
A(2,2)= b2;
RHS(1)=c1*Tg(i-1,j)+Tg(i,j-1);
RHS(2)=Ts(i,j-1);
T=A\RHS;
Tg(i,j)=T(1);
Ts(i,j)=T(2);
end
end

% Plotting the gas temperature as a function of time.
plot(1:M,Tg(50,1:M)','r')
hold on
xlabel('time steps (5.7 s in total)')
ylabel(' Gas Temperature K')
title('Graph of Gas Temperatures against  time ')
```

## A8.2 Code II: NTU thermal model (used to simulate the NTU curve in Figure 4.5)

```
% Calculate the results from using NTU method
% Enter physical parameters
h= 100;                 % Heat transfer coefficient   W m^-2K^-1
L= 0.0114;              % Control length of the channel m
den = 0.5;              % Density of air kg m^-3
Cp= 1012;               %Heat capacity J kg^-1 K^-1
DH = 1.09e-3;           % Hydraulic diameter
g_w = 0.139e-3;         % Effective wall thickness
rho_w = 2500;           % Density of monolith kg m^-3
Cp_w = 1005;            % Solid wall heat capacity J kg^-1K^-1
vel =2;                 % Air velocity m s^-1
As = pi*DH*L;           % Cross sectional area
N=100;                  % Length
t=0.00057;              % Time s
dt=0.00057;
history_Tg = Tg;
history_Ts = Ts;
Ac = (DH+0.12e-3)^2-DH^2;       % Cross sectional area of solid, m^2
Ax = DH^2;
% Initial temperature, K.
Tgo = 500;
Tso = 500;
while  t < 0.00114
% coefficients
% Biot-Fourier Number
BiFo =(h*As*t)/(Ac*L*rho_w*Cp_w);
%Number of Heat transfer Units
NTUh = (h*As)/(den*vel*Ax*Cp);
% Effectiveness factor
Et = (1-exp(-BiFo))/BiFo;
Es = (1-exp(-NTUh))/NTUh;
% Average temperature
Tg = Tgo-NTUh*(Tgo*Es/(1+Es/Et-Es)-Tso*Et/(1+Et/Es-Et));
Ts = Tso+BiFo*(Tgo*Es/(1+Es/Et-Es)-Tso*Et/(1+Et/Es-Et));
```

```
t=t+dt;
history_Tg = [history_Tg,Tg];
history_Ts = [history_Ts,Ts];
end

Tgo = 400;
Tso = 500;

while t <5.7
% Coefficients
% Biot-Fourier Number
BiFo = (h*As*t)/(Ac*L*rho_w*Cp_w);
%Number of Heat transfer Units
NTUh = (h*As)/(den*vel*Ax*Cp);
% Effectiveness factor
Et = (1-exp(-BiFo))/BiFo;
Es = (1-exp(-NTUh))/NTUh;
% Average temperature
Tg = Tgo-NTUh*(Tgo*Es/(1+Es/Et-Es)-Tso*Et/(1+Et/Es-Et));
Ts = Tso+BiFo*(Tgo*Es/(1+Es/Et-Es)-Tso*Et/(1+Et/Es-Et));
t=t+dt;
history_Tg = [history_Tg,Tg];
history_Ts = [history_Ts,Ts];
end
plot(history_Ts','*r')
hold on
xlabel ('Time steps')
ylabel (' solid Temperature at entrance ')
title ('Graph of solid Temperatures  against  time ')
```

## A8.3 Code III: 1-D heat transfer model

```
% This code contains the heat capacity of air and walls changing with temperatures, the
heat transfer coefficient, and heat conduction in solid phase as well.
% Validation of benjamin's method (50s)
% Using half implicit method to solving the model
% Two equations (solid phase and gas phase) PDE
% solid phase    kw g_w (dTs2/d2z)-h (Ts- Tb) = gwrhoCpw(dTs/dt)
% gas phase       -den Cp vel(dTg/dz) + 4/DH h (Ts-Tb) =0

clear                   % This removes any previously created variables
vel =2.34;              % Air velocity m/s
tend = 50;              % End time s
N = 100;                % Number of points in z-direction
Len = 0.15;             % Length of the monolith m
dz = Len/N;             % Step size in z-direction m
Tgo = 299;              % Initial Gas Temperature K
Tso = 293;              % Initial Solid Temperature
M =10000;               % Number of points in t-direction
dt = tend/M;            % Step size in time
kg = 0.024;             % Thermal conductivity of air w/mk
DH = 1.108e-3;          % Hydraulic diameter m
void = 0;
g_w = 0.081e-3;         % Effective wall thickness m
rho_w = 1750;           % Density of cordierite kg/m3
Tg=zeros(N,M);          % Define Tg in matrix
Ts=zeros(N,M);          % Define Ts in matrix
Cp_w=zeros(N,M);        % Solid wall heat capacity J/kg/K
Cp =zeros(N,M);         % Air heat capacity J/kg/K
vis = zeros(N,M);       % Define viscosity pa.s
kf = zeros (N,M);       % Define thermal conductivity of gas J/K/m
z=zeros (N,M);
% Defined coefficients to simplify the governing equations
alpha = zeros(N,M);
beta = zeros (N,M);
gamma = zeros (N,M);
eee=zeros(N,M);
% Set up matrix for dimensionless numbers
Re = zeros(N,M);
Pr = zeros(N,M);        % Prandtl number
Gz = zeros(N,M);        % Graetz number
h = zeros(N,M);         % Heat transfer coefficient
% Set up matrix for coefficients
a1=zeros(N,M);
b1 =zeros(N,M);
a2 = zeros(N,M);
b2 = zeros (N,M);
c1 = zeros(N,M);
c2= zeros(N,M);
RHS=ones(2,1);
RHSb=ones(2,1);
A=zeros(2,2);
A2=zeros(2,2);
% Enter initial conditions
```

```
for j=1
for i=1:N
Ts(i,j)=293;
Tg(i,j)=299;

% Calculating initial physical properties
Cp_w(i,j) = (1071+0.156*Ts(i,j)-(3.437*10^7)*Ts(i,j)^(-2))*(1-void);
Cp(i,j) = (28.09+(0.1965*10^(-2))*Tg(i,j)-(0.4799*10^(-5))*Tg(i,j)^2-(1.965*10^(-
9))*Tg(i,j)^3)*34.53;
vis(i,j) = 7.701*10^(-6)+ 4.166*10^(-8)*Tg(i,j)-7.531^(-12)*Tg(i,j)^2;
kf(i,j) = 1.679*10^(-2)+Tg(i,j)*5.073*10^(-5);
kw(i,j) = 0.9558-Ts(i,j)*2.09*10^(-4);
% Calculating initial physical properties
z (i,j) = dz*i;
Re(i,j) = (den*vel*DH)/vis(i,j);
Pr(i,j) = (Cp(i,j)*vis(i,j))/kf(i,j) ;
Gz (i,j) = Re(i,j)*Pr(i,j)*DH/z(i,j) ;
h(i,j) = (3.095 + 8.933*((1000/Gz(i,j))^(-0.5386))*(exp(-6.7275/Gz(i,j))))*kf(i,j)/DH;
% calculating initial coefficients
alpha(i,j) = (h(i,j)*dt)/(g_w*rho_w*Cp_w(i,j));
beta(i,j) = (4*h(i,j)*dz)/(vel*den*Cp(i,j)*DH);
eee(i,j) = h(i,j)/(g_w*rho_w*Cp_w(i,j));
gamma(i,j) = (h(i,j)*dz^2)/(kw(i,j)*g_w);
end
end

for j=2:M        % Time step loop
for i=2:N-1      % z step loop

% Inlet gas temperature loop as a function of time
Tg(1,j) =1.0266426857E-20*j^6 - 3.23015247029278E-16*j^5 + 3.759619051921593E-
12*j^4 - 1.87731547616258E-8*j^3 +  2.63055066311857E-5*j^2
+0.0828468360041748*j + 298.434228079564;
% calculating solid temperature at first section i =1, j = 1:M;
Ts(1,j)=((Ts(1,j-1)+eee(1,j)*dt*Tg(1,j))/(1+eee(1,j)*dt));
% calculating correlatins of physical parameters when i =1:N-1, j = 1:M;
Cp_w(1,j) = (1071+0.156*Ts(1,j-1)-(3.437*10^7)*Ts(1,j-1)^(-2))*(1-void);
Cp_w(i,j) = (1071+0.156*Ts(i,j-1)-(3.437*10^7)*Ts(i,j-1)^(-2))*(1-void);
Cp(1,j) =(28.09+(0.1965*10^(-2))*Tg(1,j-1)-(0.4799*10^(-5))*Tg(1,j-1)^2-(1.965*10^(-
9))*Tg(1,j-1)^3)*34.53;
Cp(i,j) =(28.09+(0.1965*10^(-2))*Tg(i,j-1)-(0.4799*10^(-5))*Tg(i,j-1)^2-(1.965*10^(-
9))*Tg(i,j-1)^3)*34.53;
vis(1,j) = 7.701*10^(-6)+ 4.166*10^(-8)*Tg(1,j-1)-7.531*10^(-12)*Tg(1,j-1)^2;
vis(i,j) = 7.701*10^(-6)+ 4.166*10^(-8)*Tg(i,j-1)-7.531*10^(-12)*Tg(i,j-1)^2;
kf(1,j) = 1.679*10^(-2)+Tg(1,j-1)*5.073*10^(-5);
kf(i,j) = 1.679*10^(-2)+Tg(i,j-1)*5.073*10^(-5);
kw(1,j) =0.9558-Ts(1,j-1)*2.09*10^(-4);
kw(i,j) =0.9558-Ts(i,j-1)*2.09*10^(-4);
z (1,j) =dz;
z (i,j) =dz*i;
% Calculating dimensionless numbers when i = 1:N-1, j =1:M.
Re (1,j) = (den*vel*DH)/vis(1,j) ;
Re (i,j) = (den*vel*DH)/vis(i,j) ;
Pr(1,j) = (Cp(i,j)*vis(1,j))/kf(1,j) ;
Pr(i,j) = (Cp(i,j)*vis(i,j))/kf(i,j) ;
Gz(1,j) = Re(1,j)*Pr(1,j)*DH/z(1,j) ;
```

```
Gz (i,j) = Re(i,j)*Pr(i,j)*DH/z(i,j);
h (1,j) = (3.095 + 8.933*((1000/Gz(1,j))^(-0.5386))*(exp(-6.7275/Gz(1,j))))*kf(1,j)/DH;
h (i,j) = (3.095 + 8.933*((1000/Gz(i,j))^(-0.5386))*(exp(-6.7275/Gz(i,j))))*kf(i,j)/DH;
% Calculating coefficients when i = 1:N-1, j =1:M.
alpha(1,j) = (h(1,j)*dt)/(g_w*rho_w*Cp_w(1,j));
alpha(i,j) = (h(i,j)*dt)/(g_w*rho_w*Cp_w(i,j));
beta(1,j) = (4*h(1,j)*dz)/(vel*den*Cp(1,j)*DH);
beta(i,j) = (4*h(i,j)*dz)/(vel*den*Cp(i,j)*DH);
eee(1,j) = h(1,j)/(g_w*rho_w*Cp_w(1,j));
eee(i,j) = h(i,j)/(g_w*rho_w*Cp_w(i,j));
gamma(1,j) = (h(1,j)*dz^2)/(kw(1,j)*g_w);
gamma(i,j) = (h(i,j)*dz^2)/(kw(i,j)*g_w);
% Input variables for N
Cp_w(N,j) = 1071+0.156*Ts(N,j-1)-(3.437*10^7)*Ts(N,j-1)^(-2)*(1-void);
Cp(N,j) = (28.09+(0.1965*10^(-2))*Tg(N,j-1)-(0.4799*10^(-5))*Tg(N,j-1)^2-
(1.965*10^(-9))*Tg(N,j-1)^3)*34.53;
vis(N,j) = 7.701*10^(-6)+ 4.166*10^(-8)*Tg(N,j-1)-7.531*10^(-12)*Tg(N,j-1)^2;
kf(N,j) = 1.679*10^(-2)+Tg(N,j-1)*5.073*10^(-5);
kw(N,j) = 0.9558-Ts(N,j)*2.09*10^(-4);
z (N,j) = dz*N;
% Calculating dimensionless numbers when i = N, j =1:M.
Re (N,j) = (den*vel*DH)/vis(N,j) ;                % Reynolds number
Pr(N,j) = (Cp(N,j)*vis(N,j))/kf(N,j) ;            % Prandtl number
Gz(N,j) = Re(N,j)*Pr(N,j)*DH/z(N,j) ;             % Graetz number
h (N,j) = (3.095 + 8.933*((1000/Gz(N,j))^(-0.5386))*(exp(-6.7275/Gz(N,j))))*kf(N,j)/DH;
% Calculating coefficients when i = N, j =1:M.
alpha(N,j) = (h(N,j)*dt)/(g_w*rho_w*Cp_w(N,j));
eee(N,j) = h(N,j)/(g_w*rho_w*Cp_w(N,j));
beta(N,j) = (4*h(N,j)*dz)/(vel*den*Cp(N,j)*DH);
gamma(N,j) = (h(N,j)*dz^2)/(kw(N,j)*g_w);
% Set up the coefficient from z = 1:N-1; j= 1:M
a1(1,j) =1;
a1(i,j) =1;
b1(1,j) = -1-1/alpha(1,j);
b1(i,j) = -1-1/alpha(i,j);
a2(1,j) =1+1/beta(1,j);
a2(i,j) = 1+1/beta(i,j);
b2(1,j) =-1;
b2(i,j) =-1;
% Set up the coefficient from z = N; j= 1:M
a1(N,j) =1;
b1(N,j) = -1-1/alpha(N,j);
a2(N,j) = 1+1/beta(N,j);
b2(N,j) =-1;
%  for i = 1:N-1
c1(1,j) =-1/alpha(1,j)*Ts(i,j-1)+2*(1/gamma(1,j))*Ts(i,j-1)-(1/gamma(1,j))*Ts(i+1,j-1)-
(1/gamma(1,j))*Ts(i-1,j-1);
c1(i,j) =-1/alpha(i,j)*Ts(i,j-1)+2*(1/gamma(i,j))*Ts(i,j-1)-(1/gamma(i,j))*Ts(i+1,j-1)-
(1/gamma(i,j))*Ts(i-1,j-1);
c2(1,j) = (1/beta(1,j))*Tg(i-1,j);
c2(i,j) = (1/beta(i,j))*Tg(i-1,j);
A(1,1) = a1(i,j);
A(1,2) = b1(i,j);
A(2,1) = a2(i,j);
A(2,2) = b2(i,j);
RHS(1) =c1(i,j);
```

```
RHS(2) =c2(i,j);
T=A\RHS;
Tg(i,j)=T(1);
Ts(i,j)=T(2);
% for  i=N
c1(N,j) = -1/alpha(N,j)*Ts(N,j-1);
c2(N,j) = (1/beta(N,j))*Tg(N-1,j);
A2(1,1) = a1(N,j);
A2(1,2) = b1(N,j);
A2(2,1) = a2(N,j);
A2(2,2) = b2(N,j);
RHSb(1) = c1(N,j);
RHSb(2) = c2(N,j);
T2 = A2\RHSb;
Tg(N,j) = T2(1);
Ts(N,j) = T2(2);
end
end

% Plot solid temperature profile as a function of axial distance to inlet at end of the process
plot(1:N,Ts(1:N,M)','r')
hold on
xlabel(' Axial direction along the monolith (m) ')
ylabel(' Solid Temperature (K)')
title('Transient response of solid temperature after 50s')
```

## A8.4 Flowsheets for mathematical models

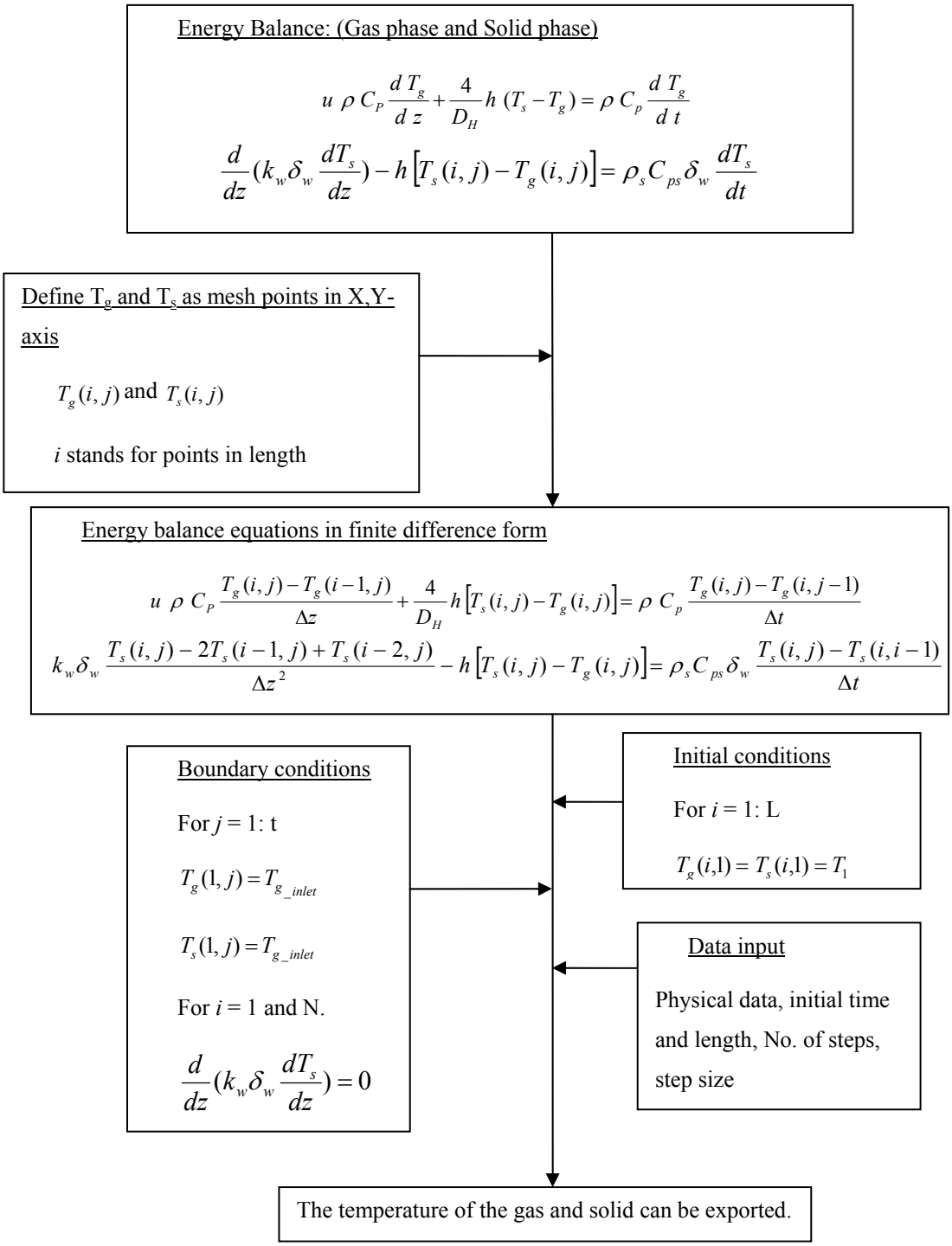


**Figure A26** Flowsheet of the 1-D heat transfer model solved using MATLAB.

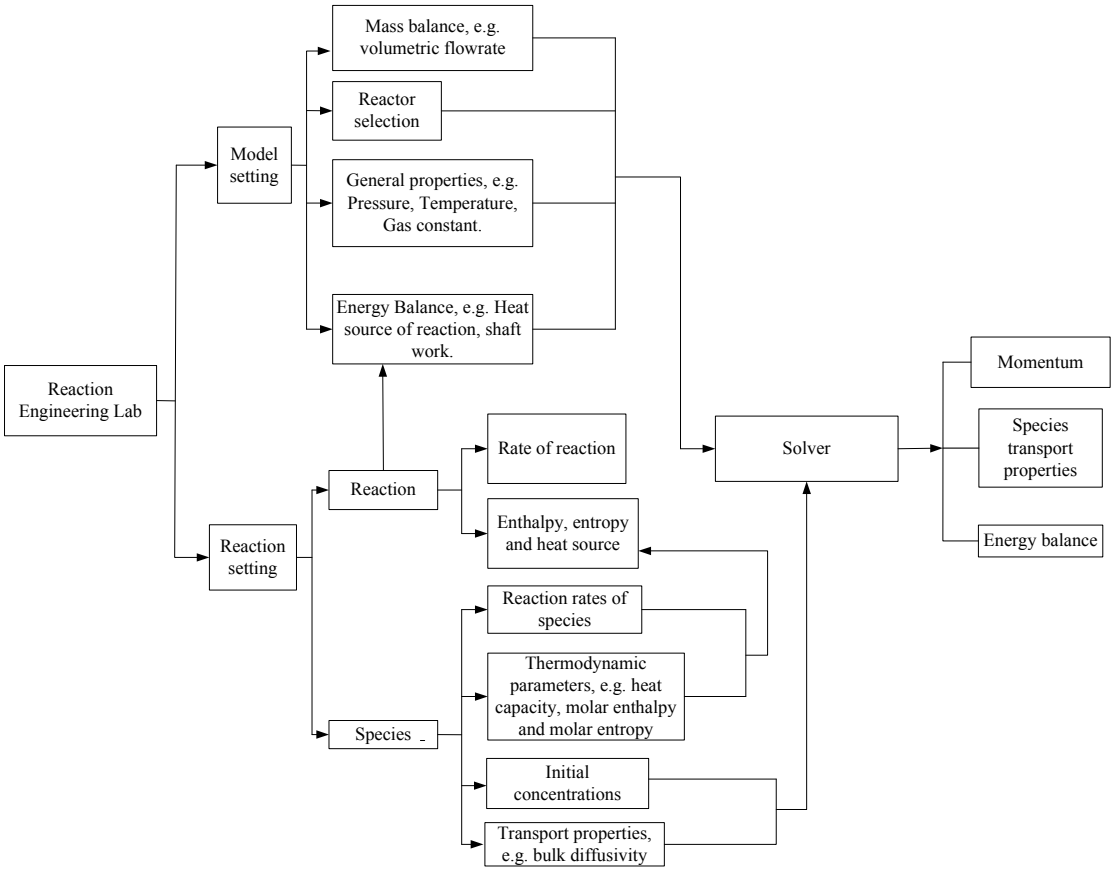


**Figure A27** Flowsheet of the Reaction Engineering Lab in COMSOL Multiphysics.

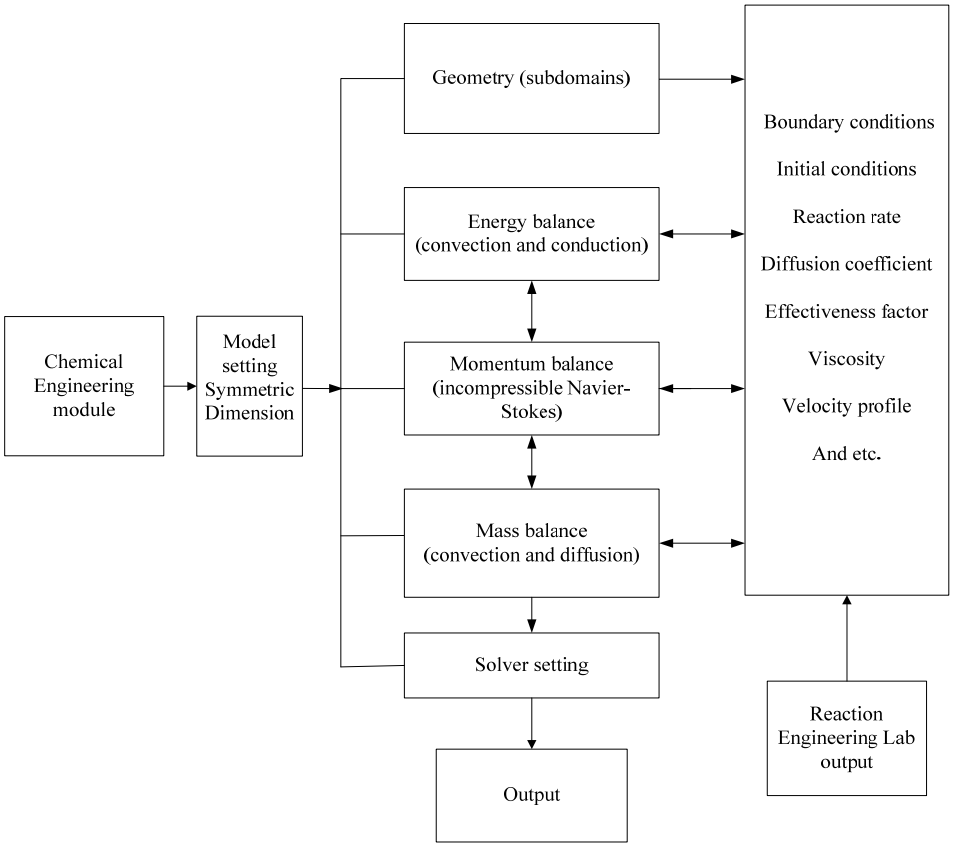


**Figure A28** Flowsheet of the Chemical Engineering Module in COMSOL Multiphysics.